

Piotr Doerffer · George N. Barakos
Marcin M. Luczak *Editors*

Recent Progress in Flow Control for Practical Flows

Results of the STADYWICO and IMESCON
Projects

 Springer

Recent Progress in Flow Control for Practical Flows

Piotr Doerffer • George N. Barakos
Marcin M. Luczak
Editors

Recent Progress in Flow Control for Practical Flows

Results of the STADYWICO and IMESCON
Projects

 Springer

Editors

Piotr Doerffer
Polish Academy of Science
Institute of Fluid-Flow Machinery
Gdansk, Poland

George N. Barakos
CFD Laboratory, School of Engineering
University of Glasgow
Glasgow, United Kingdom

Marcin M. Luczak
Polish Academy of Sciences
Institute of Fluid-Flow Machinery
Gdansk, Poland

ISBN 978-3-319-50567-1

ISBN 978-3-319-50568-8 (eBook)

DOI 10.1007/978-3-319-50568-8

Library of Congress Control Number: 2017932651

© Springer International Publishing AG 2017

This work is subject to copyright. All rights are reserved by the Publisher, whether the whole or part of the material is concerned, specifically the rights of translation, reprinting, reuse of illustrations, recitation, broadcasting, reproduction on microfilms or in any other physical way, and transmission or information storage and retrieval, electronic adaptation, computer software, or by similar or dissimilar methodology now known or hereafter developed.

The use of general descriptive names, registered names, trademarks, service marks, etc. in this publication does not imply, even in the absence of a specific statement, that such names are exempt from the relevant protective laws and regulations and therefore free for general use.

The publisher, the authors and the editors are safe to assume that the advice and information in this book are believed to be true and accurate at the date of publication. Neither the publisher nor the authors or the editors give a warranty, express or implied, with respect to the material contained herein or for any errors or omissions that may have been made. The publisher remains neutral with regard to jurisdictional claims in published maps and institutional affiliations.

Printed on acid-free paper

This Springer imprint is published by Springer Nature

The registered company is Springer International Publishing AG

The registered company address is: Gewerbestrasse 11, 6330 Cham, Switzerland

Acknowledgements

The European Commission

The editors would like to start by thanking the European Commission for their Marie Skłodowska-Curie actions (MSCA). The current research and publication were primarily made possible through funding under the MSCA project FP7-PEOPLE-2010-ITN 264672 “IMESCON” (Innovative Methods of Separated Flow Control in Aeronautics) and FP7-PEOPLE-2009-IAPP 251309 “STA-DY-WI-CO” (STAtic and DYnamic piezo-driven streamWIse vortex generators for active flow COntrol). Authors furthermore thank Ms Giuliana Donini, officer for both projects, for excellent cooperation and thorough feedback during the implementation of the projects.

About MSCA

The Marie Skłodowska-Curie actions (MSCA) provide grants at all stages of researchers’ careers, from doctoral candidates to highly experienced researchers, and encourage transnational, intersectoral and interdisciplinary mobility. For research institutions (universities, research centres and companies), MSCA offer the possibility to host talented foreign researchers and create strategic partnerships with leading institutions. The idea is to equip researchers with the necessary skills for a successful career, be it in the public or the private sector.

The MSCA are open to all domains of research and innovation, from basic research up to market take-up and innovation services. Research and innovation fields are chosen freely by the applicants (individuals and/or organisations) in a fully bottom-up manner. International mobility is prerequisite under all Marie Skłodowska-Curie actions. There are no restrictions in terms of research field, nationality or age.

Endowing researchers with new skills and a wider range of competences, while offering them attractive working conditions, is a crucial aspect of the MSCA. In addition to mobility between countries, the MSCA also seek to break the real and perceived barriers between academic and other sectors, especially business.

About ITN

The doctoral training is covered under the action Innovative Training Networks (ITN). This high-quality joint research and doctoral training is delivered by international networks that bring together universities, research centres and nonacademic organisations (companies, NGOs, charities, etc.) across Europe and beyond.

ITNs can take one of three forms:

- European Training Networks (ETN): Joint research training, involving a minimum of three partners from in and outside academia (business, museum, NGO, etc.).
- European Industrial Doctorates (EID): Joint doctoral training delivered by at least one academic partner entitled to award doctoral degrees and at least one partner from outside academia, primarily enterprise. Each participating researcher is enrolled in a doctoral programme and is jointly guided by supervisors from the academic and nonacademic sector, where they spend at least 50% of their time. The aim is to broaden the career perspective of the PhD candidate upon completion of the training.
- European Joint Doctorates (EJD): A minimum of three academic organisations form a network with the aim of delivering joint, double or multiple degrees. Joint supervision of the research fellow and a joint governance structure are mandatory. The participation of additional organisations from anywhere in the world, including from the nonacademic sector, is encouraged.

During their ITN training, researchers will develop key transferable skills common to all fields, such as entrepreneurship, management and financing of research activities and programmes, management of intellectual property rights, ethical aspects and communication.

In all cases, the recruited researchers are fully funded by the Marie Skłodowska-Curie actions, with an attractive living and mobility allowance. The host organisations receive a contribution to the research and training costs of the recruited researcher and apply good employment practices in line with the European Charter for Researchers and the European Code of Conduct for the Recruitment of Researchers.¹

¹<http://ec.europa.eu/euraxess/index.cfm/rights/europeanCharter>

The Marie Skłodowska-Curie actions support PhD candidates by financing organisations which subsequently recruit candidates to the training programmes. Therefore, PhD candidates do not apply to the Commission for the funding of their posts. Instead, they apply directly on the European Researcher Mobility portal EURAXESS.²

This research was supported in part by PL-Grid Infrastructure, and computations were performed at CI TASK Supercomputing Centre in Gdansk, Poland.

²<http://ec.europa.eu/euraxess/index.cfm/jobs/index>

Contents

Part I Introduction to Flow Control Technology		
1	Introduction and Literature Survey	3
	Vasileios Pstrikakis and George Barakos	
Part II Design of Modern Gurney Flap		
2	CFD Method for Modelling Gurney Flaps	23
	Vasileios Pstrikakis, Mark Woodgate, and George Barakos	
3	Performance Enhancement of Rotors in Hover Using Fixed Gurney Flaps	51
	Vasileios Pstrikakis, René Steijl, and George Barakos	
4	Alleviation of Retreating Side Stall Using Active Gurney Flaps	69
	Vasileios Pstrikakis, René Steijl, and George Barakos	
5	Effect of Gurney Flaps on Overall Helicopter Flight Envelope	87
	Vasileios Pstrikakis and George Barakos	
6	Active Gurney Flap Unit	105
	Ihor Berezin and R. Raczynski	
7	Gurney Flap Force Calculations	121
	Prasanta Sarkar and Radoslaw Raczynski	
Part III Design of Rod Vortex Generator		
8	Investigation of Vortex Generators on Channels and Airfoils	137
	Fernando Tejero, Piotr Doerffer, Pawel Flaszynski, and Oskar Szulc	

9	Implementation of Rod Vortex Generators on Helicopter Rotor Blades in Hover and Forward Flight Conditions	155
	Fernando Tejero, Piotr Doerffer, Paweł Flaszynski, and Oskar Szulc	
10	Retractable Rod Vortex Generator	175
	Tomasz Lewandowski	
Part IV Important Issues in Synthetic Jet Design		
11	Numerical Simulation of a Synthetic Jet Actuator for Active Flow Control	203
	Marcin Kurowski	
12	Introduction to the Synthetic Jet Flow Control and Drag Reduction Techniques	223
	Milan Matejka	
13	Experimental Results of Synthetic Jet Wind Tunnel Tests	233
	Milan Matejka	
Part V Multi Physics Co-simulation Methods		
14	Fluid –Structure Interaction Simulation	263
	Ihor Berezin, Prasanta Sarkar, and Jacek Malecki	
15	Analysis and Optimization of Flow Around Flexible Wings and Blades Using the Standard Co-simulation Interface MpCCI	283
	Nadja Wirth, Pascal Bayrasy, Bettina Landvogt, Klaus Wolf, Francesco Cecutti, and Tomasz Lewandowski	
16	Numerical Simulation of Airflow and Acoustic Field Around a Passenger Car Model Using Euler Approach and Hybrid Meshing	323
	Oskar Szulc and Piotr Doerffer	
17	Computation of Rotorcraft Stability Derivatives Using the Discrete Adjoint Method	337
	M. Biava and G. Barakos	
Part VI Structural Dynamics of Blades and Components		
18	Dynamics of the Synthetic Jet Actuator Investigation by the Numerical and Experimental Approach	359
	Rūta Rimašauskienė	
19	Thermal Synthetic Jet Actuator Investigation by Experimental Approach	375
	Rūta Rimašauskienė	
20	Modal Analysis of PZL-W-3/W-3A Sokol Main Rotor	395
	Ihor Berezin	

21 Strain Modal Analysis	405
Fabio L.M. dos Santos and Bart Peeters	
22 Uncertainty Quantification of the Main Rotor Blades Measurements	429
Marcin M. Luczak	
23 Temperature Compensation Methods for Elastic Wave Based SHM .	483
Codruț Alexandru Dan and PawełKudela	
Index	499

Part I
Introduction to Flow Control Technology

Chapter 1

Introduction and Literature Survey

Vasileios Pastrikakis and George Barakos

1.1 Introduction

Nowadays, the expectations for more efficient military and civil rotorcraft which will be faster, easier to control and invisible are very high. To achieve these goals, emphasis has been placed on control of the flow around the rotor for aerodynamic enhancement, vibration decrease and noise elimination. Modern flow control has a great influence on every major area of aeronautic engineering such as external aerodynamic enhancement, internal flows through propulsion engines, aero-acoustics and control of turbulence. The ability to change the flow behaviour to a great extent, while a small amount of energy is required, consists the gain of flow control techniques. Thus, the understanding of the stability characteristics of the flow is necessary to control it.

Referring to Hak (2001), to choose a specific type of flow control, the presence or lack of wall, the Reynolds number, the Mach number and the flow instabilities should be taken into consideration. The interrelation between different control goals shows that engineers have to make compromises to achieve at least some of the goals. The first way to classify a flow control method is by indicating whether the control is applied at the wall or away from it. Parameters such as wall surface, temperature, mass transfer, suction or injection, different additives and control devices are some examples which can influence the flow. A second classification has to do with the energy expenditure and the control loop involved. There is passive control which needs no power and no control loop and active control

V. Pastrikakis
Consulting Engineer, SoftInWay Switzerland GmbH
e-mail: v.pastrikakis@gmail.com

G. Barakos (✉)
University of Glasgow, Glasgow, UK
e-mail: George.Barakos@glasgow.ac.uk

which requires energy expenditure. As far as the active control goes, it is further divided into predetermined and reactive. The predetermined control is not affected by the particular state of flow and requires no sensors, while in reactive control the input is always adjusted based on some measurements. Reactive control can be either feedforward or feedback. Reactive feedback is classified into four categories: adaptive, physical model based, dynamical systems based and optimal control.

From this survey it is pointed out that the variety of flow control devices can be classified into two categories. The first contains fluidic mechanisms that try to change the flow behaviour by adding or removing momentum where is needed. Surface blowing circulation control, surface suction devices, jets vortex generators (VGs), synthetic jets and plasma technology are such devices. On the other hand, there are devices which do not affect directly the flow characteristics, but they contribute to the control of the flow by altering the shape of the body. Leading edge slats, drooped leading edge, trailing edge flaps and Gurney flaps are common mechanisms of this second category. However, the way these devices are used and their effectiveness on flow control are strongly related with the specific target of the control. That may be the delay of flow separation caused by dynamic stall or blade vortex interaction (BVI) or even the blade vibration decrease and noise diminution. Another significant factor which is considered when choosing the appropriate device is the type of control, as classified above (Hak 2001), the energy that will be consumed and the load penalty. These characteristics make flow control a demanding and challenging process which, however, has the potential to improve aerodynamic performance and extend the capabilities of current rotor systems. Figure 1.1 presents the interrelation between flow control objectives to give an idea of how strongly they are connected.

Considering the performance of a helicopter, the weight-speed envelope faces limitations due to the advancing blade restricting speed and due to the retreating blade stall restricting weight. In order to minimise these limitations, drag should be decreased and pitching moment should be controlled at the advancing side, while maximum lift without stall should be achieved at the retreating side. As a result, flow control devices must affect these requirements in order to be suitable for rotor application. According to Bousman's dynamic stall function (Joo et al. 2005) presented in Fig. 1.2 at the end of this survey, the flow control mechanisms will be classified in terms of increase of lift coefficient and decrease of moment coefficient.

1.2 Vortex Generators

Vortex generators were first introduced by Taylor (1947), and their principle of operation relies on the increased mixing between the external stream and the boundary layer due to longitudinal vortices produced by the VGs. Fluid particles with high momentum in the streamwise direction mix with the low-momentum viscous flow inside the boundary layer; therefore, the mean streamwise momentum of the fluid particles in the boundary layer is increased. The process provides a continuous source of momentum to counter the natural boundary layer momentum decrease and the growth of its thickness caused by viscous friction and adverse pressure gradients. Vortex generators can reduce or eliminate flow separation in

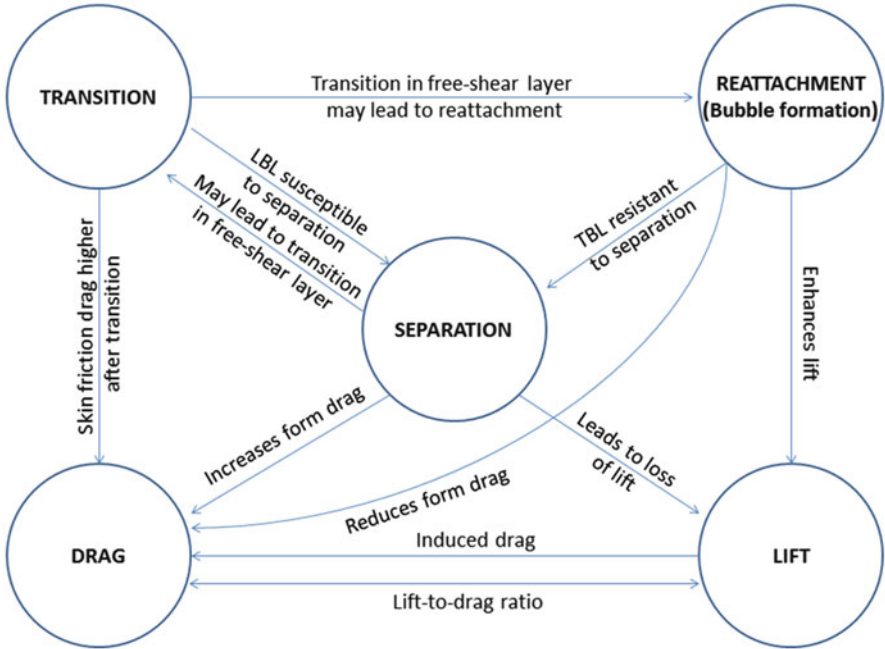
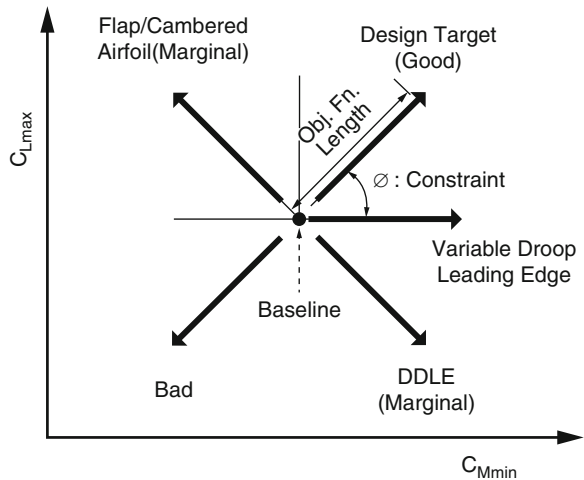


Fig. 1.1 Interrelation between flow control objectives

Fig. 1.2 Optimising for stall control—Bousman’s dynamic stall function (Joo et al. 2005)



moderate adverse pressure gradient environments. Even when separation does occur for cases of large adverse pressure gradient, the mixing action of trailing vortices will restrict the reversed flow region in the shear layer and help maintain some pressure recovery along the separated flow. Thus the effects of separation may be localised or minimised (Fig. 1.3).



Fig. 1.3 Different types of vortex generators. From left to right: delta wing, rectangular wing, delta winglets and rectangular winglets (Chu et al. 2009)

The concept of micro vortex generators was most probably first introduced by Keuthe (1972). In his work, wave-type micro VG with height of 27 and 42 % of the boundary layer thickness were installed in an aerofoil to reduce trailing edge noise by suppressing the formation of a Karman vortex street and by reducing the velocity deficit in the aerofoil wake. Since the late 1980s, these devices appeared in the literature under different names such as sub-boundary layer vortex generator (Holmes et al. 1987) (SBVG), submerged vortex generator (Rao and Kariya 1988), low-profile vortex generator (McCormic 1993) and micro vortex generator (Lin et al. 1994).

The main difference between the SBVG and the VG is in terms of the device height. In general, the velocity deficit within a turbulent boundary layer is dominant near the wall within the inner 20 % of the boundary layer thickness. In that region, an adverse external pressure gradient tends to lower the velocity and thus promotes flow separation. Although both devices operate based on a similar mechanism (generation of streamwise vortex), there are some major differences. For example, the SBVG produces a larger velocity gradient close to the wall and has a stronger- and lower-deficit region in the profile. A vortex generator achieves boundary layer control only at the penalty of possible considerable drag. A sub-boundary vortex generator produces vortices that travel downstream along the surface, causing flow mixing between the inner layers of the boundary layer. Although these SBVGs will produce extra drag as compared with a clean surface, their drag penalty is less than with VGs.

The wide range of conditions where the rotor is operating at makes the parasitic drag a particular limitation, which consists the main drawback of VGs. The only way to avoid this problem is the use of sub-boundary layer VGs as they remain within the low energy flow in the boundary layer and consequently they have low drag. On the other hand, Lin et al. (1994) and Lin (2002) used SBVGs on a multi-element aerofoil in a landing configuration and showed that VGs as small as 0.18 % of reference wing chord can effectively reduce boundary layer separation on the flap which will lead to the reduction of drag and increase of lift for a given angle of attack. In fact during his experimental study trapezoidal vanes were placed on the 25 % of the chord of the flap of a wing at flow conditions $M = 0.2$ and $Re = 5 \times 10^6$ creating counter-rotating vortices, and they achieved a 10 % lift increase, 50 % drag decrease and 100 % increase of L/D ratio.

As stated in Kenning's review (Kenning et al. 2005), the potential applications of VGs and SBVGs include control of leading edge separation, shock-induced separation and smooth surface separation. SBVGs have less parasitic drag, but in case of shock-induced separation, they must be located closer to the separation line which may be a major limitation in the unsteady application of the rotorcraft. Sub-boundary vortex generators have also been studied at ONERA by Meunier and Brunet (2008) as part of AEROMEMS Project in order to control separation on a variable sweep wing. The results of this study show that the efficiency of SBVGs is linked with local boundary thickness which depends on Reynolds number and angle of incidence. Ashill et al. (2001) also performed a separation control experiment where separation was introduced by placing a bump in the test section. The turbulent boundary layer tunnel was used with a free-stream velocity of 40 m/s and a boundary layer thickness of 40 mm over the bump. Three types of SBVGs including the micro ramp, micro vane and split micro vane (with a gap $g = 1 h$) were tested. All the devices had the same height of $h = 10$ mm, resulting in a height ratio of $h/\delta = 0.25$. Laser Doppler anemometry (LDA) was used to perform velocity measurement in streamwise and lateral planes. The velocity fields revealed a significant reduction of the separation region at the rear of the bump for all three devices; furthermore it was found that the split micro vane yielded the best results.

1.3 Air-Jet Vortex Generators

Flow separation is a complex phenomenon influenced by a combination of factors, of which adverse pressure gradients play a significant role. Adverse pressure gradients may reduce the relative motion between the various fluid particles within the boundary layer. If this relative motion is reduced to a sufficient level, the boundary layer can separate from the surface. Furnishing the boundary layer with additional momentum may allow greater penetration against adverse pressure gradients with a reduction in the magnitude of flow separation. Generating a series of longitudinal vortices over the surface of an aerofoil is one technique for achieving this aim. Transferring high-momentum free-stream fluid to the near wall region provides the boundary layer with additional momentum. The presence of a series of vortices again promotes such behaviour. An alternative to vane vortex generators is an active fluid jet vortex generator. Fluid injection via inclined and skewed wall-bounded jets act to induce longitudinal vortices for flow control, instead of solid vane vortex generators. Air-jet vortex generators (AJVGs) usually consist of an array of small orifices embedded in a surface and supplied by a pressurised air source, wherein longitudinal vortices are induced by the interaction between the jets issuing from each orifice and a free-stream fluid flow. The orifices are pitched at angle φ with respect to the surface tangent and skewed at angle ψ with respect to free-stream flow. Prior studies have highlighted the advantages of carefully selecting parameters such as the pitch and skew of the jet axis, as well as the orientation and the preference of certain orifice shapes. Prince and Khodagolian (1996) and Prince

et al. (2009) compared the effectiveness of passive and active blowing over a NACA 23012 and a NACA 63₂-217 and showed that by comparing the ratio $C_L/(C_D + C_M)$, it is obvious that active AJVGs are more effective than passive ones only at highest angles of attack. Moreover, a very important factor for the passive system is the pressure difference between the air-jet intake and exit which drives the flow through the duct. For that reason Krzysiak proposed to use the aerofoil overpressure regions as a source of the air for the AJVGs. These self-supplying air-jet vortex generators are characterised by the fact that they remain inactive at low angles of attack and only become active at higher angles of attack, close to critical values, as a result of the greater pressure difference between the upper and the lower aerofoil surfaces. However, although this type of AJVG is technically significantly simpler than the conventional one, it works well and delays separation only for Mach number up to 0.4, but for higher speeds, its influence deteriorates. Shun and Ahmed (2011) studied experimentally the exponential injection scheme over a NACA 63-421 aerofoil. The exponential jet appears to be a promising device for separation control as the velocity profile varies in space, but not time. Its main features are an injection width that increases by a given factor of e (2.71828) and a fluid injection velocity profile that also increases by the same given factor. The experiment showed that the exponential jet produces worthwhile performance gains and an increase in energy efficiency. In many cases it was found that the conventional vortex generators could be successfully replaced by the air-jet vortex generators for boundary layer control because of the ease of control accompanied by a minimal drag penalty (Prince and Khodagolian 1996). However, the complexity of the installation of AJVGs in comparison with the simplicity of the vane vortex generators has limited their practical usage. The identification of the optimum air-jet configuration is not simple and needs careful study, because the effectiveness of AJVGs depends on a number of parameters such as the pitch and skew angles, the jet mass flow rate, the ratio of the boundary layer thickness to the jet diameter, the jet Reynolds number and the ratio of mean jet velocity to mean free-stream velocity. In addition, using active or passive blowing depends on the energy required and its source such as the engine of the helicopter from where intake air can be bled away to feed the jets. In this case, the system will result in a small loss in engine efficiency, equivalent to an increase in parasitic drag which must be taken into consideration when calculating the overall efficiency of AJVGs. A research that could lead to useful conclusions concerning the application of AJVGs in helicopter rotors is conducted by Singh et al. (2006). In that study two arrays of AJVGs were located at $x/c = 0.12$ and $x/c = 0.62$ on an oscillating RAE 9645 aerofoil. The effect of operating only one or both of the arrays, as well as the influence of blowing rate, was investigated, and the results showed that blowing from the front array at $C_{\mu} = 0.01$ is more effective than blowing either from the rear array or from both arrays simultaneously. However this work is restricted to low-speed dynamic stall. For most helicopters the retreating blade operates at Mach number of about 0.4, which means that the blowing requirements may increase under these conditions and the optimum location of the arrays may also change. Furthermore, the sensitivity of AJVG at real rotor effects such as flow skew angle,

radial flow and time-varying Mach number may also be an issue. Finally, if the AJVG is used around the azimuth, then its influence on the advancing side has to be investigated.

1.4 Synthetic Jets

Synthetic jets consist of a vibrating diaphragm at the base of a small cavity just under the aerofoil surface. The diaphragm is activated electrostatically or through the use of a piezoelectric material with frequencies that span 1–14 kHz. A small hole through the surface allows the production of a stream of ring vortices travelling out from the surface as shown in the schematic (Fig. 1.4).

Hassan and Janakiram (1998) and Hassan (2001) showed by numerical study that zero-net-mass jets can, with careful selection of their peak amplitude and oscillation frequency, enhance the lift characteristics of aerofoils. Indeed, a NACA0012 was used at a free-stream Mach number of 0.6 and Reynolds number $Re = 3 \cdot 10^6$ and for jet velocities 0.05, 0.1 and 0.2. It is shown that as the jet velocity is increased, the lift is increased while the moment and drag are decreased. As far as rotor blades are concerned, two arrays of synthetic jets can be used to change the local pressure distribution near the leading edge resulting in lower temporal pressure gradients and lower blade vortex interaction noise levels. The effectiveness of these devices for lift enhancement increases with the increase of free-stream Mach number and the

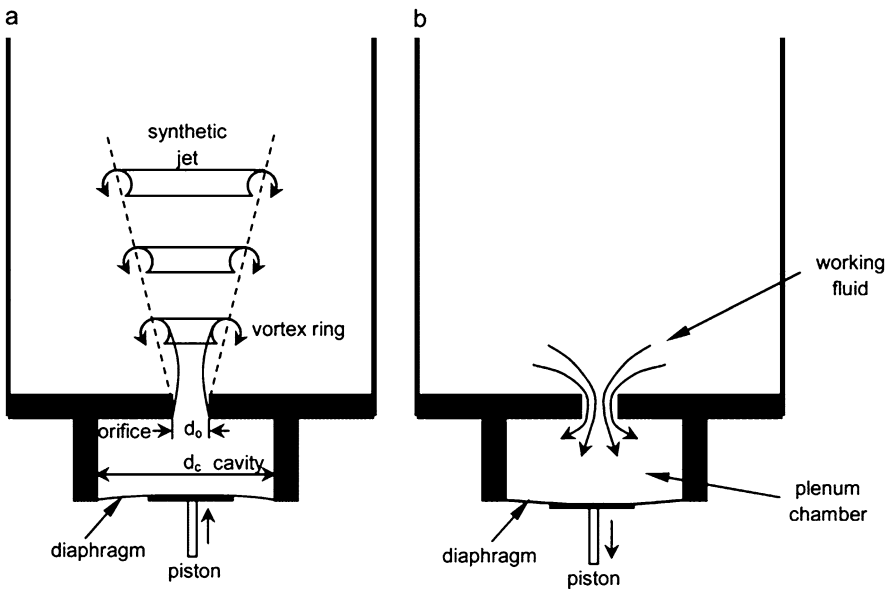


Fig. 1.4 Synthetic jet (Mushtak 2011). (a) Compression stroke. (b) Expansion stroke

decrease of the ratio between the jet Mach number and free-stream Mach number. When comparing synthetic jets with AJVGs, the advantage is that it is easier to provide power rather than air. On the other hand, researchers must always keep in mind that the implementation of any device will be pointless if the power needed exceeds the power gained by controlling the flow.

1.5 Surface Blowing Circulation

Blowing air tangentially to the aerofoil surface has been employed both at leading and trailing edges of the wings. Park and Choi (1999) showed that in the case of uniform blowing from a slot, the skin friction on the slot rapidly increased. The near wall streamwise vortices were lifted up by blowing, and as a result, the interaction of the vortices with the wall became weaker. Moreover, the lifted vortices became stronger in the downstream due to less viscous diffusion above the slot and more tilting and stretching downstream of the slot, resulting in the increase of the turbulence intensities as well as the skin friction downstream of the slot. Yu et al. (1995) investigated numerically the concept of upper-surface blowing over a NACA 0012 which has been tested in the Army's water tunnel at NASA Ames Research Centre in the early 1980s. The aerofoil was oscillating with a pitching motion of $\alpha = 10^\circ + 10^\circ \times \sin(2\pi ft)$, a reduced frequency k of 0.49 and a Reynolds number of 30,000. The tangential blowing slot was located at the quarter chord on the upper surface of the aerofoil. Three blowing rates were tested. Without blowing ($C_{\mu} = 0.0$) the aerofoil stalls at 13° . For the case of injection at twice the free-stream velocity, the blowing delays the stall until about 25° and shows a moderate amount of increase in lift. For the third case where the injection was four times the free-stream velocity, there is no sign of stall even at 30° , while the lift is higher compared to the second case. Again the power losses related to a blowing system are difficult to estimate without undertaking a full rotorcraft design study. The experimental results show that the upper-surface blowing concept delays the dynamic stall phenomenon by trapping the stall vortex. Further study with the computational method indicates that a stall vortex does not form on the airfoil when there is upper-surface blowing at the quarter chord. Although the concept seems to have some effectiveness in delaying dynamic stall, the application of these concepts to rotorcraft requires further tests on the effects of high Mach numbers and high Reynolds numbers (Fig. 1.5).

Mitchell et al. (1996) of ONERA also used blowing circulation as a method to control the vortex breakdown location. In general the vortex breakdown phenomenon can be characterised by a rapid deceleration of both the axial and swirl components of the mean velocity and, at the same time, a dramatic expansion of the vortex core. The no-blowing configuration $C_1 = 0$ of the delta wing was examined for $U = 15, 24$ and 40 m/s at $\alpha = 20, 27, 30$ and 40° . The Reynolds numbers associated with each U are, respectively, $Re_c = 9.75 \times 10^5, 1.56 \times 10^6$ and 2.6×10^6 .

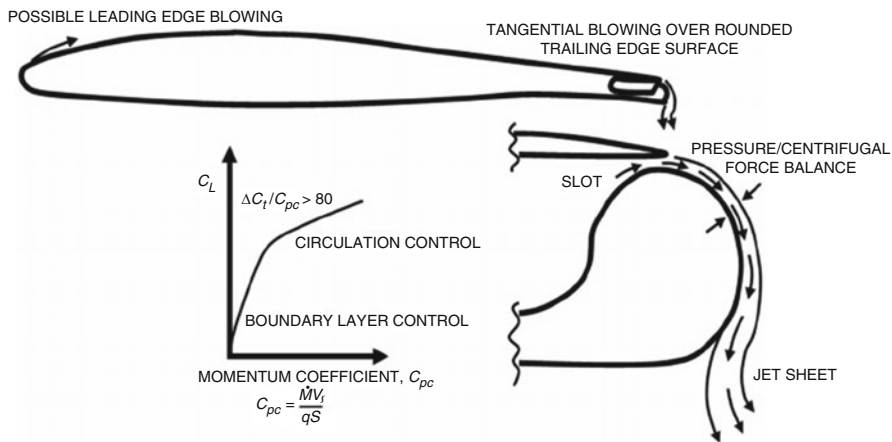


Fig. 1.5 Illustration of surface blowing circulation (Djojodihardjo et al. 2011)

Open-loop, asymmetric, blowing along the core of the portside leading edge vortex on the leeward surface of the delta wing was shown to be effective for controlling the vortex breakdown location over the delta wing.

1.6 Surface Suction

In the case of highly manoeuvrable aircraft like helicopters, suction technique can be applied to delay stall by delaying the detachment of stall vortex and taking advantage of the increased dynamic lift. The objective of Karim’s experimental study (Karim and Acharya 1994) was to reduce the dynamic stall vortex (DSV) formed on a NACA0012 by removing the reverse-flowing fluid at the same rate as it arrives in the leading edge region. It is shown that the pitch rate of the aerofoil is the main factor that influences the suction requirements, and when this rate is low, the Reynolds number becomes significant as the transition of turbulence in the shear layer makes the flow more complex. The location of the slot used for the suction is less important, as long as it is the area where the reverse-flowing fluid can be removed, and when the suction is applied in a uniform way, it requires less velocity and therefore energy rather than when it is applied in a concentrated way. As far as the suction activation goes, this should happen before the angle at which the shear layer lift-up takes place and the control should be continued as long as it is desired as if its termination before the right time will lead to an immediate formation of the dynamic stall vortex. Badran et al. (1998) and Lorber et al. (2000) investigated the effect of suction on the wing surface on vortex breakdown with leading edge suction and surface suction.

In first the case suction was found to be more effective in delaying vortex breakdown for suction slits closer to the leading edge. On the other side, the exact mechanism of how the surface suction affects the vortex breakdown was not clear. Surface suction is also being studied as a means to reduce viscous drag by delaying laminar to turbulent boundary layer transition, but as a conclusion surface suction is less effective than leading edge suction.

1.7 Plasma Technology

The last few years, researchers Kato and Breitsamter (2015), Dadfar et al. (2014) and Moralev et al. (2014) have focused on plasma technology for enhancing the flow around aerofoils and wings. Caruana (2010) describes the plasma technology and its applications on aerodynamic control for civil aircraft as part of PLASMAERO project. The technology of plasma can be classified into the family of the active means of control. The advantages of using plasma are located at the fact that their use can be of a big simplicity, their high frequency of functioning will allow a real-time control, their consumption of electric energy is reduced and no pneumatic circuit is useful. According to Post and Corke (2006), the main advantages of plasma are:

1. They are fully electronic with no mechanical parts and, therefore, are able to withstand high force loading.
2. They can be laminated onto wing surfaces and, therefore, they do not require slots or cavities.
3. They have a broad frequency response bandwidth so that they can have fast response for feedback control (Fig. 1.6).

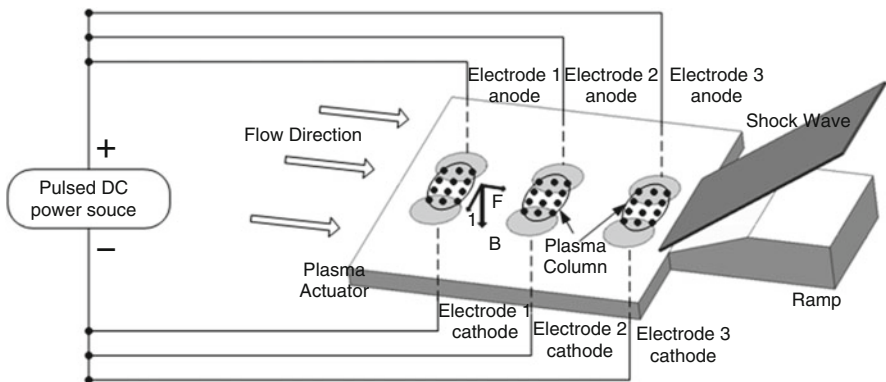


Fig. 1.6 Plasma flow control (Li et al. 2011)

The plasma actuator consists of two copper electrodes separated by a dielectric insulator. The electrodes are supplied with a high-order AC voltage. When the voltage is sufficiently high, the surrounding air ionises and plasma forms in the regions of high electrical field potential. These regions are generally located at the edges of the electrode(s) exposed to the air. The ionised air, in the presence of an electric field gradient, results in a body force on the flow. The body force is a vector that can be tailored for a given application through the orientation and design of the electrode geometry. One of the applications of plasma studied in ONERA was the separation reattachment using dielectric-barrier discharge (DBD) for the generation of plasma. For that method a nonthermal plasma is generated by the application of a high-voltage discharge between two electrodes (5–50 kV) which create an ionisation field, which generates regions where the density of one species, positive or negative ions, is dominant, and amongst the outcomes, a corresponding ionic wind due to the movement of ions at the surface of the aerofoil very close to the wall. This adds flow momentum to the main flow that can influence or modify the aerodynamic parameters like boundary layer velocities.

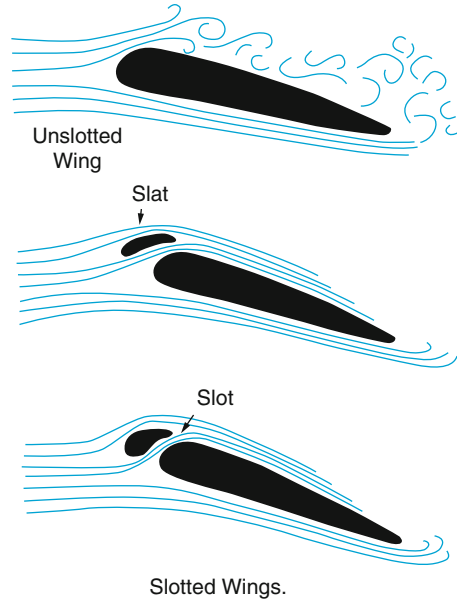
1.8 Nonfluidic Devices

1.8.1 *Leading Edge Geometries*

Putting a slot in an aerofoil to permit airflow from the lower surface to the upper surface has the potential to increase maximum lift coefficients. The maximum lift coefficient of the slotted aerofoils is significantly increased compared to that of the baseline aerofoil. However, a large drag penalty is observed for the slotted aerofoils, especially at low angles of attack (Fig. 1.7).

Apart from leading edge slats, variable droop leading edge (VDLE) has been tested in many cases both experimentally and numerically. In both (Chandrasekhara et al. 1998, 2001) studies delay of dynamic stall is observed by the use of VDLE. Dynamically drooped leading edge nose has been shown to significantly reduce or eliminate the massive flow separation and the dynamic stall vortex for a given angle of attack condition. Another case of leading edge modification is that of Huang and Mao (2002), where the performance of a wing model subjected to the influence of a leading edge control rod was tested. In fact the separation resistance of the boundary layer on a vibrating rod controlled wing is remarkable larger than the natural. More detailed results show that stall angle is delayed by around 80 %, the maximum lift coefficient is increased by 20 % and the lift to drag ratio can be increased by 50 % at large angles of attack.

Fig. 1.7 Leading edge geometries



1.8.2 Trailing Edge Flaps: Gurney Flaps

The use of Gurney flaps for lift enhancement is well established in the aerospace community, and several research works (e.g. Wang et al. 2008) document the advantages and disadvantages of these devices. The Gurney flap was introduced by Dan Gurney, and its aerodynamics was first studied by Liebeck (1978). This has been followed by numerous experimental studies (Jeffrey and Zghang 2000; Troolin et al. 2006; Lee and Su 2011). Tang and Dowell (2007) compared the loading of a NACA0012 wing section with both static and oscillating trailing edge Gurney flaps using an incompressible Navier-Stokes code against experiments conducted in a wind tunnel by them. Due to the scarcity of experimental data with dynamically deployed Gurney flaps, this set of data has been used in several computational studies (Chow and van Dam 2006; Baker et al. 2007; Kinzel et al. 2010).

The Gurney flap is a short flat plate placed at the trailing edge, perpendicular to the chord line on the pressure side of the aerofoil, and works by providing a stagnation area near the trailing edge resulting in an increase of lift. It increases the zero lift angles and keeps the lift slope constant, so there is a decrease in the stall angle. The pitching moment coefficient is also increased (i.e. more nose down) as presented in Gai and Palfrey (2003), and unless the Gurney is sized carefully, substantial drag penalties may also occur. Based on the review of flow control mechanisms (Yeo 2008), Gurney flaps are generally less than 3% of the wing chord. Previous studies (Jeffrey et al. 2008; Maughmer and Bramesfeld 2008) have concluded that the optimal height for a Gurney flap should be close to the

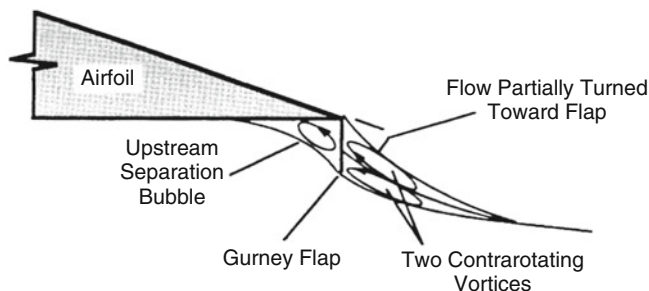


Fig. 1.8 Gurney flap

boundary layer thickness on the pressure side of the aerofoil. If the Gurney flap height is smaller than the boundary layer thickness, then its influence is significantly decreased, while increasing the size of the flap leads to a drag penalty (Fig. 1.8).

Most of the studies found in the literature are dealing with commonly used aerofoils in rotorcraft applications and try to derive conclusions concerning the potential effect of the Gurney flap on rotor blades according to two-dimensional calculations. Several researchers (Yee et al. 2007; Liu et al. 2011; Min et al. 2009) studied the effects of Gurney flaps on the blade root loads and hub vibratory loads. In their study, a Gurney flap was deployed over the entire span of the BO-105 rotor in forward flight with three different deployment schedules. A carefully chosen azimuthal deployment schedule of the Gurney flap was found to reduce the peak-to-peak variations in hub loads. The 4-per-revolution normal force at the hub was compared with the loads for a higher harmonic controlled rotor and the baseline rotor. The simulations showed that the Gurney flap deployment reduced by 80% the 4-per-revolution normal force vibration. For the same rotor in descending flight, a Gurney set at 30° angle relative to the mean chord resulted in a 40% decrease of the vertical descend rate. However, the Gurney flap resulted in local nose down pitching moment, which indicates that additional fluid structure coupling analysis for aeroelastic deformation is required.

Active Gurney flaps were also studied by Liu et al. (2011) to determine their effectiveness in reducing noise and vibration in rotorcraft, as well as improving rotor performance. Active control studies employing microflaps were conducted on a hingeless rotor configuration resembling the MBB BO-105, and various spanwise configurations of the flaps, including a single, a dual and a segmented five-flap configuration, were evaluated. Results indicate that the Gurney flap is capable of substantial reductions in blade vortex interaction (BVI) noise ranging from 3 to 6 dB. Vibration reduction ranging from 70 to 90% was also demonstrated. Vibration and noise reduction was also examined at the same time and was found that reduction in one was linked to an increase on the other. Finally, the Gurney flap appeared to be more effective in reducing the BVI noise at both advancing and retreating sides, while the plain flap was more effective in reducing the vibrations.

The effectiveness of a single active Gurney flap in reducing vibration of a UH-60A Blackhawk helicopter in high-speed flight ($\mu = 0.35$) was studied by Bae and Gandhi (2012). An elastic blade was considered, and the Gurney flap was extending from 70%R to 80%R and was deployed to amplitude of 0.5 % of the chord. The Gurney flap actuation was most influential in reducing the vertical vibratory hub force. The most effective actuation input was 4/rev, and it led to 80 % reduction.

Comparing the above studies (Min et al. 2009; Liu et al. 2011; Bae and Gandhi 2012), to the ones conducted by Milgram et al. (1998) and Viswamurthy and Ganguli (2004), it seems that a Gurney flap can have a similar effect on the vibratory loads of the rotor hub like a conventional trailing edge flap. Such a flap is used in Viswamurthy and Ganguli (2004) on a soft hingeless rotor leading to a 72% reduction of the vibratory loads. However, the advantage of using a Gurney flap compared to a trailing edge flap is on the amount of energy required for the actuation and the ease of the implementation of the Gurney flap.

A further computational study (Yeo 2008) tried to assess active control mechanisms for rotor performance enhancement. A four-bladed rotor was considered at medium (80 kt) and high (150 kt) speed forward flight cases, and the Gurney flap was assumed to be either completely deployed or retracted. A significant increase in thrust for a given power was found when the Gurney was extended from 60%R up to 100%R and activated at the retreating side, which agrees with the outcome of the study by Cheng and Celi (2005) who defined the optimum 2-per-revolution inputs in order to improve the rotor performance by either increasing the thrust of the rotor or decreasing the torque requirement. However, the positive effect of the Gurney was observed at medium speed flight while at high speed the performance improvement diminished.

Gagliardi and Barakos (2009) studied a low twist hovering rotor and the effects of trailing edge flaps on its performance. A flap located inboard resulted in hover performance similar to a blade of 6° more twist. At the same time, a reduction of the trim angles was observed. A flap located outboard did not improve the performance of the rotor although by carefully optimising its configuration similar trim benefits as for the inboard flap were achieved. The majority of the previous studies are computational, and there is a need for experimental investigations of Gurney flaps on rotors.

1.8.2.1 Actuation Mechanism

The small size of the Gurney makes it promising for high-bandwidth active control with low actuation power requirements and minimal impact to the blade structure when compared to conventional control surfaces. Piezoelectric materials could be used for the actuation mechanism of the Gurney. The existence of piezoelectric materials has been known for many years, and they have been widely researched with numerous applications such as sonar, filters, microphones and mechanical actuators. The ceramic material, for example, lead zirconate titanate (PZT), generates an electrical charge in response to a mechanical stress and also the converse; the

application of an electric field results in a mechanical strain of the ceramic material. The application of this effect can be used to apply loads to structures to achieve a desirable deformation.

1.9 Conclusions

Significant efforts have been made to delay or alleviate the retreating blade stall and improve the aerodynamic performance of rotorcraft. Passive and active control devices have been tested both experimentally and numerically mainly in aerofoils and to a lower extent in helicopters main rotors, either scaled or full models. As part of the Innovative Methods of Separated Flow Control project (IMESCON), the following study will focus on the use of active Gurney flaps as a means of controlling the retreating blade stall.

So far, Gurney flaps were used as passive control devices on race cars and recently as active control devices on rotorcraft for aerodynamic enhancement and alleviation of vibration. The control of blade stall can be addressed with a 1/rev actuation of the flap which may alter the handling qualities and the trimming of a helicopter. Thus, the main target of the current investigation is to prove that a Gurney flap can be fully deployed during hover to increase the thrusting capability of the main rotor, while in forward flight will be actuated on demand to delay or alleviate stall on the retreating side without changing the manoeuvrability of the helicopter.

References

- Ashill PR, Fulker JL, Hackett KC (2001) Research at DERA on sub boundary layer vortex generators (SBVGs). In: 39th Aerospace Sciences Meeting and Exhibit
- Badran B, McCormick S, Gursul I (1998) Control of leading-edge vortices with suction. *J Aircr* 35(1):163–165
- Bae ES, Gandhi F (2012) Upstream active gurney flap for rotorcraft vibration reduction. In: Annual Forum Proceedings—AHS International, pp 1354–1362
- Baker JP, Standish KJ, van Dam CP (2007) Two-dimensional wind tunnel and computational investigation of a microtab modified airfoil. *J Aircr* 44(2):563–572
- Caruana D (2010) Plasmas for aerodynamic control. *Plasma Phys Control Fusion*, 52(12)
- Chandrasekhara MS, Wilder MC, Carr LW (1998) Unsteady stall control using dynamically deforming airfoils. *AIAA J* 36(10):1792–1800
- Chandrasekhara MS, Wilder MC, Carr LW (2001) Compressible dynamic stall control: comparison of two approaches. *J Aircr* 38(3):448–453
- Cheng RP, Celi R (2005) Optimum two-per-revolution inputs for improved rotor performance. *J Aircr* 42:1409–1417
- Chow R, van Dam CP (2006) Unsteady computational investigations of deploying load control microtabs. *J Aircr* 43(5):1458–1469
- Chu P, He L, Tao WQ (2009) Three dimensional numerical study of flow and heat transfer enhancement using vortex generators in fin-and-tube heat exchangers. *J Heat Transfer*, 131(9):1–9

- Dadfar R, Hanifi A, Henningson DS (2015) Feedback control for laminarization of flow over wings. *Flow Turbul Combust*, 94(1):43–62
- Djojodihardjo H, Abdulhamid MF, Basri S, Abdul Majid D (2011) Numerical simulation and analysis of Coanda effect circulation control for wind-turbine application considerations. *IJUM Eng J*, Journal Special Issue, Mechanical Engineering
- Gagliardi A, Barakos GN (2009) Analysis and design of a flap-equipped low-twist rotor for hover. *J Aircr* 46(1):74–84
- Gai SL, Palfrey R (2003) Influence of trailing-edge flow control on airfoil performance. *J Aircr* 40(2):332–337
- Hak MG (2001) Flow control: the future. *J Aircr* 38(3):402–418
- Hassan AA (2001) Applications of zero-net-mass jets for enhanced rotorcraft aerodynamic performance. *J Aircr* 38(3):478–485
- Hassan AA, Janakiram RD (1998) Effects of zero-mass “synthetic” jets on the aerodynamics of the NACA-0012 airfoil. *J Am Helicopter Soc* 43:303–311
- Holmes A, Hickey P, Murphy W, Hilton D (1987) The application of sub-boundary layer vortex generators to reduce canopy “Mach rumble” interior noise on the Gulfstream III. 25th AIAA Aerospace Sciences Meeting, Aerospace Sciences Meetings. <http://dx.doi.org/10.2514/6.1987-84>
- Huang RF, Mao SW (2002) Separation control on a cantilever wing with a self-excited vibrating rod. *J Aircr* 39(4):609–615
- Jeffrey D, Zghang X (2000) Aerodynamics of gurney flaps on a single-element high-lift wing. *J Aircr* 37(2):295–301
- Jeffrey D, Zhang X, Hurst DW (2008) Aerodynamics of gurney flaps on a single-element high lift wing. *J Aircr* 45(6):2062–2067
- Joo W, Lee BS, Yee K, Lee DH (2005) Optimization of passive control devices for dynamic stall control. 43rd AIAA Aerospace Sciences Meeting and Exhibit - Meeting Papers, pp 5351
- Karim MA, Acharya M (1994) Suppression of dynamic-stall vortices over pitching airfoils by leading-edge suction. *AIAA J* 32(8):1647–1655
- Kato K, Breitsamter C (2015) Flow control on go 387 airfoil by using nanosecond pulse plasma actuator. *Fluid Mech Appl*
- Kenning OC, Kaynes IW, Miller JV (2005) The potential application of flow control to helicopter rotor blades. 30th European Rotorcraft Forum, p 129
- Keuthe AM (1972) Effect of streamwise vortices on wake properties associated with sound generation. *J Aircr* 9(10):715–719
- Kinzel MP, Maughmer MD, Duque EN (2010) Numerical investigation on the aerodynamics of oscillating airfoils with deployable gurney flaps. *AIAA J* 48(7):1457–1469
- Lee T, Su Y (2011) Lift enhancement and flow structure of airfoil with joint trailing-edge flap and gurney flap. *Exp Fluids* 50(6):1671–1684
- Li Y-H, Wu Y, Song H-M, Liang H, Jia M (2011) Plasma flow control. *Aeronautics and Astronautics book*
- Liebeck RH (1978) Design of subsonic airfoils for high lift. *J Aircr* 15(9):547–561
- Lin JC (2002) Review of research on low-profile vortex generators to control boundary-layer separation. *Prog Aerosp Sci* 38:389–420
- Lin JC, Robinson SK, McGhee RJ, Valarezo WO (1994) Separation control on high lift airfoils via micro-vortex generators. *J Aircr* 31(6):1317–1323
- Liu L, Padthe AK, Friedmann PP (2011) Computational study of microflaps with application to vibration reduction in helicopter rotors. *AIAA J* 49(7):1450–1465
- Lorber P, McCormick D, Anderson T, Wake B, MacMartin D (2000) Rotorcraft retreating blade stall control. *Fluids Conf Exhibit*
- Maughmer MD, Bramesfeld G (2008) Experimental investigation of gurney flaps. *J Aircr* 45(6):2062–2067
- McCormick DC (1993) Shock/boundary-layer interaction control with vortex generators and passive cavity. *AIAA Paper* 31(1):91–96

- Meunier M, Brunet V (2008) High lift devices performance enhancement using mechanical and air-jet vortex generators. *J Aircr* 45(6):2049–2061
- Milgram J, Chopra I, Straub F (1998) Rotors with trailing edge flaps: analysis and comparison with experimental data. *J Am Helicopter Soc* 43(4):319–332
- Min B, Sankar LN, Rajmohan N, Prasad J (2009) Computational investigation of gurney flap effect on rotors in forward flight. *J Aircr* 46(6):1957–1964
- Mitchell AM, Barberis D, Molton P, Dalery J (1996) Oscillation of vortex breakdown location and blowing control of time-averaged location. *AIAA J* 38(5):793–803
- Moralev I, Klimov A, Bityurin V, Kazansky P (2014). Lift and drag control of NACA 23012 airfoil model by surface HF plasma actuator. In: 52nd AIAA Aerospace Sciences Meeting, SciTech Mushtak A-A (2011) Experimental investigation of the use of synthetic jets for mixing in vessels. *J Fluids Eng Trans ASME* 133(9)
- Padthe AK, Liu L, Friedmann PP (2011) Numerical evaluation of microflaps for on blade control of noise and vibration. Collection of Technical Papers—AIAA/ASME/AHS/ASC Structures
- Park J, Choi H (1999) Effects of uniform blowing or suction from a spanwise slot on a turbulent boundary layer flow. *Phys Fluids* 11(10):3090–3105
- Post ML, Corke TC (2006) Separation control using plasma actuators: dynamic stall vortex control on oscillating airfoil. *AIAA J* 44(12):3125–3135
- Prince SA, Khodagolian V (1996) Low-speed static stall suppression using steady and pulsed air-jet vortex generators. *AIAA J* 49(3):642–654
- Prince SA, Khodagolian V, Singh C, Kokkalis T (2009) Aerodynamic stall suppression on airfoil using passive air-jet vortex generators. *AIAA J* 47(9):2232–2242
- Rao JR, Kariya TT (1988) Boundary layer submerged vortex generators for separation control—an explanatory study. 1st National Fluid Dynamics Conference
- Shun S, Ahmed NA (2011) Airfoil separation control using multiple-orifice air-jet vortex generators. *J Aircr* 48(6):2164–2169
- Singh C, Peake DJ, Kokkalis A, Khodagolian V, Coton FN, Galbraith RA (2006) Control of rotorcraft retreating blade stall using air-jet vortex generators. *J Aircr* 43(4):1169–1176
- Tang D, Dowell E (2007) Aerodynamic loading for an airfoil with oscillating gurney flap. *J Aircr* 44(4):1245–1257
- Taylor HD (1947) The elimination of diffuser separation by vortex generators. Rep. R-4012-3, United Aircraft Corporation Research Department
- Troolin D, Longmire E, Lai W (2006) Time resolved PIV analysis of flow over a NACA 0015 airfoil with gurney flap. *Exp Fluids* 41(2):241–254
- Viswamurthy SR, Ganguli R (2004) An optimization approach to vibration reduction in helicopter rotors with multiple trailing edge flaps. *Aerosp Sci Technol* 8(3):185–194
- Wang JJ, Li YC, Choi KS (2008) Gurney flap—lift enhancement, mechanisms and applications. *Prog Aerosp Sci* 44(1):22–47
- Yee K, Joo W, Lee DH (2007) Aerodynamic performance analysis of a gurney flap for rotorcraft applications. *J Aircr* 44(3):1003–1014
- Yeo H (2008) Assessment of active controls for rotor performance enhancement. *J Am Helicopter Soc* 53(2):152–163
- Yu YH, Lee S, McAlister KW, Tung C, Wang CM (1995) Dynamic stall control for advanced rotorcraft application. *AIAA J* 33(2):289–295

Part II
Design of Modern Gurney Flap

Chapter 2

CFD Method for Modelling Gurney Flaps

Vasileios Pastrikakis, Mark Woodgate, and George Barakos

2.1 Numerical Methods

The present work presents the necessary extensions to the HMB2 CFD solver of Liverpool to allow modelling of Gurney flaps either fixed or actuated. Several methods of implementing Gurney flaps were investigated, and it was found that modelling the flap as a discontinuity in the mesh produced results close to what Gurney flaps of some thickness would give. This also allowed a simple implementation of actuated Gurneys, and the method is demonstrated here for 2D sections, finite span wings and rotors in hover and forward flight.

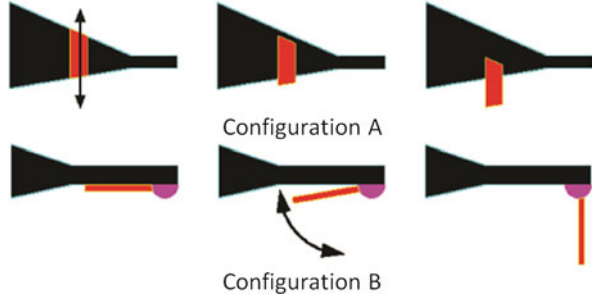
If a Gurney flap is to be added to a rotor blade, a passive device will lead to a fully deployed Gurney through the whole azimuth as in the study of Min et al. (2009), while an active Gurney could be deployed on demand. In that case, it could be fully deployed in hover flight to increase the lift capability of the rotor, while in forward flight, it could be retracted at the advancing side and deployed actively at the retreating side of the rotor. Also, due to the practicalities of implementing Gurney flaps on rotors, several configurations are possible, and the method presented can cope with these various flap designs. Two possible Gurney flap configurations are shown in Fig. 2.1.

In the first configuration, the Gurney flap is allowed to move vertically above and below the aerofoil. One obvious drawback of this option, if the Gurney is not telescopic, is that to obtain even 2–3 % c Gurney flaps, these should be placed around the 90 % chord of the aerofoil. This would reduce the overall effectiveness of

V. Pastrikakis
Consulting Engineer, SoftInWay Switzerland GmbH
e-mail: v.pastrikakis@gmail.com

M. Woodgate • G. Barakos (✉)
University of Glasgow, Glasgow, UK
e-mail: mark.woodgate@glasgow.ac.uk; George.Barakos@glasgow.ac.uk

Fig. 2.1 Proposed Gurney flap configurations



a fixed sized Gurney as discussed in the study of Wang et al. (2008). Configuration (b) is hinged at the trailing edge of the lower surface, and the Gurney is closed by rotating clockwise towards the leading edge.

2.1.1 HMB Solver

The HMB2 CFD solver (Stejil and Barakos 2008a, b; Stejil et al. 2006) was employed for this work. HMB2 solves the Navier-Stokes equations in integral form using the arbitrary Lagrangian-Eulerian formulation for time-dependent domains with moving boundaries:

$$\frac{d}{dt} \int_{V(t)} \mathbf{w} dV + \int_{\partial V(t)} (\mathbf{F}_i(\mathbf{w}) - \mathbf{F}_v(\mathbf{w})) \mathbf{n} dS = \mathbf{S} \quad (2.1)$$

The above equations form a system of conservation laws for any time-dependent control volume $V(t)$ with boundary $\partial V(t)$ and outward unit normal \mathbf{n} . The vector of conserved variables is denoted by $\mathbf{w} = [\rho, \rho u, \rho v, \rho w, \rho E]^T$, where ρ is the density, u, v, w are the Cartesian velocity components and E is the total internal energy per unit mass. \mathbf{F}_i and \mathbf{F}_v are the inviscid and viscous fluxes, respectively. For hovering rotors, the grid is fixed, and a source term, $\mathbf{S} = [0, -\rho \boldsymbol{\omega} \times \mathbf{u}_h, 0]^T$, is added to compensate for the inertial effects of the rotation. \mathbf{u}_h is the local velocity field in the rotor-fixed frame of reference.

The non-inertial frame of reference used here has two benefits over a rotating frame of reference: firstly, the energy equation is unchanged by the rotation vector $\boldsymbol{\omega}$ and, secondly, a vanishing ‘undisturbed’ velocity field occurs in contrast to the position-dependent ‘undisturbed’ velocity field in the rotating frame of reference, which is given by $-\boldsymbol{\omega} \times \mathbf{r}$.

Equation (2.1) is discretised using a cell-centred finite volume approach on structured multiblock grids. The spatial discretisation leads to a set of equations in time:

$$\frac{\partial}{\partial t} (\mathbf{w}_{i,j,k} V_{i,j,k}) = -\mathbf{R}_{i,j,k} (\mathbf{w}_{i,j,k}) \quad (2.2)$$

where \mathbf{w} and \mathbf{R} are the vectors of cell variables and residuals, respectively. Here, i, j, k are the cell indices in each of the grid blocks, and $V_{i,j,k}$ is the cell volume. The convective terms are discretised using Osher's upwind scheme (Osher and Chakravarthy 1983), MUSCL variable interpolation is used to provide high-order accuracy, and the van Albada limiter (Albada et al. 1982) is employed to prevent spurious oscillations near steep gradients. Boundary conditions are set using ghost cells on the exterior of the computational domain. For viscous flow simulations, ghost values are extrapolated at solid boundaries ensuring that the velocity takes on the solid wall velocity. Implicit time integration is employed, and the resulting linear system of equations is solved using a preconditioned generalised conjugate gradient method. For unsteady simulations, an implicit dual-time stepping method is used, based on the pseudo-time integration approach by Jameson (1991). The HMB2 method has been validated for a range of rotorcraft applications and has demonstrated good accuracy and efficiency for very demanding flows. Examples of work with HMB2 can be found in references (Steijl and Barakos 2008a, b). Several rotor trimming methods are available in HMB2 along with a blade-actuation algorithm that allows for the near-blade grid quality to be maintained on deforming meshes (Steijl et al. 2006).

The HMB2 solver has a library of turbulence closures including several one- and two-equation turbulence models and even non-Boussinesq versions of the $k-\omega$ model that is used for this work. Turbulence simulation is also possible using either the large-eddy or the detached-eddy approach. The solver was designed with parallel execution in mind, and the MPI library along with a load-balancing algorithm is used to this end. For multiblock grid generation, the ICEM-CFD Hexa commercial meshing tool is used, and CFD rotor grids with 10–30 million points and thousands of blocks are commonly used.

2.1.2 Modelling Gurney Flaps

2.1.2.1 Proposed Methods

The proposed methods for dealing with the Gurney flaps of Figs. 2.1 and 2.2 are outlined below. It should be noted that the first two methods can be implemented using part of the functionality required in overset grid methods, namely, the ability to apply wall boundary conditions to any cell face when the overset grids intersect each other and the ability to cut a hole into a grid where there is an intersection with a solid. This is shown in the second method in Fig. 2.2b.

The first method (Fig. 2.2a) uses the current grid lines within the block. In the past, when using HMB2, fixed Gurneys have been approximated by setting a solid wall boundary flag between blocks, giving the effect of a very thin flap. The code had to be extended for the active Gurney case. As an example, consider configuration

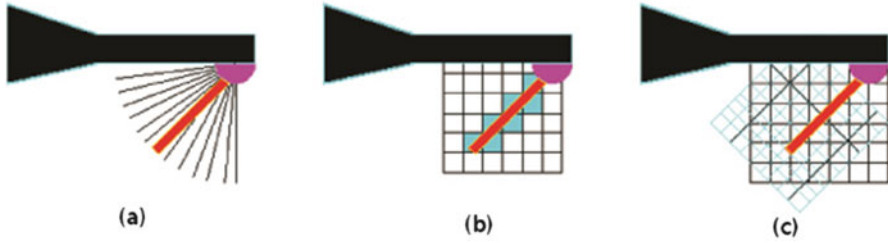


Fig. 2.2 The three possible methods for the solution of the active Gurney flap shown for configuration B of Fig. 2.1. (a) Grid lines within the block have been used, (b) computational cells are flagged as solid, (c) intersecting grids

shown in Fig. 2.2a for a case where a Gurney is aligned with a block boundary. As the Gurney moves, it will violate the requirement of HMB2 CFD solver to have a single boundary condition on each block face. In Fig. 2.2a, as the Gurney rotates, it will need to swap over from one grid line to the next. All configurations of Fig. 2.2 would be possible if the CFD method allows any face within a block to be flagged as a solid wall.

The second method (Fig. 2.2b) is one step closer to the overset grid method. Here cells are flagged as solid if they contain part of the flap. In addition to the functionality of the first method (the ability to flag any cell face as a solid wall), the second method also requires a way of flagging cells, in this case shown in shade (Fig. 2.2b), as non-computational cells or holes. After these holes have been flagged, it is a matter of finding any face that is connected to both a computational cell and a hole and flag that as a solid wall.

The final method (Fig. 2.2c) is to use two overset grids: one associated with the aerofoil and the second associated with the active Gurney. This requires all the functionality of the first two methods with additional information needed within HMB2. Firstly, it is necessary to know which cells in each grid are going to be used for computing the solution. For example, if the choice is the background grid with the minimum number of holes, one needs to know how far does the under-resolved flow next to the Gurney affects the rest of the background solution. HMB2 then requires two extra pieces of information, firstly, which cells are used in the computational domain and, secondly, how is information exchanged between grids.

The problem with moving Gurney flaps is that the solid surface of the Gurney which is surrounded by a fine CFD mesh to resolve the flow will have to come very close to the mesh around the aerofoil. The high aspect ratio and very fine grids required to resolve boundary layer flows made the use of some of the proposed methods difficult.

2.1.2.2 Implementation of the Gurney flaps

This section discusses the different methods of modelling a Gurney flap, each with its own advantages and disadvantages.

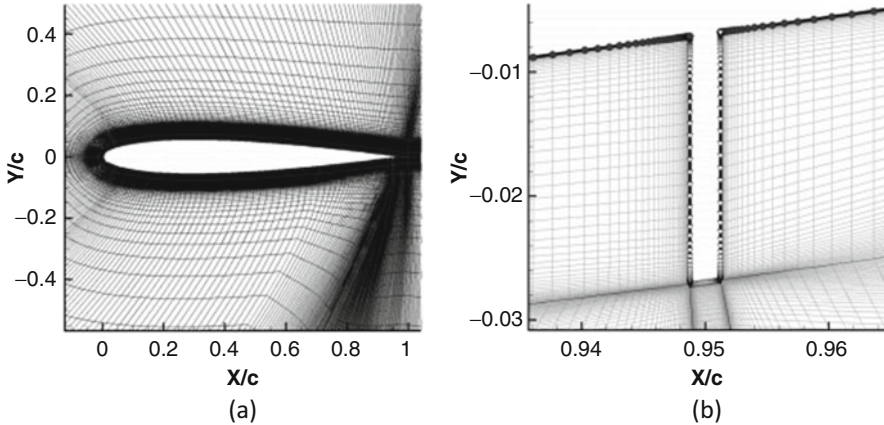


Fig. 2.3 (a) Example of a possible blocking for a Gurney at 95 % of the chord. (b) Shows a close-up of the Gurney flap. NACA 0012 aerofoil, Gurney size = 2 % chord, Gurney thickness = 0.25 % chord

Gurney Flap Modelled Within the Multiblock Mesh

The most natural way to solve a fixed steady-state Gurney flap is to include the Gurney within the multiblock grid as shown in Fig. 2.3. In this case, the Gurney flap has a well-resolved wall spacing on all sides and hence will be a benchmark solution for comparing it with solutions where the Gurney flap is approximated.

To obtain the loads on the Gurney flap alone and to be able to find its moment about a different point, for example, the Gurney hinge, two additional pieces of information are required. Firstly, a special boundary condition tag is used so the Gurney flap is identified. Secondly, additional Gurney-specific input is necessary to inform the CFD solver that computations are to be performed with a Gurney flap of a specific actuation. Figure 2.3b shows the two boundaries that need to be integrated separately for the calculation of the loads. The boundary for the aerofoil is highlighted with the solid line with the black dots, while the Gurney flap boundary is shown as the solid line with the white gradient symbol.

Gurney Flap Modelled Using Viscous Wall Boundary Condition Across a Block Face

In this case, the Gurney is assumed to be thin and is modelled along a block boundary. Since it is a restriction within HMB2 that each block face can only have one type of condition applied to it, the whole face must be part of the Gurney flap. The case, however, is computed in exactly the same way as if the Gurney had some thickness as explained in Sect. 2.1.2.2.1. The advantage of this method is that no additional effort is needed in terms of mesh generation. On the other hand, the

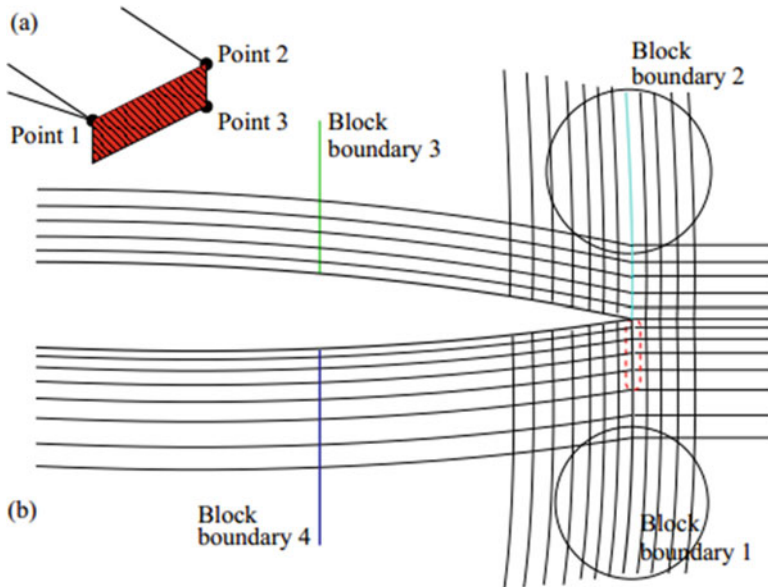


Fig. 2.4 Method for flagging a Gurney flap: (a) Gurney plane definition and (b) elimination of block boundaries 3 and 4 for not meeting the distance requirements and part of boundaries 1 and 2 for not meeting the angle requirements. Only the cell faces of the accepted block boundaries that are inside the Gurney plane will be flagged as solid (Gurney flap)

Gurney is assumed to have no thickness, and its size must coincide with the size of a block face. Figures 2.4 and 2.5 present the concept along with its extension to several cases discussed below.

Gurney Flap Modelled Using Blocked Cells Next to a Block Face

To overcome the restrictions of the previous method regarding the size of the Gurney flap, a new way of modelling thin Gurneys has been added to HMB2. This allows for any number of cells on a block face to be flagged as blocked. This means that the same grid can be used for different size flaps as well as allowing unsteady deployment of Gurney flaps along block interfaces. Figures 2.4 and 2.5 present the idea using schematics of cells and block interfaces.

For an actuated Gurney, it is important to have a robust method for blocking the correct cells. This process can be framed as a collection of computational geometry problems which have to work robustly in the very thin, high aspect ratio, cells that make up the first part of any boundary layer mesh. The algorithm is a four-stage process.

Part one is to define a planar Gurney with three points; the remaining stages are then computational geometry problems which eliminate cells until just those

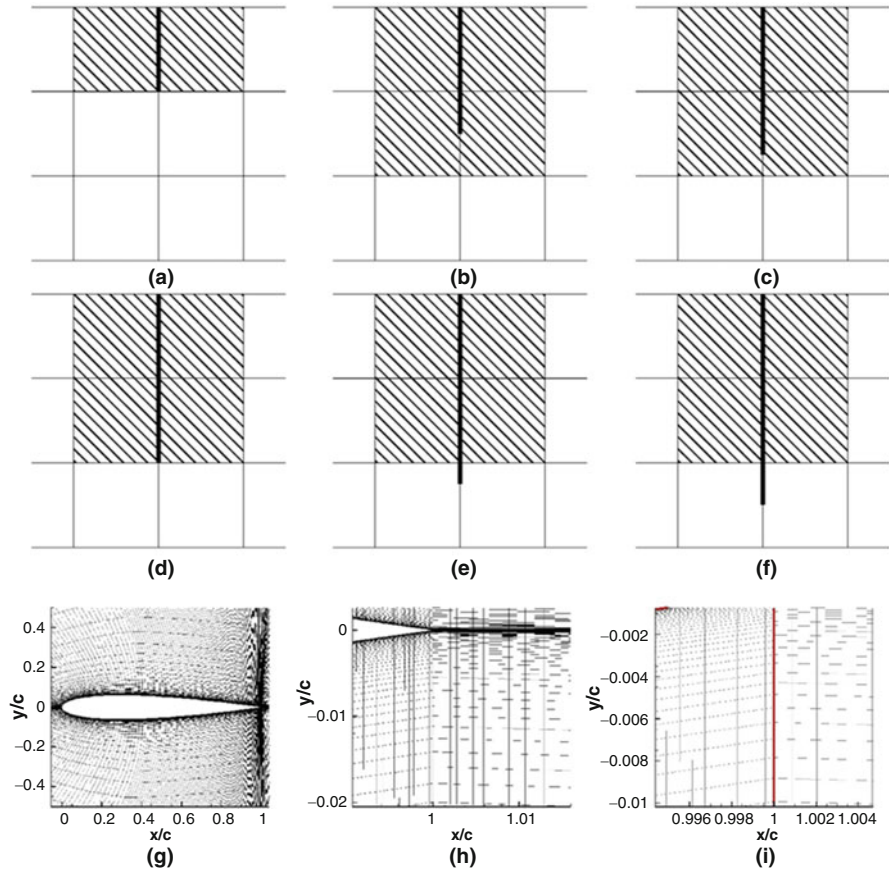


Fig. 2.5 Flagging of the cells (*shaded*) that require a wall boundary condition applied to their face to model Gurney flap (shown in *solid black line*). The Gurney flap can change in length without a change in the cells flagged as blocked. Minimal changes are needed in the CFD mesh (**g, h**), and the Gurney flap can be seen in (**i**)

representing the Gurney remain. Figure 2.4 explains how the cell faces are finally flagged as a Gurney flap. First, the block boundaries 3 and 4 are excluded as they do not meet the distance requirements between the centroid of each cell face and the planar Gurney, set by the user. Then, parts of the boundaries 1 and 2 which are inside a circle are also excluded as the angle between the normal to the face and the normal to the Gurney does not meet another user-specified tolerance. Finally, the remaining cell centres of the faces are projected onto the Gurney plane, and if they are inside the polygon formed by the Gurney, they are flagged as blocked. These cells are surrounded by the dashed line at the trailing edge of the aerofoil shown in Fig. 2.4b.

Resolution of the Length of the Gurney

For a Gurney flap of fixed height, it is always possible to place a grid point at the end of the Gurney, and hence no approximation is made if the method of blocked cell faces is used. However, if the Gurney does not end at a grid point, the semi-blocked cells must be treated in a special way. The first method is as follows: if the projection of the centre of a cell faces onto the plane described by the Gurney flap is within the Gurney, then it is flagged as blocked else it is flagged as open. Examples of this method were shown in Fig. 2.5a–f. The Gurney, shown in bold solid line, is assumed to be infinity thin and close to a block boundary, the shaded cells are flagged, and a viscous wall boundary condition is applied to the face that coincides with the Gurney. Figure 2.5a–f shows that as the Gurney extends in length, more of the cells are flagged as blocked. The length of the Gurney can only be resolved to the size of the mesh cell at its end.

To demonstrate this behaviour, three cases were computed using a Gurney at the trailing edge of a NACA 0012 aerofoil of a length approximately 1 % of the aerofoil chord. Figure 2.5g–i shows the grid and the region around the end of the Gurney flap. It can be seen that this grid has a large number of points normal to the Gurney surface to help resolve the flow.

The discretisation effect of an actuated Gurney flap was addressed with a technique that allows the flux between cells to be split according to the area of a cell exposed to the flow. The idea is to compute first the fraction of the area covered by the Gurney flap over the area of the cell face. The flux f_1 is computed on the interface between the two cells assuming no wall, and then, the flux f_2 is computed as if there is a wall boundary at the face of the cell. Finally, these fluxes are weighted by the fraction of the areas as described in the following equation:

$$f = f_1 (1 - \Delta A) + f_2 \Delta A \quad (2.3)$$

An example of the part-flux method is shown in Fig. 2.6. In Fig. 2.6a, a simple schematic of two cells is presented where a Gurney flap covers the shaded area. Figure 2.6b presents how these cells are treated in the code during the two different calculations of the fluxes before weighting them.

Figures 2.7 and 2.8 present the comparison of the results obtained for a NACA 0012 with a 2 % chord actuated Gurney flap between the full-flux and the part-flux method. Judging from Fig. 2.7, the variation of the change of the lift coefficient of the aerofoil is smoother when it is computed with the part-flux method (solid line), while with the full-flux method, rapid changes of the lift are observed while changing the size of the Gurney flap (dotted line). In Fig. 2.8, the U and V components of the velocity are presented near the Gurney flap with contours for the full-flux method and lines for the part-flux method.

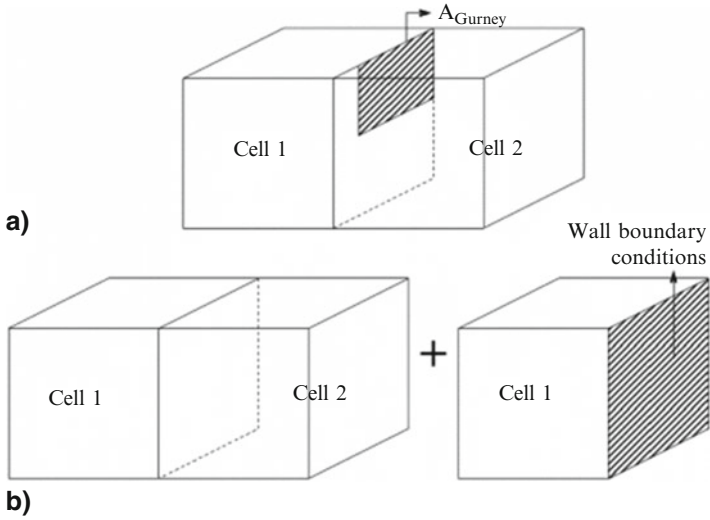
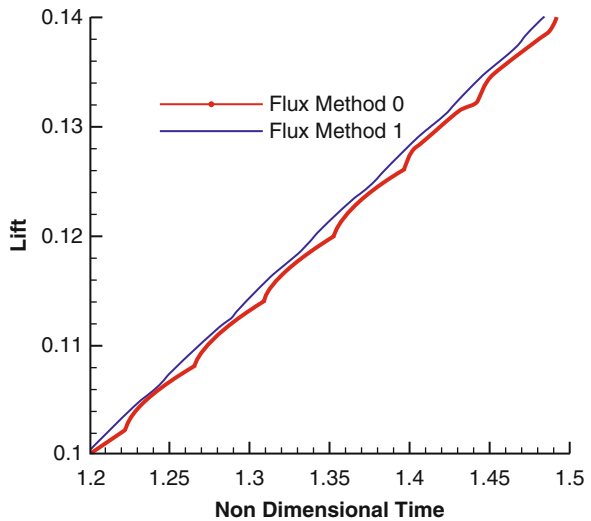


Fig. 2.6 Part-flux method description: (a) schematic of a Gurney flap covered part of the face between two cells and (b) calculation of the fluxes twice before weighting them

Fig. 2.7 Lift coefficient between the part-flux (method 1) and the full-flux (method 0) methods for a NACA 0012 aerofoil with an actuated 2% chord Gurney flap. $M = 0.2$, $Re = 2.1 \times 10^6$, $\alpha = 0$ deg, $k - \omega$ SST (Menter 1994)



Swinging Gurney

For such a case, a blocking topology is seen in Fig. 2.9. The figure shows the mesh around a NACA 0012 aerofoil with a swinging Gurney located at 95% of the chord and the modification of the blocks near the trailing edge of the aerofoil.

The method used to flag cell faces as blocked for a swinging Gurney is presented in Fig. 2.10. First, the code calculates the radius of the Gurney in the same way it

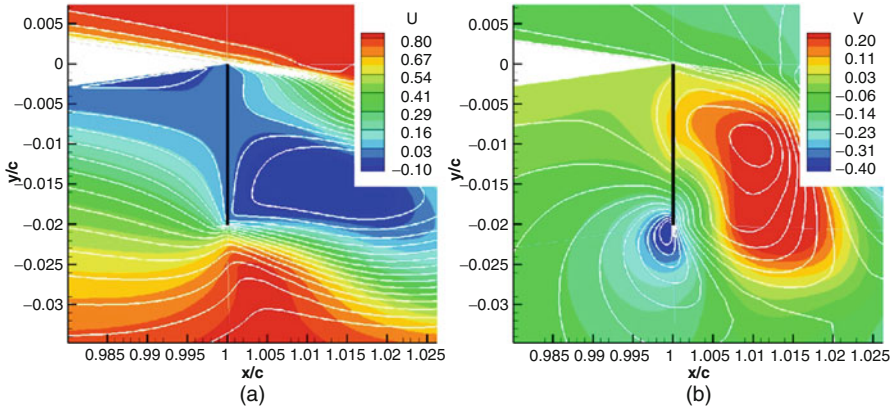
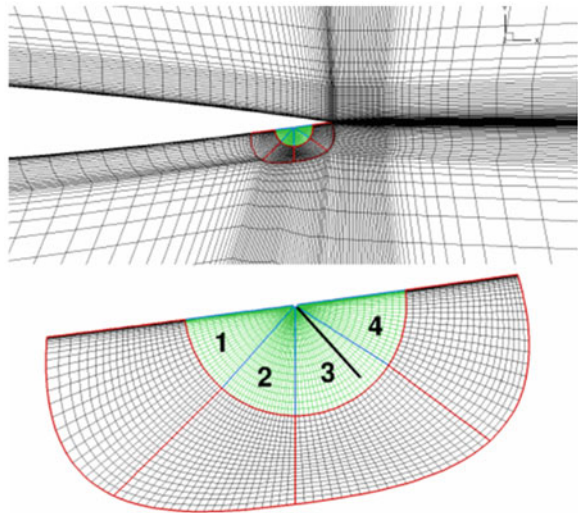


Fig. 2.8 Viscous flow around a NACA 0012 aerofoil with an actuated 2 % chord Gurney flap. The colour contours represent the solution with the full-flux method, and the white contours represent the solution with part-fluxes. $M = 0.2$, $Re = 2.1 \times 10^6$, $\alpha = 0$ deg, $k - \omega$ SST (Menter 1994). (a) Contours of U-velocity component. (b) Contours of V-velocity component

Fig. 2.9 Example of a possible blocking for a swinging Gurney at 95 % of the chord and a near view of the topology



calculated the height of the Gurney during the linear actuation. At every time step, it then computes the angle of the Gurney, and it defines the new Gurney plane as shown in Fig. 2.10a. Then for the blocks 1–4 in the near view of Fig. 2.9, the code flags the cells behind and in front of the Gurney with -1 and 1 , respectively, if they are inside the radius of the Gurney or with -2 and 2 if they are outside as presented in Fig. 2.10b. Next, the code sweeps along the grid lines and averages the flags on the nodes. The nodes with zero value will form the Gurney flap, and if the sum of

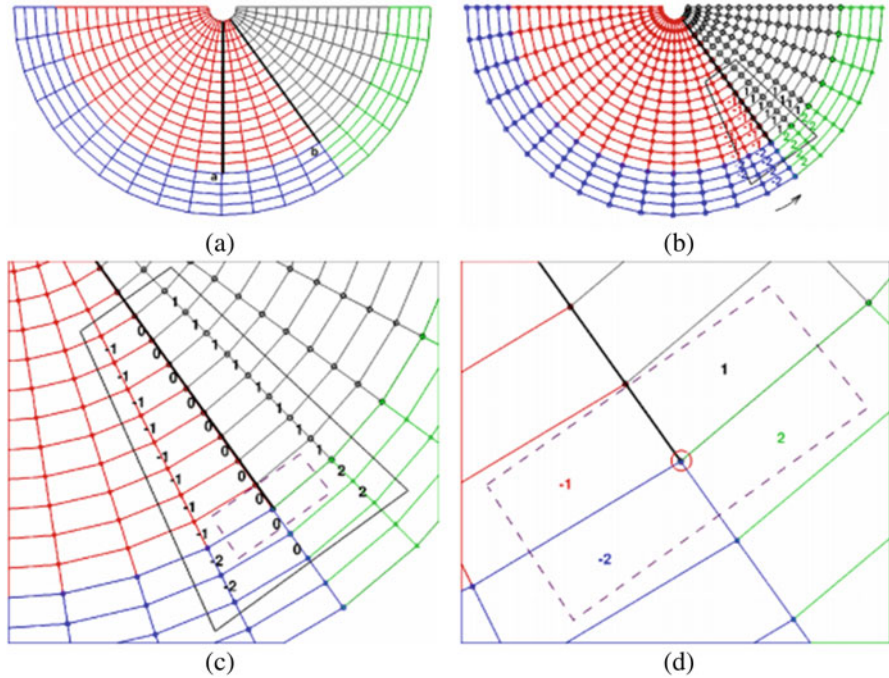


Fig. 2.10 Description of method for flagging wall faces for a swinging Gurney case with HMB2. (a) Definition of the Gurney plane. (b) Flagging cells behind and in front of the Gurney. (c) Average the flags on the nodes. (d) Definition of the end point of the Gurney

the absolute values of the four neighbour cells of a node is 6, then this node is the end of the Gurney flap as presented in Fig. 2.10c, d. Then all the cell faces up to the end point are flagged as blocked.

2.1.3 Results for Gurney Flaps in Two Dimensions

The following section demonstrates the different methods for modelling Gurney flaps that were outlined in Sect. 2.1.2.

2.1.3.1 Fixed Gurney Flap

The grid used for these calculations can be seen in Fig. 2.11. The aerofoil used is a NACA 0012 at $M = 0.2$, $Re = 2.1 \times 10^6$, $\alpha = 0$ deg. Different Gurney sizes were used from 0.5 % c up to 2 % c , and the span of the Gurney was 1 chord. The aerofoil trailing edge was refined more than the normal to resolve the boundary layer of

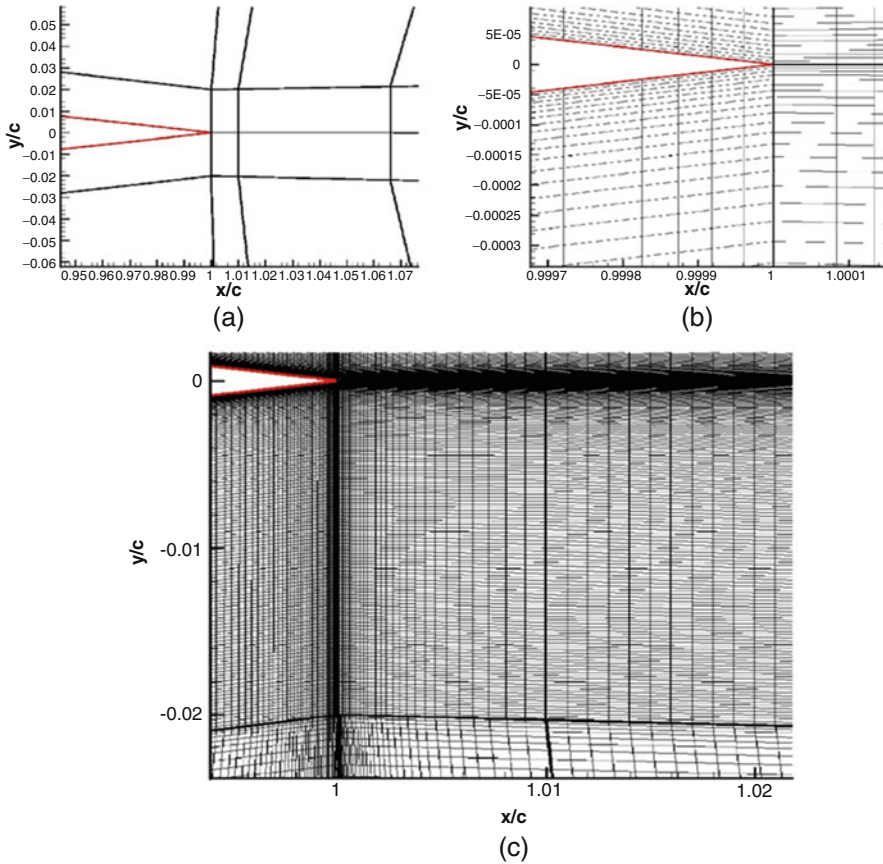


Fig. 2.11 Blocking and mesh spacing for a Gurney at the trailing edge. (a) Mesh blocks at trailing edge. (b) Detailed mesh close to trailing edge. (c) Mesh near trailing edge

the Gurney and the vortical flow structures downstream. The normal spacing to the surface of the aerofoil is $0.5 \times 10^{-6} c$ which is about an order of magnitude less than that the normal spacing to the Gurney flap. As can be seen in Fig. 2.11c, the block near the trailing edges extends in the normal direction by 2% of the chord and has been expanded in such a way so that the cells are nearly equally spaced.

This is unlike a normal aerofoil grid where the cells would keep expanding; consequently, these blocks have a large number of cells. This will give a good approximation of any Gurney flap up to a height of 2% c . The block after the trailing edge between $x/c = (1.01, 1.07)$ has a constant spacing in the x -direction again to help capture the vortical flow in the wake. Figure 2.12 shows the pressure and streamlines for four different Gurney flap sizes at conditions $M = 0.2$, $Re = 2.1 \times 10^6$, $\alpha = 0$ deg. As the Gurney increases in size, the pressure difference between the two sides of the Gurney also increases, and the flow acceleration near

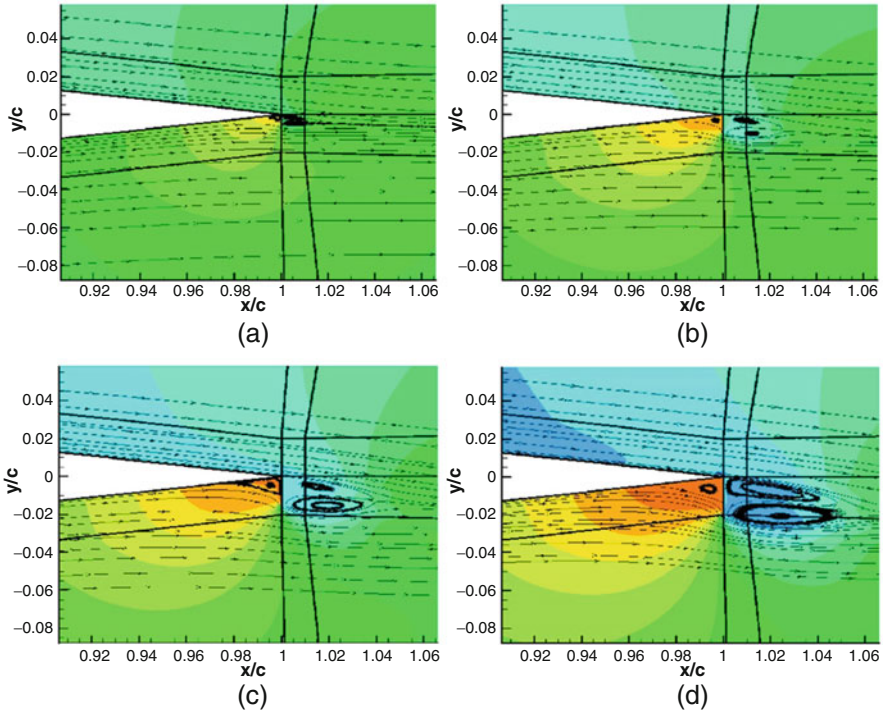


Fig. 2.12 Pressure contours and streamlines for four different heights of Gurneys. NACA 0012, $M = 0.2$, $Re = 2.1 \times 10^6$, $\alpha = 0$ deg, $k - \omega$ SST (Menter 1994). (a) $h = 0.5\%$. (b) $h = 1.0\%$. (c) $h = 1.5\%$. (d) $h = 2.0\%$

the trailing edge increases reducing the pressure behind the Gurney. The pressure in front of the Gurney increases due to the larger pocket of stagnant flow.

2.1.3.2 Resolving Flow Details Near the Gurney Flap

Several of the works published in the literature tend to model Gurney flaps using simple flow blockage that did not result in fully resolved flows. In this section, the results obtained with HMB2 for an aerofoil section near a fixed Gurney are put forward as an example of the resolution that should be sought for the Gurney flap computations. This requires fine grids but shows clearly the capability of HMB2 in resolving the details of the flow, and the results presented here should be considered as a benchmark to gauge the correct mesh resolution. In the present study, a C-type mesh of 195,000 nodes is used, 221 nodes were used in the normal direction to the surface with the spacing close to the wall being $0.00001 c$, and 189 in the wake with 80% of them used up to 50% c distance from the trailing edge. This was necessary to capture the vortices created behind the Gurney flap. Figure 2.13 shows

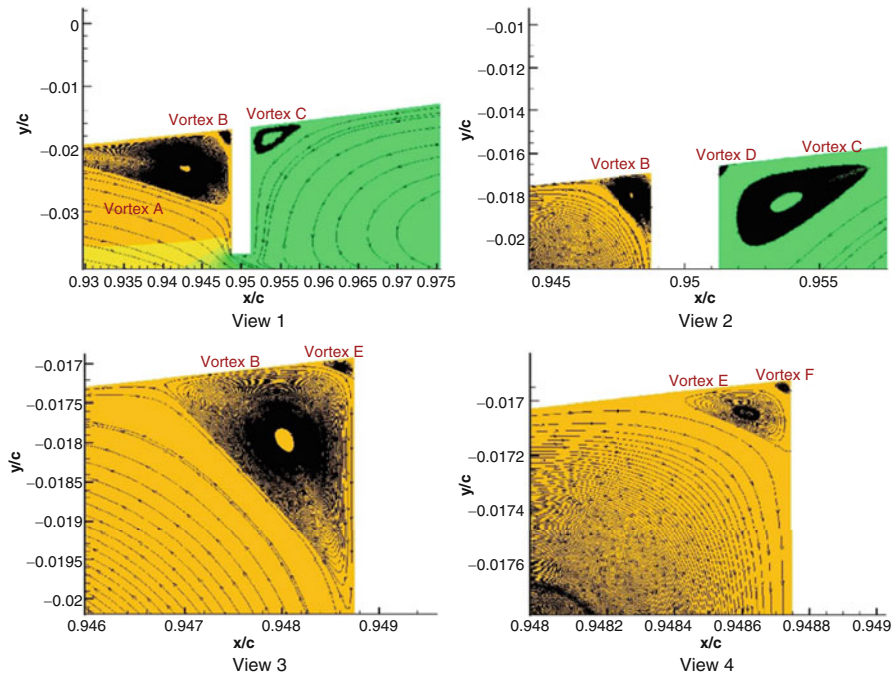


Fig. 2.13 Successive views of the flow near the aerofoil Gurney junction. Streamlines and contours of pressure coefficient are shown

several views of the flow near the corner of the Gurney flap. Pressure contours and streamlines are combined to show the successive resolution of the corner vortices expected in the aerofoil Gurney junction.

The mesh resolution is equally important behind the Gurney flap and near the trailing edge of the section especially since a blunt trailing edge is modelled. This can be seen in Fig. 2.14 where both pressure and turbulent Reynolds number fields are shown again for an NACA 0012 aerofoil with a 2 % c flap near the trailing edge. A further comparison is shown in Fig. 2.15 where results from computations for an infinitely thin Gurney are compared against results at the same conditions but for a Gurney with finite thickness. Such comparisons suggest that for most cases, the infinitely thin Gurney gives a well-resolved representation of the flow and allows easier implementation in HMB2.

Results are obtained for 2 % c Gurney flap located at 95 % c of a NACA 0012 aerofoil. For this case, some experimental data are available and the comparisons are presented in Fig. 2.16. For the clean aerofoil, the CFD results agree well with the experiments. As the size of the Gurney flap increases, there is a small overestimation of the lift and underestimation of the moment, while this difference grows as the aerofoil pitches up. The results for Gurney size 2 % c show that the pressure distribution at the suction side of the aerofoil at zero degrees of incidence

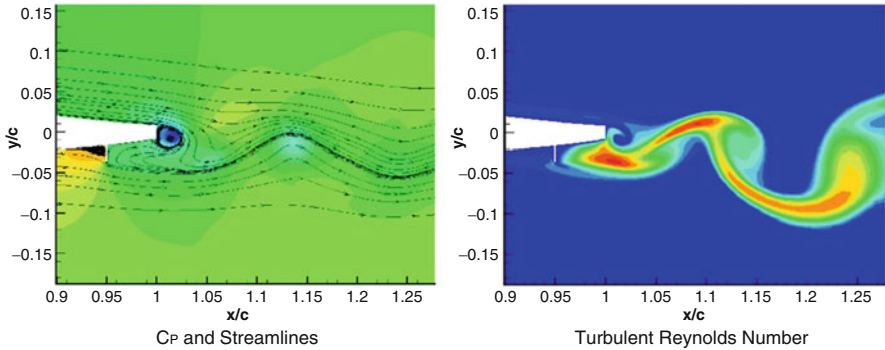


Fig. 2.14 Flow visualisation behind an aerofoil, computed unsteady with a fixed, resolved Gurney and wake. $M = 0.2$, $Re = 2.1 \times 10^6$, $\alpha = 0$ deg, $k - \omega$ SST (Menter 1994)

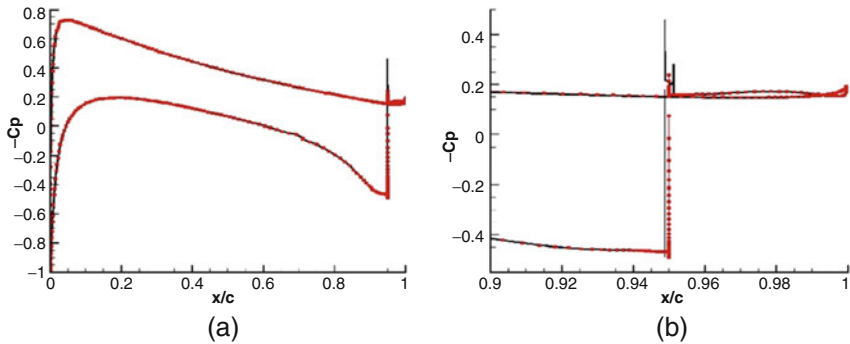


Fig. 2.15 Comparison between thick and thin Gurneys for a NACA 0012 aerofoil with a Gurney of 2% c length computed at Mach of 0.2 and zero incidence angle. Viscous computations were necessary for this case. *Dotted line* represents the case with the infinitely thin Gurney flap. **(a)** Surface pressure coefficient distribution. **(b)** Zoomed view of the surface pressure coefficient distribution near the trailing edge and Gurney

is under-predicted (Fig. 2.17), which leads to discrepancies in the lift coefficient (Fig. 2.16).

2.1.3.3 Comparison Against Thick Gurney Flap

Next, a NACA23012M aerofoil with a cavity at the trailing edge was tested actuating a virtual Gurney flap linearly. The reduced frequency selected for the oscillation of the flap was $k = 0.1$, and the period of the oscillation was 10π travel times. A non-dimensional time step of 0.001 was used. Figure 2.18 presents the way the Gurney is flagged and actuated.

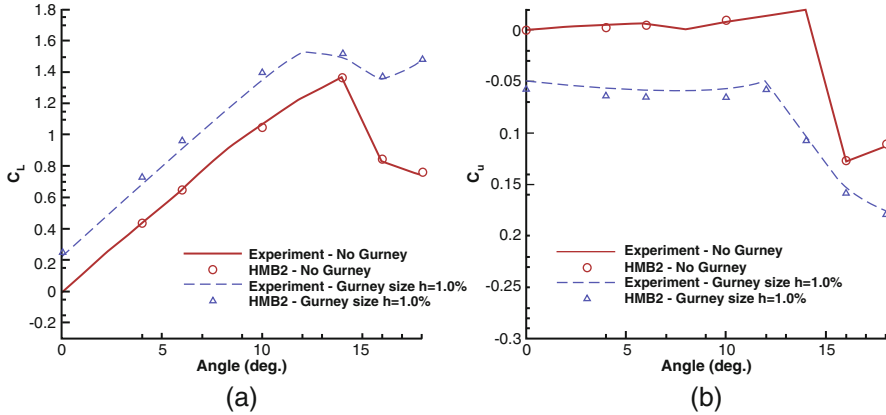


Fig. 2.16 Comparison of loads for different Gurney heights at the trailing edge against experimental data. (a) Total lift. (b) Total moment

In Fig. 2.18a, the Gurney is fully retracted inside the cavity, while in Fig. 2.18b, it is fully deployed, and it is extended by 1.5% c outside the cavity. However, the Gurney still exists inside the cavity as the hinge is always attached to the upper wall of the cavity. When the Gurney is retracted, its actual size is 53.9% of the fully deployed Gurney. Next, the unsteady computation of an actuated Gurney of 1.5% c at 0.935 c of a NACA23012M aerofoil with a cavity was compared against the same case with a thick Gurney using the Chimera technique. Figure 2.19 presents the unsteady loads for these two cases, while in Figs. 2.20, 2.21 and 2.22, vorticity contours are presented for three different time steps. As can be seen behind the Gurney flap, the vorticity magnitude shows no difference. The only difference is observed inside the cavity where it is assumed to be split into two cavities when the virtual Gurney is used. When the thick Gurney is implemented with the Chimera technique, the flow is allowed to circulate around the Gurney inside the cavity too.

2.2 3D Computations: Gurney Flaps vs Vortex Generators, Comparison Study of Aerodynamic Characteristics

2.2.1 Static Computations

To evaluate the effect of different flow control devices in preventing or delaying the separation of the flow due to stall, several unsteady calculations at fixed pitch as well as pitching-translating wing calculations were conducted as a preliminary stage. During a pitching-translating computation (dMdt), aerofoil or the wing is set to a pitching and translational motion, so that a specific section of a rotor can mimic the conditions of a rotor in forward flight.

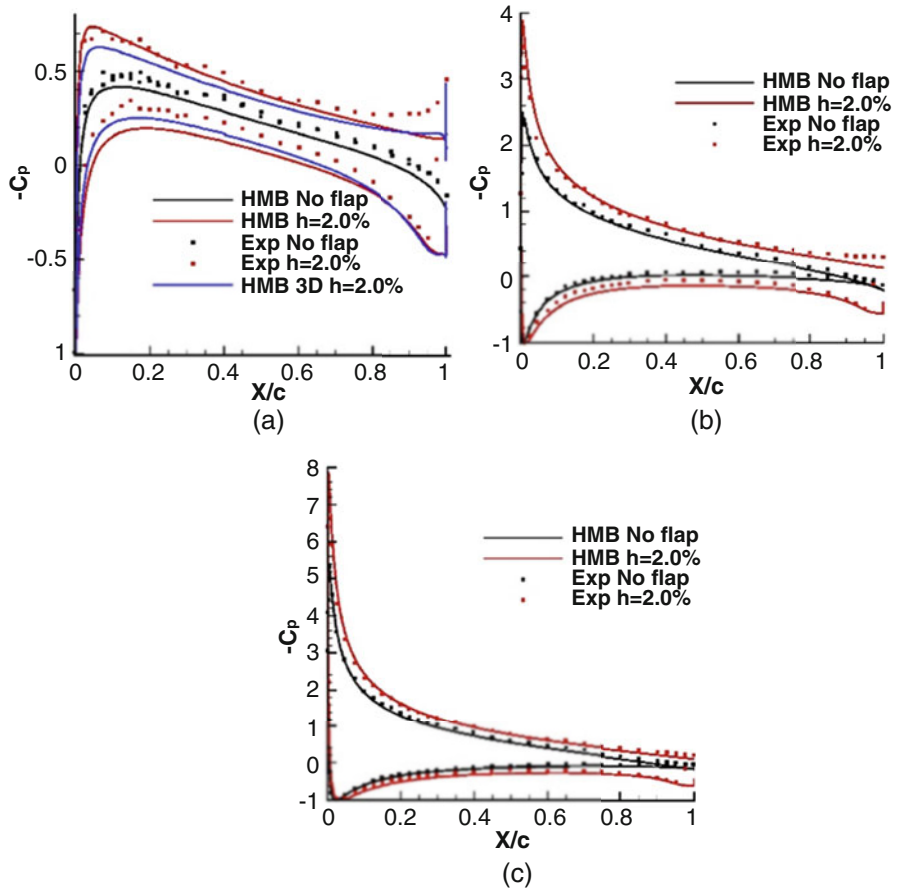


Fig. 2.17 Comparison of pressure distribution of a 2% Gurney at the trailing edge at different angles of attack. (a) Angle of attack 0° . (b) Angle of attack 6° . (c) Angle of attack 10°

Fixed Gurney flaps and vortex generators (VGs) were studied and compared for the unsteady calculations of a NACA23012M wing of $1.15c$ span at fixed pitch. NACA23012M consists the main section used on the rotor case studied in the next chapters. Twenty pairs of counterrotating vortex generator vanes were located at 20% of the chord from the leading edge. The distance between each pair was $0.05c$, and the angle at which the VGs were set to form a pair was 46° . The size of the grid was approximately four million nodes, while the sliding plane technique was used to keep that size reasonable and the mesh refined close to the VGs area where the formation of the vortices was expected. The VG specifications as well as the mesh topology and the sliding planes used are presented in Figs. 2.23, 2.24 and 2.25. Two sizes of VGs were tested, $0.005c$ and $0.01c$. It has to be noted that the sliding planes used for these cases can also be used for a rotor case with vortex generators implemented.

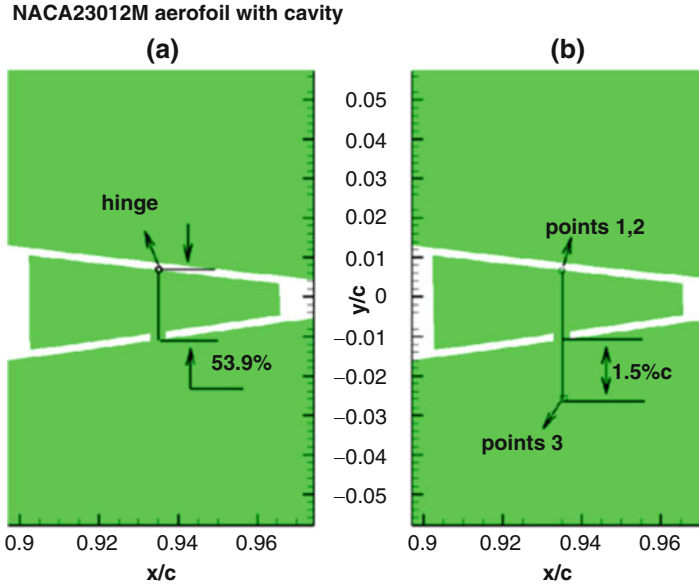


Fig. 2.18 Definition of the actuation of the virtual Gurney used for NACA23012M aerofoil with cavity

Figure 2.26 presents the fixed Gurney flap which is modelled at the trailing edge of the wing and along the whole span. The size of that Gurney is $0.01 c$, and the size of the last cell which accommodates the flap is $0.001 c$. Different Gurney sizes were tested from $0.001 c$ to $0.02 c$. The Gurney flap was modelled based on the method described in the previous section.

2D symmetry conditions were applied on the boundaries for both cases. The $k-\omega$ SST model was used, while the freestream Mach and Reynolds number were 0.2843 and 1.72×10^6 , respectively. The results are presented in Figs. 2.27, 2.28 and 2.29. Based on those results, some important remarks can be made. It is obvious that the Gurney flap increases significantly the lift coefficient, but this comes with a drag penalty and increase of the pitching down moments. On the other hand, vortex generators did not affect significantly the aerodynamic loads of the clean wing. However, the effect of VGs becomes stronger at high angles of attack. Moreover, the maximum clean lift coefficient ($L/D = 34.1$) can be achieved by using a Gurney flap at 6.7° less with an increase of the lift to drag ratio at the same time ($L/D = 54.6$), while the use of VGs will result at the same lift coefficient at 1.7° less with similar increase of the L/D ratio ($L/D = 51.5$). By decreasing the size of the Gurney flap at high angles of attack, the effect of the Gurney came closer to one of the vortex generators, while the drag and moment penalties were significantly decreased. This outcome shows that a carefully designed Gurney flap and actuation algorithm can result at the same effect as VGs at high angles of attack, while maintaining its positive effects at low angles of attack.

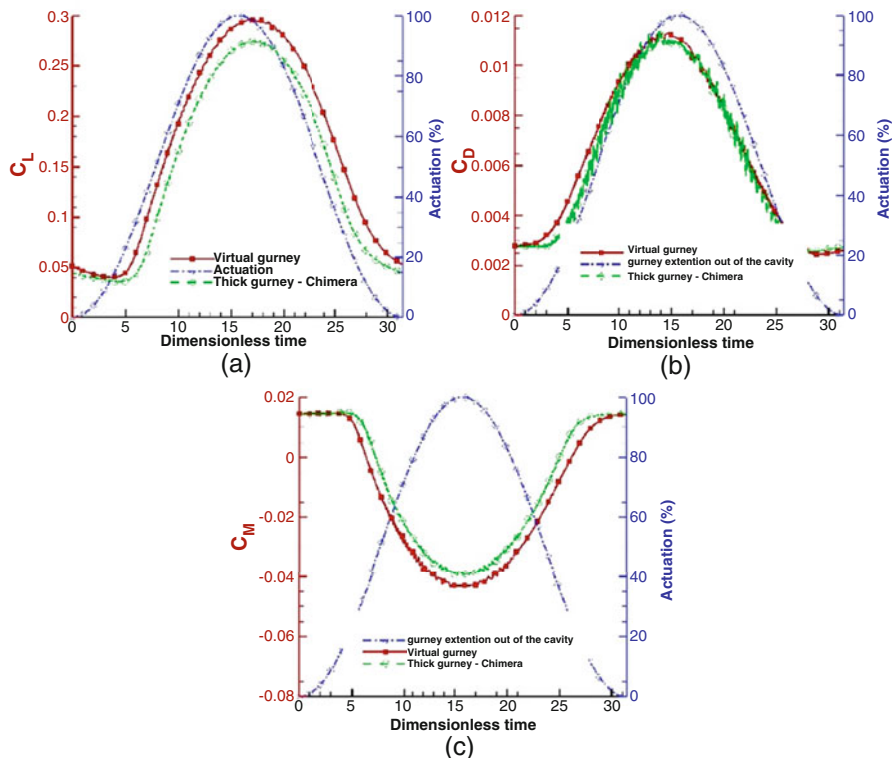


Fig. 2.19 (a) Lift, (b) drag and (c) moment coefficient comparison on NACA23012M aerofoil with cavity and a linearly actuated virtual and thick Gurney flap of 1.5% c at 93.5% c , $M = 0.2$, $Re = 0.5 \times 10^6$

2.2.2 Pitching-Translating Wing Computations

To evaluate the effect of the above flow control devices in preventing or delaying the separation of the flow due to retreating blade stall, several dMdt calculations were conducted next. For such computations, the harmonic motion of the wing is given by

$$x = x_0 + \sum_{i=1}^{nhar} x_s \sin(2kit) + x_c \cos(2kit)$$

where the x_0 is the mean translation, $nhar$ is the number of harmonics, k is the reduced frequency of the first harmonic and x_s and x_c are the coefficients of the sine and cosine contribution of each harmonic. At this study, a NACA23012M wing of 4 chords span was used again with symmetry conditions applied on the boundaries,

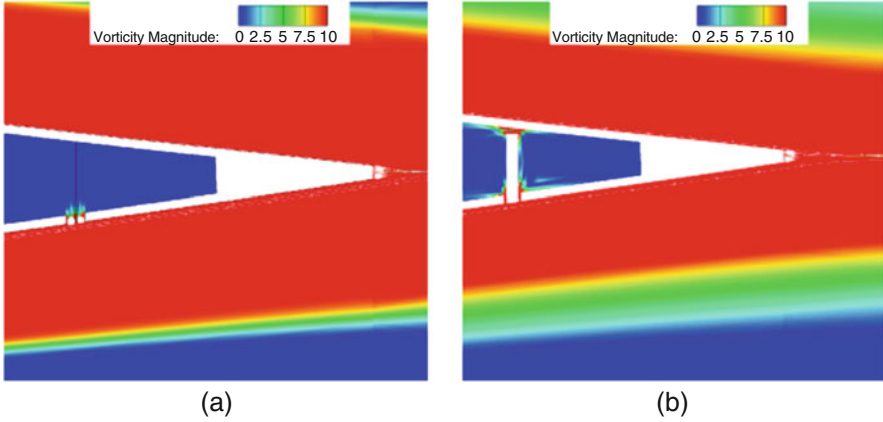


Fig. 2.20 Vorticity magnitude visualisation for a NACA23012M aerofoil with cavity and a linearly actuated virtual (a) and thick (b) Gurney flap of 1.5 % c at 93.5 % c , $M = 0.2$, $Re = 0.5 \times 10^6$. The Gurney flap is fully retracted

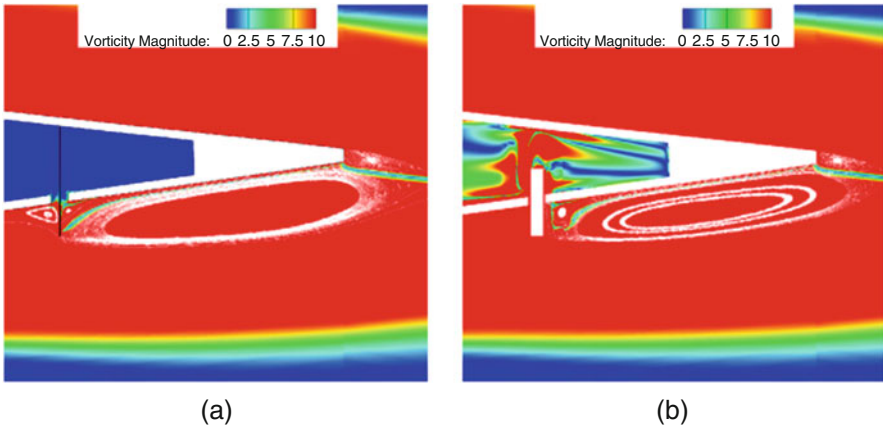


Fig. 2.21 Vorticity magnitude visualisation for a NACA23012M aerofoil with cavity and a linearly actuated virtual (a) and thick (b) Gurney flap of 1.5 % c at 93.5 % c , $M = 0.2$, $Re = 0.5 \times 10^6$. The Gurney flap is half actuated

while the pitch and translational schedule were selected based on flight test data of the W3 Sokol helicopter so that the wing experiences retreating blade stall. Both flow control devices covered 30 % of the span of the wing, and the vortex generators of size 0.01 c were fixed, while the Gurney flap of size 0.02 c was actively deployed at the retreating side. On a forward flight case of freestream speed $M_\infty = 0.2052$, a blade section experiences a flow of speed given by

$$M_{\text{section}} = M_{\text{tip}} \frac{r}{R} + M_\infty \sin(\Psi)$$

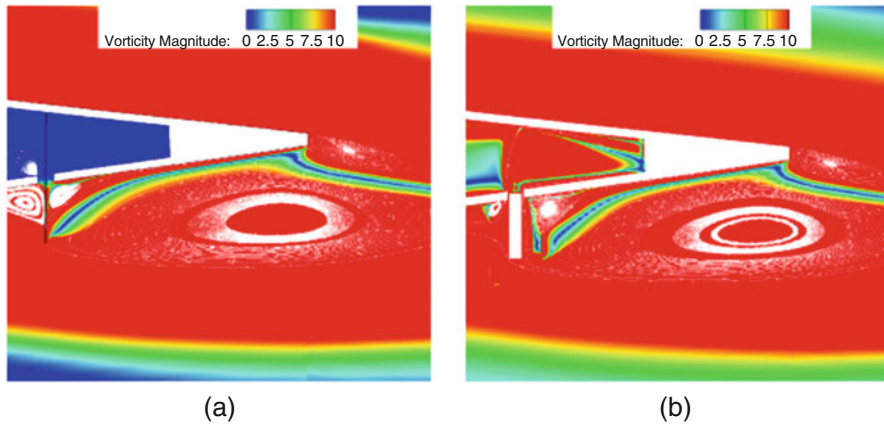


Fig. 2.22 Vorticity magnitude visualisation for a NACA23012M aerofoil with cavity and a linearly actuated virtual (a) and thick (b) Gurney flap of 1.5 % c at 93.5 % c , $M = 0.2$, $Re = 0.5 \times 10^6$. The Gurney flap is fully actuated

Although the inflow and 3D effects are not taken into account, dMdt is a very good and efficient calculation compared to a rotor case in order to approximate the forward flight effect on a blade section of a rotor.

The wing section simulating the 45 % of the blade radius of W3 Sokol main rotor is pitching down and moving forward (from positive to negative x) with high local speed at the advancing side, while at the retreating side, the local speed is decreased, and the wing is moving backward (from negative to positive x) and it is pitching up. The 20 pairs of counterrotating vortex generators did not alter the L/D ratio although they decreased the separated flow due to stall. On the other hand, the active Gurney flap increased the L/D ratio by 1.1 %. At the same time, although the separated flow was further decreased compared to the VG case, it is to be noted that the direction of the wake was slightly changed, which, in the case of a rotorcraft, may lead to blade vortex interaction. The pitching down moments that were introduced due to the Gurney can be used to alter the twist distribution on a relative soft blade in torsion which will lead to even lower collective and torque requirement.

Figures 2.30, 2.31 and 2.32 show the detached flow for three different cases used for this study. As can be seen, the active Gurney flap was the device which delayed the onset of the separation more. However, the schedule of the actuation of the Gurney must be carefully designed to lead to aerodynamic performance enhancement.

Fig. 2.23 (a) NACA23012M with 20 pairs of counterrotating vortex generators, (b) specification of vortex generator vane

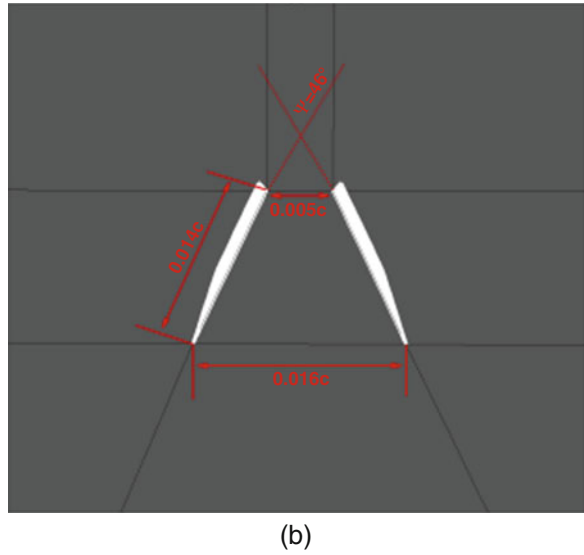
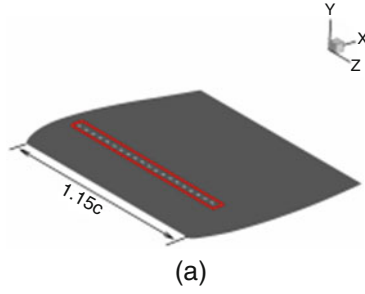
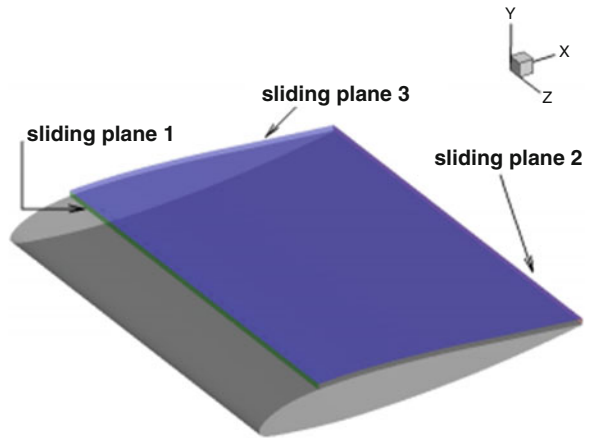


Fig. 2.24 Overview of sliding planes used for grid refinement



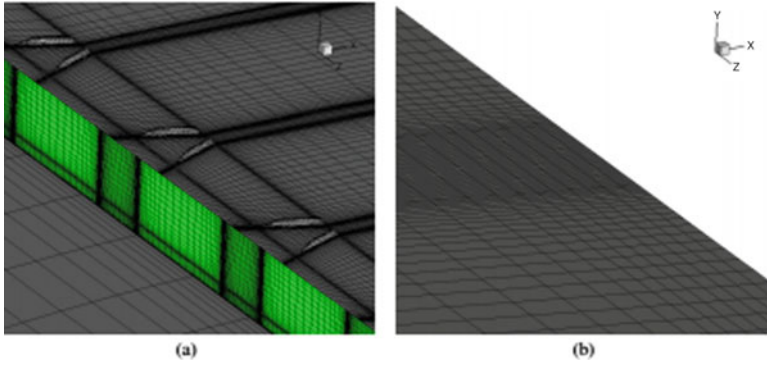


Fig. 2.25 Overview of the mesh (a) near the vortex generators and (b) near the trailing edge

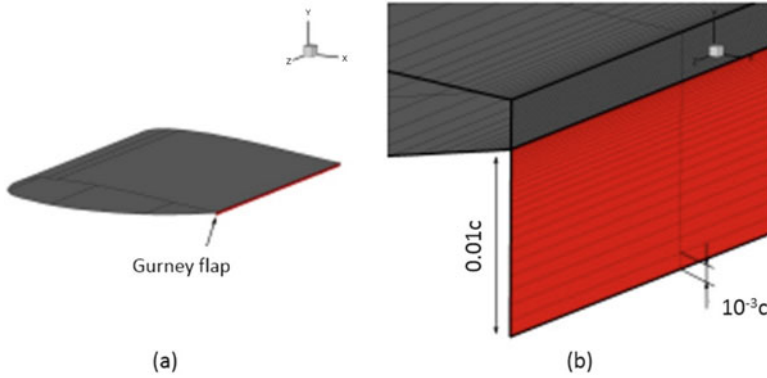
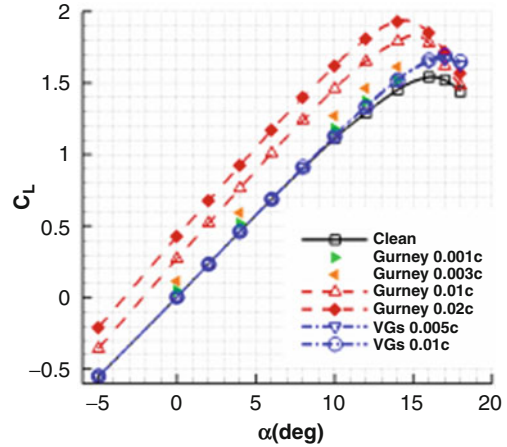


Fig. 2.26 (a) NACA23012M wing with fixed Gurney flap at the trailing edge and (b) a close view of the flap and surface mesh near the trailing edge

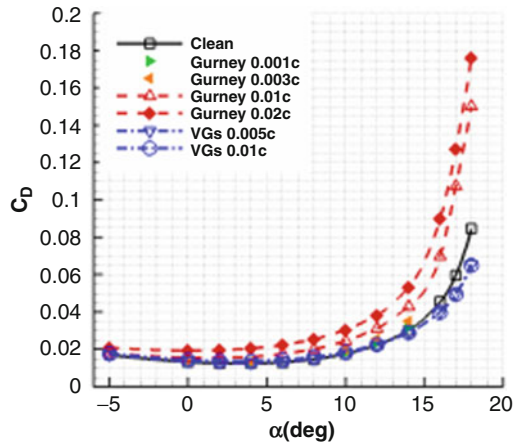
2.2.3 Observations

The main aerofoil sections used on the W3-Sokol main rotor were initially studied with CFD to investigate the change of the aerodynamic performance resulted by some modifications on the baseline NACA23012. Next, a preliminary study took place, and two flow control devices were tested on the modified NACA23012M section. The main target of the study was to identify the advantages and limitations

Fig. 2.27 (a) Lift and (b) drag coefficient comparison between Gurney flap and vortex generators for a wing NACA23012M, $M = 0.2843$, $Re = 1.72 \times 10^6$



(a)



(b)

of those mechanisms, as well as their potential use for delaying retreating blade stall separation of the flow. The active Gurney flap proved to be more effective, and it can be used to alter the aerodynamic performance of the blade not only by affecting its aerodynamics but also by changing locally the pitch of the blade section.

Fig. 2.28 (a) Lift to drag ratio and (b) moment coefficient comparisons between Gurney flap and vortex generators for a wing NACA23012M, $M = 0.2843$, $Re = 1.72 \times 10^6$. (a) is L/D and (b) is moment

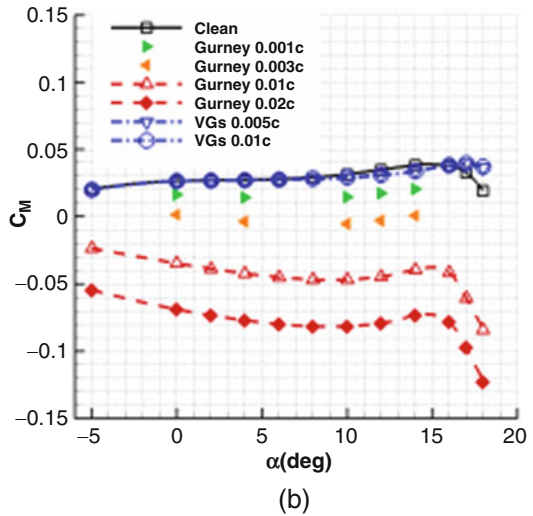
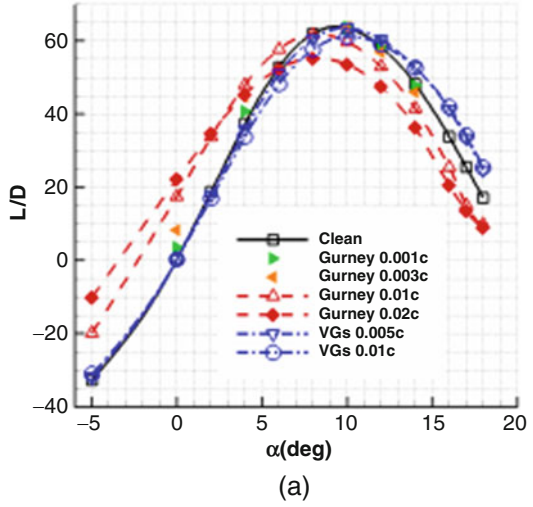
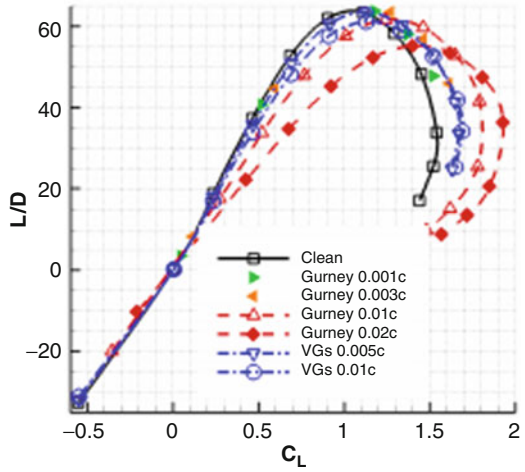


Fig. 2.29 Lift over drag ratio versus lift coefficient comparison between Gurney flap and vortex generators for a wing NACA23012M, $M = 0.2843$, $Re = 1.72 \times 10^6$



$\Psi = 270^\circ$
 $M_{local} = 0.0729$

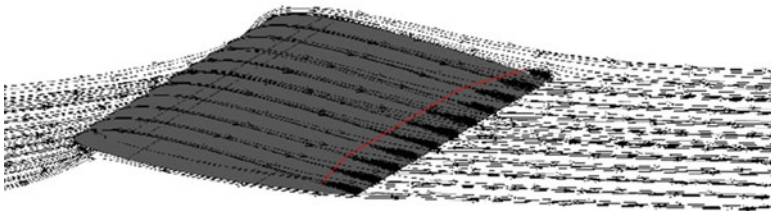


Fig. 2.30 Visualisation of the streamlines along the span of the clean wing. The red line indicates the onset of the separation

$\Psi = 270^\circ$
 $M_{local} = 0.0729$

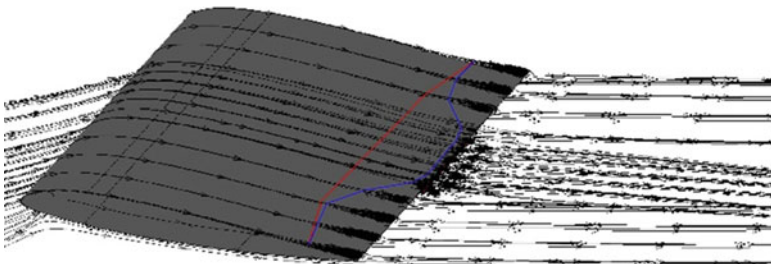


Fig. 2.31 Visualisation of the streamlines along the span of the wing with active Gurney flap. The red and blue line indicate the onset of the separation of the clean wing and the wing with active Gurney flap, respectively

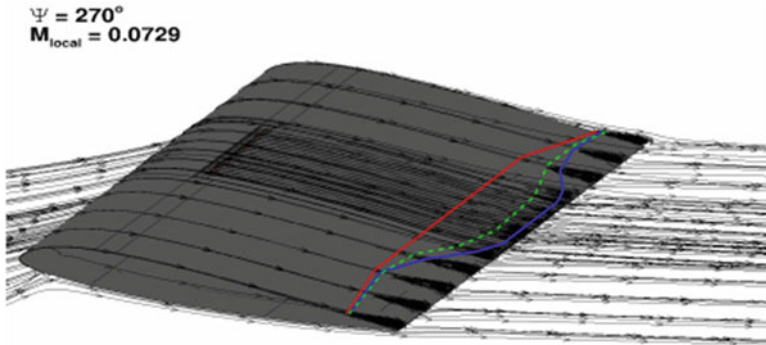


Fig. 2.32 Visualisation of the streamlines along the span of the wing with vortex generators. The *dashed green line* indicates the onset of the separation of the wing with VGs

References

- Albada GD, Leer BV, Roberts W (1982) A comparative study of computational methods in cosmic gas dynamics. *Astron Astrophys* 108:76–84
- Jameson A (1991) Time dependent calculations using multigrid, with applications to unsteady flows past airfoils and wings. Technical Report, AIAA-91-1596
- Menter FR (1994) Two-equation eddy-viscosity turbulence models for engineering applications. *AIAA J* 32(8):1598–1605
- Min B, Sankar LN, Rajmohan N, Prasad J (2009) Computational investigation of gurney flap effect on rotors in forward flight. *J Aircr* 46(6):1957–1964
- Osher S, Chakravarthy S (1983) Upwind schemes and boundary conditions with applications to Euler equations in general geometries. *Comput Phys* 50(3):447–481
- Steijl R, Barakos GN (2008a) A computational study of the advancing side lift phase problem. *J Aircr* 45(1):246–257
- Steijl R, Barakos GN (2008b) Sliding mesh algorithm for CFD analysis of helicopter rotor-fuselage aerodynamics. *Int J Numer Methods Fluids* 58(5):527–549
- Steijl R, Barakos GN, Badcock K (2006) A framework for CFD analysis of helicopter rotors in hover and forward flight. *Int J Numer Methods Fluids* 51(8):819–847
- Wang JJ, Li YC, Choi KS (2008) Gurney flap—lift enhancement, mechanisms and applications. *Progress Aerosp Sci* 44(1):22–47

Chapter 3

Performance Enhancement of Rotors in Hover Using Fixed Gurney Flaps

Vasileios Pastrikakis, René Steijl, and George Barakos

Nomenclature

Latin

a	Lift slope
c	Blade mean chord [m]
u	Mean velocity of the blade section relative to the fluid [m/sec]
c_p	Pressure coefficient
c_T	Thrust coefficient
c_Q	Torque coefficient
c_t	Sectional thrust coefficient
c_m	Sectional moment coefficient
c_q	Sectional torque coefficient
L_z	Rotor loading along the span in the thrust direction [N/m]
L_m	Rotor moment loading around the blade pitch axis [N]
L_q	Rotor moment loading around the shaft axis [N]
M	Mach number
N_b	Number of blades
P_i	Ideal induced rotor power [W]

V. Pastrikakis
Consulting Engineer, SoftInWay Switzerland GmbH
e-mail: v.pastrikakis@gmail.com

R. Steijl • G. Barakos (✉)
University of Glasgow, Glasgow, UK
e-mail: Rene.Steijl@glasgow.ac.uk; George.Barakos@glasgow.ac.uk

P	Actual rotor power [W]
R	Aspect ratio of the blade
FM	Figure of merit, $FM = P_i/P$

Greek

α	Angle of incidence [degrees]
β or β_0	Flapping angles [degrees]
γ	Rotor blade Lock number
θ or θ_0	Collective angle at 75%R [degrees]
λ	Inflow factor
μ	Advance ratio
ρ	Density [kg/m^3]
σ	Rotor solidity, $\sigma = N_b c / \pi R$

Acronyms

CFD	Computational fluid dynamics
MRB	Main rotor blade

3.1 Numerical Methods

3.1.1 Modelling Gurney Flaps

For the purposes of this study the Gurney flap on the W3-Sokol MRB is modelled by flagging any cell face within the computational mesh occupied by the flap with a solid, no-slip boundary condition. This method is implemented in the HMB3 solver and has been proved to be simple and effective.

In this case the Gurney is assumed to be thin, and is modelled along a block boundary. The same grid can be used for different size flaps as well as allowing unsteady deployment of Gurney flaps along block interfaces. The advantage of this method is that no additional effort is needed in terms of mesh generation.

3.1.2 Coupling with Structural Dynamics

For aeroelastic cases the blade was modelled as a beam and its static deformation was computed using Nastran 2005. The main structural properties needed for this analysis are the distributions of the sectional area, the chordwise and flapwise area

moments of inertia, the torsional stiffness, and the mass distribution along the span. The W3 MRB was modelled by 29 beam elements along the span and the properties were obtained by PZL Swidnik. At the root, the blade was free to flap but the lead-lag and pitching motion was not allowed. The twist of the blade was linear, $-10.6^\circ/R$.

To account for fluid/structure coupling the aerodynamic loads are extracted from the fluid solution and used in NASTRAN as nodal forces to obtain the deformed blade shape. The blade along with the mesh is deformed based on the structural shape using a method described by Dehaeze and Barakos (2012). This method first deforms the blade surface using the constant tetrahedral volume (CVT) method. Then, it obtains the updated block vertex positions via spring analogy (SAM) and, finally, it generates the full mesh via a transfinite interpolation (TFI). The same process is repeated until the loads extracted from the flow solution are converged.

3.1.3 Trimming Method

A hover trimming method based on blade-element aeroelasticity was used for this study and was described by Steijl et al. (2006). The method requires the lock number γ_L of the blade and computes an initial trim state for a hovering rotor. After estimating the collective angle θ based on the thrust coefficient, the lift slope factor of the blade section, and the solidity of the rotor, the inflow factor λ is estimated, as well as the coning angle β . HMB2 is subsequently used to compute the thrust coefficient at this particular trimming before updating the collective and the coning based on the difference between the target and the estimated thrust coefficients. The procedure consists of the following steps:

1. At start-up two options can be used:
 - (a) An initial estimate of the trim state is computed using the following equation for the collective pitch:

$$\theta_0 = \frac{6}{\sigma\alpha} C_T + \frac{3}{2} \sqrt{\frac{C_T}{2}}. \quad (3.1)$$

- (b) A user-defined initial guess for θ_0 is used.

The inflow factor λ can be obtained directly from the equation:

$$\lambda = -\sqrt{\frac{C_T}{2}} = -\frac{\sigma\alpha}{16} \left[\sqrt{1 + \frac{64}{3\sigma\alpha} \theta_0} - 1 \right]. \quad (3.2)$$

For a twisted rotor blade Eq. (3.2) gives the collective pitch at 0.75 of the rotor radius R . Then the equation for the coning angle is used:

$$\beta_0 = \frac{\gamma}{8} \left[\theta_0 + \frac{4}{3}\lambda \right]. \quad (3.3)$$

2. The mesh is subsequently deformed to account for the new rotor blade incidence and position.
3. A steady flow simulation is performed until a prescribed level of convergence is reached.
4. The collective is updated using the following relation:

$$\delta\theta_0 = \frac{C_{T,\text{target}} - C_T}{dC_T/d\theta_0}, \quad (3.4)$$

$$\frac{dC_T}{d\theta_0} = \frac{\sigma\alpha}{6} \left[1 - \frac{1}{\sqrt{1 + (64/3\sigma\alpha)\theta_0}} \right]. \quad (3.5)$$

Equation (3.3) gives the coning angle for the new collective pitch $\theta_0 + \delta\theta_0$.

5. Steps 2–4 are repeated until a constant trim state is reached.

Therefore, the coning angle β_0 depends on the Lock number and the reduced model assumptions, while the collective is independent as only the derivation of the Newton iteration is dependent on the reduced aerodynamic model.

3.2 Hover Flight Calculations

3.2.1 W3-Sokol MRB Geometry

The W3-Sokol main rotor consists of four blades made out of fibre-glass. It is a soft blade in torsion that encourages the idea of the implementation of a gurney flap in order to alter the twist distribution along the radius of the blade. Figure 3.1 presents the geometry of the original MRB. The radius of the blade is along the x -axis and the leading-edge points towards the positive y -axis as the blade is rotating counter-clockwise. Although different sections of 5-digit NACA series are used along the radius, the basic section is the NACA23012M which is created by taking some camber out of the baseline NACA23012. At 0.678R of the blade there is a trim tab of 0.1c length and 0.07R span, while from 0.75R and up to the blade tip there is a trailing edge tab of 0.05c. The tip of the blade is rounded as shown in Fig. 3.1-III (upper panel). The MRB has a blunt trailing edge. All these geometrical characteristics increased the complexity of the generated mesh. Adding a fixed Gurney within the multiblock mesh topology would increase the number of nodes and would require additional computational cost to calculate even a steady hover case. For this reason the implementation of an infinitely thin Gurney flap was essential.

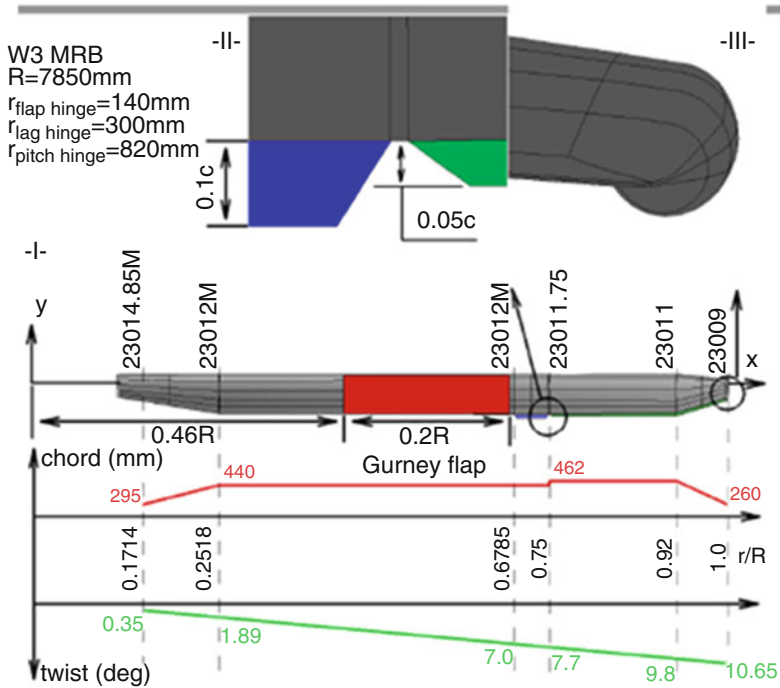


Fig. 3.1 (I) Geometry of W3-Sokol MRB, (II) close view at the trim tab and the trailing edge tab, (III) close view at the tip

For hover a Gurney flap of $0.01c$ was initially located at $0.46R$. The span of the Gurney was $0.2R$ and its location and geometry are presented in Fig. 3.1-II (upper panel). The Gurney flap was flagged using the local mesh around the blade. This allows a normal to the trailing edge flap of infinite thickness to be simulated.

The mesh used for the hover calculations consists of 5.8 million nodes. A mesh convergence study suggested that this large number of cells was needed for the blade-loads to converge. It is a combined C-type topology in the y -plane with 402 nodes along the blade and O-type topology in the x -plane with 196 nodes around every section of the blade. In the normal direction of the blade 64 nodes have been used. The domain is split into 1360 blocks and it is presented in Fig. 3.2.

For the 4-bladed W3-Sokol rotor, the periodicity boundary condition in space and time is applied in a sector of $2\pi/4$ rad. At the farfield, the inflow, and the outflow surfaces the Froude condition for hover, presented by Wake and Baeder (1996) was applied. The farfield was located 52 chords away from the tip of the blade, while the inflow and outflow boundaries are located 30 and 60 chords away from the blade, respectively.

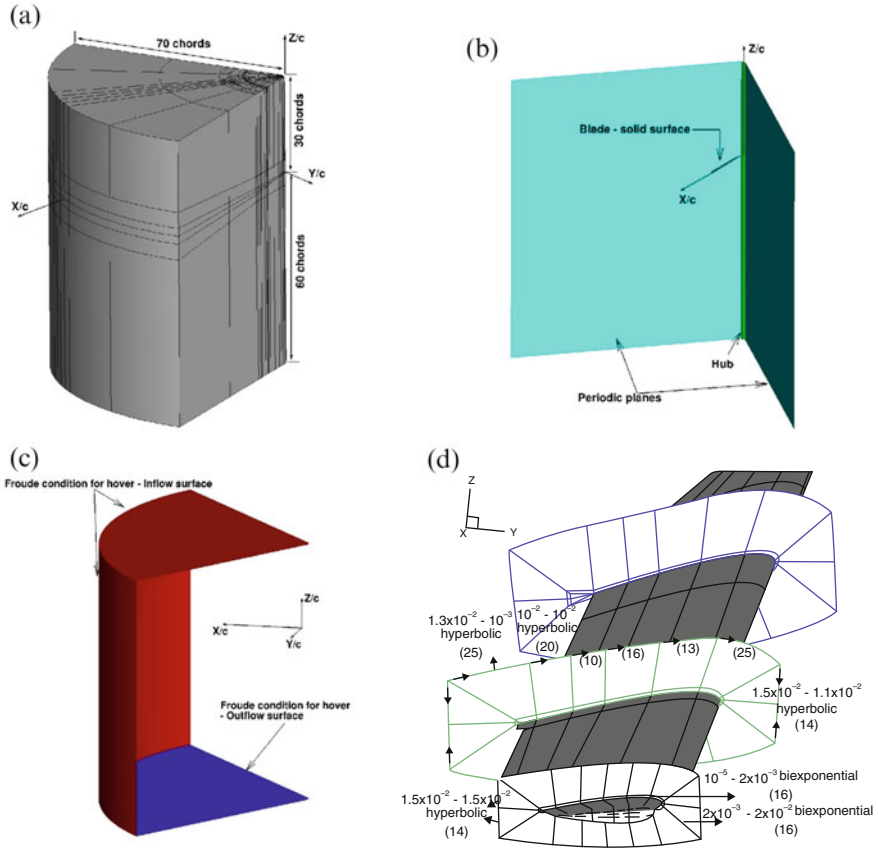


Fig. 3.2 CFD mesh and boundary conditions for the W3-Sokol rotor in hover. **(a)** Multiblock topology for a rotor in hover. **(b)** Detailed view of periodic planes. **(c)** Detailed view on inflow—outflow conditions. **(d)** Blocks around blade in hover. The numbers in brackets indicate number of nodes on the block edges

3.2.2 Rigid Blade Computations

3.2.2.1 Performance

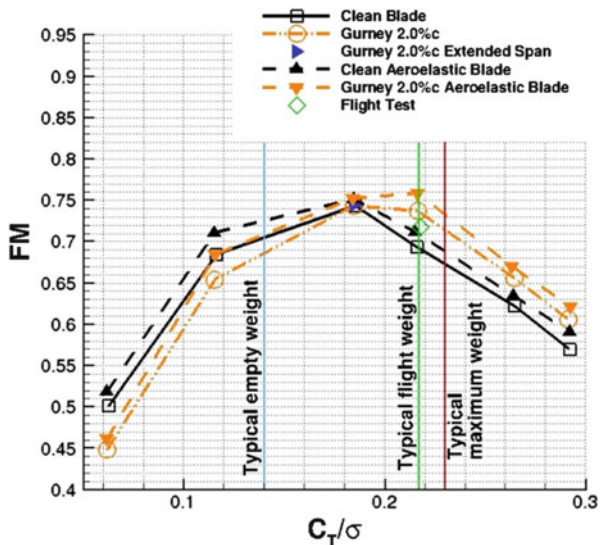
Comparative performance calculations have been conducted at six different thrust targets for the rigid clean blade using the $k-\omega$ SST turbulence model. The collective and coning angles used at every case are presented in Table 3.1. The maximum FM was 0.74 and it was observed at medium thrust settings ($C_T/\sigma = 0.185$). At the same setting the torque coefficient was $C_Q = 0.001$.

The hover performance for the clean blade as well as the blade with Gurney flaps can be seen in Figs. 3.3 and 3.4, and an enlarged view is presented in Fig. 3.5. Three vertical lines are also drawn in that figure corresponding to estimated weight

Table 3.1 Control angles and target thrust coefficients for the clean W3-Sokol blade and the blade with fixed Gurney flap of 2% of the chord (in brackets) in hover

Case	θ_0 [deg]	β_0 [deg]	C_T
1	4.5 (3.6)	1.5 (0.6)	0.0045
2	7.0 (6.1)	2.5 (1.8)	0.0082
3	10.0 (9.1)	5.0 (4.1)	0.0132
4	11.5 (10.5)	6.0 (5.2)	0.0154
5	14.0 (12.9)	6.2 (5.5)	0.0189
6	16.0 (14.4)	10.0 (8.7)	0.0209

Fig. 3.3 Figure of merit versus thrust coefficient for the W3-Sokol MRB in hover ($M_{tip} = 0.618$, $Re_{tip} = 3.74 \times 10^6$, $\sigma = 0.0714$)



cases for a typical helicopter like the W3-Sokol. In fact, the green line represents hover data provided by PZL Swidnik in order to validate the CFD methods. As demonstrated in Fig. 3.6a about 200,000 iterations were needed for a well-converged solution. If the trimmer was also employed, it added an additional number of iterations since after every re-trim the flow needs to adjust and further steps to converge.

3.2.2.2 Analysis of Rigid Blade Results

In Fig. 3.7a the surface pressure coefficient is presented and in Fig. 3.7b the C_p plots at three different sections for the clean blade can be seen. The $r/R = 0.56$ station is where the Gurney flap will be located, while in the $r/R = 0.73$ section the expected effect of the blade trim tab is observed. The trailing edge tab seems to have a similar effect, which can be seen from the pressure distribution at $r/R = 0.89$.

In Fig. 3.8a the wake of the blade is visualised using the vorticity magnitude of 0.1 s^{-1} , which shows that the vortex created at the tip of the blade interacts with the following blade at near $0.89R$, due to the wake contraction. After calculating the

Fig. 3.4 Torque versus thrust coefficient for the W3-Sokol MRB in hover ($M_{tip} = 0.618$, $Re_{tip} = 3.74 \times 10^6$, $\sigma = 0.0714$)

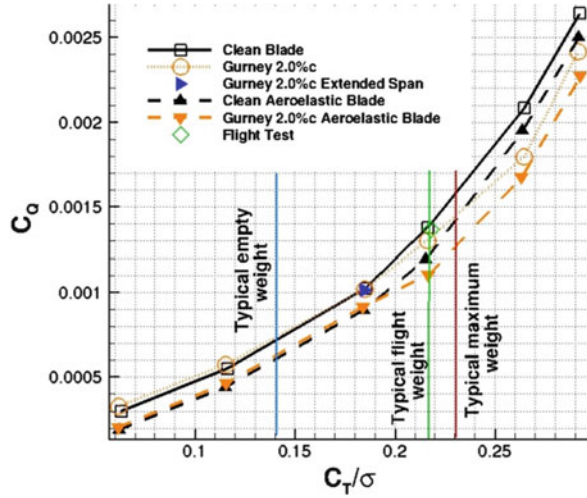
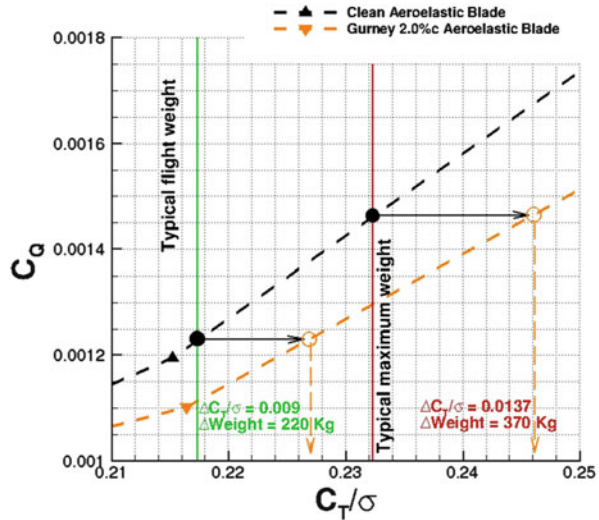


Fig. 3.5 Estimated benefit in hover flight when a Gurney flap is deployed ($M_{tip} = 0.618$, $Re_{tip} = 3.74 \times 10^6$, $\sigma = 0.0714$)



performance of the W3 rotor in hover, a Gurney flap of $0.2R$ span was implemented at $r/R = 0.46$ of the blade. The height of the flap varied from $0.3\%c$ up to $2\%c$ and the flap was assumed to be infinitely thin. Hover calculations were conducted for six thrust settings and the HMB3 trimmer was used to force the blade to reach the same thrust as the clean blade. It is pointed out that the Gurney improves the performance of the rotor above medium thrust ($C_T/\sigma = 0.185$). The most beneficial Gurney size is 2% of the chord and the maximum benefit in figure of merit was $+0.044$ at $C_T = 0.0154$ ($C_T/\sigma = 0.216$) which corresponds to 6.3% increase compared to the clean case. These results can be seen in Fig. 3.3. The Gurney effect on the wake of the blade is well captured and it is presented in Fig. 3.8b using the isosurface of

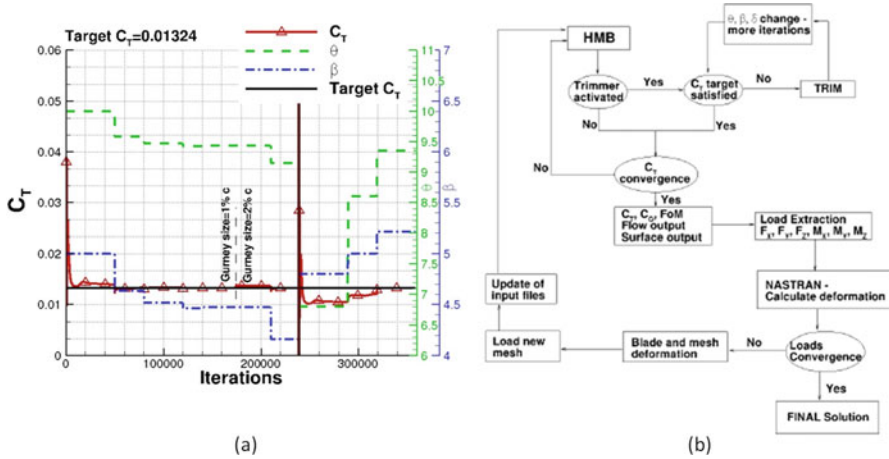


Fig. 3.6 (a) Convergence history for thrust coefficient, collective, and coning angle during aeroelastic hover computations along with trimming process. (b) Flow chart for aeroelastic calculations in hover

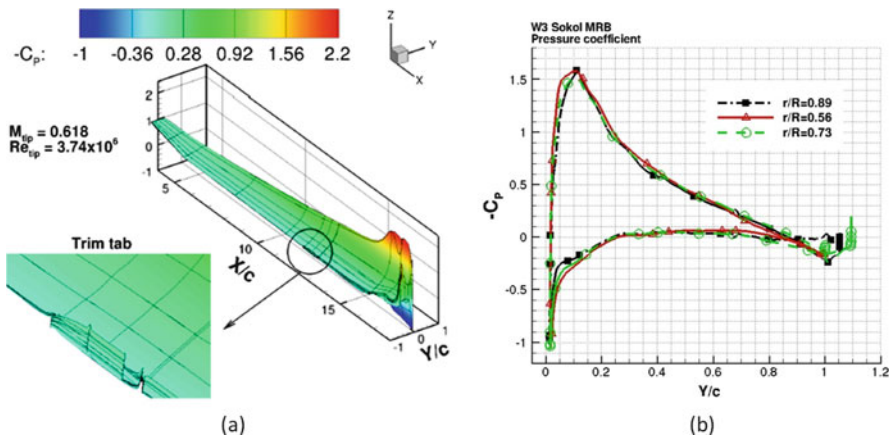
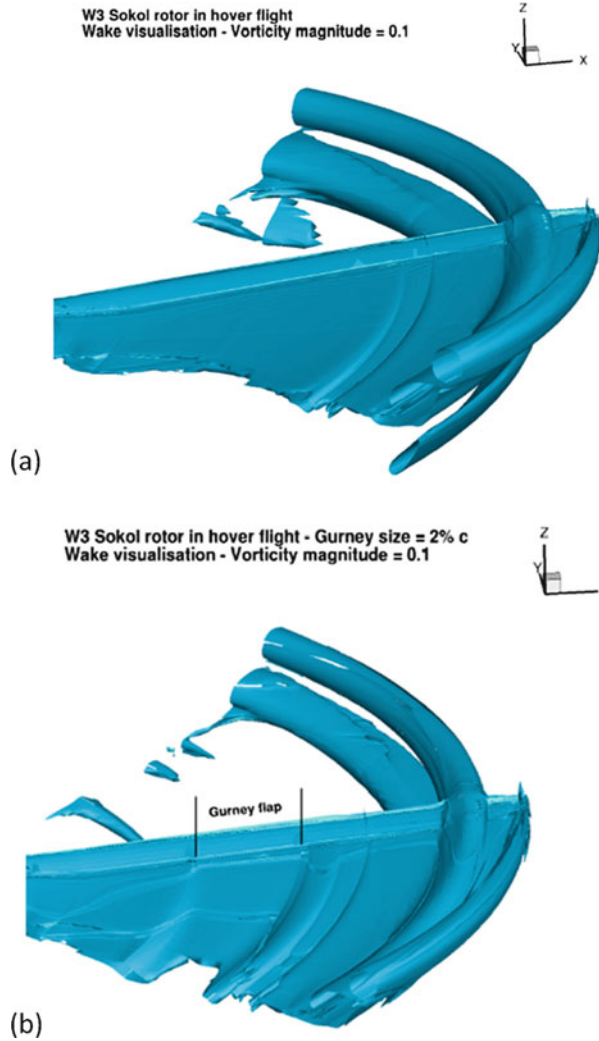


Fig. 3.7 (a) Pressure coefficient along the W3 MRB and (b) pressure coefficient at different sections of the blade normalised using the local dynamic head, $\theta = 10^\circ$, $\beta = 5^\circ$, $C_T = 0.0132$, $FM = 0.7432$, $C_Q = 0.001$

vorticity magnitude equal to 0.1 s^{-1} . For the clean case only the vortices created by the trim tab and the tip of the blade are obvious, while on the blade with the fixed Gurney the vortex generated due to the flap is observed inboard.

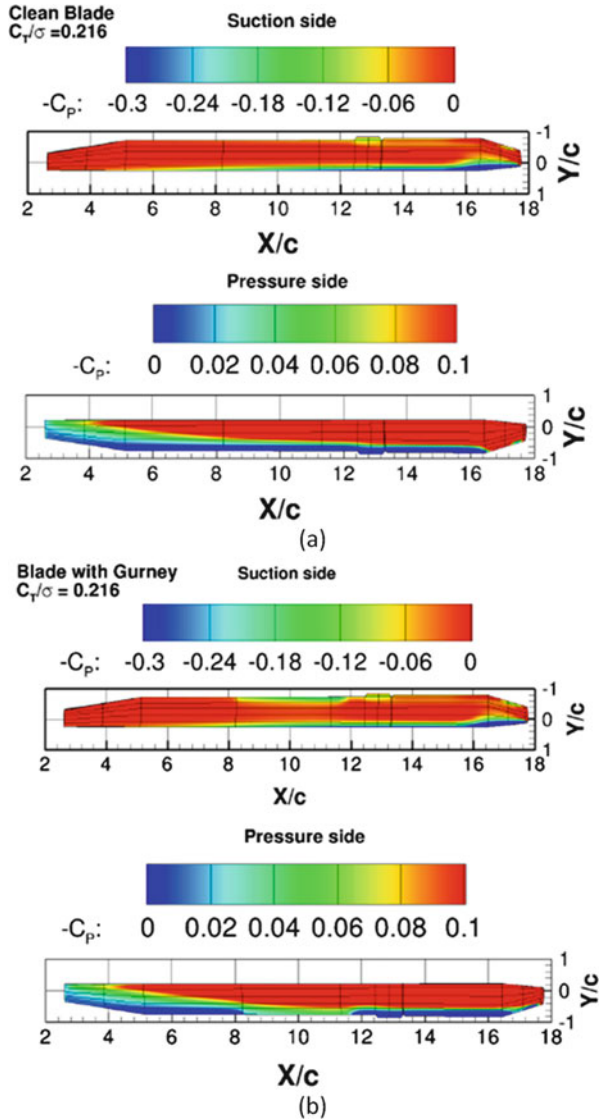
In Fig. 3.9a, b the pressure coefficient on the blade surface is presented for the blade with and without a Gurney flap. The effect of the flap on the decrease of the pressure on the suction side and the increase of the pressure on the pressure side is clear, although this effect decays rapidly away from the tips of the flap. A further comparison is conducted between the sectional pressure coefficients of both blades

Fig. 3.8 Wake visualisation on W3 MRB (a) without and (b) with Gurney flap in hover flight by using the isosurface of vorticity magnitude equal to 0.1 s^{-1} , $\theta_0 = 10^\circ$, $\beta = 5^\circ$, $C_T = 0.0132$, $FM = 0.7432$, $C_Q = 0.001$



in Fig. 3.10. It shows that a Gurney of 2% of the chord alters the pressure distribution at almost 80% of the sectional surface. At lower thrust where the collective of the blade is not very high the Gurney extends more out of the boundary layer and creates additional drag leading to a decrease of the blade performance.

Fig. 3.9 Pressure distribution on upper and lower surface of W3 MRB without Gurney (a) and with Gurney (b). Clean blade: $\theta = 11.5^\circ$, $\beta = 6^\circ$, $C_T/\sigma = 0.216$, $FM = 0.6934$, $C_Q = 0.00138$. Blade with Gurney flap: $\theta = 10.46^\circ$, $\beta = 5.21^\circ$, $C_T/\sigma = 0.216$, $FM = 0.7374$, $C_Q = 0.00129$



3.2.3 Aeroelastic Calculations

3.2.3.1 Application of the Aeroelastic Method and Trimming

Given the sectional properties of the blade, aeroelastic calculations were conducted at the same thrust settings. In Fig. 3.11 the blade is modelled using beam elements in NASTRAN to calculate the deformed shape according to the loads extracted from the flow solution. The structural properties of the blade are presented in Fig. 3.12

Fig. 3.10 Pressure coefficient at $r/R = 0.56$ —comparison between clean blade and blade with Gurney flap

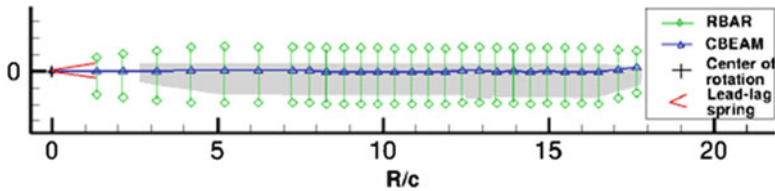
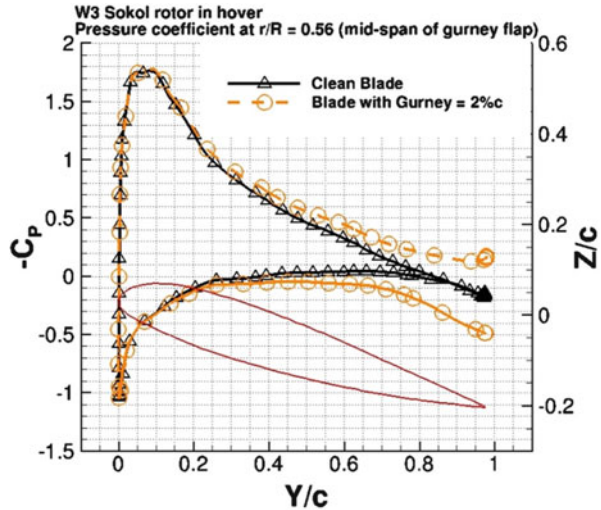


Fig. 3.11 Structural model of the W3-Sokol blade used in NASTRAN

which suggests that this blade is soft compared to more modern designs. Especially, the beamwise and the torsional stiffness are very low compared to the chordwise stiffness along the radius which allows the blade to flap and to twist more during flight.

The process of getting the final converged solution is summarised in Fig.3.6b. Having obtained the converged solution for the rigid blade the aerodynamic loads along the blade are extracted and NASTRAN is used to obtain the new deformed shape using a non-linear analysis. The mesh is then deformed according to that shape and the flow-field is updated until convergence. The trimmer is then employed to reach the required thrust coefficient and the same process is repeated until the loads converge.

3.2.3.2 Analysis of Elastic Blade Results

The black dots in Fig. 3.3 correspond to the aeroelastic calculations performed for the W3 MRB and the performance of the blade is improved. The agreement between the estimated FM and this of tests is also better. The reason for the aerodynamic enhancement is partly due to the structural properties of the blade which allow some

Fig. 3.12 Structural properties of the W3-Sokol blade used in NASTRAN

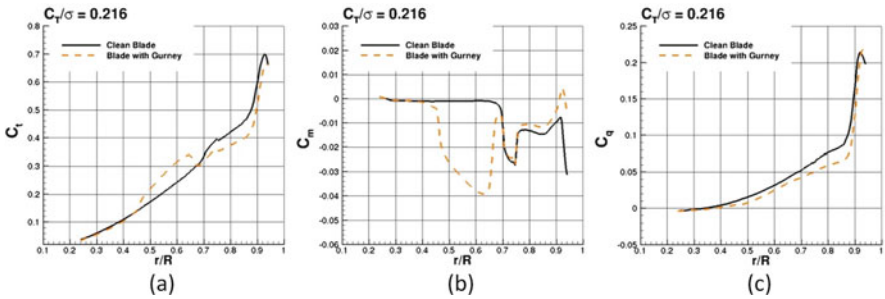
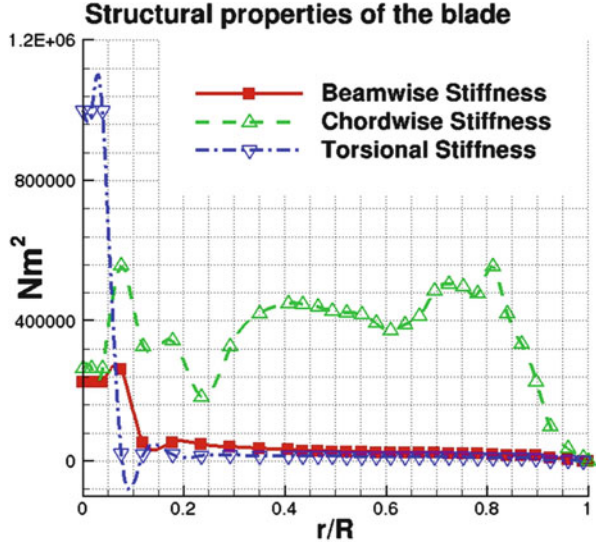


Fig. 3.13 (a) Sectional thrust coefficient, (b) pitching moment coefficient, and (c) torque coefficient of the W3 MRB with (dashed line) and without Gurney flap (solid line). Clean blade: $\theta = 11.5^\circ$, $\beta = 6^\circ$, $C_T/\sigma = 0.216$, $FM = 0.6934$, $C_Q = 0.00138$. Blade with Gurney flap: $\theta = 10.46^\circ$, $\beta = 5.21^\circ$, $C_T/\sigma = 0.216$, $FM = 0.7374$, $C_Q = 0.00129$

twist, and as a consequence, the higher twist leads to a higher figure of merit in hover as mentioned in studies by Keys et al. (2000) and Gagliardi and Barakos (2009). In Fig. 3.13 the effect of the Gurney flap on the sectional thrust, pitching moment, and torque coefficients is presented at the point where the maximum positive effect was captured. These curves were drawn using the aerodynamic loads extracted at 100 different sections along the MRB. The filled squares and the open circles correspond to the loads applied on the nodes used in the structural model. The Gurney increased the sectional thrust locally near its location, but the integrated average thrust remained the same due to trimming. As far as the torque is concerned, the Gurney flap decreased the requirements more.

At the same time the Gurney flap introduced more nose-down moments which tend to lower the collective by more than 1° as presented in Fig. 3.14. Although the

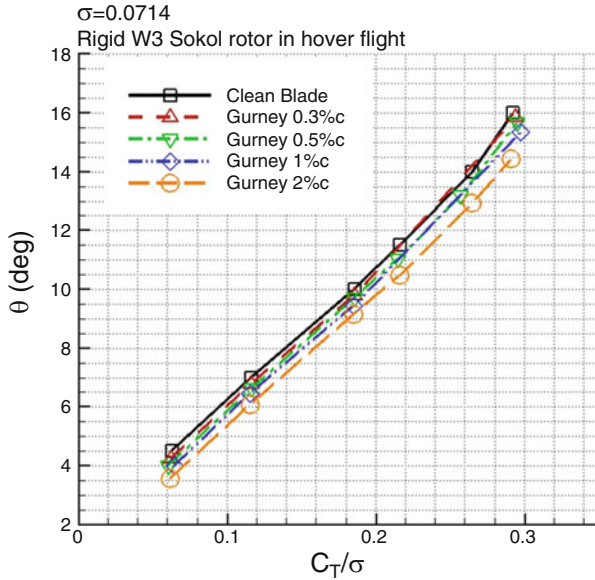
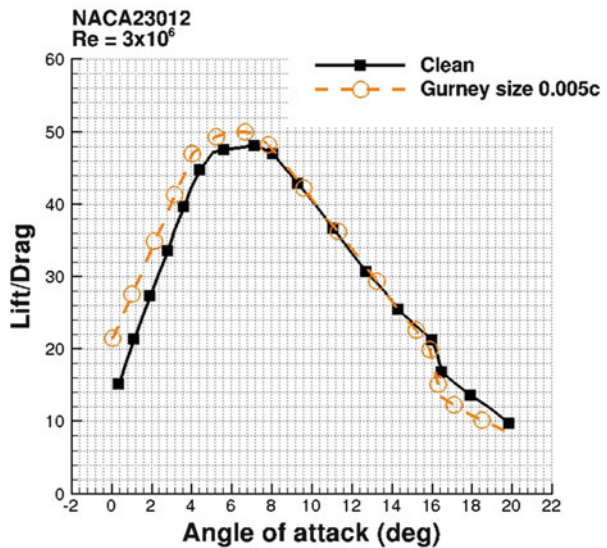


Fig. 3.14 Collective angle after trimming versus C_T/σ for different Gurney sizes on the W3 MRB in hover

Fig. 3.15 Lift over drag comparison for a NACA23012 aerofoil with (dashed line) and without a Gurney flap (solid line)



collective of the blade was further decreased by using a Gurney the overall thrust capability of the blade was maintained as extra lift was provided by the flap. This can also be explained in Fig. 3.15, which compares the lift over drag ratio for a clean NACA23012 and Gurneyed one at different incidence.

Fig. 3.16 Change of twist distribution for W3 MRB with and without Gurney flap in hover

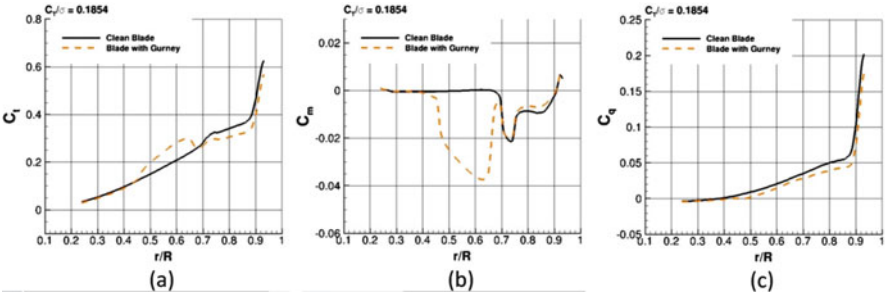
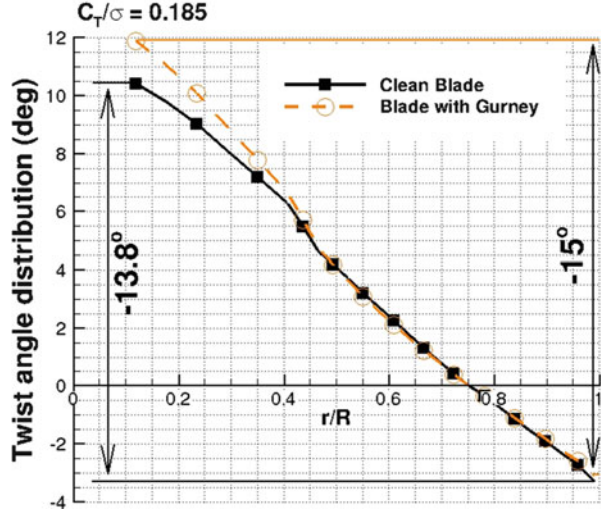


Fig. 3.17 (a) Sectional thrust coefficient, (b) pitching moment coefficient, and (c) torque coefficient of the W3 MRB with (dashed line) and without Gurney flap (solid line). Clean blade: $\theta = 10.0^\circ$, $\beta = 5^\circ$, $C_T/\sigma = 0.1853$, $FM = 0.7432$, $C_Q = 0.001$. Blade with Gurney flap: $\theta = 9.15^\circ$, $\beta = 4.16^\circ$, $C_T/\sigma = 0.1853$, $FM = 0.7429$, $C_Q = 0.001$

Finally, in Fig. 3.16, the change of the twist for both the clean blade and the blade with a Gurney flap is presented to justify the positive aerodynamic effect of the gurney by further increasing the twist by 1.2° . These results correspond to the hover case where the Gurney flap had the most beneficial effect ($C_T/\sigma = 0.216$).

The corresponding results to the lower and higher thrust cases are presented in Figs. 3.17 and 3.18. The effect of the Gurney is quantified in Fig. 3.5. For a given torque requirement it is obvious that using the Gurney a higher thrust coefficient can be reached. This C_T increase for the case of flight test data corresponds to a weight increase of 220 kg.

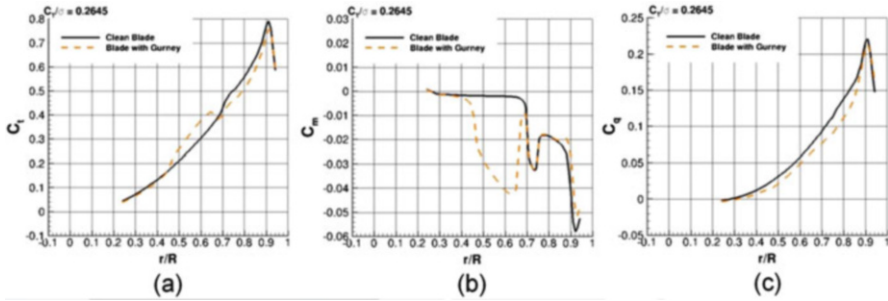


Fig. 3.18 (a) Sectional thrust coefficient, (b) pitching moment coefficient, and (c) torque coefficient of the W3 MRB with (*dashed line*) and without Gurney flap (*solid line*). Clean blade: $\theta = 14^\circ$, $\beta = 6.2^\circ$, $C_T/\sigma = 0.264$, $FM = 0.622$, $C_Q = 0.0021$. Blade with Gurney flap: $\theta = 12.92^\circ$, $\beta = 7.36^\circ$, $C_T/\sigma = 0.264$, $FM = 0.656$, $C_Q = 0.0017$

3.3 Conclusions

In this chapter the use of a Gurney flap was put forward as a means to improve the hover performance of a helicopter rotor. The basic idea is that the flap will be retracted in forward flight and deployed in hover flight only. The W3-Sokol MRB was used in this work due to the availability of the blade shape and structural properties. The maximum FM of the blade did not improve, but at high thrust settings it was enhanced by 6% over the performance of the clean blade. The effect of the Gurney flap to pitch the nose of the section down was evaluated with aeroelastic calculations and it was found that the extra lift of the Gurney in combination with the extra blade twist resulted in an increased FM. For further performance improvement a Gurney flap of bigger span could be considered. Among different sizes of Gurney the one of 2% of the chord was the most effective.

In the future, computations using a fuselage are considered and the location of the Gurney will be further optimised to maximise blade performance. The interaction of the wake generated by the rotor blade with the fuselage may affect the rotorcraft performance in such a way that relocation or a change of the Gurney size may be essential. In addition, the effect of adding a mechanism for the flap actuation on the blade structural properties should be investigated.

References

- Dehaeze F, Barakos GN (2012) Hovering rotor computations using an aeroelastic blade model. *Aeronaut J* 49(1):82–92
- Gagliardi A, Barakos GN (2009) Analysis and design of a flap-equipped low-twist rotor in hover. *J Aircr* 46(1):74–84
- Keys C, Tarzanin F, McHugh DW (2000) Effect of twist on helicopter performance and vibratory loads. In: 13th European Rotorcraft Forum. Arles, France

Nastran MSC (2005) Quick Reference Guide. MSC Software Corporation

Steijl R, Barakos GN, Badcock K (2006) A framework for CFD analysis of helicopter rotors in hover and forward flight. *Int J Numer Methods Fluids* 51(8):819–847

Wake BE, Baeder JD (1996) Evaluation of a Navier-Stokes analysis method for hover performance prediction. *J Am Helicopter Soc* 41:7–17

Chapter 4

Alleviation of Retreating Side Stall Using Active Gurney Flaps

Vasileios Pastrikakis, René Steijl, and George Barakos

Nomenclature

Latin

a	Lift slope
c	Blade mean chord [m]
u	Mean velocity of the blade section relative to the fluid [m/sec]
c_p	Pressure coefficient
c_T	Thrust coefficient
c_Q	Torque coefficient
c_t	Sectional thrust coefficient
c_m	Sectional moment coefficient
c_q	Sectional torque coefficient
L_z	Rotor loading along the span in the thrust direction [N/m]
L_m	Rotor moment loading around the blade pitch axis [N]
L_q	Rotor moment loading around the shaft axis [N]
M	Mach number
N_b	Number of blades
P_i	Ideal induced rotor power [W]
P	Actual rotor power [W]

V. Pastrikakis
Consulting Engineer, SoftInWay Switzerland GmbH
e-mail: v.pastrikakis@gmail.com

R. Steijl • G. Barakos (✉)
University of Glasgow, Glasgow, UK
e-mail: Rene.Steijl@glasgow.ac.uk; George.Barakos@glasgow.ac.uk

R	Aspect ratio of the blade
FM	Figure of merit, $FM = P_i/P$

Greek

α	Angle of incidence [degrees]
β or β_0	Flapping angles [degrees]
γ	Rotor blade Lock number
θ or θ_0	Collective angle at 75 %R [degrees]
λ	Inflow factor
μ	Advance ratio
ρ	Density [kg/m^3]
σ	Rotor solidity, $\sigma = N_b c/\pi R$

Acronyms

CFD	Computational fluid dynamics
MRB	Main rotor blade

4.1 Introduction

Losses due to flow separation are detrimental to rotor performance and normally occur at the retreating side of the rotor disc where the blade is required to operate at higher angles of attack to balance the rotor disc loads. Retreating blade stall results in highly unsteady flow and vibration. Thus, controlling the flow separation is essential. Gurney flaps are capable of providing extra lift at pitch angles below stall. Therefore, the purpose of the study is to investigate the possibility of controlling the retreating blade stall using the W3 Sokol main rotor blade as a test case.

4.2 Numerical Methods

For forward-flying rotors, the HMB2 solves the compressible flow Reynolds-averaged Navier–Stokes equations in an inertial frame of reference. The employed finite-volume discretisation accounts for moving and deforming meshes in time-accurate simulations. Consequently, a rotor in forward flight is modelled in a ‘helicopter-fixed frame of reference’, where the forward flight velocity is introduced

through the definition of the ‘free-stream’ conditions. For isolated rotors, as well as rotor/fuselage or rotor/wind tunnel cases, the rotor and rotor blade motions are then accounted for using mesh velocities. For rotor/fuselage or rotor/wind tunnel cases, the relative motion of the rotor and the fixed fuselage or tunnel is accounted for the sliding plane approach (Steijl and Barakos 2008).

4.2.1 Coupling with Structural Dynamics

A modal approach was chosen to compute the deformed shape of the blade. The final deformation is then considered as a combination of the eigenvectors of the blade. The mode shapes and frequencies are first computed using NASTRAN (2005) code. The blade structure is represented as a set of beam elements located on the elastic axis of the blade. The non-linear *PBEAM* elements of NASTRAN were used. For each section, a rigid bar (*RBAR* element) without any structural properties and rigidly linked to the chord nodes was added in front of the trailing edge and aft of the leading edge in order to assess the displacement of the blade surface. The blade lead-lag stiffness is represented as a linear elastic element.

The mode shapes and frequencies which are obtained using *NASTRAN PBEAM* beam element are the flapping and chordwise area moments of inertia and the linear mass. Other properties can be added introducing the offset between the beam element axis and the blade elastic axis as well as the radius of gyration that allows coupling between the flapwise, chordwise and torsional deformations. These data need to be specified at least at the root of the element, but can also be specified at other locations of the element.

The structural model of a blade usually contains less elements than the blade surface on the fluid mesh. Therefore, the structural solution has to be interpolated on the blade surface. The deformation of the fluid mesh is done in three main steps. Firstly, the constant volume tetrahedron (CVT) method is used to interpolate the deformed shape of the blade surface. Secondly, the block vertices are moved accordingly to the spring analogy method. Finally, the full mesh is regenerated with a transfinite interpolation (TFI). The interpolation process is described in details in Dehaeze and Barakos (2012a, b, c).

For forward-flying rotors, the modal approach is used to lower the cost of computing the blade deformations. It expresses the blade deformation as a function of the blade eigenmodes. The blade shape φ is then described as a sum of eigenvectors φ_i representing the blade displacements for each eigenmode multiplied by the coefficient α_i :

$$\varphi = \varphi_0 + \sum_{i=1}^{n_m} \alpha_i \varphi_i, \quad (4.1)$$

where φ_0 is the undeformed eigenvector. The problem is then reduced to solving for the coefficients α_i .

In the modal approach, the coefficients can be obtained by solving the differential equation:

$$\frac{\partial^2 \alpha_i}{\partial t^2} + 2\zeta_i \omega_i \frac{\partial \alpha_i}{\partial t} + \omega^2 \alpha_i = \mathbf{f} \times \varphi_i, \quad (4.2)$$

where \mathbf{f} are the external forces applied to the blade projected at each structural node, and ζ_i the structural damping coefficient.

4.2.2 Trimming Method

The trimmer used for this study is based on the blade element theory and is described by Steijl et al. (2006). The trimming method consists of an initial trim-state computation and a number of subsequent retrimming steps. The initial trim state can be obtained either offline or within the CFD solver. During retrimming, the collective pitch is updated via a Newton–Raphson process, where the simple aerodynamic model is only used to compute the derivatives of the loads with respect to control inputs. For simulations of forward-flying rotors, retrimming is carried out after completion of 1 rotor revolution using revolution-averaged integrated loads from CFD solution. The trimming method needs a target thrust coefficient C_T as input. For this study, the thrust estimate is given based on flight test data. In addition, models for the fuselage and its drag are necessary in order to compute the total drag, as a function of the advance ratio of the helicopter.

From the rotor thrust and total drag, the orientation of the tip-path plane can be obtained, i.e. the forward tilt. For a rotor at straight level conditions, the orientation of the tip-path plane can be obtained from $\sin \theta_{\text{tip}} = -D/W$, where D and W represent the total drag of the helicopter and its weight.

Assuming a fixed rotor shaft angle θ_{shaft} and known first harmonic flap coefficients β_{1s} and β_{1c} , the thrust and moment coefficients can be expressed as a function of collective and cyclic pitch angles:

$$C_T = C_T(\theta_0, \theta_{1c}, \theta_{1s})$$

$$C_{M,x} = C_{M,x}(\theta_0, \theta_{1c}, \theta_{1s})$$

$$C_{M,y} = C_{M,y}(\theta_0, \theta_{1c}, \theta_{1s}),$$

where $C_{M,x}$ and $C_{M,y}$ are the non-dimensional moments about the x -axis (rotor disc rolling moment) and y -axis (rotor disc pitching moment), respectively:

$$\begin{pmatrix} \Delta \theta_0 \\ \Delta \theta_{1s} \\ \Delta \theta_{1c} \end{pmatrix} = \begin{pmatrix} \frac{\partial C_T}{\partial \theta_0} & \frac{\partial C_T}{\partial \theta_{1s}} & \frac{\partial C_T}{\partial \theta_{1c}} \\ \frac{\partial C_{M,x}}{\partial \theta_0} & \frac{\partial C_{M,x}}{\partial \theta_{1s}} & \frac{\partial C_{M,x}}{\partial \theta_{1c}} \\ \frac{\partial C_{M,y}}{\partial \theta_0} & \frac{\partial C_{M,y}}{\partial \theta_{1s}} & \frac{\partial C_{M,y}}{\partial \theta_{1c}} \end{pmatrix}^{-1} \begin{pmatrix} C_{T,\text{target}} - C_T \\ C_{M_x,\text{target}} - C_{M_x} \\ C_{M_y,\text{target}} - C_{M_y} \end{pmatrix}. \quad (4.3)$$

The elements of the sensitivity matrix in Eq. (4.3) are the derivatives of C_T , $C_{M,x}$ and $C_{M,y}$ according to the blade element theory. Assuming a constant inflow factor λ and fixed flapping harmonics, the sensitivity matrix is:

$$\begin{pmatrix} \frac{\partial C_T}{\partial \theta_0} & \frac{\partial C_T}{\partial \theta_{1,s}} & \frac{\partial C_T}{\partial \theta_{1,c}} \\ \frac{\partial C_{M,x}}{\partial \theta_0} & \frac{\partial C_{M,x}}{\partial \theta_{1,s}} & \frac{\partial C_{M,x}}{\partial \theta_{1,c}} \\ \frac{\partial C_{M,y}}{\partial \theta_0} & \frac{\partial C_{M,y}}{\partial \theta_{1,s}} & \frac{\partial C_{M,y}}{\partial \theta_{1,c}} \end{pmatrix} = \frac{\sigma \alpha}{4} \begin{pmatrix} (\frac{2}{3} + \mu^2) & -\mu & 0 \\ \frac{2}{3}\mu & -\frac{1}{4}(1 + \frac{3}{2}\mu^2) & 0 \\ 0 & 0 & \frac{1}{4}(1 + \frac{1}{2}\mu^2) \end{pmatrix} \quad (4.4)$$

$$\begin{aligned} \delta \theta_0 &= \left[\frac{\partial C_T}{\partial \theta_0} \frac{\partial C_{M,x}}{\partial \theta_{1,s}} - \frac{\partial C_T}{\partial \theta_{1,s}} \frac{\partial C_{M,x}}{\partial \theta_0} \right]^{-1} = \left(\frac{\partial C_{M,x}}{\partial \theta_{1,s}} (C_{T,\text{target}} - C_T) + \frac{\partial C_T}{\partial \theta_{1,s}} C_{M,x} \right) \\ \delta \theta_{1,s} &= \left[\frac{\partial C_T}{\partial \theta_0} \frac{\partial C_{M,x}}{\partial \theta_{1,s}} - \frac{\partial C_T}{\partial \theta_{1,s}} \frac{\partial C_{M,x}}{\partial \theta_0} \right]^{-1} = \left(\frac{\partial C_{M,x}}{\partial \theta_0} (C_{T,\text{target}} - C_T) + \frac{\partial C_T}{\partial \theta_0} C_{M,x} \right) \\ \delta \theta_{1,c} &= -C_{M,x} / \frac{\partial C_{M,x}}{\partial \theta_{1,c}} \end{aligned} \quad (4.5)$$

Similar approaches have been used in Yang et al. (2002), Van der Ven and Boelens (2004) and Park and Kwon (2004). Yang et al. (2002) used a lifting-line technique, external to the flow solver, to obtain the derivatives of the rotor performance parameters. An alternative expensive approach is presented in Van der Ven and Boelens (2004) and Park and Kwon (2004), where the flow solver is used to determine the derivatives of the rotor performance parameters by repeating the simulation with slightly different values of the angles θ_0 , $\theta_{1,s}$ and $\theta_{1,c}$ in succession. An accurate estimate of the derivatives requires a converged flow solution for each of these different control settings. Typical trimmed rotor simulations involved up to 35 revolutions of the rotor.

4.3 W3 Main Rotor

For forward flight, a Gurney flap of 0.02c height was placed at 0.40R and had a span of 0.25R. The Gurney flap was represented in the local mesh around the blade. The mesh used for the forward flight calculations consists of 27 million nodes. It is a combined C-type topology in the chordwise plane with 402 nodes along the blade and O-type topology in the spanwise plane with 196 nodes around every section of the blade. In the normal direction of the blade, 64 nodes have been used. The domain is split in the rotor mesh which includes the rotor blade geometry and the hub and the background mesh. The flow in the interface of those two meshes is interpolated using sliding planes. The whole domain is split in 5480 blocks and it is presented in Fig. 4.1.

4.4 Flight Test Data

The flight measurements were obtained by PZL-Świdnik for four different flight cases: hover and forward flight at low, medium and high speed. A first target of

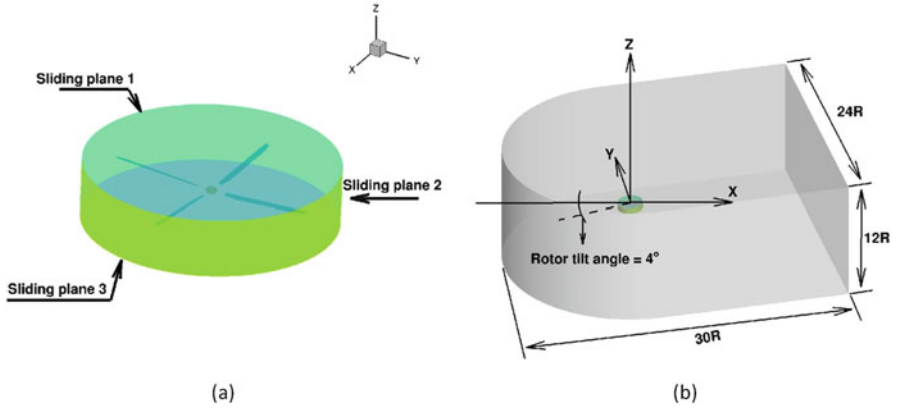
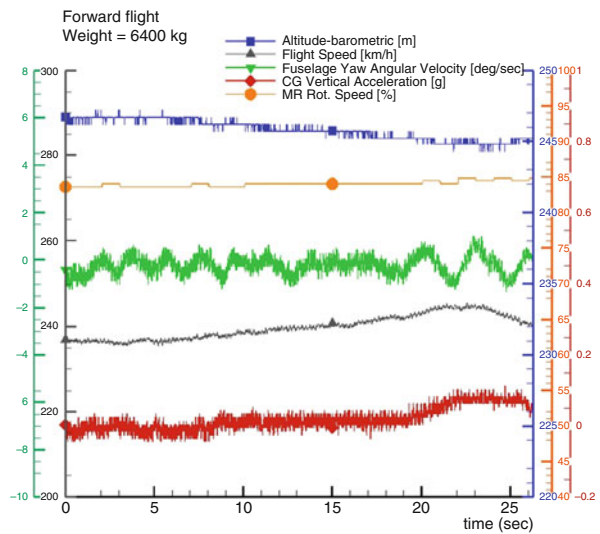


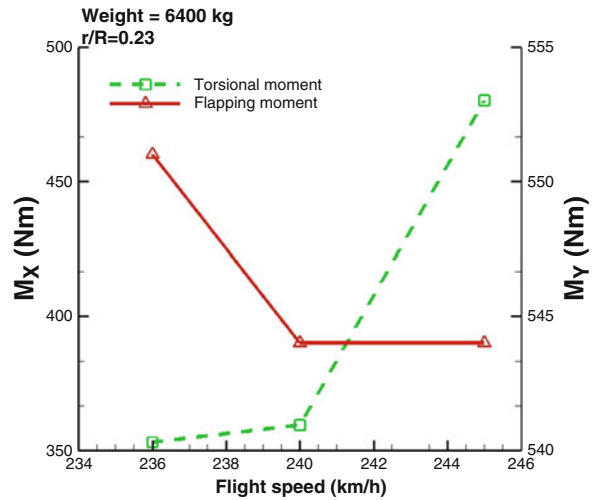
Fig. 4.1 (a) Sliding planes around W3 main rotor in forward flight and (b) overview of the computational domain used for the forward flight calculations

Fig. 4.2 Time domain flight parameters for forward flight with helicopter weight equals to 6400 kg



this work was the identification of blade stall. Data was used for a forward flight at indicated speed between 236 km/h and 245 km/h, while at the same time, the weight of the helicopter was the maximum allowed weight according to the design specifications (6400 kg), so that the indication of stall was more visible. The time domain flight parameters for that case are presented in Fig. 4.2. Figure 4.3 presents the peak to peak values for the torsional moment and the flapping bending moment at $r = 0.23R$. Figure 4.4 presents the harmonic analysis for the flap, lag and feather moments of the first blade. Based on previous flight test data processing, for a four-bladed rotor, the existence of high harmonic content frequencies which cannot be divided by 4 suggests vibrations due to stall. Table 4.1 presents the forward flight conditions of the W3 rotor.

Fig. 4.3 Peak to peak values of torsional and flapping moments at $r/R = 0.23$, helicopter weight equals to 6400 kg



4.5 Forward Flight

Figure 4.5 presents the schedule of the feathering and flap angles of the blade around the azimuth. Based on that schedule, the blade seems to operate beyond the stall limit of the NACA23012M aerofoil at the retreating side, which could be the cause for stall at inboard sections. The $k-\omega$ SST turbulence model was used and the rotor completed 4 revolutions with quarter degree steps before the loads reached convergence.

4.5.1 Rigid Blade

A separated flow region was identified at the retreating side of the rotor. Figure 4.6 presents the pressure distribution and the flowfield at 45 %R at several azimuthal positions between $\Psi = 210^\circ$ and $\Psi = 310^\circ$. Once the pressure at the leading edge of the suction side starts diverging, this is a good indication the flow separation will occur. This happens at $\Psi = 250^\circ$, and it can be seen from the streamlines and the vorticity levels near the trailing edge. The flow reattaches at $\Psi = 310^\circ$.

After processing the CFD results, Fig. 4.7 presents the stall map along with the designed actuation algorithm of the Gurney flap which had a span of $0.25R$, and its size was $0.02c$ based on the performance on the flap at the same rotor in hover. The Gurney flap is fully extracted between 200 and 300° and it is fully retracted between 30 and 120° . Figure 4.8 presents a comparison of the pressure distribution between the clean rotor and the rotor with the active Gurney as well as the flowfield for the Gurney case at inboard sections of the blade and at the retreating side of the rotor. It

Fig. 4.4 Harmonic analysis of (a) torsional, (b) flapping and (c) lagging moments of the first MRB at $r/R = 0.23$; helicopter weight equals to 6400 kg. Case conditions are presented in Table 4.1

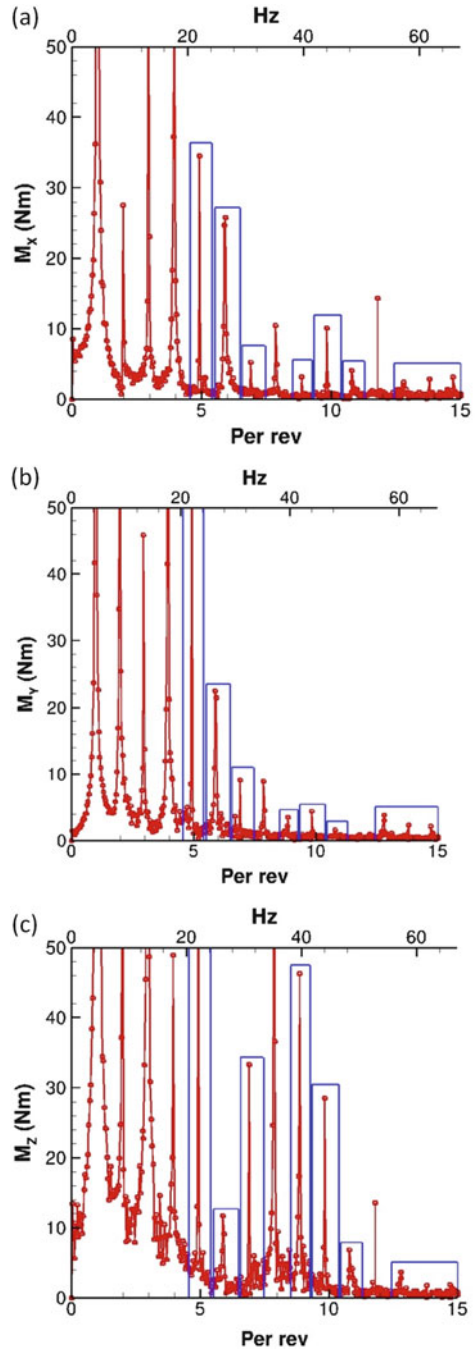
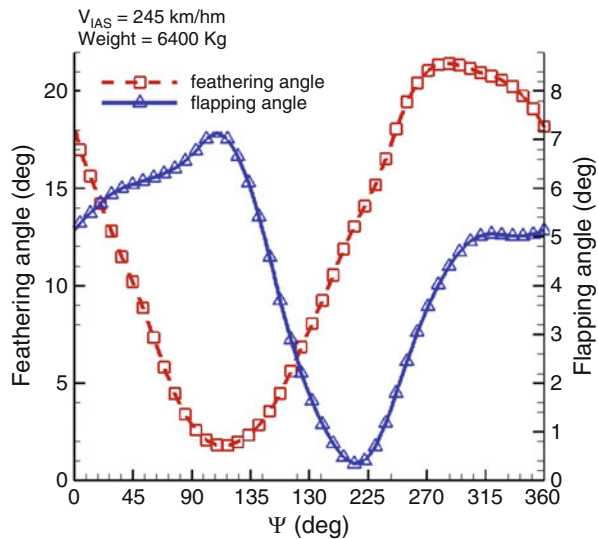


Table 4.1 Forward flight conditions for the W3 Sokol main rotor

Flight parameters	
V_{IAS}	245 km/h
M_∞	0.2052
Re_∞	1.2×10^6
μ	0.3229
θ_0	12.38°
β_0	3.55°
θ_c	-4.87°
θ_s	8.68°
β_c	-1°
β_s	-3.5°

Fig. 4.5 Schedule for the feathering and flapping angle for the W3 Sokol MRB in forward flight. Case conditions are presented in Table 4.1



is observed that the pressure coefficient diverges less if the Gurney flap is actuated indicating that the flap removed some of the stall.

Figure 4.9 presents the disc loads for the clean rotor and the rotor with the active flap along with the difference on the loads between the two cases for the rigid untrimmed rotor. The higher lift capability of the rotor when Gurney is close to full actuation is pointed out. However, the extra lift due to the Gurney flap increases the stall at the retreating side, while mostly pitch-down moments are observed at the region where the Gurney is located. The increase of the stall leads to an increase of the torque required at the same azimuthal location. When both rotors were trimmed at the same thrust setting ($C_T = 0.015$), indicative results of pressure coefficient distribution were shown in Fig. 4.10. The C_p was based on the freestream velocity, and the effect of the Gurney on decreasing the pressure on the suction side of the blade is visible. It is to be noted that the effect of the Gurney decays rapidly away from the tips of the flap.

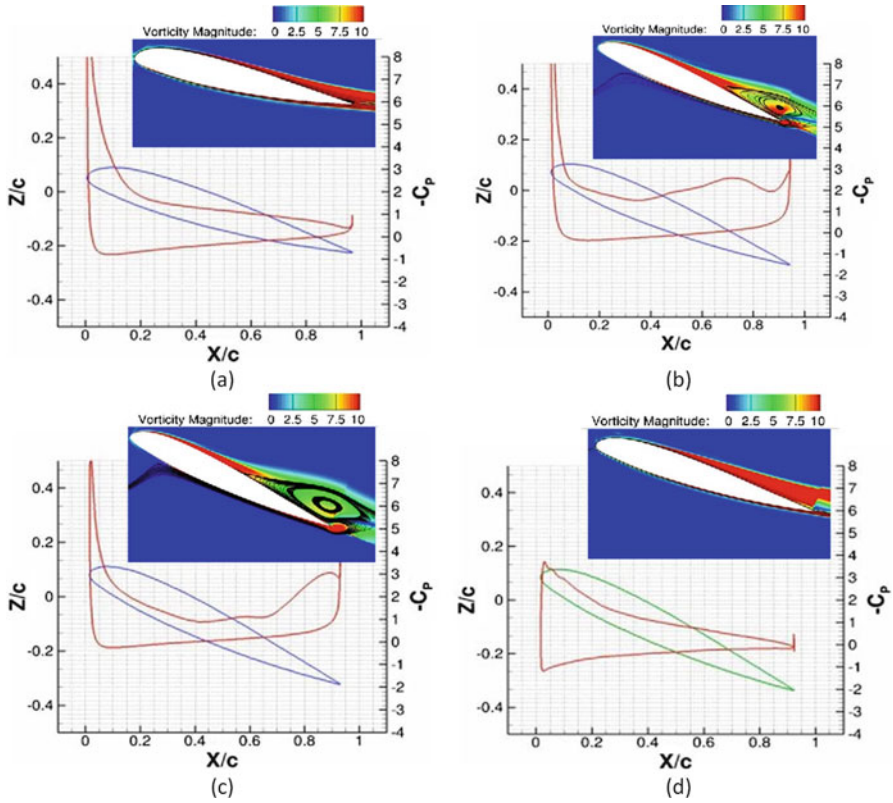


Fig. 4.6 Pressure distribution and vorticity magnitude visualisation at $r/R = 0.45$ of the W3 Sokol blade in forward flight at (a) $\Psi = 210^\circ$, (b) $\Psi = 250^\circ$, (c) $\Psi = 270^\circ$ and (d) $\Psi = 310^\circ$. Case conditions are presented in Table 4.1

4.5.2 Elastic Blade

To obtain more representative results regarding the Gurney effect on reducing the separation, both cases were treated as elastic rotors, and they were trimmed at the same thrust settings. The mode shapes of the W3 Sokol MRB based on the structural model of Fig. 4.11 were given to the solver as an initial shape of the elastic blade. Modes up to the first torsional mode were used.

The mode shapes are presented in Table 4.2, and they are mixed flapping, in-plane and torsional deformations, which made it hard to characterise them. Figure 4.12 presents the shape of the rigid and the elastic blade shapes at the back of the disc. The tip of the elastic blade is pitched down by 10° compared to the rigid, while the blade flapped upwards by almost 2° . The lagging angle was almost 3° .

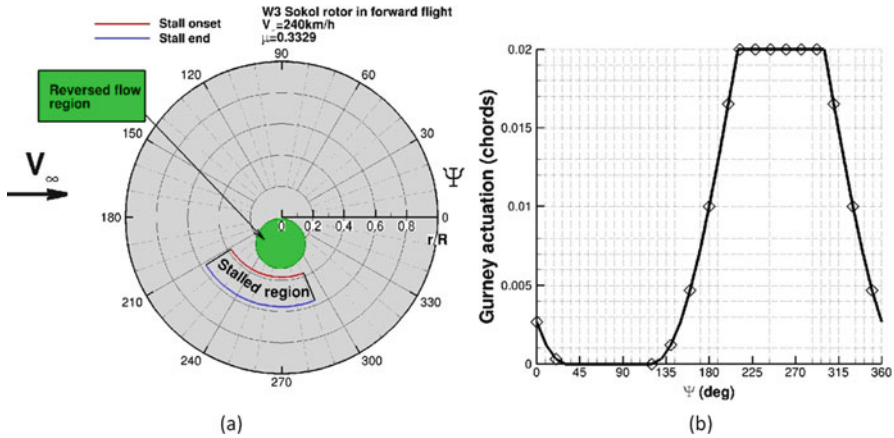


Fig. 4.7 (a) Stall map of W3 Sokol blade in forward flight and (b) actuation schedule of Gurney flap. Case conditions are presented in Table 4.1

The elastic rotor was trimmed at $C_T = 0.0117$ for both clean and Gurney cases to evaluate the effect of the flap, while the disc pitching and rolling moments were driven to zero.

Figure 4.13 presents the trimming history of the computations. For the case where the Gurney was actuated, the torque requirement of the rotor was decreased by 3.3 % (1149 kW) which corresponds to 40 KW. This reduction occurred at the retreating side of the disc because of the stall decrease.

Figure 4.14 presents streamlines near the separated region of the blade at $\Psi = 270^\circ$ along with the effect of the Gurney flap. The blade shown in Figure 4.14b is pitched down and the flow is less separated compared to the clean case. In fact, the observed benefits are due to the aerodynamic enhancement of the blade which allows the rotor to operate in lower collective, as well as the aeroelastic reshaping of the blade due to the pitching moments induced by the flap.

The increased performance of the rotor with the active Gurney flap can be evaluated using the total lift-to-drag ratio as well as the effective one as it is important to ensure that the decrease in power for the system is not due to the difference in trim state between the clean and the flapped rotor.

The effective lift-to-drag ratio is defined as: $L/D_e = L / (P/V_\infty - D)$. Based on CFD results, the drag of the clean and gurneyed rotors are 15.57 kN ($L/D = 4.03$) and 15.81 kN ($L/D = 3.97$), respectively. Thus, the effective drag for each case is $D_{e,\text{clean}} = 2.27$ kN, and $D_{e,\text{Gurney}} = 1.43$ kN, which lead to $L/D_{e,\text{clean}} = 27.66$, and $L/D_{e,\text{Gurney}} = 43.84$ (about 58 % increase compared to the clean case).

Since more data was available from flights for the W3 Sokol, CFD calculations were also performed in lower advance ratio and thrust requirements. The reason was to identify the effect of the Gurney flap along the full flight envelope of the W3 Sokol helicopter for the same actuation schedule of the flap. A complete aeroelastic trimmed computation takes about 250,000 CPU-hours to finish. The most useful

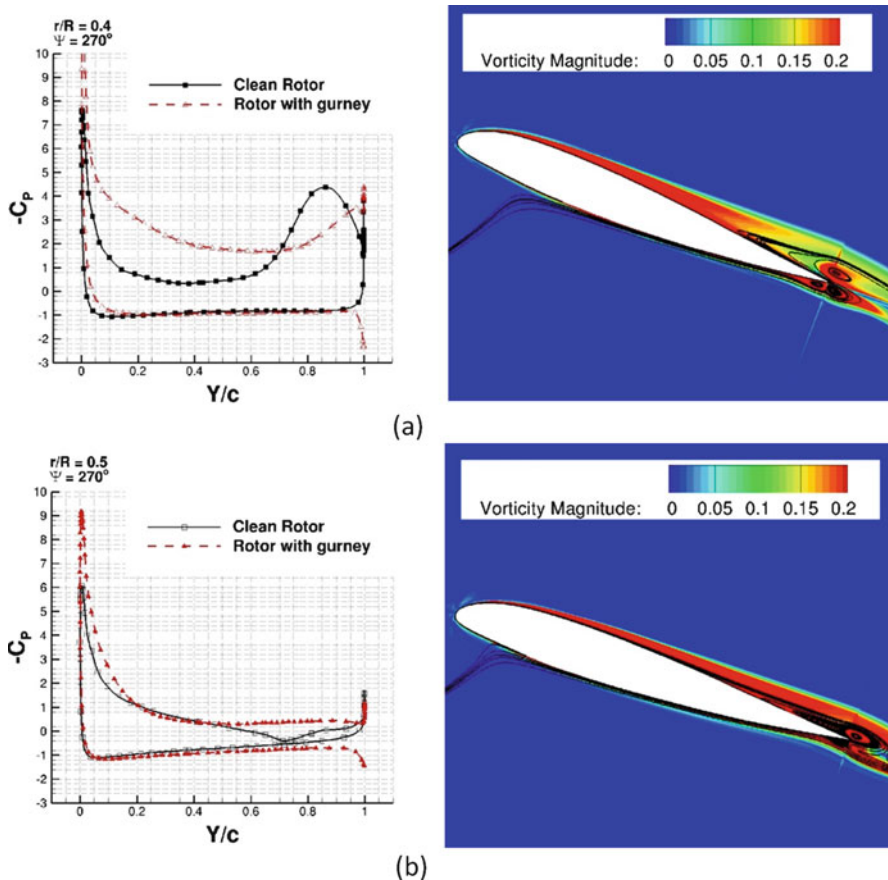


Fig. 4.8 Surface pressure coefficient and flow visualisation at $r/R = 0.4$ (a) and $r/R = 0.5$ (b). Case conditions are presented in Table 4.1

outcome of this study is the power reduction gained because of the active Gurney flap. Table 4.3 shows the effect of the flap from hover to high-speed forward flight. For this weight of the W3 Sokol, the Gurney shows some benefit in hover, although it becomes very beneficial in higher thrust requirement. During forward flight, the flap becomes beneficial close to $\mu = 0.11$. At high speed and high weight cases, the potential effect of the Gurney on the retreating blade stall alleviation enhances the aerodynamic performance of the rotor and reduces the power requirements significantly. However, Table 4.3 clearly shows that a Gurney should be deployed during hover only for high thrust requirements, while it should remain retracted at low forward flight speed.

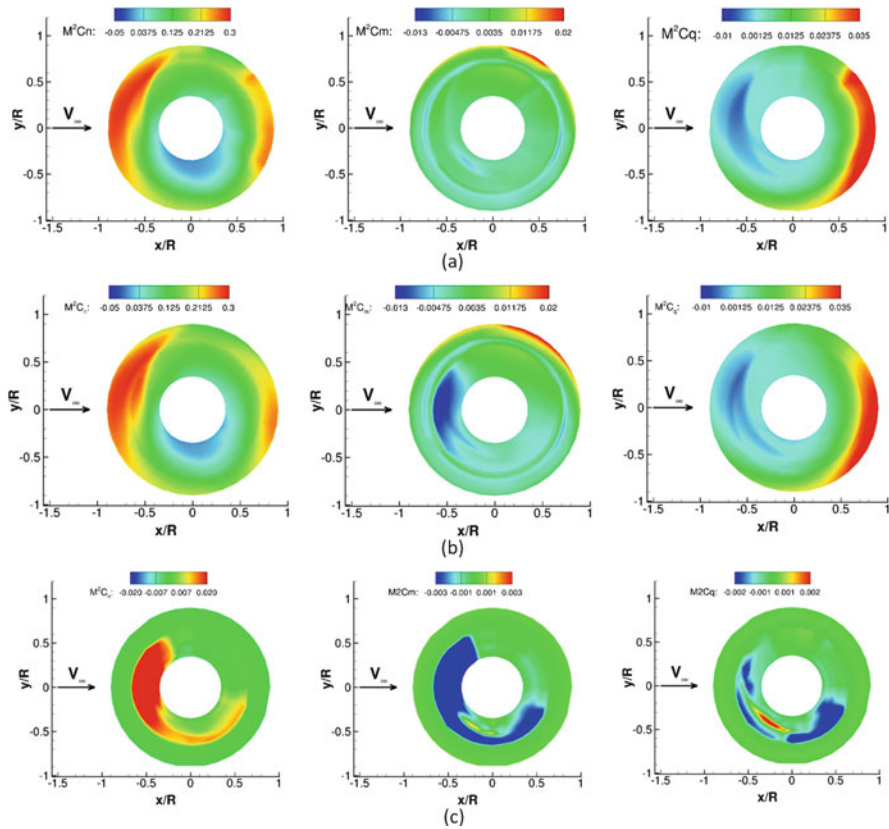


Fig. 4.9 Normal force, pitching moment and torque coefficient of the rigid untrimmed W3 Sokol MR without Gurney flap (a) and with Gurney flap (b). Load differences are presented in (c). Forward flight conditions are presented in Table 4.1

4.6 Conclusions

In this chapter, the use of a Gurney flap was put forward to improve the forward flight performance of a helicopter rotor by reducing the stall at the retreating side. The basic idea is that the flap will be actively actuated in forward flight and will be fully deployed in hover flight. The W3 Sokol MRB was used due to the availability of flight test data as well as the blade shape and structural properties. A carefully designed Gurney flap and actuation schedule proved to be essential for controlling the separation of the flow. Next, an optimisation of the Gurney location is to be considered along with closed-loop controller for the actuation of the flap. Finally, the effect of 1/rev actuation of the flap will be evaluated on the trimming and handling of a full helicopter.

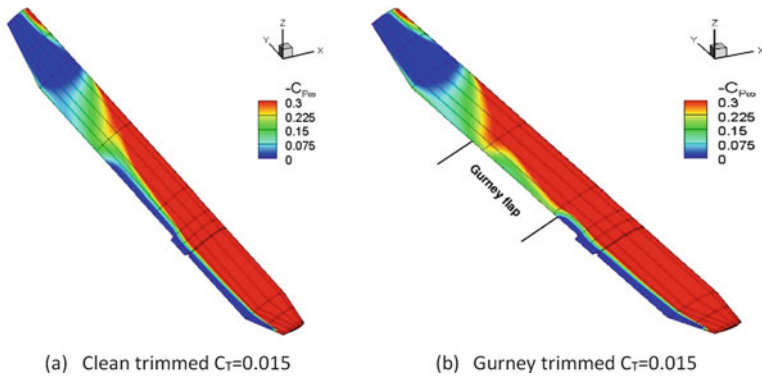


Fig. 4.10 Negative surface pressure coefficient based on the freestream velocity on clean blade (a) and (b) blade with active Gurney flap (2 % of the chord) at $\Psi = 270^\circ$; both cases trimmed at $C_T = 0.015$. W3 Sokol MR in forward flight. Case conditions are presented in Table 4.1

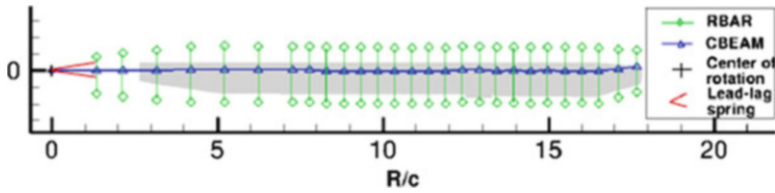
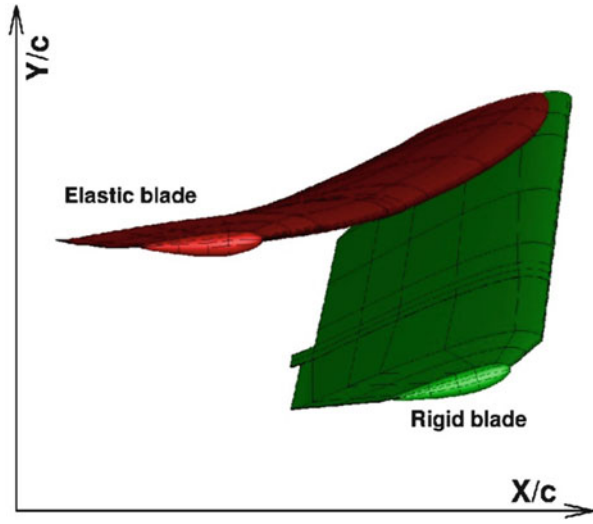


Fig. 4.11 Structural model of W3 Sokol MRB

Table 4.2 Identified modes for W3 MRB rotating at 268.485 rpm

Frequency [Hz]	Mode shape
12.17	Flapping
21.04	Flapping
21.58	In-plane
31.42	Flapping
44.02	Flapping
57.07	In-plane
60.31	Torsional

Fig. 4.12 Visualisation of the rigid and elastic W3 MRB in forward flight at $\Psi = 0^\circ$. Case conditions are presented in Table 4.1



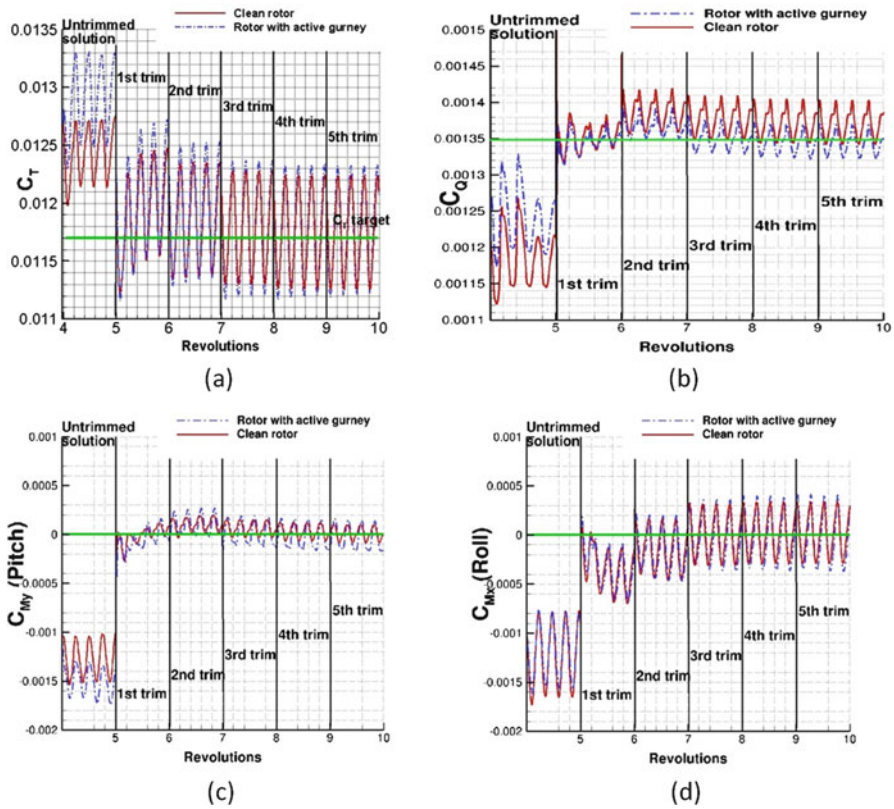
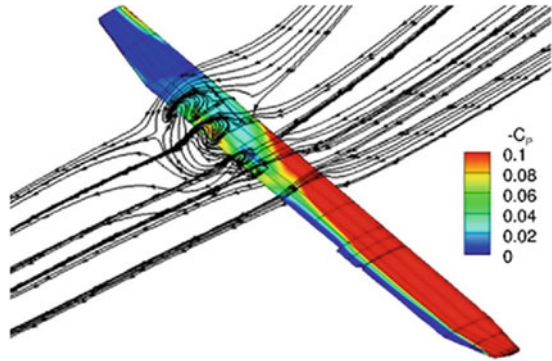
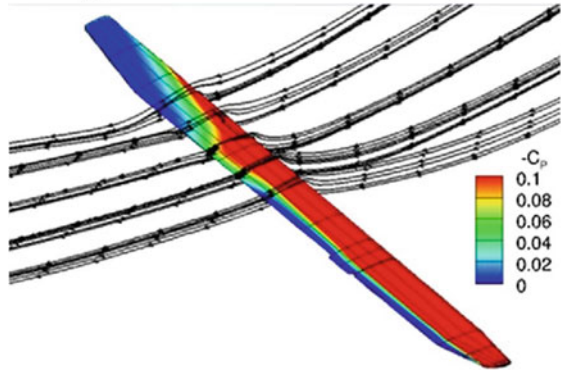


Fig. 4.13 Trimming history of (a) thrust, (b) torque, (c) rotor disc pitching moment and (d) rotor disc rolling moment of the elastic W3 Sokol MR in forward flight. Flight conditions are presented in Table 4.1

Fig. 4.14 Visualisation of the separated flow for (a) the clean blade and (b) the blade with an active Gurney flap of $0.02c$ at $\Psi = 270^\circ$ of the W3 Sokol MR in forward flight. Case conditions are presented in Table 4.1



(a) Elastic clean blade trimmed at $C_T=0.0117$



(b) Elastic blade with Gurney flap trimmed at $C_T=0.0117$

Table 4.3 Required power for clean rotor and rotor with active Gurney flap for different flight speeds and thrust settings

Advance ratio	Weight [kg]	Clean rotor—Power [HP]	Rotor with Gurney—Power [HP]	ΔP [HP]
0.0	6000	1076.7	1101.6	24.9
0.0	6400	1188.5	1205.4	16.9
0.11	6000	1034.4	1030.5	-3.9
0.11	6400	1189.6	1178.3	-11.3
0.329	6000	1365.7	1335.5	-30.2
0.3229	6400	1591.2	1542.2	-49.0

Negative ΔP indicates power benefit due to Gurney flap

References

- Dehaeze F, Barakos GN (2012) Aeroelastic CFD computations for rotor flows. In: 37th European Rotorcraft Forum, Vergiate abd Gallarate, Italy, pp 143–162
- Dehaeze F, Barakos GN (2012b) Hovering rotor computations using an aeroelastic blade model. *Aeronaut J* 116(1180):621–649
- Dehaeze F, Barakos GN (2012c) Mesh deformation method for rotor flows. *J Aircr* 49(1):82–92
- Nastran MSC (2005) Quick Reference Guide. MSC Software Corporation
- Park Y, Kwon O (2004) Simulation of unsteady rotor flow field using unstructured adaptive sliding meshes. *J Am Helicopter Soc* 49(4):391–400
- Steijl R, Barakos GN (2008) Sliding mesh algorithm for CFD analysis of helicopter rotor-fuselage aerodynamics. *Int J Numer Methods Fluids* 58(5):527–549
- Steijl R, Barakos GN, Badcock K (2006) A framework for CFD analysis of helicopter rotors in hover and forward flight. *Int J Numer Methods Fluids* 51(8):819–847
- Van der Ven H, Boelens OJ (2004) A framework for aeroelastic simulations of trimmed rotor systems in forward flight. In: 29th European Rotorcraft Forum, Marseille
- Yang Z, Sankar M, Smith M, Bauchau O (2002) Recent improvements to a hybrid method for rotors in forward flight. *J Aircr* 39(5):804–812

Chapter 5

Effect of Gurney Flaps on Overall Helicopter Flight Envelope

Vasileios Pastrikakis and George Barakos

Nomenclature

Latin

c_p	Pressure coefficient
c_T	Thrust coefficient
c_Q	Torque coefficient
c_t	Sectional thrust coefficient
c_m	Sectional moment coefficient
c_q	Sectional torque coefficient
P_i	Ideal induced rotor power [W]
P	Actual rotor power [W]
R	Aspect ratio of the blade

Greek

α	Angle of incidence [degrees]
β or β_0	Flapping angles [degrees]
γ	Rotor blade Lock number

V. Pastrikakis
Consulting Engineer, SoftInWay Switzerland GmbH
e-mail: v.pastrikakis@gmail.com

G. Barakos (✉)
University of Glasgow, Glasgow, UK
e-mail: George.Barakos@glasgow.ac.uk

θ or θ_0	Collective angle at 75%R [degrees]
λ	Inflow factor
μ	Advance ratio
ρ	Density [kg/m^3]
σ	Rotor solidity, $\sigma = N_b c / \pi R$

Acronyms

CFD	Computational fluid dynamics
MRB	Main rotor blade

5.1 Gurney Effect on Structural Properties of the Blade

The effect of different tip designs on the aeroelastic properties of a blade was studied using the S-76 blade. The idea is to compare that effect with the one due to adding a Gurney flap on the W3-Sokol blade. Four different tip designs are used; a rectangular, a tapered, a swept, and a tapered-swept as presented in Fig. 5.1. What changes between the four designs is the mass distribution, the torsional inertia of the tip segment, and the location of the elastic axis and centre of gravity at the tip. The comparison of the modes up to 125 Hz between the baseline case and the tapered-swept tip design is presented in Table 5.1. It is to be noted that the different designs did not alter the characterisation of the modes and the frequencies were shifted by less than 1% compared to the baseline tip design. This outcome shows that even such differences in the design, which lead to significant changes on the aerodynamic behaviour of the blade, will not affect significantly the aeroelastic response of the blade.

Figure 5.2 presents the properties used in NASTRAN for three different blades, the S-76, the W3-Sokol, and the UH60A, to get an insight of the different parameters used in the models. Finally, the effect of the additional mass of the Gurney flap actuation mechanism on the aeroelastic response of the blade was tested by distributing an additional 10% of the total mass of the blade at the sections where the Gurney flap was located.

Figure 5.3 presents the spoke diagram of the clean blade and a comparison against the fully instrumented blade is given in Table 5.1. Again, for the added mass, the mode shape characterisation was not altered by the Gurney flap mechanism, while the frequencies of the given modes were decreased up to 1.6%. As a result, it seems that the uncertainty due to the Gurney flap is of the same order of magnitude with the one introduced due to the different tip shape designs.

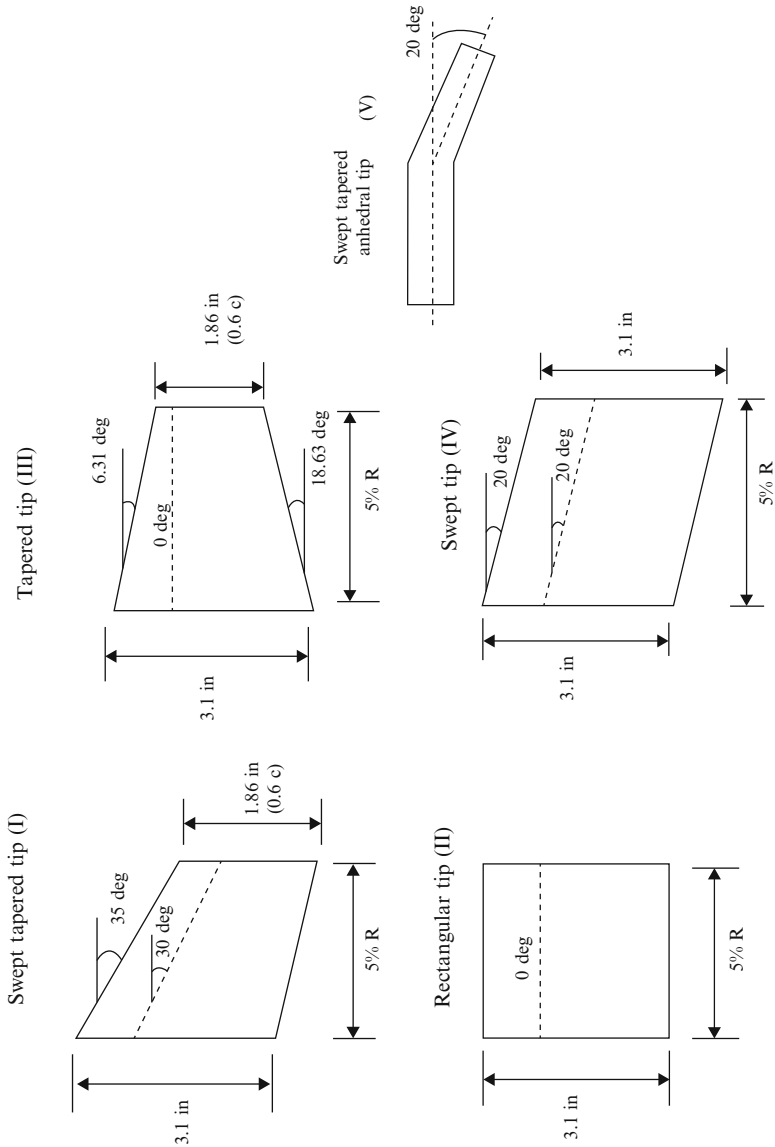


Fig. 5.1 Different tip shapes of S-76 blade (Garcia and Barakos 2015)

5.2 Closed Loop Control

For the forward flight of the W3-Sokol rotor, CFD computations for the clean rotor were used to derive the flap actuation schedule. However, in actual helicopter flight, there must be a controller that will actuate the Gurney flap based on some

Table 5.1 Mode shapes frequencies for clean blade and blade with fixed Gurney flap in hover

Mode shape	Clean blade frequency [Hz]	Blade with Gurney flap frequency [Hz]	Difference [%]
1st chordwise	3.2738	3.2551	-0.57
1st flapping	4.7496	4.7249	-0.52
2nd flapping	12.3107	12.1162	-1.58
2nd chordwise	19.7262	19.5171	-1.06
3rd flapping	21.763	21.4257	-1.55
4th flapping	33.479	33.1141	-1.09
5th flapping	47.973	47.3254	-1.35
3rd chordwise	50.1519	49.8109	-0.68
1st torsional	64.9486	64.3511	-0.92
2nd torsional	84.5769	83.3505	-1.45

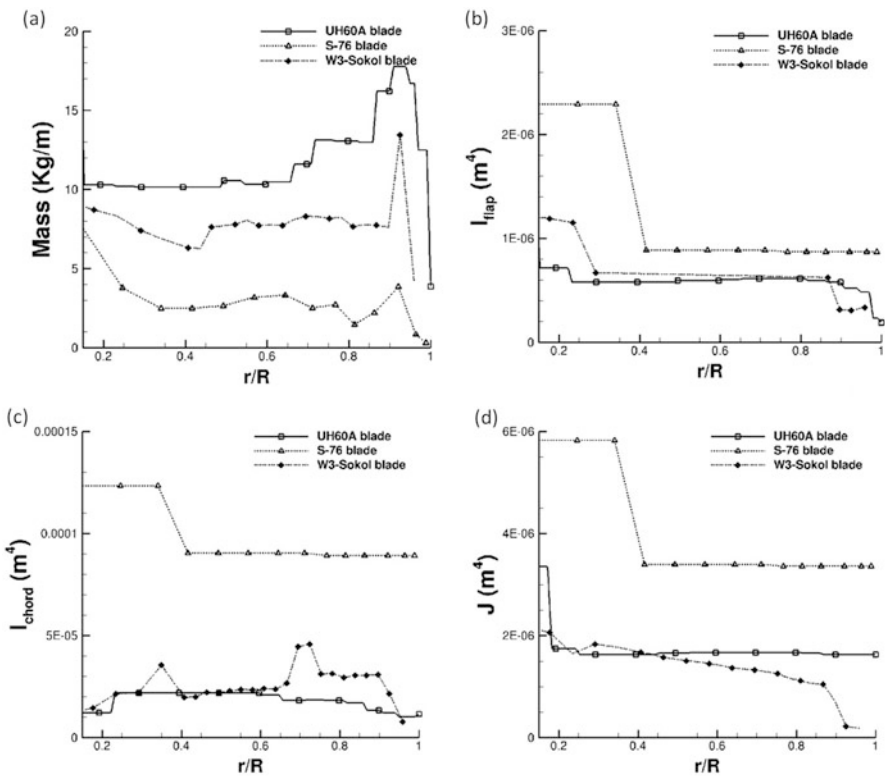


Fig. 5.2 Structural properties of different blades used for static computations. (a) Mass distribution. (b) Flapwise moment area of inertia. (c) Chordwise moment area of inertia. (d) Torsional constant

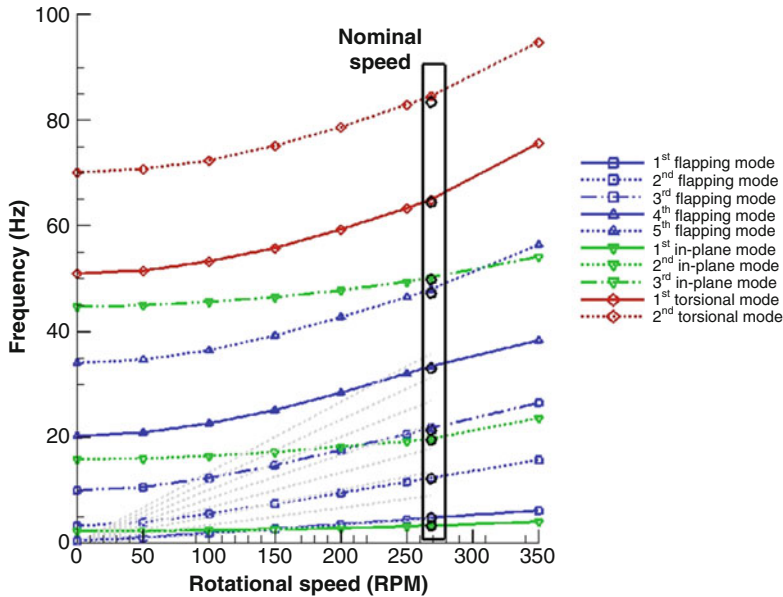


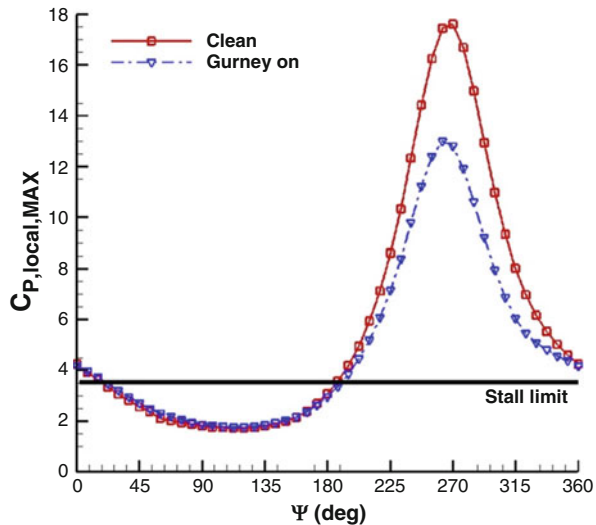
Fig. 5.3 Spoke diagram for W3-Sokol blade. Circles are used for blade with Gurney flap

observations of flight parameters. The idea is to detect the pressure divergence at the leading edge of the blade section that is indicative of stall, and if that exceeds a threshold, then the flap will be actuated. Moreover, the 1/rev actuation of the Gurney that was used in the previous chapter could introduce limitations on the handling and trimming of the helicopter. This topic was addressed by building a generic rotorcraft and performing several linear/nonlinear analyses to study its response to different control inputs.

5.2.1 2D Closed Loop Control

An NACA23012M aerofoil section was set to pitching-translating (dMdt) motion (Woodgate and Barakos 2012). The aim was to investigate retreating blade stall to identify divergence of the c_p peaks at the suction side of a blade section that could be used for the closed loop actuation of the Gurney. During the pitching-translation computations, the pressure coefficient at the leading edge increased gradually at first, and then the gradient became steeper before it reduced markedly, and it even reduced when the aerofoil stalled. The c_p threshold when the flow was about to separate was estimated close to -3.5 . Figure 5.4 compares the maximum pressure coefficient that was observed at the clean aerofoil and at the aerofoil with the active Gurney during the dMdt computations. For that particular actuation, two revolutions are needed for the flow to converge before the c_p is extracted to compute the Gurney schedule.

Fig. 5.4 Pitching-translating aerofoil— $c_{p,MAX}$ criterion



Then, the aerofoil must be trimmed at the clean mean C_L and extract the new pressure coefficient to adjust the Gurney flap deployment. After a total number of eight revolutions, the lift is trimmed, and the aerodynamic loads are presented in Fig. 5.5a–c. Figure 5.5d presents the pitching motion change of the aerofoil during the Gurney actuation and the trimming of the aerofoil. The high harmonics that appear could be justified by the fact that during the actuation, the Gurney flap sheds small vortices behind. Figures 5.6 and 5.7 show the streamlines near the trailing edge for different azimuth steps and how the separated flow is reattached after the actuation of the Gurney. It should also be mentioned that the c_p limit that defines the onset of the stall is only valid when the flow is fully attached. That means that when the flow is separated and it reattaches again, then this pressure threshold is significantly higher. In that case, $c_p = 5$ is the indicative value for the Gurney retraction, as the flow seems to be completely reattached on the aerofoil after the actuation of the flap. This can be seen in Fig. 5.8 where the flow is visualised at different steps.

5.2.2 W3-Sokol Closed Loop Control

Next, the pressure divergence criterion was used for the elastic W3-Sokol rotor at high advance ratio forward flight. The idea was to measure the pressure coefficient at different sections along the blade around the azimuth and identify Ψ , where part of the blade was experiencing stall. Figure 5.9 presents the pressure coefficient at two different sections along the blade span. Based on that criterion, the new actuation schedule of the Gurney was defined as presented in Fig. 5.10. It is observed that

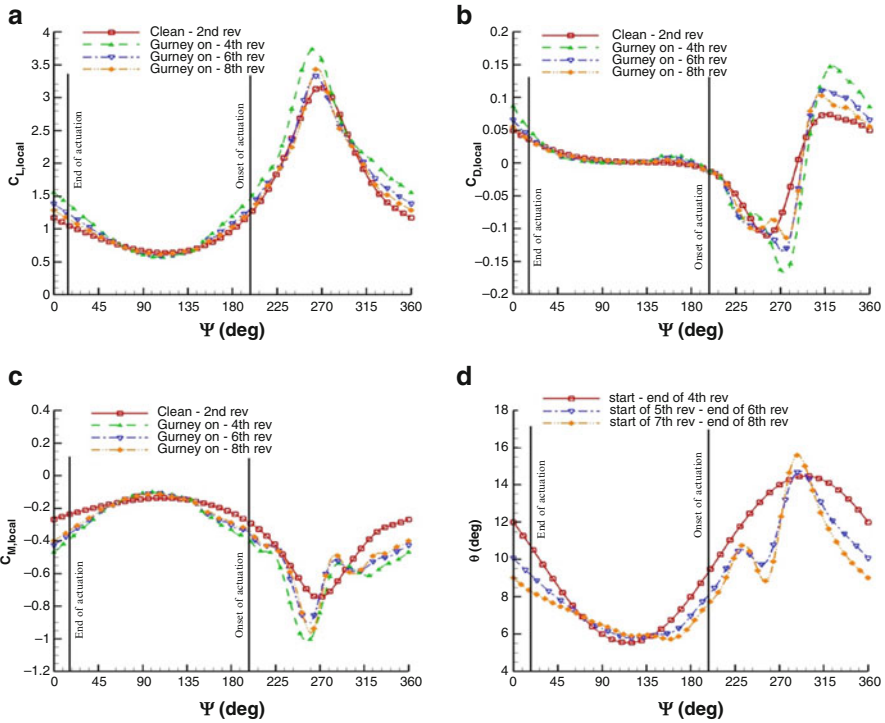


Fig. 5.5 Pitching-translating aerofoil. (a) C_L , (b) C_d , (c) C_m loads, and (d) pitching schedule during control implementation

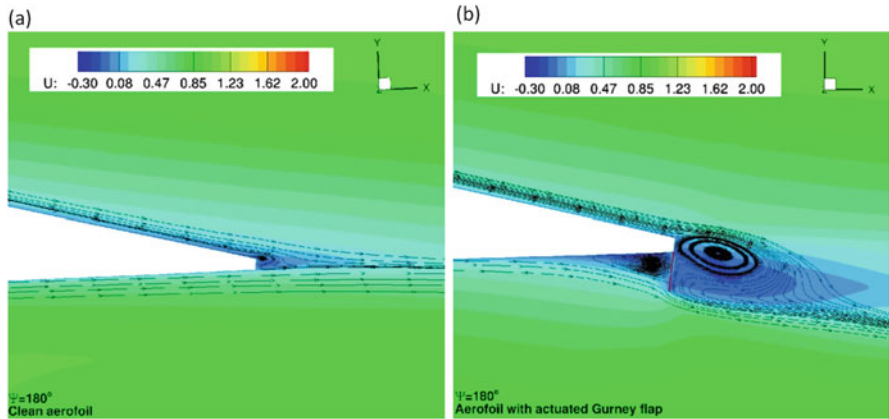


Fig. 5.6 Pitching-translating aerofoil—streamlines near the trailing edge at $\Psi = 360^\circ$. (a) Clean aerofoil. (b) Aerofoil with Gurney flap

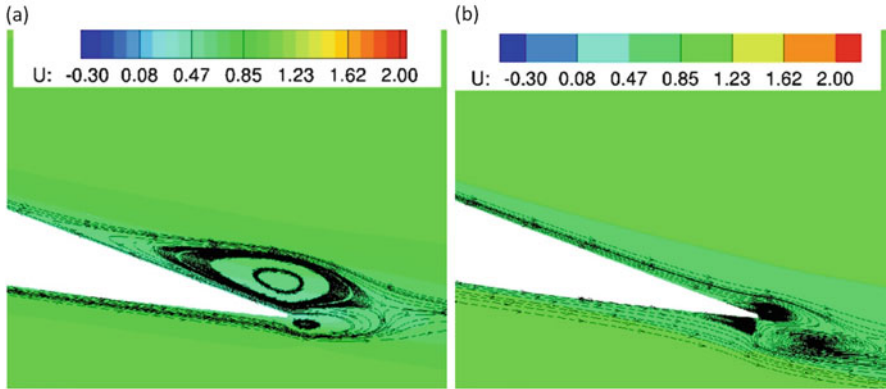


Fig. 5.7 Pitching-translating aerofoil—streamlines near the trailing edge at $\Psi = 270^\circ$. (a) Clean aerofoil. (b) Aerofoil with Gurney flap

it is very similar to the one used in the previous section for the open loop control, but this time the onset and end of the actuation took place earlier. The pressure distribution was also extracted after the actuation of the Gurney and at the end of the trimming process. Before trimming the rotor at the clean case thrust, setting the implementation of the Gurney leads the blade section in a deeper stall, while once the rotor was trimmed, the blade was pitched down, and part of the initial stall was removed. As can be seen in Fig. 5.11, the maximum pressure coefficient has decreased significantly. This fact led to a further reduction of the torque requirement predicted during the open loop control for the same flight case, which is about 0.5% (Fig. 5.12).

5.3 Effect of Gurney Flap on Full Helicopter Model

This section describes the development of a simulation model for a generic light utility helicopter (GLUH). The model is built in FLIGHTLAB environment (ART nd) for handling qualities and flight control investigations.

5.3.1 FLIGHTLAB Model

For this final analysis, the elasticity of the blade was neglected, and none of the unsteady aero models available on FLIGHTLAB was activated. The ONERA stall model was also used, but the final trim state was not significantly changed. This was done intentionally since the aim was to come up with an efficient although approximate method for these computations. The main effect of the Gurney flap was,

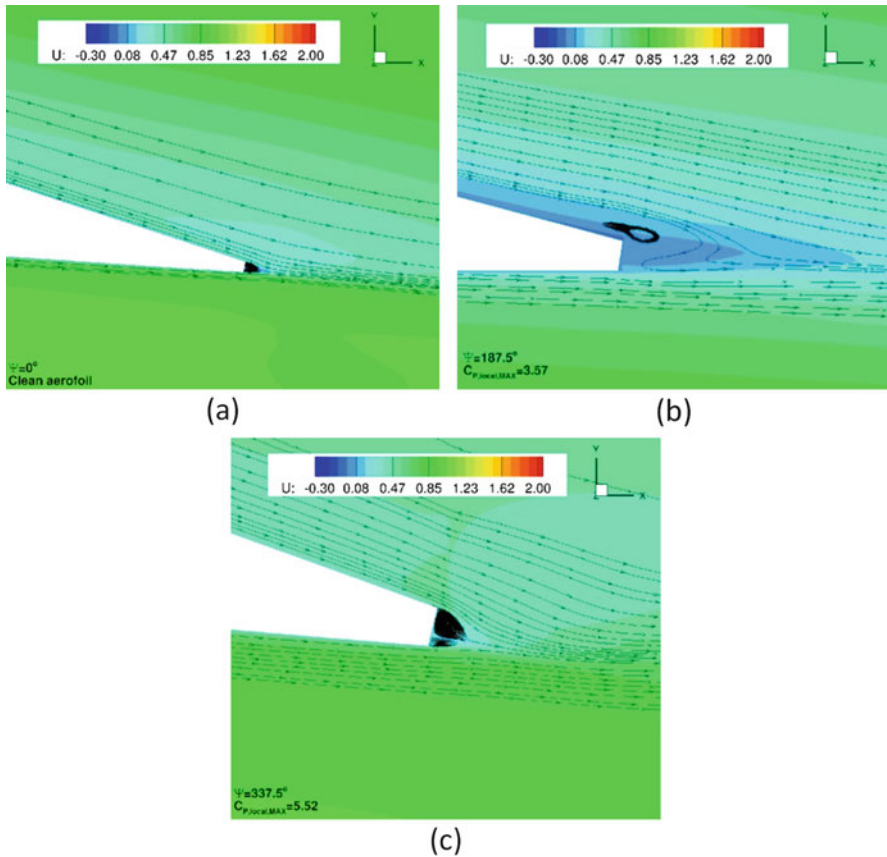


Fig. 5.8 Pitching-translating aerofoil—streamlines for clean aerofoil at (a) $\Psi = 0^\circ$, (b) $\Psi = 187.5^\circ$, and (c) $\Psi = 337.5^\circ$

however, captured even with this low fidelity method. The GLUH has a conventional configuration with high-mounted tail boom carrying fixed horizontal stabiliser and twin fins. The main rotor hub is a hingeless design with a torsion bar.

A blade element rotor module was used as the rotor model. The blade element rotor model considers rotor dynamic degrees of freedom for each individual blade, either rigid or elastic. For this study, a rigid blade was assumed. It computes the air loads with respect to the local angle of attack and Mach number and calculates blade dynamic response for no uniform blade inertial and aerodynamic properties (e.g., chord and twist).

The blade element articulated rotor model includes blade hinges for feathering, flapping, and lead-lag.

The feathering hinge is modelled via control hinge and, thus, has no degree of freedom, while the flap and lead-lag hinges are modelled with dynamic hinge of one rotational degree of freedom. Flap or lead-lag stop is modelled via nonlinear

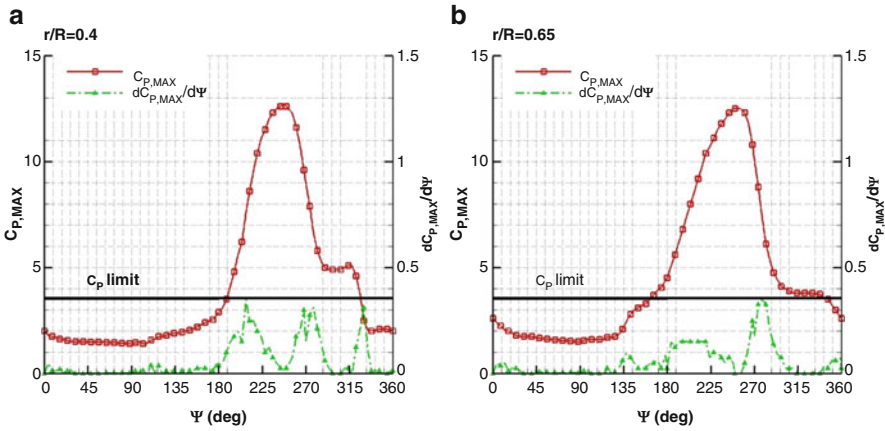


Fig. 5.9 Pressure divergence around azimuth. (a) $r/R = 0.4$. (b) $r/R = 0.65$

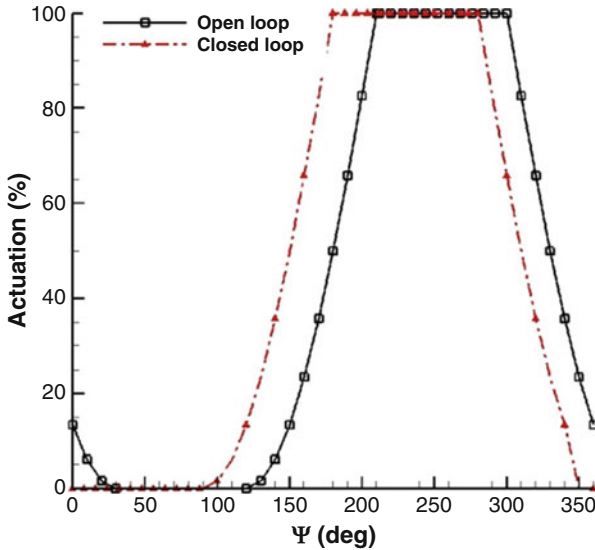


Fig. 5.10 Gurney flap actuation schedule comparison against open loop control

torsional spring/damping with further option of spring/damping dependence. The blade stop model table data are defined based on the blade flap or blade lag angle.

For the baseline model, a quasi-steady aerodynamic component was used for the air load calculation on the blade elements. The blade aerodynamic segments are defined based on the equal annuli area approach. This means that the segment length becomes finer towards the tip of the blade, while the aerodynamic loads are calculated by treating the blade sections as two-dimensional panels as described before.

Fig. 5.11
 $r/R = 0.5$ —pressure
 divergence around azimuth
 for blade with Gurney flap

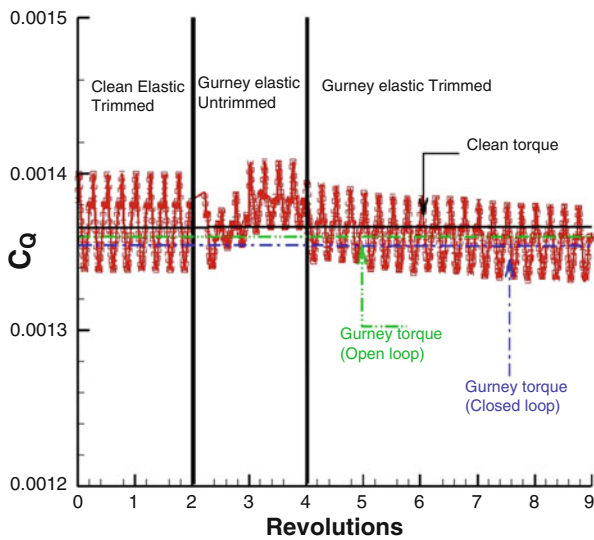
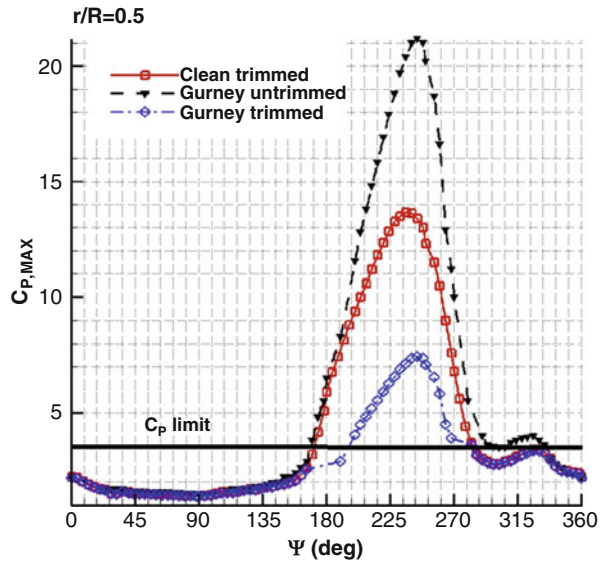


Fig. 5.12 Torque requirement for closed loop actuation of the Gurney flap

The NACA23012M sections was used, and the data were represented in table look-up form with lift, drag, and pitching moment coefficients tabulated against angle of attack (-180° to 180°) and Mach number (0–0.9 Mach). The GLUH model described in this work makes use of the Peters-He three-state dynamic wake models. This model captures the uniform and first harmonic distribution of the inflow and the transient response of these inflow components in manoeuvring flight. This

methodology also models the dynamic response of the inflow to manoeuvring flight and predicts the off-rotor components of inflow for use in interference modelling at the fuselage and tail.

FLIGHTLAB's Bailey rotor component is used to model the tail rotor. In the Bailey model, closed form expressions for rotor thrust and torque are obtained analytically by integrating the air loads over the rotor blade span and averaging them over the azimuth. Only rotor coning is considered, and hence there is no provision for blade cyclic pitch inputs. The induced velocity is computed from a uniform inflow model and included in the model. The following assumptions are employed in the derivation of the tail rotor equations:

1. Constant chord and linear twist
2. Linear lift with lift curve slope
3. Incompressible flow
4. No individual blade dynamics, except for the steady-state coning
5. Uniform induced flow over the rotor

There are several modelling options available within FLIGHTLAB for the fuselage aerodynamics, including a panel method and a simple table look-up. For the Generic model, the table look-up option was chosen where the fuselage coefficients are supplied by means of look-up tables as functions of angle of attack and sideslip angle.

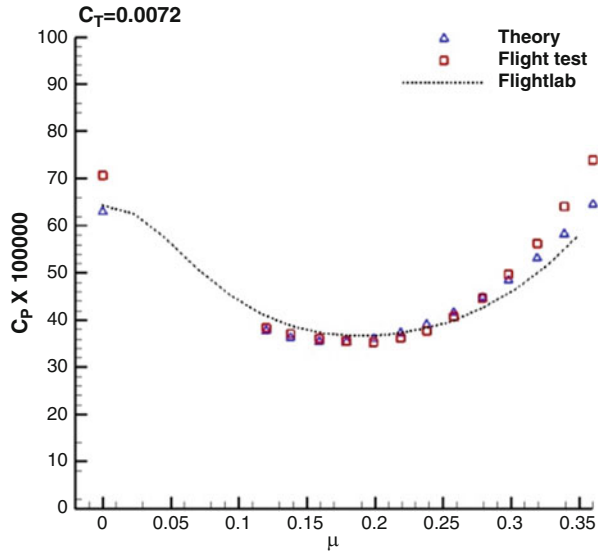
The GLUH model uses an NACA23015 aerofoil for the horizontal stabiliser and an NACA0012 for the vertical fins. Again the aerodynamic loads were imported by the use of 2D look-up tables based on the performance of these aerofoils. Regarding the power plant, two gas turbine engines PW207K of PRATT & WHITNEY company with take-off power of 630 HP each were used. The engine was modelled using the ideal engine.

Modelling the aerodynamic interactions is a challenging aspect of rotorcraft simulation. A simple and effective way of interactional modelling is by incorporating look-up tables representing the downwash/up-wash velocities at the respective aerodynamic surfaces, defined by the values of loads on the generating surface. In the absence of empirical/experimental data, the off-rotor induced velocity predicted by FLIGHTLAB's inflow model is used for the calculation of the effect of the main rotor wake on fixed aerodynamic surfaces. From the finite-state dynamic wake equations, the induced velocity at an arbitrary flow field point can be computed. The Generic model utilises this finite-state dynamic inference model for the main rotor wake effects. The main rotor wake interference is applied to both the empennage and the fuselage.

5.3.2 FLIGHTLAB Validation

Before testing the generic light utility model, FLIGHTLAB was validated using the UH-60 Black Hawk helicopter, and the results were compared against flight test

Fig. 5.13 Power coefficient for UH-60A Black Hawk helicopter. FLIGHTLAB model against theory and flight test data (Yeo et al. 2004)



data (Kufeld et al. 1994) and theory predictions. Figure 5.13 presents the power coefficient for different flight speeds. FLIGHTLAB gave good predictions between medium and high speed although it did not agree with the flight test in hover case. Moreover, the accuracy of the calculation degrades at high gross weight the same way it was observed in the previous study (Yeo et al. 2004).

5.3.3 Designed Controller for Closed Loop Analysis

The controller was designed by Kazan University, and it was based on the controller presented by Garkushenko et al. (2014). The unknown parameters and the system nonlinearity are considered as external disturbances. The controller was designed using feedback with compensation for disturbances estimated using observers. In order to simplify the procedure of the controller design, its dynamics equations are presented in the following form:

$$\begin{aligned}
 \dot{X}_1 &= R(X_3) X_2 \\
 \dot{X}_2 &= F_1(X_2, X_4, X_5, U_0, W) \\
 \dot{X}_3 &= S^{-1}(X_{32}) X_4 \\
 \dot{X}_4 &= F_2(X_2, X_4, X_5, U_1, W) \\
 \dot{X}_5 &= F_3(X_4, X_{52}, U_2)
 \end{aligned}
 \tag{5.1}$$

where $X_1 = [xyz]^T$ is the position vector; $X_2 = V$, $X_3 = n$, $X_{32} = [\theta\varphi]^T$, $X_4 = \omega$, $X_5 = [a_s b_s \delta_{\text{ped, int}}]^T$, and $X_{52} = [a_s b_s]^T$; $\delta_{\text{ped, int}}$ is the intermediate state of yaw rate feedback controller; $U_0 = [U_0^T \delta_{\text{ped}} \delta_{\text{col}}]^T$, $U_0 = \text{diag}\{-g, g \cos \theta\} u_{01}$, $u_{01} = [\sin \theta \sin \varphi]^T$; $U_2 = [\delta_{\text{lon}} \delta_{\text{lat}} \delta_{\text{ped}}]^T$, $U_1 = [\delta_{\text{ped}} \delta_{\text{col}}]^T$, δ_{ped} , and δ_{col} are the normalised pedal and collective pitch inputs, respectively; $R(X_3)$ and $S(X_{32})$ are the rotation and kinematic transformations matrices, respectively; and $W = [u_{\text{wind}} v_{\text{wind}} w_{\text{wind}}]^T$ are the wind actions in the body coordinate system.

We introduce the state vector $X = [x_1^T x_2^T x_3^T x_4^T x_5^T]^T$ and control signals vector $U = [\delta_{\text{lon}} \delta_{\text{lat}} \delta_{\text{ped}} \delta_{\text{col}}]^T$. When balancing the helicopter in hover condition, we assume $U^* = [\delta_{\text{lon}}^* \delta_{\text{lat}}^* \delta_{\text{ped}}^* \delta_{\text{col}}^*]^T$, $X^* = [x_0 y_0 z_0 0 0 0 \theta^* \varphi^* 0 0 0 a_s^* b_s^* 0]^T$. Equation (5.1) can be rewritten in terms of deviations from the trimmed condition as:

$$\begin{aligned} x &= X - X^* = [x_1^T x_2^T x_3^T x_4^T x_5^T]^T \\ u &= U - U^* = [\Delta \delta_{\text{lon}} \Delta \delta_{\text{lat}} \Delta \delta_{\text{ped}} \Delta \delta_{\text{col}}]^T \\ x_1 &= [\Delta x \Delta y \Delta z]^T, x_2 = [uvw]^T \\ x_3 &= [\Delta \theta \Delta \varphi \Delta \psi]^T, x_4 = [qpr]^T \\ x_5 &= [\Delta a_s \Delta b_s \delta_{\text{ped, int}}]^T \end{aligned} \quad (5.2)$$

Then, the resulting system of equations represented in a form suitable for the synthesis of control is given below:

$$\dot{x}_1 = R(X_3) x_2 \quad (5.3)$$

$$\dot{x}_2 = A_1(X_{31}) u_0 + f_1 \quad (5.4)$$

$$\dot{x}_3 = S^{-1}(X_{32}) x_4 \quad (5.5)$$

$$\dot{x}_4 = A_2 x_5 + f_2 \quad (5.6)$$

$$\dot{x}_5 = B_0 u_1 + f_3 \quad (5.7)$$

Here, $X_3 = X_3^* + x_3$, $X_{31} = \theta^* + \Delta \theta$, $X_{32} = X_{32}^* + x_{32}$, $x_{32} = [\Delta \theta \Delta \varphi]^T$; $u_0 = [u_{01}^T \Delta \delta_{\text{col}}]^T$, u_{01} is the virtual control for the outer loop to move the helicopter relative to the earth coordinate system; $u_1 = [\Delta \delta_{\text{lon}} \Delta \delta_{\text{lat}} \Delta \delta_{\text{ped}} \Delta \delta_{\text{col}}]^T$; f_i , $i = \overline{1, 3}$ are the vectors of generalised disturbances derived from the original Eq. (5.1) after the isolation of the terms $A_1(X_{31})u_0$, $A_2 x_5$, $B_0 u_1$, where $A_1(X_{31}) = \text{diag}\{-g, g \cos \theta, b_1\}$, b_1 is the model parameter; A_2 , B_0 are the diagonal matrices of the model parameter.

5.3.4 Synthesis of Control Law with Observers

To achieve the desired helicopter stability, it is necessary to provide compensation for the generalised disturbances f_i , $i = \overline{1, 3}$. However, as follows from Eqs. (5.3),

(5.4), (5.5), (5.6), and (5.7), the f_1 and f_2 cannot be fully compensated. Therefore, the control law is constructed so that it suppresses the generalised disturbances which affect the dynamics of the state vectors. To do this, an observer is used to construct estimates of the generalised disturbances. For the original system, represented by the equation:

$$\begin{aligned}\dot{x} &= Ax + Bu + Dw \\ y &= Cx + v\end{aligned}\tag{5.8}$$

where $x \in R^n$ is the state vector, $u \in R^m$ is the control vector, $w \in R^s$ and $v \in R^l$ are the vectors of disturbances and noise in measurements, respectively, the observer has the form:

$$\hat{x} = A\hat{x} + Bu + D\hat{w} + L_1(y - C\hat{x})\tag{5.9}$$

$$\hat{w} = \mu^{-1}(D^+L_1 + L_2)(y - C\hat{x})\tag{5.10}$$

where $D^+ = (D^T D)^{-1} D^T$, μ is an adjustable parameter, and L_1 and L_2 are the matrices of coefficients, which have to be determined. Using the observer of Eqs. (5.9) and (5.10), it is possible to achieve the desired accuracy in the estimate of the state vector coordinates and disturbances without significant increase of the coefficients of the observer matrices.

5.3.5 Handling Qualities

The main purpose of building this generic model was the observation of the Gurney flap effect on the trimming and the handling qualities of a helicopter. Typically, a 4 per rev actuation of plain flaps has been used on rotorcraft. However, in this study, a 1 per rev actuation was implemented, which could introduce additional moments on the helicopter and result in difficulties during trimming or deterioration of the handling qualities.

A comparison between nonlinear response of the body pitch rate and acceleration to a sinusoidal collective input is presented in Fig. 5.14 to evaluate the effect of a controller with the observers against a simple PID controller. The behaviour of the two systems was very different. The main difference is observed on the stability. When the PID is used, the model becomes very unstable, and once it starts diverging from the trim condition, it never goes back to the equilibrium point. However, when the robust controller is implemented, the model becomes stable again, and it goes back to the equilibrium within a very short time.

Regarding the handling qualities of the model, FLIGHTLAB is in general able to derive them. However, only one of the available tests produced meaningful results, and it is used to compare the effect of the designed controller on improving the

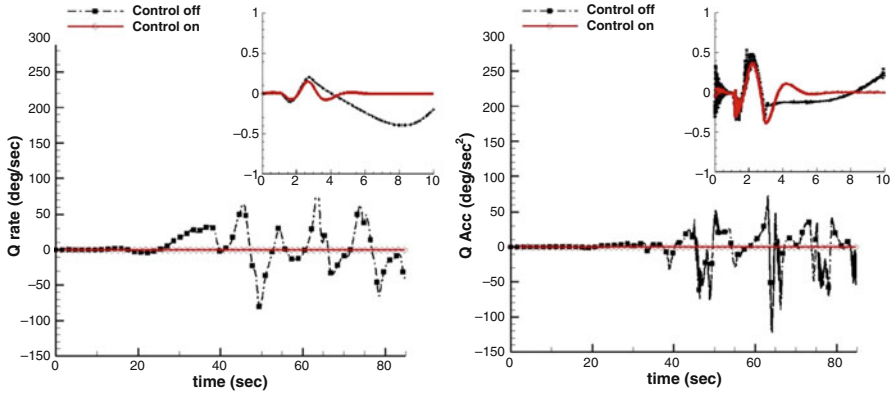


Fig. 5.14 Nonlinear response of (a) body pitch rate and (b) body pitch acceleration to sinusoidal collective input. “Control off” and “control on” correspond to PID and controller with observers, respectively

manoeuvrability of the rotorcraft. This test was related to hover and low speed requirements and especially to small-amplitude pitch (roll) attitude response to control inputs. Based on [ADS-33E-PRF \(2000\)](#), this criterion has requirements on bandwidth and phase delay to prevent tendency of pilot-induced oscillation (PIO).

The midterm response characteristics shall apply at all frequencies below the bandwidth frequency. FLIGHTLAB generated the damping ratio of roll attitude response ζ and the natural frequency of roll attitude response ω_n for the model with and without the designed controller. For the case without the controller, the following results were obtained:

$\zeta = 0.12$ and $\omega_n = 2.89$ rad/s, while for the case with the controller, it produced $\zeta = 0.40$ and $\omega_n = 0.39$. Based on the Aeronautical Design Standard Performance Specification ADS-33E-PRF, the limits on pitch (roll) oscillations are presented below. According to those limits, the model cannot be qualified (level is greater than 3), but when the controller is used, the level improves to level 1. This fact clearly presents the ability of the designed controller to improve the dynamic characteristics of the rotorcraft. Moreover, based on [Fig. 5.15](#), when the Gurney flap is implemented in the model, it does not affect the rotorcraft handling qualities.

5.4 Conclusions and Future Work

In this work, the effect of the Gurney flap on the overall flight envelope of a helicopter was studied. Some significant remarks regarding the stall identification and the actuation of the Gurney flap were observed. The active actuation of the flap can be implemented on real helicopters by observing the pressure on the suction side of the rotor blades. If the pressure diverges from a threshold, then the flap would be actuated. This 1/rev actuation might cause vibration issues and alter the trimming

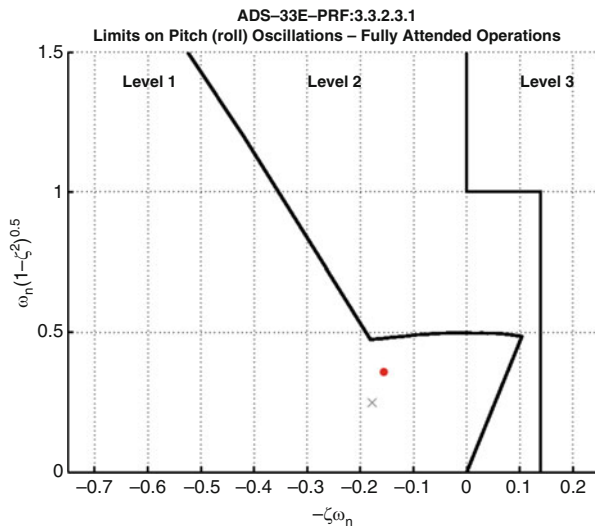


Fig. 5.15 Limits on pitch (roll) oscillations—hover and low speed. Red dot represents the clean rotor, while cross represents the rotor with the active Gurney flap

capability of the helicopter. For that reason, a generic light utility helicopter was built and tested on FLIGHTLAB with and without an active Gurney. The results showed that the flap will change neither the trimming ability of the model nor its handling qualities if there is a robust controller on the helicopter. Another issue was the possible effect of the flap on the structural dynamics of the blade. Thus, 10% of the original mass of the blade was distributed additionally on the blade, along the location of the Gurney, and a static analysis was conducted.

The mode shapes of the blade were not affected by the flap, while the frequencies of the modes at the nominal rotor speed were decreased by less than 2%. In fact, the uncertainty due to the Gurney was of the same order of magnitude of the one introduced by different tip shape designs tested for an S-76 blade.

To conclude, the potential effects of an active Gurney flap on the main rotor as well as on the response of the helicopter were studied using coupled fluid-structure dynamics. It was shown that the flap can enhance the performance of helicopters, especially at high thrust requirements, as it is an efficient flow control device for retreating blade stall alleviation. Some of the observed benefits are due to the aeroelastic reshaping of the blade due to the pitching moments induced by the flap. However, experimental data on rotors with active Gurney flaps are essential for further validation of the code and understanding of the Gurney effect on rotor aerodynamics.

In future, efforts should be directed towards the addition of the fuselage in CFD computations to study its interaction with the altered rotor wake due to the Gurney. Moreover, the effect of the flap can be further optimised by implementing multiple flaps along the rotor blade. Apart from the pressure divergence criterion that was put

forward to detect stall, other criteria should also be investigated. Finally, the active Gurney flap should be considered as a means to offload the advancing side of the rotor, and its effect should be investigated on rigid blades as well.

References

- ADS-33E-PRF (2000) Aeronautical design standard performance specification handling qualities requirements for military rotorcraft. Aviation Engineering Directorate, Redstone Arsenal, Alabama, March 21st, 2000
- ART (nd) Advanced Rotorcraft Technology. Von www.art.com abgerufen
- Garcia AJ, Barakos GN (2015) Hover performance predictions for the S-76 main rotor blade. In: AIAA 53th Aerospace Science Meeting and Exhibit, Kissimmee, FL
- Garkushenko VI, Vinogradov SS, Barakos GN (2014) Robust control synthesis for an unmanned helicopter. In: 40th European Rotorcraft Forum, Southampton, UK
- Kufeld R, Balough D, Cross J, Studebaker K, Jennison C, Bousman W (1994) Flight testing of the UH-60A airloads aircraft. In: American helicopter society 50th annual proceedings, Washington, DC
- Woodgate MA, Barakos GN (2012) Implicit computational fluid dynamics methods for fast analysis of rotor flows. *AIAA J* 50(6):1217–1244
- Yeo H, Bousman W, Johnson W (2004) Performance analysis of a utility helicopter with standard and advanced rotors. *J Am Helicopter Soc* 49(3):250–270

Chapter 6

Active Gurney Flap Unit

Ihor Berezin and R. Raczynski

6.1 Introduction

Development mass and geometric envelopes required in rotorcraft blades is still a challenge because of small actuation stroke of piezoelectric materials. Various stroke amplification mechanisms have been suggested to increase the output stroke by trading high actuation force with stroke (Lee and Chopra 2001; Thiel et al. 2006). The most common concepts use mechanical leverage amplification of stroke produced by piezoelectric or electrostrictive devices. The final design should minimize actuator weight and consider its placement so that the performance and dynamics of the rotor blade are not greatly affected. Additional constraints are imposed by reliability considerations. A set of basic requirements for use in active Gurney flap summarized by Barlas and van Kuik (2010) is as follows:

- Lightweight.
- Minimum sensitivity to temperature.
- Minimal effect on system dynamics (frequencies, mode shapes).
- Low maintenance requirements.
- As low as possible power and voltage requirements.
- Stiffness is important because of the disturbing nature of resonances within the actuator assembly.
- Fit within the limited envelope of the airfoils.
- Reliable operation in harsh environment.
- Maximum lifetime of components.
- Sufficient strength of components.

I. Berezin • R. Raczynski (✉)
WSK PZL Swidnik S.A, Swidnik, Poland
e-mail: ihor.berezin@agustawestland.com; radoslaw.raczynski@leonardocompany.com

A simple yet effective and reliable mechanism with voice coil actuator was suggested by Thiel et al. (2006). The actuator is quite simple yet robust and requires low maintenance. A number of concepts were suggested by Lee and Chopra (2001). Among them is a piezostack actuator combined with mechanical amplifier for active trailing edge control. A bidirectional L-L actuator was designed and fabricated featuring bidirectional actuation using two piezostack segments. The overall size of the prototype actuator is 8 in. length, 1.25 in. width and 0.75 in. height with ten P-804.10 piezostacks. The amplification factor of the prototype actuator is set to 15, and the preliminary bench-top testing showed about 94 % of its ideal displacement output. It was shown that integrated actuator-amplifier system is more effective in terms of stroke amplification compared to separated systems.

6.2 Gurney Flap Actuation Mechanism Concept

Unfortunately, none of these concepts can be used for PZL W-3 Sokol main rotor blade due to geometric restrictions imposed by airfoil dimensions. The goal of this chapter is to design a Gurney flap actuation mechanism with amplified piezoelectric actuators. APA500L piezostack actuator with blocked force of 550 N, full stroke of 0.47 mm, mass of 0.135 kg and dimensions of 16×49 (actuation direction) $\times 147$ mm is suggested by Cedrat Technologies.

The idea of active Gurney flap system is increase of helicopter performance. The flap would be deployed when the blade is retreating, that is, deployment frequency is $1/Rev$. Gurney flap parameters have been determined in the earlier investigations. The following dimensions are considered:

Span	$0.25R$
Height	$0.02c$
Location along radius: starting point at	$0.46R$
Location along blade chord	$0.95c$

Three concepts for deployment trajectory were considered: linear, rotational and plane flap motion. The first two would result in simple design of leverage system, but in case of linear actuation, there is not enough space inside the airfoil for housing the Gurney flap in retracted position. For rotational motion, high value of angle of rotation (around 100°) is required for full deployment. Together with high aerodynamic forces acting on the flap of this type, it makes use of this configuration impossible for the case under consideration without significant complication of the system.

Considering geometric constraints inside the airfoil and Gurney flap parameters, a system comprising of an actuator, lever amplifier and a four-rod deployment linkage is proposed (Fig. 6.1). Such kinematics of the flap ensures deployment with minimal aerodynamic resistance, yet it is compact and easily fits in retracted

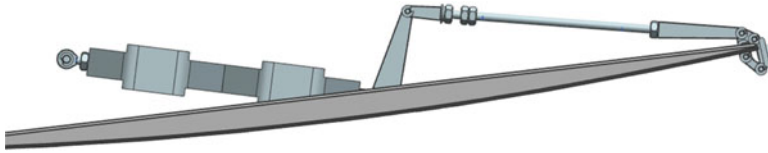


Fig. 6.1 Gurney flap actuation system

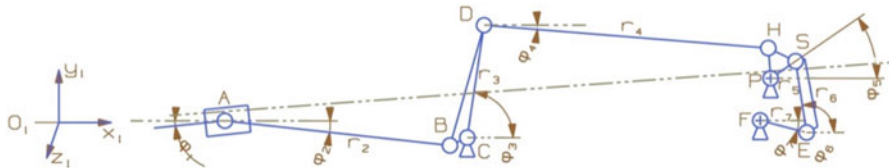


Fig. 6.2 Gurney flap actuation system kinematics

position inside the narrow toe part of the airfoil. Mass of the actuator comprises about 80% of the total active Gurney flap system. To ensure the aeroelastic stability of the airfoil section, actuator was mounted as far forward in the airfoil as space would allow.

A linear model of the mechanism was developed and used to simulate the response of the flap/actuator system. The simulation was developed to predict flap deflection as a function of actuator displacement δ as well as angular velocities ω_i , accelerations α_i and forces acting in the links. Dimensions of the links were selected to engage the maximum range of the actuator stroke and ensure Gurney flap deployment within geometrical constraints inside the airfoil. In the model, all parts are rigid.

6.2.1 Position Analysis

Let O_{xyz} (Fig. 6.2) be the global-fixed orthogonal Cartesian coordinate system. $OI_xI_yI_zI$ is a rotating (body-fixed) orthogonal Cartesian coordinate system: OI_yI parallel to Oy and OI_xI parallel to Ox . MR rotates around O with angular velocity $\Omega = \{\Omega_x \Omega_y \Omega_z\}$.

The system can be separated into three vector loops:

- Actuator loop with joints $A-C-B$
- Amplifier loop $C-D-H-P$
- Actuation loop $P-S-E-F$

Sum of vectors connecting points within every loop is zero therefore yielding a system of three vector loop equations. Position analysis is performed by projecting the vector loop equations of a mechanism onto the axes of body-fixed coordinate

system. This projection transforms a vector equation into two algebraic equations. Then, for a given value of actuator position, the algebraic equations are solved for the position of the remaining links. The first and second time derivative of the algebraic position equations provide the velocities and accelerations of the mechanism.

Vector loop equations for the system:

$$\begin{cases} \vec{r}_2 + \vec{r}_{31} - \vec{r}_{AC} = 0 \\ \vec{r}_{32} + \vec{r}_4 - \vec{r}_{CP} - \vec{r}_{51} = 0 \\ \vec{r}_{52} + \vec{r}_6 - \vec{r}_{PF} - \vec{r}_7 = 0 \end{cases}$$

Here, $\vec{r}_2 = \vec{r}_{AC} + \vec{\delta}$; \vec{r}_{31} is vector BC; \vec{r}_{51} is vector PH.

The vector loop equations are projected onto $OIxI$ and $OIyI$ axes to obtain algebraic equations:

$$\begin{cases} r_3c_2 + r_{31}c_{31} - r_{AT}c_1 = 0 \\ r_2s_2 + r_{31}s_{31} - r_{AT}s_1 = 0 \\ r_3c_3 + r_4c_4 - r_{CP}c_8 - r_{51}c_{51} = 0 \\ r_3s_3 + r_4s_4 - r_{CP}s_8 - r_{51}s_{51} = 0 \\ r_5c_5 + r_6c_6 - r_{PF}c_9 - r_7c_7 = 0 \\ r_5s_5 + r_6s_6 - r_{PF}s_9 - r_7s_7 = 0 \end{cases}$$

Here, $c_i = \cos(\varphi_i)$; $s_i = \sin(\varphi_i)$; φ_{31} is the angle between BC and CD; φ_{51} , angle between HP and PS; φ_8 , angle between CF and xI axis; and φ_9 , angle between PF and xI axis.

Solution of this system provides the position angles for the links of the mechanism. Geometry of the output linkage results in plane motion of Gurney flap (Fig. 6.3). A significant drawback of concept with plane flap motion is the inevitability of a gap in the airfoil near the flap. Dimensions of the output linkage were optimized to decrease the gap to 1.6 mm. Additional measures are to be taken to decrease negative influence of the gap.

Gurney flap deployment as a function of actuator displacement is shown on Fig. 6.4. For this case of motion, deployment fraction is calculated as factor of GF projection onto the normal to blade chord and full length of the flap, that is:

$$Gf = \frac{l_{gf} \times \sin \alpha}{l_{gf,100\%}}$$

l_{gf} is the current length of the GF outside the airfoil; α , angle between GF and blade chord; and $l_{gf,100\%} = 8.8$ mm, total height of deployed GF.

Once the $Gf(\delta)$ is known, actuator schedule as a function of blade azimuth $\delta(\Psi)$ can be retrieved by mapping required deployment schedule $Gf(\Psi)$ onto the $Gf(\delta)$.

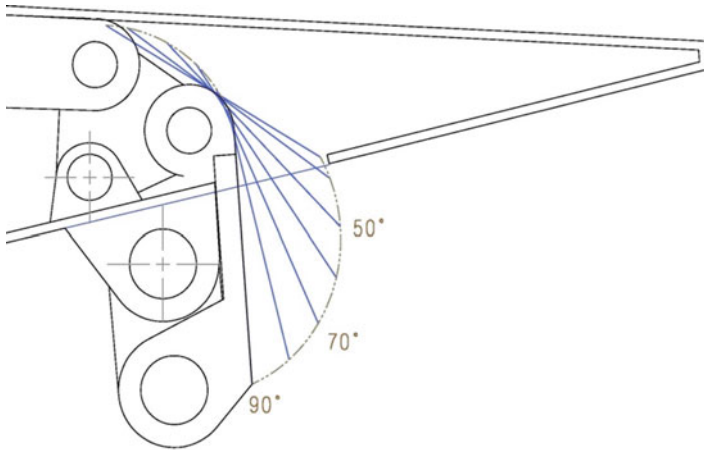
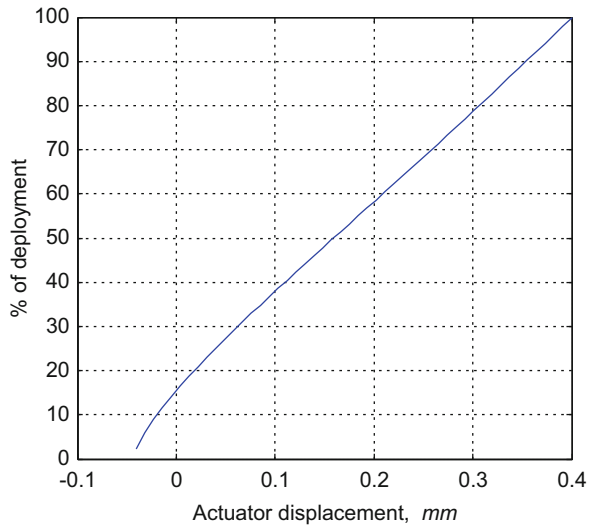


Fig. 6.3 Trajectory of Gurney flap motion

Fig. 6.4 Deployment fraction as a function of actuator displacement



6.2.2 Velocity Analysis

Velocity of a point moving with a rotating blade:

$$\vec{V}_i = \vec{V}_{O1} + \vec{\omega}_i \times \vec{r}_i = \vec{\Omega} \times \vec{r}_{OO1} + \vec{\omega}_i \times \vec{r}_i$$

Here, $\omega_i = \{\omega_{ix} \ \omega_{iy} \ \omega_{iz}\}$ is the full angular velocity vector in body-fixed reference frame. Since all the links rotate about zI axis, ω_{iz} is the only non-zero component of ω_i .

Time derivative of position equation gives the system of equations with unknown zI components of angular velocities for mechanism links.

$$\begin{cases} -\omega_2 r_2 s_2 - \omega_3 r_{31} s_{31} - V_1 c_1 = 0 \\ \omega_2 r_2 c_2 + \omega_3 r_{31} s_{31} - V_1 s_1 = 0 \\ -\omega_3 r_3 s_3 - \omega_4 r_4 s_4 + \omega_5 r_{51} s_{51} = 0 \\ \omega_3 r_3 c_3 + \omega_4 r_4 c_4 - \omega_5 r_{51} c_{51} = 0 \\ -\omega_5 r_5 s_5 + \omega_6 r_6 s_6 + \omega_7 r_7 s_7 = 0 \\ \omega_5 r_5 c_5 - \omega_6 r_6 c_6 - \omega_7 r_7 c_7 = 0 \end{cases}$$

In matrix form:

$$\begin{bmatrix} -r_2 s_2 & -r_{31} s_{31} & 0 & 0 & 0 & 0 \\ r_2 c_2 & r_{31} c_{31} & 0 & 0 & 0 & 0 \\ 0 & -r_3 s_3 & -r_4 s_4 & r_{51} s_{51} & 0 & 0 \\ 0 & r_3 c_3 & r_4 c_4 & -r_{51} c_{51} & 0 & 0 \\ 0 & 0 & 0 & -r_5 s_5 & -r_6 s_6 & r_7 s_7 \\ 0 & 0 & 0 & r_5 c_5 & r_6 c_6 & -r_7 c_7 \end{bmatrix} \begin{Bmatrix} \omega_2 \\ \omega_3 \\ \omega_4 \\ \omega_5 \\ \omega_6 \\ \omega_7 \end{Bmatrix} = \begin{Bmatrix} V_1 c_1 \\ V_1 s_1 \\ 0 \\ 0 \\ 0 \\ 0 \end{Bmatrix}$$

Acceleration analysis. Acceleration of CGs of links:

$$\begin{aligned} \vec{a}_i &= \vec{a}_{O1} + \vec{\alpha}_i \times \vec{r}_{CG,i} + \vec{\omega}_i \times (\vec{\omega}_i \times \vec{r}_{CG,i}) \\ &= \vec{\alpha}_0 \times \vec{r}_{OO1} + \vec{\Omega} \times (\vec{\Omega} \times \vec{r}_{OO1}) + \vec{\alpha}_i \times \vec{r}_{CG,i} + \vec{\omega}_i \times (\vec{\omega}_i \times \vec{r}_{CG,i}) \end{aligned}$$

Here, α_0 is angular acceleration of blade in fixed reference frame.

Values of angular accelerations α_i are calculated by differentiating the system of velocity equations and solving the resulting acceleration system of equations about acceleration unknowns. Same as with angular velocities ω_i , the only non-zero component of $\alpha_i = \{\alpha_{ix} \alpha_{iy} \alpha_{iz}\}$ zI components of angular accelerations α_{iz} :

$$\begin{cases} -\alpha_2 r_2 s_2 - \alpha_3 r_{31} s_{31} = r_2 \omega_2^2 c_2 - r_{31} \omega_3^2 c_{31} + a_1 c_1 \\ \alpha_2 r_2 c_2 + \alpha_3 r_{31} s_{31} = r_2 \omega_2^2 s_2 - r_{31} \omega_3^2 c_{31} + a_1 s_1 \\ -\alpha_3 r_3 s_3 - \alpha_4 r_4 s_4 + \alpha_5 r_{51} s_{51} = r_{32} \omega_3^2 c_3 + r_4 \omega_4^2 c_4 - r_{51} \omega_5^2 c_{51} \\ \alpha_3 r_3 c_3 + \alpha_4 r_4 c_4 - \alpha_5 r_{51} c_{51} = r_{32} \omega_3^2 s_3 + r_4 \omega_4^2 s_4 - r_{51} \omega_5^2 s_{51} \\ -\alpha_5 r_5 s_5 + \alpha_6 r_6 s_6 + \alpha_7 r_7 s_7 = r_{52} \omega_5^2 s_3 - r_6 \omega_6^2 s_6 - r_7 \omega_7^2 s_7 \\ \alpha_5 r_5 c_5 - \alpha_6 r_6 c_6 - \alpha_7 r_7 c_7 = r_{52} \omega_5^2 c_3 - r_6 \omega_6^2 c_6 - r_7 \omega_7^2 c_7 \end{cases}$$

In matrix form:

$$\begin{bmatrix} -r_2s_2 & -r_{31}s_{31} & 0 & 0 & 0 & 0 \\ r_2c_2 & r_{31}c_{31} & 0 & 0 & 0 & 0 \\ 0 & -r_3s_3 & -r_4s_4 & r_{51}s_{51} & 0 & 0 \\ 0 & r_3c_3 & r_4c_4 & -r_{51}c_{51} & 0 & 0 \\ 0 & 0 & 0 & -r_5s_5 & -r_6s_6 & r_7s_7 \\ 0 & 0 & 0 & r_5c_5 & r_6c_6 & -r_7c_7 \end{bmatrix} \begin{Bmatrix} \alpha_2 \\ \alpha_3 \\ \alpha_4 \\ \alpha_5 \\ \alpha_6 \\ \alpha_7 \end{Bmatrix} = \begin{Bmatrix} r_2\omega_2^2c_2 - r_{31}\omega_3^2c_{31} + a_1c_1 \\ r_2\omega_2^2s_2 - r_{31}\omega_3^2s_{31} + a_1s_1 \\ r_{32}\omega_3^2c_3 + r_4\omega_4^2c_4 - r_{51}\omega_5^2c_{51} \\ r_{32}\omega_3^2s_3 + r_4\omega_4^2s_4 - r_{51}\omega_5^2s_{51} \\ r_{52}\omega_5^2s_5 - r_6\omega_6^2s_6 - r_7\omega_7^2s_7 \\ r_{52}\omega_5^2c_5 - r_6\omega_6^2c_6 - r_7\omega_7^2c_7 \end{Bmatrix}$$

Mathematical model of the mechanism kinematics is capable of accounting for accelerations caused by blade flapping, lagging and twisting deflections as well as vibration deformations, but velocities and accelerations caused by these motions are not included into analysis due to their negligibly small values.

6.2.3 Dynamic Force Analysis

Actuation mechanism as a part of rotating blade is subjected to the following system of forces:

$\vec{F}_{in,i} = m_i\vec{a}_i$ —inertia forces caused by linear motion of links' centers of gravity (CGs) in body-fixed reference frame. Centrifugal forces $\vec{F}_{ci} = m_i\vec{a}_c$ are as included in this vector.

$\vec{M}_{in,i} = I_{zi}\vec{\alpha}_i$ —inertia moments by revolute motion of links around CGs in body-fixed reference frame.

$\vec{F}_{G,i} = m_i\vec{g}$ —gravitational forces.

\vec{F}_{act} —actuator force. This force is known.

\vec{F}_{GF} —maximum acceptable force on Gurney flap.

According to d'Alembert's principle, the sum of all above forces and the sum of all moments about any point equal zero. That is, the sum of input force \vec{F}_{act} and inertia forces is to be balanced by the resulting aerodynamic \vec{F}_{GF} and hinge reactions, which will be calculated as a result of the current analysis.

Figure 6.5 shows free-body diagram of input dyad 1–2 with given actuator input force \vec{F}_{act} and unknown \vec{F}_{32} and \vec{F}_{01} .

Equilibrium equations of forces ΣF^{1-2} for links 1 and 2 and moments for link 2 about point A $\Sigma M_A^{(2)}$

Fig. 6.5 Kinetic diagram for dyad 1–2

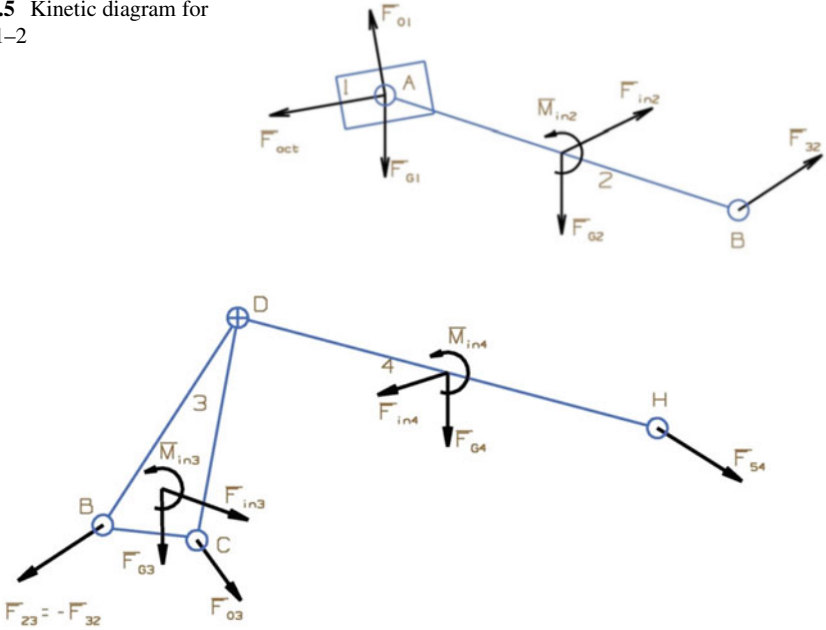


Fig. 6.6 Kinetic diagram for dyad 3–4

$$\begin{aligned} \Sigma F^{1-2} : \quad & \vec{F}_{in1} + \vec{F}_{in2} = \vec{F}_{32} + \vec{F}_{01} + \vec{F}_{G2} + \vec{F}_{G1} + \vec{F}_{act} \\ \Sigma M_A^{(2)} : \quad & \vec{M}_{in2} + r_{AG2} \times \vec{F}_{in2} = r_{AG2} \times \vec{F}_{G2} + r_{AB} \times \vec{F}_{32} \\ \Sigma M_B^{(2)} : \quad & \vec{M}_{in2} + r_{BG2} \times \vec{F}_{in2} = r_{BA} \times \vec{F}_{01} + r_{BG2} \times \vec{F}_{G2} + r_{BA} \times \vec{F}_{act} \end{aligned}$$

Solution of this system of equations provides unknown forces \vec{F}_{32} and \vec{F}_{01} .

Similarly, the forces in dyad 3–4 are calculated. Figure 6.6 shows free-body diagram of amplifier dyad 3–4 with given actuator input force $\vec{F}_{23} = -\vec{F}_{32}$ and unknown \vec{F}_{54} and \vec{F}_{03} .

Equilibrium equations of forces ΣF^{3-4} for links 3 and 4 and moments $\Sigma M_D^{(3)}$ and $\Sigma M_D^{(4)}$ about point D for link 3 and link 4:

$$\begin{aligned} \Sigma F^{1-2} : \quad & \vec{F}_{in3} + \vec{F}_{in4} = \vec{F}_{03} + \vec{F}_{54} + \vec{F}_{G3} + \vec{F}_{G4} + \vec{F}_{23} \\ \Sigma M_D^{(3)} : \quad & \vec{M}_{in3} + r_{DG3} \times \vec{F}_{in3} = r_{DC} \times \vec{F}_{03} + r_{DG3} \times \vec{F}_{G3} + r_{DB} \times \vec{F}_{23} \\ \Sigma M_D^{(4)} : \quad & \vec{M}_{in4} + r_{DG4} \times \vec{F}_{in4} = r_{DH} \times \vec{F}_{54} + r_{DG4} \times \vec{F}_{G4} \end{aligned}$$

Centrifugal forces from blade rotation produce only reaction forces in Oz direction and do not influence the mechanism kinematics. At this point, the influence of mechanism inertia on kinematics is investigated, and therefore, z components of

forces are not taken into account. Projections of vector equations onto the axes of body-fixed reference frame:

$$\begin{cases} F_{03x} + F_{54x} = F_{in3x} + F_{in4x} - F_{23x} \\ F_{03y} + F_{54y} = F_{in3y} + F_{in4y} + F_{G3} + F_{G4} - F_{23y} \\ -r_{DCy} \times F_{03x} + r_{DCx} \times F_{03y} = \left(\vec{M}_{in3} + \vec{r}_{DG3} \times \vec{F}_{in3} - \vec{r}_{DG3} \times \vec{F}_{G3} - \vec{r}_{DB} \times \vec{F}_{23} \right)_z \\ -r_{DHy} \times F_{54x} + r_{DHx} \times F_{54y} = \left(\vec{M}_{in4} + \vec{r}_{DG4} \times \vec{F}_{in4} - \vec{r}_{DG4} \times \vec{F}_{G4} \right)_z \end{cases}$$

In matrix form:

$$\begin{bmatrix} 1 & 0 & 1 & 0 \\ 0 & 1 & 0 & 1 \\ -r_{DCy} & r_{DCx} & 0 & 0 \\ 0 & 0 & -r_{DHy} & r_{DHx} \end{bmatrix} \times \begin{Bmatrix} F_{03x} \\ F_{03y} \\ F_{54x} \\ F_{54y} \end{Bmatrix} = \begin{Bmatrix} F_{in3x} + F_{in4x} - F_{23x} \\ F_{in3y} + F_{in4y} + F_{G3} + F_{G4} - F_{23y} \\ \left(\vec{M}_{in3} + \vec{r}_{DG3} \times \vec{F}_{in3} - \vec{r}_{DG3} \times \vec{F}_{G3} - \vec{r}_{DB} \times \vec{F}_{23} \right)_z \\ \left(\vec{M}_{in4} + \vec{r}_{DG4} \times \vec{F}_{in4} - \vec{r}_{DG4} \times \vec{F}_{G4} \right)_z \end{Bmatrix}$$

Output linkage 5–6 is shown on Fig. 6.7. Here, \vec{F}_{gf} is the maximum aerodynamic force on Gurney flap counterpoising actuator force. It is applied in the middle point U of flap fraction that is outside the airfoil perpendicular to the flap. Equilibrium equations ΣF^{5-6} of forces for links 5 and 6 and moments $\Sigma M_S^{(5)}$ and $\Sigma M_S^{(6)}$ about point S for links 5 and 6:

Fig. 6.7 Kinetic diagram for dyad 5–6. Actual Gurney flap is shown in red lines. Blue lines show kinematic links

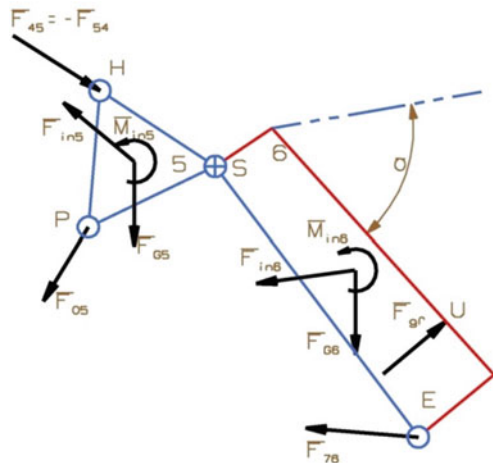
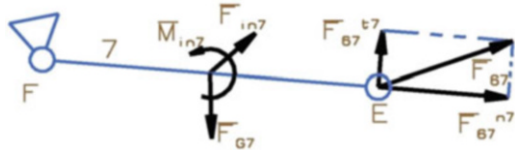


Fig. 6.8 Kinetic diagram for link 7



$$\begin{aligned}\Sigma F^{5-6} : \quad & \vec{F}_{in5} + \vec{F}_{in6} = \vec{F}_{05} + \vec{F}_{76} + \vec{F}_{Gf} + \vec{F}_{G5} + \vec{F}_{G6} + \vec{F}_{45} \\ \Sigma M_S^{(5)} : \quad & \vec{M}_{in5} + \vec{r}_{SG5} \times \vec{F}_{in5} = \vec{r}_{SP} \times \vec{F}_{05} + \vec{r}_{SG5} \times \vec{F}_{G5} + \vec{r}_{SH} \times \vec{F}_{45} \\ \Sigma M_S^{(6)} : \quad & \vec{M}_{in6} + \vec{r}_{SG6} \times \vec{F}_{in6} = \vec{r}_{SE} \times \vec{F}_{76} + \vec{r}_{SU} \times \vec{F}_{Gf} + \vec{r}_{SG6} \times \vec{F}_{G6}\end{aligned}$$

The system contains three unknowns: \vec{F}_{05} , \vec{F}_{76} and \vec{F}_{Gf} . For every force, its magnitude and direction are to be found, thus making six unknown unities to be found from four equations, and therefore, two additional constraints are required. The direction of \vec{F}_{Gf} provides the first additional constraint; it can be presented as

$$\vec{F}_{Gf} = \left| \vec{F}_{Gf} \right| \times \vec{e}_{gf} = \left| \vec{F}_{Gf} \right| \times \{ e_{gf,x} \ e_{gf,y} \} = \left| \vec{F}_{Gf} \right| \times \{ \cos(\alpha) \ \sin(\alpha) \}$$

Here, $e_{gf,x}$ and $e_{gf,y}$ are projections of unity vector \vec{e}_{gf} codirectional with \vec{F}_{Gf} onto the body-fixed coordinate system; $\left| \vec{F}_{Gf} \right|$ is the unknown norm of \vec{F}_{Gf} ; α is the angle between Gurney flap and $OIxI$.

The second constraint can be found from the equilibrium of the last link 7 (Fig. 6.8). Resultant force $\vec{F}_{67} = -\vec{F}_{76}$ on link 7 can be decomposed into force \vec{F}_{67}^n normal to trajectory of point E and \vec{F}_{67}^t tangent to the trajectory. All the other forces acting on link 7 are decomposed in the same manner.

Sum of moments on link 7 about point F

$$\Sigma M_F^{(7)} : \quad F_{67}^t \times |r_{FE}| + F_{in7}^t \times |r_{FG7}| - F_{G7}^t \times |r_{FG7}| - M_{in} = 0$$

provides the magnitude of \vec{F}_{67}^t .

Normal component \vec{F}_{67}^n is presented as a linear combination of its norm $\left| \vec{F}_{67}^n \right|$ and unity vector \vec{e}_7 .

$$\vec{F}_{67}^n = \left| \vec{F}_{67}^n \right| \times \vec{e}_7 = \left| \vec{F}_{67}^n \right| \times \{ e_{7,x} \ e_{7,y} \} = \left| \vec{F}_{67}^n \right| \times \{ \cos(\varphi_7) - \sin(\varphi_7) \}$$

Equilibrium equations for dyad 5–6 with additional constraints:

$$\begin{aligned}
\Sigma F^{5-6} : \quad \vec{F}_{in5} + \vec{F}_{in6} &= \vec{F}_{05} - \left(\vec{F}_{67}^{t7} + \left| \vec{F}_{67}^{n7} \right| \times \vec{e}_7 \right) + \left| \vec{F}_{Gf} \right| \times \vec{e}_{gf} + \vec{F}_{G5} + \vec{F}_{G6} + \vec{F}_{45} \\
\Sigma M_S^{(5)} : \quad \vec{M}_{in5} + \vec{r}_{SG5} \times \vec{F}_{in5} &= \vec{r}_{SP} \times \vec{F}_{05} + \vec{r}_{SG5} \times \vec{F}_{G5} + \vec{r}_{SH} \times \vec{F}_{45} \\
\Sigma M_S^{(6)} : \quad \vec{M}_{in6} + \vec{r}_{SG6} \times \vec{F}_{in6} \\
&= -\vec{r}_{SE} \times \vec{F}_{67}^{t7} - \vec{r}_{SE} \times \left| \vec{F}_{67}^{n7} \right| \times \vec{e}_7 + \vec{r}_{SU} \times \left| \vec{F}_{Gf} \right| \times \vec{e}_{gf} + \vec{r}_{SG6} \times \vec{F}_{G6}
\end{aligned}$$

In matrix form:

$$\begin{bmatrix} 1 & 0 & e_{gf,x} & e_{7,x} \\ 0 & 1 & e_{gf,y} & e_{7,y} \\ -r_{SPy} & r_{SPx} & 0 & 0 \\ 0 & 0 & K_{43} & K_{44} \end{bmatrix} \times \begin{Bmatrix} F_{05x} \\ F_{05y} \\ \left| \vec{F}_{Gf} \right| \\ \vec{F}_{67}^{n7} \end{Bmatrix} \\
= \begin{Bmatrix} F_{in5x} + F_{in6x} + F_{67x}^{t7} - F_{45x} \\ F_{in5y} + F_{in6y} + F_{67y}^{t7} - F_{45y} + F_{G3} + F_{G4} \\ \left(\vec{M}_{in5} + \vec{r}_{SG5} \times \vec{F}_{in5} - \vec{r}_{SG5} \times \vec{F}_{G5} - \vec{r}_{SH} \times \vec{F}_{45} \right)_z \\ \left(\vec{M}_{in6} + \vec{r}_{SG6} \times \vec{F}_{in6} - \vec{r}_{SG5} \times \vec{F}_{G5} + \vec{r}_{SE} \times \vec{F}_{67}^{t7} \right)_z \end{Bmatrix} \\
K_{43} = -r_{SUy} \times e_{gf,x} + r_{SUx} \times e_{gf,y} \\
K_{44} = r_{SEy} \times e_{7,x} - r_{SEx} \times e_{7,y}$$

The required force of the actuator is based on the aerodynamic force for the worst operation condition regarding the mechanism transmission ratio between the actuator and deployment mechanism. It can be calculated from graph on Fig. 6.9. Blue line on this graph represents the dependency of resultant force on Gurney flap with constant force on the actuator of $F_{act} = 550$ N. Obviously, the highest aerodynamic load acts on the flap when it is fully retracted. Therefore, the minimum transmission ratio is observed in fully retracted position and can be calculated as

$$n_{min} = \frac{F_{GF,100\%}}{F_{act}}$$

The block force of a single APA 500 L actuator itself is 550 N. However, force at its maximum stroke of 0.47 mm is zero, according to the product specification. To produce the required force and stroke input, serial connection of several actuators is considered. If actuators are connected in series, total displacement grows and resulting force remains constant as more elements are added, whereas in parallel connections, total force grows and displacement remains constant. Since maximum input stroke according to mechanism kinematics is set to 0.40 mm, the optimal number of serially connected actuators in every station is two. Such configuration insures maximum output force of 275 N and stroke of 0.20 mm for each actuator.

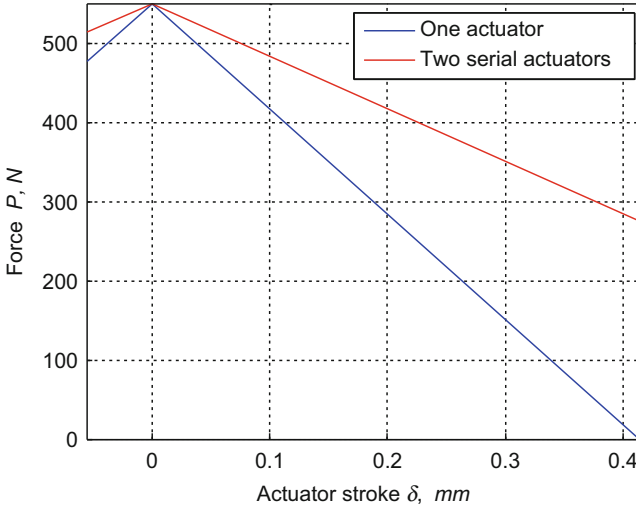


Fig. 6.9 Force-stroke characteristic a serial connection of two APA 500 L actuators

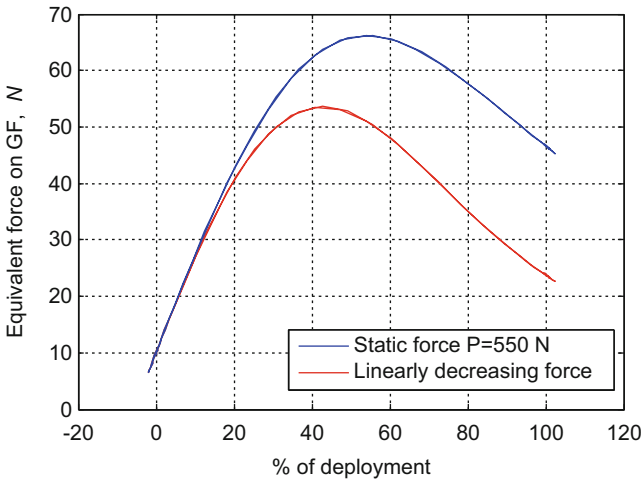


Fig. 6.10 Resultant force on Gurney flap. Constant actuator force $F_{act} = 550$ N

The force-stroke characteristic for a station consisting of two serial actuators APA 500 L is shown on Fig. 6.9.

Resultant force that can be taken by single Gurney flap actuation mechanism with maximum actuation force of $F_{act} = 550$ N is shown on Fig. 6.10. Red line of the graph represents maximum allowed force on Gurney flap with input force decreasing linearly from 550 N to 275 N. Based on Gurney flap output function, the input function for actuation station has been derived accounting for actuation mechanism kinematics. Time history for input is shown on Fig. 6.11.

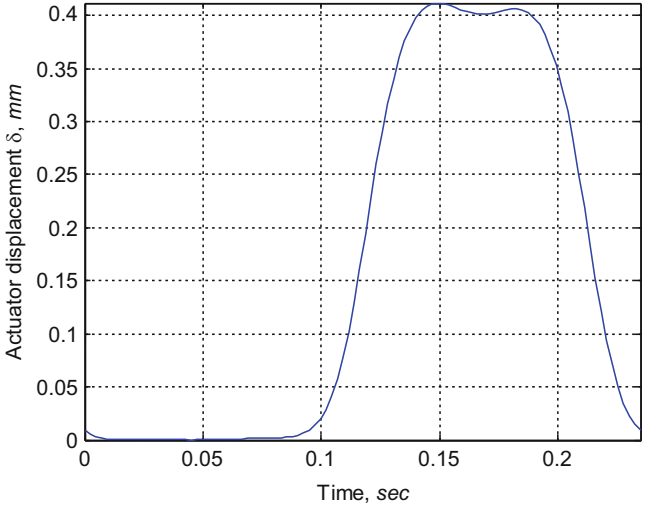


Fig. 6.11 Input displacement time history for actuator station

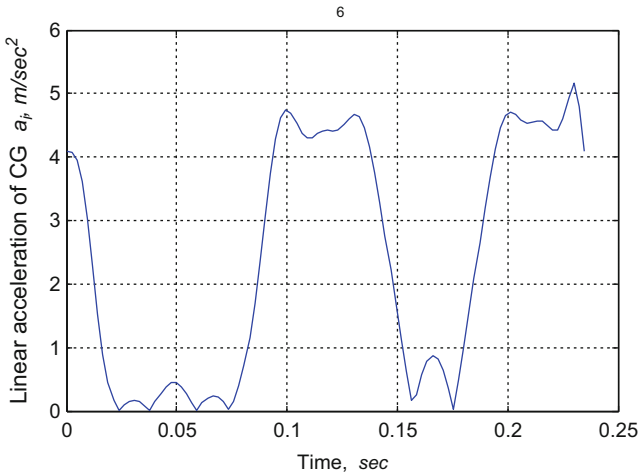


Fig. 6.12 Kinetic diagram for 1–2 dyads. Absolute value of linear acceleration of Gurney flap center of gravity

Mechanism has to work at frequency of $1/Rev$, with highest linear displacements being those of Gurney flap. Since it is also one of the most massive of the mechanism components, attention should be paid to its mass when designing and manufacturing. Gurney flap CG linear acceleration modulus is shown Fig. 6.12, and corresponding inertia force is shown on Fig. 6.13.

Graph on Fig. 6.13 shows generalized inertia force acting on the actuator during Gurney flap actuation. On this graph, positive force value corresponds to inertia

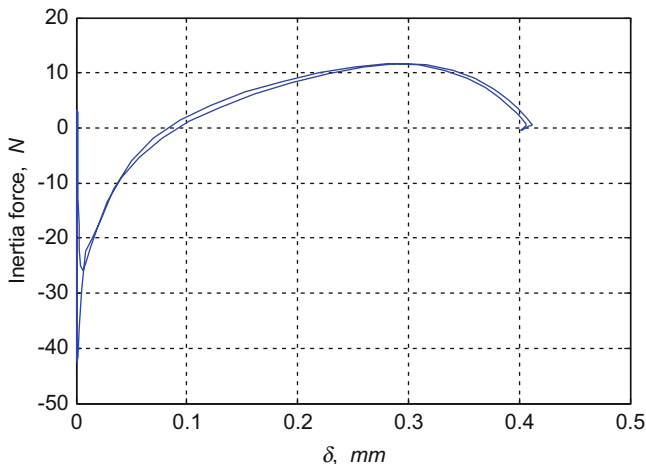


Fig. 6.13 Active Gurney flap mechanism inertia force

force direction coincident with actuation force. Attention should be paid to mass characteristics of the mechanism since the input of inertia force in overall force balance of the system is quite noticeable.

6.3 Blade Section with Active Gurney Flap

The above-described actuation mechanism concept has been implemented in mock-up of blade section with active Gurney flap. The basic requirements of the mock-up design were the following:

- Represent kinetic and dynamic properties of the actuation mechanism
- Provide possibility for wind tunnel testing
- Manufacturability
- Provide possibility for modifications and adjustments

To ensure easy access to mechanism components for assembly, adjustments and modifications, the mock-up is designed as block structure consisting of two main parts—the airfoil and active Gurney flap actuator mounted on the bottom part of the airfoil (see Fig. 6.14). Gurney flap base is connected to the airfoil with screws via threaded inserts 30 or directly into plastic body of the housing. All references to parts will be made according to this drawing. Mock-up is fully functional and suitable for wind tunnel with full operational load on Gurney flap. To simplify the design, blade twist is not included.

The most loaded part of the mechanism is the actuator frame 33. It has to secure transferring maximum load of 550 N applied by the actuators. Additionally, low

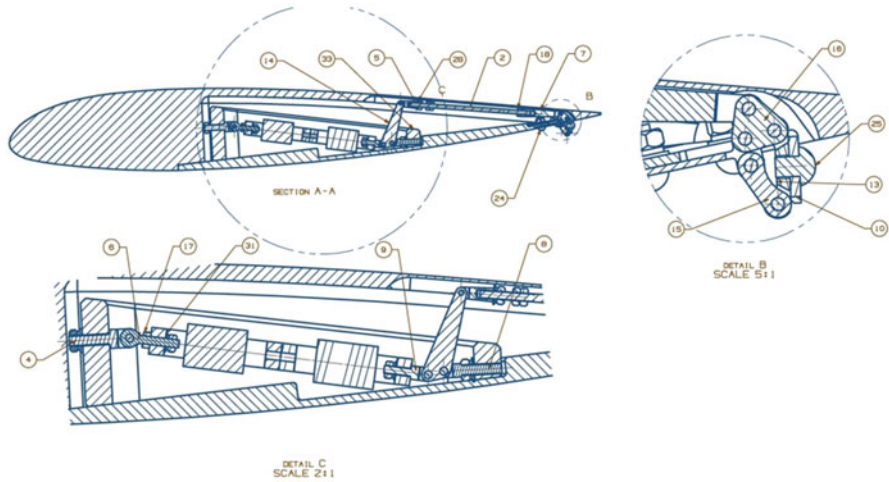


Fig. 6.14 Blade section mock-up with active Gurney flap mechanism

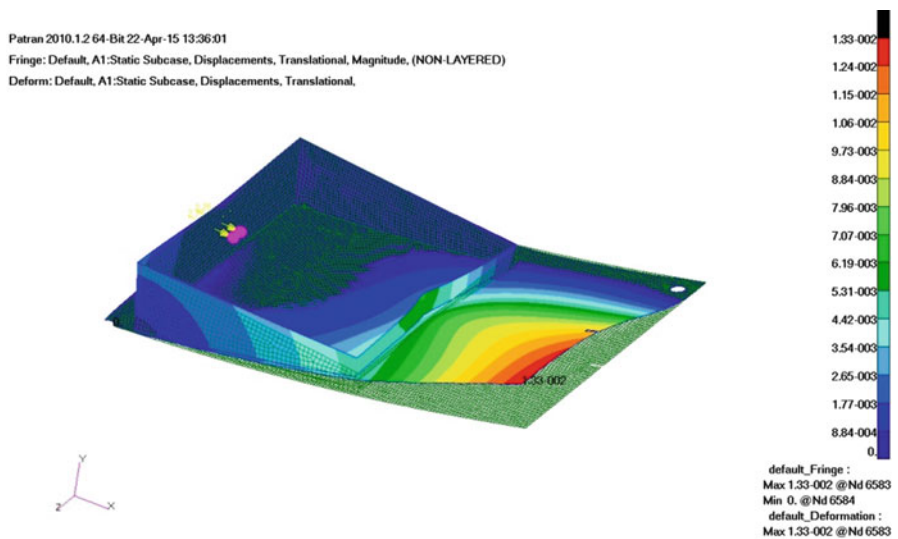


Fig. 6.15 Displacements distribution in mock-up frame loaded with maximum force of 550 N

stroke of the actuators provides requirements of high frame stiffness and backlash in the components inside the frame. Dimensions of the frame were selected based on minimum deformation criteria. Static structural analysis was performed to calculate displacements of the aluminium frame with maximum applied force of 550 N acting between the hinges of the actuator station. The model is meshed with 2D Quad4 elements. For computational efficiency, cyclic symmetry was applied, and half of the mock-up base has been modelled. Figure 6.15 displays plot of static displacements

in the mock-up. The maximum shrinkage in the direction of actuation in the actuator hinges of 0.006 mm is acceptable for normal functionality of the mock-up. For implementation of the mechanism in the real blade, the frame has to be reconsidered in terms of weight reduction.

Lever 14 transmits displacements to the Gurney flap output mechanism. Relation of lengths of lever arms provide required multiplication of displacements necessary for retracting the flap. Smooth adjustment of pulleys 2 ensures precise positioning of the flap with respect to airfoil as well as geometrical synchronization of two parallel actuator stations. Buckling analysis of pulleys showed sufficient safety ratio for the existing load conditions. Attention should be paid to synchronous retraction of parallel actuator stations, as deviations will increase the resistance forces and could damage the mechanism.

The executive body of the mechanism is Gurney flap 10. It is connected with the mechanism base with two hinged links, whose lengths are crucial for correct flap trajectory. Executive mechanism hinges 11 and 12 can be detached from the base, thus providing possibility to mechanism modification up to installing completely different executive mechanism.

The mock-up is fully functional for wind tunnel testing with maximum load on Gurney flap in retracted position of 45 N. Attention should be paid to lubrication of hinges.

6.4 Conclusions

Active Gurney flap mechanism has been developed and implemented into a blade section mock-up ready for wind tunnel testing. Based on full kinematic and dynamic analysis of the actuator system, optimal parameters were selected and tested on the mock-up. The tests revealed some drawbacks of the system such as friction and stiffness issues which can be easily removed by slight redesign of some elements of the system. Even though actuation mechanism is relatively complicated, it still can be implemented into airfoils with little space for housing Gurney flap in retracted position.

References

- Barlas TK, van Kuik GA (2010) Review of state of the art in smart rotor control research for wind turbines. *Prog Aerosp Sci* 46:1–27
- Lee T, Chopra I (2001) Design of a bidirectional piezoelectric actuator for blade trailing-edge flap. In: *Proceedings of the SPIE 4327, smart structures and materials 2001: smart structures and integrated systems*, pp 36–45
- Thiel MR, Lesieutre GA, Maughmer MD, Koopmann GH (2006) Actuation of an active gurney flap for rotorcraft applications. *AIAA Paper 2006-2181*, Newport, Rhode Island

Chapter 7

Gurney Flap Force Calculations

Prasanta Sarkar and Radoslaw Raczynski

7.1 Introduction

The Gurney flap is a small flat tab device projecting from the trailing edge of a wing. The flap is set at a right angle to the pressure surface of the airfoil, and extends generally, $1\text{--}3\%c$, where c is the wing chord. The Gurney flap improves the performance of an airfoil by increasing the lift without introducing a proportional increase in drag. The flap operates by increasing the pressure on the airfoil pressure side and decreasing the pressure on the suction side.

This trailing edge device can improve the performance of a simple airfoil to nearly the same level as a complex high-performance design and helps the boundary layer flow stay attached all the way to the trailing edge on the suction side of the airfoil. The Gurney flap improves the aerodynamic performance by increasing the maximum lift coefficient ($C_{l\max}$), decreasing the angle of attack for zero lift (α_0) and increasing the nose down pitching moment (C_m), accompanied by an increase in the drag coefficient (C_d). But with appropriate Gurney flap size based on the boundary layer thickness, a net benefit in overall lift to drag is obtained.

The Gurney flap, in theory, is a mechanically simple high-lift system which would minimize construction and maintenance costs and thus would improve helicopter performance profitability. The Gurney flap, named after original deviser Dan Gurney, is an L-shaped beam high-lift device, attached to the trailing edge on the pressure surface of a wing. The device has been widely used for high-speed racing cars to obtain stability at curves. But its applicability in the scope

P. Sarkar (✉)
Université Grenoble Alpes, LEGI, Grenoble, France
e-mail: prasanta.sarkar@univ-grenoble-alpes.fr

R. Raczynski
WSK PZL Swidnik S.A, Swidnik, Poland
e-mail: radoslaw.raczynski@leonardocompany.com

of helicopters to alleviate dynamic stall creates additional structural consideration keeping in mind the higher loading factors of the rotor blade.

The flow field structure near the trailing edge of the Gurney flap was presented by Liebeck (1978), and the presence of counterrotating recirculation vortices behind the Gurney flap was attributed for the increased aerodynamic performance. The presence of chordwise vortices shed in front of the flap and spanwise vortices shed behind the flap becomes important at high angles of attack. The enhanced pressure on the lower surface ahead of the flap means the upper surface suction can be reduced while producing the same lift. Wind tunnel tests conducted on the effect of a 1.25%*c* height Gurney flap on a Newman airfoil displayed increase in lift and a slight reduction in drag. Large increment in lift was observed for greater Gurney flap heights, but the drag increased considerably beyond approximately 2%*c* height. The study inferred that the optimal Gurney flap height should be of the order of 1–2%*c*, where *c* is the airfoil chord. Another study by Neuhart and Pendergraft (1988) found that the reason Gurney flaps are optimal at about 3% of the chord length is because that is the approximate boundary layer height. Once the flap extends outside the boundary layer, the increase in drag starts to exceed the gain in lift, and the flap is not as effective anymore. Gurney flap height greater than 2%*c* usually results in a significant increase in airfoil drag, thus degrading the improvement in airfoil performance as perceived in terms of lift-to-drag ratio by Storms and Jang (1994).

Jang et al. (1998) carried out a two-dimensional numerical study to determine the effect of a Gurney flap on a NACA 4412 airfoil, with a flap height of 0.5–3%*c*, located at the trailing edge of the airfoil. The numerical results showed that Gurney flaps increased the airfoil lift coefficient with slight penalty on drag coefficient. The study inferred that the drag coefficient was lower at higher lift coefficient than cleaner airfoil, and in comparison the lift coefficient and nose down pitching moment were increased by the Gurney flap. The flap gives rise to enhanced loading along the entire length of the airfoil, with a large increase in trailing edge loading. However, larger Gurney flaps will increase lift at the cost of increasing drag. Smith et al. (2001) performed two-dimensional steady-state simulations to determine the effect of Gurney flap on NACA 4412 and NACA 0011 airfoils and found good correlation between computed and experimental data. Addition of Gurney flap to the airfoil trailing edge increased the lift coefficient significantly with insignificant drag penalty provided proper Gurney flap height is selected.

Yoo (2000) performed fully turbulent numerical investigations using the standard *k-ε* two-equation model to determine the effect of Gurney flap on NACA 23012 airfoil. The results suggested that the Gurney flap provides a significant increase in the lift-to-drag ratio at low angle of attack and high-lift coefficient. The results showed that the Gurney flap resulted in increase of effective camber of the airfoil. Gurney flap considerably increases the aft loading of the airfoil leading to increased lift and nose down pitching moment. Most of the increased lift is generated from increase in aft loading and stronger adverse pressure gradient near the trailing edge on the lower surface.

Schatz et al. (2004) studied the effect of small micro-tab devices like Gurney flaps mounted at the lower trailing edge of an airfoil focusing on the unsteady flow

structures in the wake of Gurney flap giving rise to increased induced drag. The study inferred that the flow unsteadiness can be suppressed and reduced drag can be achieved with advanced flap concepts and trailing edge shapes. The influence of extended Gurney flap from the pressure side decreases with decreasing angle of attack due to thickening boundary layer around the flap. A flap on the suction side has an inverse effect on the airfoil with increasing negative lift at low angles of attack and decreasing influence with increasing angle of attack.

7.2 Retracting Gurney Flap

The NACA 23012 airfoil with a blunt trailing edge, which is the primary airfoil for PZL Sokol W-3 main rotor blade, is considered for the study. Flow over the airfoil at large angles of attack is very complicated and difficult to predict accurately by numerical and experimental methods. The complication in flow predictions stems from the fact that the boundary layers separate from the airfoil suction surfaces with increasing angle of attack due to adverse pressure gradients and its interaction with turbulence. The reasons for the inaccurate numerical predictions can be attributed to the inaccuracies incurred by the turbulence models used in the computations. The computational domain for the present study is at $20c$ downstream and $15c$ upstream of the airfoil, where c is the chord length of the airfoil. This domain is found to be suitable for a RANS simulation. The top and bottom far-field boundary conditions are set at $15c$ lengths from the airfoil upper and lower surface, respectively. The flow over a clean NACA 23012 airfoil and a NACA 23012 airfoil with a Gurney flap of height $2\%c$ located at $95\%c$ is studied. The Gurney flap is more effective right at the blunt trailing edge of the airfoil, but due to structural consideration and deployment and retraction requirement for a rotating rotor blade, the position is fixed at $95\%c$ of the blade chord. The mesh has 60,000 elements in the computational domain and around 500 nodes on airfoil surface. Figure 7.1 shows the schematic of an airfoil with Gurney flap.

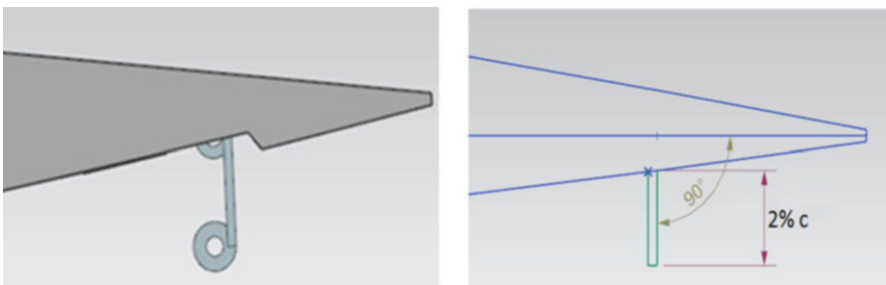


Fig. 7.1 NACA 23012 airfoil with $2\%c$ fully extended Gurney flap at 90° to the chord

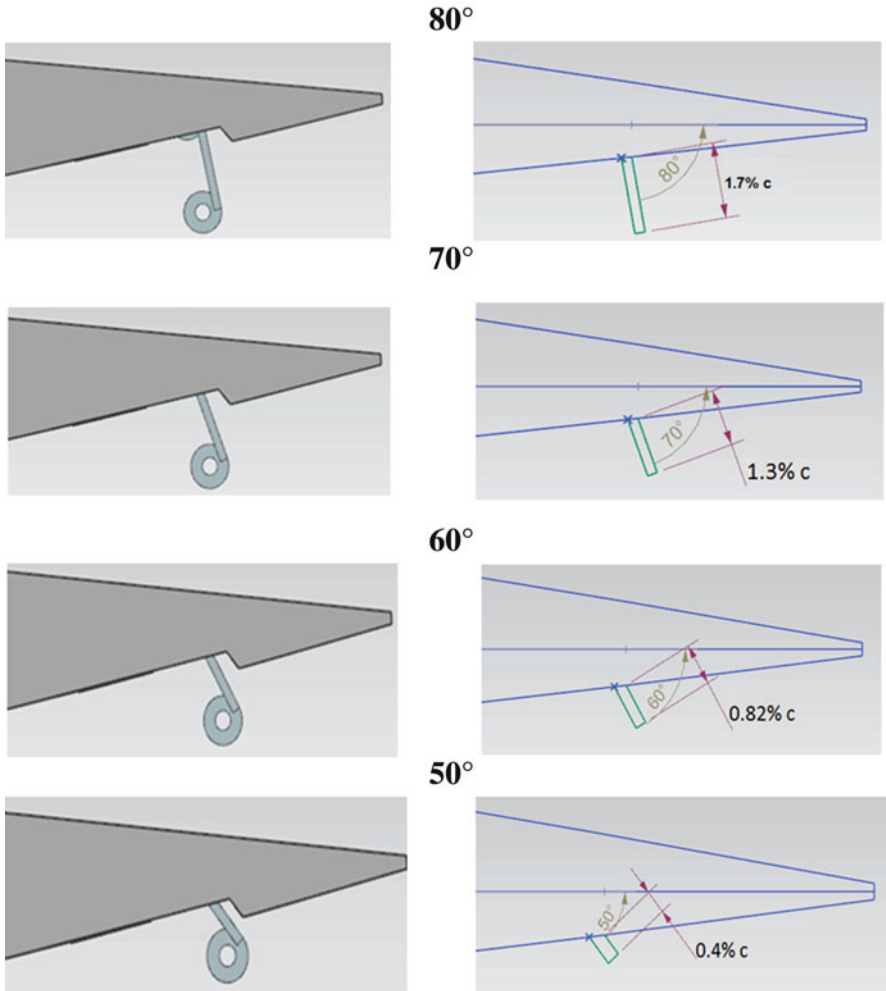


Fig. 7.2 Gurney flap deployment and retraction position as a function of angle between flap and mean airfoil chord

The deployment and retraction position of the Gurney flap with the same airfoil and computational domain is studied next (Fig. 7.2). Five different positions of the Gurney flap are considered ranging from the fully extended flap to the retracted flap, with the Gurney flap being fully extended at 90° to the chord and fully retracted at an approximate angle of 40° to the chord due to the motion imparted by the actuators. Therefore, the Gurney flap position at an interval of every 10° , i.e., at 90° , 80° , 70° , 60° , and 50° , is considered. The structured grid generated for different Gurney position cases is similar in grid density and quality as the previous cases.

The dynamic mesh model in Fluent 14.5 is used to model dynamic airfoil characteristics (Leishman, 1990) with changing interior domain shape due to pitching motion of the airfoil boundary with time. The pitching motion is prescribed by specifying the angular velocities about the center of gravity using a user-defined function (UDF) with a `DEFINE_CG_MOTION` macro on the cell zone surrounding the airfoil. The mesh is updated automatically based on the new position of the airfoil boundaries at each time step of the unsteady solver based with the defined user settings. The moving and nonmoving cell zones are grouped separately and the deforming zones separately. The mesh deformation on the deforming zone comprised of triangular cells is updated using spring-based smoothing and remeshing methods. Spring-based smoothing is implemented which idealizes the edge between any two mesh nodes as a network of interconnected springs. A spring constant factor of 0.5 is used to reduce the default damping levels on the springs and node displacement. With larger cell displacement, the cell quality deteriorates, and negative cell volumes are created if only smoothing techniques are used. Therefore, local cell and cell zone remeshing is used with maximum cell skewness limit of 0.7 and appropriate size criteria. Fluent 14.5 collects cells which exceed skewness and size limits and marks them for remeshing at every time step. It locally remeshes the collected skewed cells and locally updates with new cells if the new cells satisfy the skewness criteria. The solution in the new cells are interpolated from the existing solution. The dynamic characteristic is investigated using the inbuilt dynamic mesh deformation. Both clean airfoil and airfoil with 2% Gurney flap at mean angle of attack of 7° with pitching amplitude of 5° and pitching frequency of 4.5 Hz are studied. An unstructured dynamic grid is generated with specified grid regions for dynamic mesh capability. The zone around the airfoil consists of structured quad and pave cells, which undergo rigid body motion with no mesh deformation in the zone. The circular domain enclosing the rigid domain is the deforming zone where the mesh deformation and remeshing take place during pitching motion. The mesh is created with size and growth factor limitations so as to avoid negative cell volumes during mesh deformation in the computation. The mesh deformation settings for the spring-based smoothing and remeshing are analyzed for different cases and different control inputs to alleviate the possibility of negative cell volume after few pitching cycles and to have least effect on mesh quality. Even in the simpler case of two-dimensional numerical simulation of dynamic stall, very limited research literature is available regarding the effect of grid and temporal resolution on the accuracy of the overall aerodynamic forces. The time step is determined from the motion configuration of the pitching airfoil. As the boundary layer reattachment is very sensitive to spatial and temporal resolution, 2000 time steps per cycle are used for temporal convergence. The time step is kept low to achieve true second-order temporal discretization which is also important along with second-order spatial discretization for a time-accurate solution.

7.3 Solution Methodology

A density-based solution methodology is carried out in Ansys Fluent 14.5, which solves the coupled governing equations of continuity, momentum, and energy followed by the governing equations for additional turbulence scalars sequentially. The coupled system of equations for continuity, momentum, and energy are solved using the coupled-implicit formulation of the density-based solver, with each equation linearized implicitly with respect to all dependent variables in the set. This results in a system of linear equations for each cell in the domain, called the block system of equations. The resultant block system of equations for all the dependent variables in each cell is solved at the same time by a point implicit linear equation solver incomplete lower-upper (ILU) factorization scheme in conjunction with an algebraic multigrid (AMG) method. Pressure far-field boundary condition is used on the computational domain boundary, and no slip wall boundary condition is used on the airfoil surface. The airfoil analysis is carried out with SST $k-\omega$ turbulence model developed by Menter (1994), due to its capabilities to model adverse pressure gradient and flow separation regions with reasonable accuracy. The model effectively blends the standard $k-\omega$ model in the near-wall region and the transformed $k-\epsilon$ model in the far field. Fluent 14.5 implementation of SST $k-\omega$ turbulence model is insensitive to wall $y+$ values and, thus, imposes less restriction on the near-wall viscous mesh.

The flow is assumed to be compressible, described by the total pressure and total temperature of the flow. For an ideal gas, these quantities are related to the static pressure and temperature by the following equations:

$$\frac{P_0}{P} = \left[1 + \left(\frac{\gamma - 1}{2} \right) M^2 \right]^{\frac{\gamma}{\gamma - 1}} \quad (7.1)$$

$$\frac{T_0}{T} = 1 + \left(\frac{\gamma - 1}{2} \right) M^2 \quad (7.2)$$

where P_0 = total pressure = 101,325 Pa, P = static pressure, $\gamma = 1.4$ for air, M = Mach number, P_0 = total temperature = 311 K, and T = static temperature. The compressible form of the ideal gas law is used to determine the density of the fluid and is influenced by the flow Reynolds number and Sutherland law three coefficient method for viscosity.

Fluent 14.5 stores discrete value of the scalar at the cell centers. Second-order upwind scheme is used for spatial discretization to obtain the interpolated face values of the scalar from the cell center values for the convection terms. The diffusion terms of the scalar transport equation are central-differenced and are second-order accurate. At certain flow conditions where a converged steady-state solution could not be obtained with higher-order discretization schemes due to numerical or physical fluctuations, a first-to-higher-order blending is applied as a scaling factor to the reconstruction gradient and provides a better than first-order converged solution.

Evaluation of the gradients is needed for constructing values of a scalar at the cell faces and for computing secondary diffusion terms and velocity derivatives. Least square gradient method is used in the solution, as the method accuracy is comparable to Green-Gauss node-based gradient method and superior to the Green-Gauss cell-based gradient method. Also the least square gradient method is computationally less expensive than the node-based gradient method. The default method of standard gradient limiter is used on the second-order upwind scheme to prevent spurious oscillations in the flow field near local discontinuities or rapid change in flow field parameters. The limiting direction imposed is the default cell to face limiting, where the limited value of the reconstruction gradient is determined at cell face centers, which prohibits the linearly reconstructed field variable on the cell faces to exceed the maximum or minimum values of the neighboring cells.

The reference values of velocity, density, and temperature are updated from the pressure far-field boundary condition. The reference length is set as the chord length of the airfoil with a reference depth of unit length adopted for most cases, which gives an appropriate reference area for the calculation of force and moment coefficients. The Roe flux-difference splitting scheme is used to compute the convective fluxes, and the courant number (CFL) and under-relaxation factors are kept unchanged for flow initialization. The appropriate lift, drag and moment monitors are set up with corresponding direction vectors to monitor the local coefficient convergence along with the global residual convergence.

Solution steering capability provided with Fluent 14.5 in the density-based implicit solver is used to drive the flow solution from initial guess to converged solution, by ramping up the solution in two stages. In the first steering stage, full multigrid initialization (FMG initialization) is employed with the flow being steered from first-order accuracy to second-order accuracy at low CFL value. FMG initialization does most of the work on coarse level grids. It records the original solver settings and resets back to it once the FMG iteration is over. FMG iteration involves switching on the density-based explicit formulation and solving the Euler equations for inviscid flow using first-order discretization to obtain the approximate solution. In this second steering stage, the CFL value is adjusted by monitoring the residual history to prevent divergence and ensure fast convergence of the solution.

7.4 Results

The aerodynamic force and moment coefficients, C_l vs. α , C_d vs. α , and C_m vs. α for a clean NACA 23012 airfoil at Mach number range of 0.2–0.7, Reynolds number 4×10^6 are shown in Fig. 7.3.

The results compared with existing experimental data show that the lift coefficient at low angle of attacks is in good agreement with the experimental data. At higher angle of attack, the flow had separation region beyond which the transition from laminar to turbulent boundary layer takes place. The trailing edge separation and flow reversal phenomenon increase with further increase in angle of attack,

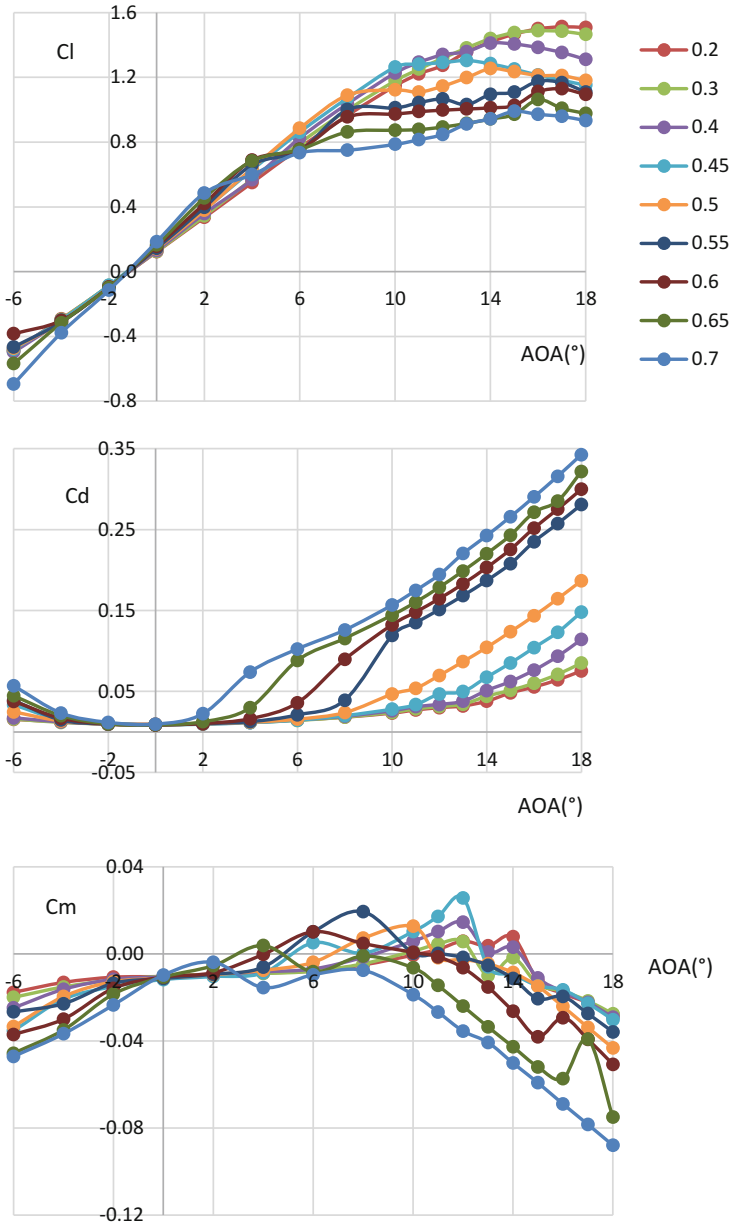


Fig. 7.3 Lift, drag, and moment coefficient over a range of angle of attack for NACA 23012 clean airfoil, $Re = 4E + 06$, $M = 0.2-0.7$

with the flow becoming nonuniform and unsteady. The performance of *SST k- ω* model in the predictions of separated flows over airfoils is satisfactory although substantial inaccuracies in the lift and drag coefficient predictions can still be expected at higher angle of attack. The *SST k- ω* turbulence model had in previous numerical studies demonstrated to overpredict the lift coefficients beyond the stall points. These overpredictions could be due to the fact that the turbulence level in the boundary layers are too high, hence developing a momentum transfer to the near-wall regions which helps the boundary layer to push through the adverse pressure gradient regions effortlessly than otherwise. The resulting delayed separation then caused the low pressure on the suction side to spread over larger area than normal which increased the lift. The high turbulence levels are caused by the fully turbulent model assumptions in the *SST k- ω* turbulence model and not properly resolving the flow transition.

The maximum lift coefficient is found for an angle of attack of 17° at 0.2 Mach number. At post-stall conditions for low Mach numbers, the flow has become unsteady around a fixed lift point. Transition to turbulence is one aspect of airfoil flows that has been demonstrated to be important in prediction of stall, with improper prediction of boundary layer energy can lead to delay in onset of stall. Transition occurs as the Reynolds number of an initially laminar flow increases. Disturbances created by discontinuities in the geometry, free-stream turbulence, and other sources are damped by relatively strong viscosity at low Reynolds numbers. At higher Reynolds numbers, strong inertial forces lead to magnification of instabilities and result in turbulent flow.

The NACA 23012 airfoil is analyzed with a 2% Gurney flap located at 95%; these results are presented in along with the data for clean NACA 23012 airfoil for comparison from the previous study. Ansys Fluent 14.5 captures the change in lift very well through the linear region of the lift curve, but it deviates somewhat at higher angle of attack.

The lift coefficient comparison for a clean airfoil and a flapped airfoil is shown for Mach number range of 0.3–0.6 in Fig. 7.4, whereas the moment coefficient comparison for both the airfoil is shown in Fig. 7.5. As shown in the results, the presence of Gurney flap increases the nose down pitching moment on an airfoil with increasing angle of attack.

The normal force exerted by flow over the airfoil on the front surface of a 2% Gurney flap for static analysis over a range of angle of attack is shown in Fig. 7.6. The normal force predictions give an account of the force to be applied by the piezoelectric actuators to hold the Gurney flap in its position. With a Gurney flap, good prediction of the lift coefficient and pitching moment coefficient for the airfoil can be observed. This improvement could be due to better prediction of lower-surface separation location with a Gurney flap. The flow physics governing the Gurney flap involves flow separation around a flat plate normal to the local flow velocity. The separation point in a clean airfoil is influenced by the boundary layer transition and development, whereas flow separation around a 2% Gurney flap would be relatively insensitive to the boundary layer properties. This would imply that a fully turbulent CFD solution would give reasonably good predictions for the

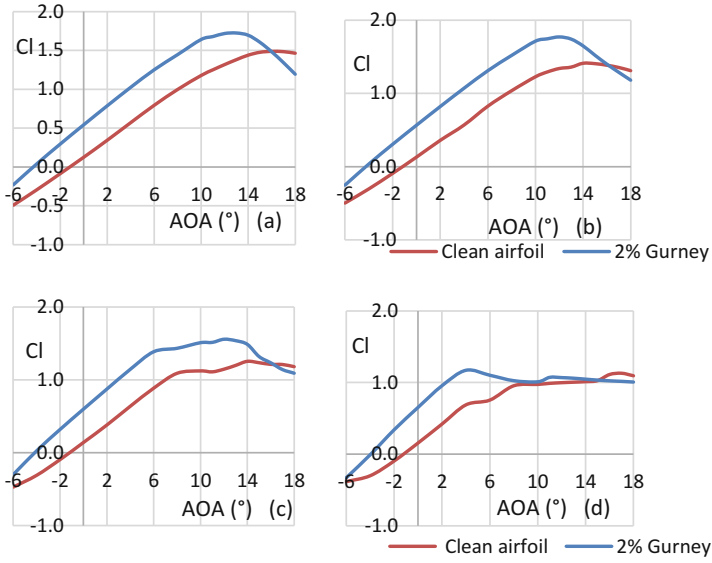


Fig. 7.4 Lift coefficient comparison for clean and 2%*c* Gurney flapped airfoil at Mach numbers (a) 0.3 (b) 0.4 (c) 0.5 (d) 0.6, $Re = 4E + 06$

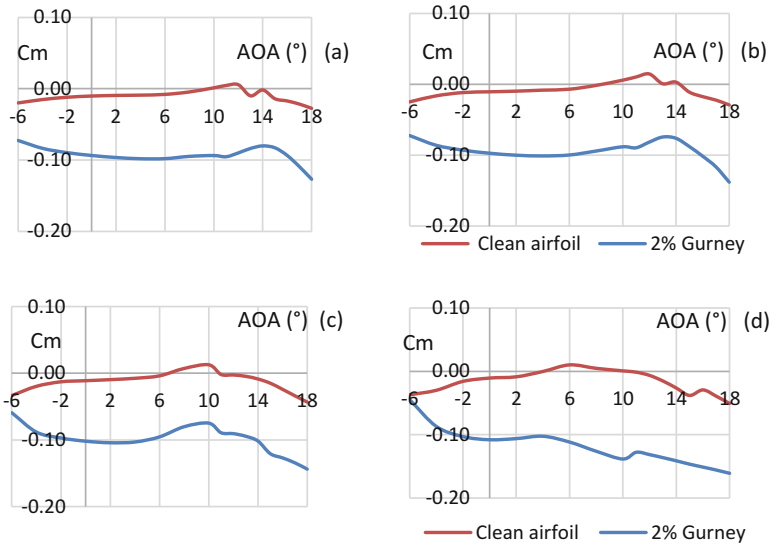


Fig. 7.5 Moment coefficient comparison for clean and 2%*c* Gurney flapped airfoil at Mach numbers (a) 0.3 (b) 0.4 (c) 0.5 (d) 0.6, $Re = 4e + 06$

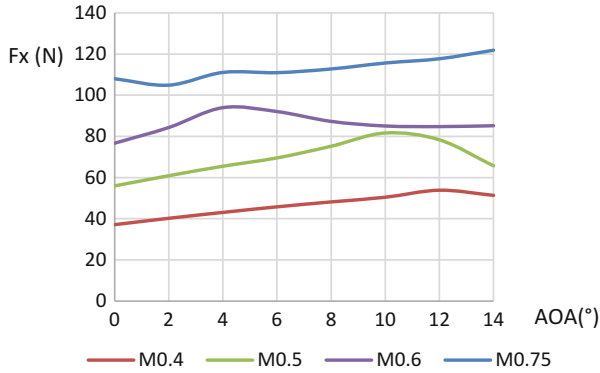


Fig. 7.6 Normal force at fully extended 2% Gurney flap front surface, $Re = 4E + 06$, $M = 0.4-0.75$

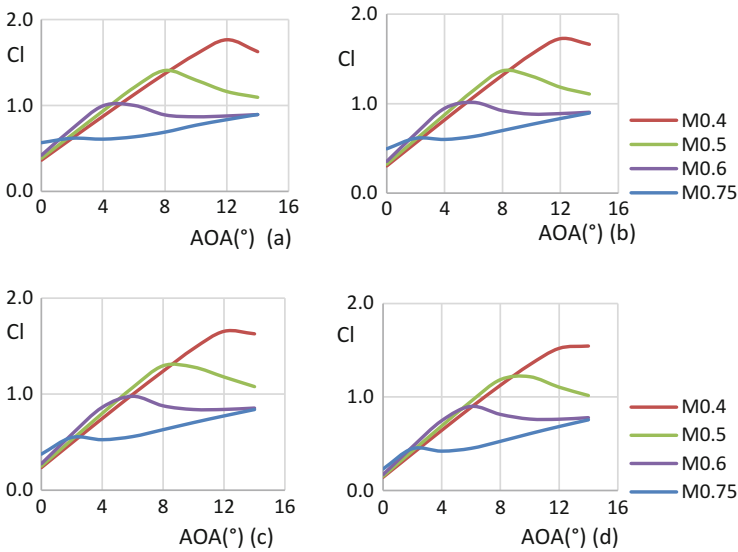


Fig. 7.7 Lift coefficient comparison at retracting Gurney flap positions (a) 80° (b) 70° (c) 60° (d) 50° , $Re = 4E + 06$, $M = 0.4-0.75$

changes in aerodynamic coefficients with lesser restrictions on the mesh boundary layer and turbulence model used. Recent research has indicated the advantages of flow control strategies in mitigating adverse flow phenomenon. While a plethora of different active flow control techniques being explored, the use of trailing edge Gurney flaps seems to be one of the more promising and cost-effective concepts. The next results in Fig. 7.7 are for a NACA 23012 with 2% Gurney flap at different retracting positions shown in Fig. 7.2.

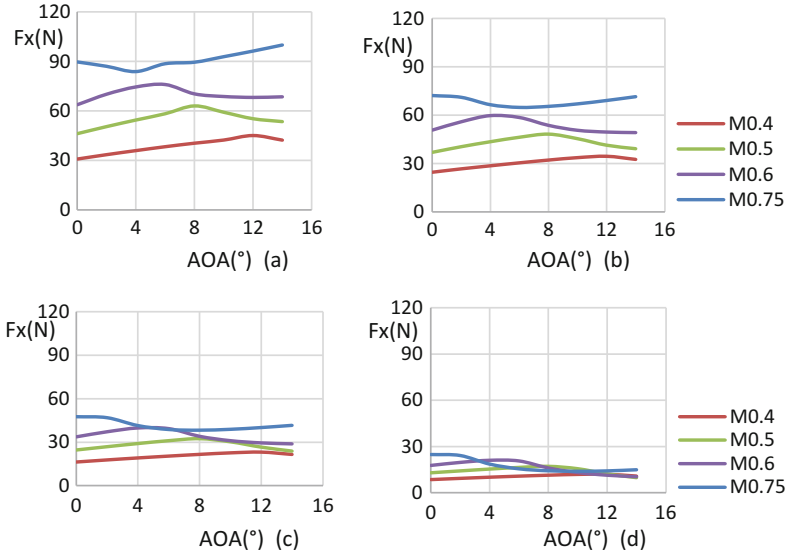


Fig. 7.8 Normal force on Gurney flap front surface comparisons at retracting Gurney flap positions (a) 80° (b) 70° (c) 60° (d) 50°, $Re = 4E + 06$, $M = 0.4-0.75$

The different Gurney flap positions are obtained from the Gurney flap actuation mechanism, and the aerodynamic coefficients and normal force on the Gurney flap front surface are plotted. The results show the decrease in lift coefficient with retracting flap evident of the reduction in effectiveness of the flap on the airfoil aerodynamic performance. The results also provide a measure of the normal force on the Gurney flap front surface to gauge the force that can be expected during deployment and retraction schedule of the flap and the estimate of force required by the actuation system to hold the Gurney flap at a certain position (Fig. 7.8).

The results obtained for the two-dimensional NACA 23012 airfoil dynamic characteristics are discussed next. The clean airfoil and airfoil with 2% Gurney flap are compared for a dynamic analysis with prescribed pitching motion.

The angle of attack scheduling of the dynamic stall analysis is

$$a(t) = a_m + a_a \sin(2\pi ft) \quad (7.3)$$

about the quarter chord at Mach number 0.4, $Re = 4 \times 10^6$. Dynamic characteristic is analyzed for mean angle of attack, $\alpha_m = 7^\circ$ with an amplitude of oscillation at $\alpha_a = 5^\circ$ and pitching frequency $f = 4.5$ Hz. The capability of Ansys Fluent 14.5 in predicting the behavior of an oscillating airfoil is assessed as a test case for the aeroelastic tool developed. For the case analyzed, hysteresis behavior of lift and moment coefficient is shown below in Fig. 7.9 along with the normal force acting on the Gurney flap front surface.

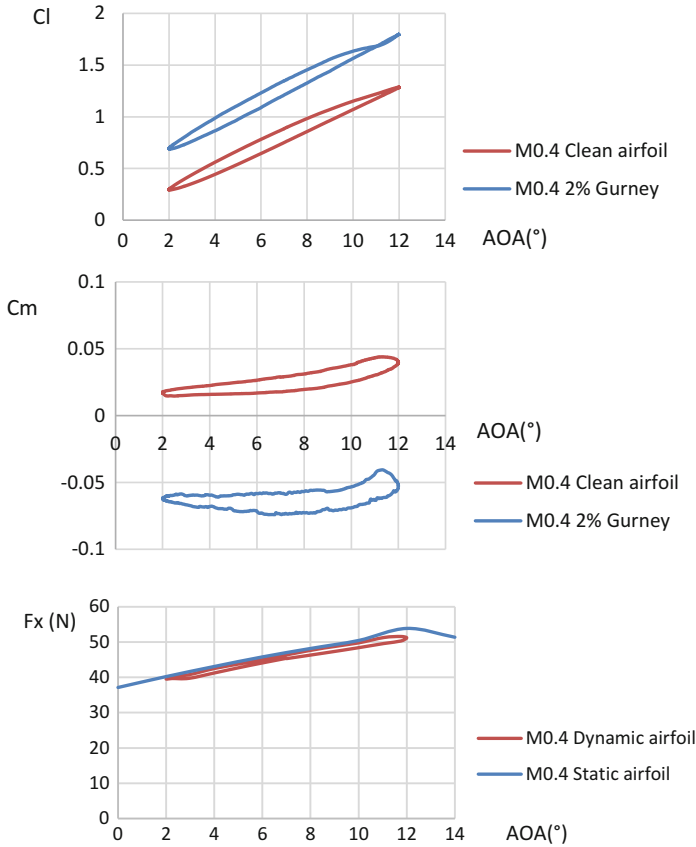


Fig. 7.9 NACA 23012 airfoil integrated coefficient variation for pitching clean and flapped airfoil in two dimensions: $\alpha(t) = 7^\circ + 5^\circ \sin(2\pi ft)$, $f = 4.5 \text{ Hz}$, $M = 0.4$, $Re = 4E + 06$

Results are averaged over two pitching cycles, where repeatability of data from cycle to cycle is observed. Modeling using URANS turbulence methods can lead to some deficiencies, including smearing of flow field characteristics due to insufficient time steps. When the cycle to cycle repeatability of the results is observed after initial pitching cycle, solution data can be obtained for analysis. The convergence of a dynamic stall simulation is determined by repeating the dynamic cycle until there is little change in the integrated forces and moments between cycles. However, this sometimes does not ensure that the simulation has converged to the correct physical behavior, with regard to reattachment and other complex flow physics. The dynamic calculation results obtained indicate in general an agreement with the static results displaying an improvement in lift and pitching moment coefficients. The estimation of force applied by the flow field at the front surface of a 2%c Gurney flap is also in agreement for both the static and dynamic analysis.

7.5 Conclusion

A computational study is performed to investigate the effects of the Gurney flap on a NACA 23012 airfoil and calculate the force imparted by the flow on the Gurney flap. The results for the advantages of the Gurney flapped airfoil over clean airfoil are found to agree well with the available experimental results. A $2\%c$ Gurney flap, where c is the chord length, is used as larger Gurney flaps will increase lift at the expense of increasing drag. The Gurney flap in comparison with a clean airfoil increases the lift coefficient and nose down pitching moment for a range of angle of attack, and a higher lift-to-drag ratio is achieved at higher lift coefficients. The separation point of the NACA 23012 airfoil with a Gurney flap is farther aft at moderate angles of attack than that of a clean airfoil. The maximum force at the Gurney flap is estimated at 120 N for a $2\%c$ height with unit length and gives an estimation of the force to be applied and number of piezoelectric actuators for the deployment and retraction of the Gurney flap, and the results are found to be similar for both static and dynamic analysis.

References

- Jang CS, Ross JC, Cummings RM (1998) Numerical investigation of an airfoil with a gurney flap. *Aircr Des* 1(2):75
- Leishman JG (1990) Dynamic stall experiments on the NACA 23012 aerofoil. *Exp Fluids* 9(1–2):49–58
- Liebeck R (1978) Design of subsonic airfoils for high lift. *J Aircr* 15(9):547–561
- Menter FR (1994) Two equation eddy viscosity turbulence models for engineering applications. *AIAA J* 32(8):1598–1605
- Neuhart D, Pendergraft O (1988) A water tunnel study of gurney flaps. National aeronautics and space administration, NASA TM-4071, NASA Langley Research Center
- Schatz M, Gunther B, Thiele F (2004) Computational modeling of the unsteady wake behind Gurney flaps. In: 2nd AIAA Flow Control Conference, Portland
- Smith DR, Amitay M, Kibens V, Parekh DE, Glezer A (2001) Aerodynamic flow control over an unconventional airfoil using synthetic jet actuators. *AIAA J* 39(3):361–370
- Storms BL, Jang CS (1994) Lift enhancement of an airfoil using a gurney flap and vortex generators. *J Aircr* 31(3):542–547
- Yoo NS (2000) Effect of the Gurney flap on a NACA 23012 airfoil. *KSME Int J* 14(9):1013–1019

Part III
Design of Rod Vortex Generator

Chapter 8

Investigation of Vortex Generators on Channels and Airfoils

Fernando Tejero, Piotr Doerffer, Pawel Flaszynski, and Oskar Szulc

Nomenclature

Latin

c	Airfoil chord [m]
C_d	Drag force coefficient [-]
C_n	Normal force coefficient [-]
C_m	Pitching moment coefficient [-]
C_p	Pressure coefficient [-]
h	Height of the rod [m]
L	Distance between VGs [m]
M	Mach number [-]
P_0	Atmospheric pressure [Pa]
P_{norm}	Normalized total pressure [-]
P_s	Static pressure [Pa]
P_t	Stagnation pressure [Pa]
$p_{\text{tot-local}}$	Local total pressure [Pa]
$p_{\text{tot-undisturbed}}$	Undisturbed total pressure [Pa]
Re	Reynolds number [-]
y^+	Nondimensional distance to the wall [-]

F. Tejero (✉) • P. Doerffer • P. Flaszynski • O. Szulc
Institute of Fluid Flow Machinery Polish Academy of Sciences, Gdansk, Poland
e-mail: fernando.tejero@imp.gda.pl

Greek

α_{VG}	Skew angle of the VG [°]
δ	Boundary layer thickness [m]
ϕ_{AJVG}	Hole diameter of the AJVG [m]
ϕ_{RVG}	Diameter of the RVG [m]
θ_{VG}	Pitch angle of the VG [°]

Acronyms

AJVG	Air-jet vortex generator
AoA	Angle of attack
CFD	Computational fluid dynamics
CFL	Courant-Friedrichs-Lewy
MEMS	Microelectromechanical systems
RANS	Reynolds-averaged Navier-Stokes
RVG	Rod vortex generator
STA-DY-WI-CO	Static and dynamic piezo-driven streamwise vortex generators for active flow control
VG	Vortex generator
VVGs	Vane vortex generator
UFAST	Unsteady effects in shock wave-induced separation

8.1 Introduction

Vortex generators (VGs) are designed to create streamwise vortices. These vortices enforce an exchange of momentum in the direction normal to the wall from the outer region. As a result, the boundary layer profiles are more full close to the wall, and the shear stress is increased. This phenomenon makes the flow stable in this critical area, and flow separation can be delayed or even eliminated. The vane vortex generators (VVGs) (or in other shapes) and air-jet vortex generators (AJVGs) are the main systems for this passive flow control device. The main advantage of VVGs with respect to AJVGs is their simpler construction, while the main disadvantage is their permanent drag penalty.

During the last years, Doerffer et al. (2009) introduced a new type of VG: rod vortex generators (RVGs). This new kind of passive flow control system is preferred over other more complex geometries (wishbones or triangles) due to its simpler manufacturing and easy activation using microelectromechanical systems (MEMS) technology. The main research concerning this new type of VG has been carried out in supersonic conditions and shock wave-boundary layer interaction.

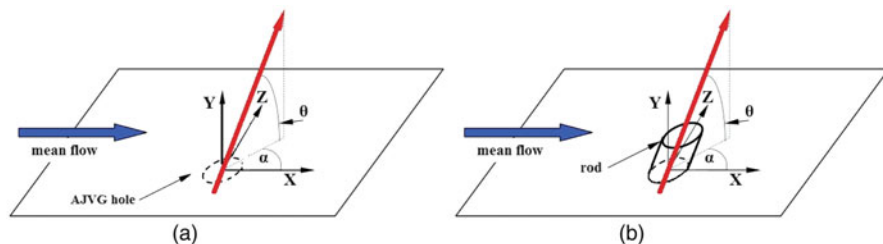


Fig. 8.1 (a) Schematic view of AJVG. (b) Schematic view of RVG

Experiments confirmed that the rods are also effective in delaying flow separation at severe conditions. Further numerical investigations assess the optimum parameters for inducing the strongest streamwise vortex, thus maximizing the dumping of the flow separation. During the 7th European Framework Programme STA-DY-WI-CO (Static and Dynamic Piezo-Driven Streamwise Vortex Generators for Active Flow Control), the piezoelectric technology was investigated to actively deploy or retract RVGs limiting the parasitic drag. On the other hand, proposed in the beginning of the 1960s by Wallis, the air-jet vortex generators are implemented as an array of small orifices placed in a line transverse to the flow direction which produce longitudinal vortices. Unlike the vane vortex generators, AJVGs do not induce a large drag penalty. Besides, they can be easily switched off in contrast to the VVGs that are mounted in a fixed manner.

The design of the most effective AJVG for given flow conditions is challenging mainly due to the large number of interrelated parameters under consideration. The optimum configuration must take into account the hole diameter (ϕ_{AJVG}) where the air jet is blown, hole spacing (L), and skew (α_{VG}) and pitch (θ_{VG}) angles (see Fig. 8.1a). The first two parameters (ϕ_{AJVG} and L) are set according to the boundary layer thickness, based on the previous research (Flaszynski and Szwaba 2007), while the angles α_{VG} and θ_{VG} should be optimized for a maximum intensity of the generated streamwise vortex. In case of RVG, following parameters should be taken into account for the most effective design: diameter and height of the rod (ϕ_{AJVG} and h , respectively), the spacing (L) between rods, and the skew (α_{VG}) and pitch (θ_{VG}) angles (see Fig. 8.1b).

8.2 Numerical Model

The present numerical investigation was carried out by means of the commercial codes Numeca Fine/Turbo and Ansys Fluent and the in-house solver FLOWer from DLR. The physical modeling was based on the Reynolds-averaged Navier-Stokes (RANS) equations closed by the Spalart-Allmaras, $k-\omega$ SST, or $k-\omega$ LEA turbulence model (depending on the case and flow solver used). The system of differential

equations was closed by a perfect gas model. The viscosity value was calculated according to the Sutherland's law. The numerical algorithm used a semi-discrete approach with a finite volume central scheme for spatial discretization and Runge-Kutta type integration of time. The CFL number was set to 2. A full multigrid strategy was implemented to improve the convergence rate. For each simulation a drop of residuals of 6.5 orders of magnitude ensured convergence of forces.

8.3 Vortex Generators on Channel Flows

8.3.1 Experimental Setup Description

The experimental investigations of supersonic nozzles have been carried out in flat and curved test sections. Previously, both nozzles were investigated within the UFAST project (*Unsteady Effects in Shock Wave Induced Separation*, Doerffer et al. 2010) providing the largest available database concerning unsteady shock wave-boundary layer interaction. The main feature of flat wall nozzle is the flow uniformity upstream of the shock wave. The appropriate shape of the upper nozzle wall allows to obtain constant Mach number (triangular area—Fig. 8.2a) upstream of the shock. On the other hand, in the curved duct, the supersonic area is generated at the convex wall. The Mach number upstream of the shock increases with mass flow rate in the nozzle, until the nozzle is choked. The intensity of the shock wave is strong at the convex wall, and it vanishes at the opposite wall (Fig. 8.2b).

Figure 8.3a presents a view of the main measurement section of the flat wall nozzle. The upper wall is shaped as a de Laval nozzle, while the lower wall is flat. Thanks to it, it is possible to obtain a constant flow velocity upstream and downstream of the jet hole. The vortex generators are placed on the flat measurement plate at the $X = 0$ mm location. During the experimental research, a standard and optimized configuration was investigated. The standard VG was treated as a reference case for the optimization process. The pressure measurement taps were located downstream of the VGs. A detailed view of the measurement plate is showed in Fig. 8.3b. To investigate the influence of both proposed vortex generators, different measurements were carried out: inlet flow conditions, static pressure distribution downstream of the VGs, stagnation pressure planes in boundary layer downstream of VGs (made by pitot probe of 0.5 mm external diameter), and oil visualization on the surface. For the AJVG case, the mass flow in the jet hole is measured with a laminar flow meter.

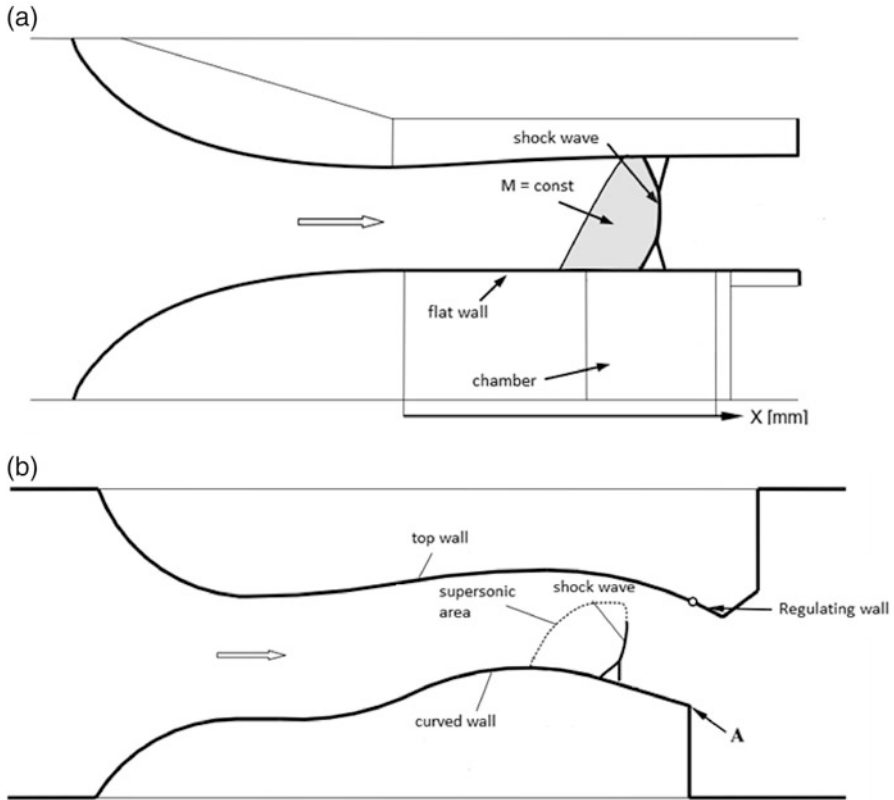


Fig. 8.2 Sketches of the test section: (a) flat and (b) curved (Doerffer et al. 2010)

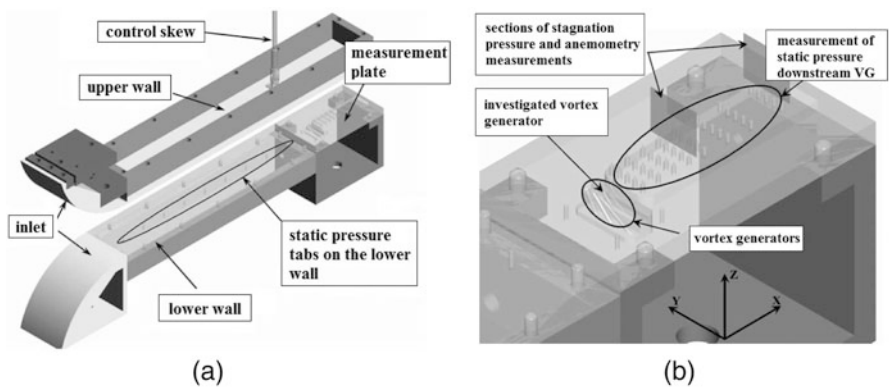


Fig. 8.3 (a) General view of subsonic and transonic nozzle. (b) Detailed view of the measurement plate

8.3.2 CFD Investigation: Basic Configuration

For the basic investigations of vortex generators, the computational domain is defined as a rectangular prism with the single VG located in the middle of the lower wall (an example of the CFD domain for the AJVG configuration is presented in Fig. 8.4). Despite the simplification (from a full nozzle to a rectangular prism) performed for the numerical simulations, the computational domain does not influence the results since the same inlet conditions as in the experiments are applied (the boundary layer was measured upstream the VGs and used as CFD boundary conditions) and the sidewall effect is too weak to influence on the generated vortex evolution. For the single AJVG case, the grid consists in 25 blocks and 2.3 million of volumes against 43 blocks and 3.0 million of volumes for the single RVG case. For both domains, the distance of the first grid point to the wall is of the order $y^+ = 1$. The grid is refined close to the vortex generator and downstream, in the streamwise vortex vicinity to reduce the numerical dissipation. The domain is formed by four types of boundary conditions: pressure inlet/outlet, symmetry at the lateral and upper sides, and viscous wall (no-slip condition and adiabatic) at the lower side of the domain (see Fig. 8.5). The flow conditions are set according to the measured data. The boundary layer profile is prescribed by the total pressure distribution at the inlet where the total temperature is also imposed. The static pressure at the outlet is set to obtain the required Mach number ($M = 0.30$). At the inlet of the AJVG hole, total conditions of the main flow are applied (passive system as described above). All presented numerical results of this section are based in Numeca Fine/Turbo solver.

The inflow conditions for studying the influence of VGs in subsonic regime were set, according to measurements, to provide $M = 0.3$ (incoming boundary layer thickness upstream of 12 mm). The vortex generator parameters were set according to the experiments: the diameter of the AJVG hole was 1 mm (≈ 0.18), and the

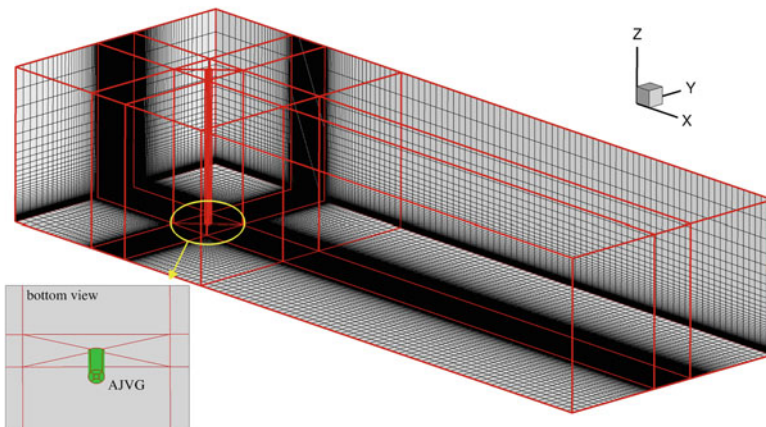


Fig. 8.4 CFD domain for the AJVG configuration

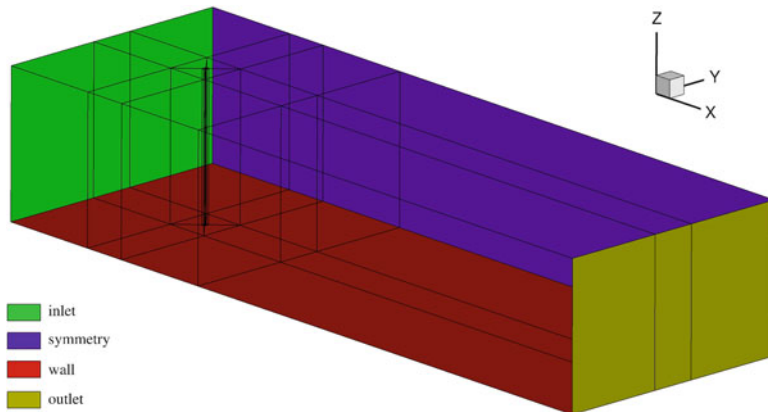


Fig. 8.5 Boundary conditions for the AJVG configuration

control angles were defined according to the standard configuration (skew of 90° and pitch equal to 45°). On the other hand, the diameter of the RVG was 2 mm with a height of 3.6 mm ($\approx 0.1\delta$) and 45° and 30° for skew and pitch angles, respectively.

A detailed insight into the flow structure in the boundary layer may be obtained by comparing total pressure in some cross sections downstream of the VGs. For this purpose, the variable normalized total pressure (P_{norm}) is defined as the ratio of total pressure between the disturbed flow by the VG and the undisturbed one. Values above 1 imply momentum transport from the outer zone of the boundary layer toward the wall, while values below 1 imply a low momentum boundary layer zone lifted off the wall.

$$P_{\text{norm}} = \frac{P_{\text{tot-local}}}{P_{\text{tot-undisturbed}}} \quad (8.1)$$

Each flow control device has been computed with the two different turbulence models (Spalart-Allmaras, $k-\omega$ SST) and compared with the available experimental data. Although there are quantitative differences between numerical results and measurements, there is a qualitative good agreement. Shapes of maximum and minimum P_{norm} are well reproduced by the computations, but the values are slightly overpredicted by CFD. This means that the measured streamwise vortex is weaker than the computed one.

Figure 8.6 compares the normalized total pressure at 48 mm downstream of the AJVG (the streamwise vortex direction of rotation is marked by an arrow in Fig. 8.6). It is worth noticing that the vortex location (placed between the maximum and minimum values of normalized total pressure) is similar for both computations and measurements and how the vortex core moves Y-positive in streamwise direction due to the air jet is blown with certain skew angle.

Results related to RVG case appear in Fig. 8.7. It is also visible how the vortex location and its intensity are satisfactorily reproduced by the numerical simulation.

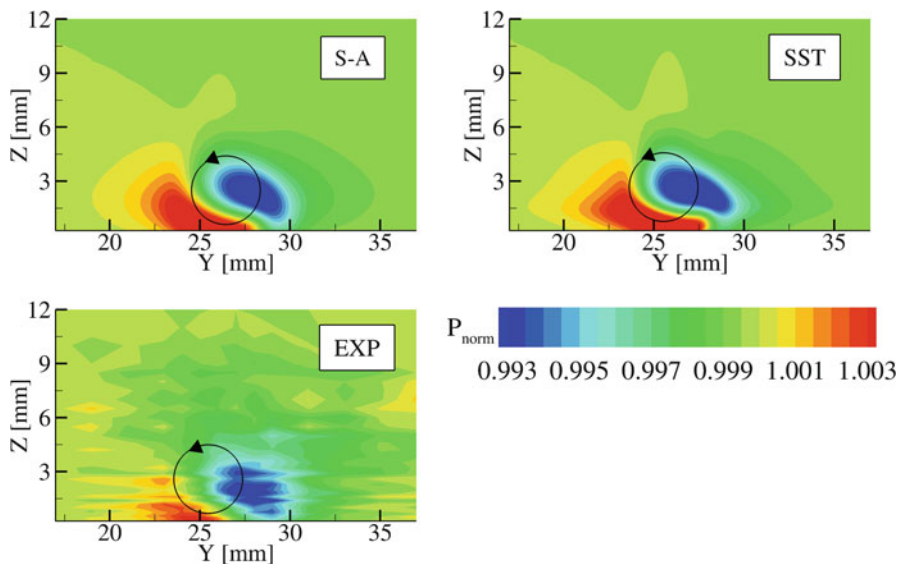


Fig. 8.6 Normalized total pressure. AJVG case, $M = 0.3$, $X = 48$ mm

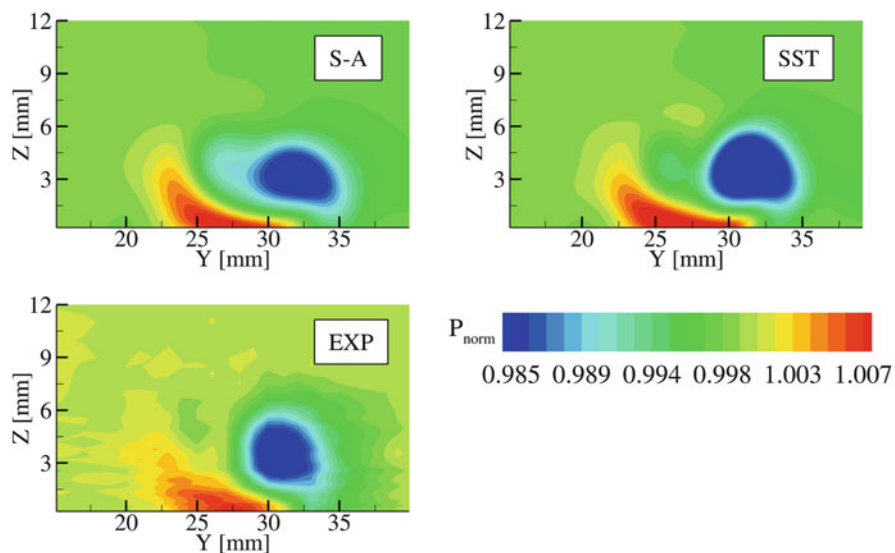


Fig. 8.7 Normalized total pressure. RVG case, $M = 0.3$, $X = 51$ mm

In this section only validation of the numerical model of vortex generators is shown and not a comparison of their effectiveness. For such comparison both VGs should work in their optimized range of skew and pitch angles.

Other inflow conditions ($M = 0.8$ and 1.45) were considered in this basic investigation of the development of streamwise vorticity. Numerical results were compared with the available measurements with success. Similar trends as for the presented case ($M = 0.3$) were obtained. More details of these flow conditions can be found in Tejero (2016).

8.3.3 CFD Investigation: Curved Wall Nozzle with RVG

Correct prediction of the flow separation, its location and reattachment lines, and size of the separation bubble is very important for accurate estimation of aerodynamic performances. In the case of a channel (nozzle) flow, accurate prediction of the flow structure by numerical methods is highly dependent on the properly resolved corner separation. The numerical investigation of the flow structure downstream of the shock wave is presented in this section. Numerical results are compared with experimental data obtained within the framework of the UFAST project. In addition, 16 rod vortex generators were placed upstream of the flow separation, and the flow structures were analyzed experimentally in the past and numerically in this section. CFD results are compared with the available measurements (boundary layer upstream of the shock wave, static pressure on the wall, oil visualization, and schlieren picture).

Figure 8.8 presents the 2D view of the mesh and its topology for the curved wall nozzle. It is divided in six zones. The zone 3 showed in Fig. 8.8 (upstream of the shock wave) consists of 145×85 cells and the zone 5 (in the shock wave location) of 281×85 cells. For the flow control cases, the rods are placed in zone 4. The distance of the first grid point from the solid walls (upper and lower) is of the order $y^+ = 1$.

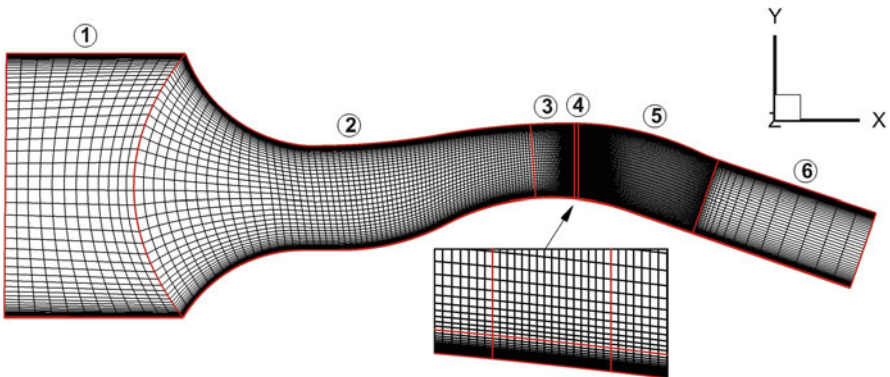
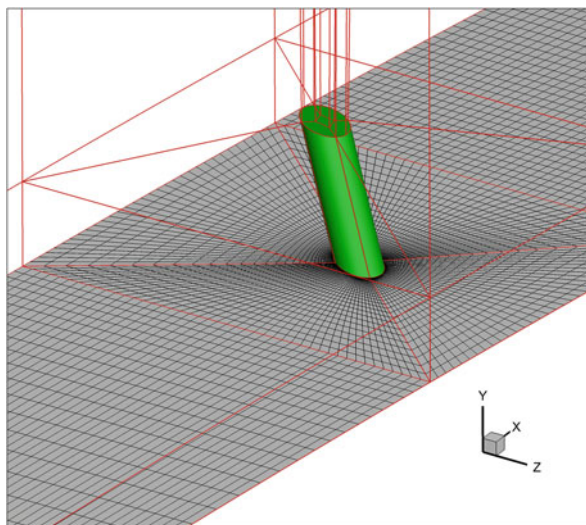


Fig. 8.8 2D view of the curved wall nozzle

Fig. 8.9 3D view of the curved wall nozzle with one RVG



For the creation of the computational domain for only one rod, the 2D model is extruded in the Z-direction (creating a 3D model), and the grid topology for one RVG is applied in zone 4. The rod is embedded in a rectangular box and an O-topology is applied (see Fig. 8.9). Computing the 2D model for the reference case or the 3D with a single rod (flow control case) neglects the influence of corner flows. For this reason, the whole nozzle was simulated as well (corner flows are resolved) increasing considerably the computational cost. It was found during the numerical investigation of the full channel that the corner flows were overpredicted leading to unphysical solutions. For this reason, the lower corners were chamfered relieving the strength of these secondary flows, obtaining more physical solutions.

The computational domain of the whole curved wall nozzle for the reference case is formed by 240 blocks and 4.86×10^6 volumes. The whole nozzle with rod vortex generators was built by extruding the 3D model for a single RVG 16 times in spanwise direction. The computational domain consists of 416 blocks and 21.67×10^6 volumes.

As far as boundary conditions are concerned, the total pressure and temperature are set to 101 KPa and 283 K, respectively, at the nozzle inlet (according to measurements). A turbulent intensity of 0.5 % and a turbulent viscosity ratio equal to 1.0 were applied during the simulations. At the nozzle outlet, the static pressure was adjusted to correspond with the measured shock wave location. The upper, lower, and side walls of the nozzle are modeled as adiabatic with no-slip condition (the same approach is applied for the rod). Against the whole nozzle, periodic boundary conditions at the side walls are applied for the simplified 3D RVG model (simulation of a single rod). In contrast to the flat wall nozzle, the curved one has been investigated with several solvers (Numeca Fine/Turbo, Ansys Fluent, and FLOWer) and turbulence models (Spalart-Allmaras, $k-\omega$ SST, or $k-\omega$ LEA).

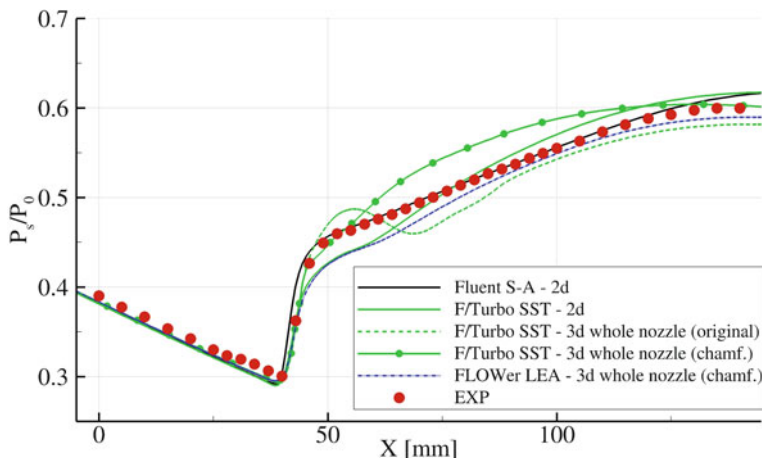


Fig. 8.10 Pressure distribution at the lower wall—reference (no flow control) case

Figure 8.10 summarizes the numerical results concerning the static pressure distribution at the lower wall for the different approaches (full channel and one rod pitch distance) and models (original and chamfered geometry) investigated. The original geometry for the whole nozzle is just presented for the Numeca Fine/Turbo solver with the SST closure (results for the rest of combinations of solvers and turbulence models were similar). For clarity of the figure, selected numerical results for different solvers, turbulence models, and geometry approaches (2D, 3D original, or 3D chamfered) are presented. Concerning the 3D simulations for the full span of the nozzle, the numerical results for Fine/Turbo suggest that there is an underprediction of the flow separation in respect of experiments, while FLOWer code overpredicts it.

Since the side wall boundary layer and corner separation are taken into account in the 3D models, the main discrepancies of the separation prediction arise from a wrong prediction of the incoming boundary layer thickness (comparison presented in Fig. 8.11). For all solvers and geometries, the incoming boundary layer (cross section located at $X = 15$ mm) is overpredicted by the numerical models with an inflow velocity lower than the experimental one. Some differences are also visible in the area of shock wave-boundary layer interaction ($X = 67$ mm). The Fine/Turbo computation of the full span of the nozzle shows a very narrow height of the bubble separation (in contrast to measured data where the height was approximately 2 mm). Once again, the overprediction of flow separation obtained with FLOWer is visible in this cross section where the height of the bubble is approximately 2.5 mm. Lastly, the traverse located after the reattachment line ($X = 145$ mm) shows an overprediction of the boundary layer due to the overestimation of the incoming one.

Figure 8.12 presents the pressure distribution along the nozzle when the RVGs are present. The RANS simulation for the chamfered nozzle with 16 rods reveals a contraction and expansion of the flow at the middle plane (more visible in the

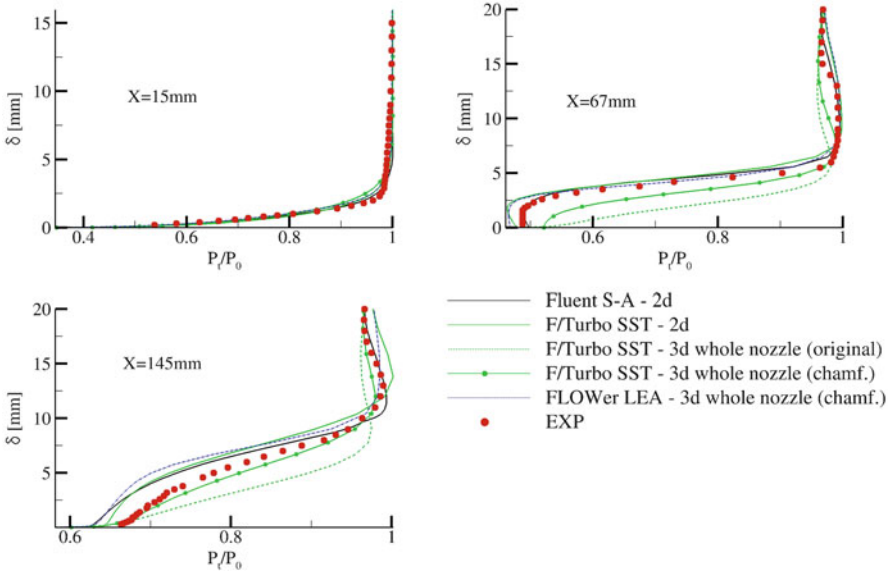


Fig. 8.11 Boundary layer comparison—reference (no flow control) case

FLOWer solution). This behavior is not due to the overprediction of the corner flow (avoided with the chamfering) but rather to the size of the separation bubble predicted by CFD. Despite the reverse flow is limited by the streamwise vortex generators (split in several bubbles), there are some large remains (they will be presented in next figures) which lead with this behavior.

Boundary layer downstream the shock wave ($X = 67$ mm and 145 mm) is presented in Fig. 8.13 where differences of boundary thickness and triple point location are visible.

Figure 8.14 compares the separation bubbles for the reference and flow control cases (whole nozzle). The reverse flow is limited by the influence of the rod vortex generators. The massive flow separation is not completely eliminated but splitted in smaller and weaker separation bubbles. Nevertheless, the positive effect of the proposed flow control device in flow separation control is evident. The separation bubble extension for the reference case is 24 mm (from $X = 47$ mm to $X = 71$ mm) for the Numeca Fine/Turbo simulation against the 44 mm (from $X = 44$ mm to $X = 88$ mm) for the FLOWer computation. The application of rod vortex generators reduces significantly the reverse flow which is in line with the observations during the measurements. This reduction was not so noticeable for the simplified models (2D for the reference case or 3D with a single RVG for the flow control case).

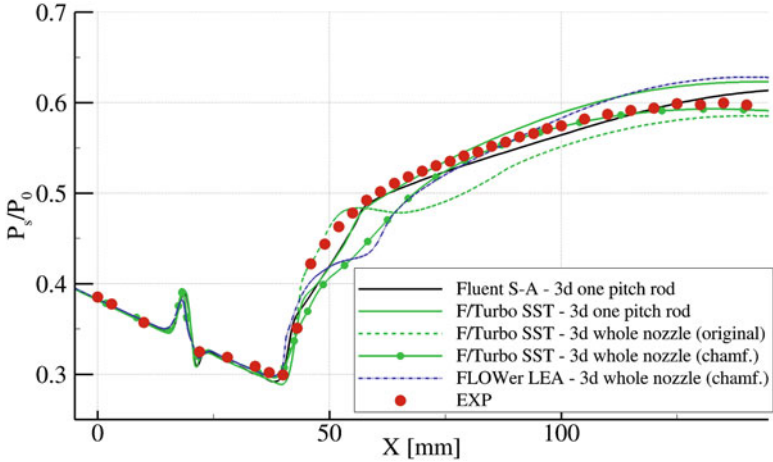


Fig. 8.12 Pressure distribution at the lower wall—RVG (flow control) case

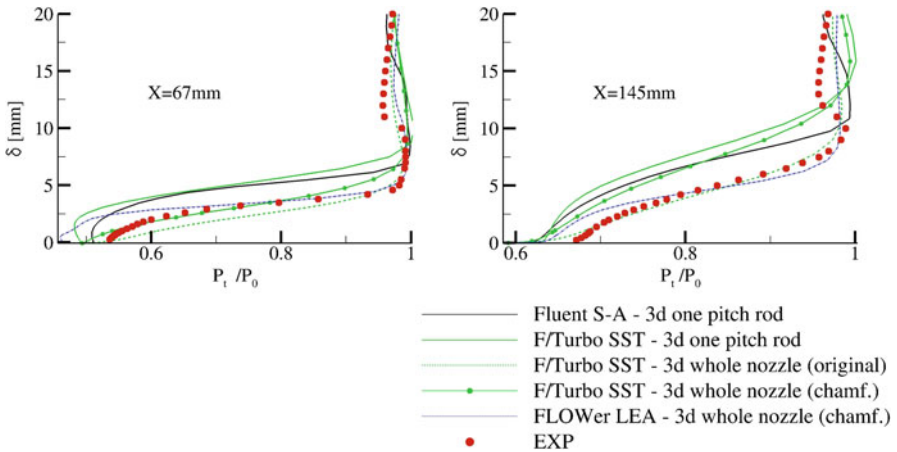


Fig. 8.13 Boundary layer comparison—RVG (flow control) case

8.4 Vortex Generators on Airfoils

The main objective of this section is to discuss the application of the proposed vortex generators (i.e., AJVGs and RVGs) on a NACA 0012 (see Tejero et al. 2015 for more details). The NACA 0012 has been chosen for this research not only due to the large available experimental database but preferably because it constitutes a basic cross section of the Caradonna-Tung model rotor—a carefully chosen configuration for implementation of the RVGs (discussed in the next chapter).

In the case of transonic conditions investigated ($M = 0.80$ and $Re = 9 \times 10^6$), the flow separation appears for angles attack above 1.4° . There is a strong shock wave-boundary layer interaction which might be controlled by the proposed flow control

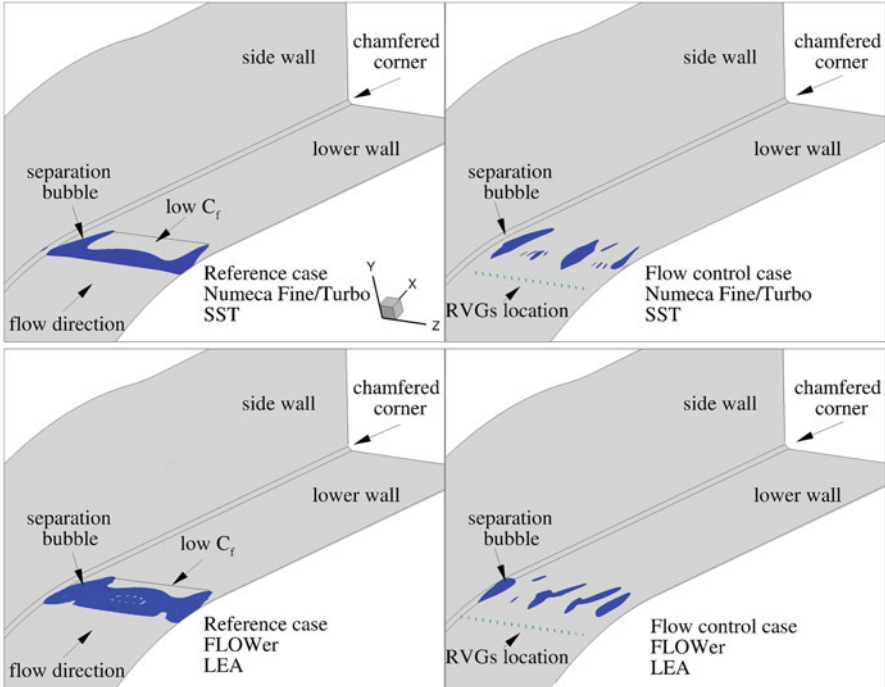


Fig. 8.14 Separation control by RVGs on the curved wall nozzle

device. The boundary layer thickness (δ) just upstream of the reverse flow location ($x/c = 0.25$) is approximately $0.01c$.

In previous investigations carried out during UFAST, Doerffer et al. (2010) suggest that the jet hole diameter should be scaled according to the boundary layer thickness (10–20% of δ) and the hole spacing should be ten times the diameter. For this reason, the diameter of the AJVG in the present investigation was set to $15\% \times \delta$ ($0.0015c$), with a spanwise distance between AJVGs (L) of $0.015c$. The skew (α_{VG}) and pitch (θ_{VG}) angles were set to 65° and 30° , respectively, which induced the strongest streamwise vortices. On the other hand, the diameter of the rod vortex generator was set to 15% of δ with a height (h) of half of boundary layer thickness and a skew and pitch angles of 45° and 30° , respectively.

For this investigation, three grids were prepared (reference, AJVG, and RVG) with the same topology and similar total number of volumes (approx. 5.5 million) in order to avoid grid influences. The computational domain was fixed to a single vortex generator with translational periodicity boundary condition in the spanwise direction. The main reason for this approach is the enormous computational cost of a full wing with an array of vortex generators. Still, the remaining task was computationally very demanding, mainly due to the complexity of the flow structures simulated.

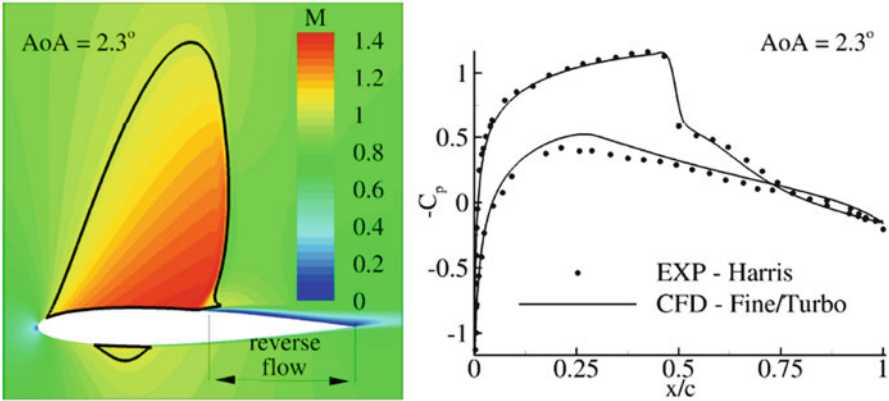


Fig. 8.15 Mach contour map and numerical validation of the NACA 0012, $M = 0.8$ and $AoA = 2.3^\circ$ (Tejero et al. 2015)

As a previous step to implement the proposed vortex generators, the numerical model for the reference case (no flow control) was validated against the available experimental data (Harris 1981). Figure 8.15 presents the Mach contour map and pressure distribution around the profile. The agreement on the suction side (where flow separation is present) is acceptable with a proper prediction of the shock wave location.

As it was mentioned above, the onset of separation is found for $AoA = 1.4^\circ$ (reattachment is also present). With increased angles of attack, the reverse flow becomes stronger, and the application of proposed vortex generators can be beneficial for aerodynamic enhancement. Besides, the detachment line moves upstream with higher incidence angles, which suggest that the location of the VGs should be also investigated. For the present flow conditions, the location of VGs at $x/c = 0.30$ showed the best aerodynamic improvement in the range of angles of attack studied.

Figures 8.16 and 8.17 present contour maps of skin friction coefficient C_f and streamlines on the suction side of the NACA 0012 profile for all configurations (reference, AJVG and RVG). For the onset of separation, $AoA = 1.4^\circ$ (Fig. 8.16), the flow reattaches to the wall, while for higher inflow angles, $AoA = 4.0^\circ$ (Fig. 8.17), the reverse flow extends until the trailing edge. The skin friction coefficient is increased downstream of the vortex generator location due to the higher shear stresses. Therefore, there is an impact in the flow separation area. In order to see better the interaction between flow control devices, the figures present the slice with three vortex generators (despite the numerical simulations were carried out for just one VG). For the $AoA = 1.4^\circ$, the flow separates at approximately $0.55c$ and reattaches at $0.70c$. With AJVG, the same location of flow detachment is maintained with more upstream reattachment at a mean value of $0.65c$, while with RVGs approximately the same reattachment position is obtained.

Figure 8.18 summarizes the effect of the proposed flow control devices on the polars (i.e., normal force C_n , drag C_d , and pitching moment C_m coefficients).

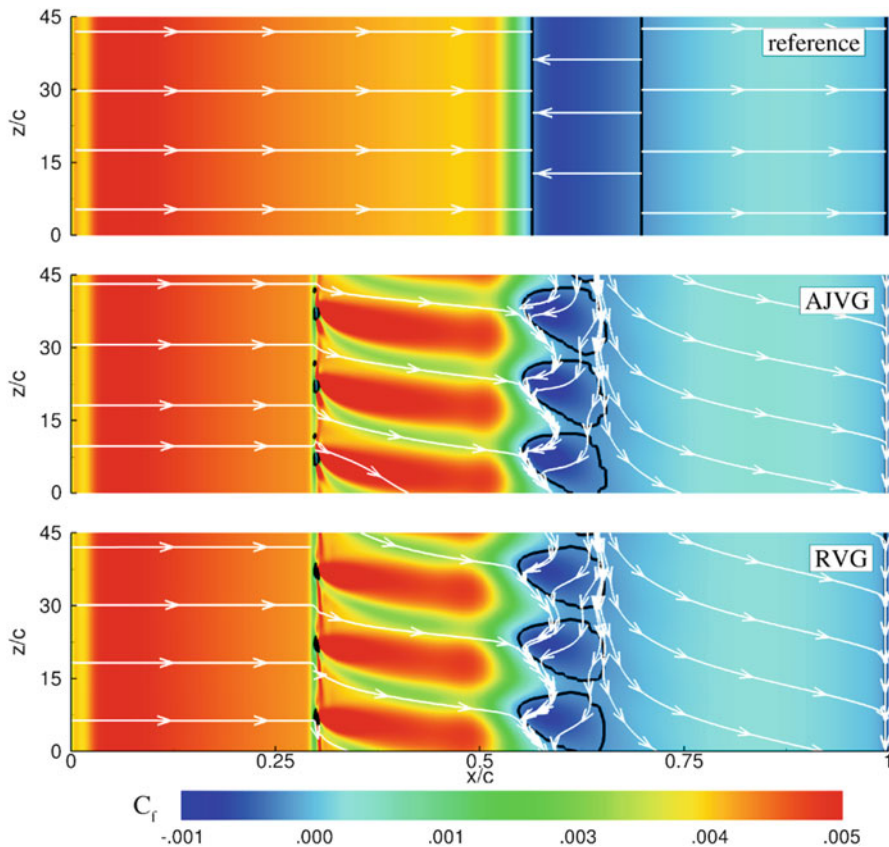


Fig. 8.16 Friction coefficient and streamlines (NACA 0012; $M = 0.8$, $\text{AoA} = 1.4^\circ$, and $\text{Re} = 9 \times 10^6$) (Tejero et al. 2015)

The flow is fully attached for angles of attack below 1.4° ; therefore no results are showed for the AJVG and RVG configurations. With increased inflow angles, flow separation develops, and the formation of streamwise vortices affects the flow separation (reducing it), thus increasing the C_n . Nevertheless, there is a drag penalty due to the implementation of VGs, but still the ratio C_n/C_d suggests that the aerodynamic performance of the NACA 0012 airfoil in transonic conditions is improved. On the other hand, the VGs increase the C_m coefficient for angles of attack above 3.0° .

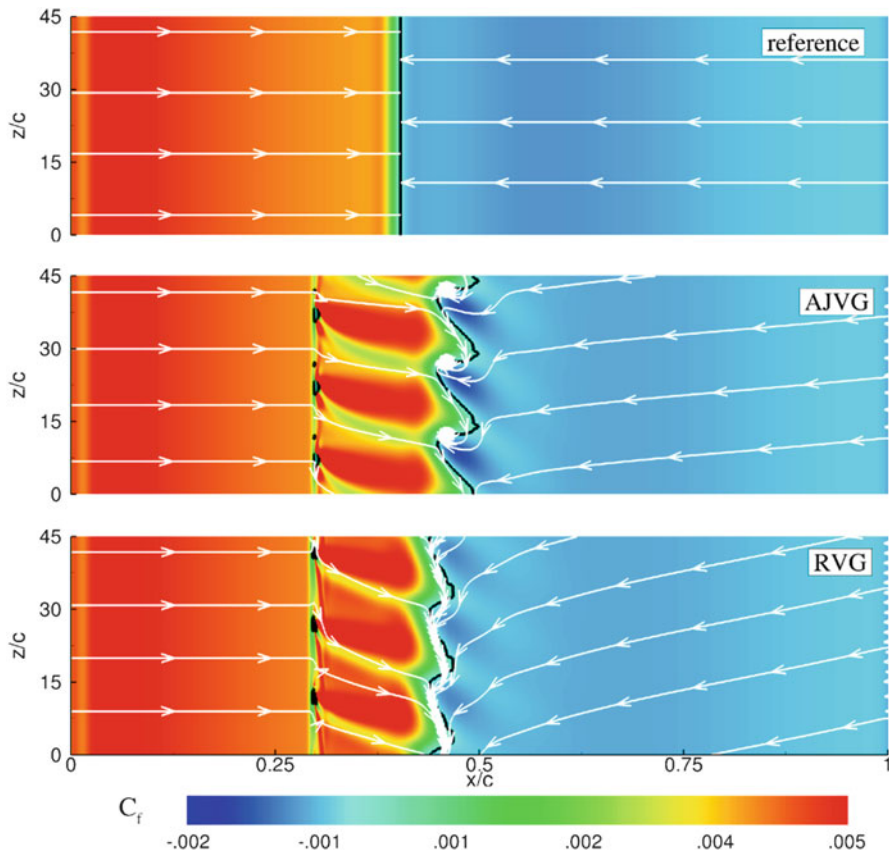


Fig. 8.17 Friction coefficient and streamlines (NACA 0012; $M = 0.8$, $AoA = 4.0^\circ$, and $Re = 9 \times 10^6$) (Tejero et al. 2015)

8.5 Conclusions

The chapter presents the numerical results of the implementation of two passive vortex generators: air-jet vortex generators (AJVGs) and rod vortex generators (RVGs).

Firstly, the investigation was focused in channel flows where the development of streamwise vortices was studied for both devices. Then, the research was extended to the study of the reduction of the flow separation induced by a strong shock wave ($M = 1.43$) on a curved wall nozzle by rod vortex generators. Experimental and numerical results showed that the proposed flow control device is suitable for separation reduction.

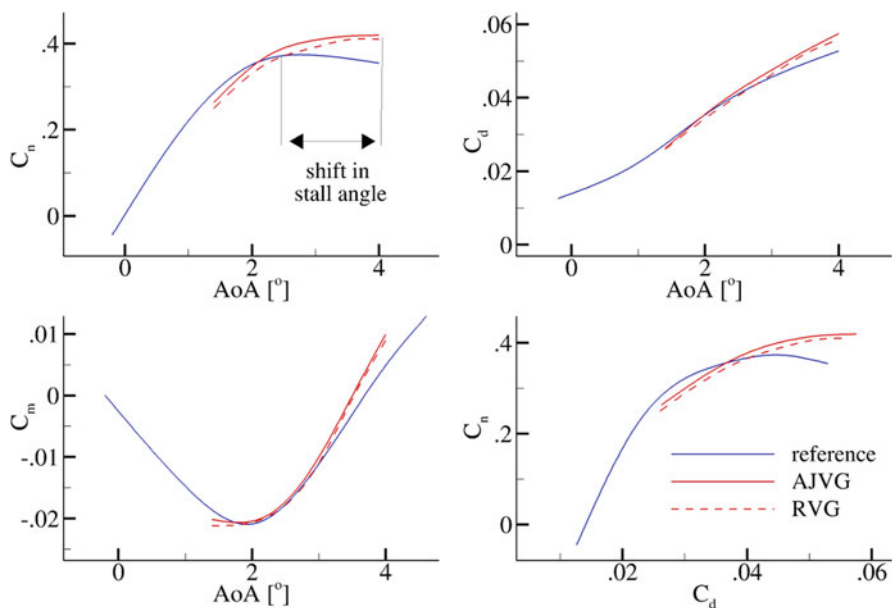


Fig. 8.18 Polar graph comparison (NACA 0012; $M = 0.8$ and $Re = 9 \cdot 10^6$)

Finally, the implementation of AJVGs and RVGs on airfoils was investigated. Both devices were effective in separation control. As a result, the normal force was increased and the stall angle was delayed significantly. Nevertheless, the implementation of VGs results in a drag penalty (but with a better ratio L/D).

References

- Doerffer P, Flaszynski P, Szwaba R (2009) Polish Patent P. 389685
- Doerffer P, Hirsch C, Dussauge JP, Babinsky H, Barakos GN (2010) Unsteady effects of shock wave induced separation. Notes on Numerical Fluid Mechanics and Multidisciplinary Design, Springer. ISBN 978-3-642-03003-1
- Flaszynski P, Szwaba R (2007) Optimization of streamwise vortex generator for subsonic flow. In: 8th International Symposium on Experimental and Computational Aerothermodynamics of Internal Flows, Lyon, France
- Harris CD (1981) Two-dimensional aerodynamic characteristics of the NACA 0012 airfoil in the Langley 8-foot transonic pressure tunnel. NASA Technical Memorandum 81927
- Kenning OC, Kaynes IW, Miller JV (2004) The potential application of flow control to helicopter rotor blades. 30th European Rotorcraft Forum, Marseilles, France, September 14–16
- Tejero F (2016) Numerical investigations of the possibilities of separation reduction on a helicopter rotor blade by means of streamwise vortices, PhD thesis
- Tejero F, Doerffer P, Szulc O (2015) Shock wave induced flow separation control by means of air-jet and rod vortex generators. TASK Quart 19(2):167–180
- Wallis RA (1960) A preliminary note on a modified type of air jet boundary layer control. Aeronautical Research Council, Rept. CP 513

Chapter 9

Implementation of Rod Vortex Generators on Helicopter Rotor Blades in Hover and Forward Flight Conditions

Fernando Tejero, Piotr Doerffer, Paweł Flaszynski, and Oskar Szulc

Nomenclature

Latin

c	Airfoil chord [m]
C_p	Pressure coefficient [-]
C_q	Torque coefficient [-]
C_T	Thrust coefficient [-]
h	Height of the rod [m]
L	Distance between VGs [m]
M	Mach number [-]
M_T	Tip Mach number [-]
R	Rotor radius [m]
Re_T	Tip Reynolds number [-]
V_∞	Forward speed [km/h]
y^+	Non dimensional distance to the wall [-]

Greek

δ	Boundary layer thickness [m]
ϕ_{RVG}	Diameter of the RVG [m]

F. Tejero (✉) • P. Doerffer • P. Flaszynski • O. Szulc
Institute of Fluid Flow Machinery Polish Academy of Sciences, Gdansk, Poland
e-mail: fernando.tejero@imp.gda.pl

ψ	Rotor azimuth [°]
θ	Blade collective [°]

Acronyms

AR	Aspect ratio
CFD	Computational fluid dynamics
CFL	Courant–Friedrichs–Lewy
C–T	Caradonna–Tung
RANS	Reynolds-averaged Navier–Stokes
RPM	Revolutions per minute
RVG	Rod vortex generator

9.1 Introduction

Based on the success of simple configurations, the application of flow control systems in more realistic geometries has also been recently considered. Several techniques have been investigated in rotorcraft applications (particularly in helicopters). The main feature of the aerodynamics of a helicopter is the unsteadiness of the flow due to its rotating parts (i.e., main and tail rotors). The non-rotating part of the helicopter, mainly the fuselage, is also exposed to large areas of reverse flow. In high-speed forward flight conditions, the massive flow separation present at the rear of the fuselage is the major component of the parasitic drag of the helicopter. In this respect, separation control for drag reduction purposes has been investigated over the past years by means of vortex generators, synthetic jets, or steady blowing (Boniface 2014)

On the rotating parts of the helicopter (main rotor blade), different flow control system might be suitable to implement. A typical aerodynamic environment for the helicopter main rotor in forward flight is shown in Fig. 9.1. On the advancing side ($0^\circ < \psi < 180^\circ$), the forward velocity is added to the blade's rotational velocity while on the retreating side ($180^\circ < \psi < 360^\circ$), the forward velocity is subtracted from the blade rotation. This unsteadiness of the flow leads to compressibility effects on the advancing side due to high Mach numbers while blade stall might be present on the retreating side if the forward flight velocity is high enough. For example, shock-wave induced flow separation on the advancing side may be controlled by vortex generators while the massive separation caused by dynamic stall may be controlled by Gurney flaps. It is important to mention that passive flow control systems (e.g., vortex generators) could be implemented in the rotor blades where they would work properly in some azimuthal positions with some drawbacks in others. For this reason, a passive system could be activated on demands. On the other hand, active flow control systems are suitable for helicopter application since they are just enabled for certain azimuthal range.

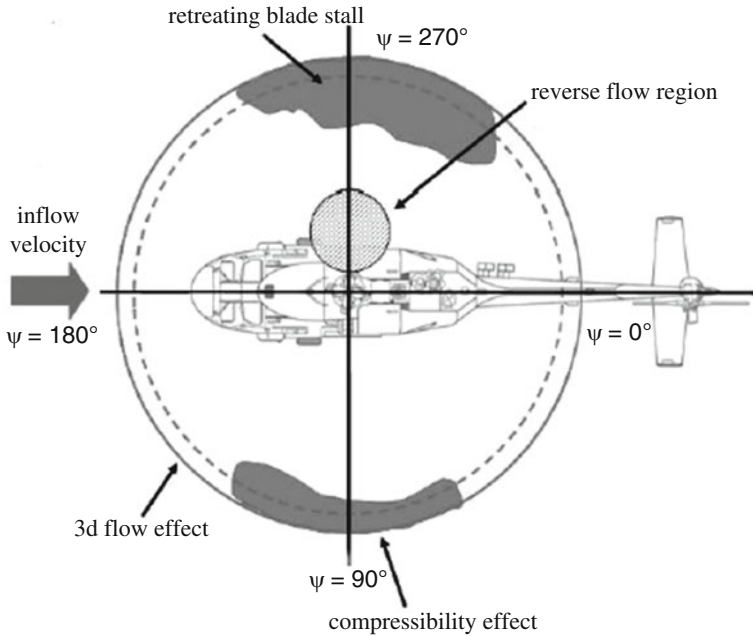


Fig. 9.1 Flow characteristics in forward flight conditions (Seddon and Newman 2011)

A list of different flow control devices have been identified as candidates to be integrated in helicopter rotor blades: vortex generators, gurney flaps, movable flaps, surface blowing circulation control, synthetic jets, surface suction, passive porous or slotted surfaces, bumps or localized shaping, and riblets. The principles of each device, with the main benefits for rotorcraft application, were recently published by Kenning et al. (2004).

9.2 Numerical Model

The numerical model as well as computational domain employed in these simulations was previously described in Tejero et al. (2016a). The present CFD investigation was carried out using the DLR (Germany) FLOWer solver. It is a rotorcraft oriented, block-structured, cell-centered code which solves the Reynolds-averaged Navier–Stokes (RANS) equations with several closures. The two-equation, LEA $k-\omega$ turbulence model was used due to its capabilities for proper prediction of transonic flows. The numerical algorithm is based on a semidiscrete approach, utilizing a finite-volume, central scheme (second order) for the spatial discretization. The same explicit, Runge–Kutta method of time integration, was used for the steady simulations of a hovering rotor, as for the internal iterations of the implicit

dual-time-stepping scheme (second order) applied for forward flight conditions. Same numerical algorithm was used in previous investigations.

The main idea of the chimera technique implemented in the ROT/CHIMERA version of the FLOWer code is to easily generate grids for complex configurations (e.g., helicopter rotors) by decomposing them into simple, independent parts. For the reference case (no flow control), the computational domain consists of a background and the blade component grids. The RVGs component grid is added for each blade to the reference setup for the flow control case.

In hovering rotor computations, the background component grid is formed by a cylinder of a height and radius equal to $6.1R$ and $4.0R$, respectively, which ensures that the rotor blades are located at least $3.0R$ from the outer boundary of the domain. Altogether, 32 computational blocks contain 4.80×10^6 volumes. The vicinity of the rotor and its wake is resolved using a central cuboid structure with a uniform block (volume size of $0.1c \times 0.1c \times 0.1c$). For forward flight simulations, a Cartesian, cuboid background component grid (see Fig. 9.2) is designed with dimensions of $16.4R \times 18.2R \times 18.2R$. Consequently, the outer boundary of the domain is positioned at least $8.0R$ from the rotor in all directions. The number of control volumes in 32 computational blocks is increased to 9.4×10^6 , much higher than for the hover setup. Again, the vicinity of the rotor is resolved using a central cuboid structure with uniform volume distribution ($0.1c \times 0.1c \times 0.1c$). For both states of flight, the blade component grid (Fig. 9.3) is C-type in streamwise

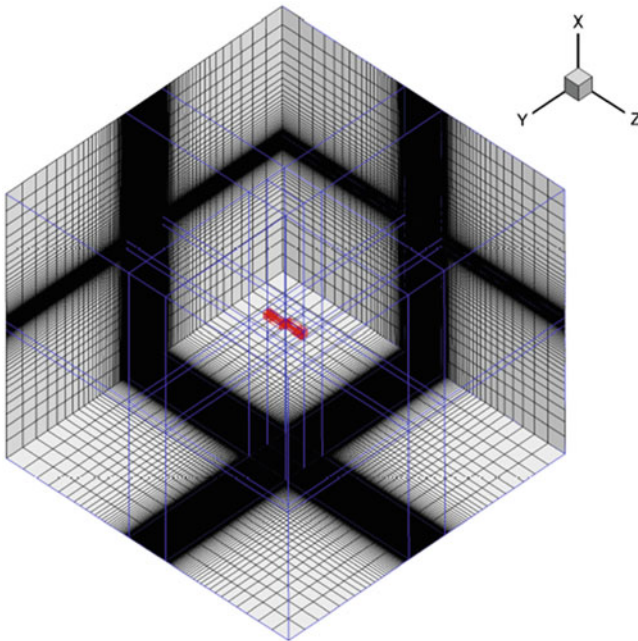


Fig. 9.2 Background component grid

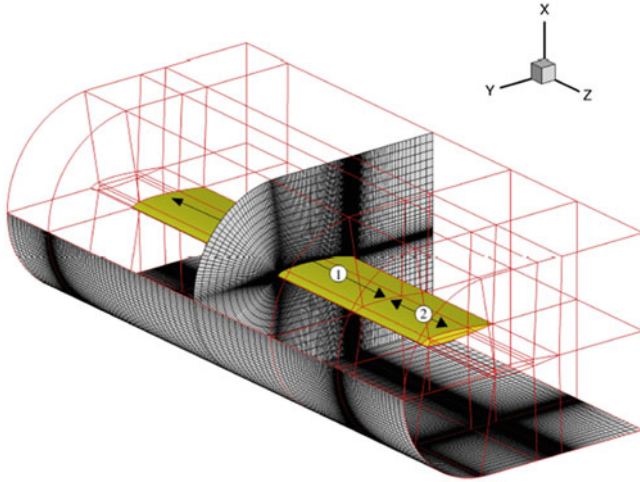


Fig. 9.3 Blade component grid

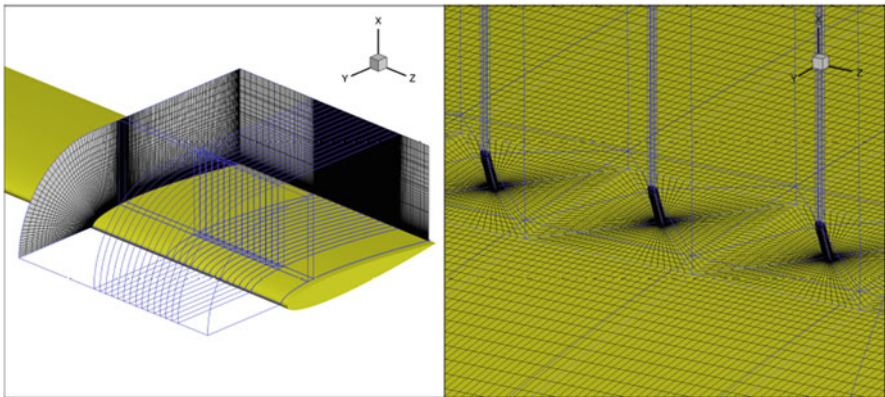


Fig. 9.4 RVG component grid and detailed view of the RVGs

and H-type in crosswise directions. It extends $1.2c$ from the blade surface in the radial and normal directions. Altogether, 40 computational blocks contain 3.9×10^6 volumes per blade.

The nondimensional distance of the first layer of cells from the solid surface of the blade is of the order $y^+ = 1$. For the flow control cases, an RVG component grid (Fig. 9.4) is added to the chimera setup. It is placed on the suction side of the blade, near the tip, where there is a significant flow separation.

Three types of boundary conditions are applied in the numerical simulation: no-slip condition with zero heat flux (adiabatic) at the rotor blades, Froude (hover), and far-field (forward flight) at the external edges of the background grids, and a

special chimera condition at the outer part of the blade component grids, which is necessary for the accurate interpolation process of flow variables between meshes.

The inclusion of the RVGs component grid leads to a significant increase of the mesh size, making the simulations computationally very demanding (37×10^6 volumes for hover and 48×10^6 volumes for forward flight conditions).

9.3 Hover Conditions

9.3.1 *Experimental Data*

The experimental data obtained by Caradonna and Tung (C–T), Caradonna and Tung (1981), is the first test data available in the literature that combines measurements of static pressure on the blade and tip vortex trajectory (see Fig. 9.5). The data was gathered in the Army Aeromechanics Laboratory’s hover test facility in the 1980s. The model rotor employed two cantilever mounted, rectangular, untwisted, and untapered NACA0012 rigid blades. The rotor was mounted on a tall column containing a drive shaft with half degree precone angle and located in the center of a large chamber with special ducting designed to eliminate room recirculation. The diameter of the rotor was 7.5 ft (2.286 m) and the chord length was 0.625 ft (0.1905 m) leading to a rotor aspect ratio of 6.0. Different rotational speeds of the rotor were applied during the experiments (from 650 RPM to 2540 RPM) which varied the tip Mach number from 0.226 to 0.890. The collective pitch ranged between 0° and 12° . Each blade was mounted with 60 pressure tubes which permits to measure five different locations—three radial locations per blade with one common. The static pressure was recorded at $r/R = 0.50, 0.68, 0.80, 0.89,$ and 0.96 . On the other hand, the wake data was acquired with a hot-wire probe mounted beneath the rotor.

9.3.2 *CFD Results*

9.3.2.1 Reference Case

The FLOWer code has been validated with a high-speed transonic case of $M_T = 0.877$, $Re_T = 3.93 \times 10^6$ and a collective pitch of $\theta = 8^\circ$. Same flow conditions have been analyzed by other researchers in the past using Euler and/or RANS approach and with/without wake models. A literature survey of the RANS results obtained for this transonic lifting hover reveals significant scatter according to experimental data (Kang and Kwon 2002; Sheng 2011).

As mentioned above, the correct prediction of the flow-field around the rotor blades requires properly resolved flow structure details. The properly captured rotor wake and the tip vortex path are necessary condition for the correct prediction of the

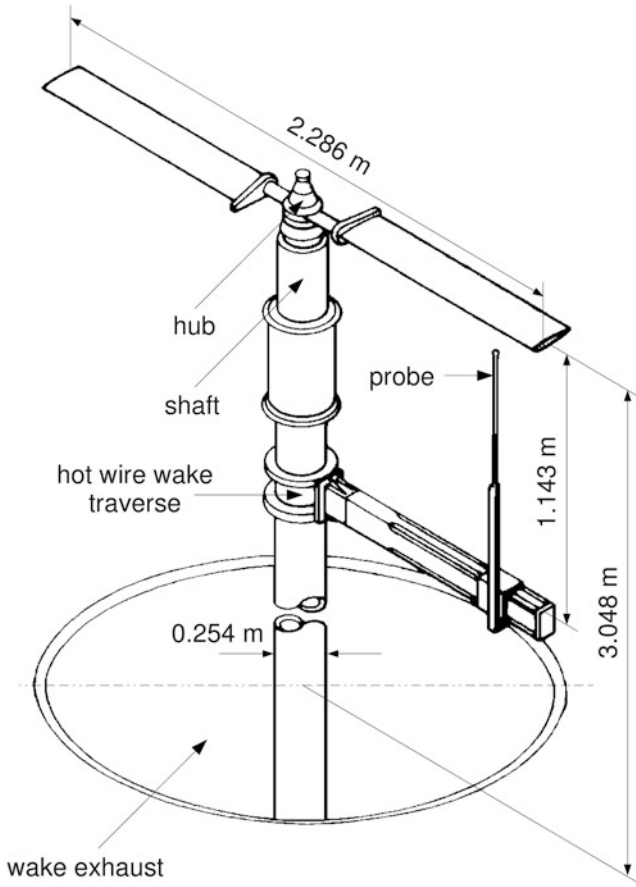


Fig. 9.5 Caradonna and Tung model helicopter rotor blade (Caradonna and Tung 1981)

rotor performance. In the present study, the rotor wake is not set externally by a wake model but it is a result of the simulation. A strong, induced vertical inflow modifies the effective angle of attack of the blades directly altering the rotor performance.

Approximately 450° of a tip vortex age is resolved in the current simulation, which is sufficient to capture the interaction of the shed vortex with the following blade at 180° . The tip vortices and trailing edge vortex sheets are diffused mainly due to the numerical viscosity of the second order central scheme applied. Below 180° the tip vortex descent and contraction rate (based on the location of the vorticity maximum) is accurately predicted by the solver FLOWer (Fig. 9.6). It is important to mention that after half rotation, the accuracy of the simulation with respect to experimental data decreases due to the wake traveling far from the wake box prepared in the background component grid.

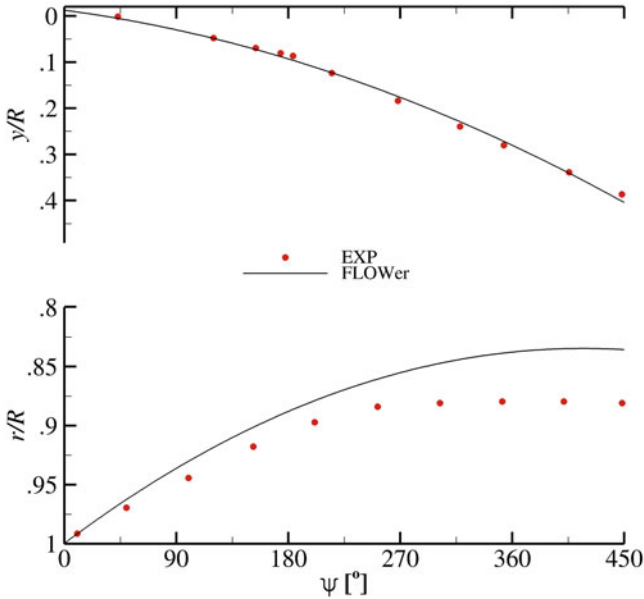


Fig. 9.6 Tip vortex descent and contraction for the C-T model rotor in transonic conditions

Figure 9.7 presents the validation of the numerical simulation in terms of comparison of pressure coefficient distributions at different cross-section in radial ($r/R = 0.50, 0.68, 0.80, 0.89,$ and 0.96). The flow is fully subsonic at the first two cross-sections ($r/R = 0.50$ and 0.68) and supersonic areas terminated by shock waves appear at the remaining sections ($r/R = 0.80, 0.89,$ and 0.96). Although there is a satisfactory agreement with the experimental C_p distributions, there is an overprediction of thrust coefficient by 15% ($C_T = 0.00545$) compared to the published value ($C_T = 0.00473$).

$$c_T = \frac{T}{\frac{1}{2}\rho AV_{\text{tip}}^2} \quad (9.1)$$

The strong shock wave at the tip of the rotor blade induces flow separation between $r/R = 0.86$ and 0.96 (with detachment line located at $x/c = 0.30$). Due to previous chapter proven that RVGs are able to control flow separation, the implementation of this flow control device on helicopter rotor blades in hover conditions will be investigated in this chapter. Upstream of the separation bubble ($x/c = 0.20$), the boundary layer thickness was $0.008c$. As suggested in the previous chapter, the dimensions of the rod vortex generators were: $\phi_{\text{RVG}} = \delta/4$, $h = \delta/2$, and $L = 2.5 \times \delta$. The spacing between the rods was increased to $L = 5 \times \delta$, reducing the total number of control volumes (14 rods are simulated instead of 28).

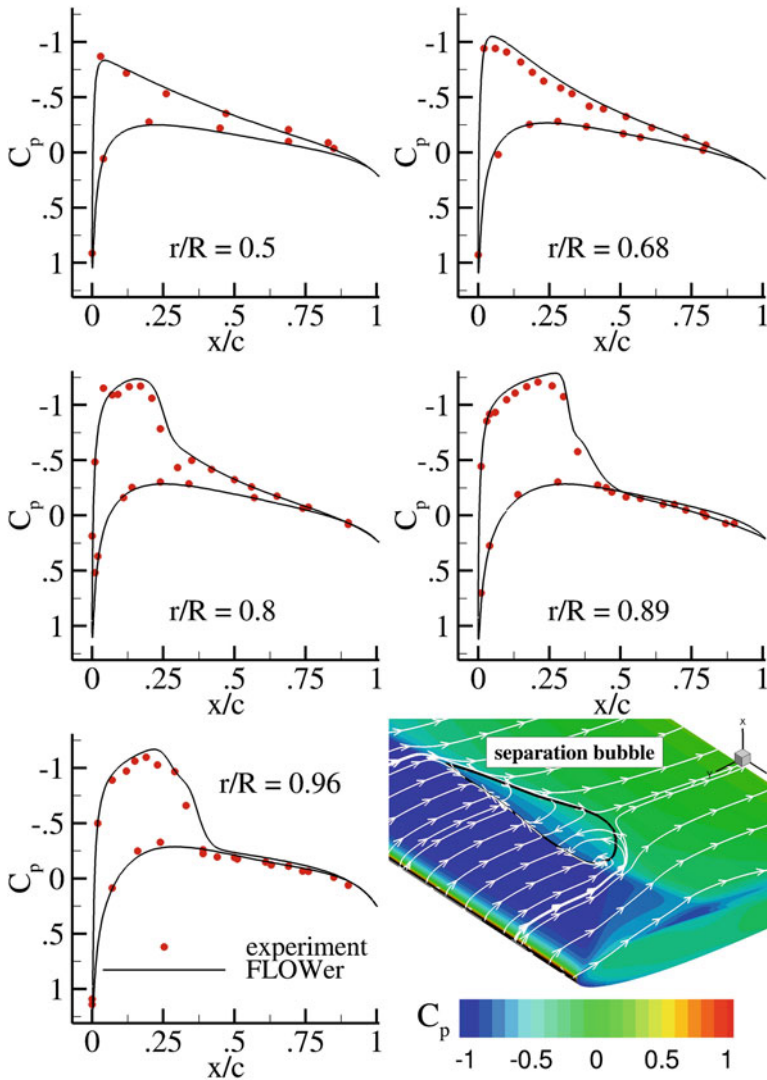


Fig. 9.7 Numerical validation of the C-T model rotor in transonic conditions and separation bubble (Tejero et al. 2016a)

9.3.2.2 Flow Control Case (RVG)

Figure 9.8 presents the development of the streamwise vortices created by the RVGs on the C-T helicopter rotor blade at five chordwise sections ($x/c = 0.22, 0.25, 0.27, 0.29,$ and 0.33). It is worth to mention that the effect of the RVGs is only visible below the edge of the boundary layer thickness where the vortex generators are submerged. For the chordwise sections upstream of the separation bubble

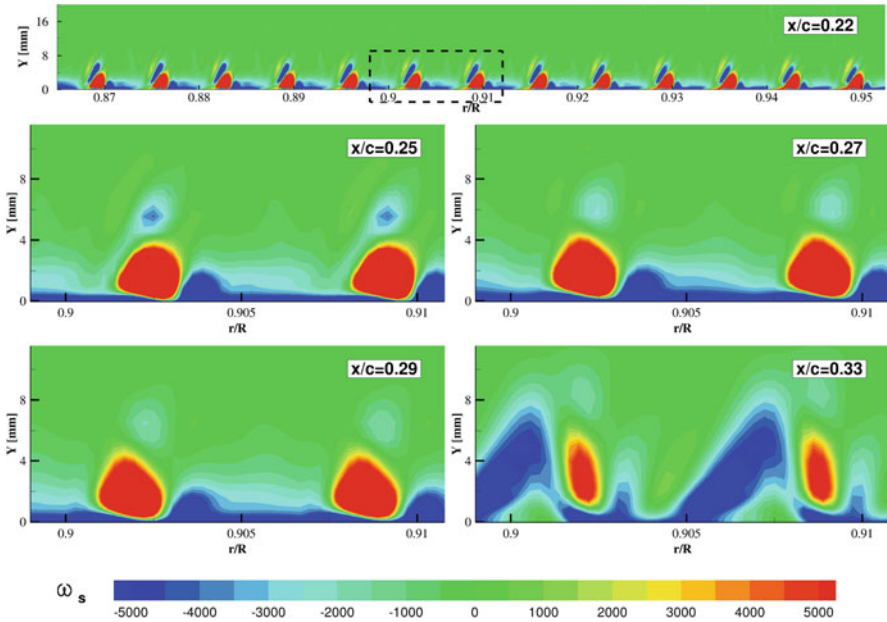


Fig. 9.8 Streamwise vortex development in the C–T model rotor in transonic conditions

($x/c = 0.22, 0.25, 0.27,$ and 0.29), the vortex develops increasing the intensity. On the other hand, when the flow separations starts ($x/c = 0.30$), the vortex core is lifted and highly dissipated (see Fig. 9.8 chordwise section $x/c = 0.33$). The numerical simulation reveals that there is a very weak vortex downstream of the reattachment point.

The numerical results of the flow past the rotor blade with the proposed passive flow control system show the possibility of reduction of the separation bubble (Fig. 9.9). The figure presents the contour map of skin friction coefficient C_f , the separation bubble (black line) and the low momentum area (red line) are marked in the figure. The proposed vortex generators increase the shear stress at the suction side of the rotor blade due to the formation of streamwise vortices. The separation bubble is not fully eliminated but reduced and spit into smaller bubbles which follow the same trends presented in channel flows and airfoils (previous chapter).

In Fig. 9.10 the boundary layer profiles are compared for the reference and flow control cases (all analyzed points are marked in Fig. 9.9). The solid lines represent a location downstream of a selected RVG ($r/R = 0.911$), while the dashed lines refer to a downstream position between two rods ($r/R = 0.922$) at four different chordwise sections ($x/c = 0.25, 0.35, 0.40,$ and 0.60). The first chordwise section ($x/c = 0.25$) is located upstream of the starting point of the flow separation, the other two sections ($x/c = 0.35$ and 0.40) refer to locations where reverse flow is present while the flow is attached to the blade for the last analyzed chordwise section ($x/c = 0.60$). The comparison of boundary layer profiles at $x/c = 0.25$ shows a big influence in the

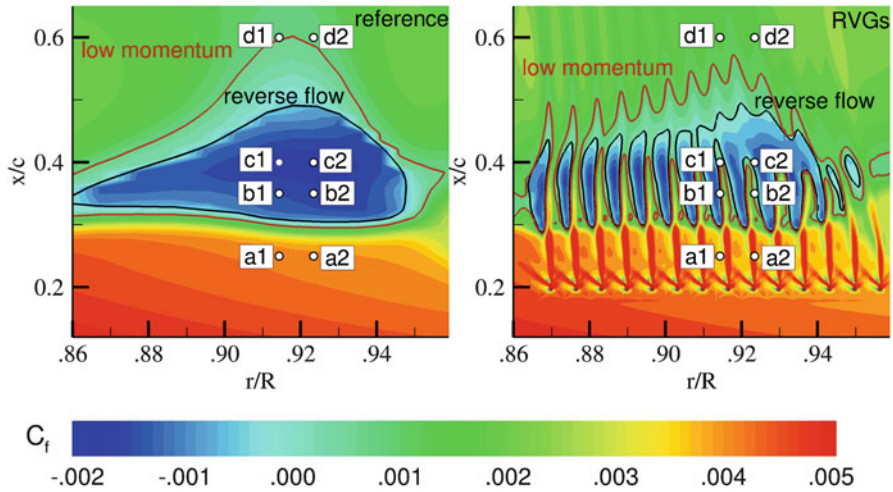


Fig. 9.9 Flow separation reduction by RVGs on the C-T model rotor in transonic conditions

radial section downstream of the rod (solid line) providing a more full profile when the proposed flow control system is applied while the boundary layer properties are similar for the radial section located between RVGs (dashed line). Traveling downstream in chordwise direction ($x/c = 0.35$), the flow separation appears in the reference case but in case of applied RVG the flow is attached in both radial sections. The other positive effect of vortex generator can be observed at $x/c = 0.40$. Although the flow is not attached at $r/R = 0.92$, the height of the separation bubble is reduced. The comparison makes evident that not only the area of the projection of the separation bubble on the surface is reduced but also the height of it. Lastly, when the flow is reattached for the reference case ($x/c = 0.60$), the effect of the streamwise vortex has been dissipated making similar boundary layer profiles for the reference and flow control cases.

The implementation of the passive flow control device of rod vortex generators on the tip of the C-T model rotor blade in transonic hover conditions increases the thrust coefficient C_T by 2.0% with respect to the reference case. The main drawback of this technology is the drag penalty associated with it (the power consumption was increased by 1.2%). The separation bubble induced at the tip of these rotor blades by a strong shock wave was limited by the proposed technology.

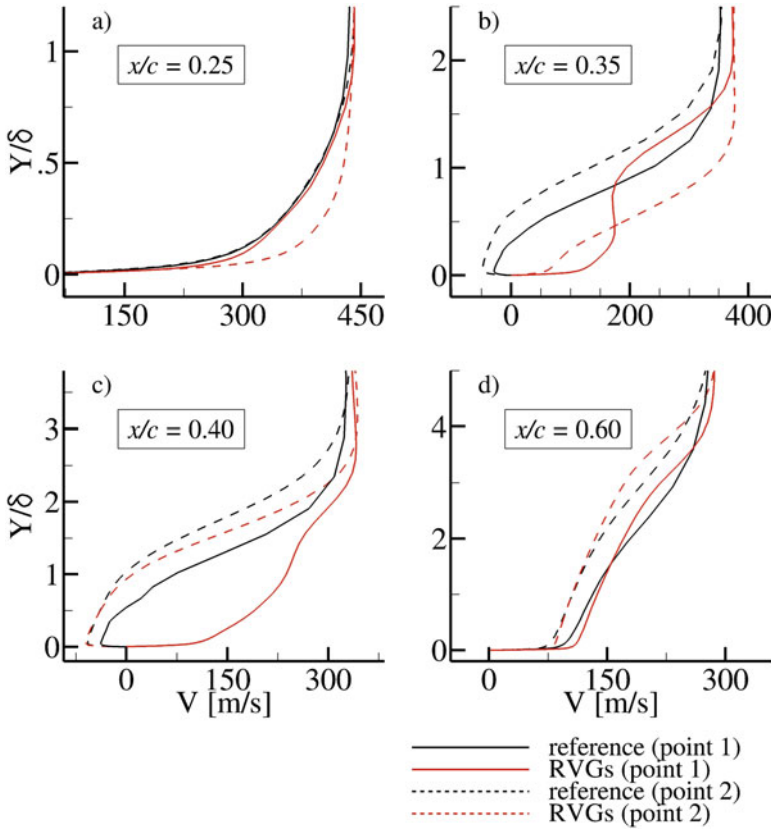


Fig. 9.10 Comparison of boundary layer thickness

9.4 Forward Flight Conditions

9.4.1 Flight Test Data

The AH-1G helicopter rotor blade (Fig. 9.11) was selected for the numerical investigation of the forward flight conditions. During The Tip Aerodynamics and Acoustics Test (TAAT), performed by Cross and Watts (1988), several arrays of absolute pressure transducers were placed on the rotor blades providing a large set of data. This flight test campaign is one of the most detailed one that can be found in the open literature so far. The data includes overall instantaneous thrust coefficients C_T , torque coefficient C_q , and the sectional normal force coefficients C_n based on the integration of the pressure data collected from the pressure transducers located on the blade. Besides, the blade motion (pitch and flap) was recorded as well.

The AH-1G is a two person, single-engine helicopter that first flew in 1965 and has been out of service for 20 years. The AH-1G 2-bladed, teetering rotor with a 540



Fig. 9.11 AH-1G helicopter rotor blade (www.airliners.net)

symmetrical airfoil section, which is a highly modified derivative of the NACA 0012 (thickness ratio = 0.0933), has a rectangular planform with a chord $c = 0.686$ m. The blades have a linear twist of -10° from the shaft to the tip (effective twist from blade root to tip is -8.48°) with a radius $R = 6.71$ m (aspect ratio $AR = 9.8$). During the TAAT test, the effective chord of the blade was increased to accommodate the instrumentation sleeve, reducing the effective aspect ratio to 9.2.

A literature survey of the published numerical results (Ahmad and Duque 1996; Yang et al. 2002) for the TAAT AH-1G campaign reveals that the low-speed flight ($V_\infty = 150$ km/h) has been simulated in the past by several researchers with success, in contrast to the higher speed flight test points where CFD calculations are very limited (i.e., medium- and high-speed flights with forward velocities of $V_\infty = 210$ km/h and 290 km/h, respectively). After the TAAT flight test campaign, one hover IGE (test point no. 2370) and six forward flight cases (test points no. 2152–2157) with increasing forward speeds (from 150 km/h to 290 km/h) were documented in Cross and Watts (1988). This section presents exemplary numerical results obtained for a subset of 3 test points. Test point no. 2157 (low-speed case, 150 km/h) was computed and validated against flight test data and compared with other CFD results found in the literature (i.e., Ahmad and Duque 1996; Yang et al. 2002). Two higher speed test cases investigated do not have similar citations available in the literature. Numerical results for test point no. 2152 (high-speed, 290 km/h) are satisfactory in terms of flight test data comparison revealing significant flow separation (shock wave induced at the advancing side and due to dynamic stall at the retreating side) (Tejero et al. 2016a, b).

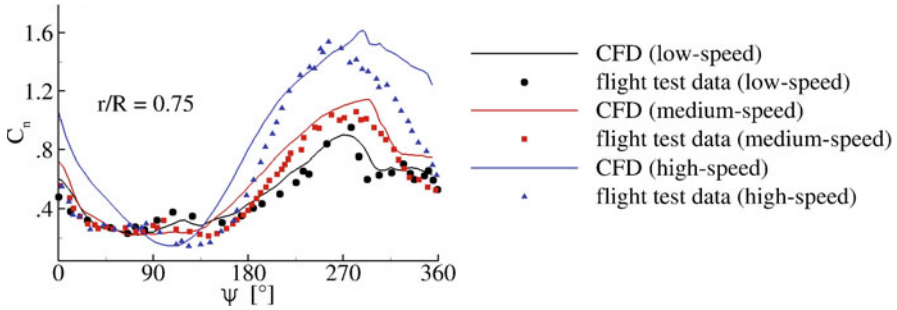


Fig. 9.12 Instantaneous normal C_n coefficient for different speed markers

9.4.2 CFD Results

9.4.2.1 Reference Case

The thrust coefficient is only overpredicted by 2% for the low-speed case ($C_T = 0.00473$), while the overprediction increases with the forward speed: 9% ($C_T = 0.00507$) for the medium-speed and 20% ($C_T = 0.00569$) for the high-speed marker. Nevertheless, the agreement is satisfactory for the complex flow conditions simulated and simplifications undertaken (e.g., neglect the influence of the fuselage). It is important to mention that during the simulations, the blade motion reported in TAAT was applied. Therefore, the rotor was not trimmed to measured thrust coefficient.

Figure 9.12 presents exemplary numerical validation for all considered forward flight cases in terms of C_n vs ψ based on integration of pressure distributions at cross-sections of the blade $r/R = 0.75$. The agreement with flight test data is satisfactory for the whole range of forward velocities analyzed. The maximum values of C_n appearing at the retreating side are well predicted by CFD. Some detailed features of the flow presented in flight test data are well reproduced by computations (for example, local maxima of C_n close to $\psi = 90^\circ$ for the low-speed case) (Tejero et al. 2016b).

Figure 9.13 presents the C_p distributions for the high-speed marker for different cross-sections and azimuthal positions. The shock wave present at $r/R = 0.86$ and $\psi = 90^\circ$ is well predicted by the numerical simulations. Besides, the two shocks (suction and pressure sides) located at $r/R = 0.99$ and $\psi = 90^\circ$ are also reproduced by the numerical simulation. On the other hand, the C_p distribution at the retreating side of the rotor blade ($r/R = 0.96$ and $\psi = 270^\circ$) is well reproduced by CFD.

Only the high-speed marker simulated showed significant flow separation to be controlled by the proposed passive flow control device. Figure 9.14 presents the skin friction coefficient (C_f) at the suction side of the AH-1G helicopter rotor blade (steps of 30°) in high-speed forward flight conditions. To simplify the figure just three colors are showed: blue color represents the areas where the flow is attached

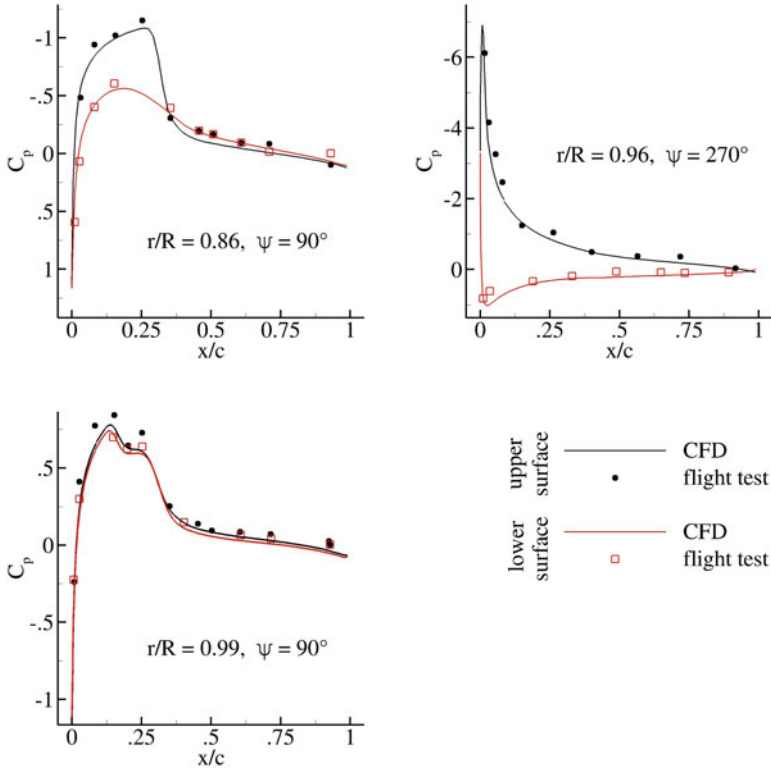


Fig. 9.13 Numerical validation in terms of pressure distribution (Tejero et al. 2016b)

to the rotor blade, the red color presents flow separation (induced by shock waves or dynamic stall), and the green color indicates the areas where the flow is attached to the surface but exerting low shear stress, $C_f < 10^{-4}$ (boundary layer close to separation).

The flow past a helicopter rotor blade in forward flight conditions is highly unsteady and therefore the boundary layer thickness is continuously changing. For this numerical investigation, the RVGs were designed with the flow properties upstream of the shock wave located at $\psi = 45^\circ$ ($\delta = 0.004c$). 18 RVGs were placed on the blade from $r/R = 0.91$ and $r/R = 0.96$ with the following dimensions: $\phi_{RVG} = \delta/4$, $h = \delta/2$, and $L = 5.0 \times \delta$.

9.4.2.2 Flow Control Case (RVG)

Figure 9.15 presents the disk loads in terms of normal (C_n) and torque (C_q) Mach scaled coefficients. The left side of the figure shows the reference case (no flow control) where it is visible how the normal force is generated by fore and aft parts of

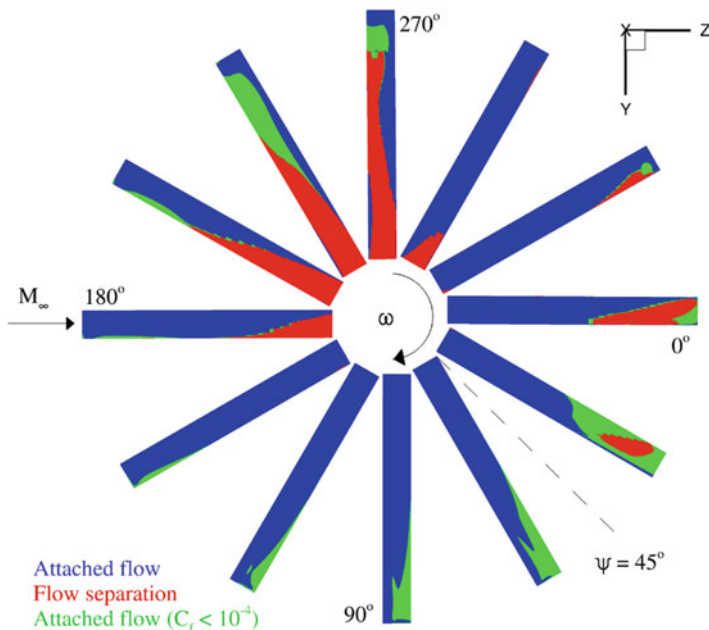


Fig. 9.14 Skin friction coefficient on the suction side of the AH-1G rotor blades in high-speed forward conditions

the rotor disk with negative values at $\psi = 90^\circ$ close to the blade tip due to negative inflow angle and at $\psi = 270^\circ$ close to the blade root caused by the reverse flow area. The torque Mach scaled is mainly generated at the retreating side. The right side of the figure presents the delta of the investigated Mach scaled coefficients (flow control minus reference case). The negative effect of the RVGs (blue) is visible only near $\psi = 0^\circ$, where the flow is massively separated from the leading edge. The rods are most effective between $\psi = 30^\circ$ and $\psi = 60^\circ$, where a strong shock wave induces flow separation. Moreover, an improvement in C_n is also evident for the remaining azimuthal positions. Even in locations not subjected to flow separation, the implementation of RVGs has a beneficial effect on aerodynamic performance, due to an increased value of the skin friction coefficient (improved boundary layer state). More details are described in Tejero et al. (2016a).

The contour map of Mach at the cross-section $r/R = 0.92$ of the azimuthal positions marked in Fig. 9.15 is presented in Fig. 9.16. The first location shows how the massive separation is still present at the retreating side when RVGs are applied. The flow separations start at the leading edge (RVGs are located in a reverse zone area) and the formation of streamwise vortices cannot be expected. On the other hand, the control of the strong shock-wave boundary layer interaction of this flow control system is visible in the second location.

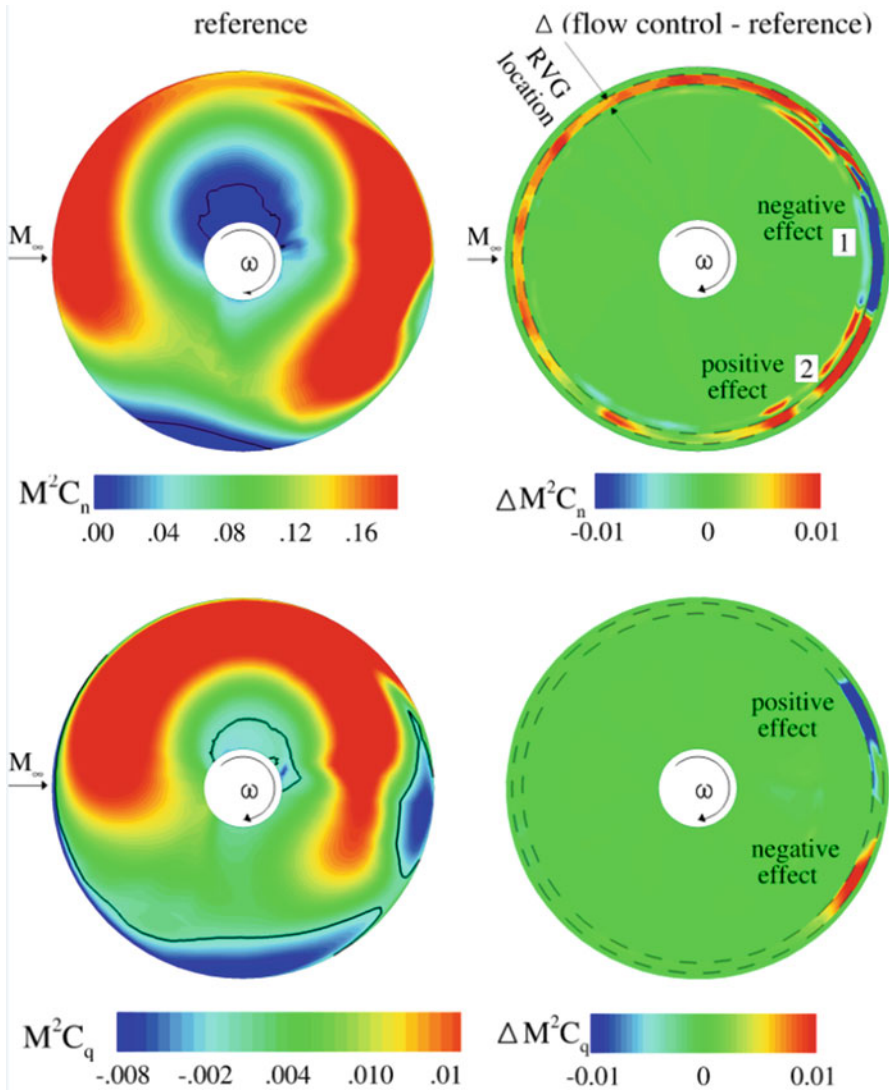


Fig. 9.15 Mach scaled normal force (C_n) and torque (C_q) coefficients for the reference case (left) and the influence of RVGs on the rotor disk (right) (Tejero et al. 2016a)

The application of RVGs in the AH-1G main helicopter rotor blade leads with an enhancement by 2.6% in the thrust coefficient with a drag penalty induced by the rods (visible in the increment of power consumption by 1.1%).

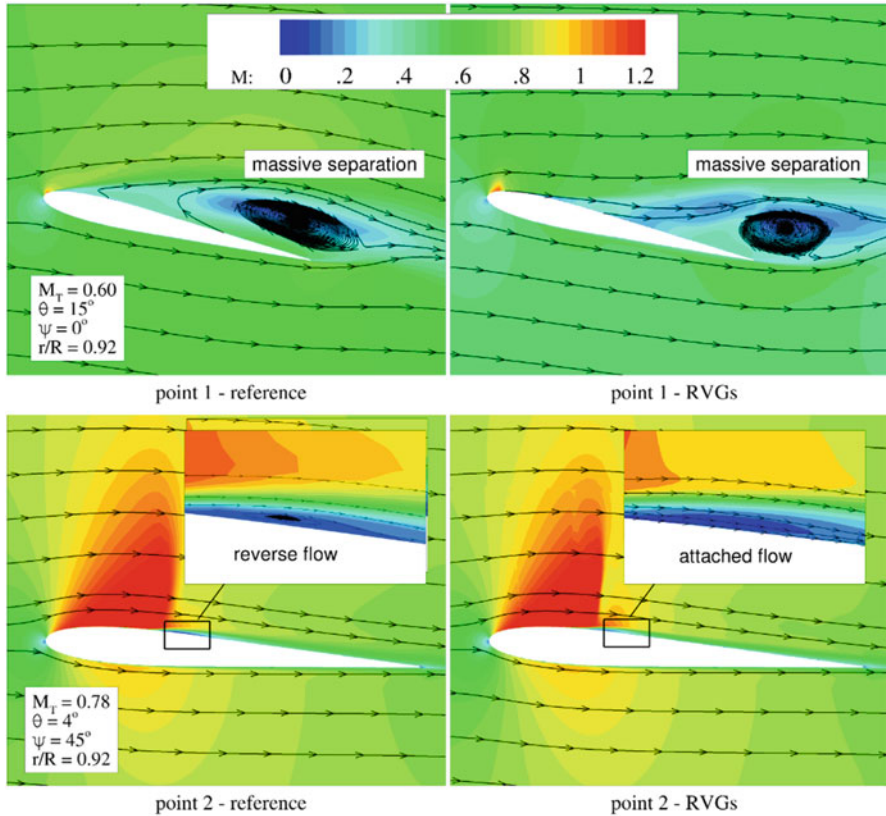


Fig. 9.16 Mach contour map and the influence of RVGs on flow separation on the AH-1G rotor blades in high-speed forward flight conditions (Tejero et al. 2016a)

9.5 Conclusions

The chapter presents the numerical investigation of the possible application of rod vortex generators on helicopter rotor blades. The Caradonna–Tung and AH-1G helicopter rotor blade were investigated in hover and forward flight conditions, respectively. The numerical models were validated with the available experimental data/flight test data. The application of the proposed passive flow control device on the suction side of both rotors leads to a separation control, which enhanced the thrust coefficient. The main drawback of the presented technology is the power consumption penalty associated with its implementation.

References

- Ahmad J, Duque EPN (1996) Helicopter rotor blade computation in unsteady flows using moving overset grids. *J Aircr* 33(1):54–60
- Boniface JC (2014) A computational framework for helicopter fuselage drag reduction using vortex generators. In: AHS 70th Annual Forum, Montreal, Canada
- Caradonna FX, Tung C (1981) Experimental and analytical studies of a model helicopter rotor in hover. NASA Technical Memorandum 81232
- Cross JL, Watts ME (1988) Tip aerodynamics and acoustics test. NASA Reference Publication 1179
- Kang HJ, Kwon OJ (2002) Unstructured mesh Navier-Stokes calculations of the flow field of a helicopter rotor in hover. *J Am Helicopter Soc* 47(2):90–99
- Kenning OC, Kaynes IW, Miller JV (2004) The potential application of flow control to helicopter rotor blades. In: 30th European Rotorcraft Forum, Marseilles, France, 14–16
- Seddon J, Newman S (2011) Basic helicopter aerodynamics, Aerospace series. Wiley, Hoboken. ISBN 9780470665015
- Sheng C (2011) A preconditioned method for rotating flows at arbitrary mach number. *Modell Simul Eng* 2011:1–17
- Tejero F, Doerffer P, Szulc O (2016a) Application of passive flow control device on helicopter rotor blades. *J Am Helicopter Soc* 61(1):1–13
- Tejero F, Doerffer P, Szulc O, Cross JL (2016b) Numerical simulation of the tip aerodynamics and acoustics test. *J Therm Sci* 25(2):153–160
- Yang Z, Sankar LN, Smith M, Bauchau O (2002) Recent improvements to a hybrid method for rotors in forward flight. *J Aircr* 39(5):804–812

Chapter 10

Retractable Rod Vortex Generator

Tomasz Lewandowski

10.1 Introduction

Growing aerodynamic loads of turbine, aircraft, wind turbine, and helicopter rotor blades increase the possibility of flow separation near the surfaces of those elements. In such situations it is necessary to use flow control methods to improve their aerodynamic performance by, for example, reducing aerodynamic drag, increasing lift force, improving heat exchange, and/or reducing noise. We distinguish between active and passive flow control methods. The passive methods include: fixed Gurney Flaps, vortex generators (VG), perforated plates over a cavity, and geometrical shape modification (Flaszynski and Tejero 2013; Doerffer and Szulc 2011; Barakos 2010). All these methods modify the flow without external energy. The active techniques, which require additional energy input, include: synthetic jets, steady suction or blowing, and active Gurney Flaps (Tang et al. 2014; Pastrikakis 2015). The active control methods can be divided into permanently set devices and controlled devices, the latter based on sensors or a control system.

RrVG is a retractable rod, which is placed on the airfoil to influence reenergizing of the boundary layer on a moving airfoil (flow control). Vortex generators are most often used to delay flow separation. To accomplish this, they are often placed on the external surfaces of vehicles and wind turbine blades. It should be noted that the rod vortex generator presented in the literature (Flaszynski and Tejero 2013) is a fixed type vortex generator (passive method). The use of retractable rod vortex generator (RrVG) with a control system (control signal) allows to activate it during the motion of the airfoil only in specified moments, which is its main advantage. The objective of the proposed system is its location on the helicopter main rotor

T. Lewandowski (✉)
Institute of Fluid-Flow Machinery Polish Academy of Sciences,
Fiszera 14 St, Gdansk, 80-231, Poland
e-mail: tomasz.lewandowski@imp.gda.pl

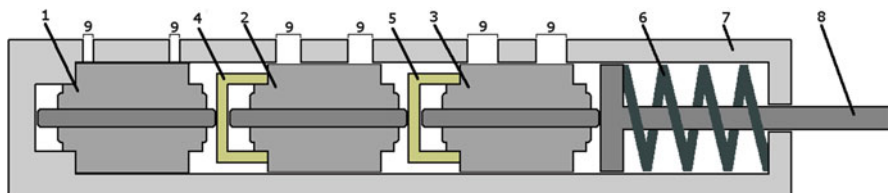


Fig. 10.1 RrVG system—cascade model

blades (Tejero et al. 2014). When constructing this element the knowledge about the structure of the fluid flow and the system control is required. Based on experiments and CFD simulations we should define the best position of RrVG on the blade in relation to the rotor axis, the best angle in relation to the main flow, and the activation moment. Another issue to be decided upon when constructing this system is the choice of the actuator element. It must be appropriately fast and has sufficient deflection.

The LMS software allows to perform a wide range of numerical simulations without the requirement of experiments in the design phase. It allows to simulate the complex system for different frequencies of action, positions, and materials performance of individual elements (parametric study).

10.1.1 Overall Description of the Model

The proposed RrVG system consists of a cascade of several elements. This is due to limitations (dimension and maximum movements) of system elements—actuators. The RrVG model is based on electromechanical components. Figure 10.1 shows the sketch cascade model of the RrVG system.

The designed RrVG system consists of three electromechanical actuators (numbered: 1, 2, 3), two connectors (4, 5), spring (6), retractable rod (8), frame (7), and connection points (9). The principle of work of the system is easy. The body of actuator 1 is clamped to the frame 7. Actuators 2 and 3 are moved by actuator (1), but they move with respect to each other. Actuators (2, 3) move the next elements. The bodies of the actuators (2, 3) are moved by connectors (4, 5). The maximum displacement of the rod (8) is equal to the sum of strokes of all actuators. The task of the spring (6) is to move back the rod. Such a type of design (a cascade) allows relatively easy reconstruction of the system when it is necessary to increase the rod displacement (in order to control the flow with thicker boundary layer). The proposed design is based on existing and easily available elements. Cascade elements for given input signals have been designed and simulated in LMS software. Simulations of cascade system operation were designed to fit and optimize the control system. The response time (activation time) and the total deflection of the rod are analyzed in the chapter depending on the assumed frictional forces and the masses of the system elements.

10.1.2 Numerical Tools

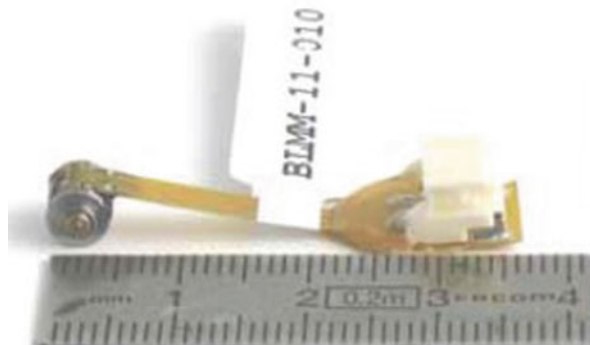
LMS Imagine Lab AMESim is an integrated simulation platform for multi-domain mechatronic systems simulation. LMS Imagine Lab AMESim offers engineers an integrated simulation platform to accurately predict the multidisciplinary performance of intelligent systems and enables you to model, simulate, and analyze multi-domain controlled systems and offers plant modeling capabilities to connect to controls design helping you assess and validate control strategies. To create a system simulation model in LMS Imagine Lab AMESim, you simply access one of the numerous LMS AMESim libraries of predefined and validated components from different physical domains (such as fluid, thermal, mechanical, electromechanical, and powertrain). All simulation library components are completely validated to guarantee the accuracy and reliability of the simulation. By selecting the required validated component from the related library, you avoid creating your own complicated code ([Siemens nd](#)).

LMS Virtual Lab (VL) is an integrated suite of 3D FE and multibody simulation software which simulates and optimizes the performance of mechanical systems for structural integrity, noise and vibration, system dynamics, and durability. LMS Virtual.Lab Motion which is part of LMS Virtual.Lab software allows you to investigate the kinematic behavior of systems – including flexible components and controllers – and to design optimally for durability performance ([Siemens nd](#)).

10.2 The BLMM Actuator

The electromechanical actuator BLMM (Bistable Linear Moving Magnet) (Fig. 10.2) is offered by CEDRAT Technologies ([CEDRAT nd](#)) which was the partner in the IMESCON project. Its main parameters are as follows: stroke of slider 0.62 mm, commutation time 0.0017 ms, total mass 1.1 g, and mass of slider 0.076 g.

Fig. 10.2 BLMM actuator
([CEDRAT nd](#))



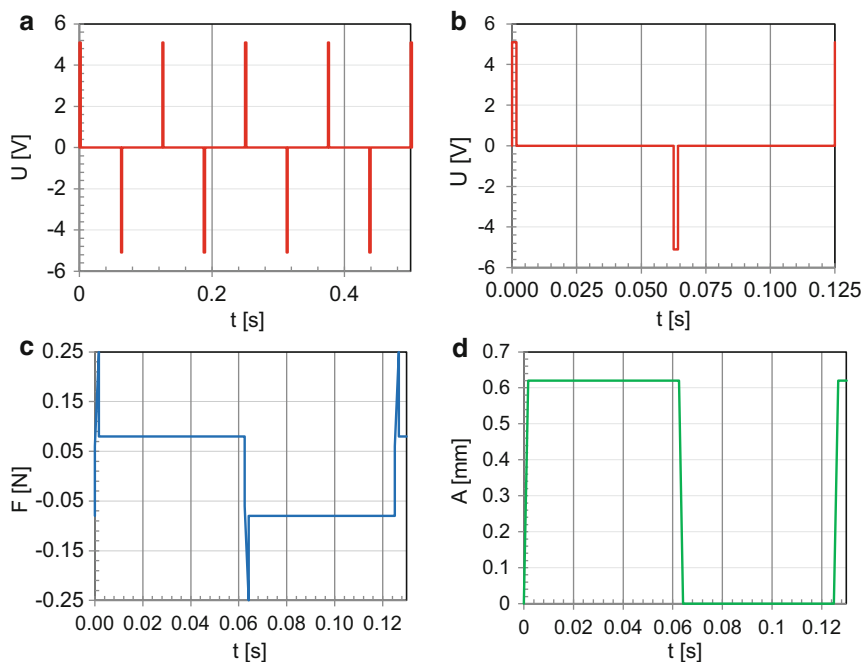


Fig. 10.3 Input and output signals for frequency 8 Hz, (a,b) voltage input signal, (b) force output signal, and (d) displacement of the slider

It makes use of a permanent magnet moving between two opposite electromagnets. BLMMs are miniature actuators, a feature which is especially attractive when a small-sized actuator is needed. The main advantages of the BLMM1 actuator are: small size, low power consumption, and fast and easy control. Input and output signals for a single actuator are presented in Fig. 10.3. The signals were determined based on manufacturer's specifications for frequency of 8 Hz. Figure 10.3a, b shows the voltage input signals in which the width of the actuation peak is 0.0017 s (commutation time).

Figure 10.3c presents the force output signal and Fig. 10.3d presents the displacement of the slider (moving part of the actuator). These signals are ideal signals for the unloaded element. Simulations have indicated the need for individual control of each actuator in the cascade.

10.3 Material Description and Friction Force

The outer body of the actuator is made of steel. Aluminum has been selected as the material of the moving elements (connectors and rod), and steel has been selected

Table 10.1 Parameters of materials

Material properties	Aluminum	Steel
Density	2710 kg/m ³	7860 kg/m ³
Young’s modulus	7e + 10 Pa	2e + 11 Pa
Poisson’s ratio	0.346	0.266
Thermal expansion	2.36e – 05 K/deg	1.17e – 05 K/deg
Yield strength	9.5e + 07 Pa	2.5e + 08 Pa

Table 10.2 Typical values of static and kinetic friction for different material combinations

Material combinations	Coefficients of static friction	Coefficients of kinetic friction
Steel–Steel	0.74	0.57
Steel–Aluminum	0.61	0.47
Steel–Teflon	0.04	0.04

as material of the frame. The material parameters are presented in Table 10.1. Additionally, the internal surface of the frame can be covered with extra lubricious shell. In the simulations, teflon (polytetrafluoroethylene—PTFE) was used as the material of extra lubricious shell. Teflon is one of the most heat-resistant synthetic materials (may operate in temperatures ranging from –200 °C to +260 °C) and has the lowest friction coefficient among all solids.

Static and kinetic coefficients of friction between two arbitrary materials are the measures of friction generated when they are in contact with each other. The friction coefficient usually varies between 0 for slippery objects and 1 for rough objects.

Typical values of static and kinetic friction coefficients for materials used in the model are presented in Table 10.2. The viscous friction between two movable surfaces depends on dimensional parameters, such as the contact area and the clearance between the two surfaces, and on fluid properties, e.g., specific gravity and viscosity. The clearances between the actuator and the frame are of the order of microns. In simulations of mechanical systems, in general, project developers often assume constant viscous friction in order to simplify the model. The value of the viscous friction coefficient for air and the clearance equal to 4 microns was equal to 0.05.

10.4 Model (1D) of RrVG System in LMS Imagine Lab AMESim

Cascade system simulations, performed in AMESim, were intended to fit and optimize the control system. The reaction time and the total deflection of the rod were analyzed depending on the assumed frictional force and the masses of the system elements. The cascade model of RrVG made in the LMS Imagine Lab AMESim is presented in Fig. 10.4.

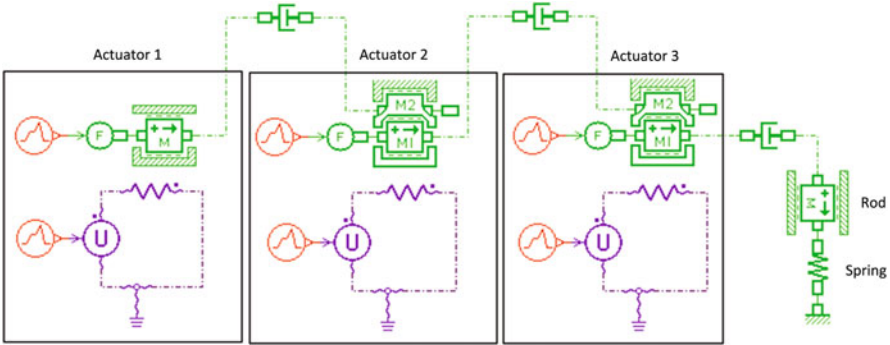


Fig. 10.4 RrVG – cascade model in Imagine Lab AMESim

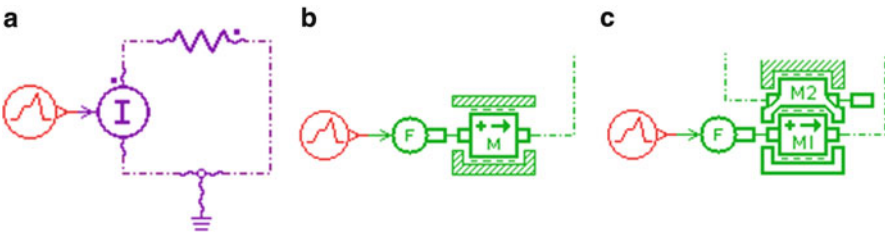


Fig. 10.5 Actuator – (a) electric part; (b) and (c) mechanical parts

The structures of all actuators are marked in the black rectangles. Each actuator consists of electrical and mechanical parts. These parts are shown in Fig. 10.5a. The electric part is represented by the resistance of the actuator, the voltage source, and the input signal submodel.

Depending on the location in the system, the mass submodels represent a single mass or combined masses. For the first actuator we have only the mass of the moving part of the actuator, because this actuator is permanently connected with the frame of the system. For other actuators, we have the sum of masses of the body of the actuator, the moving part, and the connector.

10.4.1 Description of Submodels

Input signal submodels are shown in Fig. 10.6. The element in Fig. 10.6a represents the linear signal source which can be used in electric and mechanical part. For electric part of actuator generated signal is shown in Fig. 10.3a, b but for mechanical part generated signal is shown in Fig. 10.3c.

The voltage source submodel is presented in Fig. 10.6b. The signal at port 3 controls the generated voltage on the output. Element from Fig. 10.6c converts a dimensionless signal input at port 1 to a force with the same value in N which is output at port 2.

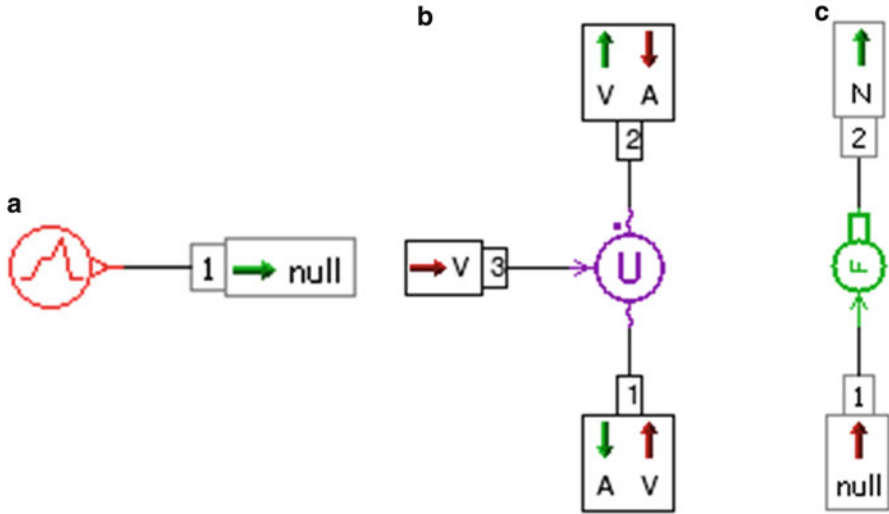


Fig. 10.6 Submodels of: (a) Signal source, (b) Voltage source, (c) Converter of signal

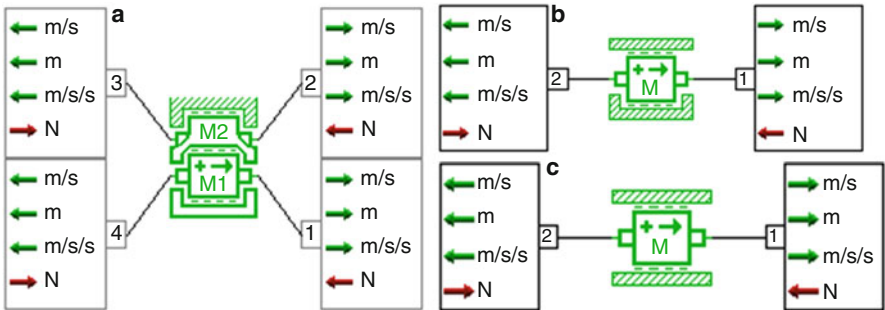


Fig. 10.7 Mass submodels

Mass submodels are presented in Fig. 10.7. Submodel in Fig. 10.7a represents the one-dimensional motion of two bodies under the action of external forces in N applied at four ports and frictional forces. One body, typically a slider, moves within the actuator body or whole actuator moves within the frame body. The displacements are limited to a specified range by inclusion of elastic end stops. In this submodel the mass $M2$ represents sum of mass body of the actuator outer body and connector. The friction force between the slider and the actuator body is modeled as Karnopp friction, stiction, Coulomb friction, viscous friction, and windage. Viscous friction and windage friction can be taken into account between the actuator and the frame body. In the cascade system, this type of mass submodel represents sum of the mass of actuator 2 and connector 1 and sum of the mass of actuator 3 and connector 2. The submodel in Fig. 10.7b

represents the one-dimensional motion of a two ports mass under the action of two external forces in N and frictional forces. The displacement is limited to a specified range by inclusion of ideal end stops. In the cascade system the submodel from Fig. 10.7b represents slider of actuator 1 which is fixed to the frame. The submodel in Fig. 10.7c represents the one-dimensional motion of a two ports mass under the action of two external forces in N and frictional forces. This mass submodel represents movable rod. All mass submodels return the velocity in m/s , the displacement in m , and the acceleration of the mass in m/s^2 for each body. For all mass submodels the inclination parameter allows for setting the inclination of the load in degrees, by the user. The friction characteristics are to be defined as follows: the coefficient of viscous friction in $N/(m/s)$; the coefficient of windage in $N/(m/s)^2$; the Coulomb friction force in N , and the stiction force in N . The windage is a force created on an object by friction when there is relative movement between air and the object. There are two possible causes of windage: the object is moving and being slowed by resistance from the air and a wind is blowing producing a force on the object. The windage force is approximately proportional to the square of the velocity. The friction coefficients between the actuator body and the slider have been set zero value because of the manufacturing specification (CEDRAT nd) of actuator there isn't information about.

Submodel in Fig. 10.8a represents an ideal mechanical spring. The submodel has two ports and gives force in N as outputs at both these ports. Connected submodels must provide velocities in m/s as inputs. The spring compression in m is calculated from the two displacement inputs. The geometrical and material parameters of the spring can be changed then the stiffness is computed using the expression for the helicoidal spring:

$$k = \frac{G \times d^4}{8 \times D^3 \times n_a} \pi r^2$$

where G is the material shear modulus N/m^2 , n_a is the number of active coils, D is the spring diameter [mm], and d is the wire diameter [mm]. Submodels in Fig. 10.8b, c represent a damper with either a constant or variable damper rating and submodel a spring-damper which combines the features of these two elements. These are additional elements in order to match input and output parameters between successive elements of system. These elements are used to obtain the continuity of the model. In the real system a permanent connection between the slider and the connector (the slider and the rod) doesn't occur in this place.

10.4.2 Analysis and Results

As mentioned before, the damper or the damper-spring was used to obtain the continuity of the model which affects the system behavior. The geometrical and material parameters of the spring were as follows: $G = 8e + 07 \text{ N/m}^2$, $n_a = 5$,

$D = 4.4$ mm, $d = 1$ mm. For these values the best result was obtained. Three positions of the system were analyzed:

- Case I: vertical position and the rod moving up,
- Case II: vertical position and the rod moving down,
- Case III: inclined position (angle 30°) and the rod moving up.

At the beginning the model was analyzed without load and friction forces in order to check the method of operation. Figure 10.9 shows displacements of cascade

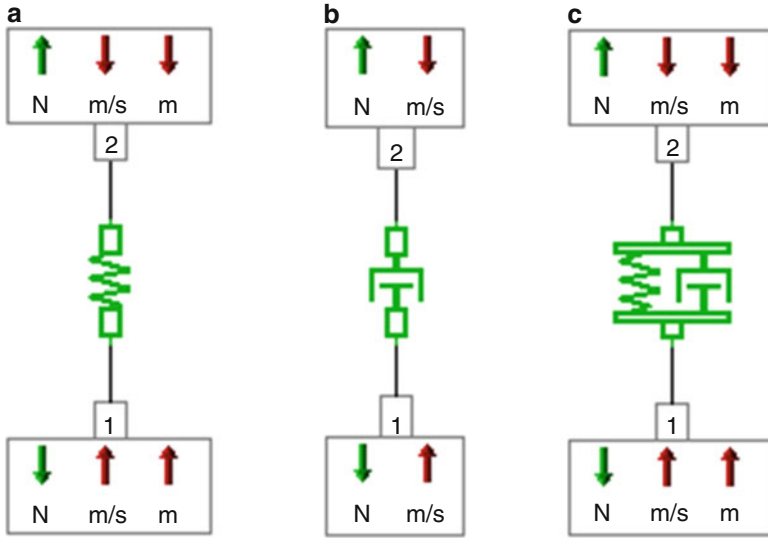


Fig. 10.8 Elements: (a) spring, (b) dumper, (c) spring-damper

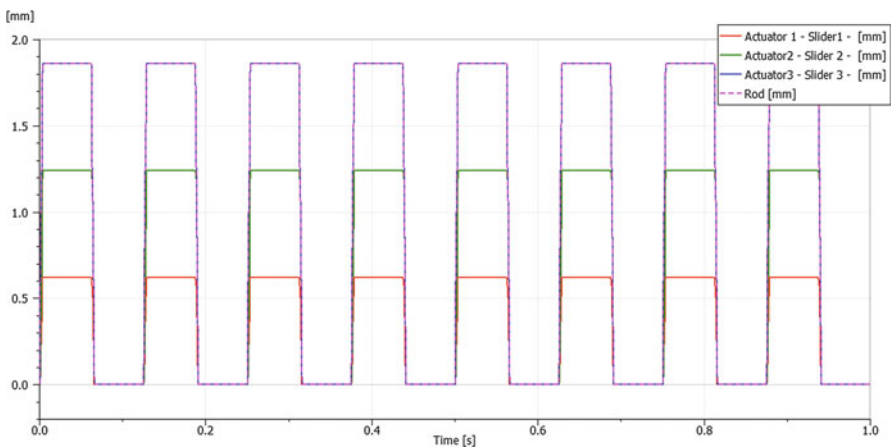


Fig. 10.9 AMESim – total displacements of sliders and rod – Case I

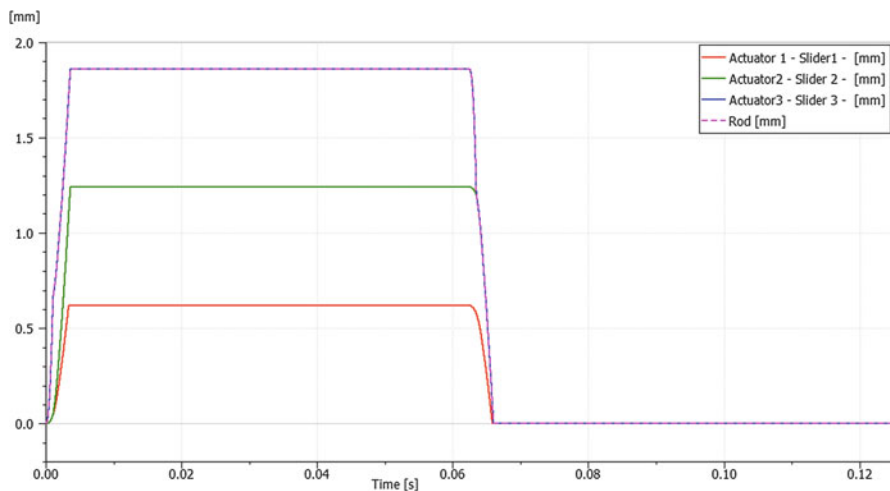


Fig. 10.10 AMESim – total displacements of sliders and rod – one period – Case I

elements as time functions for Case I. The displacements for Cases II and III look qualitatively similar, and certain differences appear only in the activation and returning times. From this figure we can see that the total displacements are consistent with the adopted assumption.

The displacement of a single slider is equal to about 0.62 mm and the sum of displacements of all sliders (displacement of the rod) is equal to 1.86 mm. The total displacement of the slider from Actuator 3 coincides with the displacement of the rod (purple line). Figure 10.10 presents one period of the signal from Fig. 10.9.

On the basis of that signal we can estimate the time of rod activation. The activation times (maximal times of rod displacement) are equal to 0.0041 s for Case I, 0.0038 s for Case II, and 0.004 s for Case III. The returning times are equal to 0.0035 s for Case I, 0.0037 s for Case II, and 0.0035 s for Case III. Since the system is analyzed without friction forces, we can assume that this is the minimum value of the rod activation time (Fig. 10.11).

The next step of the research was to use appropriate parameters of friction between the elements in order to obtain real behavior of the examined system. Figure 10.12 presents the ejecting and returning times for all cases with friction. The activation times are equal to 0.0047 s for Case I, 0.0044 s for Case II, and 0.0046 s for Case III. The returning times are equal 0.0038 s for Case I, 0.004 s for Case III, and 0.0038 s for Case III. We can see that the ejecting and returning times increased by about 15 % for the adopted/optimized friction coefficient values. On the basis of these graphs we can optimize the moment of activation and the delay time of an individual actuator.

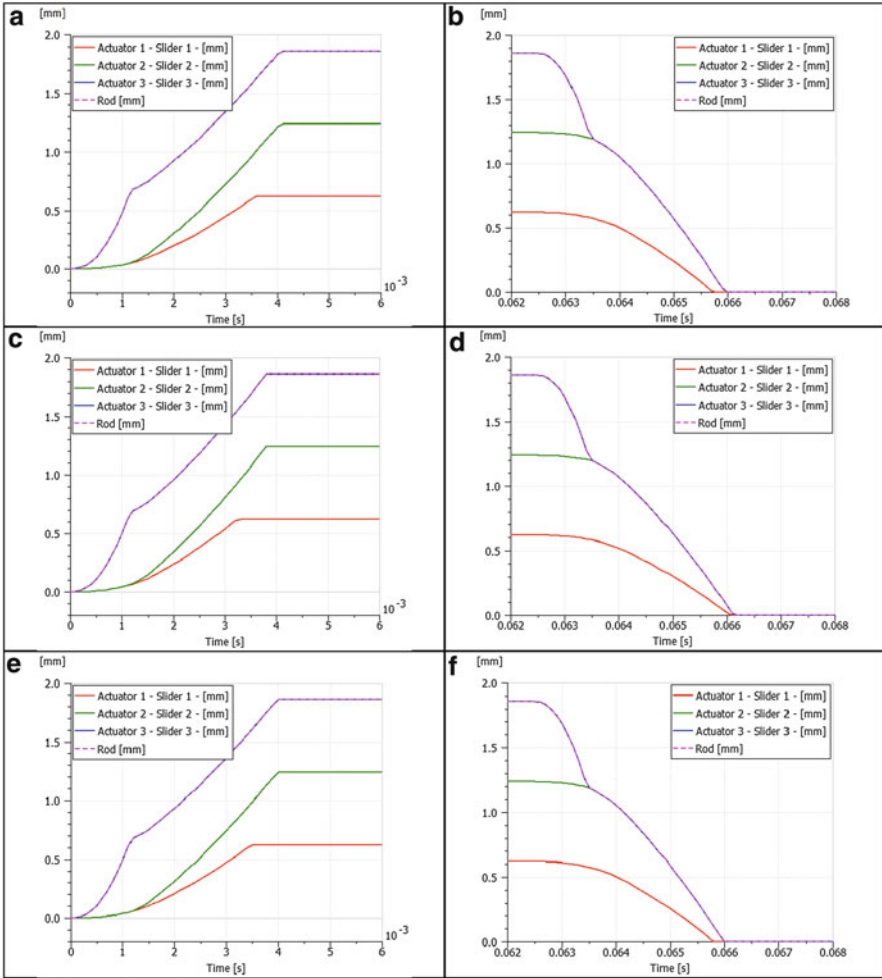


Fig. 10.11 AMESim – characteristics of ejection and return of the rod in time: (a, b) Case I, (c, d) Case II, and (e, f) Case III

10.5 Model (3D) of RrVG System in LMS Virtual Lab

The cascade model of RrVG was worked out in CATIA V5 environment integrated with LMS Virtual.Lab. The model is presented in Fig. 10.13. Starting with the geometry creation process, the bodies can be sketched, formed as solid geometries, assembled into a system of bodies, and connected by joints and forces.

The model is used both to predict loads and kinematic and dynamic behavior before the mechanical system is built, and to improve and troubleshoot the performance of the existing design. LMS Virtual.Lab offers a variety of analy-

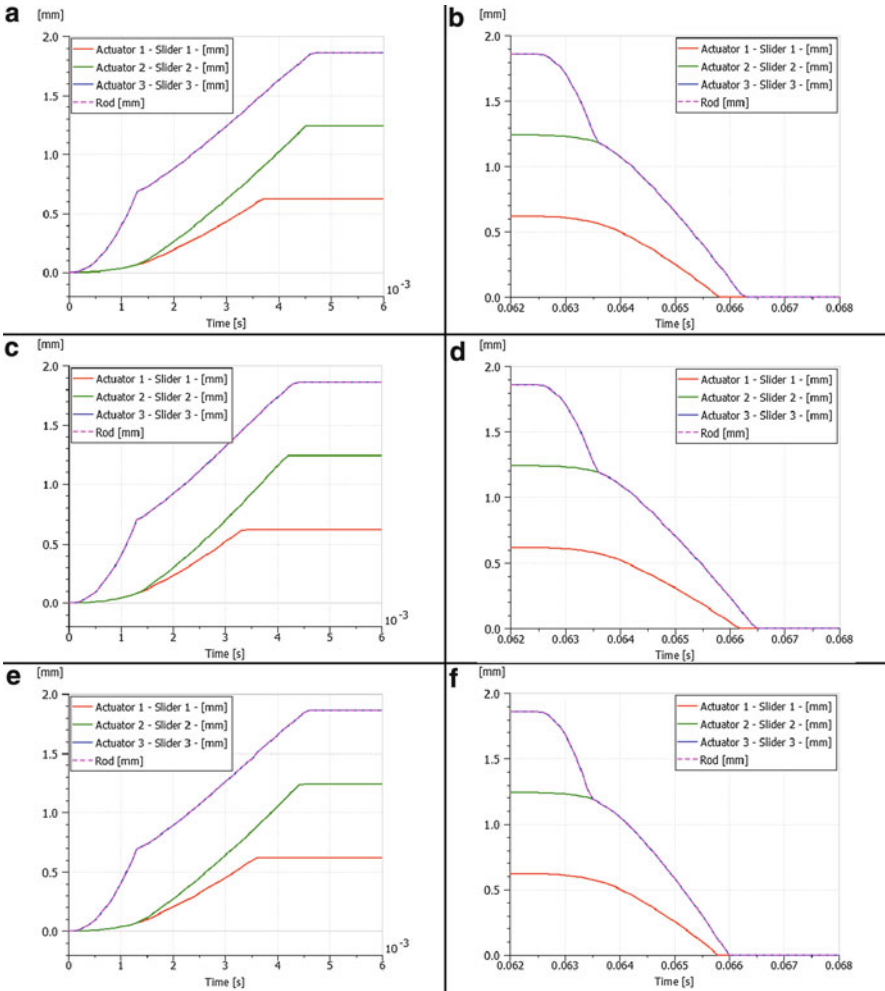


Fig. 10.12 AMESim – characteristics of ejection and return of the rod in time with friction: (a, b) Case I, (c, d) Case II and (e, f) Case III

sis types. Some types of analysis are performed sequentially. When models are first constructed, assembly analysis is run first to validate connectivity and accuracy of input. It is often useful to then run a static analysis of a dynamic system prior to running dynamic analysis to find the equilibrium position for all bodies. This ensures the dynamic run will be smooth and well behaved. Sometimes it is useful to run kinematic analysis to get body motion or path information for use in a subsequent dynamic run.

Fig. 10.13 Closed model of RrVG – cascade in LMS Virtual.Lab

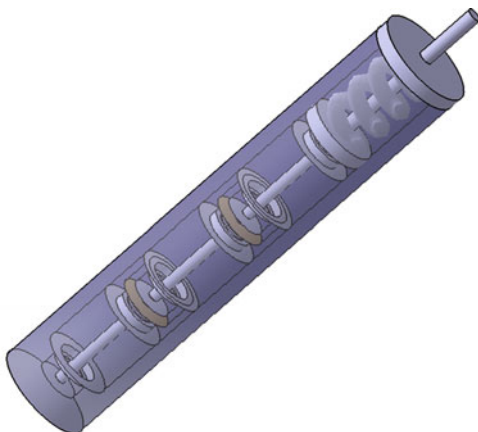
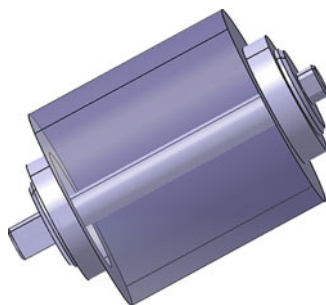


Fig. 10.14 The 3D model of BLMM actuator



10.5.1 Descriptions of Elements

The geometry and parameters (such as the mass, for instance) of the actuator were obtained from the manufacturer data (CEDRAT nd). The 3D model of the single actuator is presented in Fig. 10.14.

Figure 10.15 presents the connector and the movable rod. Figure 10.16 presents the frame with the lid of the system. Holes in the frame represent connections passing the control signal. The exact dimensions of the elements depend on the dimensions of the used actuator.

Table 10.3 presents the weights of individual elements based on the 3D model made in Virtual.Lab. The total mass of the cascade system is equal to 9.251 g (9.272 g with extra lubricious shell).

10.5.2 Kinematic Analysis

Kinematics deals with bodies connected by algebraic constraints and joints. The process of adding joints and constraints to the model involves selecting an element

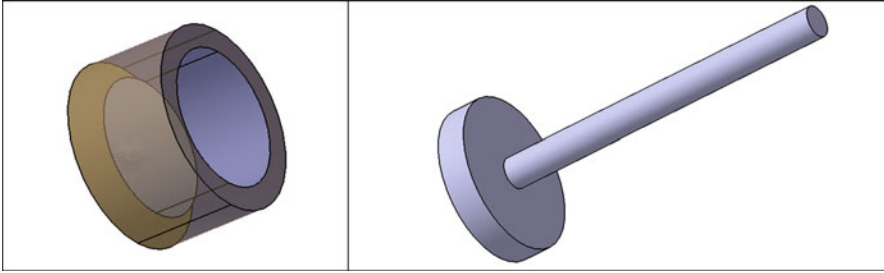


Fig. 10.15 The 3D model and characteristics of the connector and the movable rod



Fig. 10.16 The 3D model and characteristic of the frame and the frame lid

Table 10.3 Masses of elements and lubricious shell

Name of element	Material	Mass [g]
Outer body of actuator	Steel	1.024
Slider of actuator	–	0.076
Connector	Aluminum	0.088
Movable rod	Aluminum	0.079
Frame with lid	Steel	5.696
Lubricious shell	Teflon	0.021

type and picking the bodies and connection locations on the bodies. Joints define a relationship between two different bodies according to the kinematic constraints imposed by that type of joint. Each joint references geometric features on the two bodies connected by the joint. The joint also eliminates certain degrees of freedom that exist between the bodies connected by the joint. A cylindrical joint has been used between frame and movable elements in cascade. A constraint element defines a kinematic condition for one body or a relationship between two different bodies according to the type of kinematic constraint imposed. Constraints can be used to fix a point on a body to a specific location in global space, fix the distance between two points in global space, and fix the difference in the global coordinate of a point on each of the two bodies. Special constraints called drivers can be used

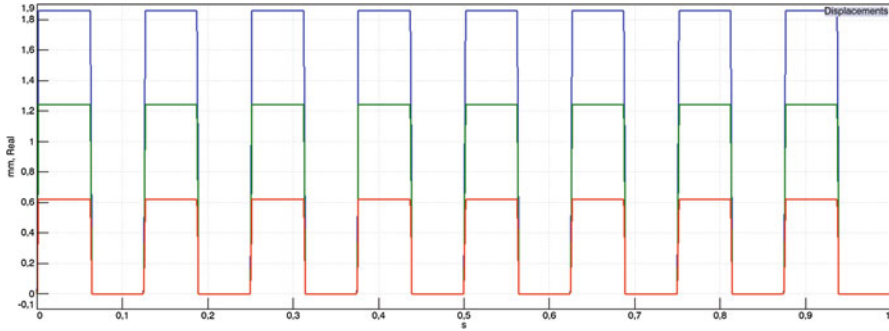


Fig. 10.17 Virtual.Lab – total displacements of sliders and rod – kinematic analysis

to define motion on a single body, between two bodies, or on a joint. Instead of a fixed constraint, these driver constraints are time varying constraints that allow you to exercise the free degrees of freedom of your mechanism. Defining a driver constraint in LMS Virtual.Lab consists of two basic steps. Step 1 is defining what you would like to drive, the position of a single body, a distance between two bodies, or a free degree of freedom on a joint. Step 2 is defining the actual driving function (Fig. 10.3d). A Joint Position Drivers were used in order to move actuator sliders and displacements of sliders respect to the frame. The initial results are presented in Fig. 10.17.

The red, green, and blue lines represent displacements of sliders for actuators 1, 2, and 3, respectively. The total displacements of the rod (purple line) coincide with the displacement of the slider from actuator 3. Analyzing the graph in Fig. 10.17 we can see that the masses and spring have no effect on the displacements. Figure 10.18 presents one period of the signal from Fig. 10.17.

Characteristics in Figs. 10.17 and 10.18 are analogical to the curves shown in Figs. 10.9 and 10.10. We can see that curves representing Virtual.Lab results are more straight than those representing AMESim results. This difference is caused by total absence of friction and connections between sliders and connectors. Additionally, the mass of the elements does not affect the movement of elements in the kinetic analysis (Fig. 10.19).

Therefore, the ejecting and returning times are equal to the commutation time (0.0017 s) of a single actuator. Results for all cases are the same for this type of analysis.

10.5.3 Dynamic Analysis

Dynamics deals with bodies, joints, and forces. The standard process of making a complete simulation involves defining the body locations and mass properties, followed by defining the constraints and kinematic joints connecting the bodies.

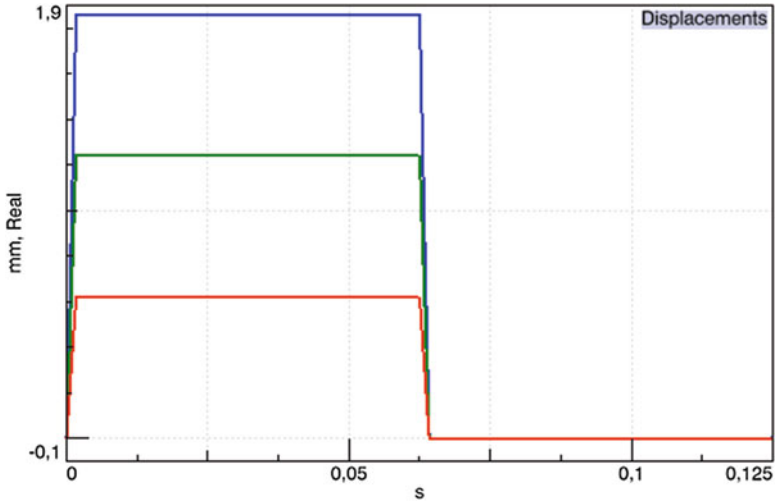


Fig. 10.18 VL – total displacements of sliders and rod – one period – kinematic analysis

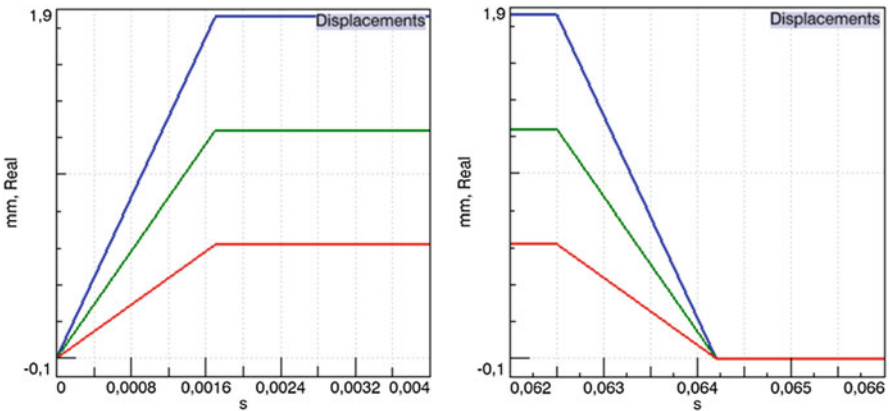


Fig. 10.19 VL – characteristics of ejection and return of the rod in time – kinematic analysis – Case I

Next, the dynamic force elements are specified. Most force elements act on one or two bodies and are a function of the position and velocity of connected bodies. Force elements do not remove any degrees of freedom from the equations of motion. They define the right-hand side terms in the equations of motion and affect the resulting body acceleration at each time step. Force elements also contribute to the solution in the case of static analysis, inverse dynamics, but not in kinematic analysis where forces are ignored. The following dynamic force elements have been specified. The Scalar Expression Force between the actuator body and the slider is applied in order to move the slider. This type of force is also used in order to add additional force as

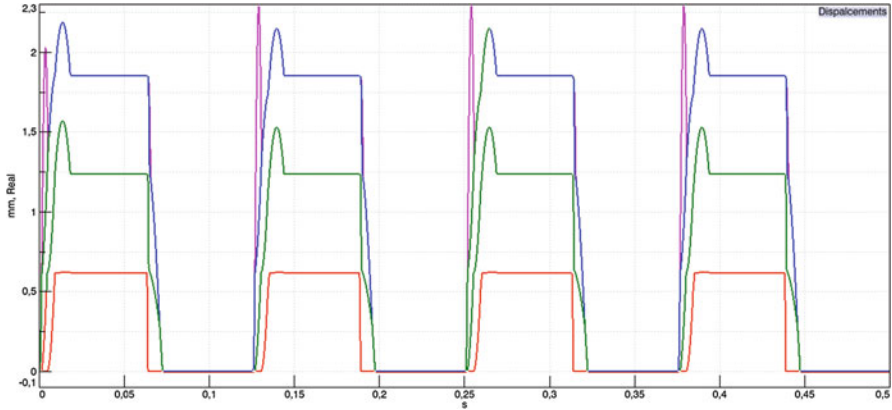


Fig. 10.20 VL – total displacements of sliders and rod – dynamic analysis Case I

the aerodynamic load. The Point-to-Point Contact force between sliders, connectors, and rod. The TSDA (“translational spring-damper-actuator”) force between the base of rod and lid of frame. This force represents the main spring which is used in model. TSDA is also used to limit the maximum displacement of the slider with respect to the actuator body.

The initial results for the dynamic analysis without friction forces for Case I are presented in Fig. 10.20. The colors of the lines are the same as in the kinematic analysis. Purple line represents the displacement of the rod and partially coincides with the displacement of the slider from actuator 3. The influence of the reaction forces between the elements is significant. The application of TSDA as the endstop results in delays in actuator’s response to the control signal. Therefore, the control signal required modification. Figure 10.21a, b presents the control signals for each actuator after modification, complemented by the dashed black line representing the initial control signal. The above-mentioned modifications consisted in changing the commutation time and shifting the control signal individually for each actuator. The distance between the following pulses activating the movement of the sliders was changed depending on which actuator was to be activated. Additionally, the control signals of actuators 2 and 3 were shifted in time.

Figure 10.22 presents the displacements of the sliders and the rod for the modified control signal. We can see that the displacement of the rod coincides with the displacement of the slider 3 from actuator 3.

Additionally, characteristic peaks appeared at the beginning of each period of displacement of an element. These peaks (short jumps of deflections) were not observed in the AMESim and kinematic results. Here, they appeared due to the fact that the system is discontinuous, and consecutive cascade elements are not permanently connected. The movement of the rod and actuators 2 and 3 is limited by the main spring which is applied in order to undo the rod. As was to be expected, the size and the shape of the peaks depend on the adopted parameters of the main spring.

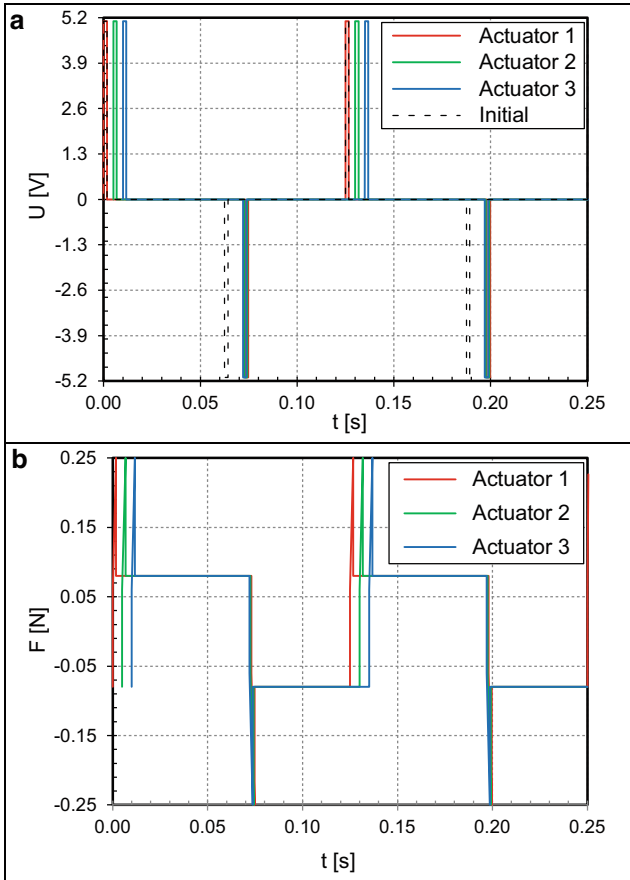


Fig. 10.21 Modified input and output signals for frequency 8 Hz, (a) voltage input signal and (b) force output signal

Spring performance is defined by such constant coefficients as: spring constant N/m, damping coefficient kg/s, and free length spring [m], defined in Virtual.Lab simulation. For excessively high values of the spring constant the rod will not be able to eject, while for very small values of the spring constant the returning time of rod is long. The damping coefficient tends to reduce the amplitude of oscillations in the system. The free length spring value defines the unreformed displacement of the spring. This value depends on the size of the system and is equal to 6.508 mm for all cases. For Case I with the modified control signal the spring constant is equal to 25 N/m and the damping coefficient is equal to 0.05 kg/s.

Each case was simulated for three different conditions: without friction force, with friction force, and with friction force and aerodynamic load of the rod. Figure 10.23a presents one period of total displacement of elements, the ejecting interval, and the returning interval from total displacement, for Case I without friction.

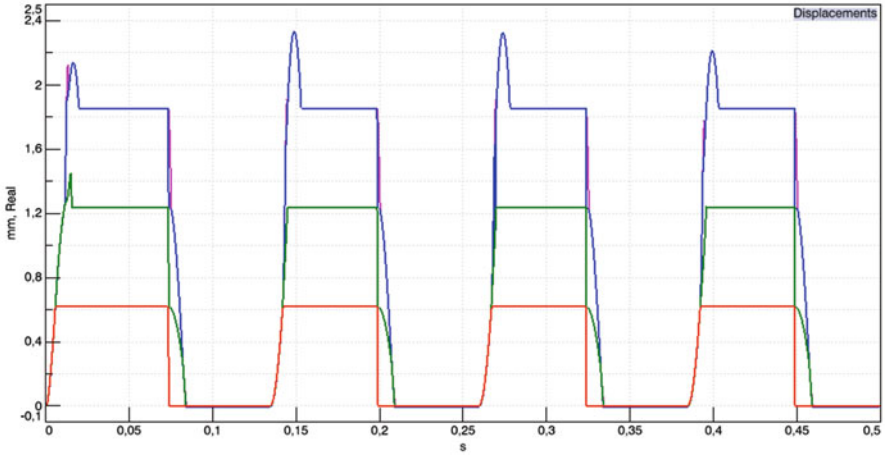


Fig. 10.22 VL – total displacements of sliders and rod after input signal modifications – dynamic analysis Case I

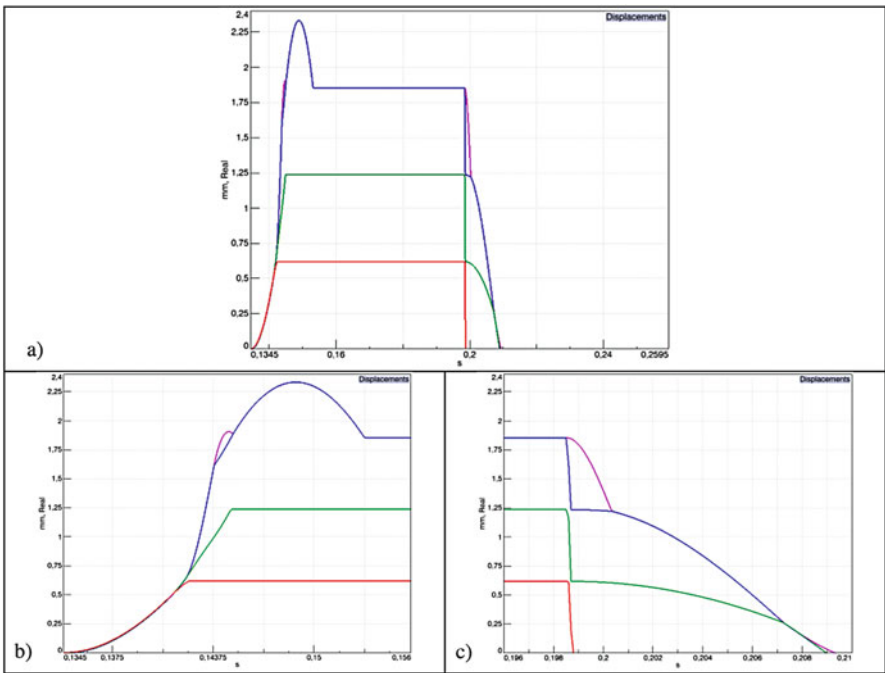


Fig. 10.23 VL – (a) Total displacements of sliders and rod – one period, (b, c) characteristics of ejection and return of the rod in time – Case I

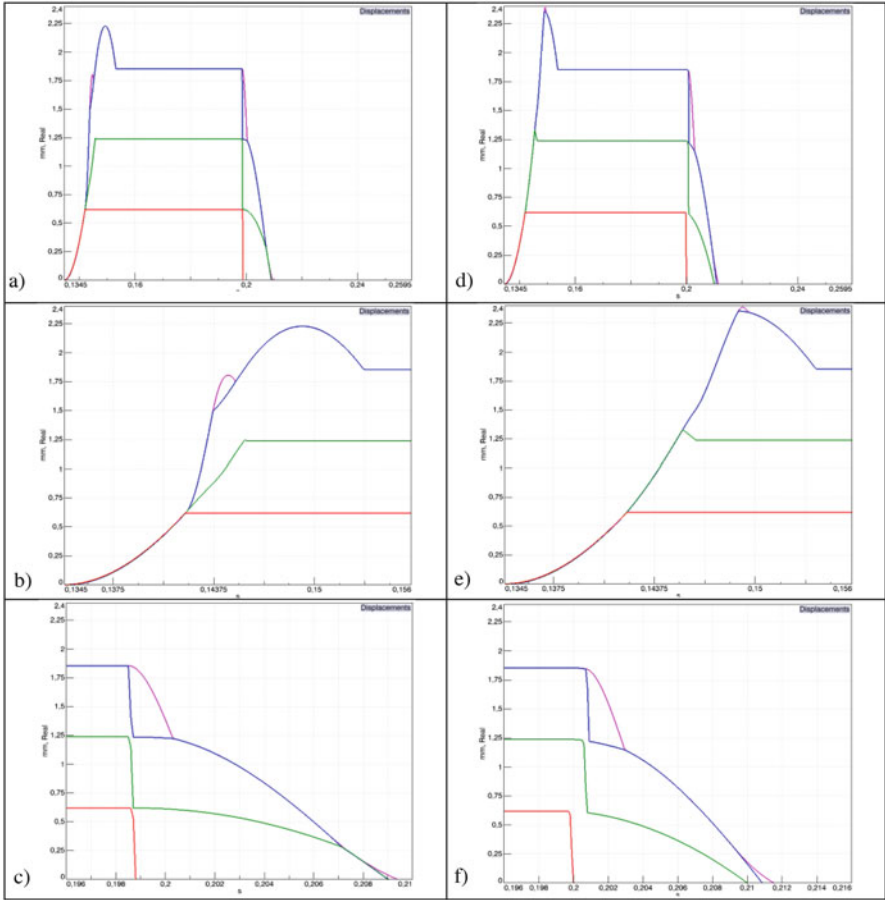


Fig. 10.24 VL – total displacements of sliders and rod, (a–c) characteristics of ejection and return of the rod in time – Case I – with friction; (d–f) Case I – with friction and aerodynamic load of rod

From Fig. 10.23b, c we can determine the ejecting and returning time of the rod to the operating deflection (≈ 1.86 mm). The eject time from the initial position of the rod up to the first moment when it achieves the operating displacement was examined. For comparison, the next figures present results for the same case but with additional friction force between the elements and aerodynamic load of the rod. Each friction element adds and removes constraints on the motion of the mechanism, therefore the number of degrees of freedom (DOF) varies as friction elements lock and unlock. Because Virtual.Lab searches for the time when locking and unlocking occurs, we may notice that the analysis is slower when these events occur.

Figure 10.24a–f presents results for Case I with friction force between the movable elements and the frame, and aerodynamic load of the rod. When the friction force was applied, the movement of the elements was slower. The aerodynamic load

Table 10.4 Ejection and return time of the rod, Case I

	Ejection time [s]	Return time [s]
Case I	0.00985	0.01075
Case I with friction	0.01115	0.01099
Case I with friction and aeroload	0.01296	0.01157

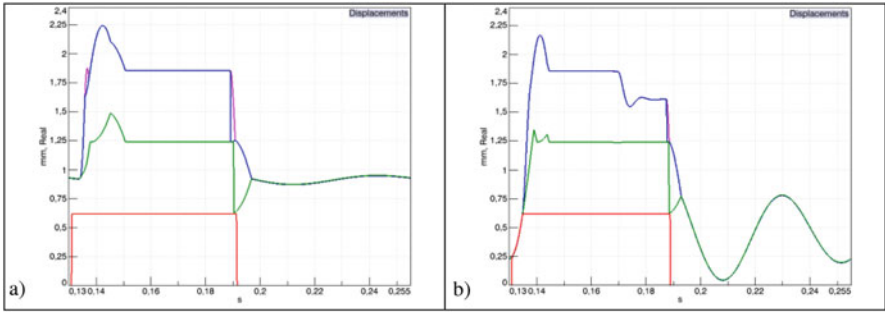


Fig. 10.25 VL – total displacements of sliders and rod – Case II for different constant spring values (a) 25 N/m (b) 50 N/m

of the rod was represented by an extra force applied to the tip of the rod. This force was changed depending on actual deflection of the rod. As a result, the observed movement of the rod was slower. The times of ejection and return of the rod for Case I are presented in Table 10.4.

For Case II, in which the system motion was reversed, the situation was completely different. It was necessary to change the control signal. Here, the initial control signal without modifications and offsets was used, see Fig. 10.3. Additionally, the parameters of the main spring were changed. Figure 10.25a presents displacement characteristics of the rod for the previous spring. We can see that the rod does not return to its initial position. Figure 10.25b presents the behavior of the system for the spring with strength enlarged by twice. For the stronger spring the system tries to return to the initial position but the displacement characteristics are deformed.

Therefore, the spring constant equal to 40 N/m was used for Case II. As a result, the system faster achieves the operating displacement, and the displacement characteristics are not deformed within the operating displacement range. However, the system does not return to its initial position and oscillates, see Fig. 10.26.

The times of ejection and return of the rod for Case II are presented in Table 10.5. The return times were undefined because the rod does not return to its initial position (Fig. 10.27).

The use of aerodynamic loads of the rod results in stronger interaction between the frame and the moving rod. For Case III (Figs. 10.28 and 10.29) the modified control signal was used (the same as in Case I) and the same the spring constant (Table 10.6).

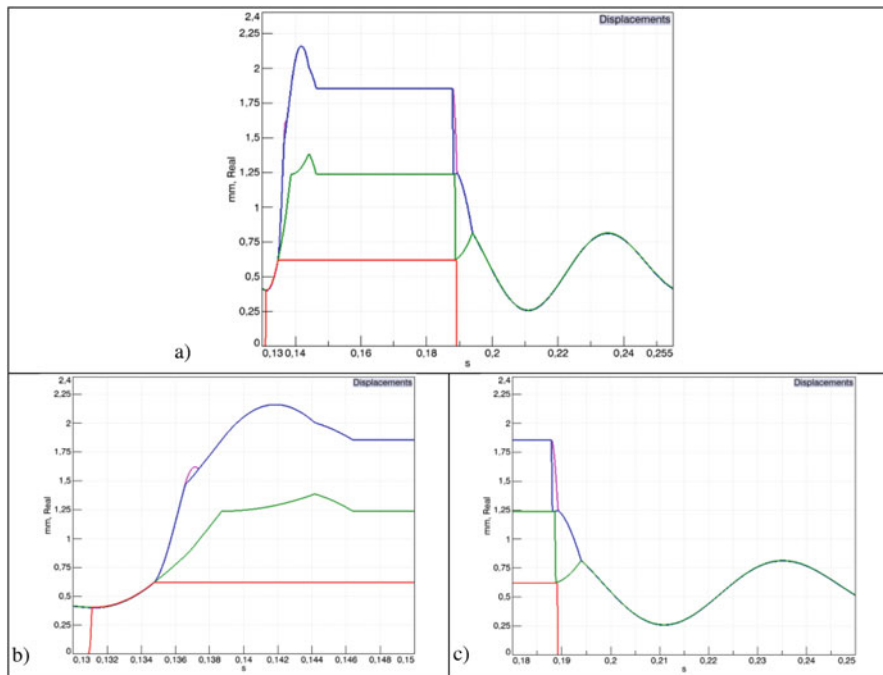


Fig. 10.26 VL – (a) Total displacements of sliders and rod – one period, (b, c) characteristics of ejection and return of the rod in time – Case II

Table 10.5 Ejection and return time of rod, Case II

	Ejection time [s]	Return time [s]
Case II	0.00783	undefined
Case I with friction	0.00788	undefined
Case I with friction and aeroload	0.00791	undefined

Table 10.6 Ejection and return time of rod, Case III

	Ejection time [s]	Return time [s]
Case III	0.01250	0.01275
Case III with friction	0.01261	0.01300
Case III with friction and aeroload	0.01290	0.01382

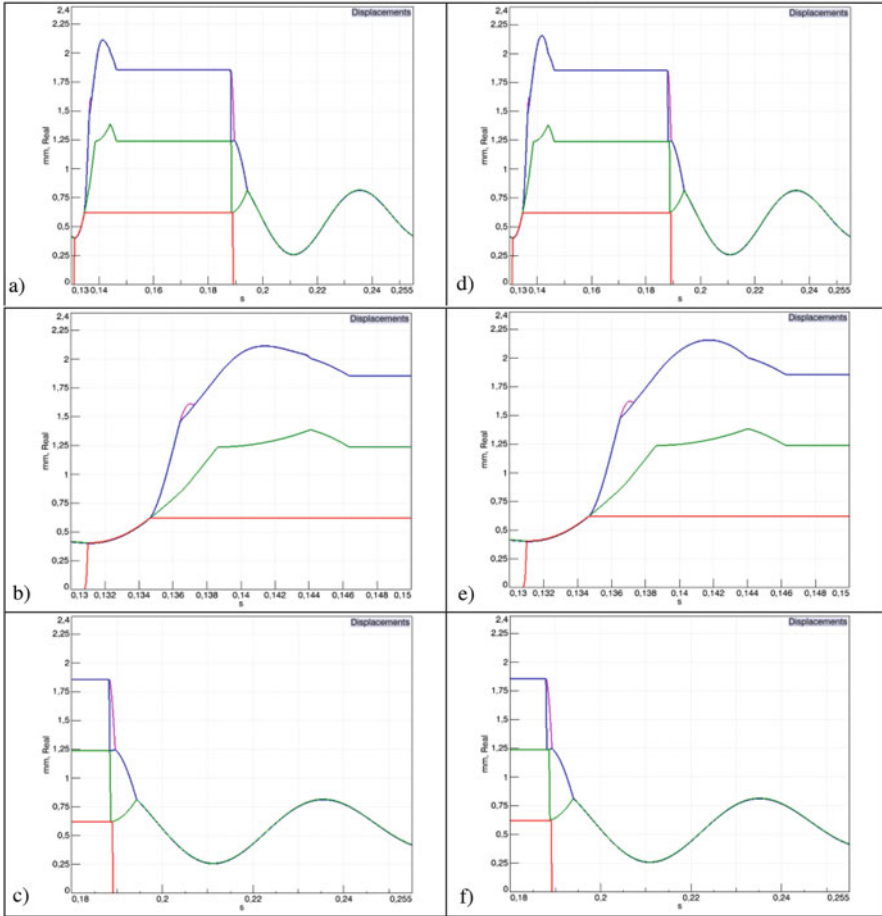


Fig. 10.27 VL – total displacements of sliders and rod, (a-c) – Case II with friction; (d-f) Case II with friction and aerodynamic load of rod

10.6 Conclusion

The main objective of the research was to build the Retractable rod Vortex Generator models using LMS software. The built models allow to analyze the system for various values of parameters. The one-dimensional model made in AMESim allowed preliminary simulation and analysis of the responses of individual moving parts. The three-dimensional model was made in VL. This model enables more realistic simulations of RrVG performance taking into account: loads of the rod, parameters of the friction force between the elements, position of the system

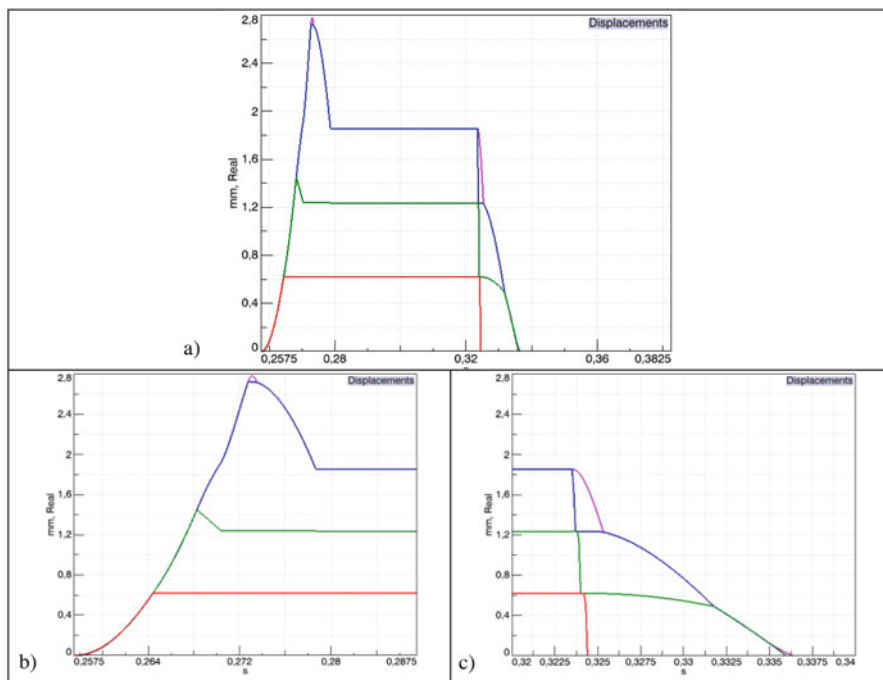


Fig. 10.28 VL – (a) Total displacements of sliders and rod – one period, (b, c) characteristics of ejection and return of the rod in time – Case III

(inclination angle), material of performance elements, and the optimized control signal. The simulation results showed the impact of the operation direction on system performance. Additionally, the change of the operation direction requires modification of parameters of individual elements (the main spring). When the system is directed down, the rod moves faster, but does not return to its original position. When typical materials (steel and aluminum) are used, the mass of the entire system is relatively low, which facilitates practical application. The simulations have shown that it is possible to obtain the time of rod ejection suitably shorter, as compared to the time of vortex generation (from the CFD results). In conclusion, the main objective of the research has been achieved.

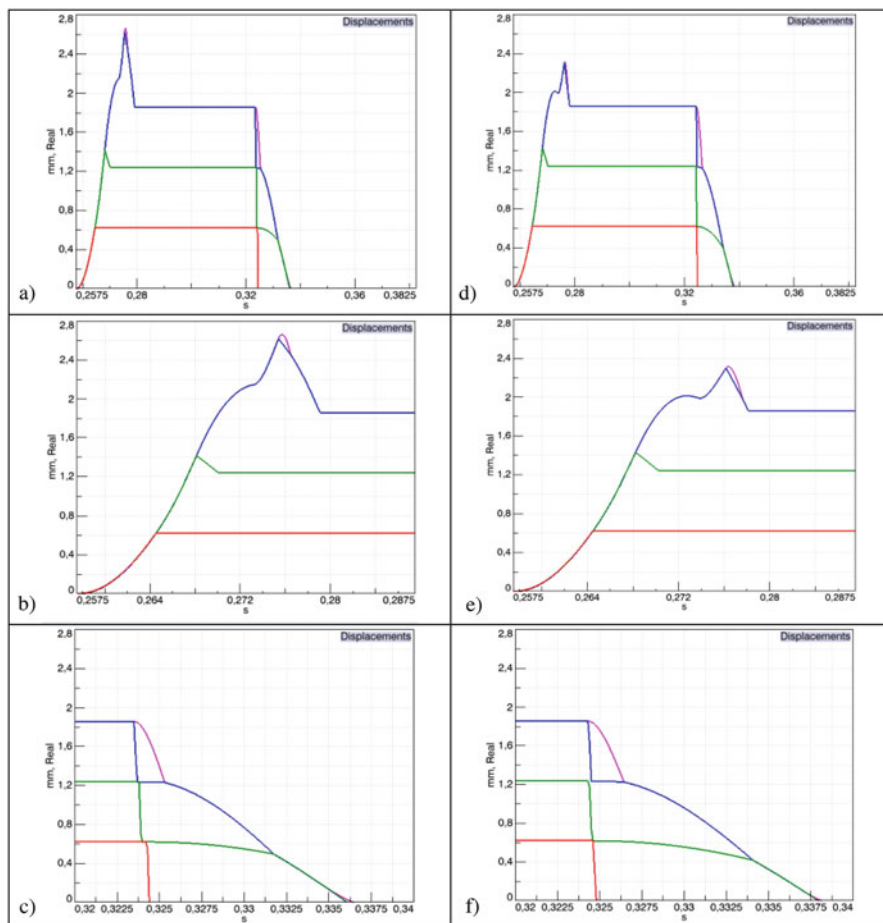


Fig. 10.29 VL – Total displacements of sliders and rod, (a–c) – Case III with friction; (d–f) Case III with friction and aerodynamic load of rod

References

Barakos G (2010) Bump at a Wall. In: Doerffer WP, Hirsch C, Dussauge J-P, Babinsky H, Barakos GN (eds) Unsteady effects of shock wave induced separation. Cambridge University Press, Cambridge, pp 13–53

CEDRAT (nd) Cedrat Technologies. Retrieved from Cedrat Technologies: <http://www.cedrat-technologies.com/en/products/users-manual/actuators.html>

Doerffer P, Szulc O (2011) Application of the passive control of shock wave to the reduction of high-speed impulsive noise. Int J Eng Syst Modell Simul 3:64

Flaszynski P, Tejero F (2013) RANS numerical simulation of effectiveness of vortex generators in a curved wall nozzle. IMP PAN

Pastrikakis V (2015) Flow control on helicopter rotors using active gurney flaps. PhD thesis, University of Liverpool

- Siemens (nd) Siemens PLM Software. Retrieved from LMS Virtual.Lab: http://www.plm.automation.siemens.com/en_us/products/lms/virtual-lab/index.shtml
- Siemens (nd) Siemens PLM Software. Retrieved from LMS Imagine.Lab Amesim: http://www.plm.automation.siemens.com/en_us/products/lms/imagine-lab/amesim/index.shtml
- Tang H, Salunkhe P, Zheng Y, Du J, Wu Y (2014) On the use of synthetic jet actuator arrays for active flow separation control. *Exp Therm Fluid Sci* 57:1–10
- Tejero F, Doerffer P, Szulc O (2014) Aerodynamic analysis of potential use of flow control devices. *J Phys Conf Ser* 530:012067

Part IV
Important Issues in Synthetic Jet Design

Chapter 11

Numerical Simulation of a Synthetic Jet Actuator for Active Flow Control

Marcin Kurowski

11.1 Introduction

Aerodynamic properties have been widely enhanced with the use of flow control devices in the engineering applications, e.g., airplanes, helicopters, and wind turbine rotors (Casalino et al. 2008; Yen and Ahmed 2013) for many years. Flow separation or transition point control can be done by passive methods which do not require any additional power supply (Gurney Flaps, vortex generators, airfoil shape modification) (Bechert et al. 2000; Shan et al. 2008) or using active devices with an additional energy input (steady blowing, synthetic jet actuators) (Gul et al. 2014). In fluid dynamics, a synthetic jet flow is a jet flow synthesized from an ambient fluid where the stream of the fluid mixes with the surrounding medium. This can be generated using an electromagnetic, piezoelectric, or mechanical driver. The synthetic jet fluid motion is obtained by an alternate suction and ejection of fluid through an orifice or a slot bounding a small cavity. This is generated by a time periodic oscillation of a diaphragm built into the cavity wall. Oscillation of the membrane is a response of the piezoelectric material to the applied voltage. During the oscillation cycle, the cavity volume alternately decreases the expelling fluid during the blowing cycle and increases the cavity volume drawing in fluid during the suction cycle. A membrane can be perpendicular or parallel to the surface in which a hole or a slot is introduced. The scheme of the synthetic jet actuator with perpendicular and parallel membranes is presented in Fig. 11.1.

M. Kurowski (✉)
Institute of Fluid-Flow Machinery, Polish Academy of Sciences, Gdansk, Poland
e-mail: marcin.kurowski@imp.gda.pl

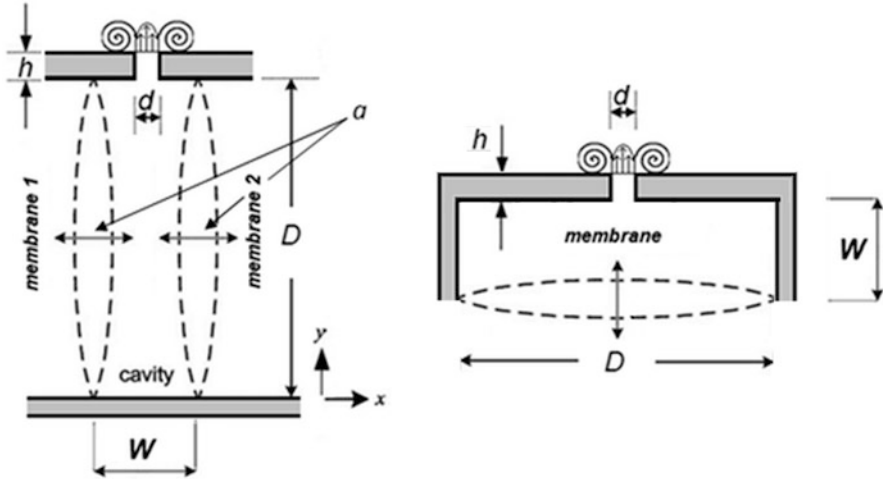


Fig. 11.1 Scheme of the synthetic jet actuator with perpendicular and parallel membranes

Many studies of the synthetic jet have been performed using simplified actuator models:

- The boundary condition at the orifice exit (the wall-normal velocity profile) (Lee and Goldstein 2002; Mallinson et al. 2001)
- The moving piston condition (Fugal et al. 2005)

The numerical modeling of the synthetic jet actuator is described in the following sections.

11.2 Initial and Updated Synthetic Jet Models

This section describes numerical simulation details of initial and updated synthetic jet models. Computational fluid dynamic (CFD) software, turbulence model used in simulation, and other simulation parameters are described. Moving–Deforming–Mesh method used for the two-dimensional (2D) CFD vibrating diaphragm simulation is presented in this section as well.

Commercial package ANSYS Fluent is used for 2D and 3D CFD simulations. Equations of conservation of mass and momentum are solved during the simulation for compressible flow. Compressibility effects have to be taken into account because of the change of the density as a result of moving diaphragm.

One can distinguish two major sections of the proposed geometry. The first region is the ambient air outside the actuator where the jet is developed and the second region includes synthetic jet actuator cavity. Ambient air and cavity are connected through a duct. The ambient air boundary conditions are specified as a pressure outlet, while all the surfaces are considered as walls.

Ambient air region is meshed with structured mesh, as well as the duct and central part of the synthetic jet actuator cavity. In cavity regions adjacent to the moving walls, a tri-pave unstructured mesh has to be used to allow membrane node displacement during the simulation. Unstructured mesh in the deforming zone is a requirement of the Moving–Deforming–Mesh feature in the software (described later). This approach allows to reduce the number of re-meshing nodes during every time step. Combination of the structured and unstructured mesh significantly reduces size of the model and as a result reduces the needed computational power and simulation time.

The shear stress transport (SST) k - ω turbulence model (Menter 1994) is a two-equation eddy-viscosity model which has been proven to be very effective in similar applications. The use of a k - ω formulation in the inner parts of the boundary layer makes the model directly usable all the way down to the wall through the viscous sub-layer; hence, the SST k - ω model can be used as a low-Re turbulence model without any extra damping functions. The SST formulation also switches to a k - ε behavior in the free stream.

By default, ANSYS Fluent updates the node positions on a dynamic zone by applying the solid-body motion equation. This implies that there is no relative motion between the nodes on the dynamic zone. However, if there is a need to control the motion of each node independently, the user-defined function DEFINE_GRID_MOTION can be used. A mesh motion UDF can, for example, update the position of each node based on the deflection due to fluid–structure interaction. Improved synthetic jet actuator model with Moving–Deforming Mesh (MDM) allows to replace surface boundary condition with deforming wall. Membrane deformation profile from finite element model can be imported as an input to CFD simulation. MDM makes possible to simulate flow in the cavity and capture the real physical phenomenon.

Initial membrane deformation profile has been written using formula:

$$y = A \sin(2\pi ft) \sin \left[\pi \left(\frac{x-l}{D} \right) \right] \quad (11.1)$$

Updated deformation profile of moving membrane used in the further simulations is given by formula

$$y = A \sin(2\pi ft) \left[1 - \left(\frac{x}{r} \right)^2 \right]^2 \quad (11.2)$$

where x is membrane displacement in x -direction [m], A is displacement amplitude [m], f is forcing frequency [Hz], t is time [s], y is y -axis coordinate, l is the distance from inlet to the actuator [m], and r is membrane radius [m].

The membrane is clamped to the chamber on the edge. Equation 11.2 describes deformation of the membrane in the area close to the wall (effect of clamp) in a more realistic method than Eq. (11.1) as it is shown in Fig. 11.2.

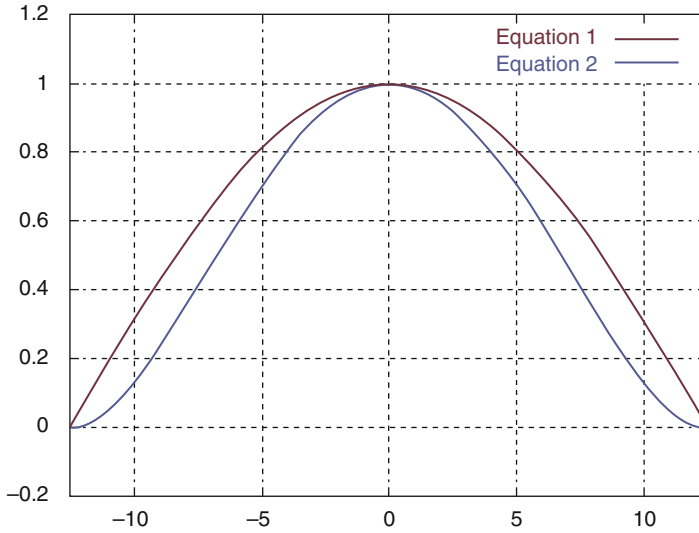


Fig. 11.2 Red line—plot of initial equation, blue line—plot of updated equation of membrane deformation

A lot of studies of the synthetic jet have been performed using simplified model of the actuator. One of the methods is based on the boundary condition at the orifice exit (the wall-normal velocity profile). Another method of representing the synthetic jet behavior is a moving piston condition. One has to notice that only the moving–deforming membrane boundary condition provides the most accurate physical phenomenon. On the other hand, use of the re-meshing method for every time step requires a lot of computational power and is time-consuming.

11.3 Shape Optimization

Velocity magnitude vectors in the blowing cycle are presented in Fig. 11.3 for initial model with straight edges. Vortices created at the orifice exit are visible.

Simulation results show reversed flow in the duct during blowing cycle which affects flow velocity on the actuator exit; therefore, duct shape has been investigated. Duct edge inclination 45° and corresponding velocity vectors are presented in Fig. 11.4. Duct edge inclination 60° and corresponding velocity vectors are presented in Fig. 11.5. Rounded duct edge and jet velocity vectors are presented in Fig. 11.6.

The best simulation results are obtained for the actuator with rounded edges. Separation area and reversed flow in the duct are minimized compared to actuator with inclined edges. Actuator geometry has been defined in the meaning of membrane diameter, orifice diameter, and actuator height and is presented in Table 11.1.

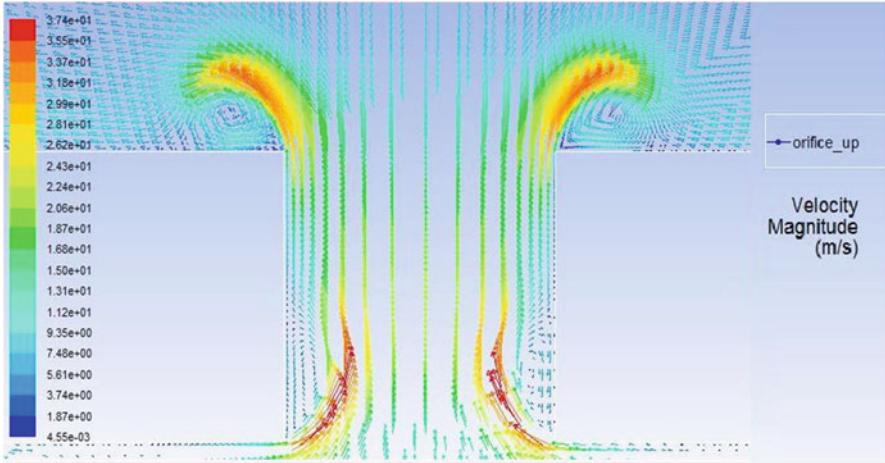


Fig. 11.3 Vectors of the velocity magnitude during the blowing cycle, initial model with straight edges

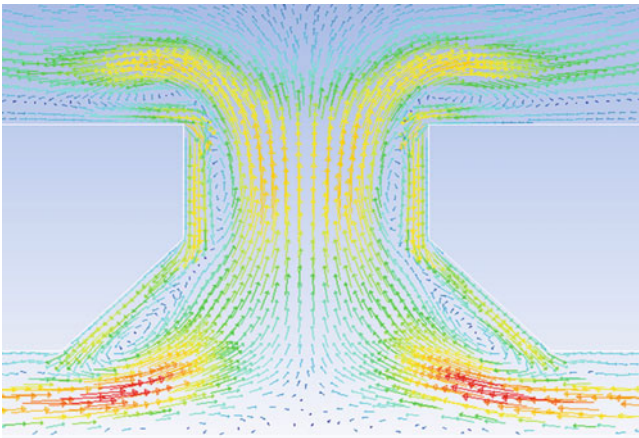


Fig. 11.4 Duct geometry with 45° edge inclination—vectors of the jet velocity magnitude

Scheme of the actuator with one and with two perpendicular membranes in cavity is presented in Fig. 11.7.

11.4 Parametric Study

There is a need to study the effect of synthetic jet individual parameters for synthetic jet flow maximization. A parametric study was carried out to find the optimal parameters. Numerical simulations of the actuator for various membrane amplitudes and different forcing frequencies were conducted. All the simulations were

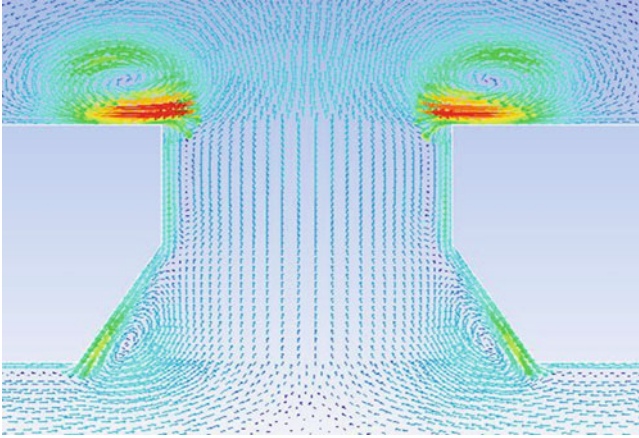


Fig. 11.5 Duct geometry with 60° edge inclination—vectors of the jet velocity magnitude

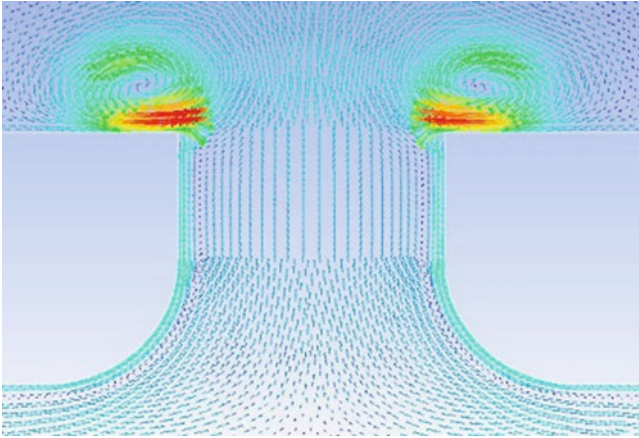
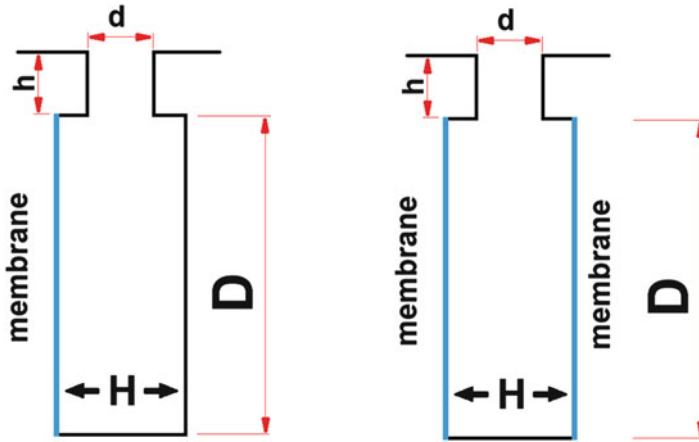


Fig. 11.6 Duct geometry with rounded edge (radius 0.5 mm)—vectors of the jet velocity magnitude

performed for two cases—for one membrane in a cavity and for two membranes in a cavity (Fig. 11.7). The influence of the vibrating membrane amplitude on the jet velocity was investigated varying the peak-to-peak displacement of the diaphragm from $a = 2e10^{-5}$ m to $a = 1e10^{-4}$ m. As the displacement amplitude increased, the change of the cavity volume increased during the cycle as well. As a result, more fluid was forced to exit the actuator during the blowing phase. It was decided to undertake a numerical simulation of an oscillating membrane in a wide range of displacement values to maximize the jet velocity. One has to keep in mind the fact that piezoelectric membrane displacement is a function of the applied voltage; therefore, the power consumption during the actuator operation can be an issue.

Table 11.1 Actuator geometry parameters

Membrane diameter D [mm]	Orifice diameter d [mm]	Orifice length h [mm]	Actuator height H [mm]
25.0	1.0	1.0	1.5
			2.0

**Fig. 11.7** Scheme of the actuator with one (*left*) and with two (*right*) membranes in the cavity

At resonant frequencies, the synthetic jet generator can generate maximum output velocity. The synthetic jet generator should be operated on its resonant frequencies to reduce the power input of energy. A preliminary design of the synthetic jet generator can be made using the lumped element modeling (LEM) (Gallas et al. 2003) method based on the electroacoustic theory. The LEM method is based on an analogy between electrical and acoustic domains. Two main forcing frequencies can be specified in the synthetic jet actuator application. One corresponds to the diaphragm natural frequency, and the other corresponds to the cavity resonant frequency (Helmholtz frequency).

11.4.1 Membrane Structural Resonance

The diaphragm natural frequency (f_{mem}) depends on the material properties, mass, and dimensions of diaphragm. Using the LEM method, the diaphragm natural frequency is given by the expression

$$f_{\text{mem}} = \frac{1}{2\pi} \sqrt{\frac{1}{M_{\text{aD}} C_{\text{aD}}}} \quad (11.3)$$

where M_{aD} is the diaphragm acoustic mass and C_{aD} is the acoustic compliance of a homogeneous clamped circular plate. From the diameter of an oscillating circular membrane in the LEM simulation, the deformation profile is exported and used as the input in the two-dimensional CFD simulations using the MDM method. Based on the LEM method, the membrane natural frequency used in the simulations is $f_{mem} = 740$ Hz.

11.4.2 Helmholtz Frequency

Thinking of the cavity resonance in terms of an oscillating mass of air can give some insight about how the physical properties of the cavity affect the resonant frequency. This can be visualized by the process of pushing extra air into the cavity where overpressure is produced. If the opening to the cavity is larger, the excess air can escape more rapidly to bring the pressure down to external conditions. This leads to a higher cavity resonant frequency. If the neck of the cavity is longer, there is more resistance to the flow of the excess air, and the resonant frequency is lowered. If the cavity volume is increased, then, it takes a greater excess mass of air to produce a given overpressure, and it therefore takes longer for that excess pressure to bring it down to external conditions. The larger cavity will have lower resonant frequency. In general the cavity resonant frequency is given by the expression

$$f_H = \frac{c}{2\pi} \sqrt{\frac{A}{VL}} \quad (11.4)$$

where c is the sound speed (m/s), A is the area of opening (m^2), V is the cavity volume (m^3), and L is the opening length (m). The synthetic jet actuator model parameters used in the presented study are given in Table 11.2.

Simulations were performed for actuator with one membrane and two membranes in the cavity. Results of the vibrating membrane amplitude influence on the jet velocity for one membrane in the cavity are presented in Fig. 11.8. Lines represent velocity magnitude V_{mag} and velocity y-component V_y (in the jet direction)

Table 11.2 Synthetic jet actuator model parameters

Peak-to-peak displacement a [mm]	Membrane diameter D [mm]	Orifice diameter d [mm]	Duct length h [mm]	Actuator height H [mm]		Number of membranes		Forcing frequency [Hz]	
0.02	25	1.0	1.0	1.5	2.0	1	2	740	1650
0.04									
0.06									
0.08									
0.10									

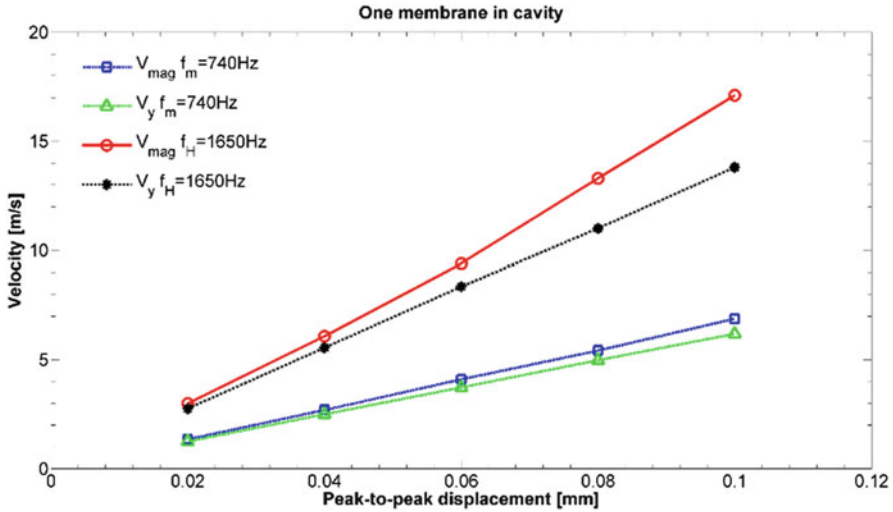


Fig. 11.8 Jet velocity for one membrane in cavity (membrane resonant frequency $f_m = 740$ Hz, cavity resonant frequency $f_H = 1650$ Hz)

for membrane resonant frequency $f_{mem} = 740$ Hz and cavity resonant frequency $f_{cav} = 1650$ Hz. All the velocity values are maximum values for the jet during the blowing cycle. Velocity magnitude and velocity y-component are calculated on the actuator exit orifice diameter. Results of the vibrating membrane amplitude influence on the jet velocity for two membranes in cavity are presented in Fig. 11.9. The membranes are actuated in the opposite phase thanks to which the cavity volume is modified twice as much as in the previous case. As it can be observed increase of the membrane displacement results in approximately linear increase of the jet velocity. The higher the membrane amplitude is the higher jet velocity from the actuator can be obtained.

Maximum jet velocities were obtained for membrane displacement $a = 0.1$ mm. For one membrane in cavity, maximum jet velocity was $V = 6.88$ m/s for $f_m = 740$ Hz. For two membranes in cavity, maximum jet velocity was $V = 14.2$ m/s for $f_m = 740$ Hz. For cavity resonant frequency $f_H = 1650$ Hz, maximum jet velocity was $V = 17.1$ m/s for one membrane in cavity and for two membranes $V = 31.5$ m/s. Ratio of jet velocities for actuator arrangement with two membranes to one membrane in cavity is presented in Table 11.3. Use of a second membrane in cavity gives jet velocity two times higher for membrane resonant frequency and for cavity resonant frequency as well.

Flow separation in the duct affects the jet velocity at the actuator exit. This can be observed in the difference between jet velocity magnitude and jet y-direction velocity component presented in Figs. 11.8 and 11.9 for one and two membranes in cavity, respectively.

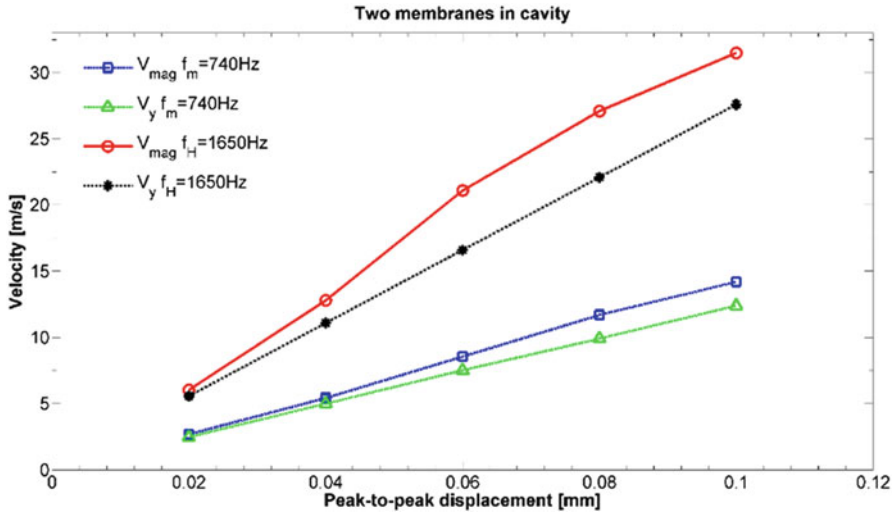


Fig. 11.9 Jet velocity for two membranes in cavity (membrane resonant frequency $f_m = 740$ Hz, cavity resonant frequency $f_H = 1650$ Hz)

Table 11.3 Ratio of jet velocities for actuators with two membranes to one membrane in cavity

Peak-to-peak displacement a [mm]	$f_m = 740$ Hz		$f_H = 1650$ Hz	
	V_{mag}	V_y	V_{mag}	V_y
0.02	2.01	1.98	2.02	2.01
0.04	2.02	2.00	2.11	2.00
0.06	2.09	2.02	2.24	1.99
0.08	2.16	1.99	2.04	2.01
0.1	2.06	2.00	1.84	2.00

Contours of velocity magnitude and vortex structure at the actuator exit in the blowing cycle for membrane peak-to-peak displacement $a = 0.06$ mm and one membrane in cavity are presented in Figs. 11.10 and 11.11. Contours of velocity magnitude and vortex structure at the actuator exit in the blowing cycle for membrane peak-to-peak displacement $a = 0.06$ mm and two membranes in cavity are presented in Figs. 11.12 and 11.13. For forcing frequency $f_m = 740$ Hz and actuator with two membranes in cavity, reversed flow area in duct is much larger compared to the case with actuator with one membrane in cavity. This phenomenon can be observed for forcing frequency $f_H = 1650$ Hz as well.

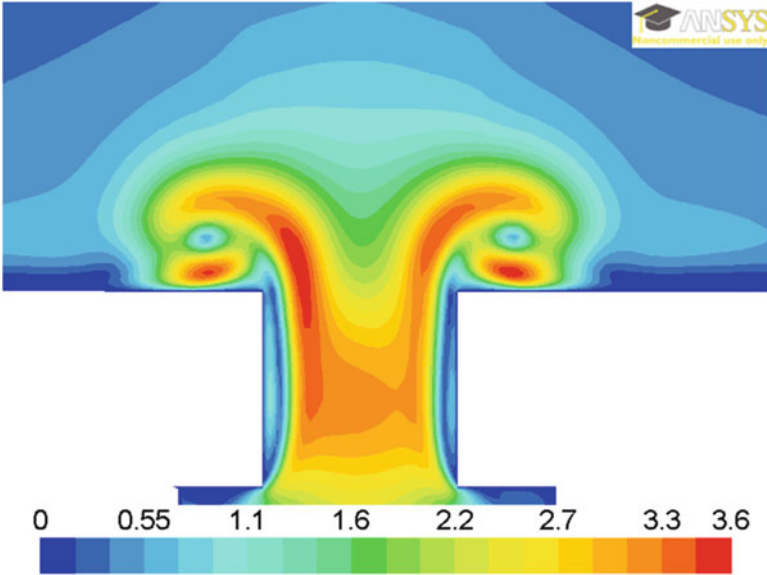


Fig. 11.10 Contours of velocity magnitude in the blowing cycle, one membrane, $f_m = 740$ Hz

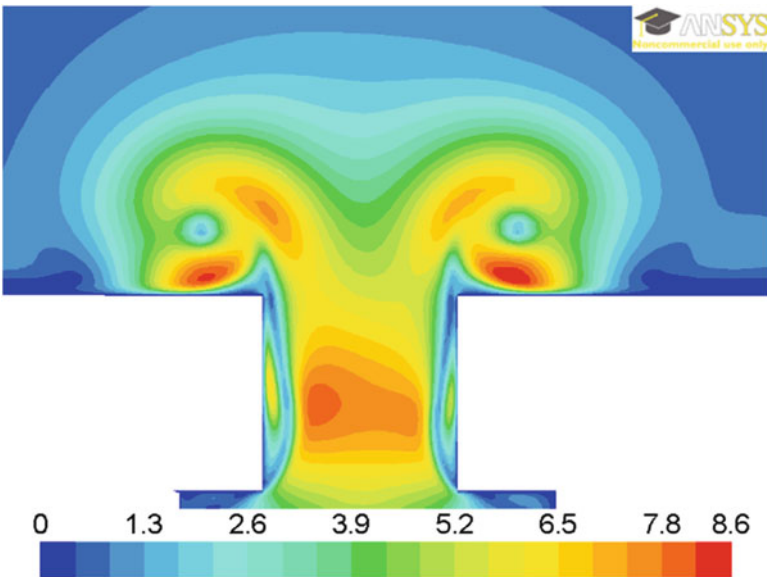


Fig. 11.11 Contours of velocity magnitude in the blowing cycle, one membrane, $f_H = 1650$ Hz

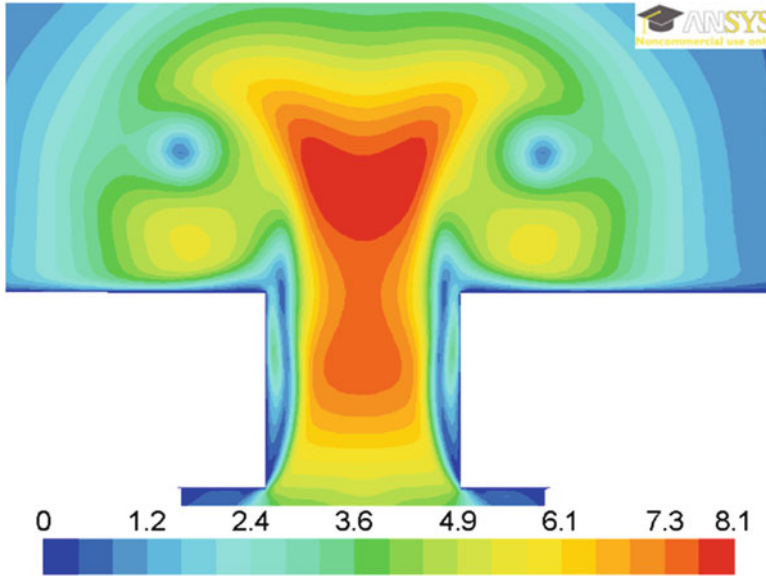


Fig. 11.12 Contours of velocity magnitude in the blowing cycle, two membranes, $f_m = 740$ Hz

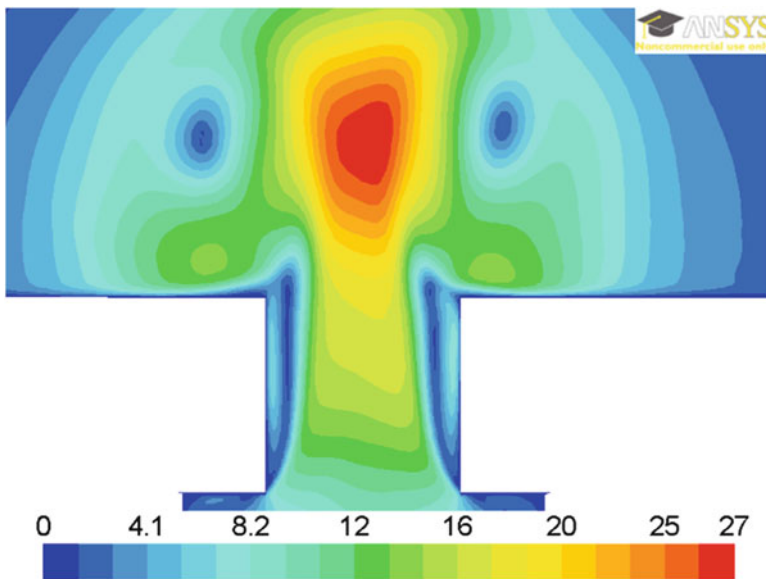


Fig. 11.13 Contours of velocity magnitude in the blowing cycle, two membranes, $f_H = 1650$ Hz

11.5 Bump for Flow Separation

Numerical simulations were performed on a bump implemented into the bottom wall of a wind tunnel section to generate flow separation due to the change of the channel geometry. Scheme of a bump used in numerical simulations is presented in Fig. 11.14.

Bump dimensions are:

- Width—80.0 mm
- Height at the beginning—min. (R_{\min}) = 10.0 mm, max. (R_{\max}) = 29.0 mm
- Height at the end— $r = 7.25$ mm
- Length (L_{bump}) = 90.0 mm

CFD model of a wind tunnel section with a bump is presented in Fig. 11.15.

Wind tunnel dimensions:

- Height $H = 90.0$ mm
- Width $W = 80.0$ mm
- Length $L = 900.0$ mm

Bump is located 270 mm from the inlet to the wind tunnel. Configurations of a bump height (R) from 10 mm up to 29 mm were investigated in simulations. In every case, radius of a bump in the end was constant $r = 7.25$ mm.

To investigate the flow field over the bump, different velocities on the inlet were applied. Minimal value of velocity in x -direction was 5 m/s, when maximal velocity in x -direction was 20 m/s. Contours of velocity magnitude for some bump geometries are presented below for two cases: inflow velocity 5 m/s and 20 m/s. It can be observed that for bump heights between 29 mm (Fig.11.16) and 20 mm

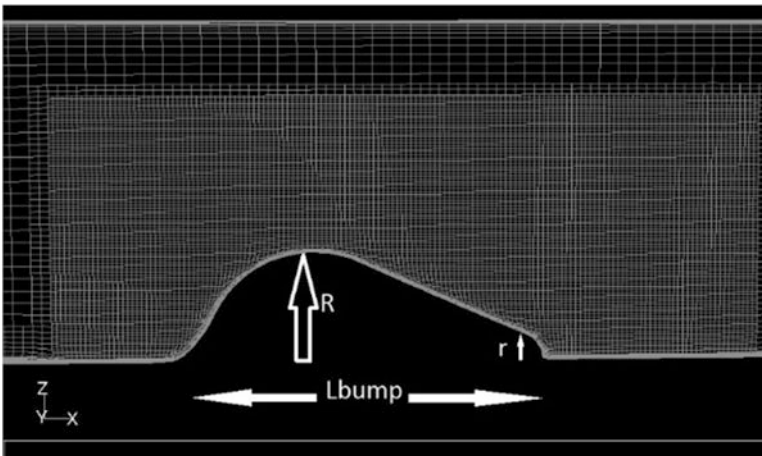


Fig. 11.14 Model of the bump used in CFD simulations

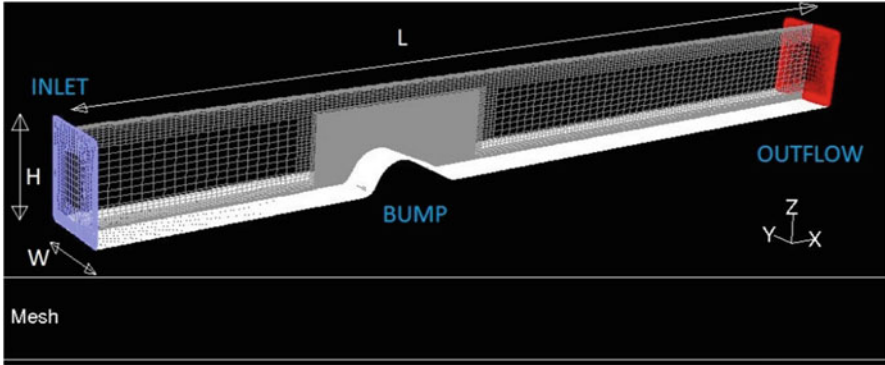


Fig. 11.15 CFD model of a wind tunnel with a bump on the bottom wall

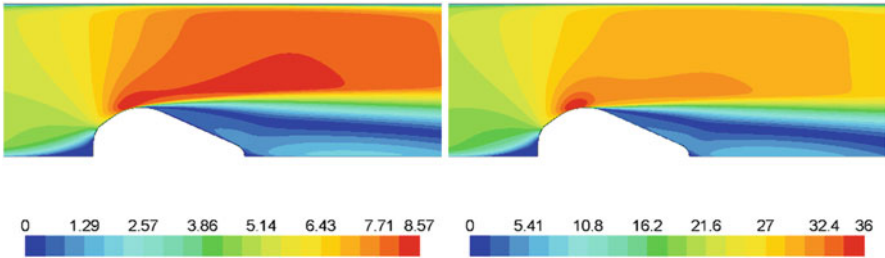


Fig. 11.16 Contours of velocity magnitude, $R = 29$ mm, $V = 5$ m/s (left), $V = 20$ m/s (right)

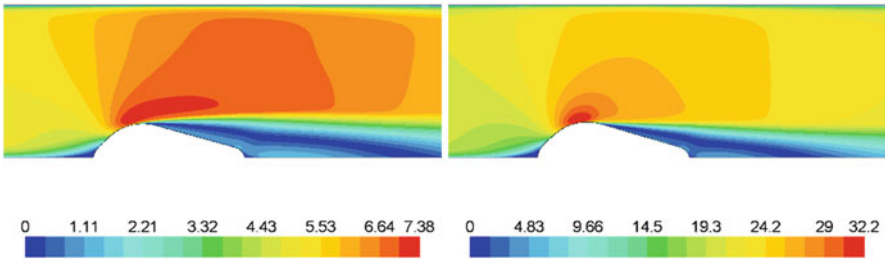


Fig. 11.17 Contours of velocity magnitude, $R = 20$ mm, $V = 5$ m/s (left), $V = 20$ m/s (right)

(Fig. 11.17), flow separates at the top of the bump. Area of the separated flow is large (indicated by the blue color), and flow is not reattached to the surface of the bump.

Contours of velocity magnitude for bump height 15 mm and inflow velocities 5 m/s and 20 m/s are presented in Fig. 11.18. Separation area is smaller than in previous cases.

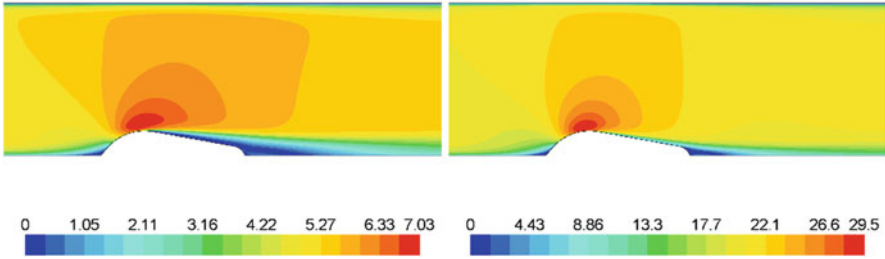


Fig. 11.18 Contours of velocity magnitude, $R = 15$ mm, $V = 5$ m/s (left), $V = 20$ m/s (right)

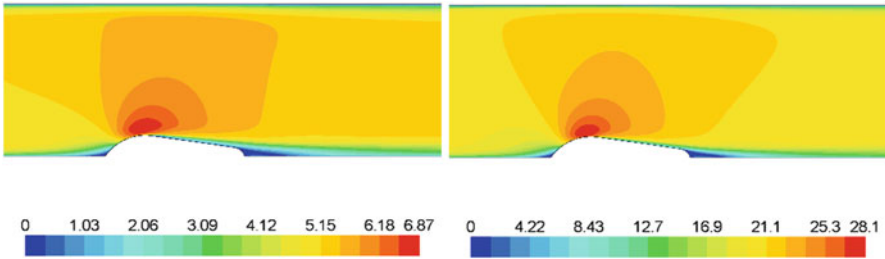


Fig. 11.19 Contours of velocity magnitude, $R = 13$ mm, $V = 5$ m/s (left), $V = 20$ m/s (right)

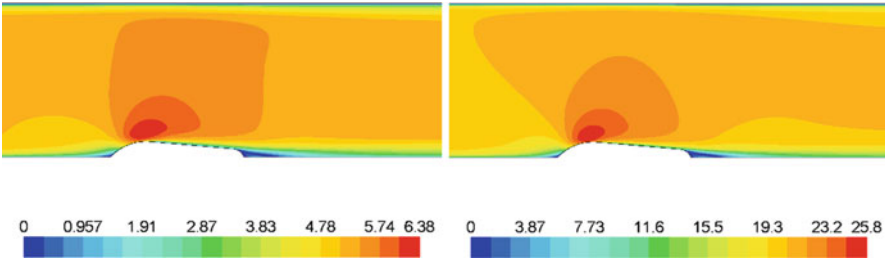


Fig. 11.20 Contours of velocity magnitude, $R = 10$ mm, $V = 5$ m/s (left), $V = 20$ m/s (right)

For bump height lower than 13 mm there is no flow separation on the bump at all, as it is presented in Figs. 11.19 and 11.20. Flow is attached to the surface of the bump along the whole distance.

Pathlines, colored by velocity magnitude, released from the top of the bump are presented in Fig. 11.21. Bump height is $R = 14$ mm and inflow velocity is 5 m/s. Flow separates on the top of the bump and reattaches to the surface. Separation bubble is clearly visible. In the future simulations, synthetic jet actuators will be placed in front of the separation bubble to investigate possibility to reduce the area of reversed flow.

Contours of velocity magnitude from the cut plane located 1 mm over the bump are presented in Fig. 11.22. Area covered by red color indicates location of the front

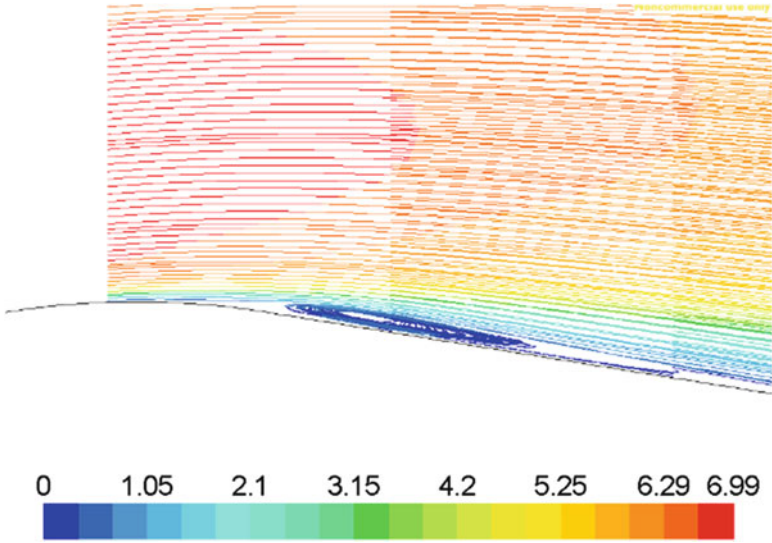


Fig. 11.21 Separation bubble for inflow velocity 5 m/s, bump height $R = 14$ mm

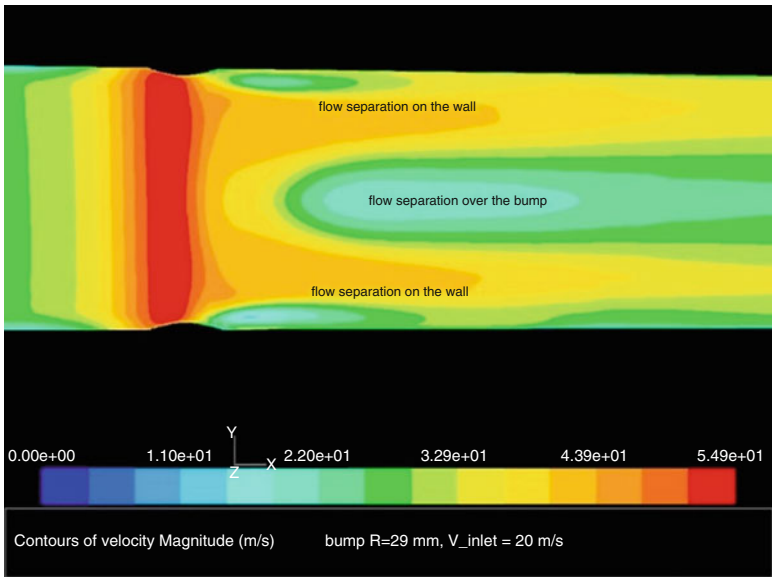


Fig. 11.22 Velocity magnitude contours for bump $R = 29$ mm, inflow velocity 20 m/s, plane cut 1 mm above the bump

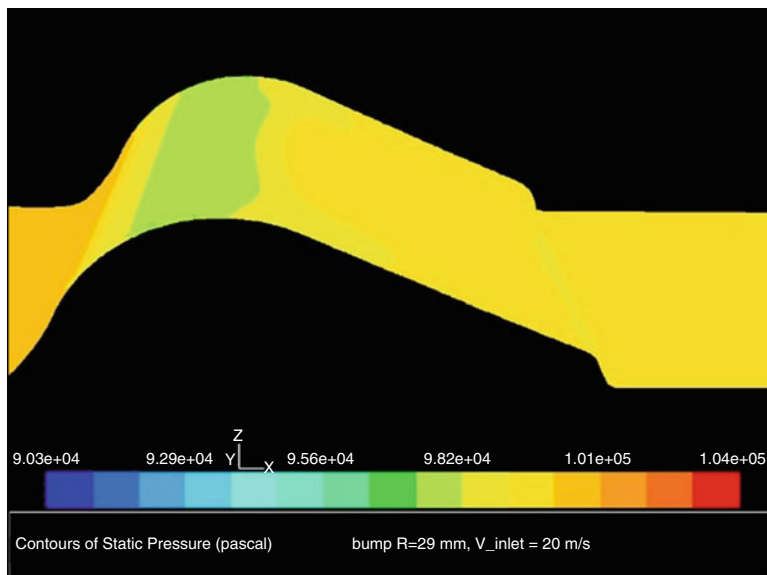


Fig. 11.23 Contours of the static pressure on the bump surface, bump $R = 29$ mm, inflow velocity 20 m/s

part of a bump. In the center of Fig. 11.22, area of lower velocity with respect to the main flow is visible. Separation on the wind tunnel walls is visible in Fig. 11.22 as well.

Contours of the static pressure on the bump surface for bump height in front part 29 mm and inflow velocity 20 m/s are presented in Fig. 11.23.

11.6 Conclusions

This chapter presents a numerical simulation of a synthetic jet actuator using the Moving–Deforming–Mesh method. The synthetic jet actuator is simulated using a membrane perpendicular to the surface arrangement. Investigations of the influence of the membrane amplitude, the forcing frequency, and cavity effect on the jet velocity were carried out, and the results are reported. Two forcing frequencies were used, one of which corresponded to the diaphragm natural frequency, and the other which corresponded to the cavity resonant frequency (Helmholtz frequency). The simulation results show that an increase in the membrane displacement results in an approximately linear increase of the jet velocity. The higher the membrane amplitude, the higher the jet velocity that can be obtained from the actuator. The use of a second membrane in the cavity gives the jet velocity two times higher for the membrane resonant frequency and for the cavity resonant frequency, as well. Maximum jet velocities were obtained for membrane displacement $a = 1 \cdot 10^{-4}$ m.

The use of a second membrane in the cavity gives the jet velocity two times higher for the membrane resonant frequency and for the cavity resonant frequency as well. This study was a preliminary study of the synthetic jet actuator for active flow control. The optimization process of the synthetic jet actuator geometry and parameters is ongoing. The numerical results obtained in these investigations are to be validated in the experimental campaign.

Appendix

Code of the user-defined function file used in the 2D synthetic jet actuator numerical simulation with Moving–Deforming–Mesh method is presented below:

```
#include "udf.h"
/* Put proper values in VALUE(variable) places */
#define freq 740 /* forcing frequency, Hz*/
#define amp 0.00008 /* peak-to-peak amplitude, meters 0.00006*/
#define L 0.025 /* chamber's width/membrane's diameter, meters*/
DEFINE_GRID_MOTION(moving_membrane, domain, dt, time, dtime)
{
    Thread *tf = DT_THREAD (dt);
    face_t f;
    Node *node_p;
    real omega, alpha, y, x;
    int n;
    /* Set/activate the deforming flag on adjacent cell zone, which */
    /* means that the cells adjacent to the deforming wall will also be */
    /* deformed, in order to avoid skewness. */
    SET_DEFORMING_THREAD_FLAG (THREAD_T0 (tf));
    omega = 2.*M_PI*freq;
    alpha = omega * CURRENT_TIME;
    begin_f_loop (f, tf)
    {
        f_node_loop (f, tf, n)
        {
            node_p = F_NODE (f, tf, n);
            /* Update the current node only if it has not been previously visited: */
            if (NODE_POS_NEED_UPDATE (node_p))
            {
                /* Set flag to indicate that the current node's position has */
                /* been updated, so that it will not be updated during a future */
                /* pass through the loop: */
                NODE_POS_UPDATED (node_p);
                y = NODE_Y (node_p);
                x = amp*sin(alpha)* ((1-((y-L)/L)*((y-L)/L))* (1-((y-L)/L)*((y-L)/L)));
                NODE_X (node_p) = x;
            }
        }
    }
    end_f_loop (f, tf);
}
```

References

- Bechert DW, Meye R, Hage W (2000) Drag reduction of airfoils with miniflaps. can we learn from dragonflies? In: Fluids 2000 conference and exhibit, Denver, CO, June 19–22, AIAA 2000–2315
- Casalino D, Diozzi F, Sannino R, Paonessa A (2008) Aircraft noise reduction technologies: a bibliographic review. *Aerosp Sci Technol* 12:1–17
- Fugal SR, Smith BL, Spall RE (2005) Displacement amplitude scaling of a twodimensional synthetic jet. *Phys Fluids* 17:045103
- Gallas Q, Holman R, Nishida T, Carroll B, Sheplak M, Cattafesta L (2003) Lumped element modeling of piezoelectric-driven synthetic jet actuators. *AIAA J* 41(2):240–247
- Gul M, Uzol O, Akmandor IS (2014) An experimental study on active flow control using synthetic jet actuators over S809 Airfoil. *J Phys Conf Ser* 524:01210
- Lee CY, Goldstein DB (2002) Two-dimensional synthetic jet simulation. *AIAA J* 40:510
- Mallinson SG, Reizes JA, Hong G (2001) An experimental and numerical study of synthetic jet flow. *Aeronaut J* 105:41
- Menter FR (1994) Two-equation eddy-viscosity turbulence models for engineering applications. *AIAA J* 32(8):1598–1605
- Shan H, Jiang L, Liu C et al (2008) Numerical study of passive and active flow separation control over a NACA0012 airfoil. *Comput Fluids* 37(8):975–992
- Yen J, Ahmed NA (2013) Enhancing vertical axis wind turbine by dynamic stall control using synthetic jets. *J Wind Eng Ind Aerodyn* 114:12–17

Chapter 12

Introduction to the Synthetic Jet Flow Control and Drag Reduction Techniques

Milan Matejka

12.1 Introduction

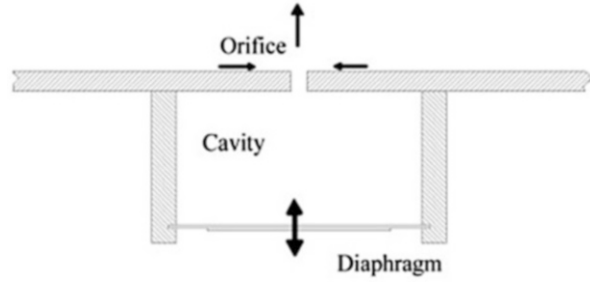
Synthetic jet—alternating blowing and suction—is a well-known shear layer active flow control technique. By means of the synthetic jet, it is possible to lower drag, to increase lift, or to intensify heat transfer in a wide range of different applications like airplanes, cars, compressors, turbines, etc. One of the first who showed that turbulent boundary layer separation can be controlled by alternating blowing and suction was Seifert et al. (1993). Chen et al. (1999) focused on the increase of mixing to intensify heat transfer, and Smith and Glezer (2002) demonstrated the possibility to use synthetic jet for jet vectoring. An important advantage of the synthetic jet, comparing to a conventional blowing or suction, is a significantly lower value of the supplied momentum needed for the same effect (Seifert et al. 1993).

The efficiency of the flow control by means of a synthetic jet depends on a correct design of the synthetic jet generator which influences creation of vortex structures. The design of the synthetic jet generator must be made in relation to the character of the flow field. The frequency of the synthetic jet should correspond to the natural vortex shedding frequency to influence separation or mixing process in the right way. This can be described like a change of the rate of vortex structures splicing. Several approaches can be used to influence the rate of vortex's structures splicing by the synthetic jet. The first case is when the exciting frequency of the synthetic jet corresponds to the natural vortex shedding frequency. Another possibility is the application of high-frequency synthetic jet with amplitude modulation (Matejka et al. 2009, 2011). Amplitude modulation is used to generate lower frequencies, which agrees with the natural vortex shedding frequency. Many authors used

M. Matejka (✉)

Researcher, Czech Technical University in Prague (CTU), Faculty of Mechanical Engineering (FME), Technická 4, 166 07, Prague, Czech Republic
e-mail: milanmatejka@hotmail.com

Fig. 12.1 The synthetic jet generator



exciting frequency of the synthetic jet much higher comparing to frequency of the natural vortex shedding frequency. This case was explained by Dandois et al. (2007).

The synthetic jet is creating vortex structures. These vortex structures originate from the interaction of the boundary layer (main flow) with pulsating stream from output orifice of the synthetic jet generator (see Fig. 12.1). The flow control should be done with minimum input power, so the synthetic jet generator should be operated on its resonant frequency. In case of resonant frequency, the velocity of the synthetic jet is maximized. Preliminary design of the synthetic jet generator can be done using lumped element modeling (LEM) (Gallas et al. 2002). LEM is based on analogy between electrical and acoustic domain, which corresponds to the synthetic jet actuator. The main assumption of LEM is that the characteristic length scales of the governing physical phenomena are larger than the geometric dimension. In this case, the acoustic wavelength must be significantly greater than the size of the synthetic jet generator.

12.2 Frequency and Intensity of the Synthetic Jet

Generally, the reason of drag reduction is in creation of vortex structures (transversal or longitudinal vortexes) which influence the character of the flow (boundary layer).

Effective application of the synthetic jet in the flow field without shock waves is formation of transversal vortex structures (Fig. 12.2). Creation of these structures must have corresponding frequency and size to influence the flow field in positive way—reducing of drag.

On the other hand, effective application of the synthetic jet in high-speed flow (with shock waves) is creation of longitudinal vortexes (Fig. 12.3). This is because creations of transversal vortexes occur arising of new shock waves, which negatively influence the flow field. Longitudinal vortexes significantly reduce the separation caused by shock wave and reduced value of drag coefficient. Interaction of high-frequency synthetic jet (which frequency is significantly higher than shedding frequency of free stream) with boundary layer is similar to interaction of continuous jet with boundary layer. Both synthetic and continuous jets can be used to generate longitudinal vortex structures. In publication (Doerffer et al. 2010), authors show

Fig. 12.2 LES simulation, synthetic jet actuation—transversal vortex (Dandois et al. 2007)

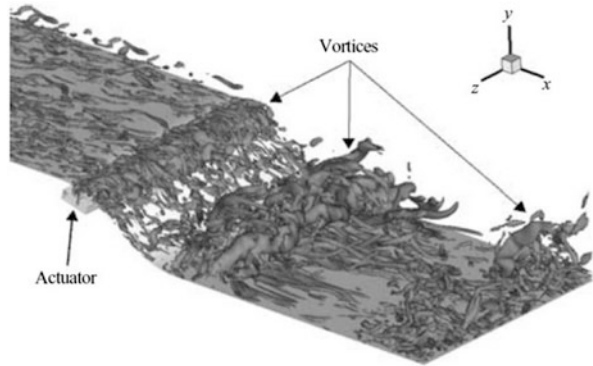
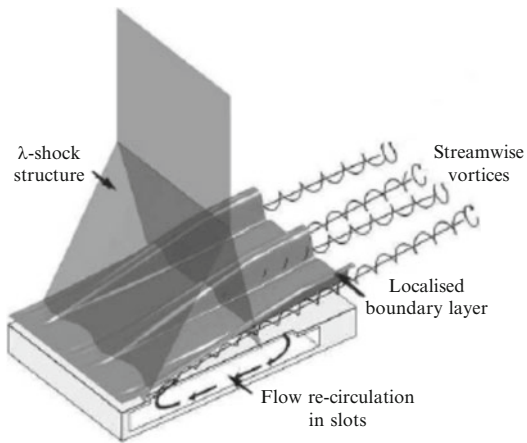


Fig. 12.3 Normal shock interaction controlled by 3D devices, creation of longitudinal vortex structures (Babinsky and Ogawa 2008)



in flow field with shock wave generation of longitudinal vortex structures using continuous jet. An important variable is the inclination of the jet to the surface and to the main flow field.

12.2.1 Frequency and Intensity of the Synthetic Jet

The efficiency of the flow control under influence of the synthetic jet strongly depends particularly on two variables. The first variable is the exciting frequency of the synthetic jet f , which should correspond to the vortex shedding frequency of the flow. Vortex shedding frequency of the flow can be measured or can be roughly calculated from nondimensional frequency F^+ :

$$F^+ = \frac{f \times X_{te}}{U_\infty} \quad (12.1)$$

Optional value of nondimensional frequency F^+ can be set at value of 1.2 (Greenblatt et al. 2005). This optimal value is also connected with the intensity of the synthetic jet, which is defined by unsteady momentum coefficient c_μ . The value of the momentum coefficient c_μ influences the intensity of the synthetic jet as well:

$$c_\mu = \frac{\rho_o \times u_o'^2 \times h}{1/2 \times \rho_\infty \times U_\infty^2 \times l} \quad (12.2)$$

where u_o' is mean velocity (in meaning of time and spatially) in output orifice of synthetic jet generator,

$$u_o' = \frac{\sqrt{\int_0^h \bar{u}_o(y)^2 dy}}{h} \quad (12.3)$$

and time mean velocity (positive part of period T)

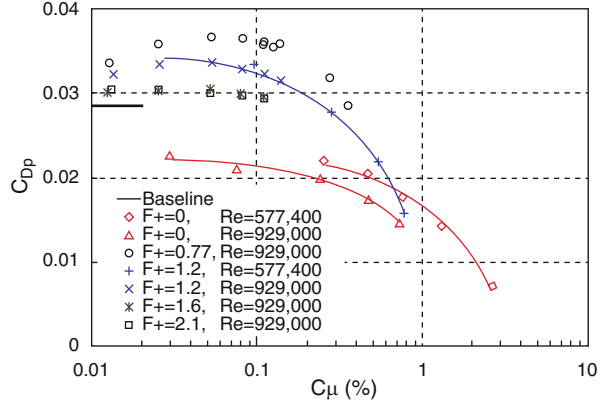
$$\bar{u}_o = \frac{2}{T} \times \int_0^{\frac{T}{2}} u_o(t) \times dt = \dots = \frac{1}{T} U_{\max} \int_0^{T/2} \sin(\omega t_s) dt_s = \frac{U_{\max}}{\pi} \quad (12.4)$$

Frequency f of the synthetic jet can be expressed from Eq. (12.1). Value of X_{te} is the distance from output orifice of the synthetic jet position to the point of reattachment—mixing length. High-output velocity of the synthetic jet can cause negative effects to the flow field, so the maximum output velocity from the synthetic jet generator should be comparable to the mean flow velocity or lower. Now, size of output orifice h from Eq. (12.2) can be calculated. Minimal value of momentum coefficient c_μ is associated with the frequency f of the synthetic jet. Optimal value of nondimensional frequency F^+ in many cases matches to the value about 1.2 (Greenblatt et al. 2005; Smith and Glezer 2002). Then minimal value of momentum coefficient c_μ corresponding to this optimal value of nondimensional frequency F^+ is about 0.2% (Greenblatt et al. 2005; see Fig. 12.4).

12.2.2 Criteria of Existence of the Synthetic Jet

The next important point is to check if the synthetic jet, defined above, fulfills criteria of existence of the synthetic jet (Trávníček et al. 2012; Holman et al. 2005; Timchenko et al. 2004). Criteria of existence of the synthetic jet is defined by nondimensional numbers: Strouhal number of output orifice of the synthetic jet generator Sh_o (12.5), Reynolds number of output orifice of the synthetic jet generator Re_o (12.6), and Stokes number of output orifice of the synthetic jet generator St_o (12.7).

Fig. 12.4 The dependence of drag coefficient C_D on the value of momentum coefficient c_μ and nondimensional frequency F^+ (Greenblatt et al. 2005)



$$Sh_o = \frac{f \times D}{\bar{u}_o} = \frac{D}{T \times \bar{u}_o} = \frac{D}{L_o} = \frac{2 \times f \times D}{\bar{U}} = \frac{Sh_H}{\pi} \quad (12.5)$$

$$Re_o = \frac{\bar{u}_o \times D}{\nu} = \frac{Re_H}{2} = \frac{Re_{\max}}{\pi} = \frac{Re_L}{L_o} \times D \quad (12.6)$$

$$St_H = \sqrt{Sh_H \times Re_H} \quad (12.7)$$

Figure 12.5 shows the area of existence of the synthetic jet. Value of Strouhal number of output orifice Sh_o must be smaller than about 2 (value of L_o/D must be greater than 0.5), and Reynolds number Re_H must be greater than about 50. Stokes number St influences the range of the synthetic jet (Brouckova et al. 2011) and shape of velocity profile in output orifice of the synthetic jet generator (Nae 2000).

12.3 Design of the Synthetic Jet Generator

The synthetic jet generator should be designed with respect to the frequency of the synthetic jet (see previous chapter) and minimum power input of the actuator. Minimum power and maximum intensity of the synthetic jet can be obtained in resonant frequencies of the synthetic jet generator.

Preliminary design of the synthetic jet generator can be done using lumped element modeling (LEM) (Gallas et al. 2002). LEM is based on analogy between electrical and acoustic domain. Schema from Fig. 12.1 represents the synthetic jet generator converted to electrical circuit (see Fig. 12.6).

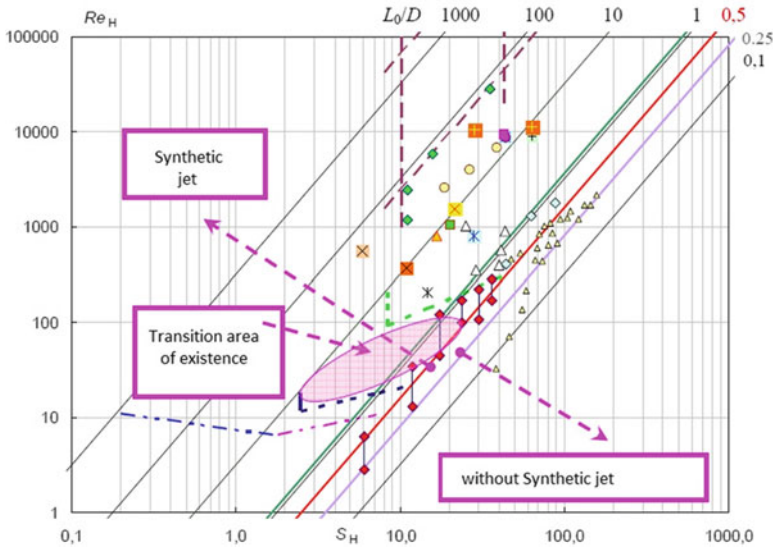


Fig. 12.5 Criteria of existence of the synthetic jet (Trávníček et al. 2012)

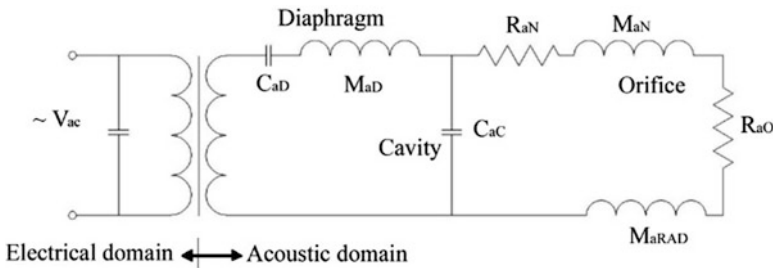


Fig. 12.6 Lumped element mode—equivalent electrical circuit

Individual parts of the synthetic jet generator components (diaphragm/membrane, cavity, and orifice) are modeled as elements of an equivalent electrical circuit using conjugate power variables. Those variables (C_{aD} , diaphragm short-circuit acoustic compliance; M_{aD} , diaphragm acoustic mass; C_{aC} , cavity acoustic compliance; M_{aN} , orifice acoustic mass; M_{aRad} , orifice acoustic radiation mass; R_{aD} , diaphragm acoustic resistance; R_{aN} , viscous orifice acoustic resistance; and R_{aO} , nonlinear orifice acoustic resistance) are expressed using electroacoustic theory (Morse and Ingard 1968; Gallas et al. 2003). Value of variables depends on geometry of generator and material properties. Impedance of electrical circuit can be calculated from abovementioned values. Impedance Z , expressed from those values, is used to calculate volume flow rate in output orifice, (12.8) and (12.9).

$$\frac{U_V}{Z} = \frac{\dot{V}}{\varphi} \quad (12.8)$$

$$da = \frac{\varphi}{C_{aD}} = \frac{\Delta V}{U_V} \quad (12.9)$$

where U_V is applied voltage, V is total flow rate, and φ is electroacoustic turns ratio. The next step is expression of flow rate volume V orifice in output orifice of the synthetic jet generator depending on exciting frequency f . All variables as flow rate in output orifice, voltage, impedance, and effective acoustic coefficient da (12.9) are functions of $s = \omega j$, where $\omega = 2\pi f$. Thereafter the related equation is

$$\frac{\dot{V}_{\text{orifice}}(s)}{U_V(s)} = \frac{da(s)}{a_4 \times s^4 + a_3 \times s^3 + a_2 \times s^2 + a_1 \times s + 1} \quad (12.10)$$

where “ a_i ” are constants determined via simple algebraic expression as a function of geometry and material properties (C_{aD} , M_{aD} , C_{aC} . . .). The output velocity can be calculated from size of area of output orifice of the synthetic jet generator and flow rate in output orifice V_{orifice} . Amplitude-frequency characteristic, dependence of velocity on exciting frequency, is shown in Fig. 12.7. One or two resonant frequencies from amplitude-frequency characteristic are obtained. Output velocity of the synthetic jet at these resonant frequencies reaches the maximum value.

Generator of the synthetic jet is suitable to use in resonant frequency, because of minimal power input comparing to power output. Then resonant frequency of the synthetic jet generator should correspond to the frequency of vortex shedding phenomena (see previous chapter). Change of dimension (size of cavity, diameter of

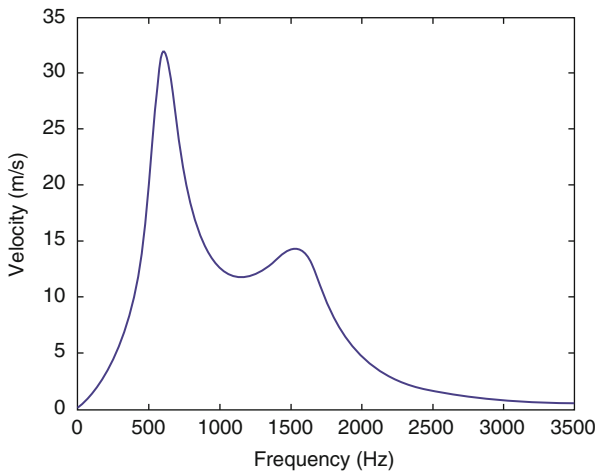


Fig. 12.7 Amplitude-frequency characteristic, dependence of velocity to exciting frequency

membrane, etc.) of the synthetic jet generator must be done, if resonant frequency of the synthetic jet generator does not correspond to the frequency of vortex shedding phenomena.

12.4 Efficiency of Flow Control

The most common goal when applying synthetic jet flow control is to minimize total losses. The energy required for application of synthetic jet needs to be included as well.

To express the local loss coefficient of total pressure can be used to formulate of the overall effectiveness of the synthetic jet control of the boundary layer, which is defined by

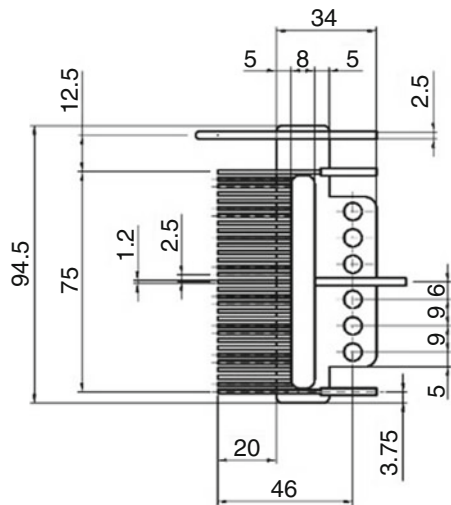
$$\xi(i) = \frac{p_{tot1} - p_{tot2}(i)}{p_{dyn1}} \tag{12.11}$$

where p_{tot1} is total pressure in cross section before the model, p_{tot2} total pressure in probe position behind the model, and p_{dyn1} is dynamic pressure in cross section before the model. Total pressure is measured by traversing total pressure probe or total pressure rake probe (Fig. 12.8).

Drag coefficient or total loss coefficient is defined as

$$c_D = \frac{2 \times F}{\rho \times A \times U_\infty} = \xi_{tot} = \frac{\sum_i \xi(i) \times A_i}{A} \tag{12.12}$$

Fig. 12.8 Total pressure rake probe



It is important to consider that the efficiency of the flow control is in relation to the power input P_{in} of the synthetic jet generator (with flow control power supply devices). Efficiency of active flow control (synthetic jet) can be derived by the efficiency of the synthetic jet η_{sj} . The specific work loss w_{loss} is calculated from the total loss coefficient and main flow velocity.

$$w_{loss} = \xi_{tot} \times \frac{1}{2} \times U_{\infty}^2 \quad (12.13)$$

The specific saved-up work w_s is derived from the difference of the total loss coefficients with and without the influence of the synthetic jet.

$$w_s = [\xi_{tot}(0) - \xi_{tot}(f)] \times \frac{1}{2} \times U_{\infty}^2 \quad (12.14)$$

Specific added work in the channel is derived as

$$w_{add} = \frac{P_{in}}{\dot{m}_{chan}} \quad (12.15)$$

where P_{in} is electric input power and \dot{m}_{chan} is mass flow rate in the channel. The efficiency of the synthetic jet η_{sj} is defined by the ratio of difference between the specific saved-up work and the added work to the specific added work. The efficiency of the synthetic jet expresses how much energy is saved in relation to the added energy. Value of efficiency of the synthetic jet can be negative.

$$\eta_{sj} = \frac{w_s - w_{add}}{w_{add}} \quad (12.16)$$

12.5 Conclusions

The development in the area of the boundary layer control brings broad possibilities in application of synthetic jet in practice. Synthetic jet application opens new options on how to design machine aerodynamics.

This chapter presented the concept of applying synthetic jets for boundary layer control. Dependencies between natural vortex shedding frequency, exciting frequency f of the synthetic jet, intensity (momentum coefficient c_{μ}) of the synthetic jet, and design of the synthetic jet generator were mentioned. Finally, the process of designing a synthetic jet generator using LEM was outlined.

References

- Babinsky H, Ogawa H (2008) SBLI control for wings and inlets. *Shock Waves* 18:89–96
- Brouckova Z, Safarik P, Travnicek Z (2011) Region of parameters of synthetic jets. *STČ, FME, CTU in Prague, Proceedings of Students Work in the Year 2010/2011*, s. 23–38
- Chen Y, Liang S, Aung K, Glezer A, Lagoda J (1999) Enhanced mixing in a simulated combustor using synthetic jet actuators. *AIAA Paper 99–0449*
- Dandois J, Garnier E, Sagaut P (2007) Numerical simulation of active separation control by a synthetic jet. *J Fluid Mech* 574:25–58
- Doerffer P, Hirsch C, Dussauge JP, Babinsky H, Barakos GN (2010) Unsteady effects of shock wave induced separation. *Notes on numerical fluid mechanics and multidisciplinary design—UFAST*, vol 114. Instytut Maszyn Przepływowych PAN, Gdańsk
- Gallas Q, Mathew J, Kaysap A, Holman R, Nishida T, Carroll B, Sheplak M, Cattafesta L (2002) Lumped element modeling of piezoelectric-driven synthetic jet actuators. *AIAA J* 2002–0125
- Gallas Q, Wang G, Papila M, Sheplak M, Cattafesta L (2003) Optimization of synthetic jet actuators. *AIAA J* 2003–0635
- Greenblatt D, Paschal BK, Yao C, Harris J (2005) A separation control CFD validation test case Part 2. Zero efflux oscillatory blowing. In: *43rd AIAA Aerospace Sciences Meeting and Exhibit*, Reno, NV 2005, *AIAA Paper 2005–0485*
- Holman R, Utturkar Y, Mittal R, Smith BL, Cattafesta L (2005) Formation criterion for synthetic jets. *AIAA J* 43(10):2110–2116
- Matejka M, Pick P, Prochazka P, Nozicka J (2009) Experimental study of influence of active methods of flow control on the flow field past cylinder. *J Flow Vis Image Process* 2009(4): 353–365
- Matejka M, Hyhlik T, Skala V (2011) Effect of synthetic jet with amplitude modulation on the flow field of hump. In: *22nd International Symposium on Transport Phenomena*. Delft, s. 31–39
- Morse MP, Ingard KU (1968) *Theoretical acoustics*. Osborne-McGraw-Hill, USA
- Nae C (2000) Unsteady flow control using synthetic jet actuator. *AIAA J*, *AIAA 2000–2403*
- Seifert A, Bachart T, Koss D, Shepshelovich M, Wagnanski I (1993) Oscillatory blowing: a tool to delay boundary layer separation. *AIAA J* 31:2052–2060
- Smith BL, Glezer A (2002) Jet vectoring using synthetic jets. *J Fluid Mech* 458:21–54
- Timchenko V, Reizes J, Leonardi E, de Vahl Davis G (2004) A criterion for the formation of micro synthetic jets. In: *ASME International Mechanical Engineering Congress and Exposition*, Anaheim, s. 197–203
- Trávníček Z, Broučková Z, Kordík J (2012) Formation criterion for synthetic jets at high Stokes numbers. *AIAA J* 50(9):2012–2017

Chapter 13

Experimental Results of Synthetic Jet Wind Tunnel Tests

Milan Matejka

13.1 Cooperation Between Czech Technical University in Prague, FME, and IMP PAN: Flow Control and Synthetic Jet Generator with Loudspeakers as Actuators

Cooperation between CTU in Prague and IMP PAN was established. Exchange of knowledge and information in the field of fluid dynamic and thermodynamics was opened. Main part of cooperation is centered to the flow control technique and technology, especially to the synthetic jet generator arrangement and synthetic jet interaction with boundary layer.

The first project was directed into the application of synthetic jet flow control on the model of bump. Experiment and numerical simulation on bump (Fig. 13.1) were carried out in cooperation with CTU in Prague, FME. These were conducted in low-speed Eiffel-type wind tunnel with 300 mm × 200 mm test section. The dimension of hump is 400 mm × 300 mm × 50 mm ($l \times w \times h$).

The design of the synthetic jet generator is based on the requirement to obtain maximum intensity of the synthetic jet with minimum input energy. Therefore, the exciting frequency of the synthetic jet generator should correspond to its resonant frequency. Two loudspeakers arranged by two in one cavity and nine cavities in one line were used with output slot in cavity. Thickness of output cavity is 1 mm and length of one cavity 20 mm. The synthetic jet actuators were excited by using amplitude-frequency modulation. Carrying frequencies $f_c = 370$ Hz is the resonant frequency of the SJ actuator, and the values of modulation frequency $f_{AM} = 60$ Hz

M. Matejka (✉)

Researcher, Czech Technical University in Prague (CTU), Faculty of Mechanical Engineering (FME), Technická 4, 166 07, Prague, Czech Republic

e-mail: milanmatejka@hotmail.com

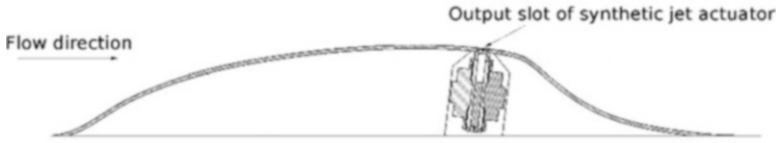


Fig. 13.1 Model—bump

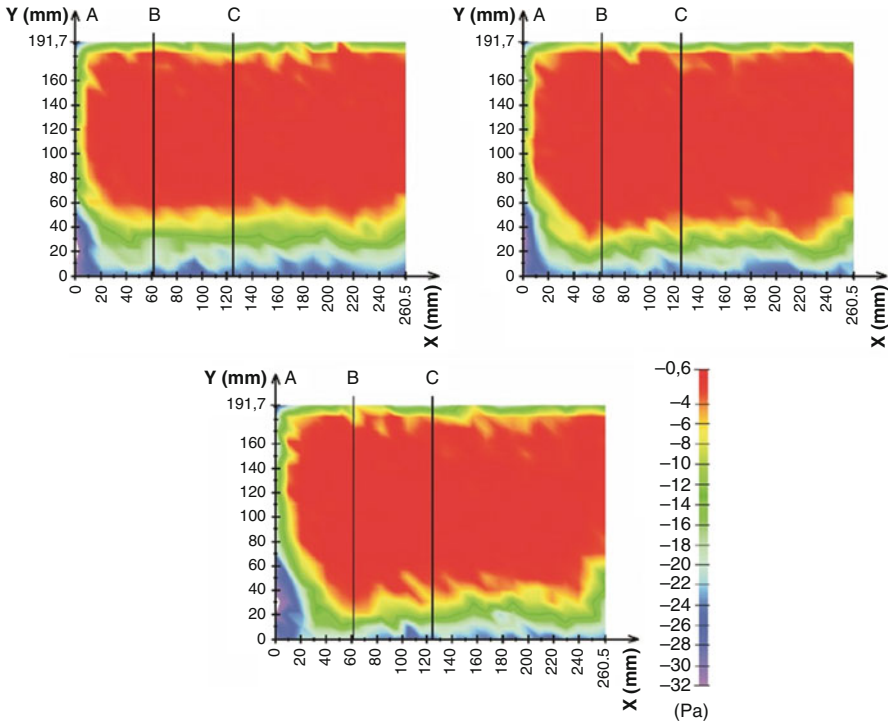


Fig. 13.2 Total pressure field (the difference to atmospheric pressure), view in the direction of the flow. From the *left*: reference conditions—no actuation, no phase shift of the synthetic jet, and phase shift of amplitude modulation of the synthetic jet

were chosen with respect to the Strouhal number F^+ (1) and oscillatory momentum coefficient c_{μ} (2). Output slot of synthetic jet actuator is perpendicular to the surface of hump, and its position is 241 mm from starting point of hump. Phase shift of consecutive actuators is possible.

In Fig. 13.2, we can see the total pressure fields in the position of 530 mm from the leading edge. In Fig. 13.3, the comparison of the total pressure distribution is shown, section (A) being 0 mm, (B) 62.5 mm, and (C) 125 mm. A positive influence of the synthetic jet on the wake size is visible in sections B and C, with the phase shift (in C) in particular. The output slot of generator of the synthetic jet starts at about 6 mm from the side of the wall; then, the effect of the synthetic jet to the flow field by the side wall cannot be visible. The visualization of the flow field with

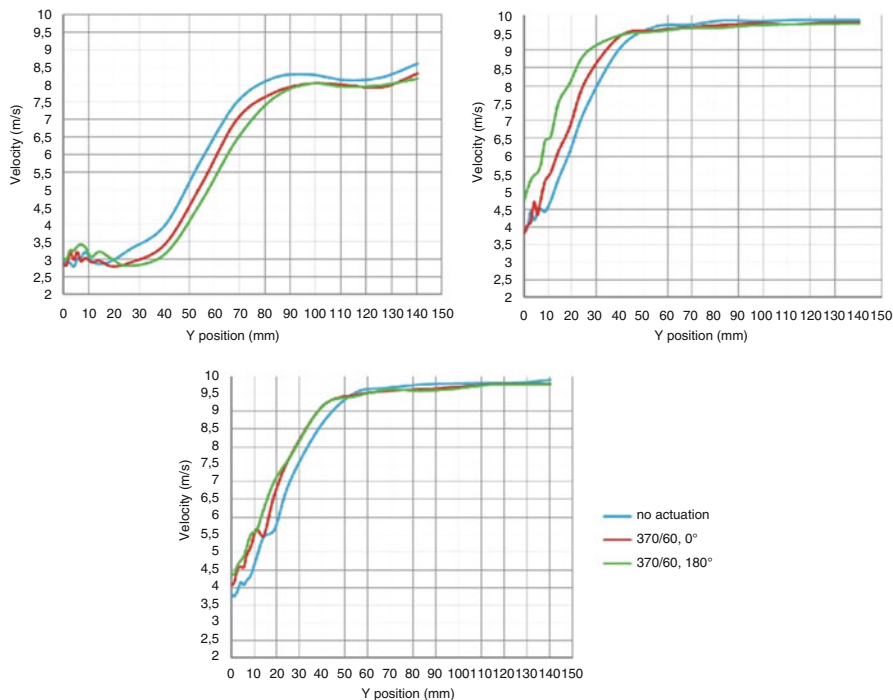


Fig. 13.3 Comparison of the total pressure distribution in sections. From the left: $X = 0$ mm (A), $X = 62.5$ mm (B), and $X = 125$ mm (C)

the influence of the synthetic jet is shown in Fig. 13.4. The size of the red (hot) area indicates a positive effect of the synthetic jet. The smaller red area corresponds to the smaller size of the recirculation area. Detailed information about numerical simulations are in the paper of Hyhlik et al. (2012).

Values of specific saved-up work w_s and efficiency of the synthetic jet η_{sj} were calculated from value of loss coefficient. From Table 13.1, it is obvious that reduction of total losses is from 16% to 31% more comparing to the value of added energy.

13.2 IMP PAN: Flow Control and Synthetic Jet Generator with Piezo-Membranes as Actuators

13.2.1 Model

Drag coefficient of the helicopter can be divided into two main parts: drag of the fuselage and drag of the rotor blades (profile and induced drag). In case of hovering

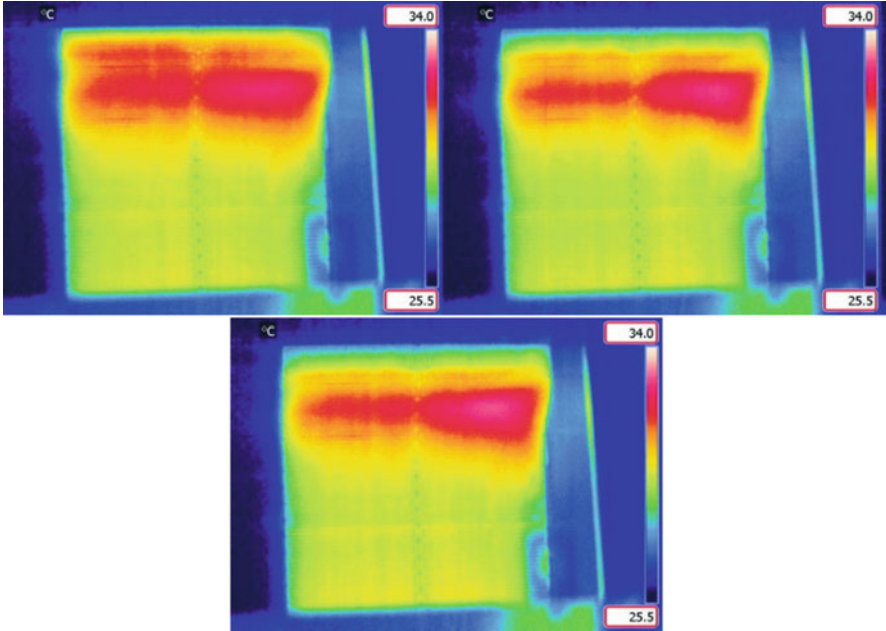


Fig. 13.4 Temperature field measured on the surface of the hump. From the *left*: no actuation, no phase shift of the synthetic jet, and phase shift of amplitude modulation of the synthetic jet

Table 13.1 Efficiency of the synthetic jet with respect to the phase shift; reduction of total losses is from 16 to 31% more comparing to the value of added energy

Exc. freq.	Phase ($^{\circ}$)	w_{add} (J/kg)	w_s (J/kg)	η_{sj} (%)
370/60	0	0.602	0.699	16.1
370/60	180	0.602	0.792	31.5

is the biggest part of drag formed due to induced drag of rotor blades and in case of forward flight it is fuselage drag. Profile drag is constant from low to mid velocities and slightly arises for high velocity. Global view to the drag of helicopter shows that more important than profile drag of rotor blade is drag of fuselage. Drag of fuselage or profile drag can be reduced by application of synthetic jet. Differences in flow control technique based on the synthetic jet exist. The explanatory of the proposal change is to investigate both longitudinal and transversal vortex structure creation by the synthetic jet at low and transonic velocities, especially techniques of longitudinal vortex structure creation using synthetic jet (Fig. 13.5).

With respect to the previous paragraph, a model with controlled boundary layer was designed in shape as half of the helicopter fuselage. The size of the model is as follows: max. high in wind tunnel 30 mm (high of model can be changed), width 80 mm, and length 90 mm. Inner part of the model is prepared for insertion of 14 synthetic jet generators in one set. Set of synthetic jet generators can be placed

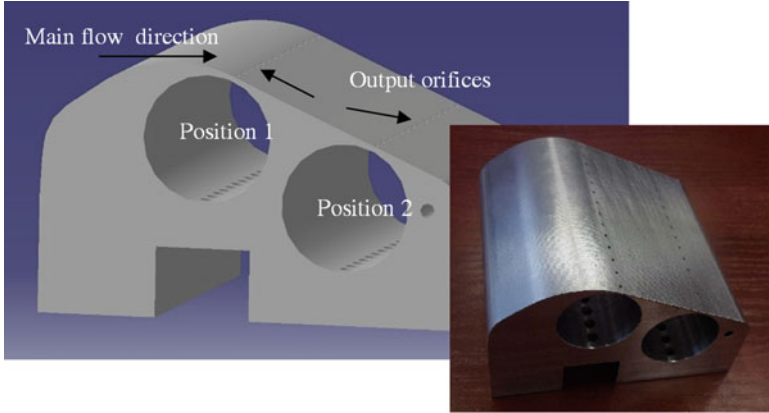


Fig. 13.5 Model with casing for the synthetic jet generator

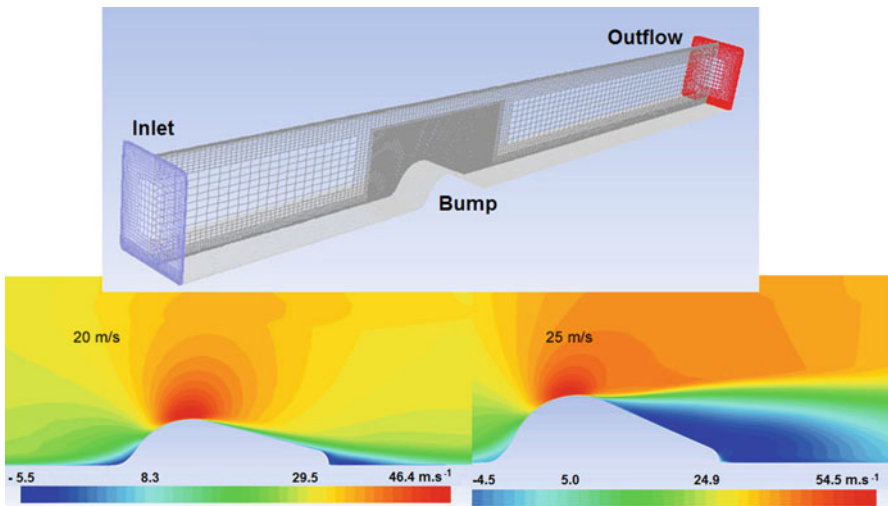


Fig. 13.6 Numerical simulation of the flow field—bump (Marcin Kurowski)

to two different positions depending on position of boundary layer separation—Position 1 or Position 2. Marked orifices are output orifices of the synthetic jet generators. Maximum high of the model can be changed by turning round the axis on the right side. Position and type of boundary layer separation can be influenced due to modification of high of the model. Shape of the model was designed with respect to the flow field using numerical simulation. Commercial software Fluent was used for numerical simulation. 3D numerical simulation and 3D model (drawing) were performed by Marcin Kurowski (Fig. 13.6.)

13.2.2 Synthetic Jet Generator

Procedure of synthetic jet generator design was introduced in Chap. 12. Design of the synthetic jet generator was prepared in coordination with model design. The synthetic jet generator was designed with respect to the character of the flow field around the model. Preliminary design of the synthetic jet generators was tested on the models of generator previously (Figs. 13.7 and 13.8). Parametric study of the synthetic jet generator with respect to the diameter of diaphragm, number of membranes in one cavity, size of cavity, and number of orifices was done. These values were used for validation of LEM to design a set of the synthetic jet generators. Dependency of piezo-membrane deflections on excitation frequency and piezo material characteristics were measured by Rūta Rimašauskienė (Fig. 13.9).

Set of the synthetic jet generator was designed as a cylinder with 14 generators. The orifices were used as an output part of the generator to have a possibility to create both, crosswise vortexes and lengthwise vortexes. Each of the generators is designed as a cavity (high of the cavity is 1.5 mm) with one output orifice (diameter 1 mm) and with one piezo-membrane (diameter of the membrane is 27 mm); see Fig. 13.10. Each of the generators can be excited independently.

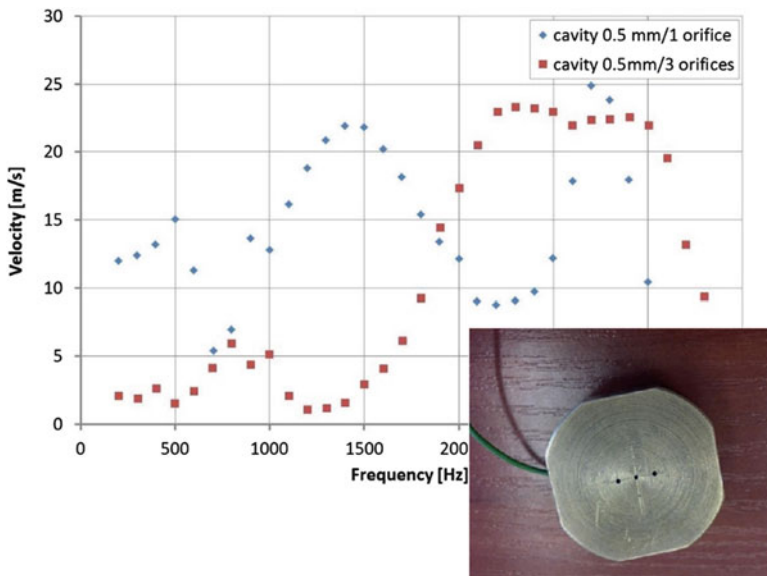


Fig. 13.7 Models of the synthetic jet generator and their amplitude-frequency characteristics

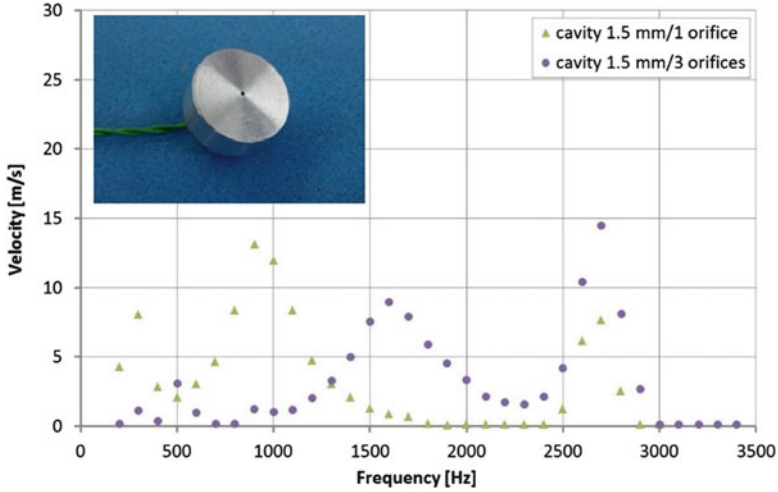


Fig. 13.8 Models of the synthetic jet generator and their amplitude-frequency characteristics

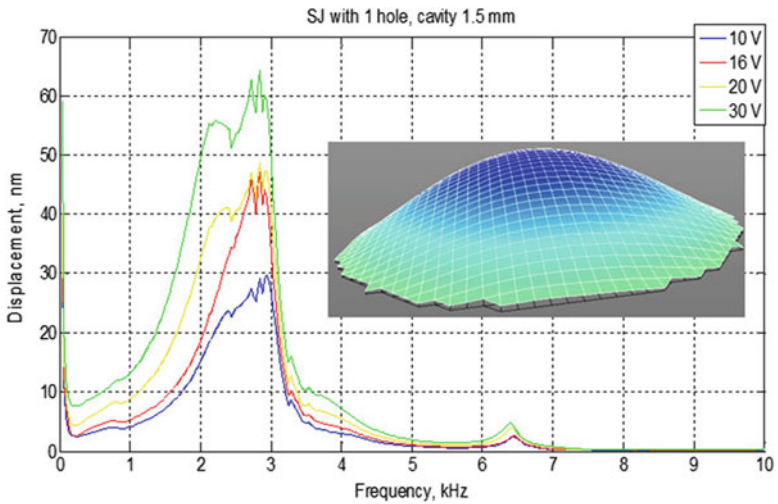


Fig. 13.9 Dependency of piezo-membrane deflections on excitation frequency (Rūta Rimašauskienė)

13.2.3 Wind Tunnel

New “Eiffel-type” wind tunnel was designed with test section in dimension 90×80×300 mm. Maximum velocity in the wind tunnel is about 40 m s⁻¹. Test section was built from plexiglass to allow using of different measurement techniques such as smoke flow field visualization, CTA measurements (hot-wire anemometer),

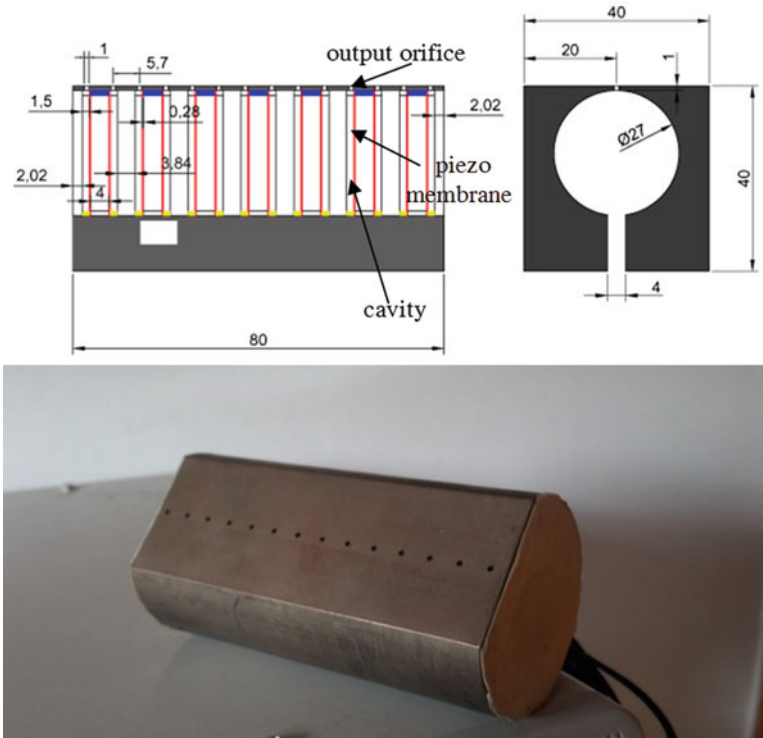


Fig. 13.10 Design of 14 synthetic jet generators in one set, one membrane in one cavity, one output orifice in one cavity

and pressure measurement. Inlet part of the wind tunnel was made from two blocks of aluminum in special shapes to reduce separation and vortex structures in the inlet of measurement test section. New radial fan (KLIMAWENT: WP-8-E, 1.5 kW, nom. 2800 rpm) was used as drive unit of the wind tunnel. Fan was placed at output part of the test section to suck the air out (Fig. 13.11). This arrangement together with proper shape of inlet part of wind tunnel allows to obtain lower value of intensity of turbulence which is needed. Fun was driven using controller with the possibility to change the revolution of the fan linearly. Characteristic of the fan is shown below.

From the first sets of velocity measurements and flow field visualizations, huge pulsation of the flow was detected. This was due to shape of inlet part of the wind tunnel and wrong setting of fan controller unit. Installation of screen into the inlet part of wind tunnel the test section or at the end of test section stabilizes the flow.

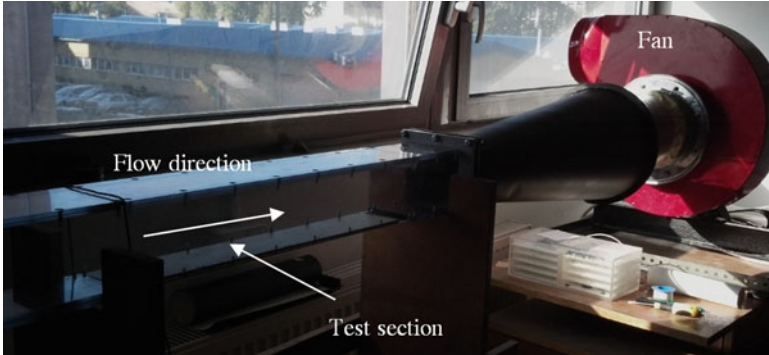


Fig. 13.11 Wind tunnel arrangement

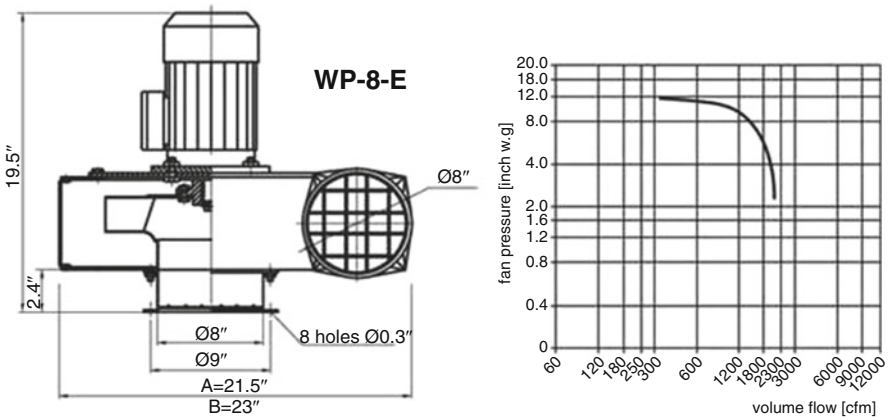


Fig. 13.12 Fan (WP-8-E) dimensions and characteristics

13.2.4 Measurement Techniques

Sets of measurement techniques are arranged to obtain total view to the flow field. All the measurement techniques can be used for different measurement conditions mentioned in special paragraph lower (Figs. 13.12, 13.13, 13.14, 13.15, 13.16, 13.17, 13.18, 13.19, 13.20, 13.21, and 13.22).

Measurement techniques:

- Smoke flow field visualization to obtain total view of the flow field, especially size and character of wake behind the bump with respect to frequency of the synthetic jet. *Equipment:* smoke generator—DANTEC.
- CTA measurements (hot-wire anemometer) were used to obtain output velocity of the synthetic jet generators, flow field velocity, and spectral density of the flow in specific points of wake (specific point of wake—about five points in

Fig. 13.13 Fan controller**Fig. 13.14** Smoke generator—DANTEC

the boundary between main flow and mixing area). Natural vortex shedding frequencies are visible from spectral density. This is needed to define (to compare) excitation frequency of the synthetic jet. These measurements must be done without influence of the synthetic jet. *Equipment: Mini CTA 54T30 DANTEC, StreamLine 90N10 Frame, CTA probe DANTEC, and cables.*

- Pressure measurement is divided into two parts: static pressure measurements and total pressure measurements. The first part is pressure measurements using static pressures in taps, which are situated on the bottom wall behind the bump. Distribution of static pressure on the bottom wall precisely describes size/shape of wake. Second part is total pressure measurements using traversing total pressure probe or total pressure rake probe. From the difference of total pressure before and behind the bump, loss coefficient can be calculated. Energy balance can be determined from the values of loss coefficients and electrical input power. *Equipment: NetScanner System 9116, max. pressure difference 2.5 kPa, max. rate 500 Hz, 16 pressure inputs, 24 V, and interface 802.3 Ethernet*



Fig. 13.15 MiniCTA 54T30 DANTEC, StreamLine 90N10 Frame, and CTA probe DANTEC

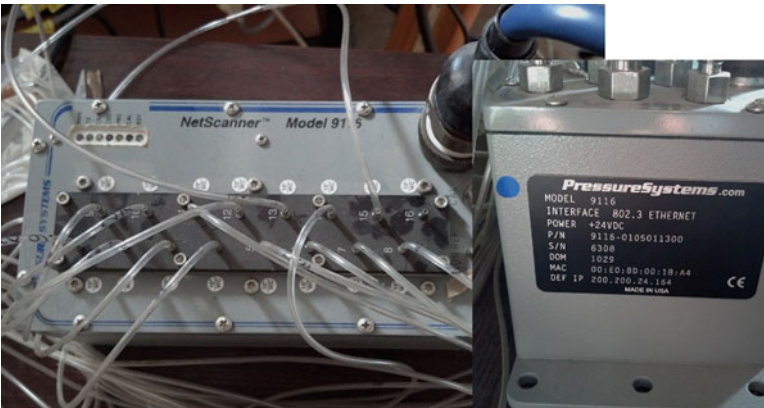


Fig. 13.16 NetScanner System 9116

13.2.5 Software Development

New homemade software were created for application of mentioned measurement techniques and for data evaluation. Software were created using LabVIEW 10 and 8.6.

User-defined miniCTA DANTEC software were created for CTA probe calibration. It can be also used for calibration of CTA probes with different equipment whose output is in voltage:

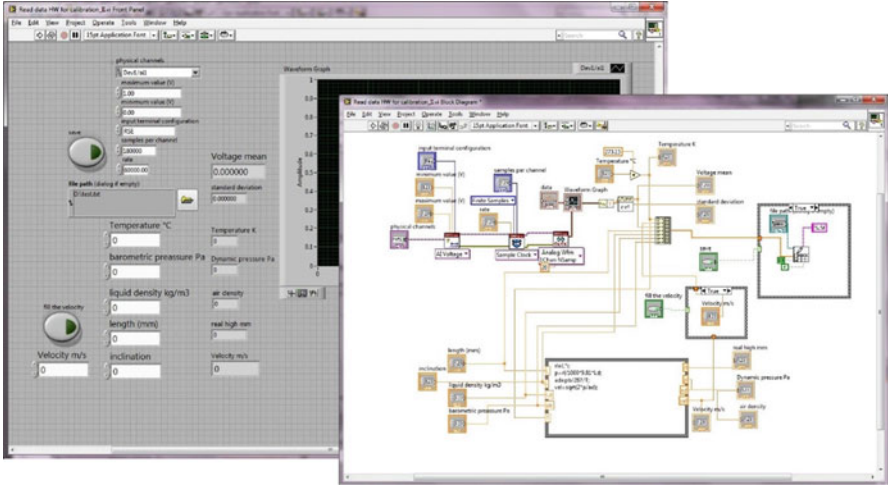


Fig. 13.17 Software for data collection from CTA probe calibration: Read data for CTA probe calibration

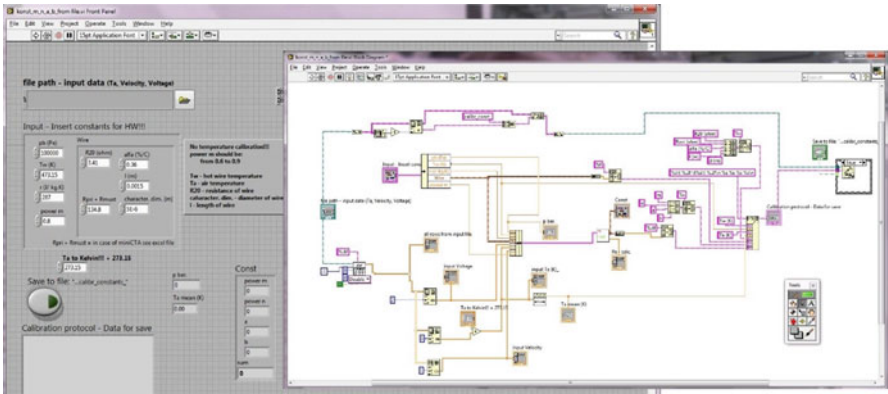


Fig. 13.18 Software for calculation of constants: Konst_m_n_a_b_from file

1. Read data for CTA probe calibration—this software is used for data collection in wind tunnel for CTA probe calibration. On right side of Fig. 13.17 is shown represents schema of the program structure in LabVIEW. On left side of the Fig. 13.17 is shown front control panel of the program. White fields must be filled:
 - (a) Physical channel—number of channel and device, channel on the connection block, and device connected into the connection block.
 - (b) Maximum input voltage—in case of miniCTA DANTEC—is 5 V.
 - (c) Minimum input voltage—in case of miniCTA DANTEC—is 0 V (for unipolar measurement cards).

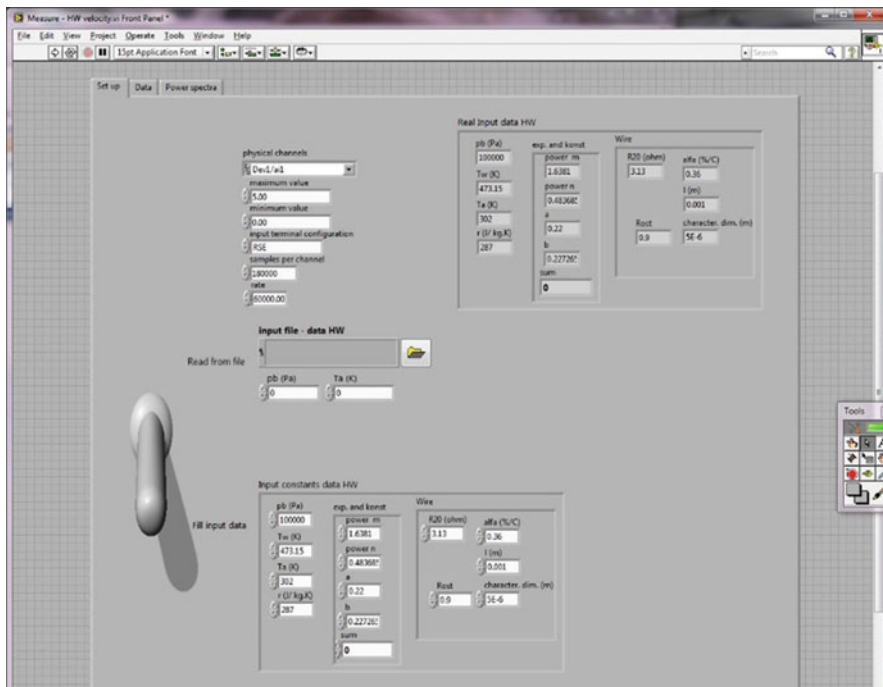


Fig. 13.19 Software for velocity measurement by CTA probe: Measure—HW velocity, Set up

- (d) Input terminal configuration—RSE (differential)—see terminal configuration of measurement card and miniCTA DANTEC.
- (e) Samples per channel and rate—rate is the frequency of data collection (min. 10 kHz), and value of sample per channel sets time of continuous measurement (e.g., rate = 10,000 Hz, samp. per. chan. = 20,000 samples; $t = 20,000/10,000 = 2$ s).
- (f) Temperature of air flows around the CTA probe.
- (g) Barometric pressure in Pa is about 100,000 Pa.
- (h) Last three white windows are values which correspond to the micromanometer, which is connected to the Prandtl probe to measure flow velocity in wind tunnel (liquid density inside the manometer (water, alcohol, etc.), length of liquid on the scale, and inclination of manometer $\frac{1}{2}$, $\frac{1}{10}$, etc.). However, the velocity can be written by keypad directly, field velocity m/s, due to push the switch (green light) “fill the velocity.”
- (i) File path and name of output file can be changed. Pressing the save switch, collected (voltage from miniCTA DANTEC) and entered actual data are written to the file.
- (j) Turn on by pressing of arrows in circle, and turn off by pressing of red dot.

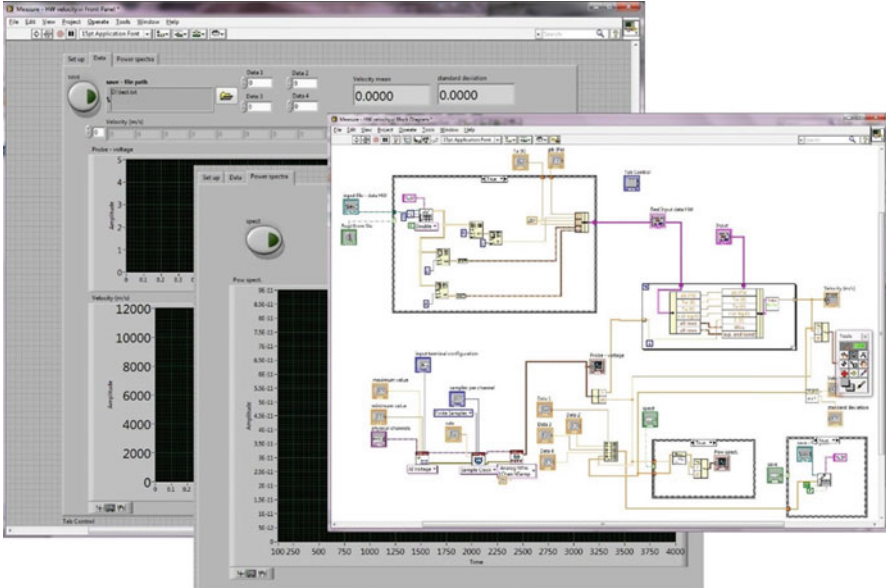


Fig. 13.20 Software for velocity measurement by CTA probe: Measure—HW velocity

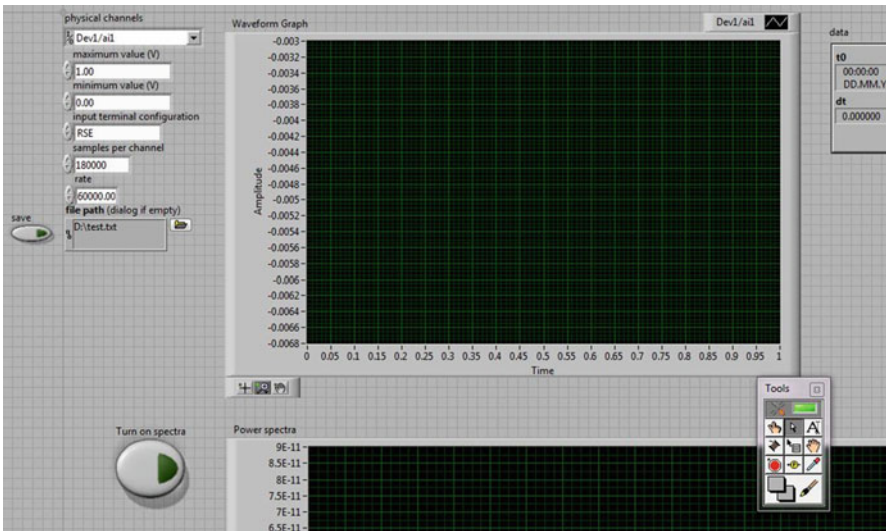


Fig. 13.21 Software for data acquisition of the analog input signal

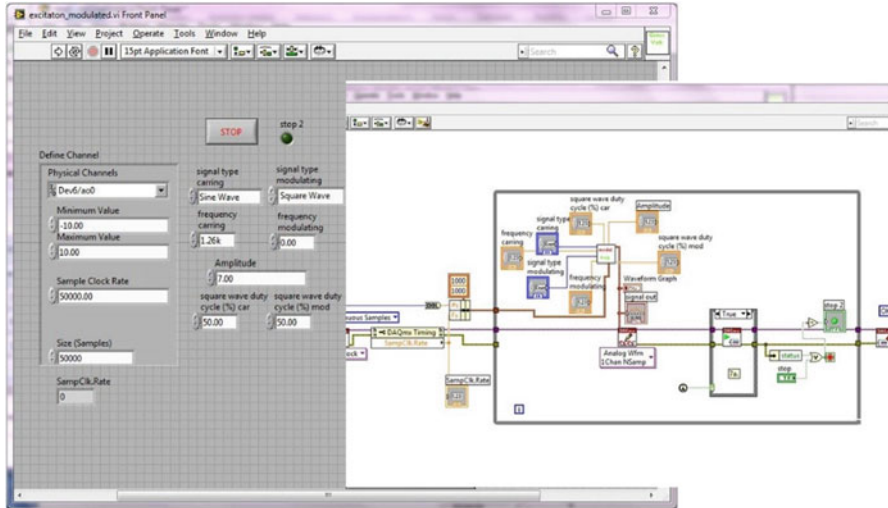


Fig. 13.22 Software for generation of synthetic jet generator excitation signal

2. Konst_m_n_a_b_from file—the next step is using calibration and King’s law (Collis-Williams formula) and data from calibration to calculate constants m , n , a , and b . From the previous step, output file (data) is used. White fields must be filled:
 - (a) File path and name of input file must be chosen.
 - (b) Barometric pressure in Pa, hot-wire temperature T_w in K, and specific heat capacitance of the air.
 - (c) Power m .
 - (d) Wire—hot-wire constants, which are usually written on the CTA probe box.
 - (e) Temperature T_a —conversion to Kelvin.
 - (f) Press the switch to save the data.
3. Measure HW velocity—software for velocity measurement using CTA probe and calibration file. Three pages are in control panel:
 - Setup—setting of hardware and input constants
 - (a) Physical channel—no. of channel and device.
 - (b) Maximum input voltage.
 - (c) Minimum input voltage.
 - (d) Terminal connection.
 - (e) Number of samples and rate.
 - (f) If the switch is up (on)—file path and name of file with calibration data (in correct data format), barometric pressure p_b in Pa, and flow temperature in K.
 - (g) If the switch is down (off)—all the data from calibration must be filled in white fields.

Data and power spectra pages—online data in graphs, switch to save the data, file path and file, and four white fields for additional data, and switch to turn on power spectra computation.

4. Other software for post-processing of data was prepared, because of change of hardware for CTA measurement (CTA—StreamLine DANTEC).
5. Spectra part I—software for data acquisition of the analog input signal (microphone, pressure transducer, etc.) was created. Power spectra of the signal can be calculated.
6. Excitation _modulated—software for generating of synthetic jet generator excitation signal, modulated carrying frequency can be used, different types of signal (sine, square, saw, etc.).

Input constants:

- (a) Define channel—physical channel (channel and device), minimum and maximum voltage value, sample clock rate in Hz, and size (number of samples in DMA memory).
- (b) Signal type—carrying and modulating frequency.
- (c) Frequency—carrying and modulating frequency.
- (d) Amplitude—carrying and modulating frequency.
- (e) Square wave duty cycle—carrying and modulating frequency.
- (f) Turn on by white arrow.
- (g) Stop by switch Stop.

All the software is uploaded on STAYWICO web pages.

13.2.6 Measurement Campaign

Three measurement techniques are used in measurement campaign:

- Flow field visualization—total view of the flow field
- CTA probe (hot-wire) measurements—frequency/power spectra of the flow
- Pressure measurement—size of wake and total loss coefficient calculation
- *Test Case 1: No*—influence of synthetic jet (SJ)
 - Velocity 20 m/s
 - *Flow field visualization*: total view of the flow field close to model and determination of position and type of boundary layer separation with respect to the velocity (20 m/s) and high of the model ($H = 15, 22, \text{ and } 30 \text{ mm}$)
 - *CTA measurement*: frequency/power spectra of the flow in the boundary between main flow and mixing area—min. three points from separation to reattachment point ($H = 15, 22, \text{ and } 30 \text{ mm}$)
 - *Pressure measurement*: static pressure measurement—determination of mixing size (length) area ($H = 15, 22, \text{ and } 30 \text{ mm}$)

Table 13.2 Excitation frequencies of the synthetic jet generator—transversal vortices

	F^+	1.2	
	Velocity (m/s)	20	
Model high (mm)	X_{te} (m)	$f_{excit.20}$ (Hz)	Voltages _{SJG} (V)
30	0.21	115	30
22	0.155	155	30
15	0.105	230	25

- **Test Case 2: Yes**—influence of SJ

Velocity 20 m/s

- Transversal vortices: Excitation frequency of the SJ corresponds to maximum peak of energy from power spectra measurements from previous Test Case 1—CTA measurements. These values of excitation frequency agree with value of frequency $f_{excit.20}$ derived from nondimensional frequency F^+ (Table 13.2).

X_{te} —mixing length value is defined based on Test Case 1, pressure measurement.

Flow Field Visualization + Static Pressure Measurement

- Transversal vortices: Application of amplitude modulation—excitation frequency of SJG is resonant frequency of the SJG ($f_1 = 1000$ Hz or $f_2 = 2700$ Hz). Excitation frequency is modulated by frequencies from Table 13.2 for all three cases ($H = 15, 22, 30$ mm). Applied voltage is 16 V (25 V) for all three cases.

Flow Field Visualization + Static Pressure Measurement

- Longitudinal vortices: Excitation frequency of SJG is one of resonant frequencies of SJG ($f_1 = 1000$ Hz or $f_2 = 2700$ Hz). Two measurements in this configuration for all three configurations ($H = 15, 22, 30$ mm):

All actuators are ON.

Every second actuator is OFF.

Flow Field Visualization + Static Pressure Measurement

- **Test Case 3: Both**—total pressure measurement for loss coefficient calculation:

- **No**—influence of the synthetic jet for all three configurations ($H = 15, 22,$ and 30 mm)
- **Yes**—with influence of synthetic jet for all three configurations ($H = 15, 22,$ and 30 mm)

Transversal vortex structures—direct excitation

Transversal vortex structures—amplitude modulation

Longitudinal vortex structures—all actuators ON

Longitudinal vortex structure—every second actuator OFF

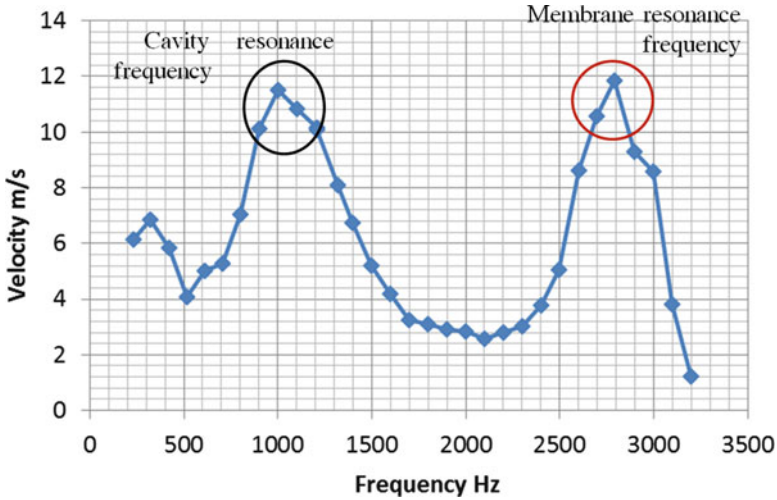


Fig. 13.23 Amplitude-frequency characteristic of the synthetic jet generator, one membrane in the cavity, voltage 16 V

13.2.7 Experimental Data

13.2.7.1 Synthetic Jet Generator

Rectangular excitation signal was used to force the piezo-membrane of the generator. All the membranes were connected parallel, which is only a possibility to actuate all together. Another possibility is separate excitation of each membrane. The amplitude-frequency characteristic of the actuator was measured using the CTA probe—miniCTA DANTEC. Figure 13.23 shows amplitude-frequency of the synthetic jet generator (generator in Position 7) with constant voltage $U = 16$ V. Maximum output velocity is about 12 m/s for both resonant frequencies (Fig. 13.23). Output velocity can be increased by increasing of voltage. Figure 13.24 demonstrates the dependency of output velocities at resonant frequencies of the generator 1000 Hz and 2750 Hz on the applied voltage 16, 30, and 35 V. Dependence of the output velocity on the voltage is almost linear.

Figure 13.25 shows the dependence of power input of set of 14 synthetic jet generators on frequency (a) and velocity (b) output on power input. In Figure 13.25 (a), two peaks are visible (elliptic marks), which are close to the resonant frequencies (Fig. 13.26).

The value of capacitance of the piezo-membranes is very important (without change of dimension of the piezo-membrane). The change of the capacitance influences the membrane resonant frequency. In other words, change of capacitance causes the shift of the piezo-membrane resonant frequency of (change of amplitude-frequency characteristic) neighboring generators (huge change of output velocity).

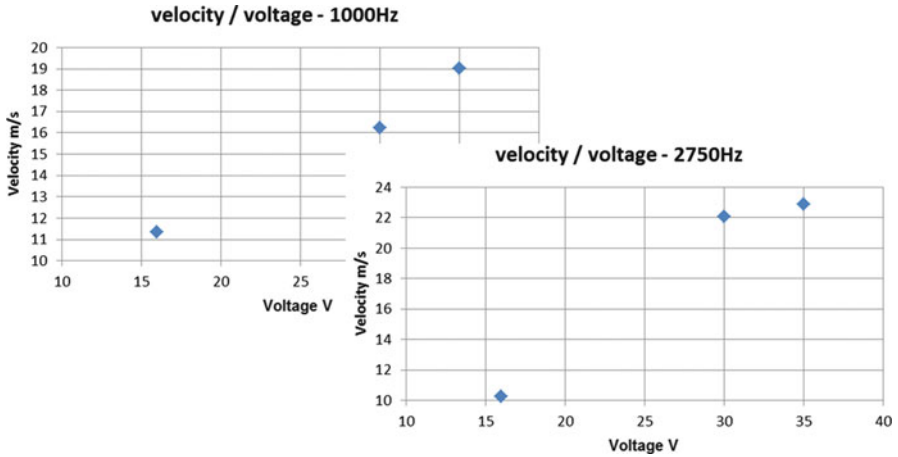


Fig. 13.24 Dependence of output velocity on voltage for resonance excitation frequencies 1000 and 2750 Hz

Two of lateral generators were modified to have a possibility to use two membranes in one cavity. This arrangement allows increasing of the output velocity. Amplitude-frequency of the synthetic jet generator with two membranes and input voltage $U = 16$ V is shown in Fig. 13.27. Figure 13.28 shows the dependence of the output velocity at resonant frequencies 800 Hz and 2450 Hz on applied voltage—16 V and 30 V. Maximum output velocity is about 45 m/s. Output velocity is more than three times higher compared with the generator with one membrane. Because of the membrane resonant frequency change, I suppose that the (SJ) generator was not tightened enough. This effect is also visible on change of output velocity (instability) at lower frequencies. In case of two membranes in one cavity, the effect of different capacitance of the piezo-membrane is also negative—lower output velocity.

In case of the excitation, frequency is lower or similar to the Helmholtz resonant frequency (the resonant frequency of the cavity), and the change of value of output velocity is less than 1 m/s (see Fig. 13.28). Change of velocity is caused especially of different positions of CTA probe due to the location of output orifice.

The amplitude-frequency characteristic, maxim output velocity, strongly depends on precise arrangement of the cavity/generator and capacitance of the piezo-membrane. Capacitance of piezo-membranes in the sets of SJ generators must be the same; otherwise it caused change of resonant frequency of the membrane and change of output velocity for each synthetic jet generator. Another possibility is separate excitation of each membrane.

Value of measured velocities is slightly lower comparing to the real velocity, because CTA probe (length of wire is about 1.2 mm) size is bigger than size of output orifice (jet).

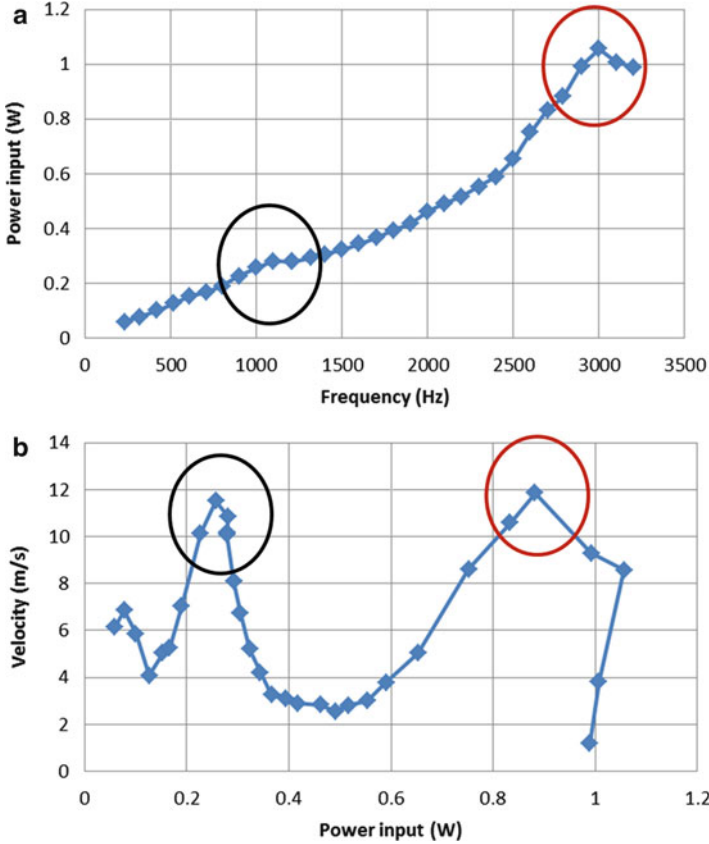


Fig. 13.25 (a) The dependence of power input (constant voltage) on excitation frequency and (b) the dependence of velocity on power input (constant voltage), power input for a set of 14 synthetic jet generators

Fig. 13.26 Amplitude-frequency characteristic of the synthetic jet generator—two membranes in cavity, voltage 16 V

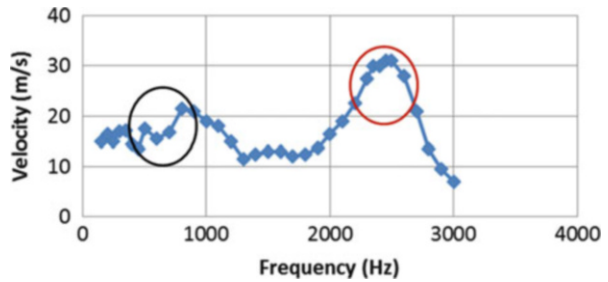


Fig. 13.27 Change of the velocity output at resonant frequencies 800 and 2450 Hz for the synthetic jet generator with two membranes in one cavity

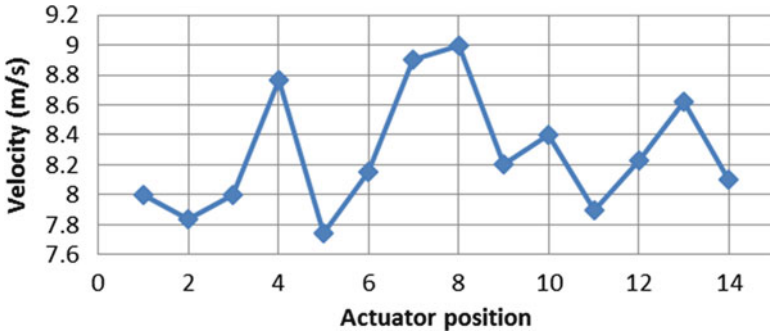
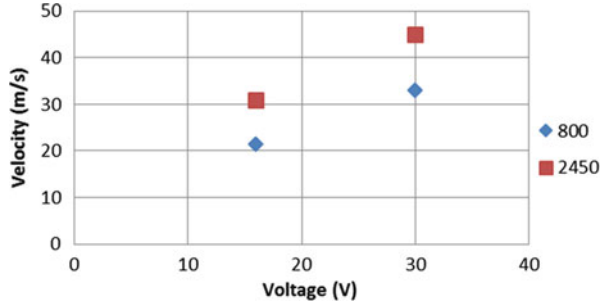


Fig. 13.28 Time-mean output velocities of the actuators for excitation frequency 200 Hz

Table 13.3 Efficiency of energy conversion of one synthetic jet generator from set, upper table two membranes in cavity and lower table one membrane in cavity, values for resonant frequencies of cavity and membrane

Two membranes in cavity					
Freq. (Hz)	Volt. (V)	P_{in} (W)	Veloc. _{out} (m/s)	P_{out} (mW)	P_{out}/P_{in} (%)
800	16	0.0375	21.5	4.7	12.53
800	30	0.225	33	16.9	7.511
2450	16	0.125	31	14	11.2
2450	30	0.525	45	42.9	8.17
One membrane in cavity					
Freq. (Hz)	Volt. (V)	P_{in} (W)	Veloc. _{out} (m/s)	P_{out} (mW)	P_{out}/P_{in} (%)
1000	16	0.0184	11.5	0.7	3.80
1000	30	0.0557	16.2	2	3.59
1000	35	0.0764	19	3.2	4.18
2750	16	0.0621	11.5	0.7	1.12
2750	30	0.2678	22	5	1.86

The efficiency of energy conversion of the synthetic jet generator with piezo-membrane is from 1 to 4% for one membrane in one cavity and from 7 to 12% for two membranes in one cavity (see Table 13.3).

To minimize power input of the synthetic jet generator and maximize intensity of synthetic jet, optimization lower resonant frequency as the first (highest) peak is recommended. This optimization lower resonant frequency must be done with respect to the flow control design procedure and value of nondimensional frequency F^+ , or amplitude modulation must be used (Matejka et al. 2009).

13.2.7.2 Wind Tunnel Measurements

From flow field visualization and pressure measurements (using Prandtl probe), huge pulsation of the flow was detected. Pulsation of velocity for time-mean velocity 20 m/s was about 8 m/s. Elimination of pulsation was minimized insertion of fine grid in output of test section.

In spite of small fluctuation of the mean flow, pressure measurement, hot-wire anemometry (CTA), and smoke field visualization were done to see the influence of the synthetic jet. Application of the synthetic jet fluctuations did not disappear, but positive changes in size of separation area were visible.

Frequency spectra of the main flow with and without influence of the synthetic jet are shown in Fig. 13.29; (a) no SJ influence, no dominant frequency is visible; (b) SJG on—excitation frequency, carrying 1000 Hz and modulation 200 Hz, 25 V (amplitude modulation)—the first peak represents actuation frequency; and (c)

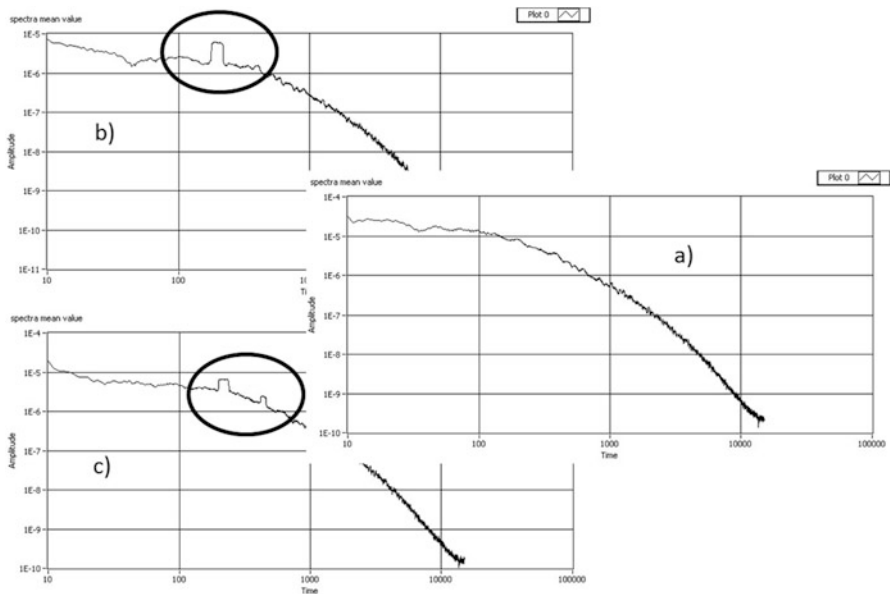


Fig. 13.29 Frequency spectra of the flow field: (a) no SJ influence, (b) SJG on (excitation frequency 200/1000 Hz, 25 V) and (c) SJG on—excitation frequency 200 Hz, 25 V; CTA measurement

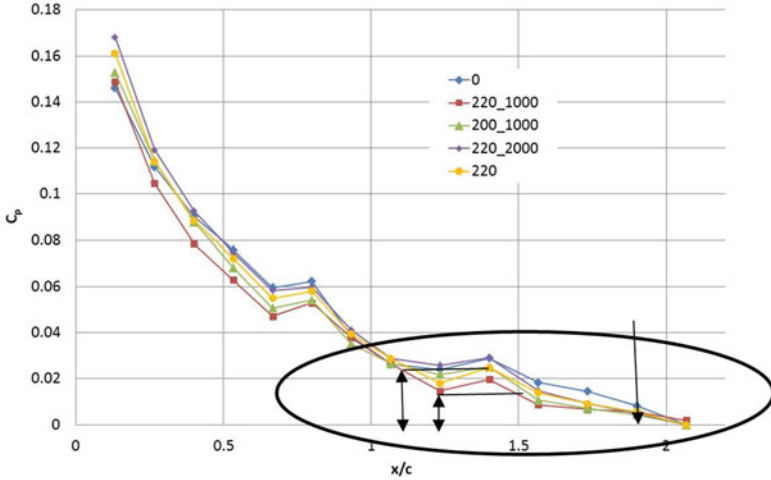


Fig. 13.30 Pressure distribution— C_p —with respect to the excitation frequency

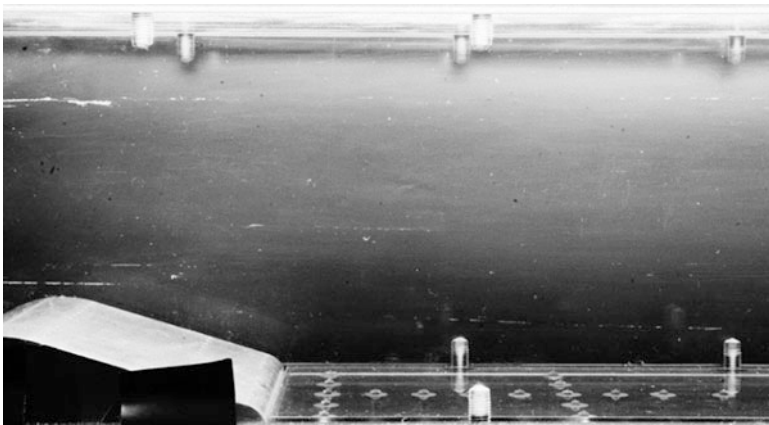


Fig. 13.31 No influence of synthetic jet

SJG on (excitation frequency 200 Hz, 25 V), the first peak represents actuation frequency. Size of these peaks is proportional to the amount of energy in vortex structures at these frequencies.

Positive influence of the synthetic jet generator is visible from pressure distribution in Fig. 13.30. Values of pressure distribution represented by C_p are lowest for excitation frequency of 220/1000 Hz. Size of separation area is shorter (x/c) and thinner (about 30%).

Figures 13.31 and 13.32 show flow field visualization and synthetic jet influence to the flow. Separation is observed in the boundary layer. For the separated flow, the smoke is present in the entire volume of the flow except the boundary layer. In case

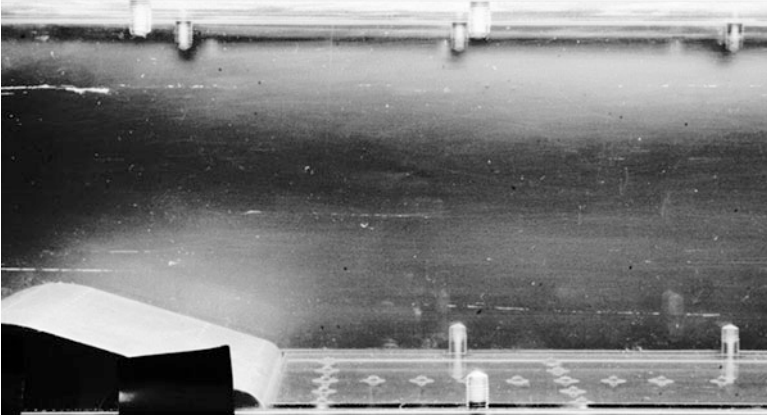


Fig. 13.32 With influence of synthetic jet—excitation frequency 200/1000 Hz, 25 V

of unseparated flow, the smoke is also present in the boundary layer. Figure 13.31, without influence of synthetic jet, clearly shows huge separation behind the bump (area without smoke). Main flow is separated and smoke goes in the direction of main flow. The second figure with influence of synthetic jet generator—excitation frequency 200/1000 Hz (amplitude modulation) and voltage 25 V—shows positive influence of the synthetic jet. Smoke is attached to the surface of the bump and lower wall of wind tunnel.

13.2.7.3 Sound Measurements

Intensity and frequency of sound of the synthetic jet generator were measured using micro piezo-microphone (type: Knowles Electronics, FG-23629-C36) (Fig. 13.33). Data from measurements were used for the simulation of synthetic jet generator influence in helicopter spectra noise annoyance (Danilo Sabbatini) (Fig. 13.34).

13.3 Conclusions

Set of synthetic jet generators in fixed configuration were designed and produced with respect to the nature of the flow field. Parametric study of the design of the synthetic jet generator was made possible with the proposed setup. Model of bump representing fuselage of helicopter was designed and produced. New wind tunnel was built. Software for measurement, data collection, and data processing were prepared and introduced. Experimental campaign on the test bench of the synthetic jet stack incorporated in the bump in wind tunnel was performed.

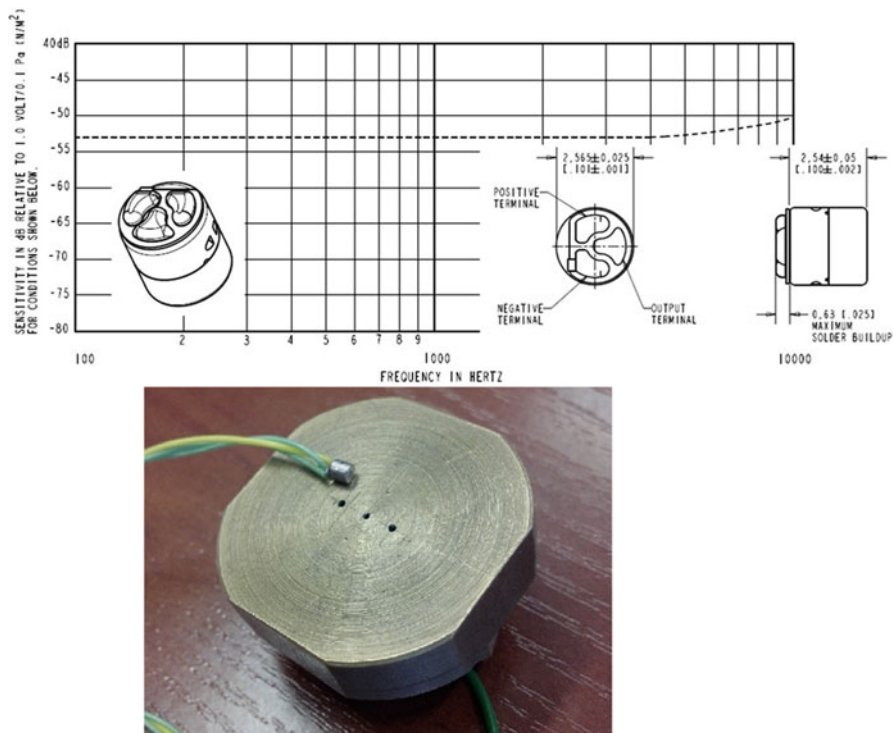


Fig. 13.33 Synthetic jet generator with microphone and microphone characteristics

From experimental data obtained, the conversion efficiency from the electric power input to the jet flow is from 2 to 12% (output velocity about 50 m/s, diameter of membrane 27 mm). Efficiency of application of synthetic jet flow control is from 15 to 30% (in case of application of lower efficiency synthetic jet generator—efficiency less than 2%). This means that using synthetic jet can be obtained saving about 30% more energy than was used for the synthetic jet actuation. When all the electronic equipment is included, value reaches about 20%. Experimental data was obtained in incompressible flow condition—transversal vortices were used to control boundary layer. In case of compressible flow, the efficiency of flow control will be lower. My estimation is about 5–7%.

Application of flow control technique on helicopter (fuselage or rotor blade) includes also mass of the devices (generators, electronic, etc.). My estimation is that total mass of all the device (device optimized and designed for application on helicopter) can be less than 15 kg for both, flow control on the fuselage and on rotor blade.

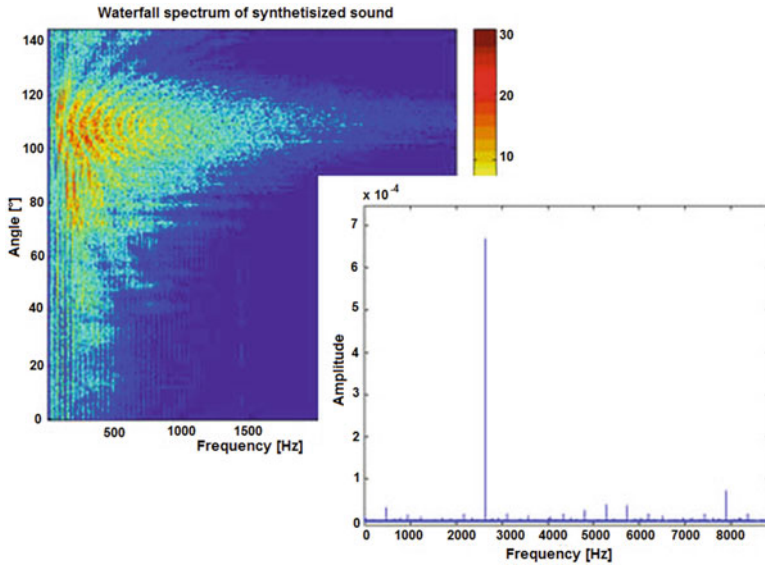


Fig. 13.34 Simulation of synthetic jet generator influence in helicopter spectra noise (Danilo Sabbatini)

Table 13.4 Parameters significantly influencing the design of the synthetic jet generator

		Synthetic jet generator design										
		Input values										
		Diaphragm				Cavity				Orifice		
		<i>D</i>	<i>h</i>	Num.	Deflect.	Vol.	<i>d</i>	<i>l</i>	Num.	Volt.	Freq.	Exist. _{SJ}
Output values	Veloc. _{out}	1	2	1	2	1	1	2	2	1	1	1
	Intens. _{jet}	1	2	1	2	1	1	2	1	1	1	1
	Freq. _{res.}	1	1	2	x	1	1	1	1	x	x	2
	Power _{in}	2	2	2	x	x	x	x	x	1	1	x

1, important; 2, less important; x, independent

13.3.1 Summary of Flow Control Parameters and Data Measurements Overview

The influence of parameters such as diameter, thickness, deflection, and number of diaphragm (piezo-membrane); cavity volume; diameter, length, and number of output orifice; voltage; and frequency and criteria existence of SJ to the output velocity, intensity of jet, resonance frequency, and power input is shown in Table 13.4.

Table 13.5 shows variants measured in parametric study of the synthetic jet generator. The most important variables are output velocity, power input, and amplitude-frequency characteristics.

Table 13.5 Measured test case configuration of the synthetic jet generators

		Input values					
		<i>D</i> _{diaph.}	No. _{of diaph.}	Vol. _{cavity}	No. _{of orif.}	Voltage	Freq.
Output values	Veloc. _{out}	YES	YES	YES	YES	YES	YES
	Power _{in}	YES	YES	YES	YES	YES	YES
	A–F char.	YES	YES	YES	YES	YES	YES
	Deflec. _{diaph.}	YES	x	YES	YES	YES	YES
	Sound _{int.}	x	x	x	x	YES	YES

Table 13.6 Parameters significantly influencing the flow control efficiency

		Flow control					
		Input values					
		Flow vel.	Char. dim.	NVSFreq.	Mix.leng.	Jet vel.	Outp. orif.
Output values	Excit. Freq	1	x	1	1	x	x
	Momen.coef	1	1	2	x	1	1
	Jet veloc.	1	x	x	x	x	1

1, important; 2, less important; x, independent

Table 13.7 Summarization of measurement campaign—interesting connection between the most important parameters

		Input values					
		Carr. F.	Modul. F.	Jet int.	Power _{in}	Model geom.	Type of vortex
Output values	Size of wake	x	x	x	x	x	x
	Flow field veloc.	x	x			x	x
	Loss coeff.	x	x	x	x	x	x
	Vortex struct.	x	x	x	x	x	x
	Efficien. of SJ	x	x	x	x	x	x

The importance of influence of flow velocity, dimension of “model,” nature vortex shedding frequency/nondimensional frequency, mixing length, jet velocity and size to output orifice to exciting frequency, momentum coefficient, and output velocity is shown in Table 13.6.

Table 13.7 summarizes the measurement campaign—mutual influence of the most important values of flow field, SJ generator, and type of vortexes such as carrying and modulation frequency, jet intensity, power input, model geometry, type of vortex (transversal × longitudinal) to the size of wake, flow field velocity, loss coefficient, vortex structure in the flow, and SJ efficiency.

References

- Hyhlík T, Matějka M, Skála V, Doerffer P (2012) Experimental and numerical investigation of separation controlled flow over hump. THMT 7, 24–27.9, Palermo, Italy, ISBN: 978-1-56700-302-4
- Matějka M, Pick P, Procházka P, Nožička J (2009) Experimental study of influence of active methods of flow control on the flow field past cylinder. Journal of Flow Visualization and Image Processing, vol. 2009, no. 4, s. 353–365

Part V
Multi Physics Co-simulation Methods

Chapter 14

Fluid–Structure Interaction Simulation

Ihor Berezin, Prasanta Sarkar, and Jacek Malecki

14.1 Introduction

Computational methods for fluid–solid interaction (FSI) simulations can be classified as tightly or loosely coupled. The tightly coupled (monolithic) approach solves the fluid and solid equations in a single computational domain using a single numerical framework. The unified treatment of both media tends to improve stability of this method. However, this coupling approach often suffers from the ill conditioning of the associated matrices and from the inability to use existing fluid and solid solvers. These two disadvantages are addressed with the loosely coupled (partitioned) approach, which uses separate and independent techniques for the fluid and solid subdomains and exchanges data along the fluid–solid interfaces (i.e., transfer of jump conditions for kinematic compatibility and dynamic equilibrium) via a fixed point iteration scheme. The loosely coupled approach can thus take full advantage of existing, well-developed, and tested codes for fluid and solid analysis. Solvers with disparate discretization scheme can be “plugged” into a loosely coupled framework, with the only changes of obtaining the appropriate boundary conditions from the framework.

The loose coupling approach presents two key areas of challenges. The first one is concerned with the stability, accuracy, and convergence of staggered time-integration schemes used for the partitioned approach. The second one deals with data transfer between differing mesh representations of the fluid and the solid

I. Berezin (✉) • J. Malecki
WSK PZL Swidnik, S.A, Swidnik, Poland
e-mail: berezin.ih@gmail.com; malecki.jacek@finmeccanica.com

P. Sarkar
Université Grenoble Alpes, LEGI, Grenoble, France
e-mail: prasanta.sarkar@univ-grenoble-alpes.fr

subdomains. Such meshes are in general nonmatching (i.e., have incompatible nodal connectivity and positions along the interface) because of differing mesh resolution requirements or discretization schemes (Jaiman et al. 2005).

Fluid–structure coupled computations require an interface between the flow domain and the structural domain. The flow domain R_f and the structural domain R_s are coupled by exchange of forces and displacements through the wetted structural wall Γ . Usually, different definitions of displacements, velocities, and forces are applied on the two sides of the interface. In the most general case, the geometry is discretized in two different ways, owing to different requirements for the solution of the structural and flow equations, respectively. The solution of the flow usually requires an accurate description of the boundary. On the other hand, for the purpose of structural analysis, the body is often simplified by combinations of beam-like, platelike, or other types of structural elements. While the structural surface is not accurately modeled in this way, the essential static and dynamic behavior can be captured efficiently. Even if the structural and flow discretization are both chosen to model the same boundary surface, the computational nodes for the structure usually do not coincide with those used for the flow. Again, this is because the flow computation requires a higher resolution than the structural analysis, due to the need for resolving smaller scales. An approach for data exchange between the two domains is necessary, which may involve a combination of interpolation and extrapolation, depending on the severity of the mismatch (Sadeghi et al. 2004; De Boer et al. 2007).

An appropriate fluid–structure interface takes account of the following requirements concerning transfer of displacements and forces. A detailed discussion on the issues of interpolation, extrapolation, conservativeness, and other requirements for fluid–structure interfaces is presented by Brown (1997):

1. Accurate, physically sound recovery of the deformation of the wetted surface, given its representation on the structural grid.
 - (a) Exact representation of rigid body motions: If the structural grid is subject to a rigid body motion, the displacement transfer should result in the same motion for the wetted surface. Exact representation of these base modes will improve the accuracy of the treatment of general deformations.
 - (b) Smoothness: If the deformation of the structural grid is smooth, the aerodynamic grid should also be smoothly deformed.
 - (c) Physical deformations: In order to restrict deformations of the wetted surface to physically reasonable shapes, the application of physical relations (e.g., for an elastic continuum) is preferred over the use of arbitrary extrapolation/interpolation techniques.
2. Accurate, conservative load transfer.
 - (a) Smoothness: If the load distribution on the wetted surface is smooth, the load on the representative structural grid should also be smooth. However, it may also be important that load discontinuities (e.g., in transonic flow) be accurately transferred to the structural grid.

- (b) Conservation of energy: The projected forces perform work on the moving structural grid. The accurate computation of the energy that is extracted from the flow is essential to the prediction of utter stability. The work on the structural grid has to be identical to the work performed by the aerodynamic load on the moving wetted surface. Energy conservation is achieved by an appropriate combination of load and displacement transfer methods.

To evaluate the integrated framework for transient fluid–structure interaction, FSI analysis is performed for a 2D section of W3 main rotor blade. CFD and structural (CSM) models share the same interface Γ with nonmatching meshes in fluid and structural domain. Commercial software packages ANSYS Fluent 13.0 and MSC Nastran 2010.1 are used for fluid and structural solutions with fluid–structure interface and overall FSI solution control performed with Matlab r2007b. Attention should be paid to software versions, for compatibility with other versions hasn't been checked. Both CFD and CSM models are defined as fully transient with CFD mesh updating in the end of every time step t_n .

Assuming that the fluid, solid, and mesh motion solutions are known at time t_n , solution of the coupled FSI system at time t_{n+1} is obtained using the following explicit coupling procedure (Fig. 14.1):

1. Solve aerodynamic system for the current time step ($t_n = t_{n-1} + \Delta t_c$).
2. Integrate fluid loads onto structural domain.
3. Solve structural dynamics problem for time $0 < t_n < \Delta t_c$ with initial conditions (nodal displacements u , velocities \dot{u} , and accelerations \ddot{u}) calculated as result of solution on time step t_{n-1} .
4. Interpolate displacements δ_s of the wetted surface Γ_s onto fluid surface Γ_f .
5. Update mesh in the fluid domain according to the interpolated displacements, and create new CFD mesh for step t_{n+1} .

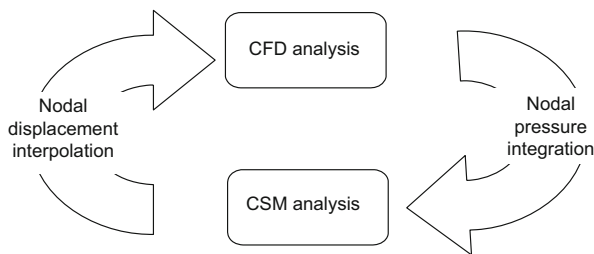


Fig. 14.1 FSI cycle flowchart

14.2 CFD Analysis

The role of CFD in fluid structure interaction can be categorized into the following:

- (a) To predict the actual fluid motion
- (b) To predict the force induced on the airfoil by the fluid motion
- (c) To determine how an airfoil subjected to fluid-induced force changes its motion and how such an airfoil in motion causes a change in the fluid motion

Fluid flow analysis aims to determine the relationship between fluid flow velocity and pressure on the airfoil which is subject to a geometric boundary condition, i.e., the fluid–solid interface. The airfoil section used for developing the case for fluid structure interaction study was taken from 0.52R section of the PZL W3 Sokol main rotor blade, where R is the blade radius. The dynamic characteristics of a pitching NACA 23012 airfoil were studied to develop a methodology capable of conducting CFD analysis of hovering rotors and rotor blade aeroelastic analysis similar to the work carried out by Steijl et al. (2006) and Lee et al. (2008).

Mesh created around the airfoil consists of structured quad and paves cell zone (Fig. 14.2). The structured cell zone undergoes only rigid body motion with no deformation in the zone when rigid body motion is desired with no surface deformation (Fig. 14.3). The airfoil surface has 904 nodes around it, substantially increased to have a better control and smooth airfoil surface deformation. A thin elliptical region was created around the airfoil with quad elements to contain the boundary layer. The circular domain enclosing the rigid domain is the deforming zone where the maximum mesh deformation and re-meshing takes place during pitching motion. The mesh was created with size and growth factor limitations so as to avoid negative cell volumes during mesh deformation in the computation. The y^+ value, which is the scaled normal distance from the wall, was kept over 30. This was due to the need to avoid highly skewed thin rectangular cells near the wall. The presence of thin rectangular cells near the wall can lead to negative volumes in case of airfoil surface deformation, which is hard to control at a later stage in

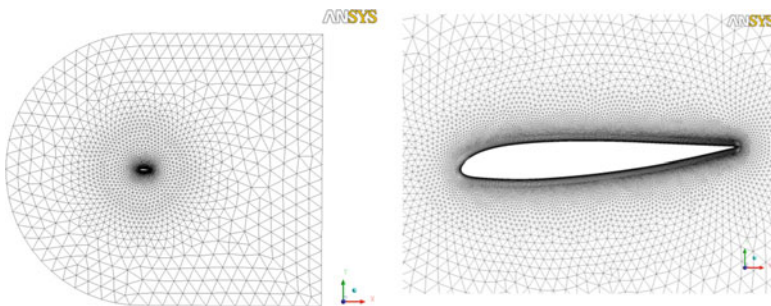


Fig. 14.2 Computational domain used for NACA 23012 FSI calculations

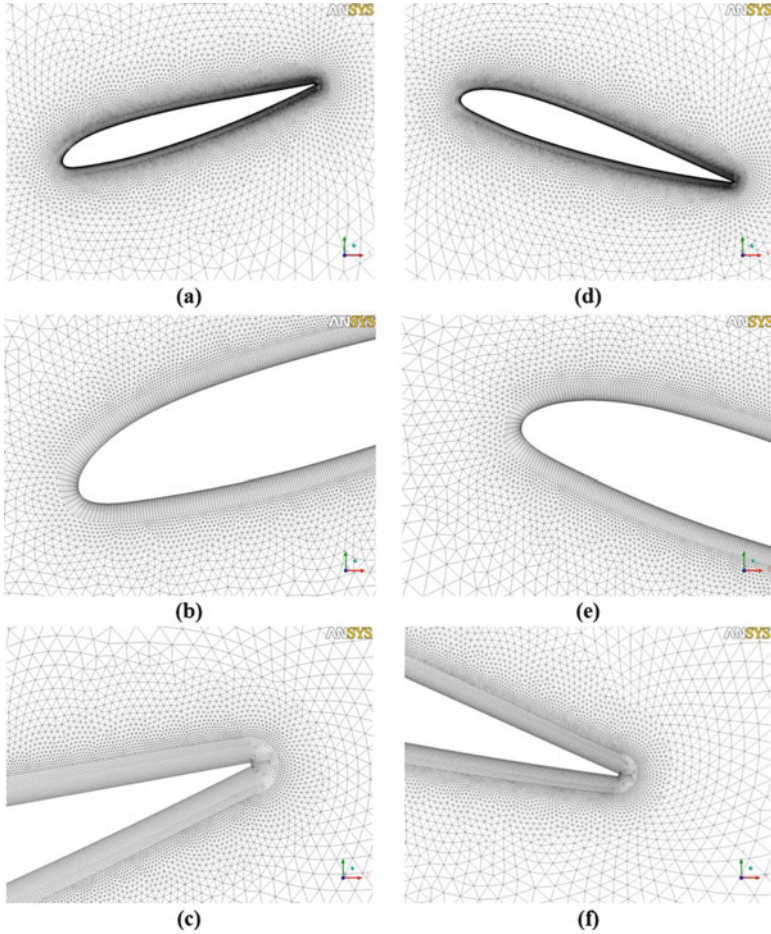


Fig. 14.3 NACA 23012 pitching airfoil (a–c) mesh deformation, downstroke; (d–f) mesh deformation, upstroke

between computation. Also static numerical investigation on the airfoil with $y^+ = 1$ has given similar results with SST $k-\omega$, thus validating the models non-dependence on y^+ value. The boundary layer was generated with a growth factor of 1.05 with 25 layers. The grid around the elliptical region is made using triangular cells with a maximum growth factor of 1.2 and maximum grid size based on airfoil characteristic length.

The mesh is solved with the initial airfoil position at each time step of the unsteady solver. Previous dynamic stall evaluations identified boundary layer reattachment as the feature most sensitive to spatial and temporal resolution. Based on numerical study of stall onset and flow reattachment, studies reaffirmed the sensitivity of reattachment to time step size and recommended 1000–2000 time

steps per cycle with 100 sub-iterations for temporal convergence. The time implicit or dual time-stepping formulation is used to obtain unsteady flow solution, with the time-dependent terms being discretized in an implicit way using second-order Euler backward difference in time with the addition of a low Mach number preconditioned pseudo-time derivative.

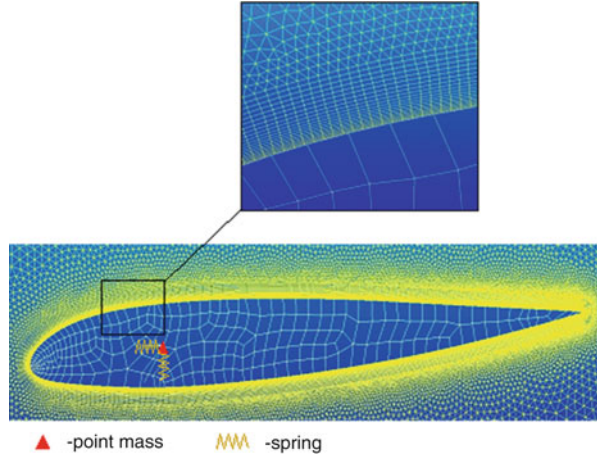
As rotor flow field computations are characterized by viscous unsteady flow and body motion, the flow field requires a simulation based on the unsteady Navier–Stokes equations. These equations were simulated discretely using the unsteady Reynolds-averaged Navier–Stokes model equations. Density-based implicit solution methodology was used, as although explicit methods can be computationally less expensive for a single time step, they have strict stability requirements and time step limitations. Pressure far-field boundary condition was used on the computational domain boundary, and no-slip wall boundary condition was used on the airfoil surface. The computation was carried out with SST k - ω turbulence model with second-order upwind scheme for spatial discretization of the convection terms and central differenced for the diffusion terms.

The fluid–solid interface is subjected to a very important assumption of zero fluid velocity (no-slip condition) over the entire surface of an airfoil. The assumption arises from the viscosity of the fluid, as the fluid particle will completely come to rest on the airfoil surface due to uneven roughness. A point implicit linear equation solver incomplete lower upper (ILU) factorization scheme is used in conjunction with an algebraic multigrid (AMG) method to solve the resultant block system of equations for all dependent variables in each cell at the same time with second-order implicit Euler backward difference in time for temporal discretization. The complete solution method was automated using TUI journal file and coupled with the FSI routine developed with the force and moment coefficients being monitored along with airfoil motion and mesh quality. The flow is assumed to be compressible, characterized by the total pressure and total temperature of the flow. The compressible form of the ideal gas law is used to determine the density of the fluid and is influenced by the flow Reynolds number and Sutherland law three coefficients method for viscosity.

14.3 Coupling: Surface Pressure Integration

Structural model is developed in MSC Nastran with shell elements, whose stiffness is intended to represent the magnitude of surface displacements under aerodynamic load. It was shown that the influence of blade surface deformation is negligible compared to airfoil rigid body motions. Therefore, precise model of internal blade structure is not needed in this case and can be represented with simplified mesh. Section inertia and stiffness properties are modeled as a system of point mass and spring system. Concentrated mass is applied to the blade pitch axis with three springs representing flapping, lagging, and pitching stiffness of the blade

Fig. 14.4 CSM and CFD domains for fluid–structure interaction simulation



connected to the same load (Fig. 14.4). Inertia and stiffness properties represent blade dynamical properties within first flapping, first lagging, and first pitching frequencies.

Fluid and structural solvers are integrated in time synchronously, thus there is a need for a continual transfer of load and motion at the interface. Temporal coupling and updating is performed between CFD and CSM solvers. It is likely for time steps required in fluid and structural domains to be different, as the solvers generally employ different time integrators and different grid resolutions. However, a common time step Δt_c is used herein to focus on spatial variation issues. This time step is determined by minimal time step in fluid and structural domain:

$$\Delta t_c = \min (\Delta t_f, \Delta t_s) \quad (14.1)$$

where Δt_f and Δt_s are fluid and structural domain time steps, respectively.

At each FSI cycle, two interface boundary conditions corresponding to continuity of tractions and velocities must be satisfied along the fluid–solid interface Γ . Let t_f and u_f denote the fluid traction vector and the fluid displacement fields along Γ_f , respectively, and t_s and u_s denote the solid traction vector and the solid displacement fields along Γ_s . The equilibrium of tractions and compatibility of velocity field can be expressed as (Sadeghi et al. 2004):

$$\begin{aligned} t_s &= t_f \\ u_s &= u_f \end{aligned} \quad (14.2)$$

where

$$\begin{aligned} t_f &= -p_f n_f + \sigma_f n_f \text{ and} \\ t_s &= \sigma_s n_s \end{aligned}$$

where p_f is the fluid pressure along the interface, σ_f and σ_s are the fluid viscous tensor and structural stress tensor, respectively, and n_f and n_s are the normal at the fluid interface Γ_f and solid interface Γ_s , respectively.

In general, while the fluid system addresses the traction field vector t_f on the element surfaces on the interface, the structural system is solved based on a set of concentrated forces at the nodes on the interface. A distributed fluid load, therefore, must be transferred into equivalent nodal forces along the solid interface. Such a transformation must satisfy conservation of loads, i.e., the solid nodal load vector must yield the same net load vector as the original distributed fluid traction loads. However, the conservation of loads can be satisfied by an infinite number of possible nodal load vectors. To be physically consistent and meaningful, the transformation of load must also be highly accurate, i.e., to have a small error in a specific norm, and, preferably, the conservation of energy should be satisfied. For the evaluation of the energy, the definition of the virtual work can be conveniently used (Sadeghi et al. 2004; Farhat et al. 1998).

In Jaiman et al. (2005), it is shown that the resulting force vector in structural nodes j on interface of solid domain Γ_s can be calculated as follows:

$$F_s^j = \int_{\Gamma} N_s^i \tilde{t}_f d\Gamma \quad (14.3)$$

where N_s^i —standard element shape functions associated with node i of the fluid domain expressed in natural coordinates of corresponding structural element; \tilde{t}_f —approximate traction in the corresponding nodes.

14.4 Structural Analysis

Once aerodynamic load is retrieved, structural dynamics simulation is performed with MSC Nastran. CSM model is fully transient. For a 2D case, interface is formulated as linear elements; however, the same approach can be used for 3D FSI with plane (quadrilateral or triangular) interface elements.

For convenience, structural model is divided into several parts:

- **bdf*—control file containing information about solution parameters, links to mesh, time controls, and load files
- **model*—model mesh with nodes, connectivity, element properties, and boundary conditions
- **force.load*—nodal forces
- **tabled1.load*—timed load history, refer to TABLED1 in Nastran Reference Guide for details
- **tstep.load*—time step parameters, refer to TSTEP in Nastran Reference Guide for details
- **tic.load*—initial conditions, refer to TIC in Nastran Reference Guide for details

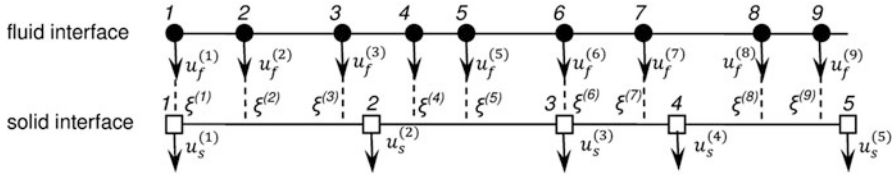


Fig. 14.5 Node projection-based load transfer

Blade section is fixed to ground via three springs—two linear in x and y direction and a torsional spring in rz direction (see Fig. 14.4). By application of corresponding displacements to spring base, the effect of swash plate motion can be simulated.

On every FSI loop, structural dynamics solution is performed for time $0 < t < t_n$ with 20 solution substeps. Initial conditions are applied based upon results of previous solution or are set to zero on the first loop. Initial conditions (displacements and velocities) are applied to the model on the first substep of solution. Resulting nodal displacements, velocities, and accelerations are recorded on the last substep only for space-saving purpose. When structural analysis is done, displacement vector in the interface nodes is extracted and passed forward to CFD interface with interpolation procedure (Fig. 14.5).

Load is step changed between FSI loops. However, to avoid impact effect in the beginning of the simulation, load increases linearly within first revolution of MR. In this case, load multiplier $\mu = 0 \dots 1$ is split proportionally between loops representing first revolution. Within one loop, load multiplier is linearly changed from μ_{n-1} to μ_n . Another method to reach dynamic stabilization faster is using static preload of the blade. Blade vibrations occur about the static equilibrium position, and starting of the simulation from state close to equilibrium speeds up system transferring to steady-state vibrations (Fig. 14.5).

14.5 Coupling: Displacements Interpolation Between Fluid and Structural Interfaces

Node projection scheme (Farhat et al. 1998) is used for interpolation of displacements between CSM and CFD interfaces. According to this scheme, fluid nodes are projected onto the solid surface elements to extract displacements from the solid interface nodes. Let N_s^i be a shape function associated with the fluid node i projected onto corresponding structural element. This scheme can be outlined as follows:

1. Associate each fluid node on Γ_f with the closest solid interface element on Γ_s . Associativity table is generated with fluid nodes assigned to structural elements.
2. Determine the projection of the fluid nodes onto the corresponding solid element. Since interfaces are assumed to be matching, each fluid node can be determined in terms of natural coordinates $\xi(i)$ determined based on element shape functions.

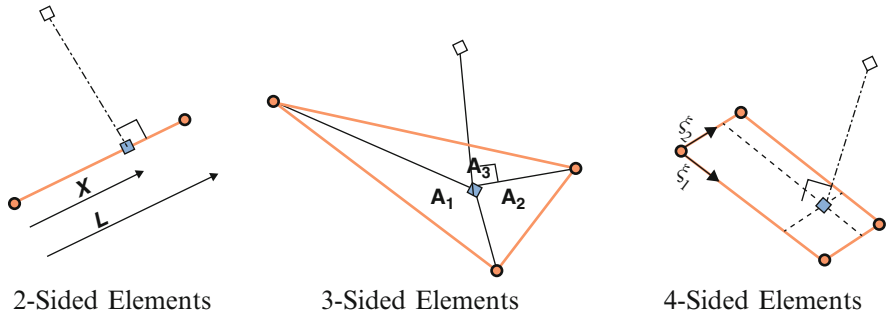


Fig. 14.6 Elements with node projections

Figure 14.6 shows element shape functions for 1D and 2D interface elements. Element shape functions are defined as follows:

Two-sided elements	Three-sided elements	Four-sided elements
$N_1(\xi_1, \xi_2) = \xi_1 = \frac{x}{L}$	$N_1(\xi_1, \xi_2) = \xi_1 = \frac{A_1}{A_T}$	$N_1(\xi_1, \xi_2) = (1 - \xi_1)(1 - \xi_2)$
$N_2(\xi_1, \xi_2) = \xi_2 = 1 - \xi_1$	$N_2(\xi_1, \xi_2) = \xi_2 = \frac{A_2}{A_T}$	$N_2(\xi_1, \xi_2) = \xi_1(1 - \xi_2)$
	$N_3(\xi_1, \xi_2) = 1 - (\xi_1 + \xi_2) = \frac{A_3}{A_T}$	$N_3(\xi_1, \xi_2) = \xi_1 \xi_2$
	$A_T = A_1 + A_2 + A_3$	$N_4(\xi_1, \xi_2) = (1 - \xi_1)\xi_2$

3. Multiply u_j inside the solid element with $N_s^i(\xi^i)$. The extracted displacement vector on fluid node is defined as

$$u_f^i = \sum_{j=1}^{m_s} N_s^i(\xi^i) u_s^j \tag{14.4}$$

Interpolation of displacements between meshes shows (Fig. 14.7) good results in terms of accuracy, smoothness, and displacements conservation. Attention should be paid in case of nonmatching interfaces when using this procedure, because shape functions in this case might not represent interpolation correctly.

14.6 CFD Mesh Updating

Fluid mesh updating is performed using spring analogy concept (Dehaeze and Barakos 2012) adjusted for use with the FSI tool. New interface structural mesh is created from fluid nodes coordinates and connectivity and solved with MSC Nastran with displacements obtained after CSM solution as boundary conditions. A code for generating structural mesh based upon node coordinates and connectivity of fluid

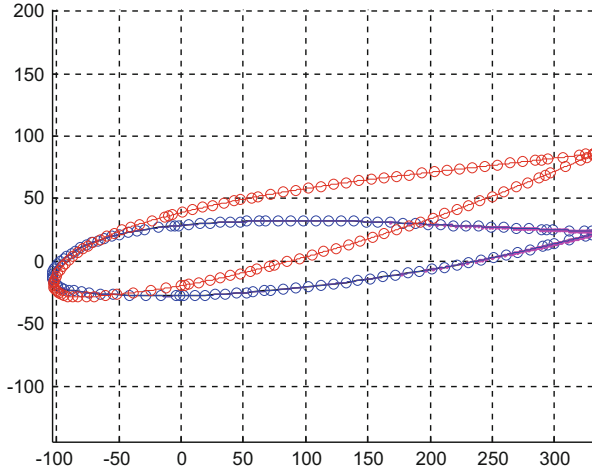


Fig. 14.7 Structural surface displacements and interpolated fluid surface deformation. Lines–fluid interface, dots–structural interface

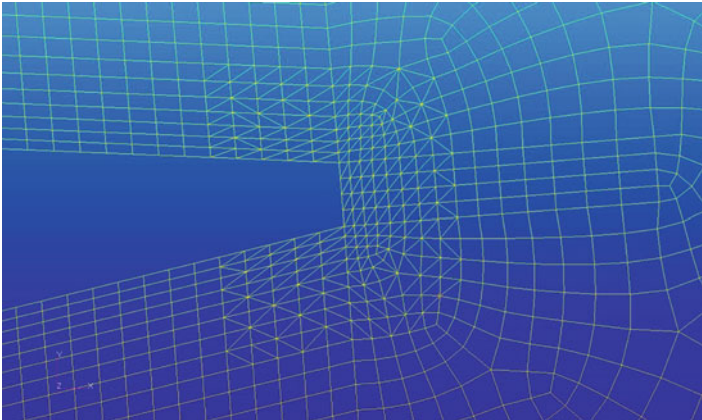


Fig. 14.8 Interface structural mesh in the trailing edge region

domain mesh has been developed. Fluid mesh degradation was observed at high angle of attack due to excessive deformation of interface mesh beams in the trailing edge region. To avoid this problem, diagonal beams were added to split quadrilateral fluid faces surrounding trailing edge into triangular ones (see Fig. 14.8). Such approach ensures higher stiffness of interface mesh close to trailing edge with the same nodes and coordinates as in the fluid mesh.

Similar to the main structural dynamics solution, interface mesh model is also separated into control file **.bdf*, mesh file **.model*, and load file **disp.load*. For a 2D case, fluid faces are converted into structural beam elements. The surrounding structured mesh region around the airfoil has high stiffness and thus undergoing

less deformation with the maximum deformation being transferred to the external fluid mesh. Rigid body displacements of the airfoil are transferred mostly to outer regions of mesh and dynamic zone experiences only blade surface deformations. The deformation method used gave better control over mesh deformation for non-prescribed motion with the mesh orthogonal quality staying over 0.7 for most of the cases.

Nodal displacement vector u_i is applied with nodes belonging to pressure far-field zone fully constrained. Static structural problem for interface structural mesh is solved. The resulting nodal displacements are added to the coordinates of nodes, and nodes coordinates are updated.

Fluid–structure interaction simulation is controlled with Matlab script developed at PZL. Figure 14.9 shows flow diagram for coupled analysis. It can be seen that interfaces matching is performed only once at the beginning of the analysis. Fluid–structure ($F-S$) transfer matrix (depending on pressure integration method can be either linear operator, independent matrix, or inverse of structure–fluid ($S-F$) matrix) and $S-F$ matrices do not change during mesh deformation assuming that fluid Γ_f and structure Γ_s interfaces do not separate. Solution data is stored in the working directory. Solution data includes Fluent *.cas and *.dat files, Fluent pressure and velocities contour plots *.hmf, Nastran output files *.f06, simulation log file, and solution summary. Generally, Fluent and Nastran files are required only for restarting the simulation at any iteration and debugging purposes. For disk space-saving purpose, the number of backup files can be controlled; recommended number of backup files is 10 last loops plus every 10th loop.

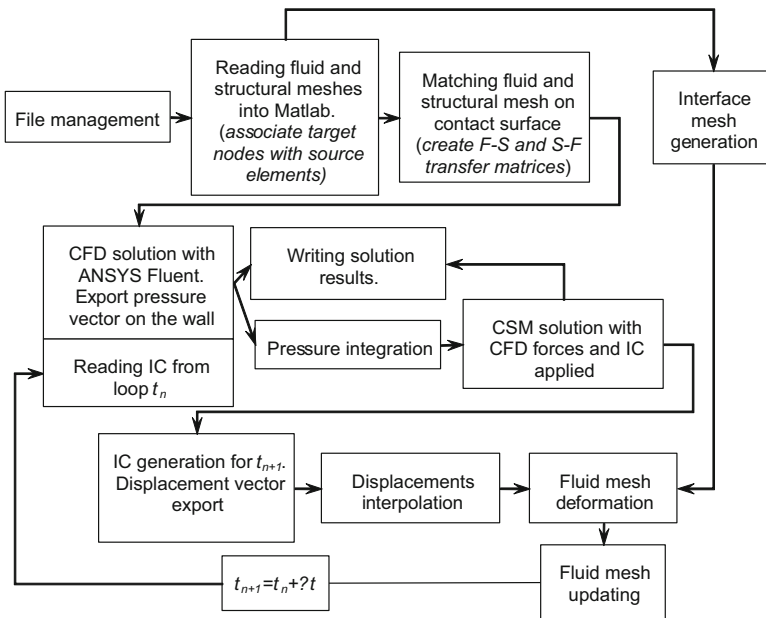


Fig. 14.9 Flow diagram of FSI simulation

14.7 Results

FSI simulation is performed for blade section with the following parameters:

- Mach number $M = 0.34$
- Incidence angle $\alpha = 7.69^\circ$; <geometric angle 4.9° >
- Temperature $T = 304$ K
- Blade mass $m = 0.343$ kg
- Flap stiffness $K_y = 120$ N/mm
- Lag stiffness $K_x = 294.5$ N/mm
- Pitch stiffness $K_{r_z} = 4583$ Nm/rad

Computations are performed on two-core Intel Xeon 5130 at 200 GHz and 8GB RAM for 412 loops using the same time step for fluid, mesh motion, and solid solvers. CFD domain consists of 41328 cells; size of CSM mesh is 330 nodes. Since CFD problem is transient, time required for its solution varies with amount of mesh deformation. High airfoil displacements require more iteration for CFD to converge. For the current simulation, general time resolution is set to 120 loops per one rotor revolution with 100 iterations on every loop and maximum of 70 substeps per iteration. Although rotation about MR axis is not accounted for in the model, it is incorporated in time calculations for convenience.

The dynamics of NACA 23012 airfoil aeroelastic behavior is studied with and without structural damping of the airfoil motion. For a given angle of attack, Fluent simulates the pressure distribution over the airfoil which is used to calculate the aerodynamic coefficients and airfoil displacement. The first case simulated a high-amplitude response at an initial angle of attack of 7.69° with Reynolds number of 4×10^6 at a flow Mach number of 0.34. A zero component of the velocity in the z -direction was assigned to obtain a two-dimensional fluid behavior. As lift is a component of the force perpendicular to the direction of a uniform flow, the x -component of fluid force acting on the airfoil surface, F_y , was used in this analysis. This lift, F_y , associated with the coefficient of lift, C_L , is shown in the following expression,

$$C_L = \frac{2F_y}{\rho v^2 S} \quad (14.5)$$

where S is a reference area that corresponds to projected area of the airfoil to the flow. In this analysis, projected area was obtained by multiplying the chord by the thickness, $S = 0.44$ m². From the Fig. 14.10, the growing displacement and subsequent lift coefficients can be observed. The simulation was carried out with low stiffness to check the mesh deformation validity at high angle of attacks and large deformations as shown below. The relative importance of the Reynolds number, i.e., ratio of the inertial forces to the viscous forces for the flow conditions, is quantified

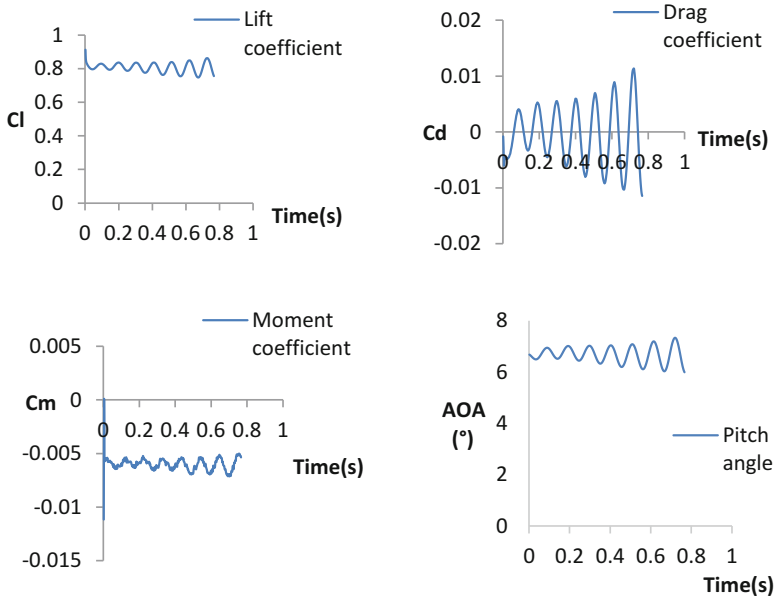


Fig. 14.10 Force and moment coefficient evolution over time for equilibrium condition, $M = 0.34$, $Re = 4E + 06$

by taking L as the characteristic length of the airfoil and U as characteristic velocity of flow. The dimensionless Navier–Stokes equation depends only on the Reynolds number as it represents a dimensionless flow velocity.

Simulations with low torsional stiffness and impact load were run to confirm FSI applicability to a wide range of accelerations and displacements as well as troubleshoot load and motion transfer procedures. Amplitude of blade section motion is shown on Figs. 14.11 and 14.12 that shows time history results of test simulation.

In this case, high-pitching motion amplitude is achieved, with maximum angle of attack reaching the value of 19.1° and CFD divergence occurs. The airfoil in the high-amplitude test case underwent high displacements in flapping and pitching directions for three load cycles beyond which the angle of attack increased considerably and vortex shedding was observed from both the leading and trailing edge. The test case was used as a benchmark to validate the capability of the tool to simulate aeroelastic response and undergo a wide range of motion and mesh deformation. Despite excessive translation of the airfoil, displacement and force transfer between fluid and structural domains is still properly performed within the whole range of motion.

To investigate actual motion of the blade under fluid loads, another simulation was performed. For this case, model is statically preloaded before dynamic simulation to approach reduces the dynamic effect of abrupt force application.

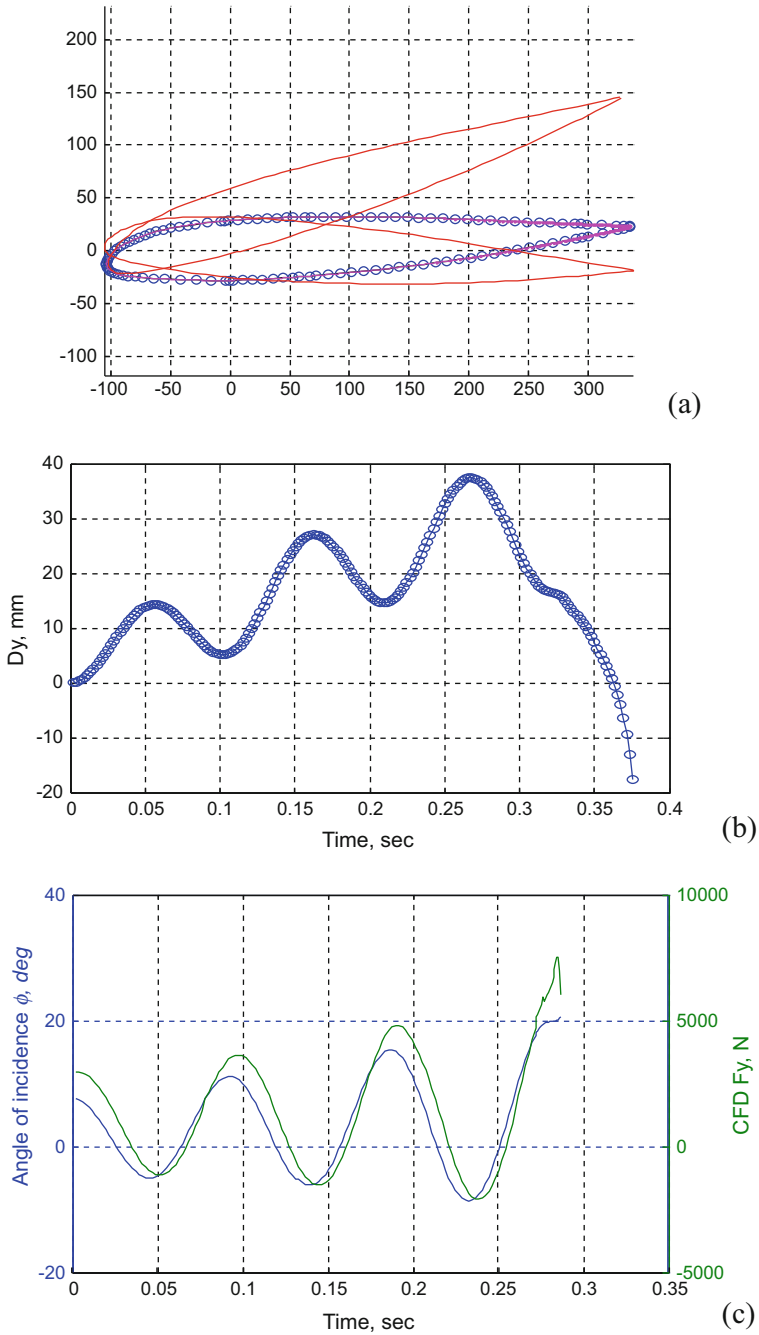
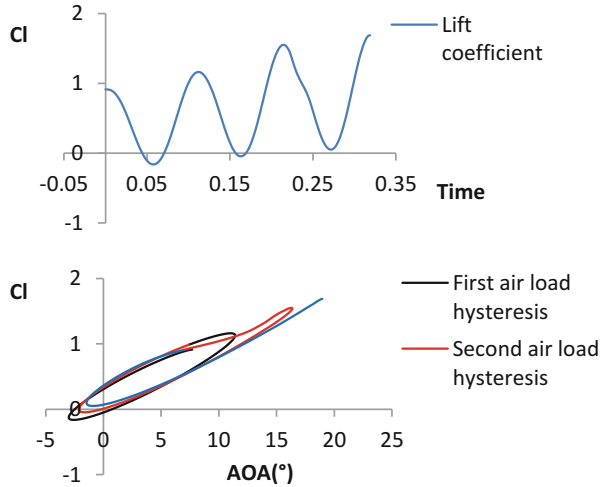


Fig. 14.11 Results of excessive displacement simulation. (a) Flapping motion of the blade; (b) pitching motion and lift force; (c) angle of incidence

Fig. 14.12 Lift coefficient evolution over time and lift coefficient hysteresis over incidences and pitching cycle for high-amplitude case, $Re = 4E + 6$, $M = 0.34$



Preload FSI simulation is performed for static fluid and structural models. After 10 static loops, as the system approaches static equilibrium, full dynamic simulation is launched. Preload significantly decreases acceleration on the initial loops of motion and reduces distortions from instantaneous load application.

The solutions obtained till 0.8 s corresponding to three rotor revolutions are shown in Figs. 14.13 and 14.14, which shows the instabilities and aerodynamic coefficients increasing with time. Both the flap and pitch motions of the airfoil are simple harmonic in nature, and the airfoil oscillates unboundedly with increasing amplitude in time.

14.8 Conclusions

A numerically stable loosely coupled fluid–structure interaction model is proposed employing commercial finite element solvers ANSYS Fluent and MSC Nastran and controlled by Matlab. Interface load transfer algorithm suggested in this chapter is applicable to wide range of blade motions up until critical blade pitch angles. A method for fluid mesh deformation updating based on Nastran solver is proposed. The method is characterized with high controllability of fluid mesh distortion and robust displacements transfer.

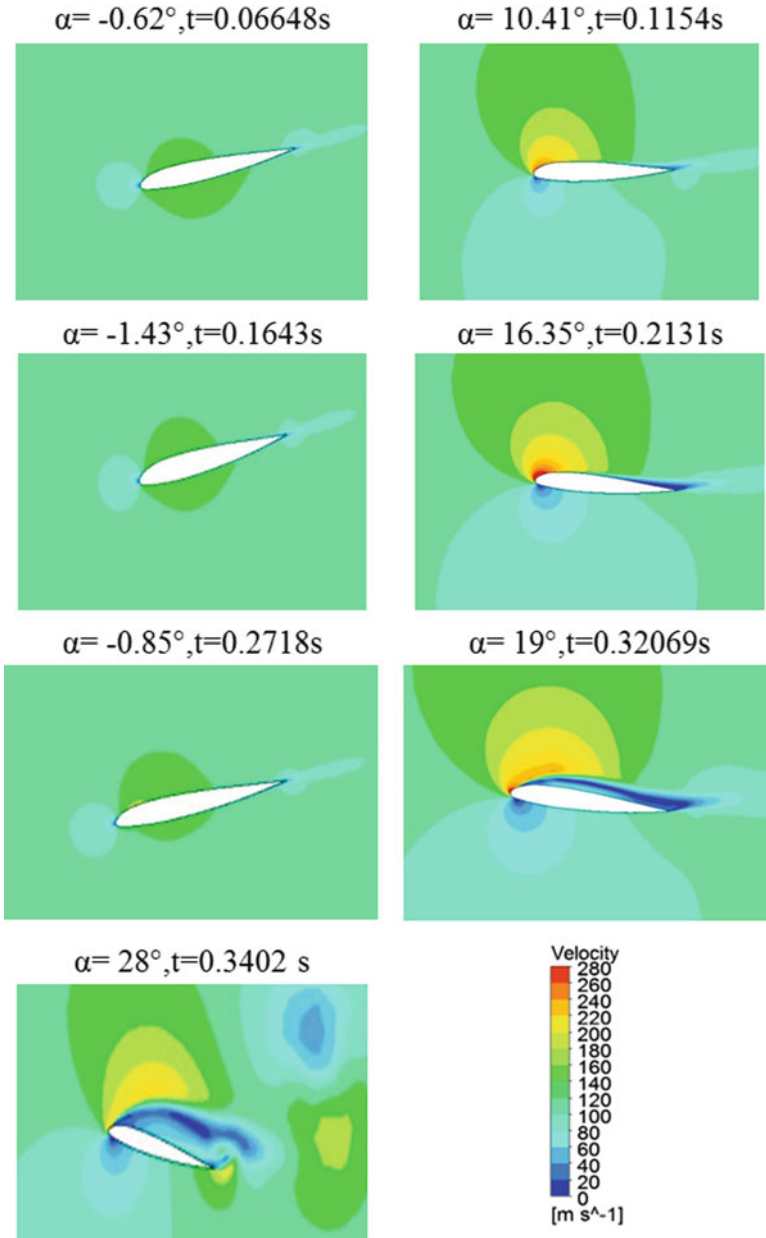


Fig. 14.13 Velocity contours for the airfoil motion at different time interval, $Re = 4E + 6$, $M = 0.34$

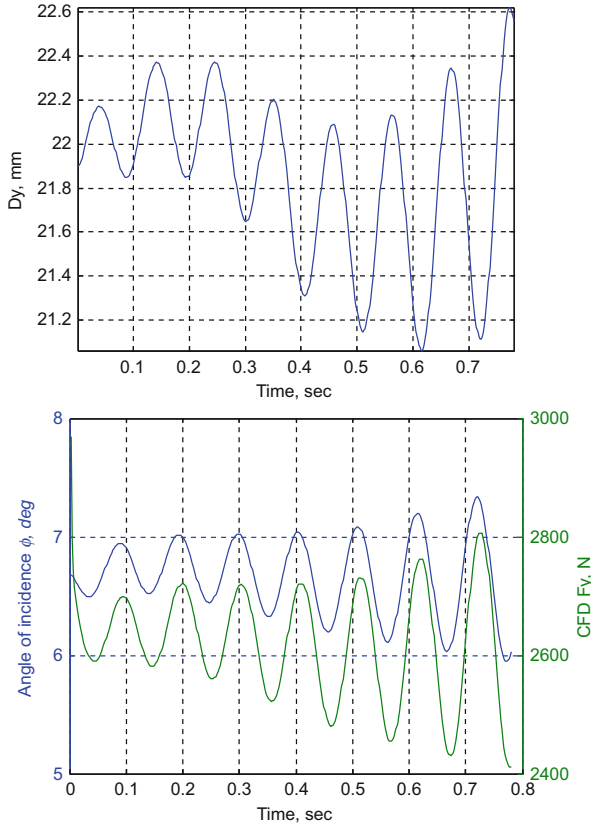


Fig. 14.14 Time history results for dynamic simulation with static preload

References

- Brown SA (1997). Displacement extrapolations for CFD+CSM aeroelastic analysis. AIAA-97-1090, Kissimmee, FL, USA
- De Boer A, van Zuijlen AH, Bijl H (2007) Review of coupling methods for non-matching meshes. *Comput Methods Appl Mech Eng* 196(8):1515–1525
- Dehaeze F, Barakos GN (2012) Mesh deformation method for rotor flows. *J Aircr* 49(1)
- Farhat C, Lesoinne M, LeTallec P (1998) Load and motion transfer algorithms for fluid/structure interaction problems with non-matching discrete interfaces: momentum and energy conservation, optimal discretization and application to aeroelasticity. *Comput Methods Appl Mech Eng* 157:95–114
- Jaiman RK, Jiao X, Geubelle PH, Loth E (2005) Assessment of conservative load transfer for fluid–solid interface with non-matching meshes. *Numer Methods Eng* 64(15):2014–2038
- Lee H, et al (2008) Coupled CFD/CSD analysis of a hovering rotor using high fidelity unsteady aerodynamics and a geometrically exact rotor blade analysis. In: 34th European Rotorcraft Forum, Liverpool, UK

- Sadeghi M, Liu F, Lai KL, Tsai HM (2004). Application of three-dimensional interfaces for data transfer in aeroelastic computations. In: 22nd Applied Aerodynamics Conference and Exhibit, Providence, RI
- Steijl R, Barakos GN, Badcock K (2006) A framework for CFD analysis of helicopter rotors in hover and forward flight. *Int J Numer Methods Fluids* 51(8):819–847

Chapter 15

Analysis and Optimization of Flow Around Flexible Wings and Blades Using the Standard Co-simulation Interface MpCCI

Nadja Wirth, Pascal Bayrasy, Bettina Landvogt, Klaus Wolf, Francesco Cecutti, and Tomasz Lewandowski

15.1 Introduction

Fluid–structure interactions (FSI) are one of the most widespread multiphysics phenomena: the interaction between a deformable structure and a surrounding fluid. For a realistic prediction it is necessary to consider the influence of the fluid forces—modeled in a computational fluid dynamics (CFD) code—to the structural deformation—simulated with finite element analyses (FEA)—and vice versa.

These multi-disciplinary simulations have many different applications: in the automotive area, for wind turbines and for wings, propellers, and other deformable parts on airplanes or helicopters.

Two different simulation approaches can be used for the solution of these problems: either the solution with one single software package (if available) or the coupling between a CFD and an FEA simulation utilizing an interface between the two codes. The second solution is a lot more flexible and offers the possibility to use the customized simulation tools for each discipline. Both simulation tools—CFD and FEA—are running at the same time and exchange repeatedly data at

N. Wirth • P. Bayrasy • K. Wolf (✉) • F. Cecutti
Fraunhofer Institute for Algorithms and Scientific Computing SCAI, Schloss Birlinghoven,
53757 Sankt Augustin, Germany
e-mail: klaus.wolf@scai.fraunhofer.de

B. Landvogt
scapos AG, Schloss Birlinghoven, 53757 Sankt Augustin, Germany
e-mail: bettina.landvogt@scapos.com

T. Lewandowski
Institute of Fluid-Flow Machinery Polish Academy of Sciences, Fiszerza 14 St.,
Gdansk 80-231, Poland
e-mail: tomasz.lewandowski@imp.gda.pl

pre-defined time or iteration steps. The coupling interface is taking care of the synchronization between the two codes and the necessary geometric associations and interpolations.

The interface software tool set MpCCI builds a framework for multi-physical and multi-disciplinary simulations.

15.2 The General Concepts of MpCCI

The MpCCI software tools provide an application independent *interface* for the direct one-way or bi-directional coupling of different simulation codes. This section is based on the manuals and webpages for the MpCCI toolset (cf. MpCCI Manual 2015, MpCCI Cpl 2017, MpCCI Map 2017).

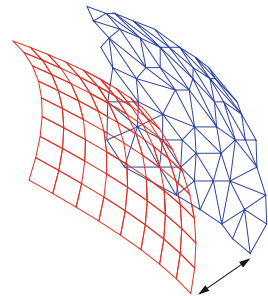
MpCCI is developed independently from simulation software vendors and is “de facto” the neutral standard for simulation code coupling. The interface supports the established commercial and open-source simulation codes from the areas FEA, electromagnetics (EMAG), CFD, multi-body systems (MBS), and others. Fluid–structure interaction, magneto-hydro dynamics, or thermal radiation define only a subset of multi-physical processes covered by MpCCI.

Since MpCCI builds an interface between different simulation tools, it provides methods and algorithms to enable a seamless data transfer between the meshes, which are not compatible in general, cf. Fig. 15.1. The algorithms are presented in Sect. 15.2.3.

Depending on the degree of the physics interactions, the MpCCI software provides two solutions for different engineering applications:

- *MpCCI CouplingEnvironment* couples different simulation codes at run-time which require a high degree of interactions (see Sect. 15.2.1).
- *MpCCI FSIMapper* transfers fluid or electro-magnetic loads from a simulation result file as boundary condition to an FEA analysis (see Sect. 15.2.2).

Fig. 15.1 Data transfer between two non-matching grids (distance exaggerated) cf. MpCCI Manual (2015)



15.2.1 Co-simulation with MpCCI CouplingEnvironment

MpCCI CouplingEnvironment offers a general framework to build a co-simulation application based on different simulation codes. The goal is to achieve a concurrent converged simulation result considering all physical effects at once.

To this purpose, MpCCI CouplingEnvironment will automatically exchange the data between the meshes of two or more simulation codes by using the best-fit interpolation method and considering the nature of the quantities exchanged. The co-simulation application can exchange nearly any kind of data between the coupled codes; e.g., energy and momentum sources, material properties, boundary condition values, mesh definitions, or global quantities. The details of the data exchange are automatically handled by a coupling manager behind the concise interface of MpCCI CouplingEnvironment (cf. MpCCI Cpl 2017).

MpCCI CouplingEnvironment employs a staggered approach solution strategy for all co-simulation problems which can be defined as

- a *globally explicit coupling method*: the coupled fields are exchanged only once per coupling step. This approach is applicable to problems with weak physics coupling.
- an *implicit iterative coupling method*: the coupled fields are exchanged several times per coupling step until an overall stabilized solution is achieved before advancing to the next coupling step. This approach is applicable to problems with strong physics coupling.

Complementary to the coupling method MpCCI CouplingEnvironment offers two coupling algorithms, Gauss–Seidel and Jacobi (Fig. 15.2):

- *Gauss–Seidel coupling scheme* is also known as serial or “Ping-Pong” algorithm where one code waits while the partner code proceeds.
- *Jacobi coupling scheme* is also known as parallel algorithm where both analysis codes run concurrently.

MpCCI CouplingEnvironment supports different coupling analysis solutions depending on the focused phenomena:

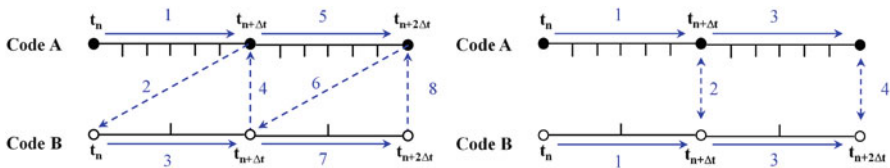


Fig. 15.2 Flow diagram for Gauss–Seidel coupling scheme (left) and Jacobi coupling scheme (right). $t_{n+\Delta t}$ represents the physical time t at time step $n + \Delta t$. Δt is the coupling time step size (cf. MpCCI Cpl 2017)

- Coupling analysis of steady state solutions:
For stationary problems, it is assumed that there is exactly one solution of the coupled problem, which shall be found. The coupling algorithm does not have a big influence on the solution in this case.
- Coupling analysis of transient solutions:
Typical applications focus on the transient effect of the coupled solution, e.g., pressure oscillation, heat dissipation, etc. The fully transient analysis provides an accurate solution. As the solution is dominated by the time component several co-simulation approaches are supported by MpCCI CouplingEnvironment:
 - Fixed coupling time step size: in this configuration both simulations are constrained to use the same coupling time step size during the complete co-simulation. The time step size is equally defined in each application in this case and there is no need to exchange this time information.
 - Exchange of time step size: instead of using a fixed coupling time step size it is also possible to use adaptive time stepping. In this case the time step size is determined by one code and sent to the partner code, which changes its own time step to the received value.
 - Non-matching time step size: codes may run at different local time stepping and also exchange data at non-matching points in time. MpCCI Coupling-Environment takes care of a proper interpolation in time for the coupled physical quantities. MpCCI CouplingEnvironment offers three different methods for the data time-interpolation: constant, linear, and cubic.
- Coupling analysis of mixed solutions steady state and transient:
A fully transient coupling is challenging because of the great disparities of the physical models between the coupled domains (e.g., fluid-structure, fluid-electromagnetics, FEM structural analysis, and discrete element models for particles) and the high computational time. The main difficulty is due to the significant discrepancy of characteristic times since the transient phenomena in the fluid usually take place at a much smaller time scale than those in the solid. The fully transient coupling method describing the transient effects in both coupled domains leads to a highly accurate solution but might be too expensive for some applications. As a computationally cheaper mode you can couple transient models with a sequence of steady state models.

The supported simulation codes are shown in Fig. 15.3. MpCCI Coupling-Environment directly implements the simulation code API provided by the software vendor and is provided as an add-on plugin solution to the simulation codes. Any in-house codes can be connected in the same manner to the MpCCI framework. There are no needs to modify any existing simulation codes installation. The MpCCI CouplingEnvironment software is installed beside the higher number of commercial simulation codes supported.

To ensure best interoperability between the supported simulation codes MpCCI CouplingEnvironment has established a standardization of coupling procedures independent from the utilized codes and coupling quantities definition: energy

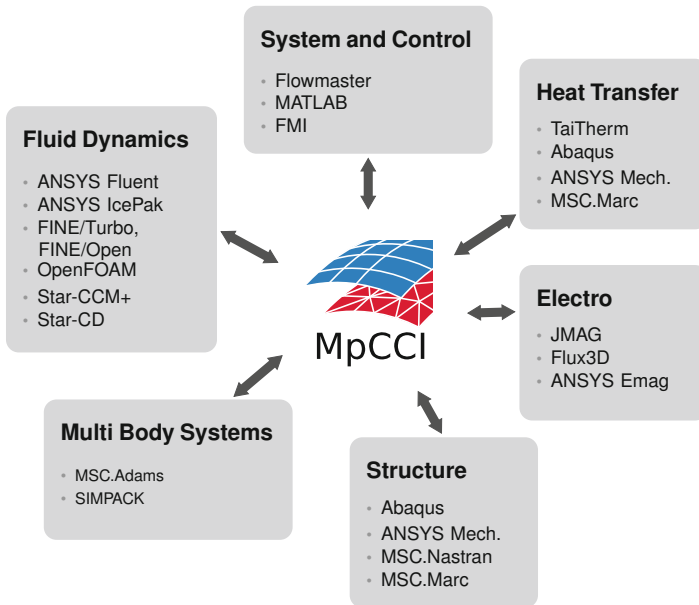


Fig. 15.3 MpCCI CouplingEnvironment's list of supported simulation codes (January 2017)

sources, e.g., joule heat; momentum sources, e.g., Lorentz forces; boundary conditions values, e.g., temperature, pressure.

The MpCCI CouplingEnvironment graphical interface provides a guided method to configure the co-simulation application: the engineer can combine several simulation model files, define the application field which consists of selecting the physical quantities to exchange on the coupled interface, and finally choose the best-fit coupling method. With the start of the coupling, MpCCI CouplingEnvironment will directly launch the involved simulation codes from their standard installation and exchange the data as chosen by the user.

15.2.2 Uni-Directional Data Transfer with MpCCI FSIMapper

For many problems the influence of the fluid flow on the FEA solution is more significant than vice versa, e.g., when structural deformation caused by thermal expansion or pressure loading does not affect the flow field. Thus, a one-way transfer of the fluid solution to the solid solver as boundary condition is a time saving and good approximation to a co-simulation. MpCCI FSIMapper is a file-based tool to address application cases where a single one-way transfer is sufficient (cf. MpCCI Map 2017).

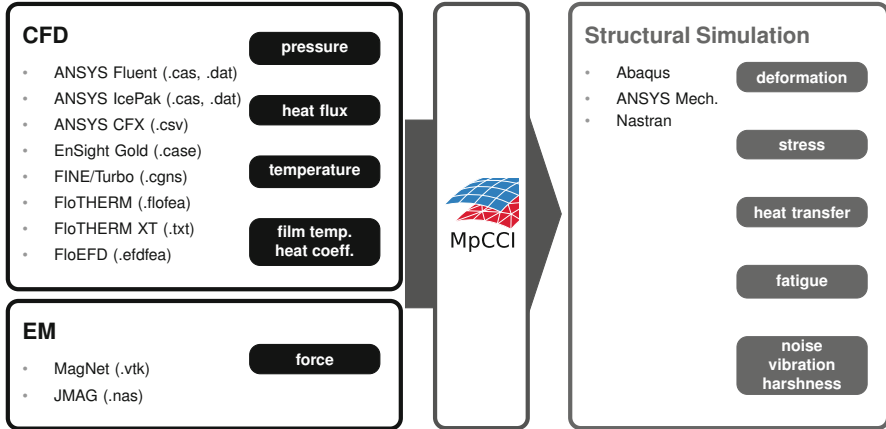


Fig. 15.4 Schematic view of the capabilities of MpCCI FSIMapper. In the *left*, the importable file formats are listed, in the *right* the available solver formats for exporting the mapping result (January 2017)

MpCCI FSIMapper allows to read data of various CFD result formats as well as an EMAG result format (see Fig. 15.4). The universal EnSight Gold format can be exported by diverse CFD tools which enlarges the practicability.

Thermal and mechanical loads can be transferred to an FEA model to be used in a subsequent structural analysis. The tool exports a file including the mapped boundary conditions using the syntax of Abaqus, ANSYS Mechanical, or Nastran.

The quantities that can be transferred are volume temperature, film temperature, wall heat transfer coefficient, the wall heat flux, pressure, and forces.

Robust and efficient interpolation schemes allow the data transfer for different discretization accuracy (mesh density, element type) or even in non-matching model regions using extrapolation.

The mapping of static, transient (only MagNet .vtk, EnSight Gold .case), and harmonic (only FINE/Turbo .cgns, EnSight Gold .case) results is offered. A Fourier transformation of transient force or pressure data is provided in order to create the loading for NVH analyses.

If the models between the mapping shall take place are defined in different unit systems or their position and orientation differ from each other, MpCCI FSIMapper provides, on the one hand, an automatic and, on the other hand, a user defined transformation (translation and rotation) in order to generate geometrically coinciding models. Also, the mapping between periodic models which differ only with respect to their section shape is possible, cf. Fig. 15.5.

In the context of frozen-rotor analyses the simple mapping of the thermal or mechanical loading would lead to an unbalanced structural behavior. In order to produce a blade-wise average, MpCCI FSIMapper offers the possibility to build an “average over rotation,” where the mean is built over sections defined by a certain pitch angle.

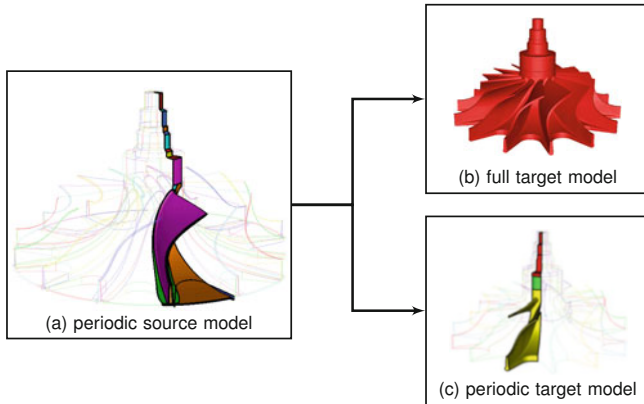


Fig. 15.5 Possibilities of mapping between periodic and full models with MpCCI FSIMapper. The source CFD mesh is a periodic passage of the rotor build around one single blade (a). The target mesh can be the full rotor (b) or a different section (c), here a passage containing parts of two neighboring blades due to planar cutting faces, cf. MpCCI Turbo (2017)

The tool not only has a graphical user interface but can also be used in batch.

15.2.3 Association and Interpolation Methods

MpCCI as interface software handles the data transfer between the involved simulation codes. Since the discretizations differ from each other in general, mapping algorithms—consisting of association and interpolation methods—are implemented (cf. MpCCI Cpl 2017, MpCCI Cpl 2017).

15.2.3.1 Association

The first step of the data transfer is the neighborhood search, where the nodes of the target mesh are associated with elements of the source model. It is based on a k -d-tree implementation for an efficient searching algorithm and is based on different geometrical parameters:

- *Normal distance* and *Tangential distance* (for surface meshes): searching distance for the closest element in normal and tangential direction (Fig. 15.6a).
- *Distance* (for volume meshes): searching distance for closest element.
- *Multiplicity*: parameter to control the search distance (Fig. 15.6b).
- *Node tolerance*: to find doubly defined nodes for meshes with multiple parts.

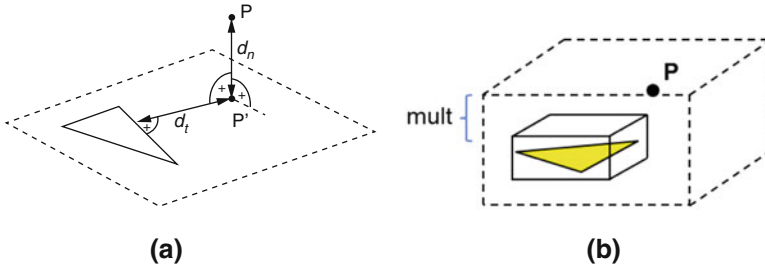


Fig. 15.6 Normal distance d_n and tangential distance d_t for a point P and multiplicity factor parameter. (a) Normal and tangential distance. (b) Multiplicity, cf. MpCCI Manual (2015)

15.2.3.2 Interpolation

With the node-element relations (target node n associated with source element e), the actual data transfer can be realized. The main interpolation algorithm uses the finite element formulation of the associated element e , i.e., the shape functions $\{\Phi_1^{(e)}, \Phi_2^{(e)}, \dots, \Phi_N^{(e)}\}$, where N is the number of nodes of element e . For the shape functions it holds that

$$\Phi_i^{(e)}(\xi_j) = \begin{cases} 1, & \text{if } i = j \\ 0, & \text{if } i \neq j \end{cases}$$

with ξ_j the relative coordinate of node n_j in element e .

Two cases have to be distinguished:

- *non-integral quantities* (like pressure, density, and temperature), which are independent of the element size
- *integral quantities* (like force), which have to be adapted to the element size in order to preserve the integral.

The mapped value w of a *non-integral quantity* at a certain node n of the target mesh is given by the linear combination of the finite element ansatz functions evaluated at the relative position ξ of the node in the associated element e :

$$w = \sum_{i=1}^N w_i^{(e)} \cdot \Phi_i^{(e)}(\xi) \tag{15.1}$$

The factors $w_i^{(e)}$ denote the quantity values at node n_i of the element e . Figure 15.7 illustrates the formula for linear shape functions.

In the interpolation scheme of *integral quantities*, the size and shape of the involved elements are included. The mapped value w at the target node is derived by

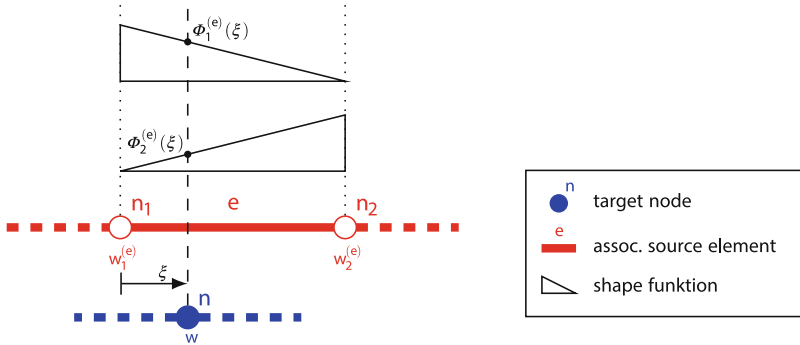


Fig. 15.7 Mapping of a non-integral quantity illustrated for linear finite elements in 2D

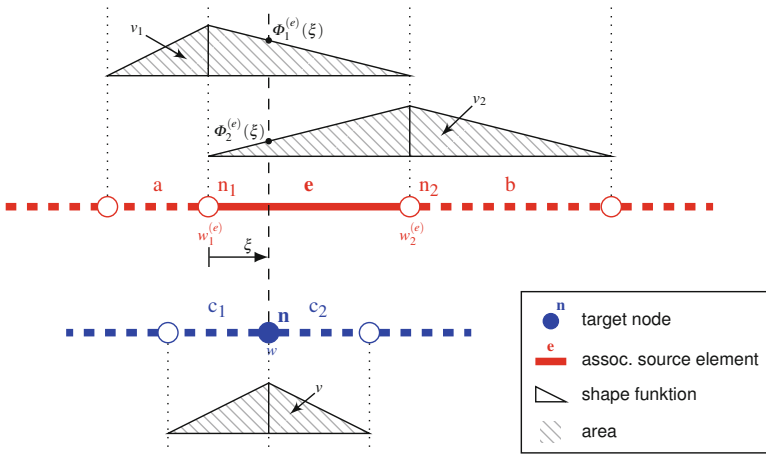


Fig. 15.8 Mapping of an integral quantity illustrated for linear finite elements in 2D

$$w = \left(\sum_{i=1}^N \frac{w_i^{(e)}}{v_i} \cdot \Phi_i^{(e)}(\xi) \right) \cdot v \quad (15.2)$$

where the nodal volume v_i is the sum of the integrals of $\Phi_i^{(a_j)}$ over the elements a_j , $j = 1, \dots, M$ attached to node n_i . v is defined equivalently with respect to the target node and its attached elements. Figure 15.8 illustrates the formula for linear shape functions.

Both interpolation schemes use the *nodal* values of the source element to map the data to a target *node*. If the source data is given as *element*-based quantity or the target simulation code uses *element*-based boundary conditions, the quantities are transformed to the respective needs of the interpolation or the target code using the nodal volumes.

Besides this *shape-function* interpolation method, MpCCI FSIMapper knows the *nearest* and the *weighted-element* mapping algorithms.

If a target node was not associated with a source element (a so-called orphan node), then a default value or an extrapolated value is assigned.

15.3 Examples

15.3.1 *Coupled Fluid–Structure Interaction Simulations for the HIRENASD Aero-Elastic Benchmark Cases*

15.3.1.1 Description of the HIRENASD Benchmark Cases

Verification and validation of simulation results is very important and gets even more crucial when the simulation models become more complicated. For coupled fluid–structure interaction (FSI) simulations, for instance, not only the two stand-alone models have to be validated but also the combination of both models. To assess the quality of the simulation results experimental measurements for test cases are necessary. The simulation results then can be compared to these measured values.

To check the quality of FSI simulations with MpCCI, the HIRENASD (**H**igh **R**eynolds **N**umber **A**erostructural **D**ynamics) benchmark cases have been investigated (cf. HIRENASD 2010, Landvogt 2014). These consist of a series of measurements that have been conducted at the Technical University of Aachen and measured in the European Transonic Windtunnel (ETW) from 2006 to 2008, funded by the German Research Foundation (DFG).

These measurements focused on the investigation of an elastic wing model for transonic flow conditions, which are characterized by strong non-linearities, shock waves, and shock-induced steady state or unsteady flow detachment. Unsteady fluid–structure interactions can occur as a result of possible shock-induced vibrations leading to an interesting validation possibility for FSI simulations.

In the cryogen conditions of the ETW, parameters like Mach number, Reynolds number, and dynamic pressure can be set independently. Using a half model, Reynolds numbers of up to 80 million and high transonic Mach numbers can be tested. The test envelope of the benchmark measurements, which covers realistic flight conditions for a large transport aircraft, is depicted in Fig. 15.9a.

The wing (see Fig. 15.9b), that was used for the experimental measurements, has a span width of 1.3 m and a profile that is typical for a wing of a big passenger aircraft. To record quantity values (i.e., pressure, velocity, or displacement) during the test runs the wing was equipped with about 250 miniature pressure sensors, 11 acceleration sensors, 22 strain sensors, and several surface markers for optical displacement measurement.

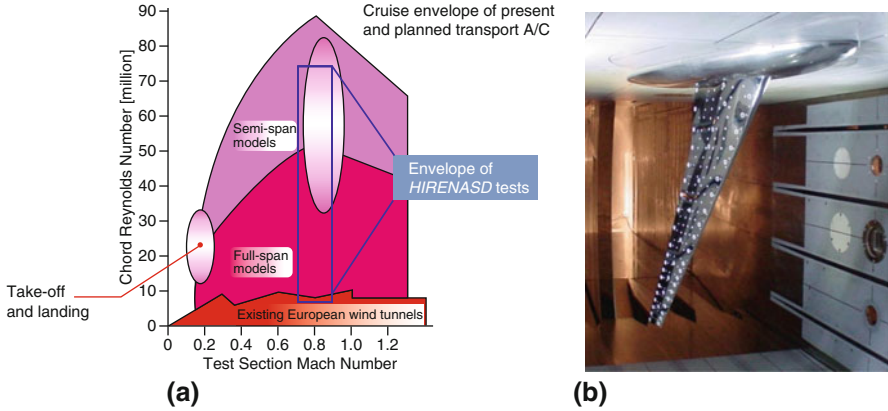


Fig. 15.9 Test envelope and experimental setup of the HIRENASD benchmark. (a) Test envelope of the HIRENASD benchmarks. (b) The HIRENASD wing model in the wind tunnel (figures from HIRENASD 2010)

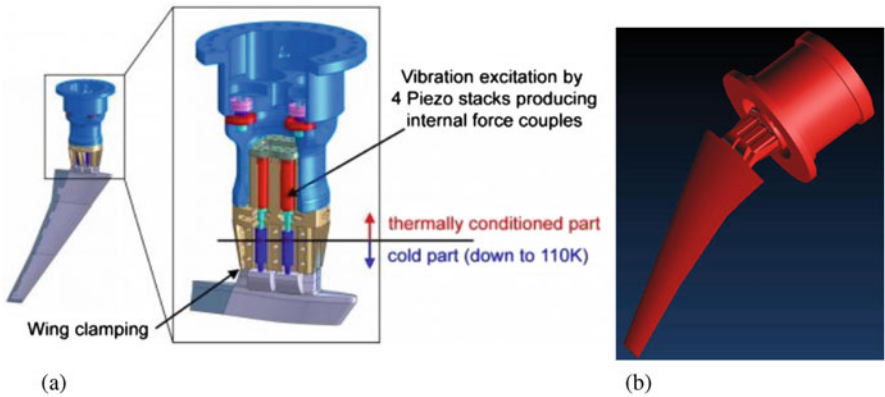


Fig. 15.10 FEA model of the wing and clamping mechanism. (a) Clamping mechanism of the wing in the wind tunnel. (b) FEA model of the wing (figures taken from HIRENASD 2010)

15.3.1.2 FEA and CFD Simulation Models

As a first step, the fluid and structure dynamics models for the wing have to be set up independently. For the coupled simulation of the HIRENASD benchmark cases MSC.Nastran was used for the FEA part and the CFD simulations were performed with Fluent.

The FEA model consists of the wing itself and the necessary equipment to fix the wing in the wind tunnel and achieve the experimental test conditions. Figure 15.10a shows the clamping mechanism of the wing in the wind tunnel and the necessary excitation and temperature control parts that are located outside of the wind tunnel.

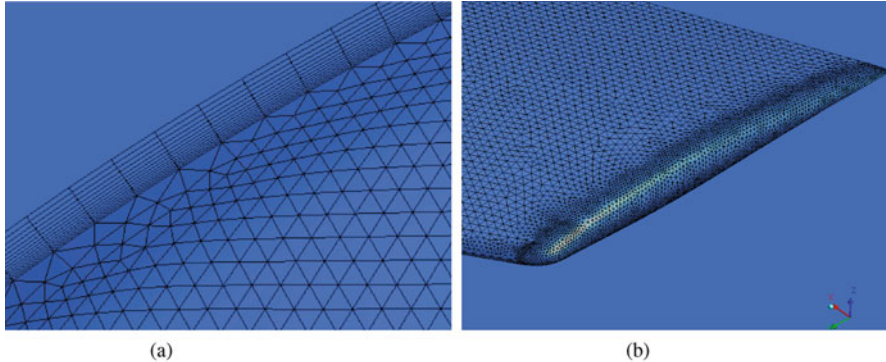


Fig. 15.11 Screenshots of the CFD mesh for the HIRENASD wing. (a) Boundary layer. (b) Wing tip

The MSC.Nastran model incorporates all of these parts and consists of approximately 200,000 second-order tetrahedral elements. The material properties of the wing are set accordingly to the benchmark experiments: the Young's modulus is $2.1 \cdot 10^{11}$ Pa and the density is 7860 kg/m^3 . The Poisson number (with an average value of approximately 0.3125) and the thermal expansion coefficient (approx. $1.3 \cdot 10^{-5}$) are both defined to be dependent on the temperature T .

CFD simulations are performed on a mesh consisting of 15 million tetrahedral and prismatic elements and using 14 boundary layers on the boundary of the wing and the fuselage mock-up. The boundary layer and the meshed wing tip are depicted in Fig. 15.11.

For steady state simulations an implicit density-based solver is used. Then, the steady state solution is used as an initial condition for the transient simulations, employing a density-based, second-order implicit solver. Turbulence is handled by the Spalart–Allmaras model. The density of air is computed using the ideal gas model for all cases.

The rest of the boundary conditions and material properties have to be set according to the investigated test conditions. The results presented here, for example, have been simulated using a Mach number of 0.8 and a Reynolds number of 7 million.

This leads to a viscosity of air of 1.54434 kg/ms , an operating pressure of $137,764 \text{ Pa}$, and an inlet pressure of $76,239 \text{ Pa}$ at a temperature of 265.957 K .

15.3.1.3 FSI Coupling and Results

Using the stand-alone CFD and FEA models the coupling can be easily set up with MpCCI CouplingEnvironment.

The coupling surface, on which quantities will be exchanged and interpolated, is the surface of the wing. In the MSC.Nastran model, the volume elements have to

be covered by a “wetted surface” which can be read and used by MpCCI Coupling-Environment; for Fluent no changes in the stand-alone CFD model are necessary.

The quantities that are exchanged between the two codes are selected: the relative wall force is sent from Fluent to MSC.Nastran and the new nodal positions are sent in the other direction. The morphing of the Fluent mesh is automatically activated by MpCCI CouplingEnvironment for all coupled simulations involving a deforming mesh.

Experimental measurements have been conducted for steady state and for transient flow conditions for the HIRENASD benchmark cases. Transient explicitly coupled simulations can be started using the MpCCI CouplingEnvironment GUI: Fluent, MSC.Nastran, and MpCCI CouplingEnvironment start running and then exchange the respective data each time step.

Generally, MpCCI CouplingEnvironment can also couple steady state simulations or even mixed (steady state with transient) simulations. However, for MSC.Nastran some manual modifications are necessary to obtain a steady state coupled solution using the MSC.Nastran SOL 144. The workflow for such a coupled simulation is depicted in Fig. 15.12.

To be able to compare the simulation results with the experimental measurements the location of the pressure sensors on the wing are defined as monitor points in Fluent (see Fig. 15.13).

As an exemplary result Fig. 15.14 shows the experimental measurements and the coupled simulation results for three sections of the wing.

Looking at Fig. 15.14 reveals that the results of the coupled FSI simulation do match to the experimental measurements. For all different boundary conditions and simulation types, the simulation results near the wing tip (i.e., Section 7) are much closer to the experimental measurements than the results close to the fuselage attached to the wing (i.e., Section 1). This is probably due to the much more complicated flow behavior close to the fuselage and aircraft body.

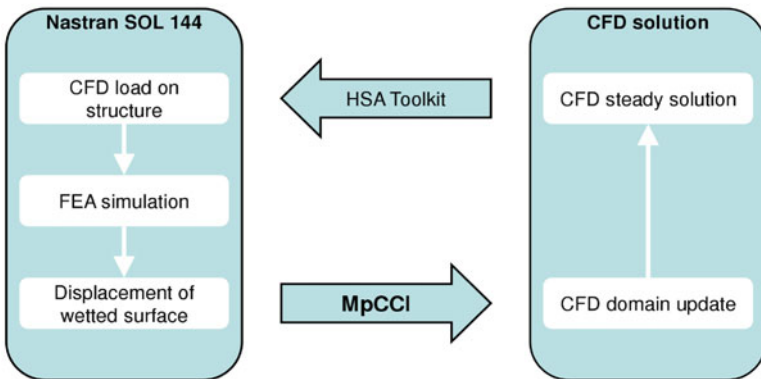


Fig. 15.12 Workflow for using MSC.Nastran SOL 144 with MpCCI CouplingEnvironment

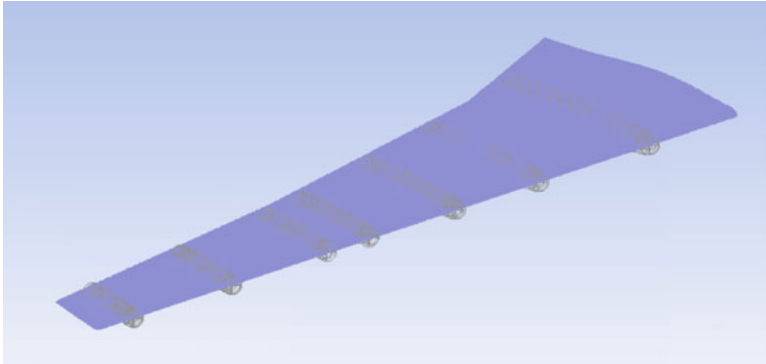


Fig. 15.13 Pressure sensor locations on the CFD model in Fluent

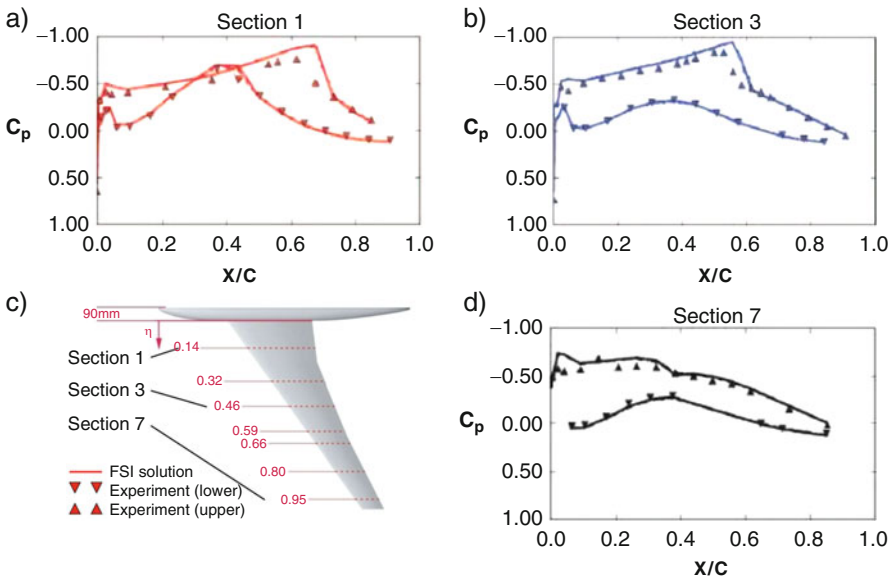


Fig. 15.14 Result of coupled FSI simulations on three sections of the wing, $Ma = 0.8$, $Re = 7$ million. Comparison of pressure coefficient to experimentally measured data. Part (c) shows the position of the three investigated sections (1, 3 and 7) on the wing and the legend, Part (a) shows Section 1 (close to the fuselage), Part (b) shows Section 3 (middle of the wing) and Part (d) shows Section 7 (close to the wing tip)

15.3.1.4 Summary

Summarizing, the setup of the coupled simulation with MpCCI Coupling-Environment using the two stand-alone FEA and CFD models is really straightforward and easy. The results show a good match to the experimental measurements.

However, there are certain drawbacks and difficulties when performing coupled FSI simulations: the computation time required to obtain a solution can be quite high and is usually dominated by the CFD part of the solution. Furthermore, the morphing of the CFD mesh might be difficult, although in most cases for wings the displacements are not too big. Still, the mesh quality cannot always be maintained. In the area of aero-elastic simulations several extensions of the current MpCCI CouplingEnvironment functionalities might be worth considering. Particularly, different types of coupling algorithms and their respective advantages and disadvantages need to be investigated and integrated into MpCCI CouplingEnvironment. After an iterative implicit coupling algorithm that was introduced in MpCCI CouplingEnvironment 4.2, the next version MpCCI CouplingEnvironment 4.5 will include Quasi-Newton methods for implicit coupling. Additionally, extensions for different coupling schemes (mixed coupling, subcycling, predictor-corrector approaches) might be investigated in the future.

15.3.2 FSI-Benchmarks for NACA 4415

15.3.2.1 Introduction

With the growing possibilities of today's supercomputers the interest in Multiphysics simulations has increased in recent years. Such simulations require high computational power. This chapter presents a structural and aerodynamic analysis, coupled together by a fluid-structure interaction loop. The obtained simulation results have demonstrated the potential of the MpCCI software in Multiphysics simulations based on the flow around the NACA 4415 airfoil. The simulations showed the influence of oscillations and deflections on the flow structure over the airfoil.

Part of the STADYWICO project concerned "advanced rotor configuration": an intelligent active flow control system should be investigated using coupled multiphysics simulation.

A CFD simulation (performed by Fluent) and an FEA simulation (done using MSC.Nastran) are coupled through MpCCI.

The task proved to be extremely difficult due to the size of grids and the required computing resources. The industrial partner of the project within the task entitled "innovative rotor blades" suggested to use the NACA 4415 profile for the rotor blade.

The NACA 4415 is an asymmetrical airfoil. It has a maximum camber of 4% located 40% (0.4 chords) from the leading edge with a maximum thickness of 15% of the chord. This airfoil profile was used in the FSI simulations. The coupled airfoil simulations aimed at finding the optimal location of Retractable rod Vortex Generators (RrVG) on the airfoil.

15.3.2.2 FEA Model

The geometry of the structural model was created in Autodesk Inventor. The mesh and boundary conditions were generated using the SimXpert software, a pre-processing tool for MSC.Nastran. The option/functionality of OpenFSI type, necessary for proper configuration, and start of MpCCI is available by default in this software. Thanks to this feature, which occurs in the immediate neighborhood of the fluid, the Wetted Surface boundary condition can be imposed on the surfaces. On that surface, the data between cooperating solvers are exchanged. Figure 15.15a shows the mesh of the structural model.

The 3D grid of the structural model of the airfoil has been created with CTETRA (Four-Side Solid Element) solid element. The CTETRA element, which is used widely to model complicated systems (i.e., extrusions with many sharp turns and fillets, turbine blades), is presented in Fig. 15.15b. The surface of the whole model, except the fixed end (surface on the left), is defined as the Wetted Surface boundary condition and can be selected as a coupling component. In Case C1 aluminum has been selected as the material of the airfoil. In the two remaining cases, C2 and C3, the Young's modulus was changed from that of aluminum in order to obtain a more elastic airfoil. The parameters of the examined solids are presented in Table 15.1.

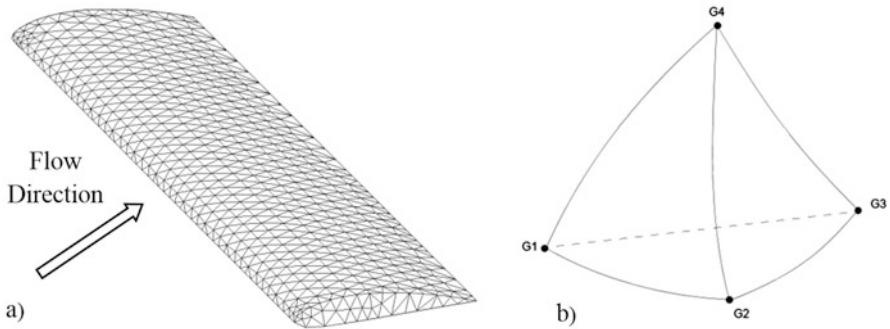


Fig. 15.15 (a) Mesh of the structural model, (b) Solid element

Table 15.1 Solid parameters

Case	C1	C2 and C3
Material	Aluminum	No aluminum
Density	2710 kg/m ³	2710 kg/m ³
Young's modulus	70 GPa	7 GPa
Poisson's ratio	0.346	0.346
Span	1 m	1 m
Chord length	0.204 m	0.204 m

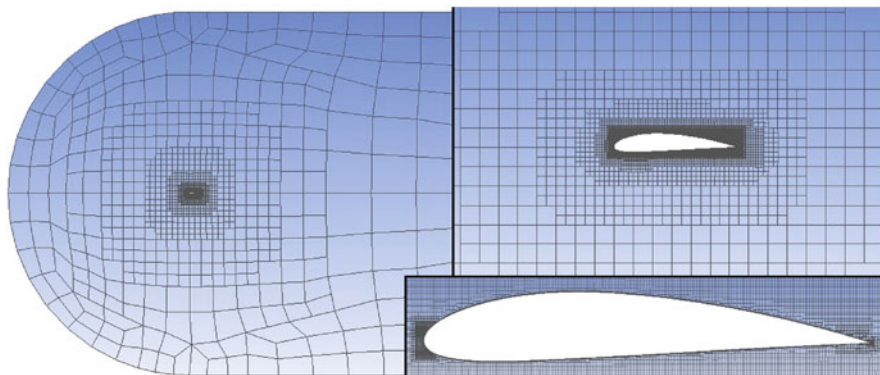


Fig. 15.16 Unstructured mesh around the profile

15.3.2.3 CFD Model

The initial CFD simulations were performed on the 2D model in order to assess the ability of the CFD code to predict the structure of the flow around the airfoil and to perform validation (comparison with the experimental data (Gregorek et al. 1995)). The unstructured grid of the 3D model, created with hexahedral elements, is presented in Fig. 15.16. The mesh was generated by Hexpress/NUMECA.

The designed mesh consists of 4.4 millions of cells. The Reynolds number based on the chord length of the airfoil cross section and free-stream flow conditions was set to $1.0 \cdot 10^6$ for case C1 and to $2.0 \cdot 10^6$ for cases C2 and C3. The one-equation Spalart–Allmaras turbulence model was used. The boundary conditions were set up using the pressure-far-field, which makes use of characteristic pieces of information to determine the flow variables at the boundaries. The pressure-far-field conditions are used to model the free-stream condition at infinity. Furthermore, the ideal gas assumption and the Sutherland formula for viscosity were used.

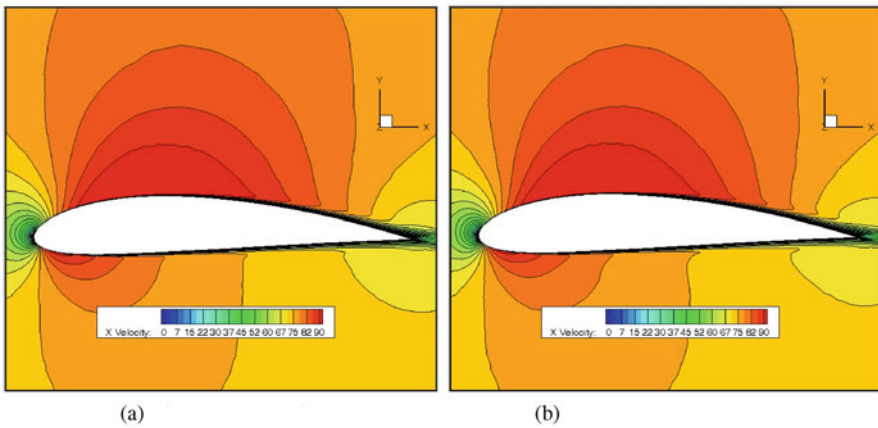
The mesh resolution near the solid wall boundaries was assumed in such a way that y^+ was approximately equal to one. The values of the coefficients are comparable with those from the 2D simulation and the experiment (Gregorek et al. 1995). Detailed boundary conditions are presented in Table 15.2. The computations were performed for an unsteady state and for the time step size depending on material parameters of the FE model. In all cases the flow is in the X direction.

15.3.2.4 FSI Simulation of Airfoil

In the further analysis of the results we will focus mainly on qualitative differences between the flow pattern with and without airfoil deflection. The applied flow control devices (like vortex generators) had fixed positions and changes in the structure of the flow on the surface of the airfoil might affect their performance.

Table 15.2 Boundary conditions of the flow

Case	C1	C2	C3
Static pressure	101 325 Pa	101 325 Pa	101 325 Pa
Mach number	0.216	0.432	0.432
Temperature	300 K	300 K	300 K
Span (R)	1 m	1 m	1 m
Chord length	0.204 m	0.204 m	0.204 m
Angles of attack (AoA)	0°	16°	16°
Reynolds number	$1.0 \cdot 10^6$	$2.0 \cdot 10^6$	$2.0 \cdot 10^6$

**Fig. 15.17** Case C1, X velocity contours at 75 % of span. (a) Without deformation. (b) with maximal deformation

Case C1

The first case was analyzed for material parameters which characterize aluminum. It is a relatively inflexible material. The time step size was equal to $t = 2 \cdot 10^{-5}$ s and the angle of attack was equal to $\text{AoA} = 0^\circ$. For such angle of attack, flow conditions, and solid parameters of airfoil the maximal displacement of the airfoil tip was not very significant (1.7mm). Therefore, the effect of the airfoil deformation on the flow structure was minimal. Figure 15.17 presents X velocity contours for the airfoil without deformation (a) and for the maximal deformation of the airfoil (b).

The detailed analysis of the deformation of the airfoil is presented in Figs. 15.18, 15.19, 15.20, and 15.21. As can be seen from Figs. 15.18 and 15.19, due to certain flexibility of the airfoil the tip starts to move under the influence of aerodynamic load. For the case with zero value of the angle of attack, at the beginning the leading edge of the airfoil goes down and then starts to go up, similarly to the trailing edge. The non-synchronized movement of the edges generates the torque along the airfoil. Figure 15.20 shows these differences directly. The deflections of the airfoil trailing edge are bigger than those of the leading edge.

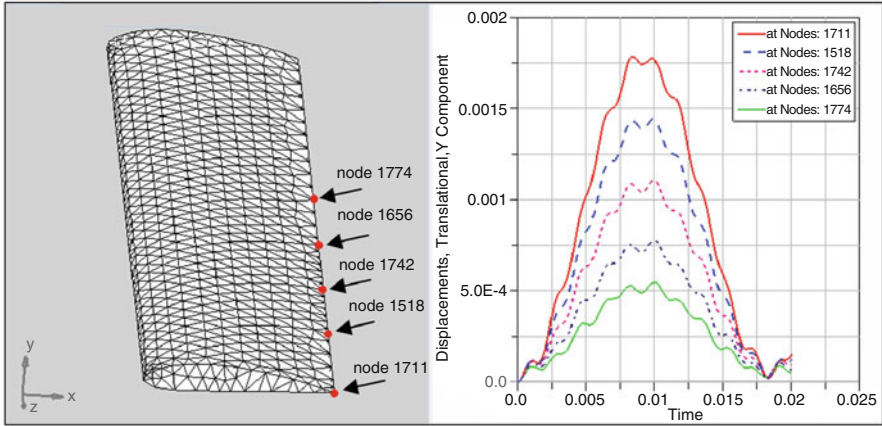


Fig. 15.18 Case C1, displacements of nodes on the airfoil trailing edge in Y direction

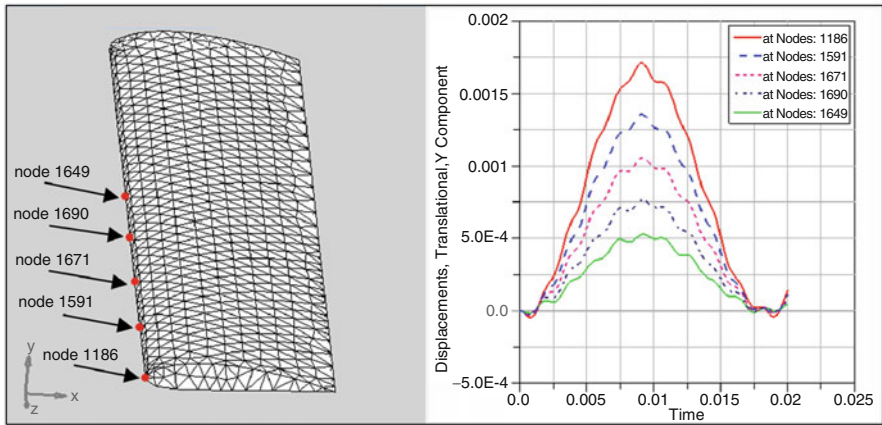


Fig. 15.19 Case C1, displacements of nodes on the airfoil leading edge in Y direction

Figure 15.21 presents oscillations of nodes on the airfoil tip in X direction (flow direction). Furthermore, these deflections occur at different points of time, which leads to instantaneous changes of the angle of attack. Figure 15.22 shows the von Mises stress tensor of the airfoil due to the flow. The areas of maximum values are located near the fixing of the airfoil. The Von Mises equivalent stress criterion is used by engineers to check whether the designed construction will withstand a given load.

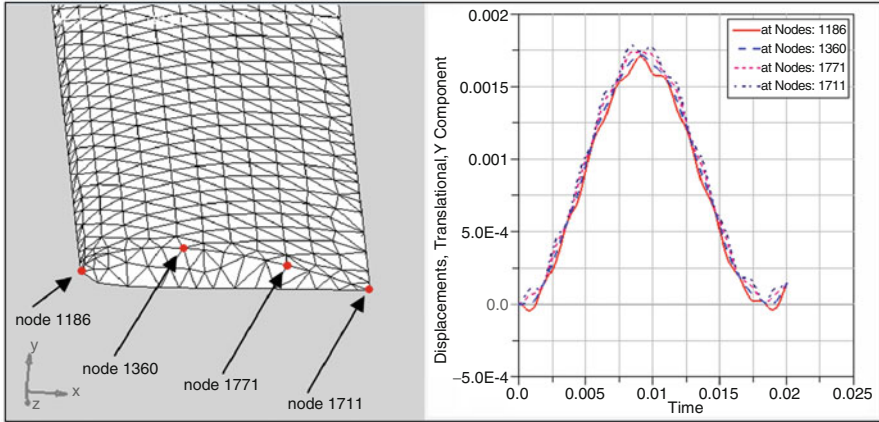


Fig. 15.20 Case C1, displacements of nodes on the airfoil tip in Y direction

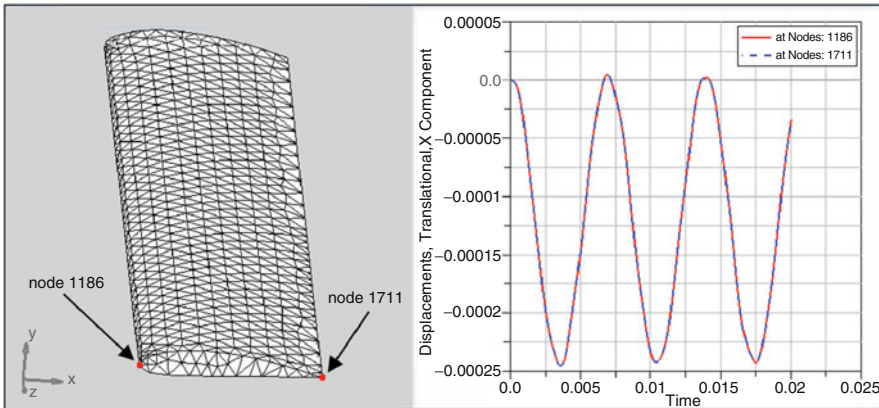


Fig. 15.21 Case C1, displacements of nodes on the airfoil tip in X direction

Case C2

The second case C2 was for the material the Young’s modulus of which was changed in order to obtain more elastic airfoil. The time step size was equal to $t = 5 \cdot 10^{-6}$ s and the angle of attack was equal to $AoA = 16^\circ$. In this case the maximal displacement of the airfoil tip was equal to 5.4 mm.

Figure 15.23 presents X velocity contours in the cross section situated at the distance of 0.25R from the airfoil tip. We can see a small flow separation a little ahead of the trailing edge. More insight into the flow structure is given in the next figures. Figures 15.24 and 15.25 present the cross sections for the same position but

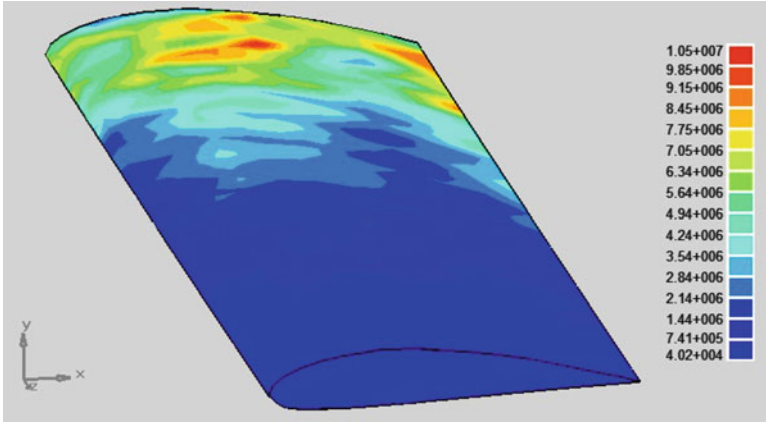
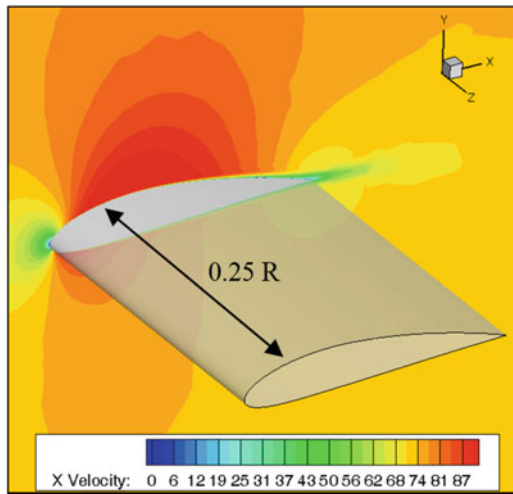


Fig. 15.22 Case C1, Von Mises stress tensor for maximum tip deflection

Fig. 15.23 Case C2, X velocity contour at 75% of span



different time points. The black horizontal line indicates the level $y = 0$ in order to visualize the movement of the airfoil. We can see some changes in the contours in Figs. 15.24 and 15.25 for the deflected airfoil. As the time passes, the separation formed at the airfoil trailing edge begins to increase.

The displacement of the stagnation point is shown in Fig. 15.25. The observed changes in the position of the stagnation point confirm the appearance of local changes of the angle of attack. These changes depend on the time and distance from the clamping point of the airfoil.

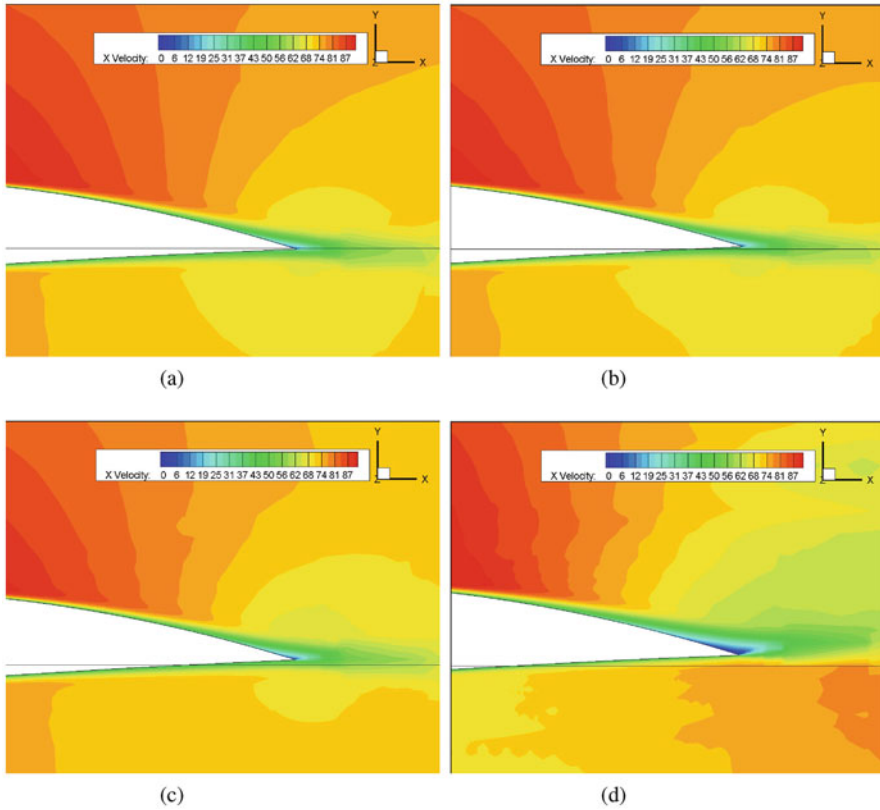


Fig. 15.24 Case C2, X velocity contours and trailing edge displacement. (a) $t = 0.1012$ s. (b) $t = 0.1044$ s. (c) $t = 0.1084$ s. (d) $t = 0.1122$ s

Case C3

In this case, the Young's modulus of the material was the same as in Case C2. The time step size was equal to $t = 4 \cdot 10^{-6}$ s and the angle of attack was equal to 16° . The main object in this case was to obtain larger deflection of the airfoil and to examine the effect of this deflection on flow separation. In this case the maximal displacement of the airfoil tip was equal to 11 mm. Figure 15.26 compares static pressure contours on the deformed airfoil (FSI simulation) and the undeformed airfoil (CFD simulation). Despite the fact that the differences are small, we can see that the instantaneous angle of attack of the airfoil tip changes.

The greatest flow separation for this case and conditions appears in the middle of the airfoil. Figure 15.27 presents X velocity contours for the section situated at 50% of span.

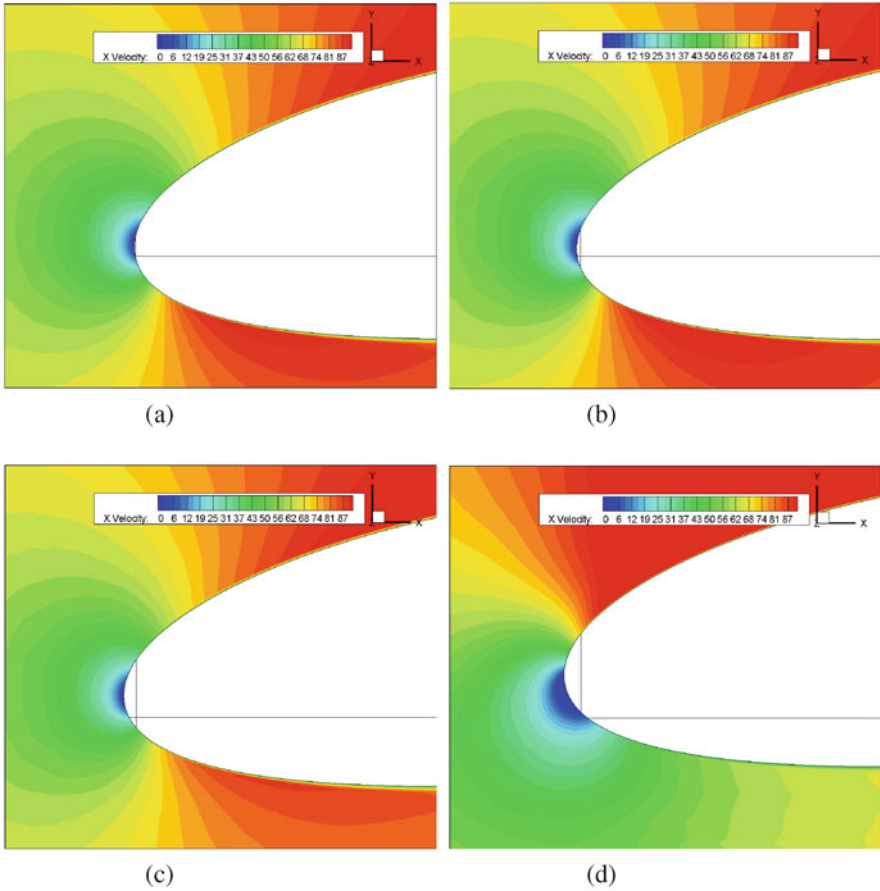
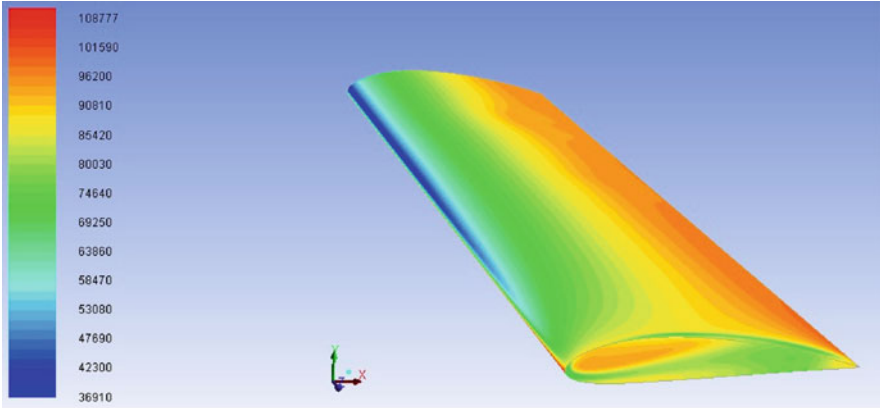


Fig. 15.25 Case C2, X velocity contours and leading edge displacement. (a) $t = 0.1012$ s. (b) $t = 0.1044$ s. (c) $t = 0.1084$ s. (d) $t = 0.1122$ s

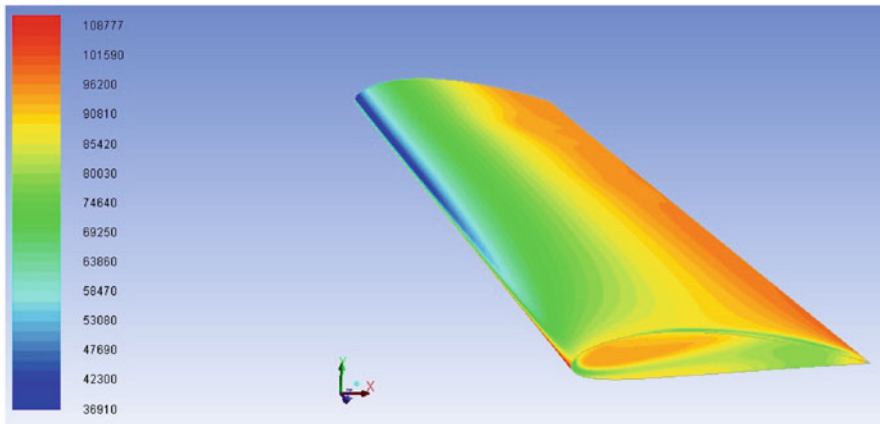
Figure 15.28 presents positions of tip cross sections of the airfoil without deformation (blue line) and for the maximal airfoil deformation (red line). For this case, the airfoil deflection in the flow direction is clearly visible and is equal to 3 mm.

15.3.2.5 Summary

The task proved to be extremely difficult due to large sizes of the used grids and the required computing resources. The obtained results have shown that the calculations are very sensitive to the time step size. Cases of bigger airfoil tip displacements require smaller time step sizes. Although the flow grid contained only 4.4 millions



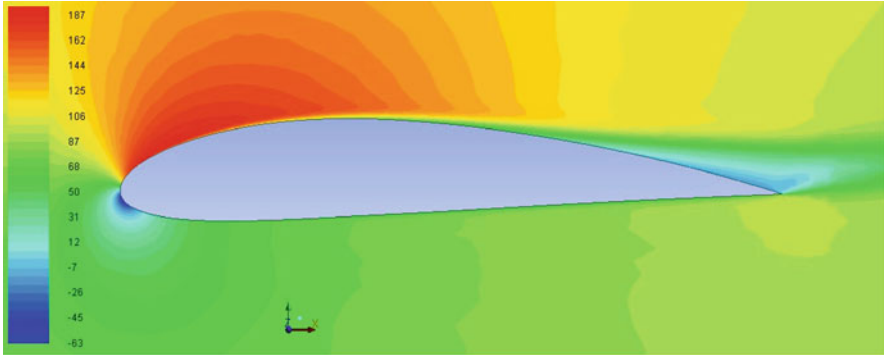
(a)



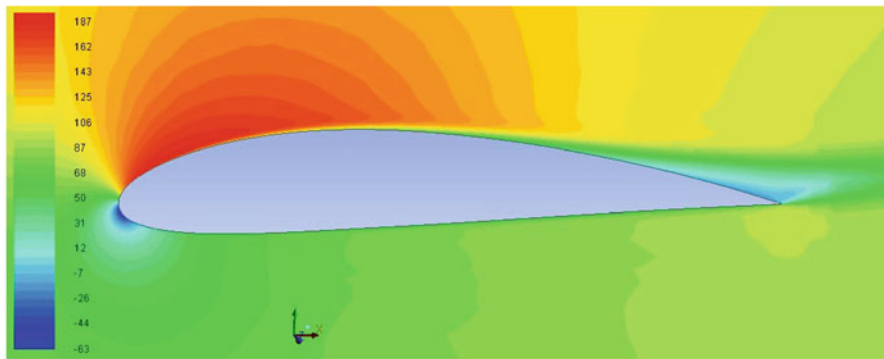
(b)

Fig. 15.26 Case C3, static pressure contours on the airfoil. (a) Undeformed airfoil. (b) Deformed airfoil

cells, this part of computation required large computing resources. The simulations showed that oscillations and deflections of the airfoil due to aerodynamic effects generate instantaneous changes of the angle of attack of the airfoil. Consequently, the flow control devices are likely to be influenced by changes of the torque which acts on the airfoil.



(a)



(b)

Fig. 15.27 Case C3, X velocity contours at 50 % of span. (a) Undeformed airfoil. (b) Deformed airfoil

15.3.3 *Airfoil FSI Optimization Using a Coupled Fluent-MpCCI-MATLAB Workflow in modeFRONTIER*

15.3.3.1 Introduction

In this paper a coupled FSI simulation is used as a solution block within an optimization task. In particular, the aim of this work is to optimize the performance of airfoils for small size propelled aircraft, performing an aero-elastic simulation.

The article is based on Cecutti (2015).

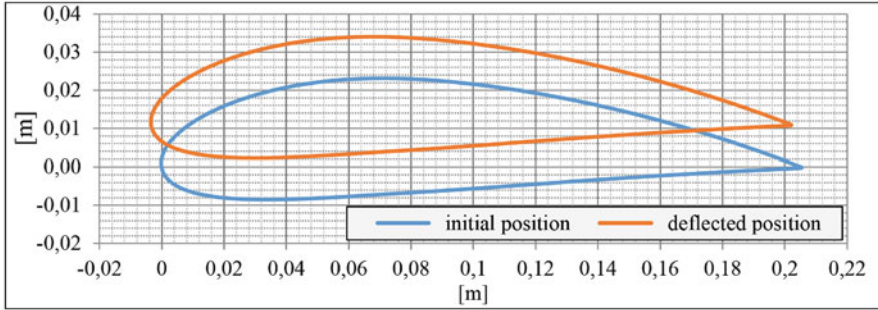


Fig. 15.28 Case C3, positions of airfoil cross sections

Airfoil Performance

Performances of airfoils are given by the forces that are generated when they are exposed to a fluid flow. In particular, the most important forces to be considered are the following:

- *Lift force L* : this is the force orthogonal to the oncoming flow direction. In the case of aircraft, it is the force allowing them to fly.
- *Drag force D* : this force is parallel to the oncoming flow. It always opposes to the direction of the flight, and is responsible for the biggest part of fuel consumption.

Writing these two forces in their dimensionless forms, the lift and drag coefficients (C_L and C_D) are obtained. Lift and drag coefficients are independent from size and fluid dynamic factors when similar flows are considered, and therefore are more suitable to describe airfoil performances.

Target of this Optimization Work

The present optimization work is meant to find the airfoil geometry providing the best possible performance. The two following objectives are considered:

- Maximization of the lift coefficient
- Minimization of the drag coefficient.

For the evaluation of these coefficients, the aero-elastic deformation of the wing structure given by the fluid flow is considered during the simulation. Such interaction can, on the one hand, make the airfoil reach an equilibrium position, leading to a stable behavior, or, on the other hand, cause vibration and divergence. For safety reasons, several constraints are applied in order to avoid unstable configurations or excessive deformations.

Considering the multi-objective nature of the optimization, the expected result is not a single optimal airfoil, but rather the set of best compromises between the two objectives: this set of solutions takes the name of Pareto front.

15.3.3.2 Optimization Workflow and Design Space

The optimization is organized by the software modeFRONTIER which is a mono- and multi-objective optimization tool, capable of providing optimized solutions for a broad range of engineering problems. In order to find the maxima or minima of the objective function, modeFRONTIER applies optimization algorithms to iteratively suggest promising wing geometries. For each chosen geometry, the performance (building the objectives) is examined. This builds two loops:

- Optimization loop, handled by modeFRONTIER
- FSI loop, handled by MpCCI CouplingEnvironment

where the optimization loop is external and contains the FSI loop.

In the FSI loop, the aero-elastic simulation is carried out to evaluate the performance of a single airfoil shape.

The overall interaction of the programs adopted is represented in Fig. 15.29.

Optimization Workflow

The workflow which is run through in each optimization iteration is shown in Fig. 15.30. Due to the presence of many blocks, it appears complicated, but four fundamental nodes can be observed:

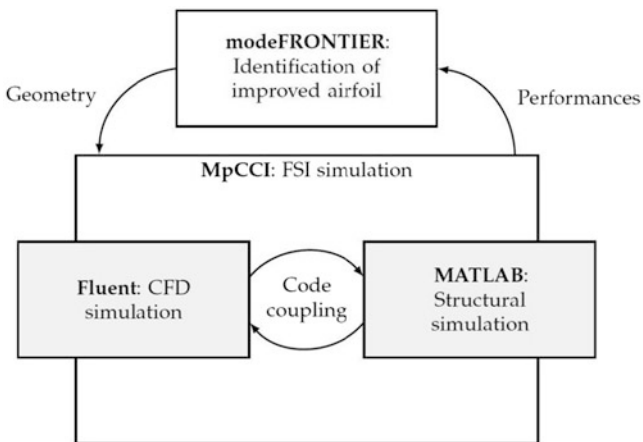


Fig. 15.29 Interactions among the programs adopted, cf. Cecutti (2015)

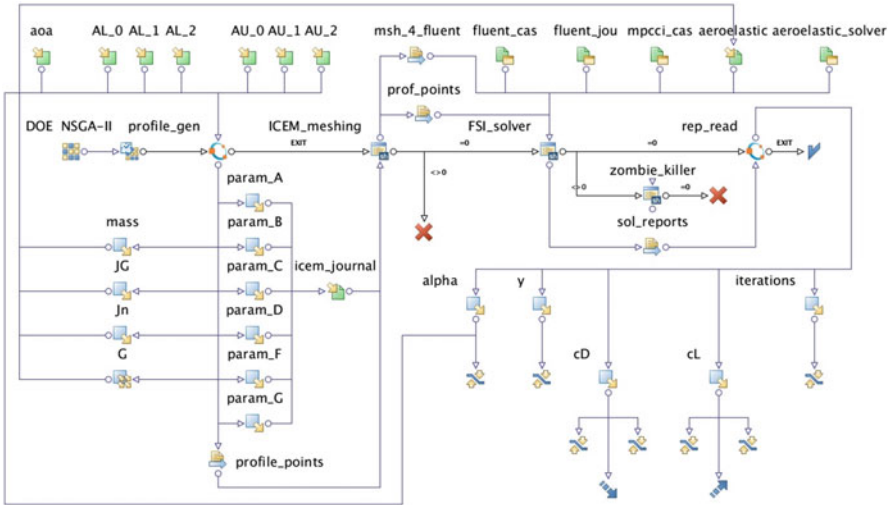


Fig. 15.30 FSI optimization workflow, cf. Cecutti (2015)

- profile_gen_block: the airfoil surface is built, starting from given values of the geometric parameters
- ICEM_meshing_block: the mesh around the airfoil is generated
- FSI_solver_block: the aero-elastic simulation is accomplished
- rep_read_block: the results from the FSI simulation are read.

Design Space and Geometric Parametrization of the Airfoil Shape

To efficiently represent the design space in a parametric way, the CST (Class/Shape Transformation) method is adopted (cf. Kulfan 2008). This method is chosen for its flexibility and its capability to provide smooth airfoil shapes in an intuitive way. The CST method represents the typical 'round nose/sharp aft end' geometry of low speed airfoils (cf. Fig. 15.31) with the following equation:

$$\zeta(\psi) = \sqrt{\psi} \cdot (1 - \psi) \cdot f(\psi)$$

where

- $\psi \in [0, 1]$ is the normalized x coordinate
- ζ is the normalized y coordinate
- $\sqrt{\psi}$ provides the round nose at the leading edge
- $(1 - \psi)$ provides a sharp trailing edge
- $f(\psi)$ is a general analytic function describing the airfoil shape.

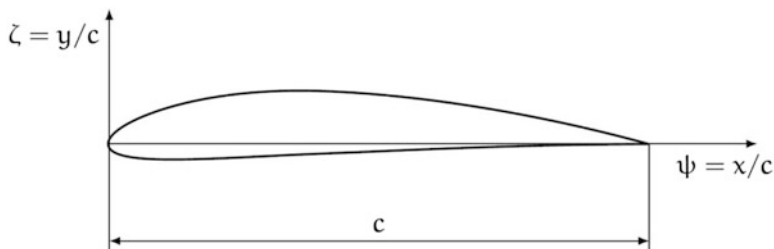


Fig. 15.31 Round nose/sharp aft end airfoil geometry, cf. Cecutti (2015)

15.3.3.3 The FSI Loop

The FSI loop calculates the performance of a certain wing shape under consideration of the steady wing deflection (translational and rotational). This fluid–structure interaction is simulated by a coupling between the CFD simulation tool Fluent and MATLAB where the solution of the structural equations of motion are computed. At run-time the wing deformation and the fluid forces are iteratively exchanged until a convergent equilibrium is reached.

The CFD Simulation

The flow around the airfoil is simulated by Fluent solving the two-dimensional incompressible isothermal steady state Reynolds-averaged Navier–Stokes equations. The computation is performed on a *C-type far field shape* domain around the airfoil, see Fig. 15.32a. The mesh (cf. Fig. 15.32b) is built by a dynamic blocking procedure, which takes the airfoil shape into account. The $k - \epsilon$ -turbulence model with the Kato-Launder correction is used.

The mesh deformation due to translational and rotational wing movement during the coupling is handled by a mesh smoothing in Fluent.

The Structural Simulation

The wing structure is modeled as a two degree of freedom system (translation y , rotation α) as shown in Fig. 15.33b, where the wing's cross section is rigid. The flexural and torsional stiffness of the cantilevered wing are represented by springs, whose stiffnesses k and k_t are developed by the linear beam theory and are dependent on the section's moment of inertia.

The flexural and torsional damping coefficients are defined by the damping ratio and the systems critical damping.

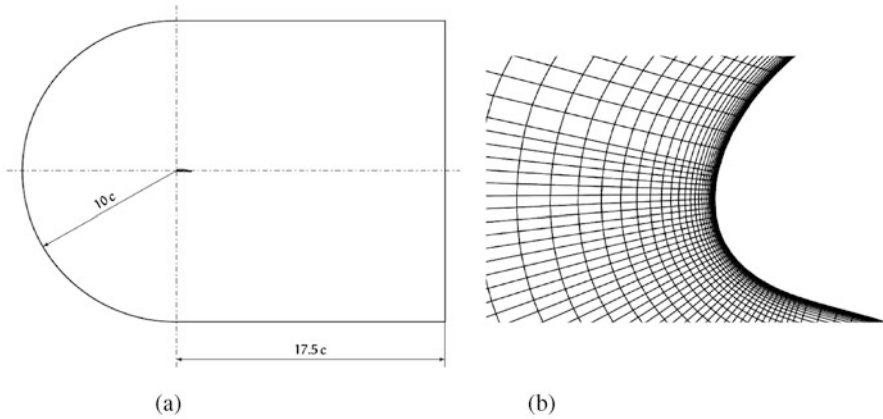


Fig. 15.32 CFD mesh. (a) CFD domain. (b) Mesh at airfoil's leading edge, cf. Cecutti (2015)

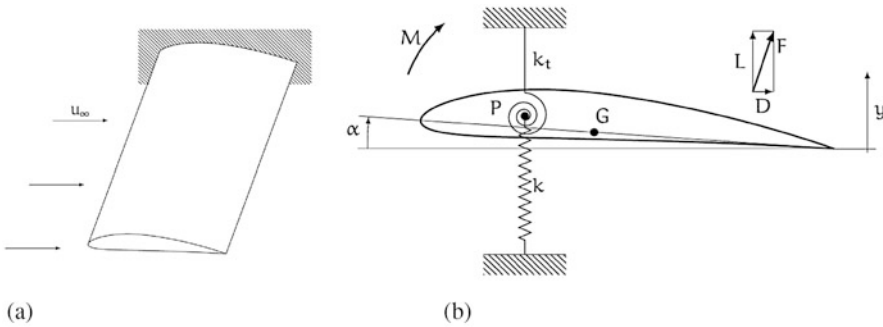


Fig. 15.33 Structural wing modeling. (a) Cantilevered wing geometry. (b) Model of two-dimensional wing, cf. Cecutti (2015)

The transient equations of motion are solved by MATLAB. The external load is provided by the resulting surface loads (force $F = L + D$ and moment M) acting on the wing in the fluid flow.

The Coupled Simulation

The FSI analysis is carried out through an iterative process. Here, the two solvers are run in parallel and periodically exchange the necessary information (cf. Fig. 15.34).

The layout of the information exchange has a deep influence on both the quickness and the accuracy of the calculation. In fact, a too frequent information exchange may lead to more accurate results, but dramatically slows down the calculation; conversely, a low information exchange frequency speeds up the simulation, but may spoil the reliability of the results.

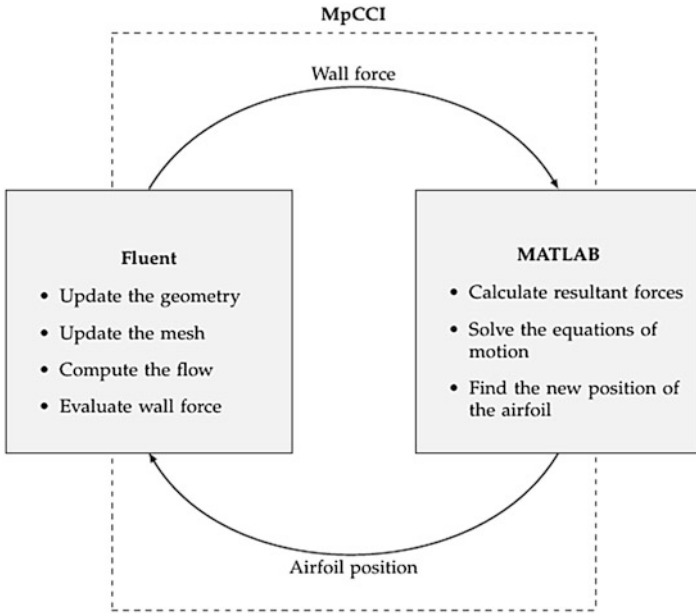


Fig. 15.34 Interaction between the solvers in the MpCCI framework, cf. Cecutti (2015)

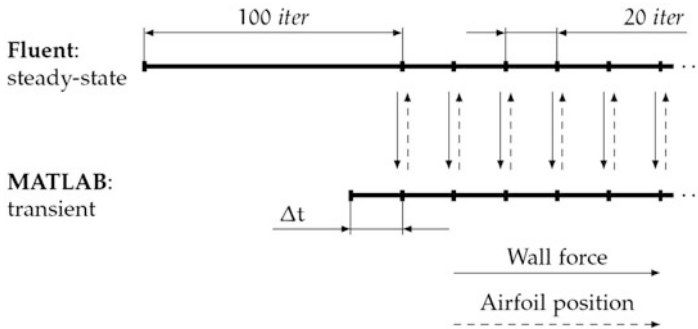


Fig. 15.35 Information exchange layout, cf. Cecutti (2015)

In Fig. 15.35, the chosen information exchange layout for this work is represented. A mixed steady state/transient approach for the overall FSI simulation is obtained by running a steady state fluid dynamic computation while performing a transient structural analysis. This method surely provides a quick computation, but requires caution in order to achieve the desired accuracy in the results.

The FSI simulation starts uncoupled, with Fluent performing 100 iterations. This strategy helps to start the coupling when the fluid flow is already well approximated. After the coupling starts, Fluent performs subcycling for a faster and smoother convergence.

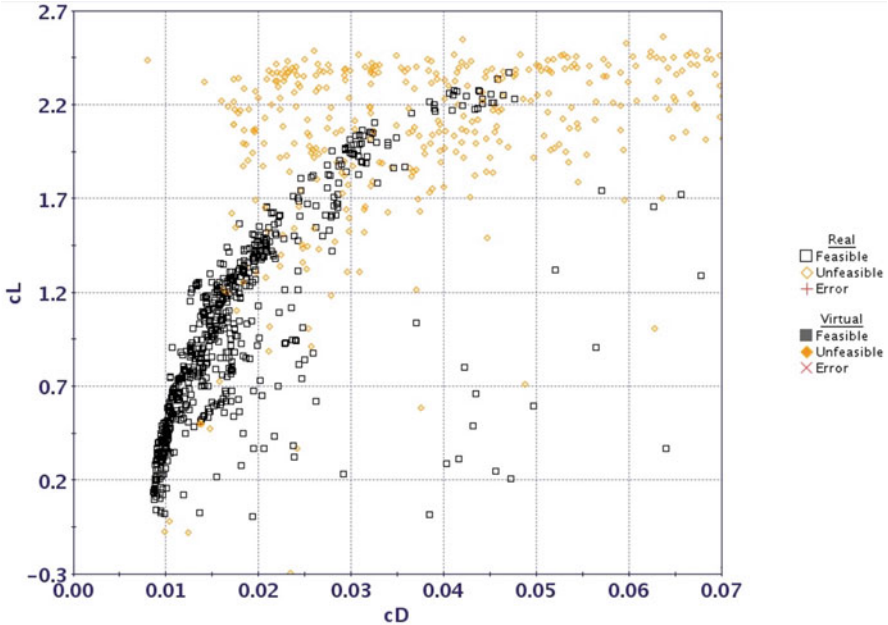


Fig. 15.36 Design scatter with respect to objectives, cf. Cecutti (2015)

15.3.3.4 Results of the Coupled Optimization Workflow

The optimization carried out in this work clearly identifies a Pareto front, as shown in Fig. 15.36. The front obtained has 61 valid designs. By analyzing the airfoil shapes on the Pareto front, the following general trend can be observed:

- Low C_L and C_D zone: here, airfoils with low thickness, camber, and angle of attack can be noticed. These shapes can be commonly seen on light and ultra-light aircraft. An example is shown in Fig. 15.37a.
- High C_L and C_D zone: in this zone, the airfoils assume high angles of attack and cambered shapes, looking like wings with extended flaps, as shown in Fig. 15.37b. Such airfoil shapes are not suitable to the considered speed, therefore big displacements and instabilities are often reached. In order to provide feasible designs, thick airfoil shapes are generated by modeFRONTIER.

15.3.4 Static Deformations and Vibrations of Turbine Blades

In turbomachinery, the pressure field deforms the blades of the stationary guide vanes and the rotating blades. Moreover, due to interactions between rotating and

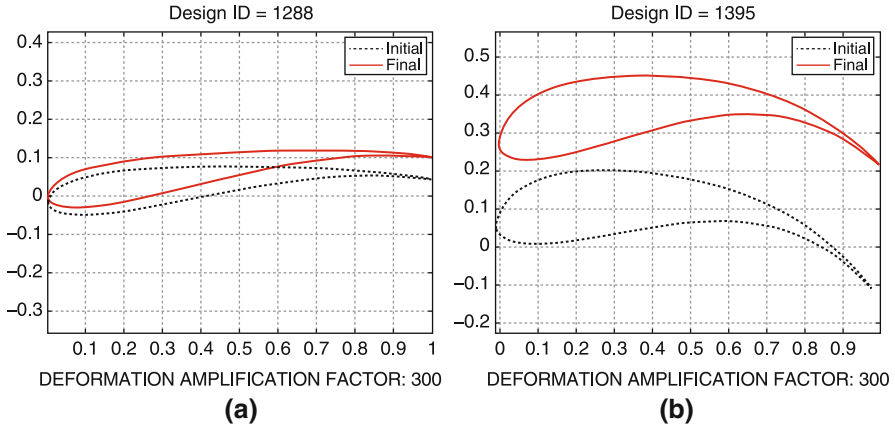


Fig. 15.37 Two different airfoil shapes on the Pareto front. (a) Design 1256: $C_L = 1.22$, $C_D = 1.28 \cdot 10^{-2}$. (b) Design 1395: $C_L = 2.37$, cf. Cecutti (2015)

stationary turbomachinery components, the transient fluid flow is characterized by periodic pressure fluctuations. Those oscillations excite vibrations of the blades.

For a first assessment of the static deformation and the vibration amplitudes of the blades, the static pressure and the pressure excitations, which are the result of a harmonic CFD simulation, are mapped by MpCCI FSIMapper to a structural model. In a subsequent structural simulation, the blade's deformation and oscillation is calculated, where the latter is done in the frequency domain.

15.3.4.1 Problem Description

The considered turbine configuration is shown in Fig. 15.38. The flow passes radially 13 stator blades. The 14-bladed rotor is turned by the relaxing gas which leaves the turbine in the axial direction. Further information about the example and the methodological background can be found in Wirth and Oeckerath (2015).

The static deformation and the blade vibrations of the rotor are to be calculated. The corresponding simulation and mapping workflow is shown in Fig. 15.39.

15.3.4.2 CFD Simulation

A possibility of approximating the transient steady state behavior of the flow field is a finite Fourier decomposition into periodic oscillations as developed by He (2010) and He and Ning (1998). This approach is used in the Nonlinear Harmonic (NLH) method implemented in Numeca's turbine simulation software FINE/Turbo (Vilmin et al. 2006). It decomposes, e.g., the pressure $p(\mathbf{r}, t)$ at position \mathbf{r} and time t into the time-averaged pressure $\bar{p}(\mathbf{r})$ and periodic fluctuations around this mean value.

Fig. 15.38 Considered turbomachinery configuration vibrations, cf. Wirth and Oeckerath (2015)

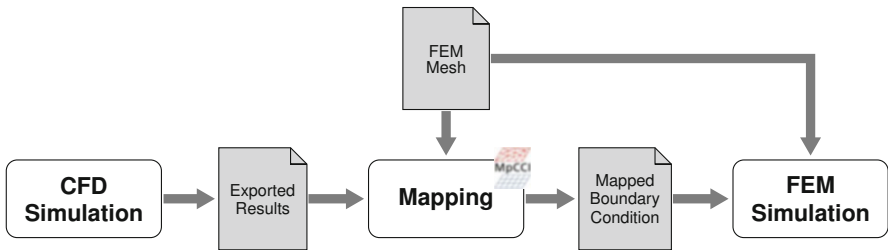
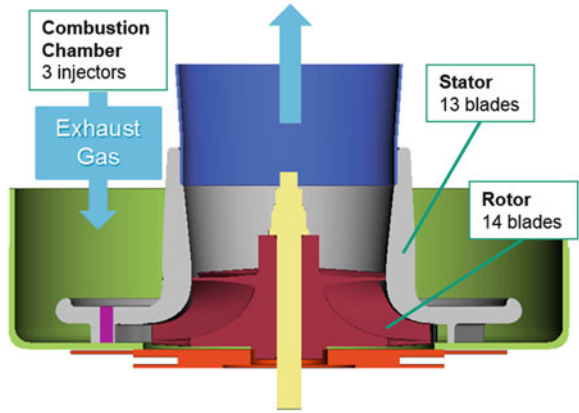


Fig. 15.39 Simulation workflow for the calculation of flow-induced deformations and vibrations

The periodic oscillations are split into K frequency terms which correspond to multiples of the blade passing frequency ω , also called harmonics [see Eq. (15.3)].

$$p(\mathbf{r}, t) = \bar{p}(\mathbf{r}) + \sum_{\substack{k=-K \\ k \neq 0}}^K \tilde{p}_k(\mathbf{r}) \cdot e^{ik\omega t} \quad (15.3)$$

The factor $\tilde{p}_k(\mathbf{r}) \in \mathbb{C}$ denotes the complex amplitude of the k -th harmonic pressure. It can be reformulated as magnitude and phase lag (using Euler’s formula) of the pressure oscillation at frequency $k \cdot \omega$ which excites blade vibration. The time-averaged variable $\bar{p}(\mathbf{r})$ corresponds to the static pressure load. The reader is referred to Vilmin et al. (2006) for a more detailed explanation of the NLH method.

In the present example, the harmonic CFD simulation is performed on a structured hexa mesh of one periodic rotor and stator blade passage with the blade passing frequency $\omega = 20.8$ kHz. The static pressure and the first $K = 3$ pressure harmonics are computed (magnitudes see Fig. 15.40) which together approximate the transient pressure behavior.

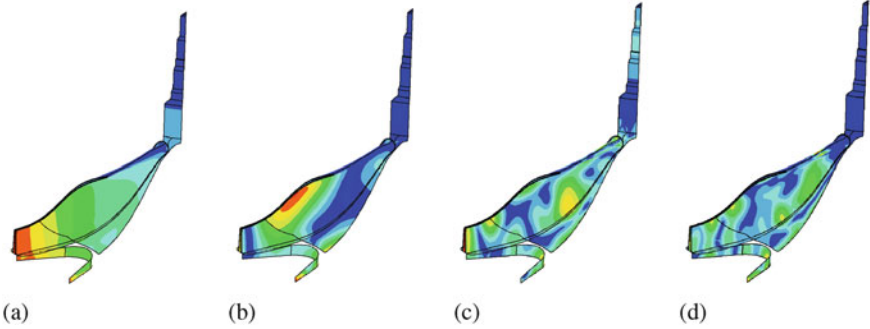


Fig. 15.40 Mean pressure \bar{p} and the first three harmonic pressure magnitudes $\|\tilde{p}\|$ as a result of the Nonlinear Harmonic method in FINE/Turbo. (a) time-averaged pressure. (b) 1. harmonic pressure at $\omega_1 = 20.8$ kHz. (c) 2. harmonic pressure at $\omega_2 = 41.6$ kHz. (d) 3. harmonic pressure at $\omega_3 = 62.4$ kHz, cf. Wirth and Oeckerath (2015)

15.3.4.3 Mapping

The static pressure \bar{p} and the three pressure excitations $\tilde{p}_k \in \mathbb{C}$, $k = 1, 2, 3$ are mapped by MpCCI FSIMapper to the wetted surface of a structural periodic model of the rotor. The section is meshed by second-order tetra elements and it exhibits planar cutting faces and thus comprises parts of two adjacent blades, cf. Fig. 15.42.

Since the CFD and the FEA mesh do not coincide geometrically, the corresponding full model data of the CFD result is created using the periodicity information. In this way, the data is provided on the whole wetted surface of the periodic target mesh.

The static pressure is revolved by copying the data from section to section. To provide the complex data $d^{(1)} \in \mathbb{C}$ —representing the magnitude and phase of an oscillation—from a periodic model to the remaining sectors $s = 2, \dots, n$, Eq. (15.4) is applied (He 2010; Wildheim 1981a,b,c).

$$d^{(s)} = e^{-i(s-1)\sigma_{\text{ND}}} \cdot d^{(1)} \quad (15.4)$$

The oscillation experiences a temporal phase shift, the inter-blade phase angle:

$$\sigma_{\text{ND}} = \pm \frac{2\pi \cdot \text{ND}}{n} \quad (15.5)$$

This blade-to-blade phase difference is dependent on the data's nodal diameter $0 \leq \text{ND} \leq \lfloor \frac{n}{2} \rfloor \in \mathbb{N}$ which is derived by the turbomachinery configuration, see Wildheim (1981a,b,c).

The specific inter-blade phase angles σ_{ND} of the three harmonic pressure fields are listed in Table 15.3.

Table 15.3 Inter-blade phase angles of the harmonic pressure fields

k	ND	σ_{ND} [°]
1	1	25.71
2	2	51.43
3	3	77.14

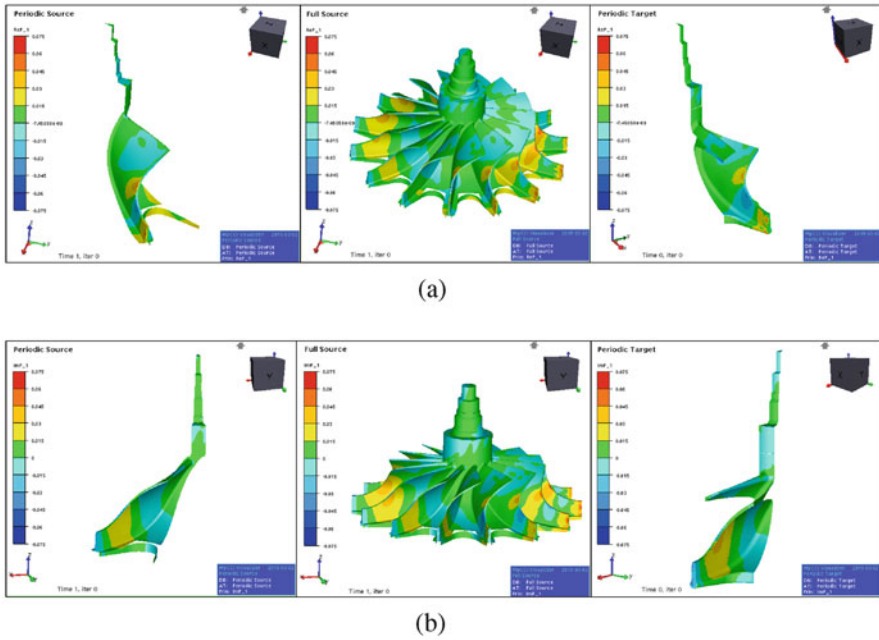


Fig. 15.41 Cyclic symmetry mapping procedure demonstrated for the first harmonic pressure with MpCCI FSIMapper. The data on the periodic source model (*left*) is “rotated” using the inter-blade phase angle to build the full source mesh (*middle*). These data are mapped to the periodic target model (*right*) (a) Real part. (b) Imaginary part, cf. Wirth and Oeckerath (2015)

With Eq.(15.4) and Table 15.3, the three harmonic pressure fields are revolved to the full source model and are mapped to the structural mesh. The visualization of the mapping process of the first pressure harmonic is shown in Fig. 15.41.

The mapping process exports loading files comprising the static pressure and the three pressure harmonics defined for the surface of the structural mesh. The three pressure excitations are defined by the real and imaginary part of their complex amplitude.

15.3.4.4 FEA Simulation

Since structural vibration analyses work in the frequency domain and thus the exciting load needs to be given as frequency dependent complex data, harmonic

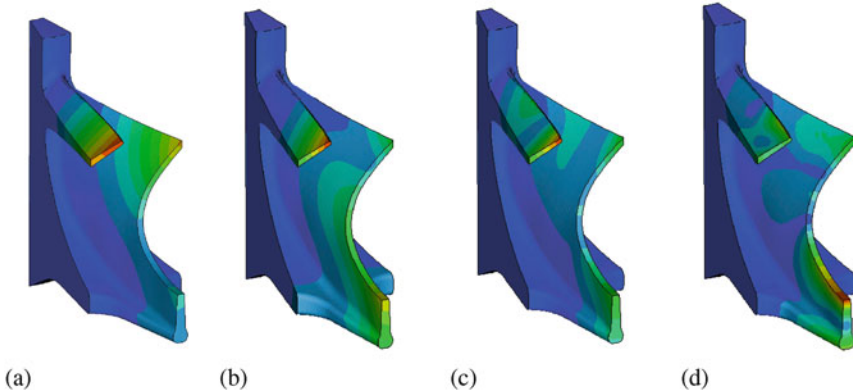


Fig. 15.42 Magnitude of resulting displacements for the time-averaged pressure and the first three pressure harmonics. Color range scaled to the particular maximum. Simulation result of frequency response analysis in Abaqus. **(a)** Time-averaged deformation. **(b)** 1. harmonic deformation at $\omega_1 = 20.8$ kHz. **(c)** 2. harmonic deformation at $\omega_2 = 41.6$ kHz. **(d)** 3. harmonic deformation at $\omega_3 = 62.4$ kHz, cf. Wirth and Oeckerath (2015)

CFD results meet by definition the demands on the loading for those analyses. In the case of transient CFD results, the pressure fluctuations can be transformed by the Fourier decomposition to meet that requirement.

First, the static deformation of the blades are computed, taking into account the mapped time-averaged pressure. The result is shown in Fig. 15.42a. The maximal deformation caused by the mean pressure is located in the blade tip at trailing edge (near outlet).

Based on the static result, three frequency response analyses are performed, each for a different harmonic pressure excitation. The deformation magnitudes are shown in Fig. 15.42, where each color range is scaled to its maximal amplitude.

15.3.4.5 Summary

In this turbomachinery example, the static and the dynamic deformation of the rotor blades induced by the steady state fluid flow has been simulated. The pressure load has been calculated by a harmonic CFD simulation, whose result consists of a time-averaged pressure \bar{p} and three harmonic pressure fields \tilde{p}_k . The harmonic pressures are represented by scalar complex fields, which are equivalent to pressure oscillations at the corresponding frequency $k \cdot \omega$ with a certain magnitude and phase shift. The CFD results have been mapped by MpCCI FSIMapper to a structural periodic model of the rotor. Since the periodic section of the source and the target model did not coincide geometrically, the data of the source mesh was revolved in order to produce the data of the full rotor. For static and dynamic loading, different algorithms apply. With the exported include files consisting of the static and the dynamic loading acting on the wetted surface of the structural mesh, the deformation and vibration simulation has been performed.

15.4 Conclusion and Outlook

The examples in this article showed how coupled CFD and FEA tools can be used to analyze typical applications in aircraft design and turbomachinery:

- Within benchmarks for **High Reynolds Number Aerostructural Dynamics** (HIRENASD) applications the coupled Fluent-MSC.Nastran setup showed a good conformity with measurement data from experiments.
- In a second case a NACA 4415 airfoil was modeled—the simulations showed that oscillations and deflections of the airfoil due to aerodynamic effects generate instantaneous changes of the angle of attack of the airfoil.
- An airfoil shape was optimized using a coupled Fluent-MATLAB simulation in a modeFRONTIER workflow.
- Finally in the fourth case static deformations and vibrations of turbine blades were modeled using a file-based mapping of harmonic pressure data.

In all four examples the vendor neutral interface MpCCI was used. MpCCI as an interface software tool set supports a high number of commercial simulation codes and comes with an open API that can be used to connect in-house codes to MpCCI. Because of the flexible setup—concerning the different supported coupling schemes and quantities—MpCCI can be adapted to many different requirements.

During the last years there has been an increasing demand for coupling CFD or FEA simulation codes with multi-body system simulation software. This might have interesting applications in the area of active flow control, e.g., when simulating the behavior of control elements on airplane wings or helicopter rotors. Also the possibility to couple with MATLAB allows to implement active flow controls.

The next versions of MpCCI CouplingEnvironment will focus on the automatic coupled part association between the two simulation codes—thereby saving a lot of manually setup work—and on new coupling algorithms. The currently available iteratively implicit transient coupling will be extended by a new implicit coupling method, implementing a Quasi-Newton method.

References

- Cecutti F (2015) Airfoil FSI optimization using a coupled fluent-MpCCI-MATLAB workflow in modeFRONTIER. Master's thesis, University of Trieste, Italy
- Gregorek GM, Reuss RL, Hoffmann MJ (1995) Effects of surface roughness and vortex generators on the NACA 4415 Airfoil. The Ohio State University, Columbus. NREL/TP-442-6472
- He L (2010) Fourier methods for turbomachinery applications. *Prog Aerosp Sci* 46(8):329–341
- He L, Ning W (1998) Efficient approach for analysis of unsteady viscous flows in turbomachines. *AIAA J* 36(11):2005–2012
- HIRENASD (2010) High Reynolds Number Aerostructural Dynamics - HIRENASD Project Page.<http://heinrich.lufmech.rwth-aachen.de/>. Accessed 05 Jan 2017
- Kulfan BM (2008) Universal parametric geometry representation method. *J Aircr* 45(1):142–158

- Landvogt B (2014) Coupled fluid-structure-interaction simulations for aero-elastic benchmark cases. In: Proceedings NAFEMS European conference on multiphysics simulation (Manchester, UK)
- MpCCI Manual (2015) Fraunhofer Institute for Algorithms and Scientific Computing SCAI, MpCCI 4.4.2 Documentation, Part V User Manual, <http://www.mpcci.de/content/dam/scai/mpcci/documents/MpCCIdoc.pdf>. Accessed 05 Jan 2017
- MpCCI Cpl (2017) MpCCI CouplingEnvironment, <http://www.mpcci.de/en/mpcci-software/mpcci-couplingenvironment.html>. Accessed 05 Jan 2017
- MpCCI Map (2017) MpCCI FSIMapper, <http://www.mpcci.de/en/mpcci-software/fsimapper.html>. Accessed 05 Jan 2017
- MpCCI Turbo (2017) MpCCI Turbomachinery Applications. <http://www.mpcci.de/en/application-areas/turbomachinery-applications.html>
- Vilmin S, Lorrain E, Hirsch Ch, Swoboda M (2006) Unsteady flow modeling across the rotor/stator interface using the nonlinear harmonic method, GT2006-90210. ASME Turbo Expo 2009: Power for Land, Sea and Air (Barcelona), vol 6, pp 1227–1237
- Wildheim J (1981a) Excitation of rotating circumferentially periodic structures. *J Sound Vib* 75(3):397–416
- Wildheim J (1981b) Excitation of rotationally periodic structures. *J Appl Mech* 46(4):878–882
- Wildheim J (1981c) Vibrations of rotating circumferentially periodic structures. *Q J Mech Appl Math* 34(2):213–229
- Wirth N, Oeckerath A (2015) Analysis of flow-induced vibrations in turbomachinery by mapping of complex fluid pressures. *Int J Multiphys* 9(2):195–208

Chapter 16

Numerical Simulation of Airflow and Acoustic Field Around a Passenger Car Model Using Euler Approach and Hybrid Meshing

Oskar Szulc and Piotr Doerffer

Nomenclature

Latin

c_d	Drag coefficient
f	Frequency [Hz]
L	Vehicle length [m]
OASPL	Overall Sound Pressure Level dB
p'	Acoustic pressure [Pa]
p'_{rms}	Root-mean-square of acoustic pressure [Pa]
Re	Reynolds number
T	Period [s]
V	Vehicle speed [km/h]

Greek

Δx	Grid spacing [m]
Δt	Time step [s]
λ	Acoustic wave length [m]

O. Szulc (✉) • P. Doerffer
Institute of Fluid-Flow Machinery, Gdańsk, Poland
e-mail: Oskar.Szulc@imp.gda.pl

Acronyms

CAA	Computational aeroacoustics
CAD	Computer-aided design
CFD	Computational fluid dynamics
DES	Detached eddy simulation
IMP PAN	Institute of Fluid-Flow Machinery, Polish Academy of Sciences
LES	Large eddy simulation
RMS	Root mean square
STADYWICO	STAtic and DYnamic piezo-driven streamWise vortex generators for active flow COntrol
URANS	Unsteady Reynolds-averaged Navier–Stokes

16.1 Introduction

Active flow control methods under research in the STADYWICO project (e.g., piezo-driven streamwise vortex generators) have not only impact on the aerodynamic performance but also significantly alter the level of generated noise. Therefore, it is important to include the acoustic predictions next to the structural and fluid flow analysis to increase the probability for future industrial applications. It has been proposed that by using recent achievements in CFD (e.g., hybrid grids) and high performance supercomputers, it is possible to directly resolve low-frequency part of the acoustic field generated by the flow of air past the complete passenger car without any need for additional modeling, connecting numerical simulation of fluid flow with propagation of the acoustic pressure fluctuations into the near-field. Using this method of simulation, the main sources of the aerodynamic noise are identified in the close proximity of the object, but no far-field propagation is resolved. The numerical model is general and allows for future analysis of influence of various new flow control methods and complex flow cases currently investigated at IMP PAN.

It is evident that a design of a passenger car is not only limited by the external styling and safety requirements. The airflow around the car body and various exterior accessories has significant impact on the fuel consumption, performance, and wind noise. Recently, passenger comfort is one of the most important automotive attributes for car manufacturers. The flow of air that causes aerodynamic noise affects directly passenger's comfort and requires specially designed methods of control. Numerical identification of the aerodynamic sources is considered as a necessary step in order to control the noise.

The wind noise is one of the major contributors to the overall acoustic signature of a car and becomes dominant on the exterior and in the interior above certain forward velocity V , usually close to 100 km/h (Gloerfelt 2009). Other sources coexist, i.e., engine with intake and exhaust ducts, gearbox, differential, tires, etc.

Two major sources of the external aerodynamic noise are rearview side mirrors (Nouzawa et al. 2011) and underbody of the car (Moron et al. 2011). A strong, unsteady vortex is shed from the mirror, traveling downstream, oscillating and exciting the side windows near the driver's and front passenger's heads causing high-frequency tonal components. On the other hand, the strongest acoustic pressure fluctuations are generated below the car by the underbody components (including wheelhouses), dominated by low-frequency contents and shielded from the passenger's compartment by the floor. Apart from side mirrors and underbody, other components of the car are known to have their contribution to the generated aerodynamic noise, i.e., roof antennas and carrier systems, door handles, windscreen wipers, sunroofs, open windows, and various tiny gaps (i.e., door gaps and rain gutters). Even the shear motion of the turbulent boundary layer over the windscreen and side windows is heard in the passenger compartment due to close location to passenger's ears.

16.2 Surface Model and Hole Searcher

The simplest nonlinear model of fluid flow, derived directly from mass, momentum, and energy conservation principles, allowing for density variations in time and sound wave propagation is based on the inviscid Euler equations. A numerical solution of this set of partial differential equations is much simpler than for more complicated models that include turbulence closures (e.g., URANS, DES, or LES) but still very demanding in terms of computing power and solution time for a detailed industrial car shape. The exemplary CAD model of Nissan 350z (Numeca International, Belgium) consists of more than 200 distinct surfaces (Fig. 16.1). This medium-size, exterior model of the vehicle contains majority of the car components that are known to have impact on the generated level of the aerodynamic noise. The largest surfaces, i.e., bonnet, roof, front and rear bumpers, doors, wheels, side windows, windshield, and fenders, are creating a basic shape. Additionally, medium-size surfaces, i.e., wheel rims, grills, side mirrors, lights, door handles, as well as simplified underbody parts, are added creating a more elaborated view. Finally, the smallest details, i.e., radio antenna, windscreen wipers, and various tiny gaps and edges, are building the final shape of the object. The vehicle surface model is prepared for grid generation with Hexpress/Viewer tool from Fine/Open flow simulation package developed by Numeca International.

The CAD model of Nissan 350z is not directly suitable for CFD simulations since it contains various gaps between elements. For example, in the front of the car, there is a tiny distance left between the front fender and the mudguard allowing the air to flow into the engine compartment. Another example might be a gap between the front fender and the driver's door letting the outside air to enter the interior of the car. In order to generate the computational grid of the exterior of the car, the watertight surface of the vehicle needs to be prepared. A special tool called Hole

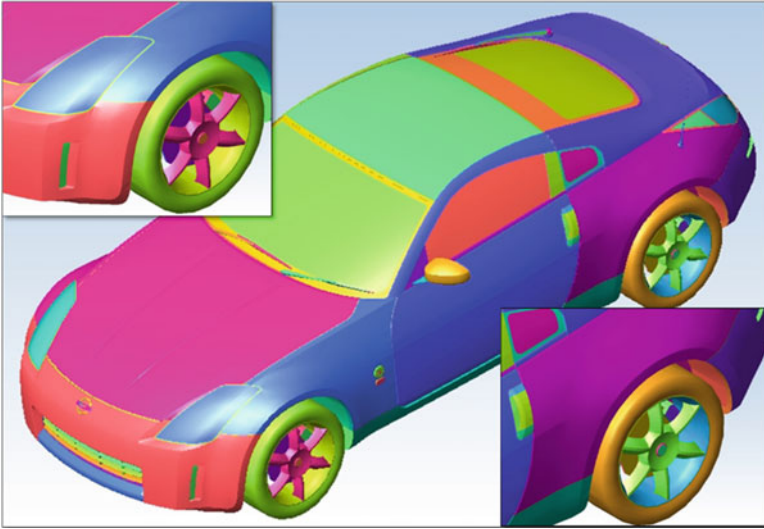


Fig. 16.1 Surface model of Nissan 350z (Numeca)

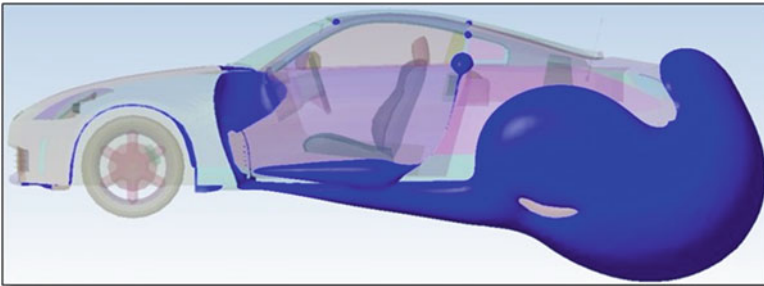


Fig. 16.2 Surface hole searcher—example front closing surface

Searcher from Fine/Open package is designed for this purpose. The algorithm is adding special surface to the project closing the outside surface of the car, making it watertight and suitable for the grid generation. This multistage process is based on a solution of the thermal conductivity problem from a well-defined heat source placed in the interior of the vehicle. The resulting iso-surfaces of the temperature fit perfectly as secondary surfaces, closing any tiny gaps of the CAD model. The first auxiliary surface (marked by blue color) that was used for closing the most forward gap between the front fender and mudguard is presented in Fig. 16.2. The remaining part of the surface is useless and cut out. Each gap requires its own closing surface. The final, combined closing surface of the whole vehicle, making the geometry watertight, is presented in Fig. 16.3.

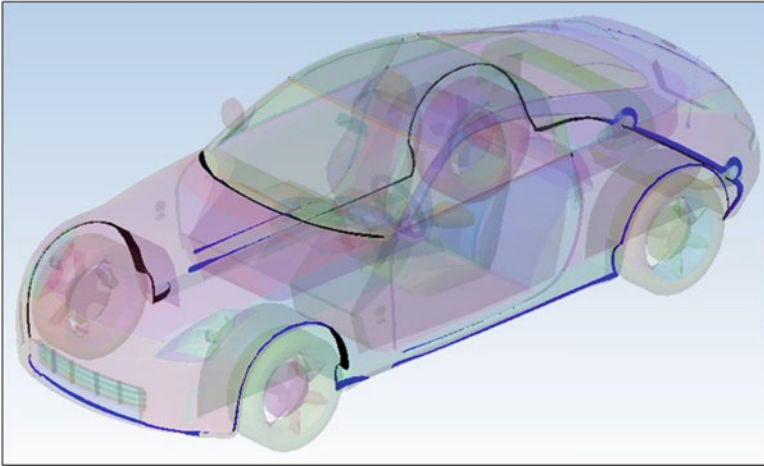


Fig. 16.3 Surface hole searcher—final car closing surface

16.3 Surface and Volume Refinements

The hybrid mesh generation process is initiated by setting the surface and grid refinement levels, which control the mesh density and distribution over various surfaces and in the volume around the vehicle. This necessary step is crucial for proper capturing of the shape of the vehicle and has a direct impact on the quality of the obtained numerical results. The largest panels are grouped in the family called “large components” including the bonnet, fenders, doors, roof, windscreen, side and rear windows, lights, front and rear bumpers, tailgate, and floor (see Fig. 16.4). Medium-size details are put together in the “medium components” family including wheels (tires and rims), front grill, rearview mirrors, and door handles. The next level of refinement is called “small components” family and contains smaller details of the car: front and rear windscreen wipers and some finer parts of the rims, doorsteps, door handles, and lights, as well as majority of the gaps between different large components of the car. Finally, the “tiny components” family is built of the smallest objects present and various sharp corners, for example, the Nissan logo at the front bonnet and side fenders, outer edges of the rims, and radio antenna. All families are hierarchical in type—the larger component family contains all finer families of components.

A three-dimensional computational domain surrounding the surface model of Nissan 350z is stretching 100 m away from the vehicle in each direction (23 times the car length L), resulting in span of $200 \text{ m} \times 200 \text{ m} \times 100 \text{ m}$ (see Fig. 16.5). At the outer surface, the wind velocity of $V = 100 \text{ km/h}$ is set as a “far-field” type boundary condition (blue color), while the car surface and the ground are modeled as inviscid walls (black color). The atmospheric conditions with forward velocity of 100 km/h result in a Reynolds number of $\text{Re} = 8 \times 10^6$. The volume between the car and ground surfaces and the outer edges of the computational domain is

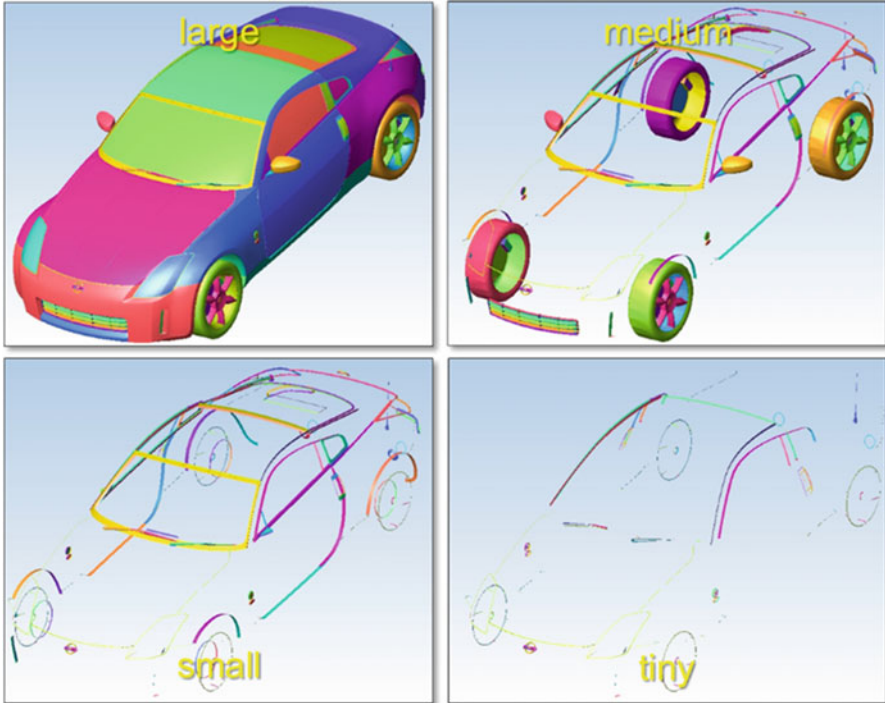


Fig. 16.4 Surface refinements—families of components

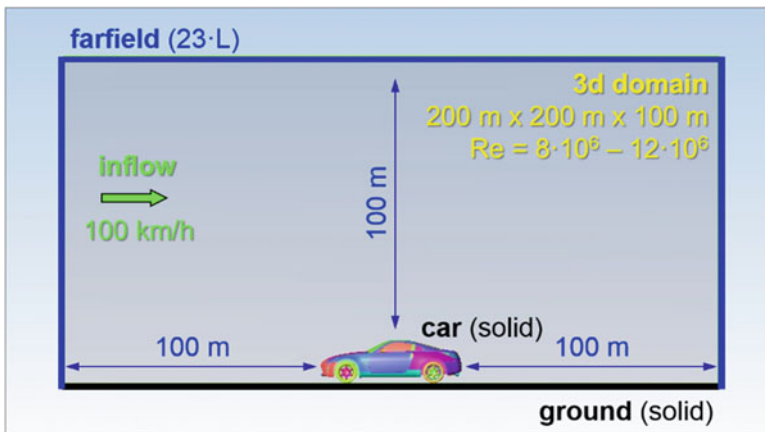


Fig. 16.5 Computational domain

filled with a hybrid (unstructured) grid consisting of various type elements to allow prediction of flow-field quantities at every mesh point surrounding the model. This step is performed with Hexpress/Hybrid tool from Fine/Open package developed

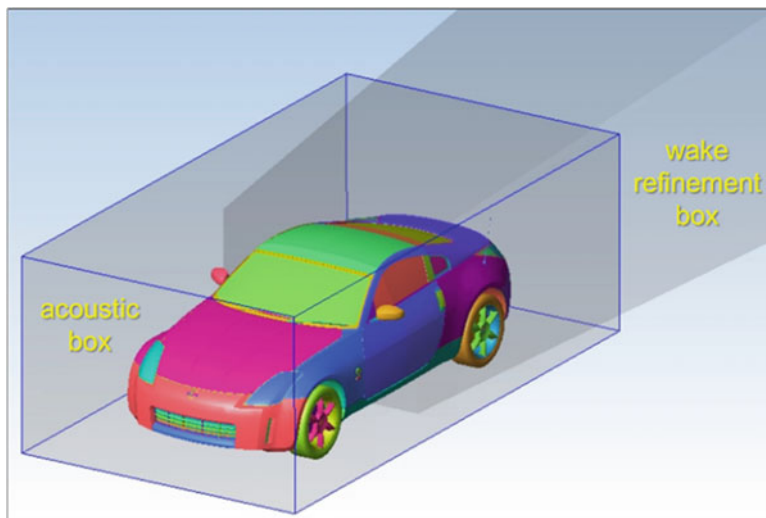


Fig. 16.6 Volume refinements

by Numeca International. The grid coarsens with the distance from the vehicle, reaching in the far-field cell size of approx. 8 m.

The density of the volume grid in the vicinity of the vehicle is controlled by “box refinements”. Usually, for a pure flow-field simulation, two sets of box refinements are prepared: one near the car itself and the other in the wake behind it. For the acoustic analysis, the box refinements surrounding the vehicle are interchanged with a much denser (higher spatial resolution) refinement called “the acoustic box” (see Fig. 16.6). The “acoustic box” is stretching by 0.5 m in every direction from the car and has a uniform grid spacing of $\Delta x = 10$ mm, thus allowing for a resolution of 6 points per wavelength λ up to a frequency of acoustic pressure fluctuations of $f = 5$ kHz. To assure a similar resolution in time domain, a time-step Δt of 33 μ s is set, resulting in 6 points per period T of acoustic fluctuations up to $f = 5$ kHz. Using Euler methodology and combining CFD and CAA using hybrid grid treatment, low-frequency fluctuations are resolved in the near-field of the car together with the flow without any need for modeling. A very similar approach has proved to be a valuable tool of analysis of the noise generated by a helicopter rotor (Szulc et al. 2015).

16.4 Surface and Volume Grids

The volume grid generation process is preceded by a surface mesh generation. The surface refinement levels, defined according to families of components, are taken into account by the algorithm resulting in capturing of the vehicle shape, the ground and far-field surfaces with a sufficient accuracy (Fig. 16.7). Even such small components as Nissan logos, grill, and details of the wheels are captured. The

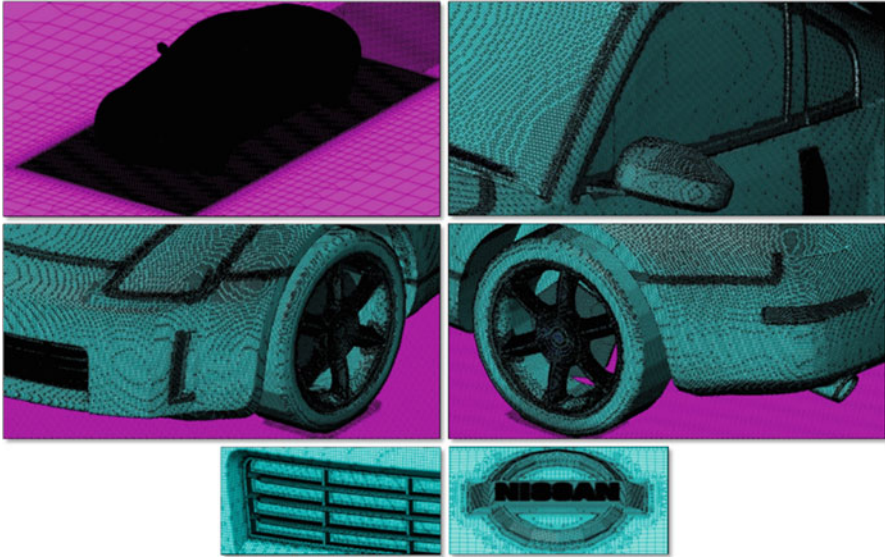


Fig. 16.7 Surface grid

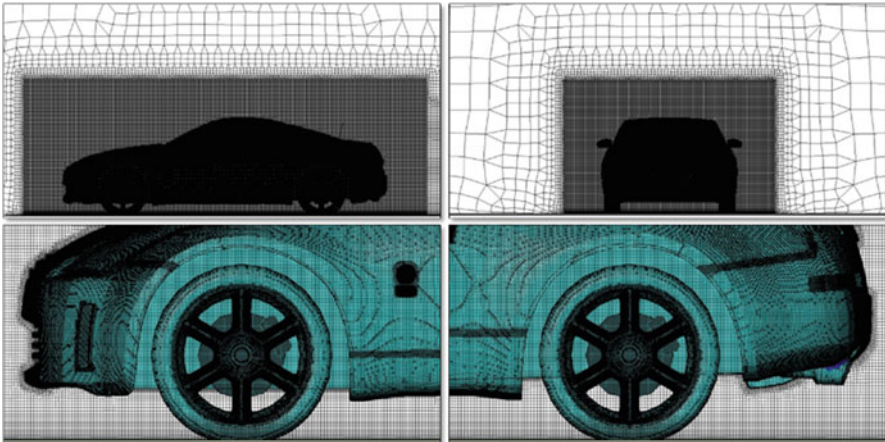


Fig. 16.8 Volume grid

projections of the “acoustic box” and “wake refinement box” on the ground are visible in Fig. 16.7 as well.

The most time-consuming process of the initial volume grid generation requires 24 GB of RAM memory and takes approx. 5 h of computing time on an Intel Core i7 desktop computer using all available CPU cores. The final stage of mesh generation consists of an automated process designed to increase the near-wall resolution and takes approx. 2–3 CPU h. The inviscid volume grid for the industrial car shape of Nissan 350z is ready for analysis and consists of 44×10^6 of control volumes with

75% of hexahedral (most desirable) and 25% of other type (i.e., tetrahedral, prisms, and pyramids) elements (Fig. 16.8).

16.5 Steady Flow Solution

The Euranus/Hybrid flow solver from Fine/Open package developed by Numeca International is solving numerically Euler (inviscid) equations of gasdynamics in steady (time-independent) mode using finite volume method of second-order accuracy in space and an explicit Runge–Kutta type integration in time. Since the computational model is very large, a massively parallel supercomputer of high-performance computing centers affiliated in the PL-Grid Consortium (e.g., TASK Supercomputing Centre in Gdansk, Poland) is required to perform a simulation in a reasonable time. Even the steady-state solution of the flow-field around Nissan 350z consumes 64 GB of RAM memory and with 24 CPU cores ($4 \times$ Intel Xeon 6-core processor) lasts for approx. 6 days (10,000 iterations) creating 35 GB of output data.

The visualizations of streamlines of the airflow around the vehicle are presented in Fig. 16.9 from various views. Large vortical structures are created and shed behind the mirrors and in the wake of the car revealing complexity of the flow. Since the flow is inviscid in nature, maximum velocities are reached at the surface and marked by colors (blue, low-speed airflow; red, high-speed airflow). The largest velocities of airflow (red color) are obtained at the edges of the rearview mirrors, tires, and wheelhouses—locations known to have large impact on the generated level

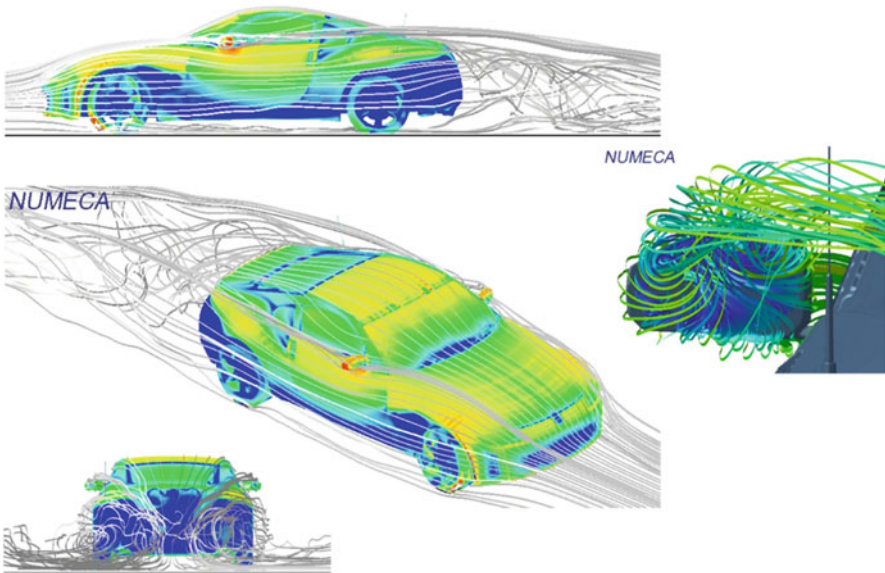


Fig. 16.9 Steady flow-field around Nissan 350z at $V = 100$ km/h

of noise. Medium velocities (yellow-green colors) are visible over the whole upper part of the vehicle. Low wind-speed areas (blue color) are visible at the front grill (stagnation region), along the lower half of all doors and front and rear fenders, in the wheelhouses and near the tailgate at the back of the vehicle, under the influence of the vortical wake generated behind the car. Some tiny gaps are subjected to low velocities of air as well. The only publically available data that may be used for verification of the Nissan 350z flow-field is a measured drag force coefficient c_d . The experimental value of $c_d = 0.31$ is overpredicted by CFD by approx. 10% ($c_d = 0.34$), which is fully understandable from the point of view of a simplification in form of an inviscid flow assumption. The steady-flow solution constitutes an initial condition for a full, unsteady numerical simulation of the flow around the vehicle, designed to deliver low-frequency part of the acoustic spectrum in the near-field of the car. The initial (transient) part of the solution is shortened, and the final fluctuating flow-field and pressure field are more readily obtained with less user effort and computer power.

16.6 Acoustic Analysis

Starting from the initial steady solution, the simulation is progressed in time using a dual-time-stepping approach of Jameson with second-order accuracy. It was decided to limit the temporal accuracy of the solution (time step Δt) from $33 \mu\text{s}$ to 0.8 ms to speed up the calculation within the bounds of the available (limited) computing time. Still, fine spatial resolution was kept unmodified. This modification limited the accuracy of the initial acoustic analysis down to a frequency of $f = 200 \text{ Hz}$ (with $6p/\lambda$) allowing for detection of the acoustic perturbations up to a frequency of $f = 600 \text{ Hz}$. However, the main physical mechanisms of the aerodynamic noise generation are present in the solutions. The numerical simulation lasted for 15 days (500 time steps) using similar computer resources as for the steady-state case. When a quasi-steady flow oscillation developed, the acoustic pressure data has been recorded to the disk (55 GB) at predefined surfaces (ground and car surfaces) for post-processing. At each grid node of the ground and car surface, the acoustic pressure p' is averaged using the root-mean-square definition. The resulting data is referenced to human hearing threshold ($20 \mu\text{Pa}$) and transformed to a logarithmic scale forming the overall sound pressure level (OASPL) in dB. No acoustic weighting is applied to the OASPL in any form.

An example visualization of the root-mean-square of pressure fluctuations p'_{rms} and overall sound pressure level (OASPL) at the ground surface below the car is presented in Fig. 16.10. Major contributors (sources of noise) are readily visible in red color located in the wake behind the car. Just aft of the front and rear tires and tire-ground intersections' intense vortex sheets are formed with high level of pressure fluctuations. High values of OASPL of approx. 130 dB are resulting from the dominating low-frequency contents ($f < 20\text{Hz}$) inaudible by human ear that is not filtered out in the presented results. Fortunately, the floor panel is well insulated damping the acoustic wave propagation into the interior of the car. The view of

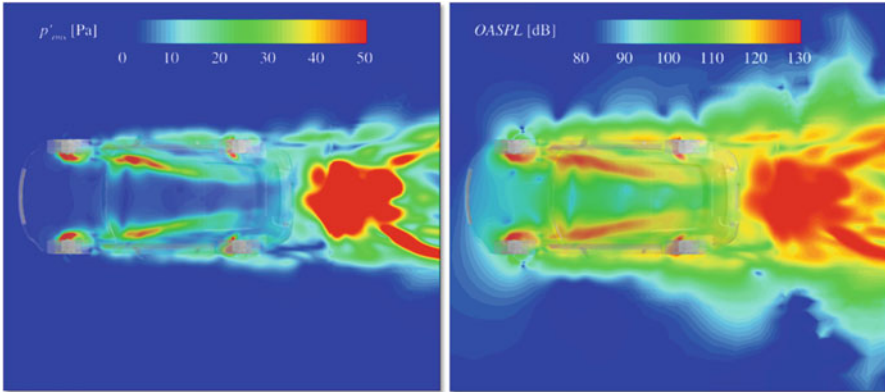


Fig. 16.10 Acoustic pressure fluctuations at ground surface

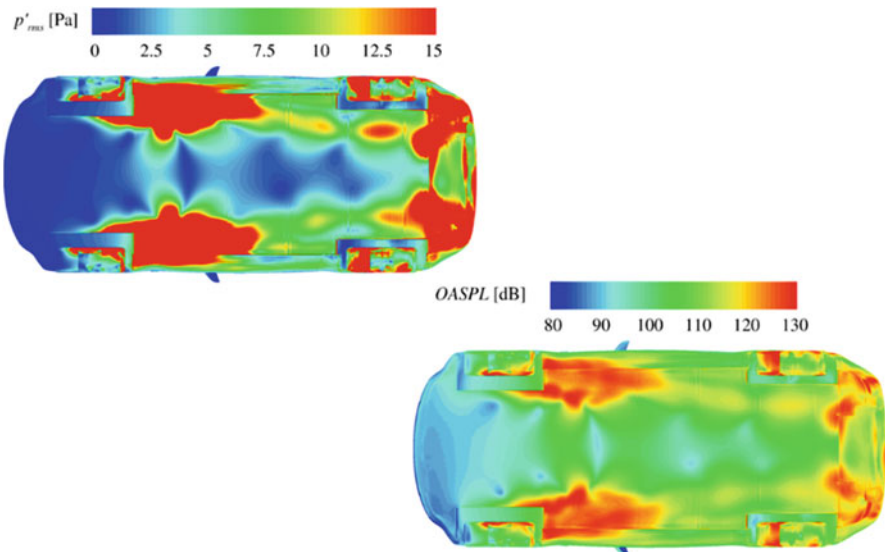


Fig. 16.11 Acoustic pressure fluctuations at floor surface

the acoustic pressure fluctuations at the floor panel, located just above the ground surface, is visible in Fig. 16.11. Here the evident peaks are at the inner edges of front tires and in the wake behind them that is interfering with front parts of both doorsteps. Rear tires are subjected to high-pressure fluctuations influenced by highly unsteady vortical wake behind the car increasing the p'_{rms} value at the whole rear of the vehicle. The maximum values of p'_{rms} are reduced from 50 Pa down to 15 Pa compared to Fig. 16.10 which includes the projection of the volume behind the car (wake) on the ground surface.

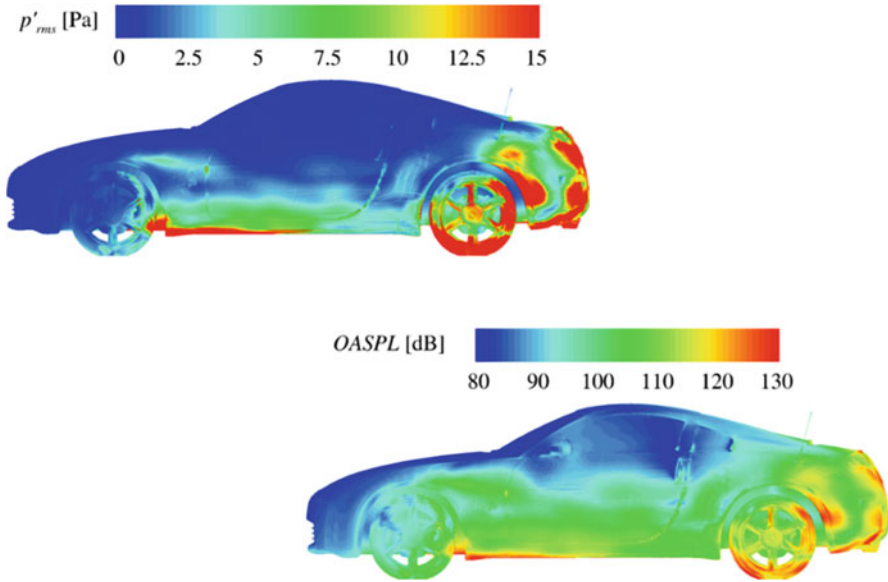


Fig. 16.12 Acoustic pressure fluctuations at exterior car surface

The most informative visualization of the acoustic sources present at the surface of the car is presented in Fig. 16.12 in a form of a side view of the vehicle. It is evident that two main sources are present in the numerical results. The pressure oscillations are the highest in the front wheelhouses and along the front part of doorsteps, reaching approx. half of the door height. More downstream rear wheels and rims reveal a region of increased noise connected with the rear bumper and tailgate surface subjected to the wake. It is worth to notice that the simulation did not detect the interaction between the vortices created and shed behind the rearview mirrors hitting the side windows—a well-known source of annoying wind noise.

The close-up of the rearview mirror area is depicted in Fig. 16.13 by limiting the OASPL scale to 90 dB. Still the interaction of the wake of the mirror with the side windows is barely visible. The maximum level of acoustic pressure fluctuations is located at the outer part of the mirror, in the area of high flow velocity. The area of high noise due to flow under the car is also noticeable at the door surface. This lack of detection of the rearview mirror–side window interference source of noise is directly connected with the limitations of the current numerical method focused on low-frequency ($f < 200$ Hz) pressure fluctuations only, while this phenomenon is emitting tonal noise in higher-frequency range of approx. 2–5 kHz, depending on the car's forward velocity and mirror shape. The numerical simulation with the originally planned, small time-step Δt of 22 μs would possibly resolve this phenomenon as well.

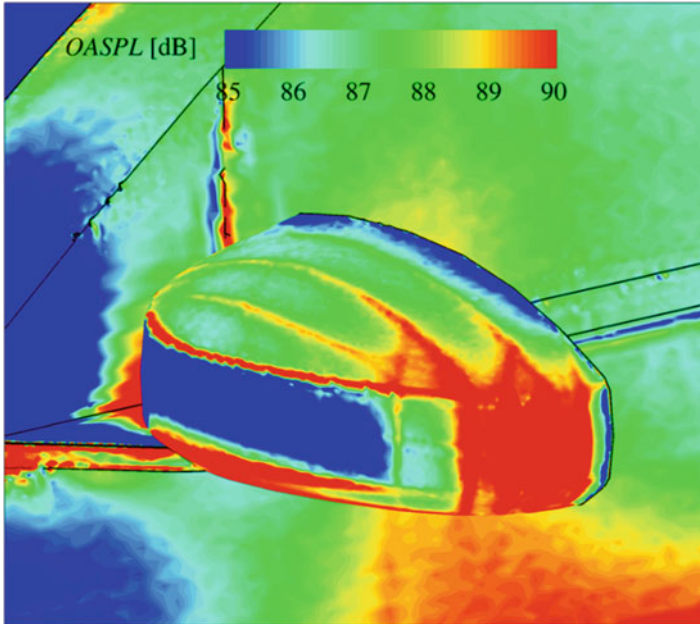


Fig. 16.13 Acoustic pressure fluctuations at rearview mirror surface

16.7 Summary

The method of the quantification of the main aerodynamic sources of noise generated by the flow of air around the industrial car shape has been developed. It has been proven that using a sufficiently detailed surface model of the vehicle and simplified Euler modeling of the flow on hybrid grids, designed to capture the near-field sound wave propagation, it is possible to locate major contributors to noise level. It is also evident that the methodology is very efficient and could be easily extended to allow for more complex turbulent flow modeling (URANS, DES, or LES). Thanks to a constant increase of an available computing power, it is possible to refine the spatial and temporal resolution of the combined CFD–CAA simulation to a point when the additional acoustic modeling is no longer necessary—the acoustic pressure fluctuations are an inherent part of the overall flow-field solution.

References

- Gloerfelt X (2009). Noise from automotive components. VKI Lecture Series: Aerodynamic Noise From Wall-Bounded Flows, Brussels
- Moron P, Hazir A, Crouse B, Powell R, Neuhierl B, Wiedemann J (2011) Hybrid technique for underbody noise transmission of wind noise. Society of Automotive Engineers Technical Paper 2011-01-1700
- Nouzawa T, Li Y, Kasaki N, Nakamura T (2011) Structure of aerodynamic noise sources generated in production vehicle. *J Environ Eng* 6(3):604–614
- Szulc O, Doerffer P, Tejero F, Zoltak J, Malecki J (2015) Numerical analysis of High-Speed Impulsive (HSI) noise of PZL W3-A “Sokol” (Falcon) helicopter main rotor in forward flight. *Task Q* 19(2):181–196

Chapter 17

Computation of Rotorcraft Stability Derivatives Using the Discrete Adjoint Method

M. Biava and G. Barakos

17.1 Introduction

Simulation of rotorcraft flight mechanics is extremely challenging, because of the nonlinearity and unsteadiness of rotor flows. For many applications, however, it is possible to consider only small deviations from a given steady flight condition, and to describe the flight dynamics behavior by means of a linearized model, defined by a set of aerodynamic derivatives. These derivatives can be obtained via finite differences (FDs) of computational fluid dynamics (CFD) simulations (Woodgate and Barakos 2012), and two or more complete flow solutions are required to compute each derivative, depending upon the order of the FD approximation. A more efficient way to obtain the aerodynamic derivatives with CFD is via analytic sensitivity methods (Limache and Cliff 2000; Mader and Martins 2011). The basic idea is to write any aerodynamic force and moment coefficient I as a function of the flow variables \mathbf{W} and of the input flight dynamics variable of interest x (e.g., angle of attack, sideslip, Mach number, etc.), that is, $I = I[\mathbf{W}(x), x]$. The flow variables are subject to satisfy the fluid dynamics governing equations, such as the Navier–Stokes (NS) equations, which can be written in compact form as

$$\mathbf{R}[\mathbf{W}(x), x] = 0 \tag{17.1}$$

Formally, taking the derivative of I with respect to x , we obtain

$$\frac{DI}{Dx} = \frac{\partial I}{\partial x} + \frac{\partial I}{\partial \mathbf{W}} + \frac{\partial \mathbf{W}}{\partial x} \tag{17.2}$$

M. Biava • G. Barakos (✉)
University of Glasgow, Glasgow, UK
e-mail: George.Barakos@glasgow.ac.uk

which represents the tangent form of the sensitivity equation. All the partial derivatives appearing on the right-hand side can be computed with limited effort, with the exception of $\partial\mathbf{W}/\partial x$, which represents the variation of the flow variables with respect to the flight dynamic variable. This last term may be obtained by differentiating the governing Eq. (17.1) to yield the following linear system for the unknown $\partial\mathbf{W}/\partial x$:

$$\frac{DR}{Dx} = 0 \rightarrow \frac{\partial\mathbf{R}}{\partial\mathbf{W}} \frac{\partial\mathbf{W}}{\partial x} = -\frac{\partial\mathbf{R}}{\partial x} \quad (17.3)$$

Therefore, the computation of a flow derivative is reduced to the solution of the nonlinear governing flow Eq. (17.1) plus the solution of the linear system (17.3). This linear problem is, however, usually hard to compute, because the Jacobian matrix $\partial\mathbf{R}/\partial\mathbf{W}$ is characterized by a high stiffness, and the solution time is usually comparable to that of the base flow. Also, the right-hand side of Eq. (17.3) depends upon the input variable x , and therefore, like with finite differencing, the computational cost for computing aerodynamic derivatives scales with the number of flight dynamics variables. Nevertheless, the sensitivity-equation approach requires the solution of only one linear system of equations for each derivative, and does not suffer of cancellation errors, yielding results accurate up to machine precision. Instead, using second-order FDs, for instance, two nonlinear problems have to be solved to compute each derivative.

The sensitivity problem (17.2) and (17.3) can be recast in dual form by introducing the adjoint-variable vector λ as the solution of the following linear system (Giles and Pierce 2000):

$$\left(\frac{\partial\mathbf{R}}{\partial\mathbf{W}}\right)^T \lambda = -\left(\frac{\partial I}{\partial\mathbf{W}}\right)^T \quad (17.4)$$

Substituting Eq. (17.4) into Eq. (17.2), and using Eq. (17.3) we obtain

$$\frac{DI}{Dx} = \frac{\partial I}{\partial x} - \lambda^T \frac{\partial\mathbf{R}}{\partial\mathbf{W}} \frac{\partial\mathbf{W}}{\partial x} \rightarrow \frac{DI}{Dx} = \frac{\partial I}{\partial x} - \lambda^T \frac{\partial\mathbf{R}}{\partial x} \quad (17.5)$$

The computational cost of the dual sensitivity problem (17.4) and (17.5) scales with the number of outputs, because the right-hand side of Eq. (17.4) depends on I , but it is independent of the input parameters. The choice between using the direct or dual sensitivity problem consequently depends on the balance between the number of outputs and the number of inputs. The two methods should perform equally well in computing the flight-mechanic derivatives, because the number of output force and moment coefficients is similar to the number of input flight-mechanic parameters.

The calculation of the partial derivatives appearing in the sensitivity equation can be done manually, by deriving analytical expressions and writing the necessary computer code. Nonetheless, this approach can be tedious if the flow equations

involve complex terms. Recent advances in automatic differentiation (AD) tools (Griewank and Walther 2008; Griewank 2003; Bartholomew-Biggs et al. 2000), however, enable to produce the computer code for the differentials of flow equation terms directly from the source code of the CFD solver (Giering et al. 2005; Mader et al. 2008; Jones et al. 2011).

The present work describes the development of the sensitivity-equation approach by means of AD in the CFD solver Helicopter Multi-Block (HMB2) (Steijl et al. 2006; Barakos et al. 2005) of Glasgow and AgustaWestland. As followed in the works of Mader et al. (2008) and Jones et al. (2011), the individual functions of the CFD solver have been automatically differentiated and assembled afterward to build the necessary terms in the sensitivity equation, both in tangent and adjoint forms. The linear system associated with the sensitivity problem is solved using a matrix-free version of the fully implicit fixed-point iteration scheme of the base-flow solver. The resulting code is able to compute the aerodynamic derivatives of rotors at a fraction of the cost required by finite differencing. The method is demonstrated for the aerodynamic sensitivities of the inviscid flow around the ONERA 7AD rotor in hover, and for the turbulent flow around the S-76 rotor in hover. The extension of the method to rotors in forward flight using the harmonic-balance formulation of the flow equations is presented in Biava et al. (2016).

17.2 Background on AD and the Discrete Adjoint

The first application of the adjoint method to fluid dynamics is dated back to 1974 with the pioneering work of Pironneau (1974), in which adjoint methods and control theory were applied to drag minimization. Starting from the late 1980s, the first applications to CFD problems begin to appear, with the works of Jameson (1988, 1990) and Jameson et al. (1998). They exploited the adjoint method and control theory for aerodynamic shape optimization in conjunction with CFD techniques, whose complexity increased over the years from the solution of the potential flow equations to that of the NS equations (Jameson et al. 1997; Reuther and Jameson 1994; Reuther et al. 1996). The derivation of the adjoint problem in these works is based on the continuous approach (CA), in which the adjoint equations are analytically derived from the primary flow equations and discretized afterward.

The alternative discrete approach (DA) to the adjoint problem consists in deriving the adjoint equations directly from the discretized formulation of the flow equations. This has been pursued in the works of Elliott and Peraire (1997), Anderson and Bonhaus (1999), and Mavriplis (2007) in the context of aerodynamic shape optimization with unstructured meshes. A fairly complete overview of the development of continuous and discrete adjoint methods in the last two decades of the twentieth century can be found in Newman et al. (1999). Both CA and DA have advantages and disadvantages, as pointed out by Giles and Pierce (2000). These are summarized in Table 17.1.

Table 17.1 Advantages and disadvantages of the continuous and discrete adjoint approaches (Biava et al. 2016)

DA	CA
It provides the exact gradients, because the discrete adjoint operator is simply the transpose of the matrix arising from the discretization of the primary flow equations	It gives an approximation to the continuous gradient based on some alternative discretization
The implementation requires less coding effort, especially if AD is employed	It requires hand coding of the discretization scheme applied to the continuous adjoint equations
The straight application of AD to the CFD code produces inefficient adjoint code, so that the application of AD to individual nonlinear functions and partial recoding is necessary	The continuous code is often considerably simpler than the discrete in terms of operation count and memory requirements, as well as easier to implement
The derivation of the adjoint equations and BCs is purely algebraic, and gives no insight in the physics of the problem	It gives a more clear interpretation of the physics behind the adjoint variables and of the associated BCs

The implementation of the DA for flow equations involving complex terms (upwinding terms, terms depending on spectral radii, source terms appearing in turbulence models, etc.) is not straightforward. A technique to tackle the problem of deriving the discrete adjoint in such complex cases is AD, in which the adjoint code to evaluate the gradients is obtained by directly manipulating the original CFD code, as in the work of Mohammadi (1997a, b). This approach has grown in popularity and was later pursued by other research groups (Giering et al. 2005; Mader et al. 2008; Jones et al. 2011; Müller and Cusdin 2005; Marta et al. 2007). AD may be obtained by means of source-transformation tools or via operator overloading in programming languages, such as FORTRAN 90 and C++. Tools that use source-code transformation add new statements to the original source code that compute the derivatives of the original statements. The operator-overloading approach consists of a new user-defined type that is used instead of floating points. This new type includes not only the value of the original variable, but its derivative as well. The operator-overloading approach results in fewer changes to the original code, but is usually less efficient (Griewank and Walther 2008). AD tools are available for a variety of programming languages. ADIFOR (Carle and Fagan 2000), TAF (Giering et al. 2005), and TAMC (Gockenbach 2000) are some of the tools available for FORTRAN. TAPENADE (Hascoët and Pascual 2004; Anon (nd) [The TAPENADE Tutorial](#)) supports both FORTRAN 90 and C. A complete list of AD tools available for each programming language may be found in (Anon (nd) [Community Portal for Automatic Differentiation](#)).

There are two different modes of operation for AD of a computer code: the forward (or tangent) mode and the reverse (or adjoint) mode. The forward mode uses the chain rule to propagate the required derivatives in the same direction of the original computer code. The cost of forward AD is proportional to the number of

inputs of the computed function. In the reverse mode, the derivatives are propagated backward, from the last statement of the code to the first. The reverse mode is analogous to the adjoint method, and the cost is proportional to the number of outputs of the computed function. However, the memory requirements of the reverse mode can be considerably higher, because the storage of intermediate results of the function evaluation is required for the backward propagation of the derivatives.

It is to be noted that AD cannot be applied directly to the whole residual-evaluation chain to produce the adjoint of the flow equations, because it would lead to an inefficient code in terms of memory and CPU time. A more realistic goal for AD is in assisting the derivation of the discrete adjoint by hand differentiation, by automatically differentiating, and by transposing individual source-code functions. This approach was adopted, for instance, in Mader et al. (2008) and in Jones et al. (2011), and was also followed here.

17.3 Past Work on Adjoint for Aircraft and Rotorcraft Applications

The introduction of AD, the advances in techniques for solving the adjoint problem, and the growing power of computing hardware allowed the application of the adjoint method to more complex cases. Also, driven by the industrial need of more realistic flight-mechanic models, the related research widened its initial objective of aerodynamic shape optimization to make space to novel applications, such as aeromechanics. In the work of Limache and Cliff (2000) and of Mader and Martins (2011, 2012), for instance, the aerodynamic derivatives of airfoil and wings are computed by solving the sensitivity problem.

This concept was then extended to compute the sensitivities of time-periodic-flow solutions, such as those generated by turbomachinery and helicopters, by applying the adjoint method to the time-spectral formulation of the flow equations, which reduces the time-dependent problem to a steady problem in the frequency domain. This was described by Mader and Martins (2012) and Choi et al. (2014) for helicopter applications, and by Huang and Ekici (2014) in the context of turbomachinery. The adjoint development in these works is, however, limited to inviscid flows.

In the context of the discrete adjoint, full account of the viscous effects and linearization of the Reynolds-averaged Navier–Stokes (RANS) equations coupled with a turbulence model has been attempted by several authors (Dwight and Brezillon 2006; Lyu et al. 2013; Marta et al. 2013; Thomas et al. 2013; Osusky and Zingg 2013). Applications to realistic aerodynamic optimization problems can also be found in Lyu and Martins (2014) for fixed-wing aircraft, and in Mani and Mavriplis (2009) for rotorcraft.

These past works highlighted the efficiency of the sensitivity-equation approach for aerodynamic shape optimization and for aeromechanics applications. They also showed the difficulties associated with the convergence of the sensitivity equation

and the demanding memory requirements of adjoint solvers, which can represent a limiting factor for realistic large-scale applications. The objective of the present work was to partially overcome these drawbacks, while keeping the efficiency and accuracy of the sensitivity-problem approach for the computation of aerodynamic derivatives. The novelty of the work is the detailed description of the development of a low memory, fully implicit adjoint solver for the RANS equations. The low-memory footprint is achieved by using AD to compute on-the-fly terms involving the flow-equation residual Jacobian, which is never stored explicitly.

17.4 HMB2 Flow Solver

The following contains a brief outline of the approach used in the Helicopter Multi-Block solver version 2.0. The NS equations are discretized using a cell-centered finite volume approach. The computational domain is divided into a finite number of nonoverlapping control volumes V_{ijk} , and the governing equations are applied to each cell. Also, the NS equations are rewritten in a curvilinear coordinate system, which simplifies the formulation of the discretized terms because body-conforming meshes are adopted here. The spatial discretization of the NS equations leads to a set of ordinary differential equations in real time:

$$\frac{d}{dt} (\mathbf{W}_{ijk} V_{ijk}) = -\mathbf{R}_{ijk} (\mathbf{W}) \quad (17.6)$$

in which \mathbf{W} and \mathbf{R} are the vectors of cell conserved variables and residuals, respectively. The convective terms are discretized using Osher's upwind scheme for its robustness, accuracy, and stability properties. The MUSCL variable extrapolation is used to provide second-order accuracy with the van Albada limiter to prevent spurious oscillations around shock waves. Boundary conditions (BCs) are set using ghost cells on the exterior of the computational domain. At the far field, ghost cells are set at the freestream conditions. At solid boundaries, the no-slip condition is set for viscous flows, or ghost values are extrapolated from the interior (ensuring the normal component of the velocity on the solid wall is zero) for Euler flow.

The integration in time of Eq. (17.6) to a steady-state solution is performed using a fully implicit time-marching scheme by

$$\frac{\mathbf{W}_{ijk}^{n+1} - \mathbf{W}_{ijk}^n}{\Delta t} = -\frac{1}{V_{ijk}} \mathbf{R}_{ijk} (\mathbf{W}_{ijk}^{n+1}) \quad (17.7)$$

in which $n + 1$ denotes the real time $(n + 1) \Delta t$. For steady-state problems, the real time is replaced by a pseudotime τ , which is also used for unsteady problems in the dual time-stepping scheme of Jameson (1991). Equation (17.7) represents a system of nonlinear algebraic equations, and to simplify the solution procedure, the flux residual $\mathbf{R}_{ijk} (\mathbf{W}_{ijk}^{n+1})$ is linearized in time as follows:

$$\mathbf{R}_{ijk}(\mathbf{W}_{ijk}^{n+1}) \approx \mathbf{R}_{ijk}(\mathbf{W}_{ijk}^n) + \frac{\partial \mathbf{R}_{ijk}}{\partial \mathbf{W}_{ijk}} \Delta \mathbf{W}_{ijk} \quad (17.8)$$

in which $\Delta \mathbf{W}_{ijk} = \mathbf{W}_{ijk}^{n+1} - \mathbf{W}_{ijk}^n$. Equation (17.7) now becomes the following linear system:

$$\left[\frac{V_{ijk}}{\Delta t} \mathbf{I} + \frac{\partial \mathbf{R}_{ijk}}{\partial \mathbf{W}_{ijk}} \right] = -\mathbf{R}_{ijk}(\mathbf{W}_{ijk}^n) \quad (17.9)$$

which is solved with a generalized conjugate-gradient (GCG) iterative solver (Axelsson 1994). Because at steady state the left-hand side of Eq. (17.10) must go to zero, the Jacobian $\partial \mathbf{R} / \partial \mathbf{W}$ can be approximated by evaluating the derivatives of the residuals with a first-order scheme for the inviscid fluxes. The first-order Jacobian requires less storage and, being more dissipative, ensures a better convergence rate to the GCG iterations. The steady-state solver for the turbulent case is formulated and solved in an identical manner to that described for the mean flow.

17.5 Fully Implicit Tangent and Adjoint Solvers

To compute the aerodynamic sensitivities, we need to solve either the linear system (17.3) for the tangent formulation or the discrete adjoint Eq. (17.4), and then use the sensitivity Eqs. (17.2) or (17.5), respectively. These linear systems become stiff as the dimension of the flow problem increases, and therefore, a suitable preconditioner is required to stabilize the solution algorithm. Another way to tackle the stiffness problem is to reformulate the linear system as a fixed-point iteration problem (Christianson 1998; Giles 2002), in which an approximation of the linear system matrix, with better convergence properties, is introduced as a preconditioner to advance the solution at each iteration. The fixed-point iterative schemes read:

$$\widehat{J} \Delta \mathbf{W}_x^{n+1} = -\frac{\partial \mathbf{R}}{\partial x} - J \mathbf{W}_x^n, \quad \text{tangent form} \quad (17.10)$$

$$\widehat{J} \Delta \lambda^{n+1} = -\left(\frac{\partial \mathbf{R}}{\partial x} \right) - J^T \lambda^n, \quad \text{adjoint form} \quad (17.11)$$

in which

$$j = \frac{\partial \mathbf{R}}{\partial \mathbf{W}}, \quad \widehat{J} = \frac{V}{\Delta t} \mathbf{I} + \left[\frac{\partial \mathbf{R}}{\partial \mathbf{W}} \right]^{1\text{st}}$$

$$\mathbf{W}_x = \frac{\partial \mathbf{W}}{\partial x}, \quad \Delta \mathbf{W}_x^{n+1} = \mathbf{W}_x^{n+1} - \mathbf{W}_x^n \quad \text{and} \quad \Delta \lambda^{n+1} = \lambda^{n+1} - \lambda^n$$

The matrix J is the flow-equation residual Jacobian. The natural choice for the preconditioner \hat{J} is the matrix used for the base flow iterative scheme (17.9), the sum of a stabilizing time-derivative term and of the first-order flow-equation residual Jacobian, which approximates J and is more diagonally dominant. The fixed-point iteration (17.10) is solved using the GCG iterative solver. In the adjoint iteration (17.11), the system matrix is the transpose of the preconditioner \hat{J} , and the linear system can be solved with a slightly modified version of the GCG solver that implicitly performs the matrix transposition.

The iteration schemes (17.10) and (17.11) do not require the full exact Jacobian J , but only the matrix–vector product Jv or $J^T v$. As explained later in this section, the computer code to perform the former product can be obtained by AD in tangent mode of the flow steady residual function, whereas the code for the latter product can be obtained with AD of the same function in adjoint mode. This avoids the necessity of storing J , and hence, the computation of sensitivities adds only a small memory overhead to the base solver.

There are two options for applying the preconditioning matrix \hat{J} . The first is to form explicitly \hat{J} by computing analytically the low order Jacobian terms. This is done by the same code used for the base flow implicit method. Because the GCG solver only requires the matrix–vector product, the second option is to use the automatically differentiated residual function to compute directly $\hat{J}v$ for scheme (17.10) or $\hat{J}^T v$ for scheme (17.11). This is accomplished by the same set of functions used for Jv and $J^T v$, with the only difference that the (differentiated) MUSCL extrapolation is not being performed. In this case, a special version of the GCG linear solver is invoked that calls the differentiated code instead of the explicit matrix–vector product.

17.5.1 Computation of the Product Jv

To produce the matrix–vector product of the residual Jacobian J and a generic vector v , we have isolated the CFD solver code that computes the steady-flow residuals. In particular, the steps involved in the computation of the residuals have been grouped in the single function `steady_residual`, described by the pseudocode of Fig. 17.1. (The calls to the turbulence-modeling functions have been omitted in this discussion for simplicity.) The inputs for the function are the vector \dot{X} of mesh velocities, the vector N of surface normals (the mesh metrics), the solution vector W , and the freestream Mach number M_∞ . The function produces as output the steady residual vector R .

The differentiated version of `steady_residual` in tangent mode, named `steady_residual_d`, has been hand coded, and it simply calls the differentiated version of the inner functions present in the original statements, as shown by the pseudocode in Fig. 17.2. The inner functions have been instead differentiated individually by means of the source-transformation tool TAPENADE, operated in tangent mode. As a convention, the functions differentiated in tangent mode are identified by the postfix “_d” appended to the base name.

```

steady_residual(Xdot, N, W, M, R)
{
    // Set the boundary and halo cells
    call set_boundary(Xdot, N, W, M);

    // Exchange data at block/inter-processor boundaries
    call exchange_halo_cells(W);

    // Calculate residual looping over the blocks
    do for each mesh block
    {
        // Compute inviscid terms with Osher's scheme
        call inviscid_Osher(Xdot, N, W, M, R);

        // Compute viscous terms
        call viscous(N, W, M, R);
    }
}

```

Fig. 17.1 Pseudocode for the computation of the steady residual vector

```

steady_residual_d(Xdot, Xdot_d, N, N_d, W, W_d, M, M_d, R, R_d)
{
    // Set the boundary and halo cells
    call set_boundary_d(Xdot, Xdot_d, N, N_d, W, W_d, M, M_d);

    // Exchange data at block/inter-processor boundaries
    call exchange_halo_cells_d(W, W_d);

    // Calculate residual differentials looping over the blocks
    do for each mesh block
    {
        // Compute inviscid terms differentials
        call inviscid_Osher_d(Xdot, Xdot_d, N, N_d,
                               W, W_d, M, M_d, R, R_d);

        // Compute viscous terms differentials
        call viscous_d(N, N_d, W, W_d, M, M_d, R, R_d);
    }
}

```

Fig. 17.2 Pseudocode for the steady residual function differentiated in tangent mode

The application of the source-transformation tool to the complex HMB2 solver functions, which are written in C language, was not straightforward, and some hand coding was needed before and after the AD. For each function to be differentiated, the required manual modifications were as follows:

1. Before differentiation: The function was modified so that all input and output quantities appeared explicitly as dummy arguments in the function interface, eliminating any access through global variables.
2. Before differentiation: The “\$AD II-LOOP” directive was added before loops, in which each iteration does not depend on a value that is computed by another iteration. There are many loops of this kind in a typical CFD code, such as loops over the mesh elements to compute metric terms, fluxes and residuals, and loops over the surface mesh elements to perform loads integration. The directive instructs TAPENADE to treat this type of loops in a more efficient way when reverse differentiation is performed.
3. After differentiation: For efficiency, most of the data arrays in HMB2 are allocated in a contiguous memory area and accessed through pointer arithmetics. The differentiation tool sometimes does not handle correctly the pointer arithmetics, and data access must be manually corrected in the generated code.

Note that, differently from the Adjoint method proposed by Mader and Martins (2011), the present approach does not need rewriting of the residual-evaluation code, transforming the original-flux calculation loop over the computational control-volume faces to a complete single control-volume evaluation. This, in fact, is only needed to exploit the sparsity pattern of the Jacobian matrix when computing explicitly its elements. Because the present solver relies only on the computation of a single matrix–vector product Jv or $J^T v$ at each fixed-point iteration, the original CFD code loops can be differentiated directly both in forward and reverse modes, provided that the directive “\$AD II-LOOP” is specified before the loops to obtain an efficient code also when using the reverse mode.

The differentiated residual function `steady_residual_d` has the additional arguments $\delta\dot{X}$, δN , δW , δM_∞ , and δR (`Xdot_d`, `N_d`, `W_d`, `M_d`, and `R_d` in the pseudocode, respectively) that represent the differentials of the quantities involved in the residuals computation. For any value of the input differentials, the action of `steady_residual_d` is to compute the consequent variation of the residual vector, that is

$$\delta R = \frac{\partial R}{\partial \dot{X}} \delta \dot{X} + \frac{\partial R}{\partial N} \delta N + \frac{\partial R}{\partial W} \delta W + \frac{\partial R}{\partial M_\infty} \delta M_\infty, \quad (17.12)$$

The third term on the right-hand side is the product between the exact residuals Jacobian matrix with an arbitrary vector of solution variations. Thus, using `steady_residual_d` with $\delta\dot{X} = 0$, $\delta N = 0$, $\delta W = W_x^n$, $\delta M_\infty = 0$ produces the matrix–vector product necessary to compute the right-hand side of the fixed-point iteration (17.10).

Note that additional memory is necessary to solve Eq. (17.3) via the fixed-point iterations (17.10), because storing the differentials $\delta\mathbf{X}$, $\delta\mathbf{N}$, $\delta\mathbf{W}$, $\delta\mathbf{M}_\infty$, and $\delta\mathbf{R}$ is now needed. This, however, represents only 10–15% of the memory used by the implicit solver for the base flow.

17.5.2 Computation of the Product $J^T \mathbf{v}$

The computation of the matrix–vector product $J^T \mathbf{v}$ requires the differentiation, in adjoint mode, of the steady residual function. As for the tangent-mode case, the adjoint code for the main function `steady_residual_b` has been manually coded, whereas the inner functions have been differentiated using TAPENADE in the reverse mode. The functions differentiated in adjoint mode are labeled by the addition of the postfix “_b” to the base name. The pseudocode for `steady_residual_b` is shown in Fig. 17.3.

```

steady_residual_b(Xdot, Xdot_b, N, N_b, W, W_b, M, M_b, R, R_b)
{
    // Set the boundary and halo cells
    call set_boundary(Xdot, N, W, M);

    // Exchange data at block/inter-processor boundaries
    call exchange_halo_cells(W);

    // Calculate residual differentials looping over the blocks
    do for each mesh block
    {
        // Compute viscous terms differentials
        call viscous_b(N, N_b, W, W_b, M, M_b, R, R_b);

        // Compute inviscid terms differentials
        call inviscid_Osher_b(Xdot, Xdot_b, N, N_b,
                               W, W_b, M, M_b, R, R_b);
    }

    // Exchange differentials at block/inter-processor boundaries
    call exchange_halo_cells_b(W_b);

    // Set the differentials at boundary and halo cells
    call set_boundary_b(Xdot, Xdot_b, N, N_b, W, W_b, M, M_b);
}

```

Fig. 17.3 Pseudocode for the steady residual function differentiated in reverse mode

Note that the adjoint code is more complex with respect to the tangent-mode code. There are calls to the nondifferentiated functions at the beginning, in what is called the forward sweep, in which all the quantities needed during the subsequent back propagation of the derivatives are calculated. The back propagation of derivatives is performed in the reverse sweep, in which the differentiated versions of the functions called in the original statements are executed in reverse order. Also, not every call to nondifferentiated function is present in the forward sweep of the adjoint code, like the call to `inviscid_osher`, for instance, because the values computed by these functions are not needed during the reverse sweep.

For any value of the input residual differentials $\delta\mathbf{R}$ (`R_b` in the pseudocode), the action of the adjoint code in `steady_residual_b` is to compute the vectors $\delta\dot{\mathbf{X}}$, $\delta\mathbf{N}$, $\delta\mathbf{W}$, and δM_∞ (`Xdot_b`, `N_b`, `P_b`, and `M_b` in the pseudocode, respectively) of weighted partial derivatives of the residuals:

$$\delta\dot{\mathbf{X}} = \left(\frac{\partial\mathbf{R}}{\partial\dot{\mathbf{X}}} \right) \delta\mathbf{R} \quad (17.13)$$

$$\delta\mathbf{N} = \left(\frac{\partial\mathbf{R}}{\partial\mathbf{N}} \right) \delta\mathbf{R} \quad (17.14)$$

$$\delta\mathbf{W} = \left(\frac{\partial\mathbf{R}}{\partial\mathbf{W}} \right) \delta\mathbf{R} \quad (17.15)$$

$$\delta M_\infty = \left(\frac{\partial\mathbf{R}}{\partial M_\infty} \right) \delta\mathbf{R} \quad (17.16)$$

It is interesting to observe that the role of the dual variables $\delta\dot{\mathbf{X}}$, $\delta\mathbf{N}$, $\delta\mathbf{W}$, δM_∞ , and $\delta\mathbf{R}$ in the differentiated function `steady_residual_d` is reversed in function `steady_residual_b`: input quantities in the former are output in the latter, and vice versa.

The vector $\delta\mathbf{W}$ is the product between the transpose of the exact residual Jacobian matrix and an arbitrary vector. It follows that a call of `steady_residual_b` with $\delta\mathbf{R} = \boldsymbol{\lambda}^n$ produces the matrix–vector product appearing in the right-hand side of the fixed-point iteration (17.11).

The additional memory for `steady_residual_b` is due to the storage needed for the variables $\delta\dot{\mathbf{X}}$, $\delta\mathbf{N}$, $\delta\mathbf{W}$, δM_∞ , and $\delta\mathbf{R}$. This needs to be added to the memory allocated temporarily by the inner functions differentiated in the reverse mode by TAPENADE. The reverse-mode differentiated code requires, in fact, to save some of the quantities computed during the forward sweep, when they are necessary to back propagate derivatives at certain stages of the reverse sweep. The temporary storage allocated by the reverse differentiated routines called by `steady_residual_b` is, however, very small.

17.6 Aerodynamic Sensitivities for Rotors in Hover

Hover computations are performed in HMB2 formulating the equations in the rotating reference frame of the rotor, so that the solution is steady. Periodic BCs are also used to take advantage of the symmetry of the problem, allowing for the discretization of a single rotor blade.

With respect to the sensitivities of rotorcraft in hover, the outputs I of interest are the thrust coefficient $C_T = T / (\rho A \Omega^2 R^2)$ and the torque coefficient $C_Q = Q / (\rho A \Omega^2 R^3)$, whereas the independent parameters x are the collective pitch θ , the flap angle β , and the vertical velocity w (see Fig. 17.4). A brief description of the sensitivity equation terms required to compute the aerodynamic derivatives for rotors in hovering flight follows.

17.6.1 Treatment of the Terms $\partial R / \partial \theta, \partial R / \partial \beta$

These partial derivatives represent the variation of the residual vector R due to a change of the pitch or flap angle. For the computation of any of these two terms, it is convenient to express the derivative as follows:

$$\frac{\partial R}{\partial x} = \frac{\partial R}{\partial N} \frac{\partial N}{\partial X} \frac{\partial X}{\partial x}, \quad x \in \{\alpha, \beta\} \tag{17.17}$$

Recalling that the action of the steady residual function differentiated in tangent mode is given by Eq. (17.17), the desired term $\partial R / \partial x$ can be computed by a single call to `steady_residual_d` with $\delta \dot{X} = 0, \delta N = \partial N / \partial X \partial X / \partial x, \delta W = W_x, \delta M_\infty = 0$.

The term $\partial N / \partial X$ can be obtained by tangent differentiation of the function computing the mesh metrics, whereas the term $\partial X / \partial x$, with $x \in \{\alpha, \beta\}$, is computed by differentiation in tangent mode of a mesh-deformation function based

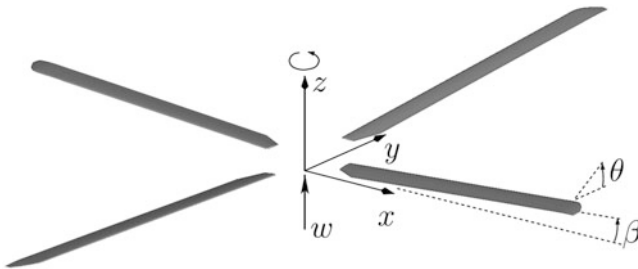


Fig. 17.4 Pseudocode for the steady residual function differentiated in reverse mode (Biava et al. 2016)

on inverse distance weighting (IDW) (Shepard 1968). This function evaluates the mesh differentials due to a rigid rotation around the pitch or flap axis of the blade surface, and of the consequent volume mesh deformation, which is set up so as to keep the other mesh boundaries (periodic planes and far field) fixed.

17.6.2 Treatment of the Term $\partial \mathbf{R} / \partial w$

These partial derivatives represent the variation of the residual vector \mathbf{R} due to a variation of the velocity along the rotor axis of rotation. The computation of these terms requires expressing the derivative as

$$\frac{\partial \mathbf{R}}{\partial w} = \frac{\partial \mathbf{R}}{\partial \dot{\mathbf{X}}} \frac{\partial \dot{\mathbf{X}}}{\partial w} \quad (17.18)$$

The right-hand side of Eq. (17.18) can be computed by a single call to the function `steady_residual_d` with $\delta \dot{\mathbf{X}} = 0$, $\delta \mathbf{N} = \partial \mathbf{R} / \partial \dot{\mathbf{X}} \partial \dot{\mathbf{X}} / \partial w$, $\delta \mathbf{W} = \mathbf{W}_x^n$, $\delta M_\infty = 0$. The derivative $\partial \dot{\mathbf{X}} / \partial w$ is easy to compute, as it represents a uniform variation of the mesh velocities in the direction of the rotor-rotation axis.

17.6.3 Treatment of the Terms $\partial I / \partial \theta$, $\partial I / \partial \beta$

These partial derivatives represent the direct dependence of force and moment coefficients upon the pitch and flap angle. They can be computed by expressing the derivative as

$$\frac{\partial I}{\partial x} = \frac{\partial I}{\partial \mathbf{N}} \frac{\partial \mathbf{N}}{\partial \mathbf{X}} \frac{\partial \mathbf{X}}{\partial x}, \quad x \in \{\alpha, \beta\} \quad (17.19)$$

and computing $\partial \mathbf{X} / \partial x$ as described in Sect. 17.6.1.

17.7 Numerical Results

17.7.1 Inviscid ONERA 7AD Rotor in Hover

To verify the computation of aerodynamic sensitivities for rotors, the inviscid flow around the ONERA 7AD rotor in hover flight was computed. The tip Mach number was $M_{\text{tip}} = 0.6612$ and the collective pitch was $\theta_{0.7} = 7.5$ deg. A multi-block mesh with 880,000 cells per blade was used, and the effect of the other blades

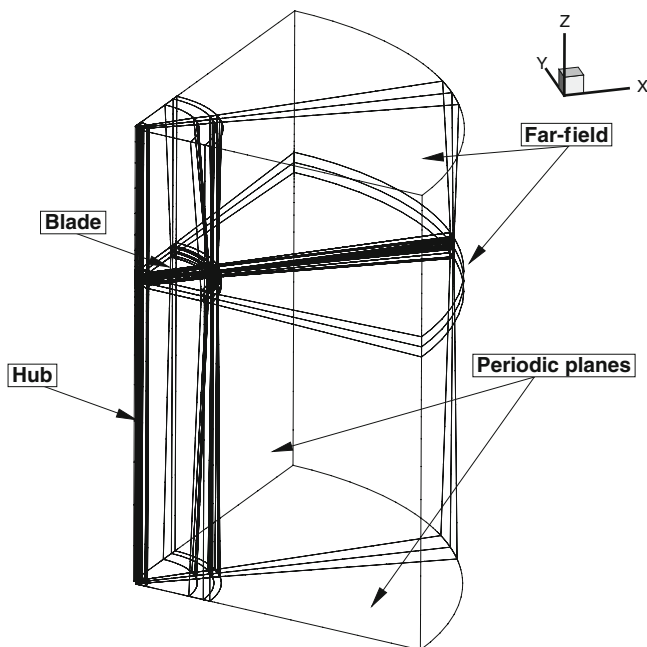


Fig. 17.5 Mesh topology for the 7AD rotor in hover (Biava et al. 2016)

Table 17.2 HMB2 sensitivity results for the ONERA 7AD rotor

	C_T	C_Q
θ	0.1191865	0.0125512
θ_{tw}	-0.0044539	-0.0009800

was accounted for using periodic BCs (see Fig. 17.5). At the far-field boundaries, Froude conditions were imposed to better represent the flow induced by the rotor and to avoid the formation of artificial recirculation regions. The Courant–Friedrichs–Lewy (CFL) number for the base-flow and tangent solvers was set to 8.

The derivatives of the thrust coefficient C_T and of the torque coefficient C_Q computed with HMB2 solving the sensitivity equation in tangent and adjoint modes are shown in Table 17.2, in which θ denotes the collective angle of the rotor and θ_{tw} the blade-twist angle centered at 70% of the blade span. Because no sensitivity result is available in the literature for this rotor, the sensitivities computed with the automatically differentiated code were compared with those obtained via the second-order centered FDs. The comparison relative to the collective-angle sensitivity is shown in Table 17.3, in which a good agreement between the two methods can be observed.

The method for computing the partial derivatives with respect to the collective angle is based on the chain-rule expansion (17.17) and mesh deformation using IDW, differentiated with AD. The variation of the control angle is introduced as a differential deformation field, which represents a rotation of the blade surface that

Table 17.3 Comparison of collective-angle sensitivity computed with AD and FD for the ONERA 7AD rotor

	$\partial C_T / \partial \theta$	$\partial C_Q / \partial \theta$
HMB2 AD tangent	0.1191865	0.0125512
HMB2 AD adjoint	0.1191865	0.0125512
HMB2 FD	0.1200453	0.0125287
Difference, %	0.730	0.180

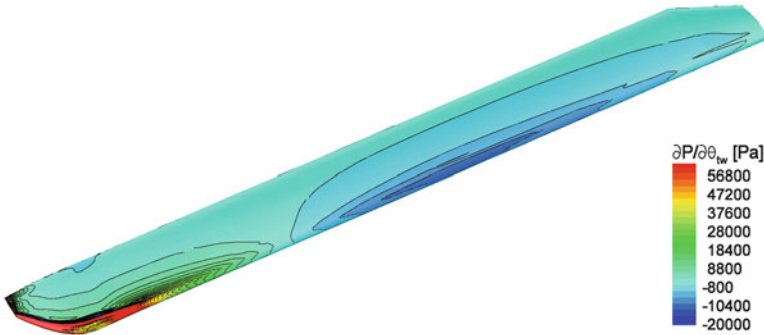


Fig. 17.6 Surface pressure sensitivity to the twist angle for the ONERA 7AD rotor (Biava et al. 2016)

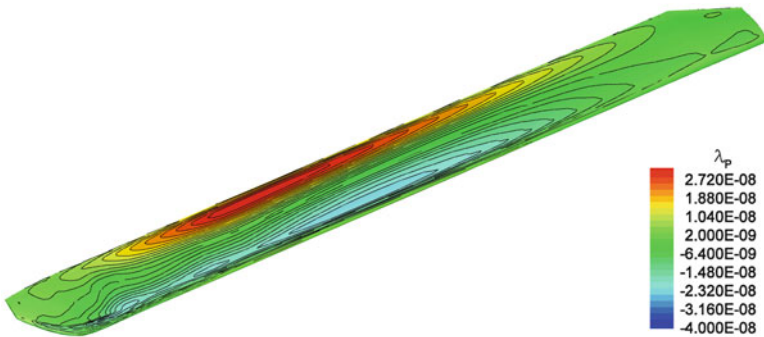


Fig. 17.7 Pressure equation adjoint variable of the thrust coefficient for the ONERA 7AD rotor (Biava et al. 2016)

vanishes at the hub, the far field, and the periodic planes. The method is general and allows computing the flow derivative with respect to an arbitrary deformation of the blade, a feature particularly useful for the application of the adjoint method in aerodynamic shape optimization. For instance, Fig. 17.6 shows the surface distribution of the pressure derivative with respect to a twist variation centered at the blade section with $r/R = 0.7$, whereas Fig. 17.7 shows the distribution of the adjoint variable of the thrust coefficient C_T relative to the pressure equation.

17.7.2 Viscous Flow Around the S-76 Rotor in Hover

An accurate estimation of rotor flight-mechanic derivatives requires high-fidelity modeling of the flow. The sensitivity-equation approach has been therefore extended to the full three-dimensional RANS equations completed with the $k\text{-}\omega$ turbulence model (Wilcox 1988). To demonstrate the method, the flow sensitivity of an S-76 rotor in hover flight (Balch and Lombardi 1985) was analyzed, with viscosity and turbulence model.

The tip Mach number was $M_{\text{Tip}} = 0.65$, the Reynolds number was $\text{Re} = 1.1 \cdot 10^6$, and the collective pitch was $\theta_{0.75} = 7.5$ deg. The mesh had 9 million cells per blade, and the effect of the other blades was modeled with periodic BCs. At the far-field boundaries, Froude conditions were imposed. The CFL number for the base-flow solver and for the tangent solver was set to 3.

Note that the second-order Jacobian of the flow equations for the S-76 mesh needs about 52 GB of memory storage. It is clear that memory requirement poses a severe limit to the application of methods needing explicit storage of the Jacobian matrix. The matrix-free approach, on the other hand, alleviates this memory requirement and proves to be particularly suited for large-scale applications.

The derivatives of the thrust coefficient C_T and of the torque coefficient C_Q computed with HMB2 solving the sensitivity equation in tangent mode are shown in Table 17.4. A fairly good agreement was found between the obtained sensitivity of the thrust coefficient with respect to the collective, and the theoretical value computed by

$$\frac{\partial C_T}{\partial \theta} = \frac{\sigma a}{6} \left[1 - \frac{1}{\sqrt{1 + 64 + (3\sigma a)\theta}} \right] \quad (17.20)$$

In Eq. (17.20), $\sigma = 0.0704$ and $a = 6.113$. Note that the Euler computation for the ONERA 7AD case overestimates the derivative $\partial C_T / \partial \theta$, and that high-fidelity flow modeling leads to a better estimate. Table 17.5 shows a comparison between the collective-angle sensitivity computed with AD and the second-order centered FD. The relative error is less than 0.6% for both the thrust and torque coefficients.

Table 17.4 HMB2 sensitivity results for the S-76 rotor

	C_T	C_Q
θ	0.0922836	0.0090250
θ_{tw}	-0.0035866	-0.0006710

Table 17.5 Comparison of collective-angle sensitivity computed with AD and FD for the S-76 rotor

	$\partial C_T / \partial \theta$	$\partial C_Q / \partial \theta$
HMB2 AD tangent	0.0922836	0.0090250
HMB2 FD	0.0917879	0.0089743
Difference, %	0.537	0.562

17.8 Conclusions

This chapter presented the implementation and assessment of AD and the discrete adjoint method for the computation of rotorcraft stability derivatives with CFD. The method benefits from the fully implicit formulation of the adjoint solver, and achieves a low-memory footprint by avoiding the storage of the high-order Jacobian. After implementation, the aerodynamic derivatives for rotors in hover were computed, and the results were found to agree with FD computations. The cost for solving the sensitivity equation with the fully implicit method was shown to be lower than that of the nonlinear base flow solution, even for complex turbulent flow cases.

References

- Anderson WK, Bonhaus DL (1999) Airfoil design on unstructured grids for turbulent flows. *AIAA J* 37(2):185–191
- Anon (nd) Community portal for automatic differentiation. Retrieved 5 1, 2015, from <http://www.autodiff.org>
- Anon (nd) The TAPENADE tutorial. Retrieved 5 1, 2015, from <http://www-sop.inria.fr/tropics/tapenade.html>
- Axelsson O (1994) *Iterative Solution Methods*. Cambridge Univ. Press, Cambridge, MA
- Balch DT, Lombardi J (1985) Experimental study of main rotor tip geometry and tail rotor interactions in hover, vol I, Text and Figures. NASA CR 177336, NASA
- Barakos G, Steijl R, Badcock K, Brocklehurst A (2005) 31st European Rotorcraft Forum [CD-ROM]. Societies, Council of European Aerospace, Development of CFD Capability for Full Helicopter Engineering Analysis
- Bartholomew-Biggs MC, Brown S, Christianson B, Dixon LC (2000) Automatic differentiation of algorithms. *J Comput Appl Math* 124:171–190
- Biava M, Woodgate M, Barakos GN (2016) Fully implicit discrete adjoint methods for rotorcraft applications. *AIAA J* 54(2):735–749
- Carle A, Fagan, M (2000) ADIFOR 3.0 overview. TR CAAM-TR-00-02, Rice University, Houston, TX
- Choi S, Lee K, Potsdam M, Alonso JJ (2014) Helicopter rotor design using a time-spectral and adjoint-based method. *J Aircr* 51(2):412–423
- Christianson B (1998) Reverse accumulation and implicit functions. *Optimization Methods and Software* 9(4):307–322
- Dwight RP, Brezillon J (2006) Effect of approximations of the discrete adjoint on gradient-based optimization. *AIAA J* 44(12):3022–3031
- Elliott J, Peraire J (1997) Practical three-dimensional aerodynamic design and optimization using unstructured meshes. *AIAA J* 35(9):1479–1485
- Giering R, Kaminski T, Slawig T (2005) Generating efficient derivative code with TAF: adjoint and tangent linear Euler flow around an airfoil. *Futur Gener Comput Syst* 21(8):1345–1355
- Giles MB (2002) On the iterative solution of adjoint equations. In: Corliss G, Faure C, Griewank A, Hascoët L, Naumann U (eds) *Automatic differentiation of algorithms*. Springer, New York, pp 145–151
- Giles MB, Pierce NA (2000) An introduction to the adjoint approach to design. *Flow Turbul Combust* 65(3–4):393–415

- Gockenbach MS (2000) Understanding code generated by TAMC. IAAA Paper, Department of Computational and Applied Mathematics, Rice University, Houston, TX
- Griewank A (2003) A mathematical view of automatic differentiation. *Acta Numer* 12:321–398
- Griewank A, Walther A (2008) Evaluating derivatives: principles and techniques of algorithmic differentiation, 2nd edn. SIAM, Philadelphia
- Hascoët L, Pascual V (2004) TAPENADE 2.1 user's guide. Tech. rep., Institut National de Recherche en Informatique et en Automatique, Sophia Antipolis, France
- Huang H, Ekici K (2014) A discrete adjoint harmonic balance method for turbomachinery shape optimization. *Aerosp Sci Technol* 39:481–490
- Jameson A (1988) Aerodynamic design via control theory. *J Sci Comput* 3(3):233–260
- Jameson A (1990) Control theory for optimum design of aerodynamic shapes. In: Proceedings of the IEEE conference on decision and control, vol 1. Institute of Electrical and Electronics Engineers, New York, pp 176–179
- Jameson A (1991) Time dependent calculations using multigrid with application to unsteady flows past airfoils and wings. In: 10th computational fluid dynamics conference, Honolulu, HI, June 24–26. AIAA Paper
- Jameson A, Martinelli L, Pierce NA (1998) Optimum aerodynamic design using the Navier–Stokes equations. *Theor Comput Fluid Dyn* 10(1–4):213–237
- Jameson A, Pierce NA, Martinelli L (1997) Optimum aerodynamic design using the Navier–Stokes equations. In: 35th AIAA aerospace sciences meeting and exhibit, Reno, NV, Jan 6–9, AIAA paper 97–0101, pp 1–22
- Jones D, Müller J-D, Christakopoulos F (2011) Preparation and assembly of discrete adjoint CFD codes. *Comput Fluids* 46(1):282–286
- Limache AC, Cliff EM (2000) Aerodynamic sensitivity theory for rotary stability derivatives. *J Aircr* 37(4):676–683
- Lyu Z, Martins JR (2014) Aerodynamic design optimization studies of a blended-wing-body aircraft. *J Aircr* 51(5):1604–1617
- Lyu Z, Kenway GK, Paige C, Martins JR (2013) Automatic differentiation adjoint of the Reynolds-averaged Navier–Stokes equations with a turbulence model. In: 21st AIAA computational fluid dynamics conference, San Diego, CA, 24–27 June 2013
- Mader CA, Martins JR (2011) Computation of aircraft stability derivatives using an automatic differentiation adjoint approach. *AIAA J* 49(12):2737–2750
- Mader CA, Martins JR (2012) Derivatives for time-spectral computational fluid dynamics using an automatic differentiation adjoint. *AIAA J* 50(12):2809–2819
- Mader CA, Martins JR, Alonso JJ, Weide ED (2008) ADjoint: an approach for the rapid development of discrete adjoint solvers. *AIAA J* 46(4):863–873
- Mani K, Mavriplis DJ (2009) Adjoint-based sensitivity formulation for fully coupled unsteady aeroelasticity problems. *AIAA J* 47(8):1902–1915
- Marta AC, Mader CA, Martins JR, Van Der Weide E, Alonso JJ (2007) A methodology for the development of discrete adjoint solvers using automatic differentiation tools. *Int J Comput Fluid Dyn* 21(9–10):307–327
- Marta AC, Shankaran S, Wang Q, Venugopal P (2013) Interpretation of adjoint solutions for turbomachinery flows. *AIAA J* 51(7):1733–1744
- Mavriplis D (2007) Discrete adjoint-based approach for optimization problems on three-dimensional unstructured meshes. *AIAA J* 45(4):740–750
- Mohammadi B (1997) Optimal shape design, reverse mode of automatic differentiation and turbulence. In: 35th aerospace sciences meeting and exhibit, Reno, NV, AIAA paper 97–0099
- Mohammadi B (1997) Practical application to fluid flows of automatic differentiation for design problems. Inverse design and optimization methods. Lecture series 1997–05, von Karman Institute for Fluid Dynamics, Rhode Saint Genese, Belgium, pp M1–M34

- Müller J-D, Cusdin P (2005) On the performance of discrete adjoint CFD codes using automatic differentiation. *Int J Numer Methods Fluids* 47(8–9):939–945
- Newman JC, Taylor AC, Barnwell RW, Newman PA, Hou GJ (1999) Overview of sensitivity analysis and shape optimization for complex aerodynamic configurations. *J Aircr* 36(1):87–96
- Osusky L, Zingg DW (2013) Application of an efficient Newton-Krylov algorithm for aerodynamic shape optimization based on the Reynolds-averaged Navier–Stokes equations. In: 21st AIAA computational fluid dynamics conference, San Diego, CA, June 24–27, 2013, pp 1–18
- Pironneau O (1974) On optimum design in fluid mechanics. *J Fluid Mech* 64(1):97–110
- Reuther J, Jameson A (1994) Control theory based airfoil design using the Euler equations. In: AIAA/USAF/NASA/ISSMO symposium on multidisciplinary analysis and optimization, 94, Columbia, MD, AIAA Paper 1994-CP4272, pp 1–17
- Reuther J, Jameson A, Farmer J, Martinelli L, Saunders D (1996) Aerodynamic shape optimization of complex aircraft configurations via an adjoint formulation. In: 34th AIAA aerospace sciences meeting and exhibit, Reno, NV, Jan 15–18, 1996, AIAA Paper 1996-0094
- Shepard D (1968) A two-dimensional interpolation function for irregularly-spaced data. In: Proceedings of the 1968 23rd ACM national conference, Association for Computing Machinery, New York, pp 517–524
- Steijl R, Barakos GN, Badcock K (2006) A framework for CFD analysis of helicopter rotors in hover and forward flight. *Int J Numer Methods Fluids* 51(8):819–847
- Thomas JP, Dowell EH, Hall KC (2013) Discrete adjoint method for nonlinear aeroelastic sensitivities for compressible and viscous flows. In: 54th AIAA/ASME/ASCE/AHS/ASC structures, structural dynamics, and materials conference, Boston, pp 6144–6152
- Wilcox DC (1988) Re-assessment of the scale-determining equation for advanced turbulence models. *AIAA J* 26(11):1299–1310
- Woodgate M, Barakos G (2012) Implicit computational fluid dynamics methods for fast analysis of rotor flows. *AIAA J* 50(6):1217–1244

Part VI
Structural Dynamics of Blades
and Components

Chapter 18

Dynamics of the Synthetic Jet Actuator Investigation by the Numerical and Experimental Approach

Rūta Rimašauskienė

18.1 Introduction

The study of synthetic jets (SJ) emerged as an intriguing new field in the past few years. In fluid dynamics, synthetic jet flow is a jet flow synthesized from ambient fluid (Yang et al. 2009; Qayoum Gupta et al. 2010). A jet flow is such flow of a fluid where a stream of fluid mixes with surrounding medium. Synthetic jet flow can be generated in a number of ways, for example, using electromagnetic, piezoelectric or even mechanical driver, such as a piston. Each installation moves a diaphragm up and down hundreds of times per second, sucking the surrounding fluid into a chamber and then expelling it.

This chapter presents numerical and experimental modal analysis of piezoelectric actuator Sonox P502, analogical analysis of the brass diaphragm with bonded piezoelectric actuator Sonox P502 and sound transducer LD-BZPN-2030, which can be used as the diaphragm in the structure of the synthetic jet generator. The aim of these investigations was to compare theoretical and experimental data that are important for control of synthetic jet devices. And to check FE model in Ansys 12.1 software because later it was included into co-simulation platform MpCCI and extended with sensory system. As it is known, in order to obtain proper control of flow, it is necessary to find the most suitable mode shapes and achieve the maximum displacement of the diaphragm.

Using scanning laser vibrometer Polytec 3D, vibration mode shapes and displacements of piezoelectric actuator and brass diaphragms were defined in a way of changing control frequencies.

R. Rimašauskienė (✉)

Department of Production Engineering, Kaunas University of Technology, Studentų St. 56,
Kaunas LT-51424, Lithuania

e-mail: ruta.rimasauskiene@ktu.lt

Numerical simulations of piezoelectric actuator, brass diaphragm with bonded actuator and sound transducer LD-BZPN-2030 (which can be used as the diaphragm) were performed aiming to validate operating principle through the modal analysis. The simulations were performed using FEM software ANSYS 12.0. Modal analysis of piezoelectric actuator Sonox P502, brass diaphragms with piezoelectric actuator and sound transducer LD-BZPN-2030 was performed aimed to find proper resonance frequencies and mode shapes. The results of modal analysis showed that mode shapes are similar to experimentally identified shapes.

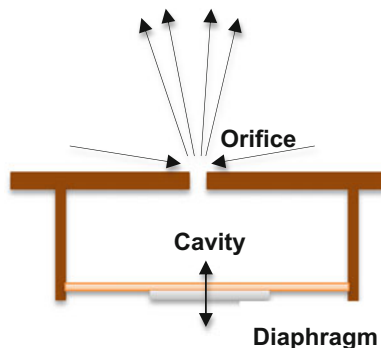
During experimental analysis discrepancies of the experimental and numerical results were found. Therefore it was decided to change FE model in order to obtain better results and smaller differences between numerical and experimental results.

18.2 Structure of Synthetic Jet Generator and Results of Numerical Simulation

Usually, synthetic jet's chamber consists of a diaphragm oscillating in a circular space and an orifice opposite to the diaphragm (Fig. 18.1). The oscillation of a diaphragm generates two, intake and exhaust, flows in the orifice. The intake flow separates and forms a vortex sheet that rolls up into a single vortex as it moves away from the orifice at its self-induced velocity. If the velocity is high enough, entrance to the chamber is prevented and the air jet forms. Thus a linear momentum is transferred into the flow system even though net mass injection is zero. Consequently, these jets are also called “zero net mass flux” jets (Yang et al. 2009; Qayoum Gupta et al. 2010).

Finite element method was used to perform modal frequency analysis and to calculate shapes of the piezoelectric actuators (with electrodes) and diaphragms surfaces movements. Natural frequencies and modal shapes of the surfaces were found. Numerical simulations of piezoelectric actuator and active diaphragms with piezoelectric actuators were performed aiming to validate actuator's operation

Fig. 18.1 Scheme of the synthetic jet generator



pattern through modal analysis. FEM software ANSYS Multiphysics 12.1 was employed for the simulation. FE models for actuator Sonox P502 (diameter 10 mm, thickness 0.5 mm), brass diaphragm (diameter 20 mm, thickness 0.15 mm) with bonded piezoelectric actuator and sound transducer LD-BZPN-2030 (diameter 20 mm, thickness 0.15 mm) were built.

Modal analysis of piezoelectric actuator and diaphragms with bonded piezoelectric actuator were performed in order to find proper resonance frequencies and shapes of the surfaces.

18.2.1 FE (Finite Element) Model of Piezoelectric Actuator Sonox P502

For the study, piezoelectric actuator Sonox P502 (diameter 10 mm, thickness 0.5 mm) manufactured by the company *CeramTec* was selected. These types of piezoelectric actuators are used in aviation because of their ability to work in different environments.

The properties of piezoceramic material of Sonox P502 are $S_{11}^E = S_{22}^E = 18.5p \left(\frac{m^2}{N}\right)$, $S_{33}^E = 20.7p \left(\frac{m^2}{N}\right)$, $S_{12}^E = -6.29p \left(\frac{m^2}{N}\right)$, $S_{13}^E = -6.23p \left(\frac{m^2}{N}\right)$, $S_{44}^E = S_{55}^E = 33.2p \left(\frac{m^2}{N}\right)$, $S_{66}^E = 52.3p \left(\frac{m^2}{N}\right)$, $d_{31} = d_{32} = -185\frac{pC}{N}$, $d_{33} = 440\frac{pC}{N}$, $d_{15} = d_{24} = 560\frac{pC}{N}$, $\epsilon_{11}^T = \epsilon_{22}^T = 1950\epsilon_0$, $\epsilon_{33}^T = 1850\epsilon_0$ (Trindade and Benjeddou 2011). Actuators are used mainly in mixed systems where piezoelectric ceramics are used as an ultrasonic transducer on the one hand and as a receiver on the other hand.

Sonox P502 is made from specifically created high-performance materials with a high rate of thermal and temporal stability. For this reason, it is extremely suitable for automotive and aircrafts industry applications in a range of temperatures from -40 to $+160$ °C.

Standard electrodes are silver or nickel-gold plated. Special electrode configurations are feasible to achieve enhanced functionality. Metal plating can be applied with or without insulation margin. The standard insulation margin is ≤ 0.3 mm.

Modal analysis of piezoelectric actuator was performed in order to find proper resonance frequencies and shapes. The electrodes were tightly fixed at the bottom and in place where they contacted a piezo disc (Fig. 18.2).

Examination of the results of modal analysis showed that vibration modes No. 1 (963.28 Hz), No. 2 (5.68 kHz) and No. 3 (12.26 kHz) (Fig. 18.3) are interesting and useful for further investigation.

The surface shapes of piezoelectric actuators were investigated. Excitation voltage of ± 100 V was selected. The test involved frequencies from 0 to 30 kHz, every 0.25 kHz.

Using finite element method shapes of the piezoelectric actuator Sonox P502 at three above-mentioned resonance frequencies were found. This means that the

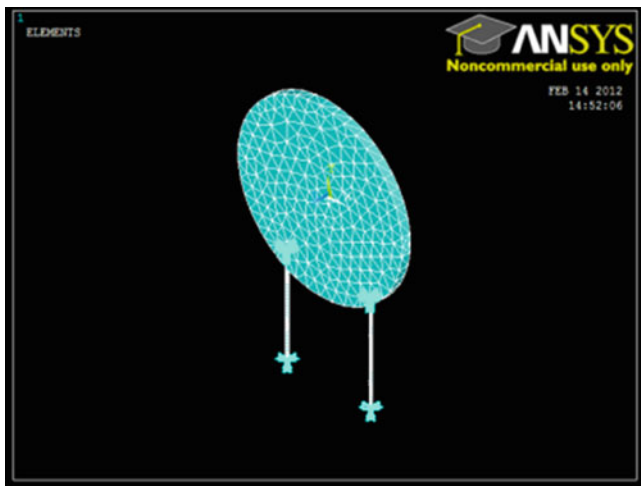


Fig. 18.2 Model of the piezoelectric actuator in Ansys 12.1

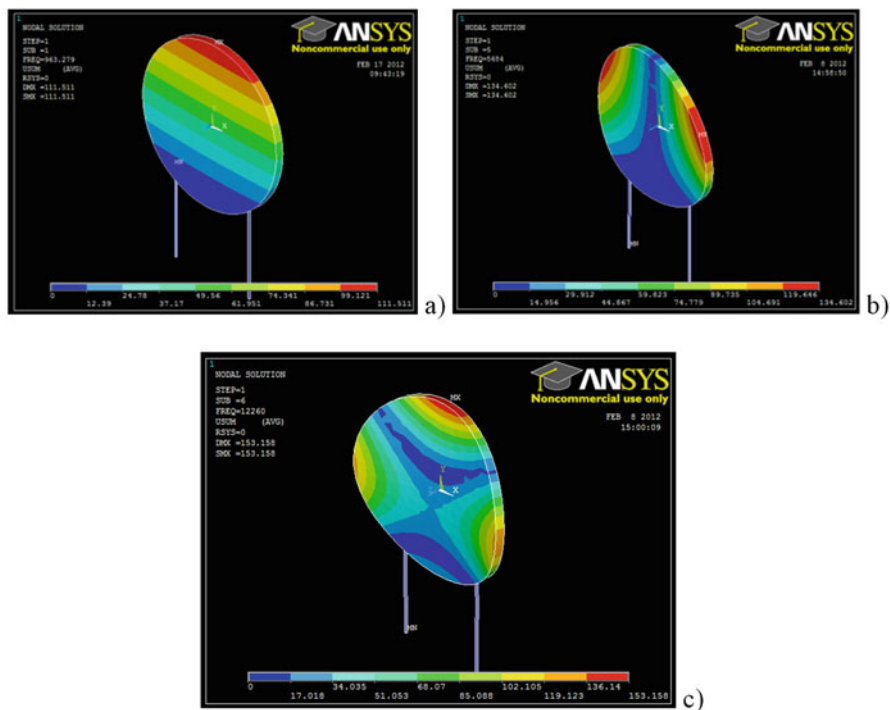


Fig. 18.3 Vibration modes of the piezoelectric actuator: (a) the first mode ($f = 963.28$ Hz), (b) the second mode ($f = 5.68$ kHz), (c) the third mode ($f = 12.26$ kHz)

actuator was analysed in a way of modal analysis. And lately it was very important to compare numerical and experimental results (Rimašauskienė and Ostachowicz 2012).

18.2.2 FE Model of the Brass Diaphragm with Bonded Piezoelectric Actuator Sonox P502

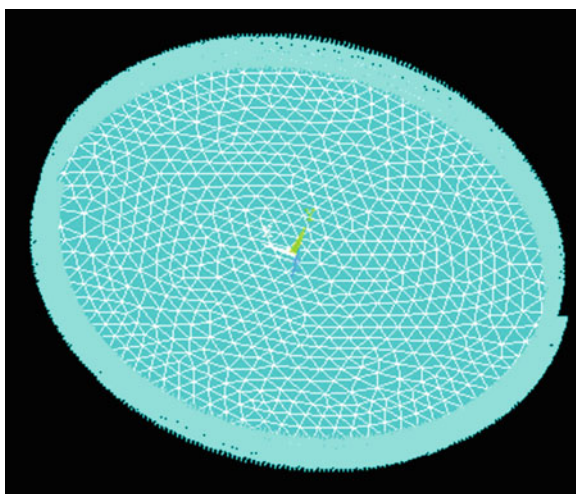
Aiming to perform modal analysis and to find resonance frequencies and mode shapes of diaphragm with piezoelectric actuator Sonox P502 surfaces finite element method was used.

Numerical simulations of the brass diaphragm with bonded actuator Sonox P502 were performed aiming to validate actuator's operation pattern through modal analysis. The simulation was performed using FEM software ANSYS 12.1 (Rimašauskienė et al. 2015).

In numerical simulation of the brass diaphragm with bonded piezoelectric actuator Sonox P502, the edge of the diaphragm was fixed tightly (Fig. 18.4). All volumes were meshed by 3 coupled-field tetrahedral finite element SOLID 98. Material properties required for the analysis of piezoelectric materials (permittivity, piezoelectric matrix, elastic coefficient matrix, density) were entered into the programme. During analysis with diaphragm, brass material properties were entered additionally. Properties of brass: density 8400 kg/m^3 , Young's modulus 100 GPa and Poisson's ratio 0.31.

Using FE modal analysis, natural resonant frequencies and mode shapes of the brass diaphragm (diameter 20 mm, thicknesses 0.15 mm) with bonded piezoelectric actuator Sonox P502 were found.

Fig. 18.4 Finite element model of the brass diaphragm with bonded piezoelectric actuator in Ansys 12.1



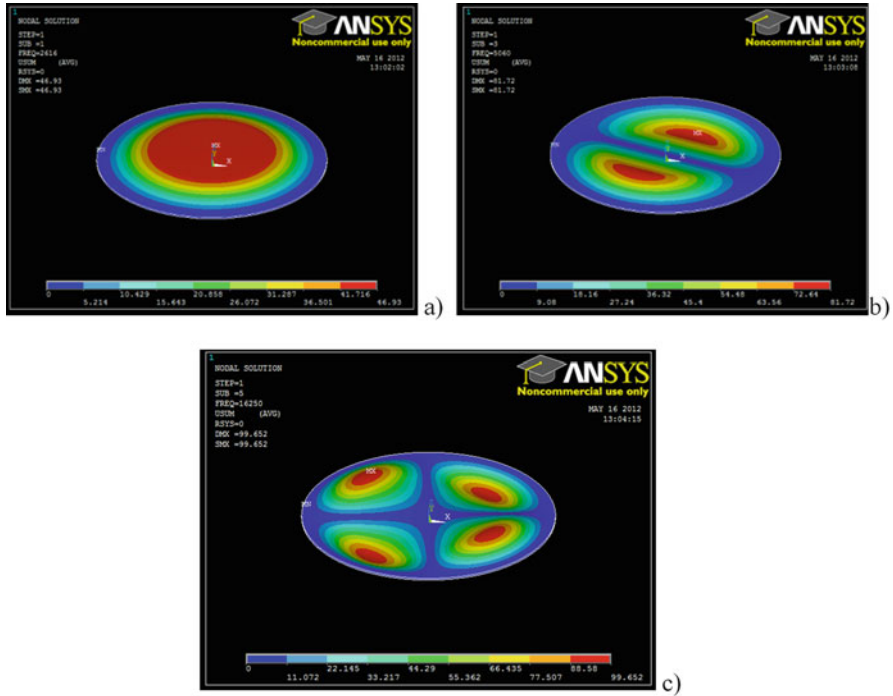


Fig. 18.5 Mode shapes of a diaphragm with piezoelectric actuator: (a) the first mode ($f = 2.615$ kHz), (b) the second mode ($f = 5.06$ kHz), (c) the third mode ($f = 16.25$ kHz)

The examination of the results of modal analysis disclosed that vibration modes No. 1 (2.615 Hz), No. 2 (5.06 kHz) and No. 3 (16.25 kHz) (Fig. 18.5) are interesting and useful for further investigation (Rimašauskienė et al. 2015).

18.2.3 FE Model of Sound Transducer LD-BZPN-2030

A proposal to perform modal analysis and to find resonance frequencies and mode shapes of sound transducer LD-BZPN-2030 surface finite element method was used. Finite element model of diaphragm looks similar as diaphragms with bonded actuator Sonox P502 (Fig. 18.4).

Using FE modal analysis, natural resonant frequencies and mode shapes of diaphragm LD-BZPN-2030 (diameter 20 mm, thicknesses 0.15 mm) with piezoelectric actuator were found.

The examination of the results of modal analysis disclosed that vibration modes No. 1 (4.77 Hz), No. 2 (10.06 kHz) and No. 3 (16.12 kHz) (Fig. 18.6) are interesting and useful for further investigation (Rimašauskienė et al. 2015).

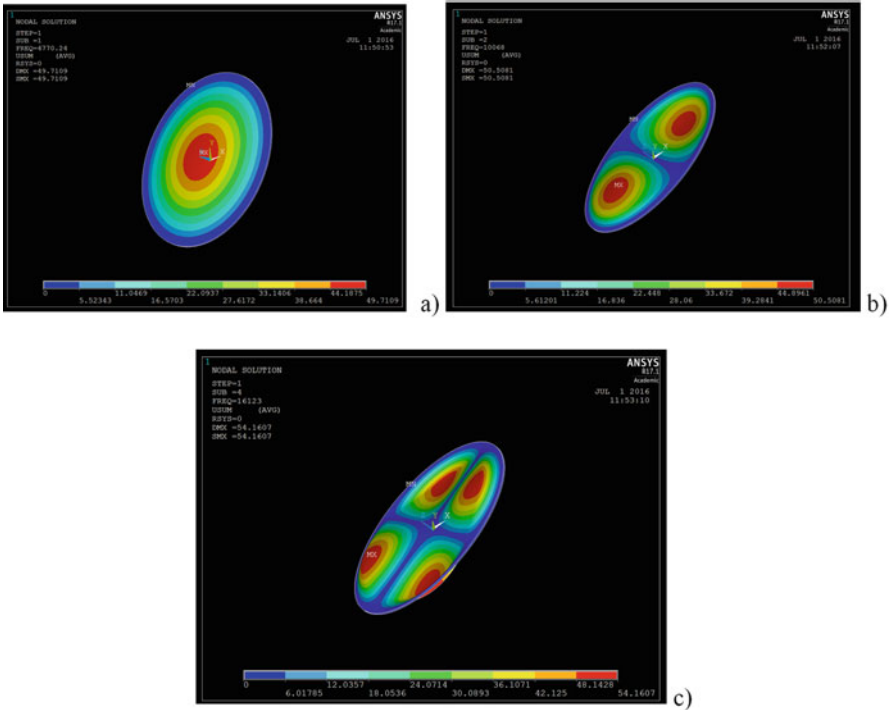


Fig. 18.6 Mode shapes of a diaphragm LD-BZPN-2030: (a) the first mode ($f = 4.77$ kHz), (b) the second mode ($f = 10.06$ kHz), (c) the third mode ($f = 16.12$ kHz)

18.3 Experimental Equipment and Results of Experimental Analysis

Experimental analysis of dynamic characteristics of piezoelectric actuator Sonox P502 and brass diaphragms with piezoelectric actuators was carried out in order to find out what frequency would allow achieving the largest displacement of surfaces and what mode shapes of the piezoelectric actuator and brass diaphragm surfaces are at various resonance frequencies.

18.3.1 Description of Experimental Equipment

Various types of laser vibrometers can be distinguished. The simplest vibrometers allow measuring only velocity of vibrations along the laser beam in one point (manual positioning of laser head). More sophisticated versions of vibrometers allow automatic scanning of velocity of vibration in a defined measuring mesh

(scanning laser vibrometer). But they also measure velocity along the laser beam only. The third type of vibrometers allows measuring three components of vibration velocity simultaneously (3D laser scanning vibrometer).

Laser vibrometer operates on a basis of Doppler effect. A vibrometer registers changes in frequency of a light beam reflecting from vibrating surface.

A fundamental advantage of laser vibrometry is a non-contact measurement. This eliminates detrimental effects of adding mass related to the sensor at a measured point. Another advantage of laser vibrometry is a possibility of 3D measurement of vibrations. This measurement technique allows registering object vibration components in a plane perpendicular to the investigated surface as well as in one parallel to it.

Laser vibrometry allows measuring vibrations in frequencies from close to 0–24 MHz, as well as a wide range of vibration velocities—from 20 nm/s to 20 m/s.

All mentioned advantages make laser vibrometry one of the most effective non-contact measurement techniques that allow registering vibrations of structures and propagations of elastic waves.

Measurements were performed using 3D scanning laser vibrometer Polytec® PSV 400 (Fig. 18.7). This vibrometer consists of three laser scanning heads, a control unit with built-in signal generator and PC with vibrometer software. It should be mentioned that during the experimental analysis, only 1D measurements, using one laser scanning head, were conducted. Only vibration velocity along the laser beam (without a plane component) was recorded.

During the measurement, vibration displacements instead of velocities were extracted. It is possible to measure velocity or displacement; however it should be underlined that vibrometer measures velocity and calculates displacements based on velocities measured. The measured surface in some cases was covered with retroreflective tape in order to enhance the signal to noise ratio (SNR).

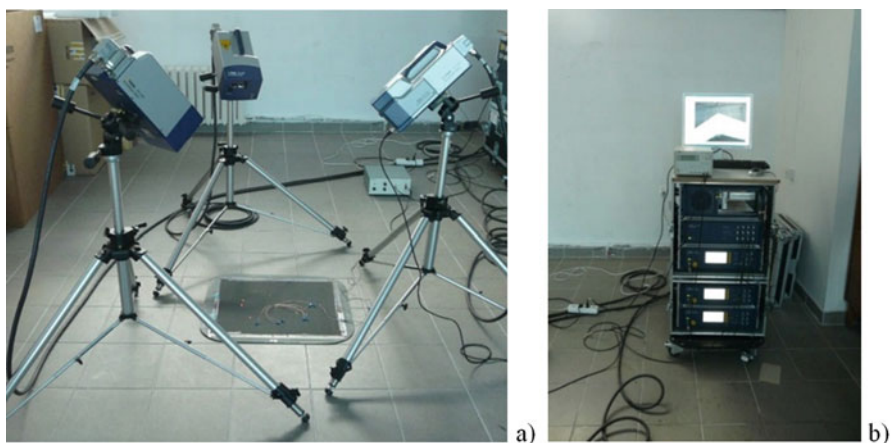


Fig. 18.7 Polytec 3D laser vibrometer: (a) three scanning heads for 3D vibration measurement, (b) control unit

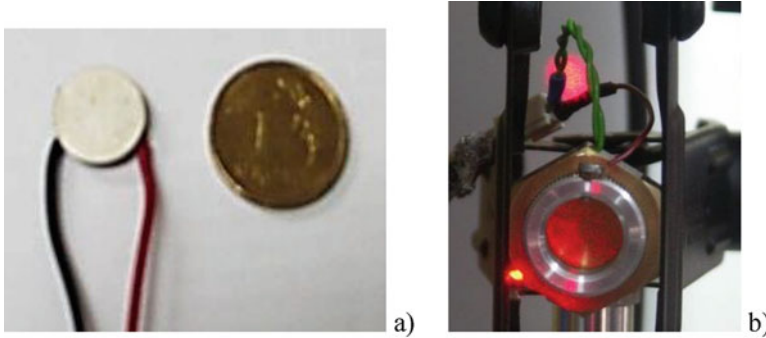


Fig. 18.8 Experimental equipment: (a) piezoelectric actuator Sonox P502, (b) brass diaphragm with piezoelectric actuators fixed inside the chamber

Laser scanning vibrometry is ideally suitable for modal tests because it provides an unambiguous phase reference, highly precise measurement without mass loading problems and a high spatial resolution for detailed FEM correlations.

During the experimental analysis, piezoelectric actuator Sonox P502 was excited by sinusoidal voltage. In the first case, piezoelectric actuator was fixed by electrodes (Fig. 18.7a); in the second and third cases, brass diaphragms were fixed tightly inside the chamber of a synthetic jet (Fig. 18.8b) (Rimašauskienė and Ostachowicz 2012).

Using 3D laser vibrometer *Polytec® PSV 400* and computer with specifically designed programme PSV 8.8, the dependences of displacements on frequency were found. During the experiments, excitation voltages were kept constant, frequency varied, and the displacement of piezoelectric actuator and brass diaphragms surfaces were measured (Rimašauskienė and Ostachowicz 2012).

During the experimental analysis, piezoelectric actuator Sonox P502 was excited by sinusoidal voltage. Literature tells that vibrations can be described in trigonometric functions or complex numbers. It is useful to note that piezoceramics exciting with a help of sinusoidal voltage courses harmonic vibrations. A harmonic vibration is described in frequency, amplitude and zero phase angles as follows (Rimašauskienė and Ostachowicz 2012):

$$U(t) = A \cos(\omega t + \varphi_0) \quad (18.1)$$

where

$$\omega = 2\pi f \quad (18.2)$$

A , amplitude; ω , angular frequency; φ_0 , zero phase angle; and f , frequency.

With a help of the addition theorems, it is possible to rewrite Eq. (18.1) as

$$U(t) = A \cos \varphi_0 \cos \omega t - A \sin \varphi_0 \sin \omega t \quad (18.3)$$

$A_{\cos} = A \cos \varphi_0$, amplitude of the cosine part; $A_{\sin} = A \sin \varphi_0$, amplitude of the sine part.

A harmonic vibration can be described as a superposition of a sinusoidal and cosinusoidal vibration whose amplitudes depend on the zero phase angles.

18.3.2 Experimental Analysis of Piezoelectric Actuator Sonox P502 and Brass Diaphragms with Piezoelectric Actuators

Using experimental equipment resonance frequencies and mode shapes of piezoelectric actuator Sonox P502 were found. The piezoelectric actuator was excited by sinusoidal voltage ± 100 V. Figure 18.9 shows that the biggest displacement of the surface of piezoelectric actuator was obtained in the third resonance frequency (12.29 kHz). Maximum displacement of the surface of piezoelectric actuator was 3.2 nm. And in the first resonance frequency (1.59 kHz), it was 2.2 nm.

Figure 18.10 presented the mode shapes of the surface of piezoelectric actuator Sonox P502 in the first three resonance frequencies. In order to improve the validity of a model, it was useful to make an experimental analysis and to recognize shapes of this actuator.

After measurements, piezoelectric actuator Sonox P502 was bonded to the centre of the brass diaphragm (diameter 20 mm, thickness 0.15 mm). And the same

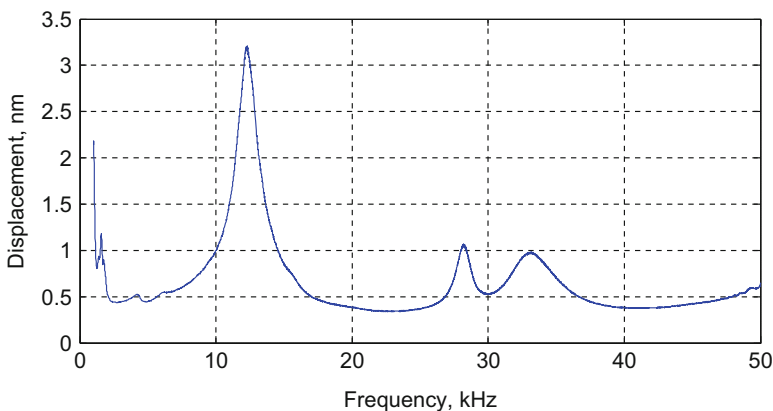


Fig. 18.9 Dependence of the displacement of surface of piezoelectric actuator Sonox P502 on frequency (voltage ± 100 V)

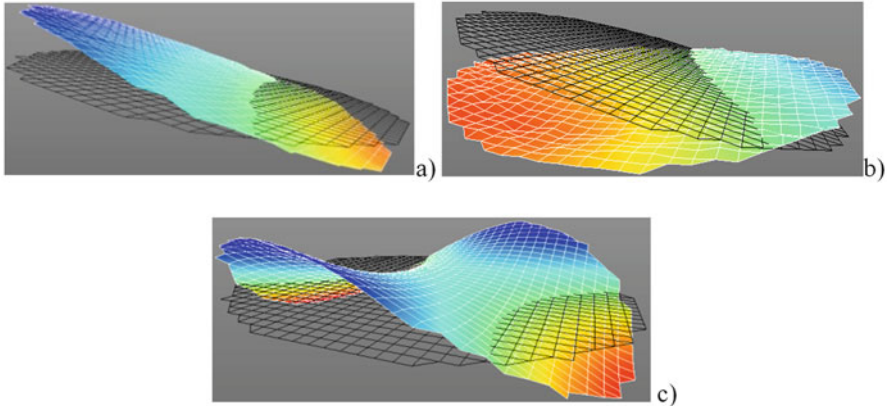


Fig. 18.10 Experimental mode shapes of the surface of piezoelectric actuator Sonox P502: (a) frequency 1.59 kHz, (b) frequency 4.22 kHz, (c) frequency 12.29 kHz

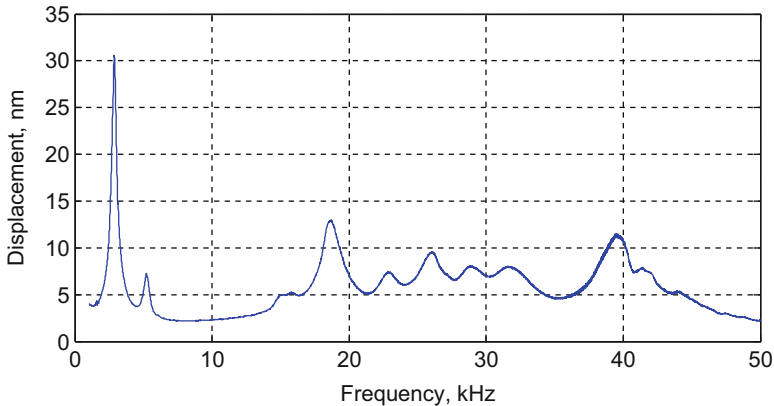


Fig. 18.11 Dependence of the displacement of the surface of the brass diaphragm with bonded piezoelectric actuator Sonox P502 on frequency (voltage ± 100 V)

experimental analysis was repeated for the surface of the brass diaphragm. As it was expected, the largest displacement was obtained in the first resonance frequency; it was 30 nm (Fig. 18.11).

It means that in this case, the displacement was more than ten times bigger than in the analysis of piezoelectric actuator. The most effective mode shape for synthetic jet generator is the first one (Fig. 18.12), since the largest displacement enables creating the strongest flow out of the cavity of the device.

The last experimental analysis with sound transducer LD-BZPN-2030 was repeated. Parameters of the brass diaphragm were diameter 20 mm and thickness 0.15 mm. The piezoelectric actuator of LD-BZPN-2030 was excited by sinusoidal voltage ± 20 V. Figure 18.13 shows that the biggest displacement of the surface of

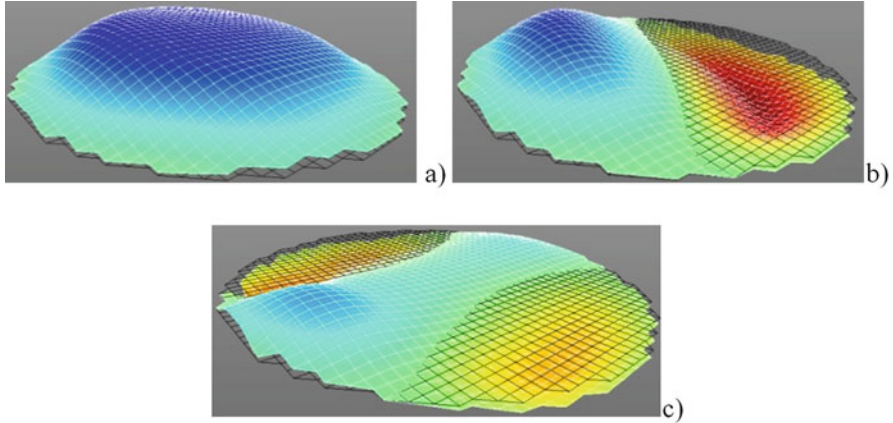


Fig. 18.12 Experimental shapes of the surface of the brass diaphragm with piezoelectric actuator Sonox P502: (a) frequency 2.85 kHz, (b) frequency 5.22 kHz, (c) frequency 15.77 kHz

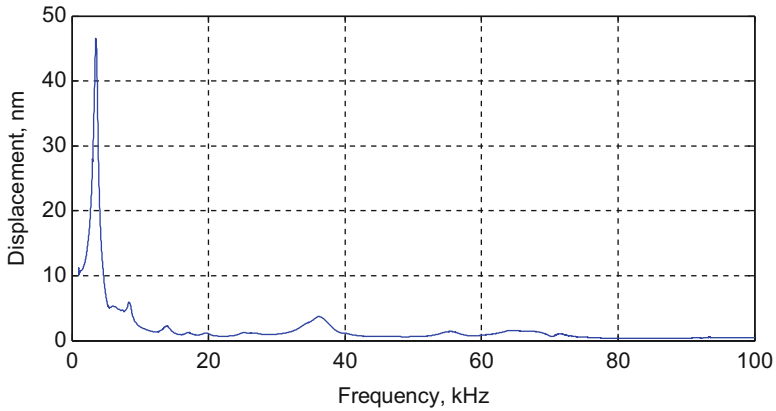


Fig. 18.13 Dependence of the displacement of surface of LD-BZPN-2030 on frequency (voltage ± 100 V)

diaphragm was obtained in the first resonance frequency (3.52 kHz). The maximum displacement of the surface of LD-BZPN-2030 was 47.3 nm. And in the second resonance frequency (8.36 kHz), it was 5.7 nm, in the third (13.84 kHz)—2.8 nm.

Figure 18.14 presents the mode shapes of the surface of LD-BZPN-2030 in the first three resonance frequencies.

It is important to mention that the first resonance frequency and the mode shape of the diaphragms are mostly relevant for flow control devices. However, aiming to improve the validity of numerical model, the first three mode shapes of diaphragms were analysed.

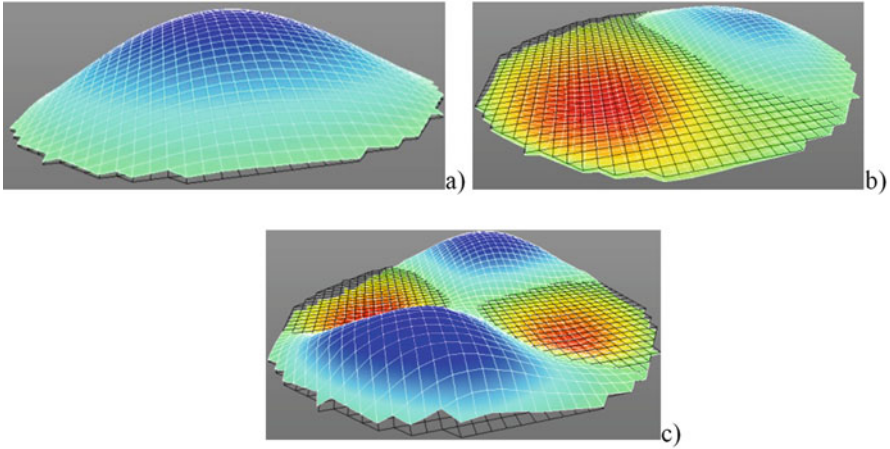


Fig. 18.14 Experimental shapes of the surface of LD-BZPN-2030: (a) frequency 3.52 kHz, (b) frequency 8.36 kHz, (c) frequency 13.84 kHz

Table 18.1 Comparison of the analytical and experimental resonance frequencies of piezoelectric actuator Sonox P502

Mode number	Analytical natural resonance frequency (kHz)	Experimental resonance frequency (kHz)	Error (%)
1	0.96	1.56	37.5
2	5.68	4.22	34.5
3	12.26	12.29	0.24

18.4 Comparison of the Results

One of the tasks of the study was to compare the numerical and experimental results, as this was the only way to check if the results are coincident.

The very important step was to compare numerical and experimental resonance frequencies. Table 18.1 discloses the differences between calculated and experimental frequencies of piezoelectric actuator Sonox P502. The biggest difference between the experimental and numerical results was found at a first resonance frequency of 37.5%. It could be explained that it was not very easy to develop a suitable model for the finite element analysis. Piezoelectric material is very complicated for numerical simulation. Resonance frequencies and shapes of piezoelectric actuator strongly depended on the positions of electrodes (Rimašauskienė and Ostachowicz 2012).

Second very serious reason for the difference in resonance frequencies was the preparation of piezoelectric actuator Sonox P502 for the experiments. Table 18.2 shows the results of two piezoelectric actuators of the same kind. Difference between resonances frequencies of the two discs varied from 3.33 to 30.16%. It might be explained as the dependence from electrodes. Electrodes were soldered

Table 18.2 Resonance frequencies comparison of the two identical piezoelectric actuators

Mode number	The first disc (kHz)	The second disc (kHz)	Error (%)
1	1.09	1.56	30.16
2	3.56	4.22	15.64
3	11.88	12.29	3.33

Table 18.3 Comparison the analytical and experimental resonance frequencies of the brass diaphragm with bonded piezoelectric actuator Sonox P502

Mode number	Analytical natural resonance frequency (kHz)	Experimental resonance frequency (kHz)	Error (%)
1	2.62	2.85	8.07
2	5.06	5.22	3.07
3	16.25	15.77	3.04

Table 18.4 Comparison the analytical and experimental resonance frequencies of diaphragm LD-BZPN-2030

Mode number	Analytical natural resonance frequency (kHz)	Experimental resonance frequency (kHz)	Error (%)
1	4.77	3.52	26.02
2	10.06	8.36	16.89
3	16.12	13.84	14.14

to the piezoelectric actuator manually. This means that it was not possible to solder them into the same place of the disc surface and with the same amount of the soldering material. As it is known, piezoelectric materials are very sensitive, and their parameters can be changed by various factors (Rimašauskienė and Ostachowicz 2012).

The next step was to compare numerical and experimental resonance frequencies of the brass diaphragm with bonded piezoelectric actuator Sonox P502. Table 18.3 discloses the differences between calculated and experimental frequencies of the brass diaphragm with bonded piezoelectric actuator Sonox P502. The biggest difference between the experimental and numerical results was found at a first resonance frequency of 8.07% (Rimašauskienė and Ostachowicz 2012).

The last comparison of numerical and experimental resonance frequencies of LD-BZPN-2030 was performed. Table 18.4 discloses the differences between calculated and experimental frequencies of diaphragm LD-BZPN-2030. The biggest difference between the experimental and numerical results was found at a first resonance frequency of 26.02%. The big difference can be explained by the lack of piezoelectric parameters because producer does not present information about the piezoelectric material which is used in the structure of LD-BZPN-2030.

18.5 Changing of the Numerical Tools

Performing project was planned that FEM models of the piezoelectric actuators will be included into AMESim platform in order to extend them with sensory system, open and closed control loops.

One of the best solutions to create diaphragms with piezoelectric actuators model was to use ANSYS Multiphysics 12.1. ANSYS Multiphysics software offers a comprehensive product solution for both multiphysics and single physics analysis. The product includes structural, thermal, fluid and both high- and low-frequency electromagnetic analysis. The product also contains solutions for both direct and sequentially coupled physics problems including direct coupled-field elements and the ANSYS multi-field solver.

Possible piezoelectric analysis types (available in the ANSYS Multiphysics) are static, modal, prestressed modal, harmonic, prestressed harmonic and transient. But during project performance were found some kind of difficulties and we had to change platform from AMESim to MpCCI.

18.6 Conclusion

This chapter presents both numerical and experimental investigations of piezoelectric actuator and diaphragms, which could be used in structure of the synthetic jet device. FE models of the piezoelectric actuator Sonox P502, brass membrane with bonded piezoelectric actuator Sonox P502 and sound transducer LD-BZPN-2030 were built; resonance frequencies and shape modes of the surfaces were found. Analogical data were found by experimental analysis. The comparison of analytical and experimental results and explanation of differences are presented in the chapter.

The conducted research can help in the creation of the synthetic jet device design.

References

- Qayoum Gupta A, Panigrahi PK, Muralidhar K (2010) Influence of amplitude and frequency modulation on flow created by a synthetic jet actuator. *Sens Actuators A* 162:36–50
- Rimašauskienė R, Ostachowicz W (2012) Investigation of characteristics of piezoelectric actuator used for synthetic jet flow control. In: *Mechanika 2012: proceedings of the 17th international conference* ISSN 1822–2951, pp 251–256
- Rimašauskienė R, Rimašauskas M, Jūrėnas V, Ostachowicz W, Matejka M (2015) Numerical and experimental analysis of membrane with piezoelectric element used for synthetic jet flow control. *Mechanika* 21(1):64–69
- Trindade MA, Benjeddou A (2011) Finite element homogenization technique for the characterization of d15 shear piezoelectric macro-fibre composites. *Smart Mater Struct* 20:1–17
- Yang AS, Ro JJ, Yang MT, Chang WH (2009) Investigation of piezoelectrically generated synthetic jet flow. *J Vis* 12:9–16

Chapter 19

Thermal Synthetic Jet Actuator Investigation by Experimental Approach

Rūta Rimašauskienė

19.1 Introduction

The importance and the growing use of intelligent materials in aero crafts applications affect scientists to perform even greater analysis of the following materials characteristics. Synthetic jet generators are widely researched in controlling the airflow of aero crafts aiming to enhance their lifting and manoeuvrability, control stalls and reduce the noise (Kim and Kim 2009). Practical application of this technology faces the following problems: weight, size, response time, force and the complexity of controlling airflows.

The study of synthetic jets emerged as an intrigue new field in the past few years. In fluid dynamics, synthetic jet flow is a jet flow synthesized from ambient fluid (Mautner 2004; Jain et al. 2011). A typical synthetic jet generator consists of an enclosed cavity with one or more openings (orifice) on one side. The other face has a diaphragm for actuation. The oscillatory motion of the diaphragm leads to alternate suction and ejection of the fluid between the cavity and the cross stream. During the suction stroke, the opening acts as a sink and entrains the near-wall low-momentum fluid into the cavity, while during the expulsion stroke, a fluid jet is formed. There is net momentum injection into the cross stream without any additional mass accumulation (Qayoum et al. 2010). A jet flow is such flow of a fluid where a stream of fluid mixes with surrounding medium. Synthetic jet flow can be generated in a number of ways, for example, using electromagnetic, piezoelectric or even mechanical driver, such as a piston. Each installation moves a diaphragm up and down hundreds of times per second, sucking the surrounding fluid into a chamber and then expelling it.

R. Rimašauskienė (✉)

Department of Production Engineering, Kaunas University of Technology, Studentų St. 56,
Kaunas, LT-51424, Lithuania

e-mail: ruta.rimasauskiene@ktu.lt

The actuators have to possess enough power to produce required displacement. Previous designs involved piezoelectric diaphragms in generating a synthetic jet (Smith and Glezer 1998; Lee et al. 2003). A lot of studies have covered the development of the piezoelectric actuator as well as the general behaviour and performance of the synthetic jet produced. Results indicated that excitation frequency and cavity orifice were important factors affecting the size and formation of coherent structures in synthetic jet flow (Tan and Zhang 2013). The only drawback is the space required to integrate them. A piezoelectric diaphragm consists of a diaphragm made from a flexible material onto which a piezoelectric actuator is bonded. The piezoelectric actuator excites diaphragm bending modes by contracting and extending at a defined frequency.

Important to mention is that it is necessary to research thermal characteristics of the diaphragms creating synthetic jet generators with piezoelectric materials. Particularly, piezoelectric actuators are used aiming to obtain the maximum displacements that are possible when a piezoelectric actuator operates under maximum excitation voltage and at the resonance frequency. The theory suggests that working in such modes, the temperature of the piezoelectric elements extremely increases, and it can reach maximum point (Curie temperature). The development of various devices with piezoelectric elements requires knowing maximum allowable excitation voltages and frequencies. These data is essential not only for piezoceramic itself but also for the device where it is used in Kim et al. (2006). High temperatures might cause deformation or other changes of mechanical properties of some materials used in the structure of the device. This might influence the life time and operational characteristics of the synthetic jet generator (Heidary and Eslami 2006).

This chapter presents experimental analysis of the piezoelectric actuator Sonox P502, own-produced diaphragm with bonded piezoelectric actuator Sonox P502 and analogical analysis of the sound transducer LD-BZPN-2030. The aim of these investigations was to find the highest displacements of the piezoelectric diaphragms, to research the resonance frequencies and to verify temperature of the elements. As it is known, in order to obtain proper control of synthetic jet flow, it is necessary to find the most suitable mode shapes and achieve the maximum displacement of the diaphragm. The task of this research was to find experimental data that are important for control of synthetic jet generator.

19.2 Experimental Equipment and Design of Synthetic Jet Generator

Using scanning laser vibrometer (Polytec: frequency response up to 1.5 MHz, displacement measurement range as low as 1 nm and a computer with installed PSV 8.8 software were carried out), displacements and resonance frequencies of piezoelectric actuator Sonox P502, own-made diaphragm with bonded piezoelectric actuator Sonox P502 and piezoelectric sound transducer LD-BZPN-2030 were defined.

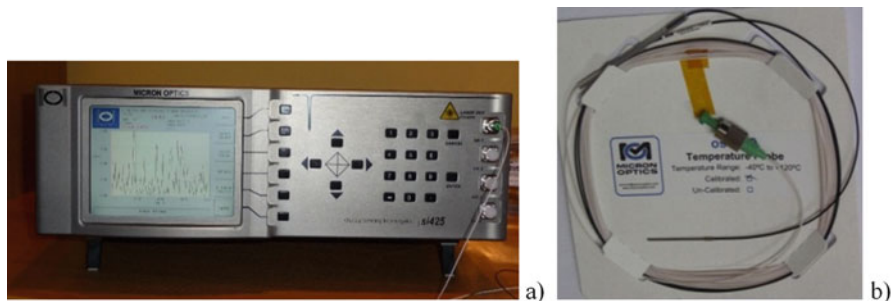


Fig. 19.1 Thermal measurements devices: (a) interrogator for FBG sensors, (b) temperature probe

During the experiments with fibre Bragg grating (FBG), the experimental stand consisted of an interrogator (Micron Optics, si425-500) (Fig. 19.1a) and FBG temperature probe (os4200) (Fig. 19.1b). The FBG sensor was dedicated to measure the temperature variations of the surface of piezoelectric actuator and diaphragms.

A synthetic jet is created at the slot by oscillation and deflection of a diaphragm attached to the bottom of the jet chamber. In some cases, synthetic jet chamber consists of a diaphragm oscillating in a circular space and an orifice opposite to the diaphragm (Fig. 19.2). The oscillation of a diaphragm generates two, intake and exhaust, flows in the orifice. The intake flow separates and forms a vortex sheet that rolls up into a single vortex as it moves away from the orifice at its self-induced velocity. If the velocity is enough high, the entrance to the chamber becomes limited and the air jet forms. Thus, a linear momentum is transferred to the flow system even if net mass injection is equal to zero. Consequently, these jets are also called “zero net mass flux” jets (Yang et al. 2009; Qayoum et al. 2010). It is important to mention that synthetic jet is very sensitive to the parameters of the generator, i.e. sizes and forms of its cavity and orifice, displacement and velocity of the diaphragm, etc.

The chapter analyses piezoelectric actuator Sonox P502 (Fig. 19.3) and two different piezoelectric diaphragms which could be used in the design of the synthetic jet generator.

One of them is sound transducer LD-BZPN-2030 (dimensions of the diaphragm: diameter 20 mm, thickness 0.15 mm; dimensions of the piezoelectric actuator: diameter 15 mm; thickness 0.3 mm) (Fig. 19.4) and other own-made brass diaphragm (diameter 20 mm, thickness 0.15) with bonded piezoelectric actuator Sonox P502 (diameter 10 mm, thickness 0.5 mm) (Fig. 19.5). Piezoelectric actuator Sonox P502 manufactured by the company *CeramTec* was selected for research (Trindade and Benjeddou 2011). As it is known from scientific sources, piezoelectric materials acquire the highest displacement in the first resonance frequencies, but working in such conditions the temperature of these materials can grow rapidly. Synthetic jet generator’s control extremely depends on a displacement of the diaphragm, that is why it is necessary to investigate the most appropriate working regimes of a piezoelectric diaphragm. Thermal analysis of the piezoelectric diaphragms was made in the few first resonance frequencies and results were presented in this chapter.

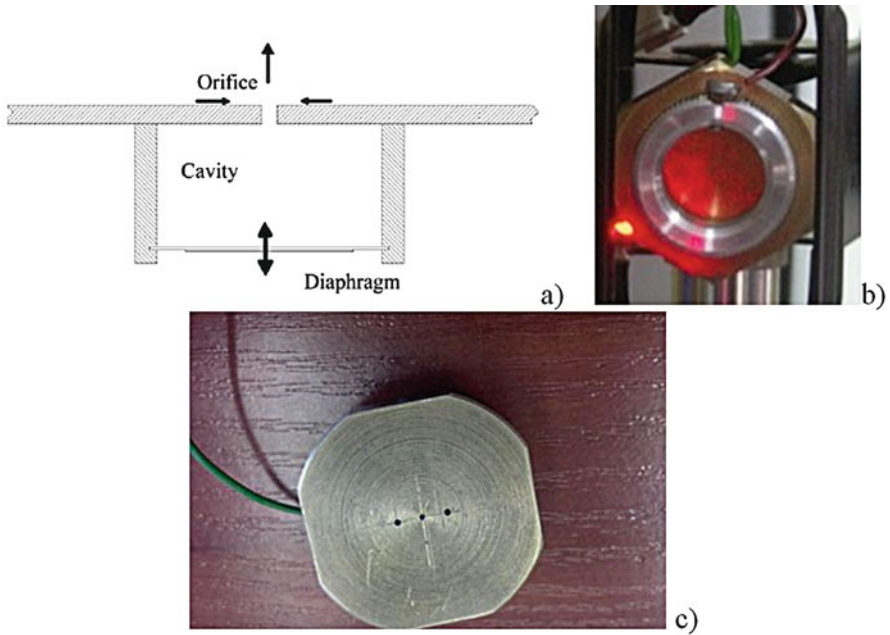


Fig. 19.2 Structure of the synthetic jet generator: (a) schematic design, (b) experimental model (back view), (c) experimental model (front view)

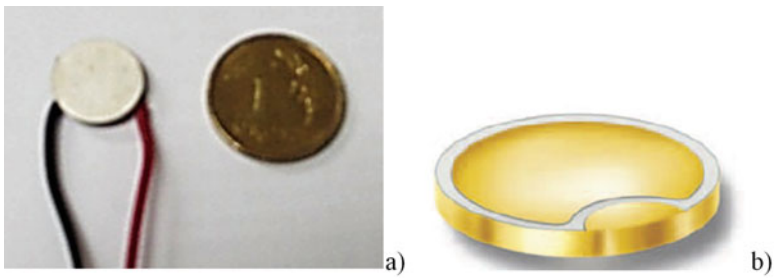


Fig. 19.3 Piezoelectric actuator Sonox P502: (a) real view, (b) configuration of the electrodes

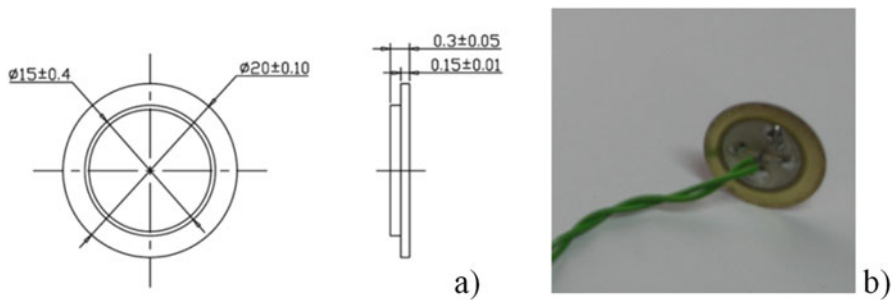


Fig. 19.4 Sound transducer LD-BZPN-2030: (a) dimensions of the components, (b) real element

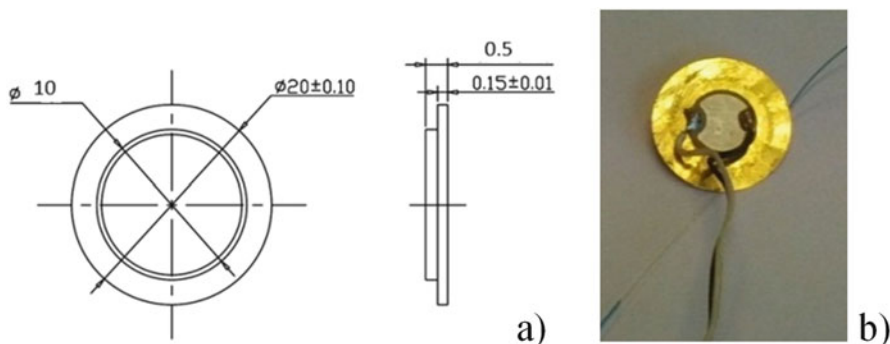


Fig. 19.5 Piezoelectric diaphragm with bonded actuator Sonox P502: (a) dimensions of the components, (b) real element

19.3 Results of Thermal Analysis

19.3.1 Results of the Experimental Analysis of Piezoelectric Actuator Sonox P502

At the beginning it was aimed to identify resonance frequencies of piezoelectric actuators having excited them by maximum voltage. With a help of laser vibrometer, resonance frequencies and surface displacements were determined.

It was defined that maximum displacements occur at the first resonance frequencies. Therefore in the chapter analysis of the first three resonance frequencies, i.e. discloses thermal characteristics of piezoelectric actuator were presented. It should be mentioned that piezoelectric actuators were fixed just by the electrodes.

First, piezoelectric disc Sonox P502 manufactured by the company *CeramTec* was analysed. The dependence of piezoelectric actuator Sonox P502 surface displacement at various frequencies (voltage ± 200 V) was found (Fig. 19.6).

Figure 19.6 shows that working at the first resonance frequency 0.93 kHz (voltage ± 200 V) delivered the biggest displacement (about 8.15 nm) of the surface of piezoelectric actuator. If piezoceramic element is working under the highest excitation voltage at the first resonance frequency, the temperature is not growing rapidly. After 1.5 min it achieved 35 °C and became stable (Fig. 19.7a).

But working continuously at the second resonance frequency temperature was growing extremely rapidly, and the electrodes fell down after 20–30 s. The temperature was too high for the electrode welding solder and they were disconnected. It was a problem of our research.

Theory suggests that different dielectric ceramic bodies are heating up at different excitation voltages. If cooling of piezoceramic elements is not ensured, the increased temperature increases losses and causes thermal destruction of polarity. The best mechanical and piezoelectric properties of piezoelectric actuator Sonox P502 when it is working up to 160 °C are kept. Therefore, the experiment at the

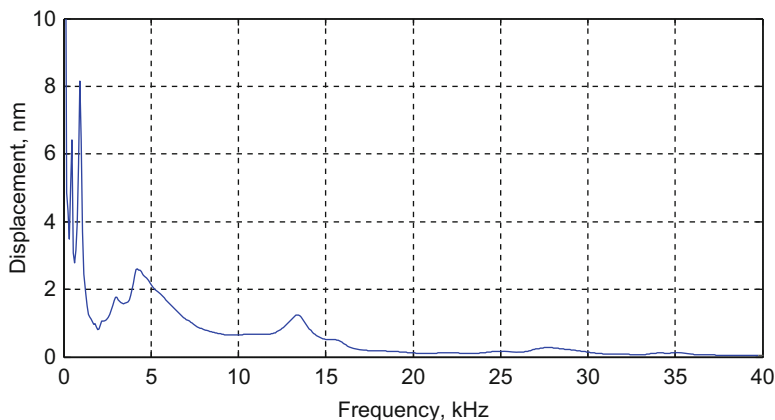


Fig. 19.6 The dependence of piezoelectric actuator Sonox P502 surface displacement on frequency ($U = \pm 200$ V)

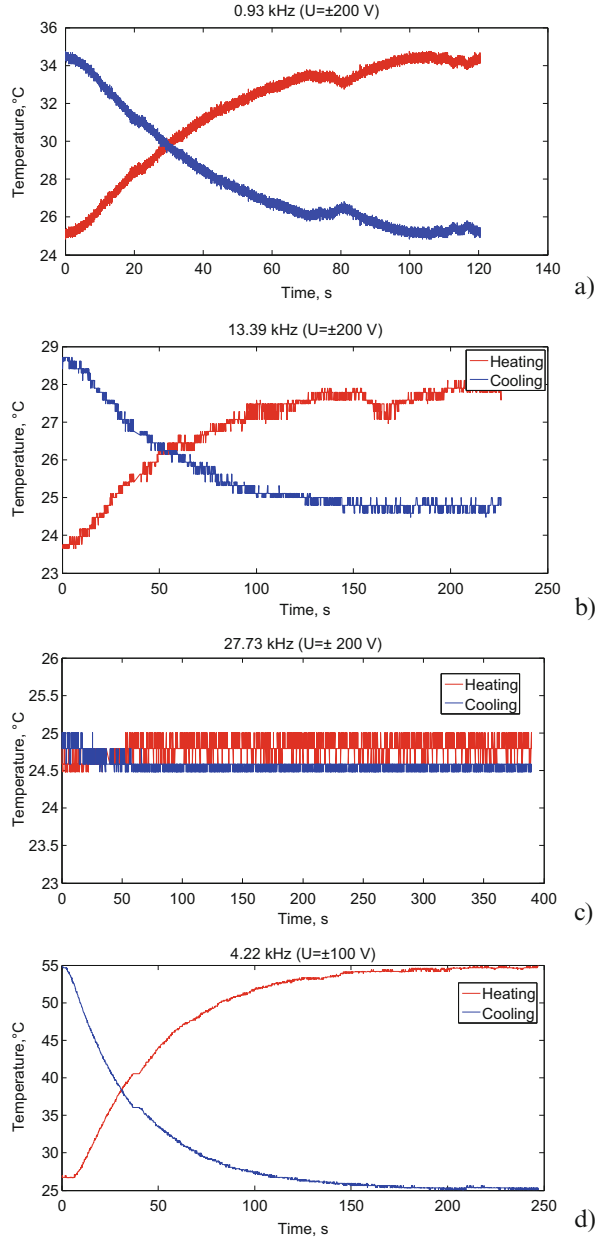
second resonance frequency was repeated by keeping different excitation voltages (± 100 V) (Fig. 19.7d), because ± 200 V was too high.

At the third frequency (13.39 kHz), temperature reached 28°C in 200 s and became almost linear (Fig. 19.7b). It should be noted, that on the same time it was cooling down, like in the experiment with the first resonance frequency. During the experiment with the fourth resonance frequency, thermal dependence remains almost constant (Fig. 19.7c). The same process was observed at next frequencies too.

In the next steps of the thermal analysis, the excitation voltage was changed from ± 200 V to ± 100 V. It must be said that such a big change of voltage was not very useful, since the displacement of the surface of piezoelectric actuator became smaller than 1 nm. But from the other side, it was the possibility to find thermal characteristics of piezoelectric disc Sonox P502 at the second resonance frequency. Curves in Fig. 19.7d show that temperature was growing quite fast and reached 55°C in 150 s. Cooling process lasted for the same time. At the third resonance frequency (13.39 kHz), temperature reached just 26°C . It means the temperature changed only by 1.5°C . At the fourth resonance frequency, temperature acted seemingly as in the case with the voltage of ± 200 V. It means that, working at the first three resonances, frequencies' temperature is growing, but it is possible to achieve the biggest displacement of the piezoelectric actuator's surface.

Experimental results of piezoelectric disc Sonox P502 made clear that the best way to get the biggest displacement for the system is to use the first resonance frequency. It is possible to conclude that cooling of piezoelectric actuator must be ensured. Otherwise it is not possible to work in the best working modes, since they will destroy piezoceramic elements.

Fig. 19.7 The dependence of temperature on time: **(a)** frequency 0.93 kHz, voltage ± 200 V; **(b)** frequency 13.39 kHz, voltage ± 200 V; **(c)** frequency 27.73 kHz, voltage ± 200 V; **(d)** frequency 4.22 kHz, voltage ± 100 V



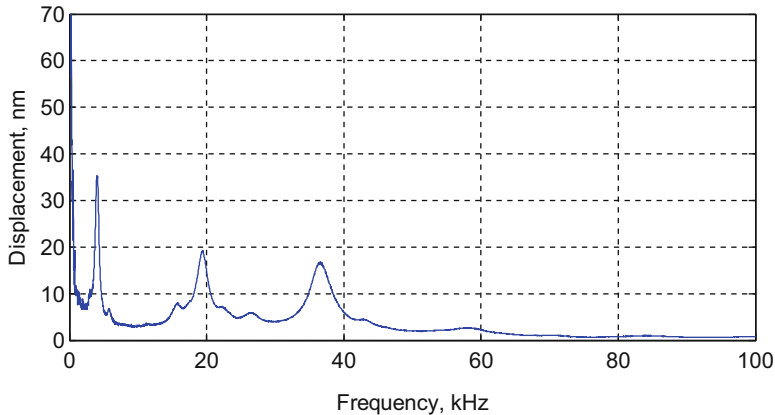


Fig. 19.8 Dependence of the displacement of surface of diaphragm with piezoelectric actuator Sonox P502 (fixed by electrodes) on frequency ($U = \pm 100$ V)

19.3.2 Results of the Experimental Analysis of Diaphragm with Bonded Piezoelectric Actuator Sonox P502

Analogue analysis was made with brass membrane with glued piezoelectric actuator Sonox P502 (Fig. 19.5). With a help of experimental equipment, resonance frequencies and surface displacements of piezoelectric diaphragm were found. During experimental analysis with the own-made diaphragm, the piezoelectric actuator Sonox P502 was excited by sinusoidal voltage $U = \pm 100$ V. The first measurement with a diaphragm fixed by electrodes was made. Figure 19.8 shows that the highest displacement of the surface of the piezoelectric diaphragm with bonded actuator Sonox P502 (Fig. 19.5) was obtained at the second resonance frequency (5.86 kHz). Maximum displacement of the surface of piezoelectric diaphragm was 35 nm. In contrast, at the first resonance frequency (4.11 kHz), it was 28 nm; in the third (15.76 kHz) it was less when 10 nm. Next at the fourth (19.46 kHz) and fifth (37.69 kHz) resonance frequencies displacements of the diaphragm surface were around 20 nm (Rimašauskienė et al. 2014).

Theory suggests that different dielectric ceramic bodies are heating up at different excitation voltages. If cooling of piezoceramic elements is not ensured, the increased temperature increases losses and causes thermal destruction of polarity. The best mechanical and piezoelectric properties of piezoceramic Sonox P502 are kept when it is working up to 160 °C. Due to this reason, it was very important to test thermal characteristics of the diaphragm with piezoelectric actuator Sonox P502 at different resonance frequencies. Thermal experimental analysis at five resonance frequencies of diaphragm was conducted in 120 s. It was sufficient time to notice the stabilization of the diaphragm temperature.

Initial temperature of the laboratory room was around 27 °C. Figure 19.9a shows that temperature at the first resonance frequency was almost stable (voltage $U = \pm 100$ V). The highest difference of the temperatures was equal to about 4 °C at the fourth resonance frequency (19.46 kHz) (Fig. 19.9d). Consequently, it is possible to make a decision that this difference will not affect working conditions of the synthetic jet generator (Rimašauskienė et al. 2014).

After that next part of the experimental analysis with brass diaphragm with bonded piezoelectric actuator Sonox P502 was done. Diaphragm was fixed in the brass and aluminium chamber of the synthetic jet generator (Fig. 19.2b, c). One side of the diaphragm was covered by the generators components. From one side piezoelectric diaphragm was open; from another it has just three small open orifices (diameter 1 mm). The cooling of the piezoelectric diaphragm from external effects was reduced.

At the beginning resonance frequencies and displacements of the fixed piezoelectric diaphragm were found. Figure 19.10 shows that the highest displacement of the surface of the fixed piezoelectric diaphragm with bonded actuator Sonox P502 was obtained at the first resonance frequency (2.88 kHz). Maximum displacement of the surface of piezoelectric diaphragm was 31 nm. However, at the other resonance frequencies, it was less than 13 nm. In order to get the appropriate velocity of the synthetic jet, the right resonance frequency of the piezoelectric actuator should be used. In this case, the first resonance frequency (2.88 kHz) with which the highest displacement of the diaphragm surface was achieved is the most appropriate solution.

The main task of this research was to verify thermal characteristics of the membrane working in different work conditions. The dependences of the temperature on time were checked at different resonance frequencies. Excitation voltage of the piezoelectric actuator Sonox P502 was ± 100 V. Initial temperature on the laboratory room was around 27 °C like in the first part of the experimental analysis of the brass membrane with bonded piezoelectric actuator (Rimašauskienė et al. 2014).

Figure 19.11 shows that temperature was stable in the first five resonance frequencies ($U = \pm 100$ V). The biggest difference of temperatures about 2 °C was found. In this case, stability of the temperature can be explained as heat transmission of the synthetic jet generator material. Generally, it is possible to say that brass diaphragm with bonded piezoelectric actuator Sonox P502 can be used in the design of the synthetic jet generator. Piezoelectric actuator will not be overheated in this structure; it just arises with the question how powerful it will be in synthetic jet generation (Rimašauskienė et al. 2014).

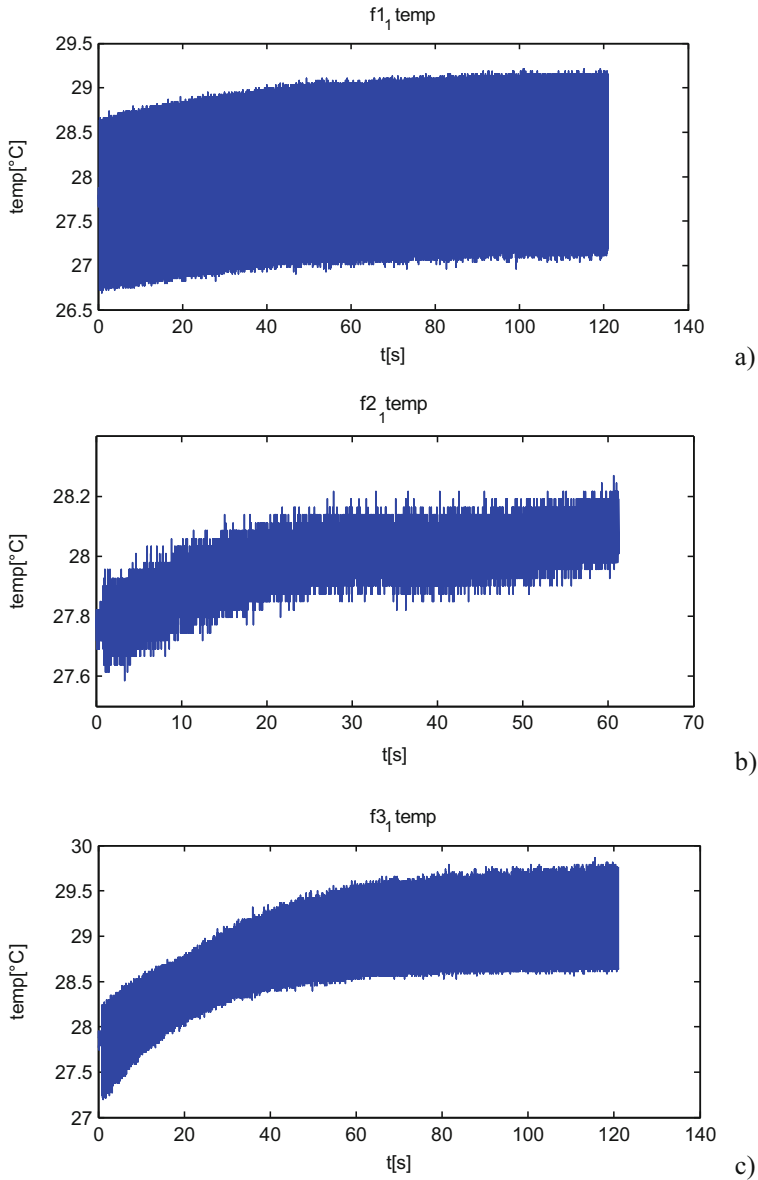


Fig. 19.9 The dependence of temperature on time: (a) frequency 4.11 kHz, (b) frequency 5.86 kHz, (c) frequency 15.76 kHz, (d) frequency 19.46 kHz, (e) frequency 37.69 kHz ($U = \pm 100$ V)

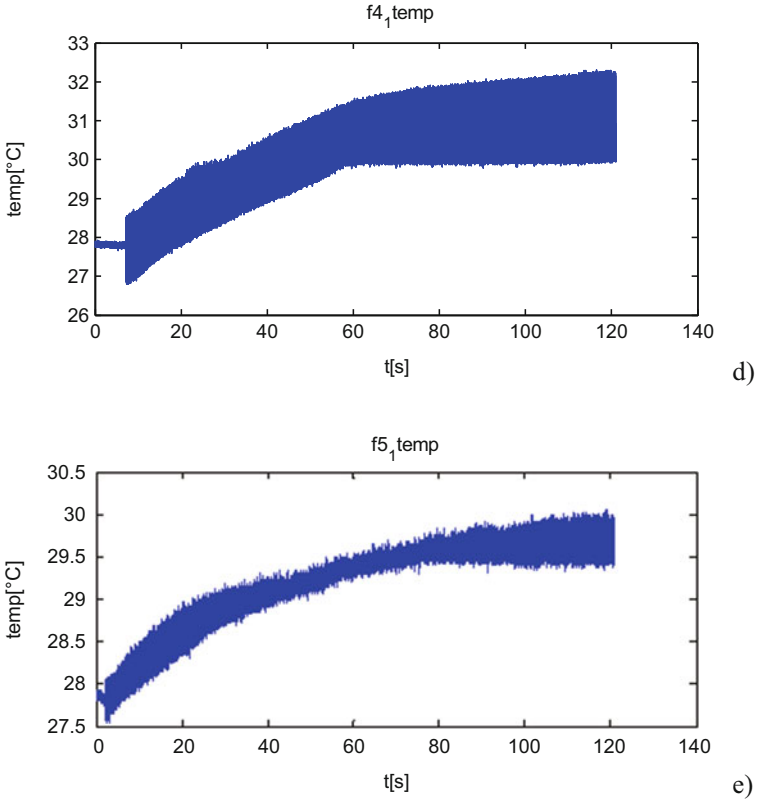


Fig. 19.9 (continued)

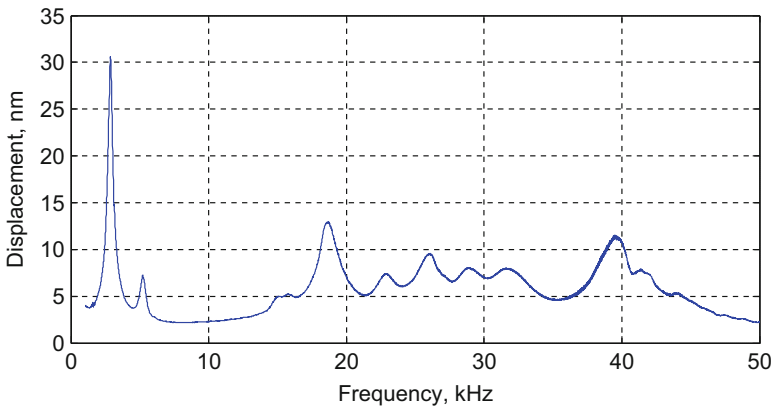


Fig. 19.10 Dependence of the displacement of surface of diaphragm with piezoelectric actuator Sonox P502 on frequency (diaphragm fixed in the chamber) ($U = \pm 100$ V)

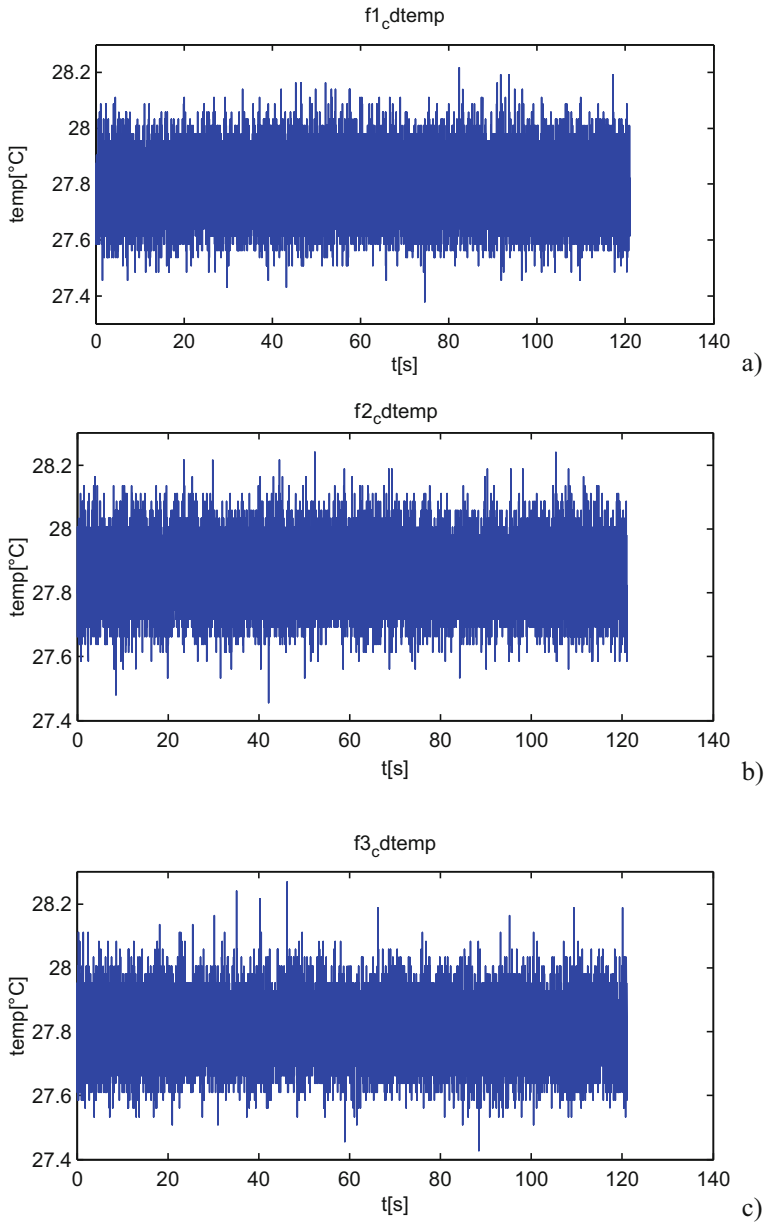


Fig. 19.11 The dependence of temperature on time: (a) frequency 2.88 kHz, (b) frequency 5.2 kHz, (c) frequency 15.63 kHz, (d) frequency 18.72 kHz, (e) frequency 22.88 kHz ($U = \pm 100$ V)

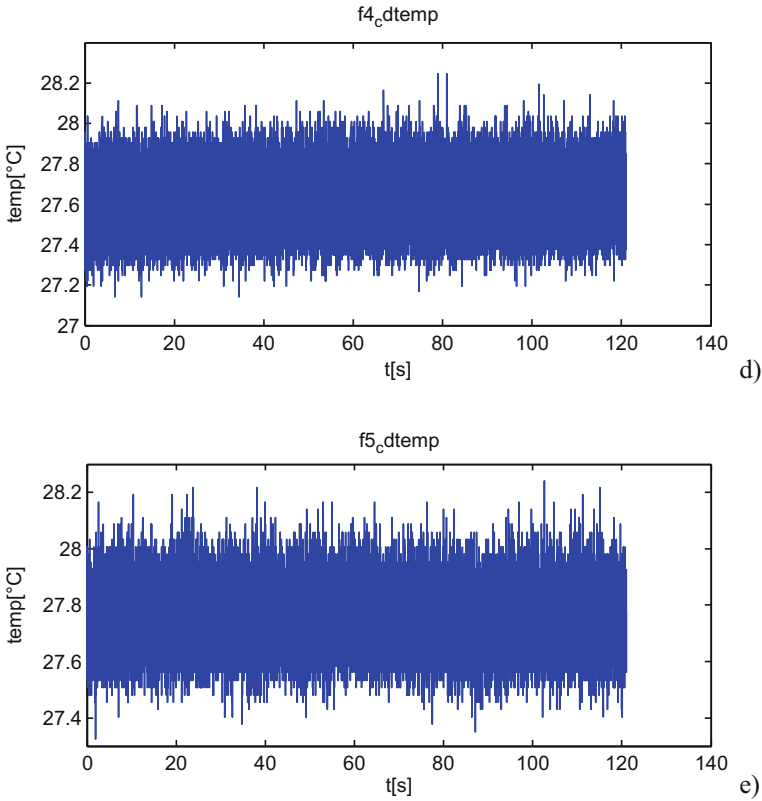


Fig. 19.11 (continued)

19.4 Results of the Experimental Analysis of Sound Transducer LD-BZPN-2030

In order to find the better solution for synthetic jet generation, sound transducer LD-BZPN-2030 (Fig. 19.4) was chosen and analysed. Using Polytec laser vibrometer dependence of the displacement of surface of sound transducer LD-BZPN-2030 diaphragm (fixed by electrodes) on frequency (Fig. 19.12) was found. The highest displacement (140 nm) of the diaphragm surface at the fourth resonance frequency (5.16 kHz) was found. At the first resonance frequency (1.25 kHz), the displacement of 85 nm was achieved ($U = \pm 20$ V).

In the same consistency as thermal experimental analysis with own manufactured piezoelectric diaphragm with actuator Sonox P502, analysis with sound transducer LD-BZPN-2030 was repeated. Figure 19.13 shows that very substantial growing of the temperature was not noticed. Initial temperature of the laboratory room was around 24 °C. The highest difference of the temperatures was found about 1.5 °C

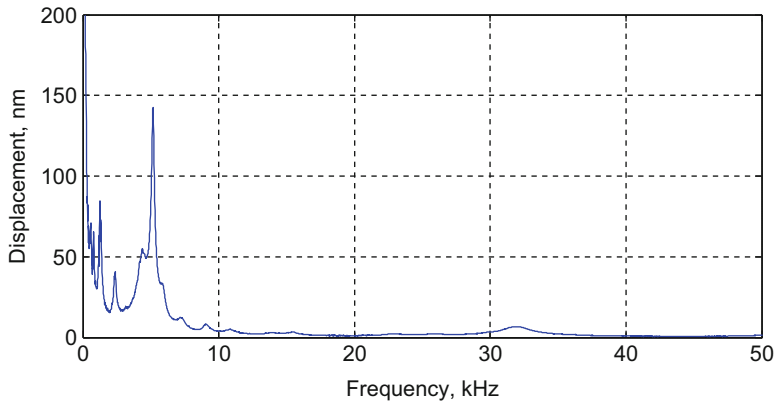


Fig. 19.12 Dependence of the displacement of surface of sound transducer LD-BZPN-2030 diaphragm (fixed by electrodes) on frequency ($U = \pm 20$ V)

at the fifth resonance frequency (31.96 kHz) (Fig. 19.13d). While analysing sound transducer at different resonance frequencies, high increase of the temperature was not noticed and it was stable during 120 s (Rimašauskienė et al. 2014).

Next part of the experimental analysis with piezoelectric sound transducer LD-BZPN-2030 was done. Diaphragm was fixed in the brass and aluminium chamber of the synthetic jet generator (Fig. 19.2b, c). One side of the diaphragm was covered by the generator's components.

At the beginning resonance frequencies and displacements of the surface of the fixed piezoelectric sound transducer LD-BZPN-2030 were found. Figure 19.14 shows that the highest displacement of the surface of the fixed piezoelectric sound transducer LD-BZPN-2030 diaphragm was obtained at the first resonance frequency (3.57 kHz). Maximum displacement of the surface of sound transducer LD-BZPN-2030 diaphragm was 47 nm. However, at the other resonance frequencies, it was less than 5 nm. In this case, the first resonance frequency (3.57 kHz) with which the highest displacement of the diaphragm surface was achieved is the most appropriate solution for synthetic jet generator design.

Figure 19.15 shows that the temperature was stable at the first four resonance frequencies ($U = \pm 20$ V). In this case, stability of the temperature can be explained as heat transmission of the synthetic jet generator material as in experimental analysis with piezoelectric diaphragm with bonded actuator Sonox P502. In conclusion, it is possible to say that sound transducer LD-BZPN-2030 can be used in the design of the synthetic jet generator also. Piezoelectric actuator will not be overheated in this structure, and velocity of the synthetic jet will be achieved higher than working with brass diaphragm with glued piezoelectric actuator Sonox P502 (Rimašauskienė et al. 2014).

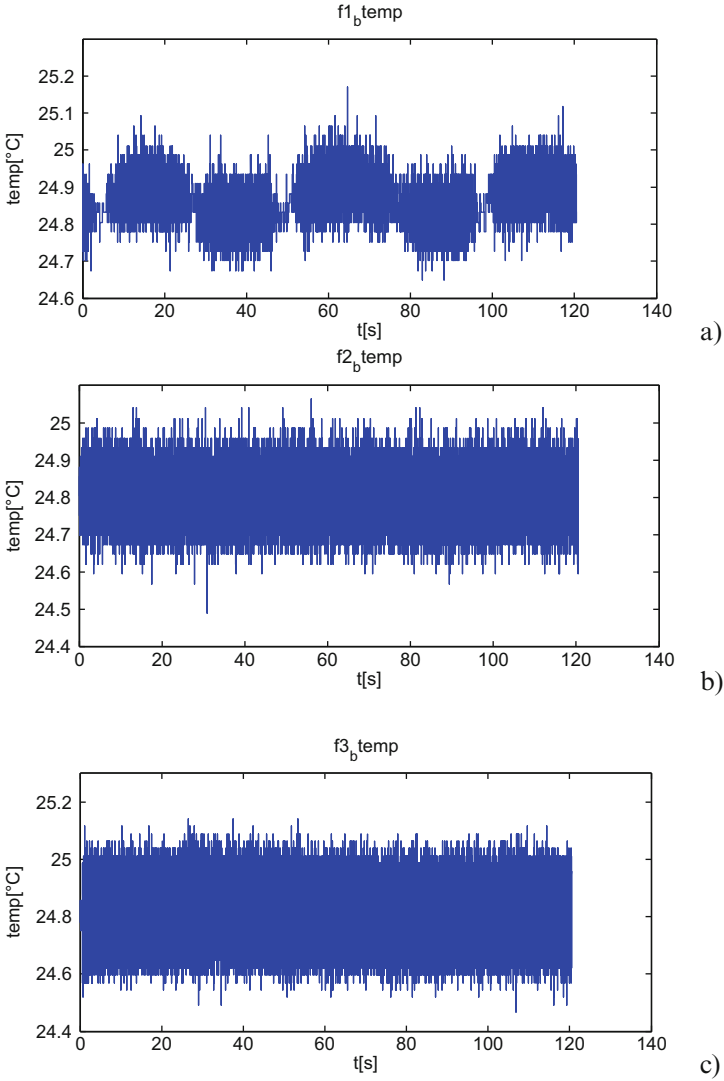


Fig. 19.13 The dependence of temperature on time: (a) frequency 1.25 kHz, (b) frequency 2.36 kHz, (c) frequency 4.39 kHz, (d) frequency 5.16 kHz, (e) frequency 31.96 kHz ($U = \pm 20$ V)

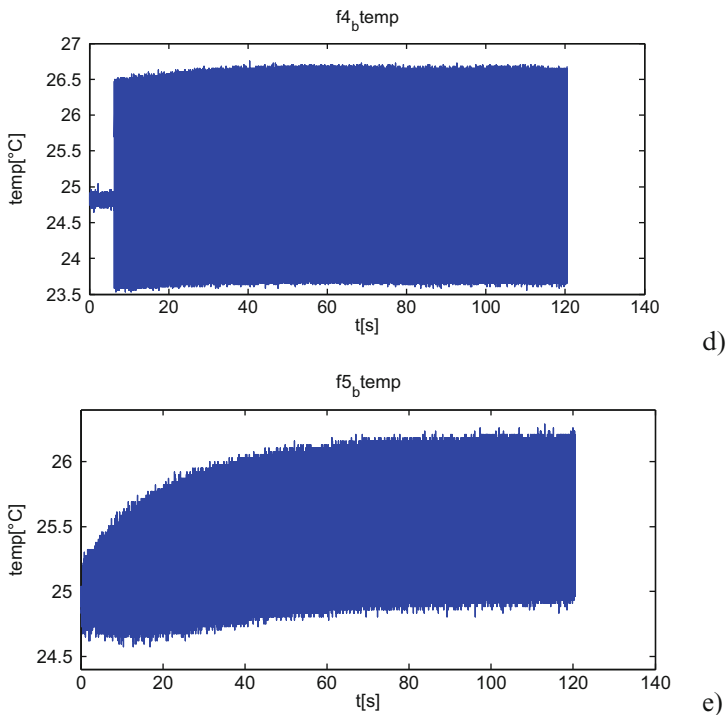


Fig. 19.13 (continued)

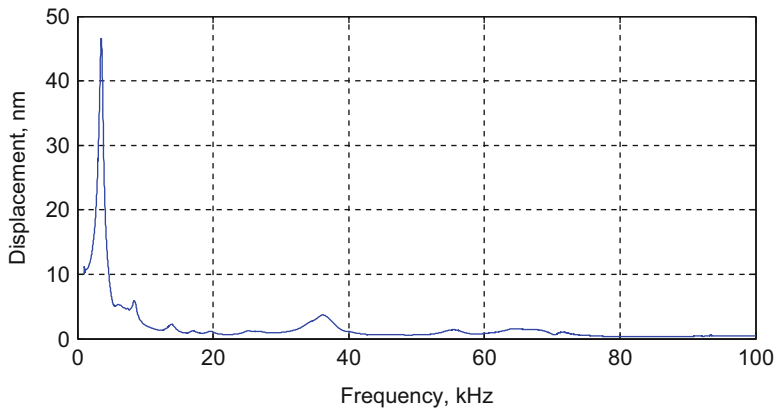


Fig. 19.14 Dependence of the displacement of surface of diaphragm on frequency (diaphragm fixed in the chamber) ($U = \pm 20$ V)

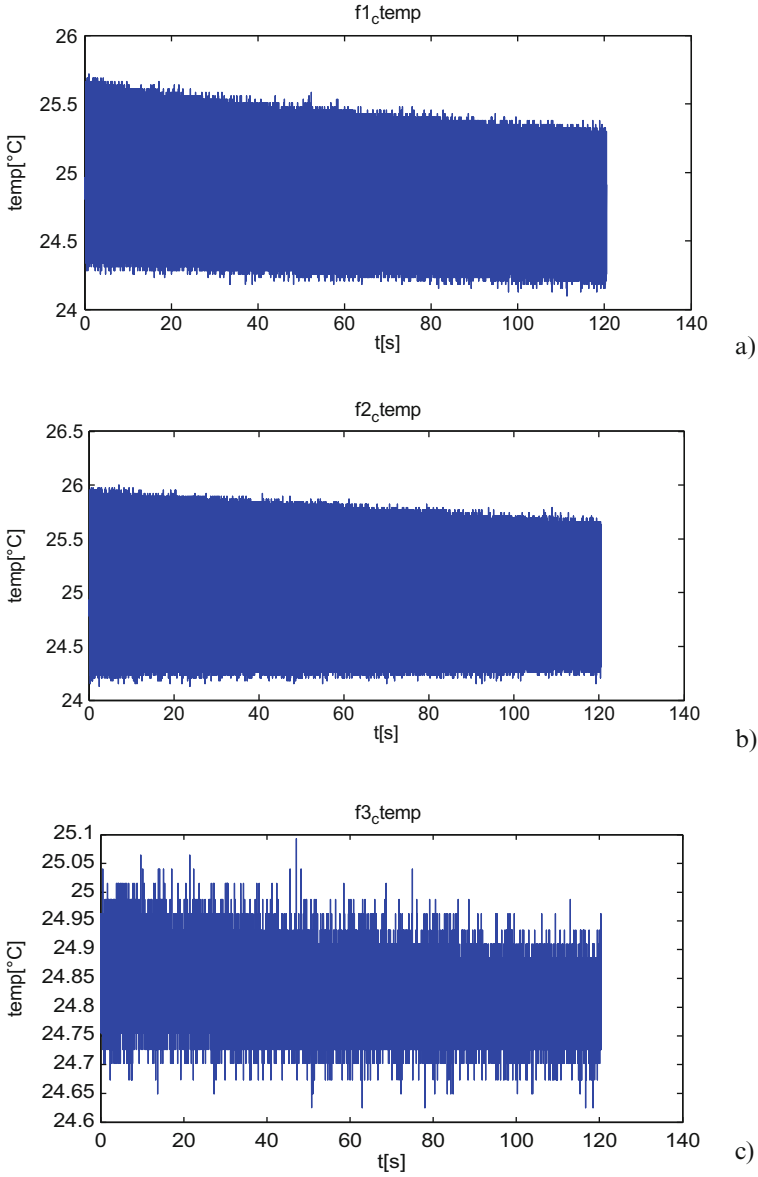


Fig. 19.15 The dependence of temperature on time: **(a)** frequency 3.57 kHz, **(b)** frequency 8.36 kHz, **(c)** frequency 13.84 kHz, **(d)** frequency 17.05 kHz ($U = \pm 20$ V)

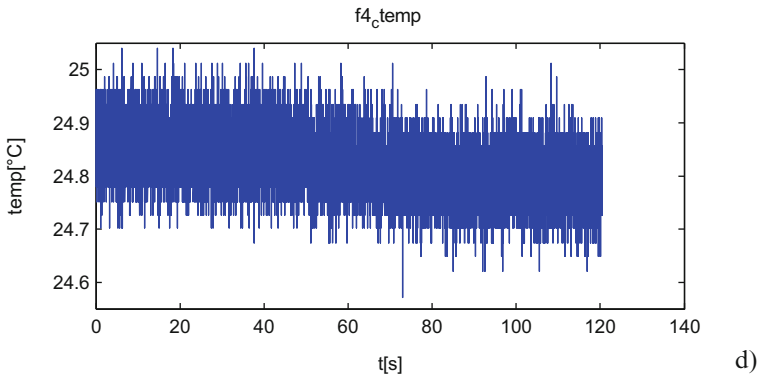


Fig. 19.15 (continued)

19.5 Conclusions

This chapter analyses and presents the dependence of the displacement of piezoelectric actuator Sonox P502, diaphragm with bonded actuator Sonox P502 and sound transducer LD-BZPN-2030 on frequency. In all cases, the highest displacement of the fixed in the synthetic jet generator chamber diaphragms surfaces was obtained at the first resonance frequency.

In the present study, it was proved that temperature generated by piezoelectric actuator will not affect working conditions of the piezoelectric diaphragms and synthetic jet generators. Stable thermal characteristics of the fixed piezoelectric diaphragms in the synthetic jet generator's chamber were observed. The stability of the temperature can be explained as high heat transmission of the elements of the synthetic jet generator.

References

- Heidary F, Eslami MR (2006) Piezo-control of forced vibrations of a thermoelastic composite plate. *Compos Struct* 74:99–105
- Jain M, Puranik B, Agrawal A (2011) A numerical investigation of effects of cavity and orifice parameters on the characteristics of a synthetic jet flow. *Sens Actuators A* 165:351–366
- Kim H, Kim C (2009) Separation control on NACA23012 using synthetic jet. *Aerosp Sci Technol* 13:172–182
- Kim JC, Chung JT, Lee DJ, Kim YK, Kim JW, Hwang SW, Ju BK, Yun SK, Park HW (2006) Development of temperature feedback control system for piezo-actuated display package. *Sens Actuators A* 151:213–219
- Lee C, Hong G, Ha QP, Mallinson SG (2003) A piezoelectrically actuated micro synthetic jet for active flow control. *Sens Actuators A* 108:168–174

- Mautner T (2004) Application of the synthetic jet concept to low Reynolds number biosensor microfluidic flows for enhanced mixing: a numerical study using the lattice Boltzmann method. *Biosens Bioelectron* 19:1409–1419
- Qayoum A, Gupta V, Panigrahi RK, Muralidhar K (2010) Influence of amplitude and frequency modulation on flow created by a synthetic jet actuator. *Sens Actuators A* 162:36–50
- Rimašauskienė R, Rimašauskas M, Mieloszyk M, Wandowski T, Malinowski P, Ostachowicz W (2014) Experimental investigation of thermal characteristics of synthetic jet generator's diaphragm with piezoelectric actuator. In: AIP conference proceedings: 11th international conference on vibration measurements by laser and noncontact techniques—AIVELA, Ancona, Italy, 25–27 June 2014, vol 1600, pp 94–102
- Smith BL, Glezer A (1998) The formation and evolution of synthetic jets. *Phys Fluids* 10:2281–2297
- Tan XM, Zhang JZ (2013) Flow and heat transfer characteristics under synthetic jets impingement driven by piezoelectric actuator. *Exp Thermal Fluid Sci* 48:134–146
- Trindade MA, Benjeddou A (2011) Finite element homogenization technique for the characterization of d15 shear piezoelectric macro-fibre composites. *Smart Mater Struct* 20:1–17
- Yang AS, Ro JJ, Yang MT, Chang WH (2009) Investigation of piezoelectrically generated synthetic jet flow. *J Vis* 12:9–16

Chapter 20

Modal Analysis of PZL-W-3/W-3A Sokol

Main Rotor

Ihor Berezin

20.1 Isolated Blade Natural Frequencies and Mode Shapes

Dynamic response of a rotor is determined by interference of the blades through the blade hub. To simplify analysis, in the first step the hub parts are not taken into account, thus providing background for investigation of isolated blade vibration response in conditions where it is not influenced by external factors. Extensive data collected during laboratory testing performed at PZL Swidnik provides broad possibilities for dynamic model verification.

Relatively simple structural and topological beam model can capture the complex behavior of sophisticated anisotropic nonhomogeneous rotor blades provided that appropriate elastic and inertial properties are taken into account (Weller and Minneck 1978). This approach does not encounter explicitly the geometry of blade cross sections, its internal structure, and material properties, but they are assumed via generalized stiffness and mass characteristics measured during laboratory tests and implemented into the mechanical model.

Due to the complex structure of the cross sections as well as the use of composite materials with orthotropic elastic properties, the helicopter blades are usually characterized with coupled bending-torsion vibrations (Bramwell et al. 2001; Mil et al. 1966). Coupling is induced mainly by the offset between the shear center (SC) and center of gravity (CG). Reduced mass applied out of the SC causes additional torque (in this case, the distance between the SC and CG acts as a lever arm), therefore causing the blade to undergo additional twist during bending vibrations. Unfortunately, limited data concerning SC locations is available from the results of laboratory tests. As a first approximation, the SC was assumed to be located on the blade pitch axis.

I. Berezin (✉)
WSK PZL Swidnik S.A, Swidnik, Poland
e-mail: berezin.ih@gmail.com

Stiffness and mass distributions required for modeling of an actual PZL-W-3/W-3A helicopter main rotor blade have been determined during laboratory testing performed at PZL. The characteristics include bending stiffness in chordwise (EI_y) and beamwise (EI_z) directions of the blade as well as torsional stiffness GI_x . Available laboratory test data of blade stiffness distribution have been measured with respect to blade chord and blade pitch axis.

The blade is represented as a straight 3D elastic beam coincident with blade pitch axis, with elastic and inertial characteristics distributed along the span corresponding to those of an actual blade used on PZL-W-3/W-3A helicopter. Variation of properties along the span is handled by introducing a series of elements with intermittent elastic and inertial properties (Fig. 20.1). Beam properties within each section $i = 1 \dots n$ are set to be constant. Masses m_i and mass moments of inertia J_{xi} , J_{yi} , J_{zi} are implemented as point mass elements M_i located at the corresponding CG coordinates for each blade section. Mass elements are connected to the investigated beam using rigid elements. Such representation of inertia properties is in good correlation with the physics of beam deformation and vibrations. Horizontal, vertical, and pitch hinges are modeled with revolute joint elements.

To simulate the effect of blade modifications, a full structural 3D model of the middle section corresponding to active gurney flap span has been developed (Fig. 20.2). A multilayer composite structure has been modeled with orthotropic shell elements. Internal structures of the blade were modeled with isotropic and

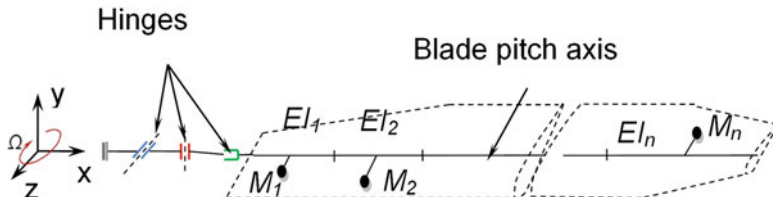


Fig. 20.1 Schematic of the blade model with beam elements

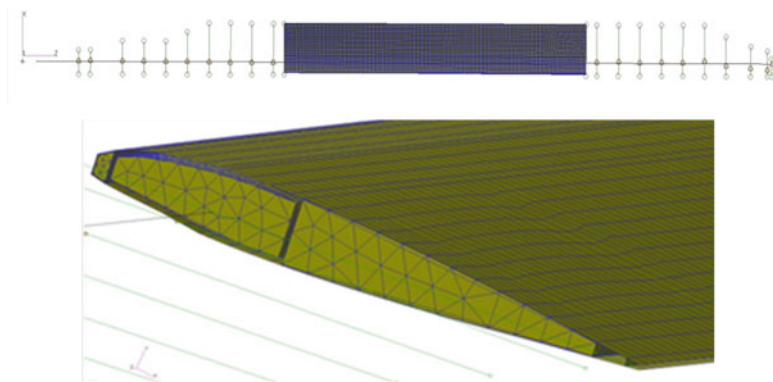


Fig. 20.2 FEM beam model of the blade with 3D middle section

orthotropic 3D elements and connected to outer shell structure with glued contact-type interface. For precise tracking of blade deflections in the 3D region, marker points projected onto blade pitch axis were introduced and connected to the rest of the model with rigid connections.

The model has been verified with the blade presented in Weller and Minneck (1978) prior to analysis of an actual blade to ensure its applicability to coupled bending-torsion modal analysis. In the verification problem, separate bending and rotational natural modes as well as coupled bending-torsion natural modes were calculated. For the case of simply supported beam with uniform stiffness and mass distribution, the values of natural frequencies for all cases determined with the described model are within $\pm 0.5\%$ of the target values. It has been shown that if the location of the shear center is not taken into account, the discrepancy increases to $\pm 5\%$. Verification analysis has been followed by the analysis of the PZL-W-3/W-3A helicopter blade natural frequencies.

Laboratory modal tests of the blades were performed with step sine excitation with frequency band from 3 to 50 Hz and data acquisition in 60 locations. Two sets of boundary conditions are considered in the laboratory tests and calculations:

- *Cantilever blade with hinges* free and additional suspension provided by rubber springs. Pitch hinge is blocked.
- *Hingeless cantilever blade* fixed at the horizontal hinge location with vertical and pitch hinges blocked (Fig. 20.3).

Finally, modal characteristics were calculated based upon methodology suggested by Weller and Minneck (1978) and implemented at PZL Swidnik in BLD software. Comparison of the results is shown in Table 20.1.

For more convenient interpretation of modal testing results, the mode identification procedure is introduced: natural modes are identified by plane in which principal vibration occurs (v beamwise, h chordwise, t torsional) and number of

Fig. 20.3 Laboratory test setup for cantilever blade modal testing

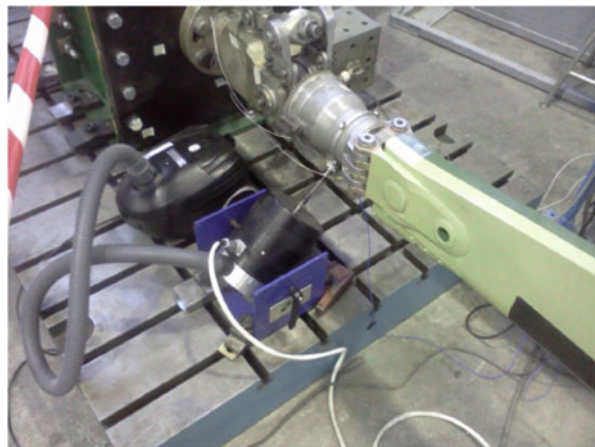


Table 20.1 Comparison of natural frequencies calculated with FEM, BLD, and lab tests

Cantilever blade			Fully articulated blade		
	FEM-test	FEM-BLD		FEM-test	FEM-BLD
			v0	–	–2.33%
v1	–12.90%	–4.93%	v1	–5.99%	1.11%
v2	–0.29%	–1.00%	v2	–1.47%	1.83%
v3	3.73%	2.21%	v3	–0.08%	2.21%
v4	6.61%	2.33%	v4(t)	3.21%	6.53%
v5	9.69%	3.97%	v5(t)	5.14%	10.00%
v6	6.49%	4.01%			
v7	8.86%	5.00%			
v8	8.30%	–			
			h0	–0.08%	–4.51%
h1	–7.01%	–7.95%	h1	3.21%	–2.57%
h2	–3.52%	–4.56%	h2	–8.31%	–6.98%
h3	0.47%	–4.61%	h3	4.72%	–4.80%
h4	3.68%				
t0	–0.91%	–1.33%	t0	2.99%	–0.30%
t1	3.75%	–1.19%	t1	4.72%	–0.31%
t2	1.18%	–2.17%			

corresponding nodes. For this purpose, a subroutine has been developed. The criterion used for identification of vibration plane is effective modal mass, calculated in the corresponding directions.

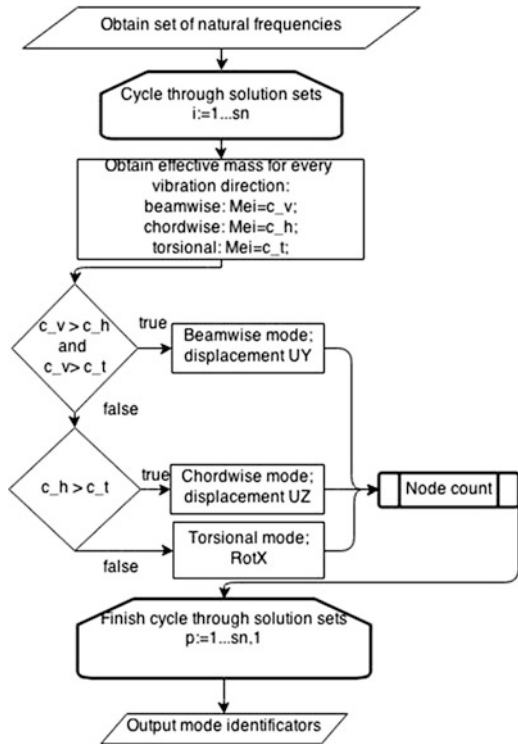
$$M_{ei} = \frac{\gamma_i^2}{\{\varphi\}_i^T [M] \{\varphi\}_i}$$

here $\gamma_i = \{\varphi\}_i^T [M] \{D\}$ —modal participation factor; $\{\varphi\}_i$ —eigenvector normalized to generalized mass; $[M]$ —mass matrix; $\{D\}$ —vector describing excitation direction.

Effective modal mass M_{ei} is calculated for each mode in every vibration direction y (beamwise), z (chordwise), or rx (torsional). Its maximum value within one mode corresponds to principal vibration direction. Then the number of nodes for this direction is calculated. Flowchart of the subroutine is shown in Fig. 20.4.

Natural mode shapes obtained during analysis are plotted in Fig. 20.5 in the coordinates of normalized displacements in the principal vibration direction vs

Fig. 20.4 Flowchart of mode identification



distance from the center of rotation. Since strong coupling between bending and torsional vibrations is observed for higher frequencies, some mode shapes cannot be identified unambiguously as ones in beamwise, chordwise, and torsional direction. This effect is considerably amplified in case if bending and torsional natural frequencies are approaching close values. For this reason the separation of mode shapes is provisional in certain cases. Thus, clear distinction could not be made for torsional and bending modes v_4 , v_5 , and h_1 neither during laboratory testing nor after FEM simulation.

Results of modeling of a single blade without hub and fixtures with FEM are in good correspondence with the results obtained during laboratory testing and BLD. Since BLD has been used at PZL for a long time and the results obtained from this software have been verified by broad experimental database, the further results of modal analysis will be compared to BLD. Discrepancy between some modes is caused by uncertainties in shear center definition. However, this model is sufficient for the comparative study of blade modifications.

Modal assurance criterion (MAC) has been used as a measure of consistency between the mode shapes calculated with FEM and ones determined from the BLD to determine validity of calculated mode shapes. MAC between two vectors $\{\varphi\}_X$ and $\{\varphi\}_Y$ is calculated as follows:

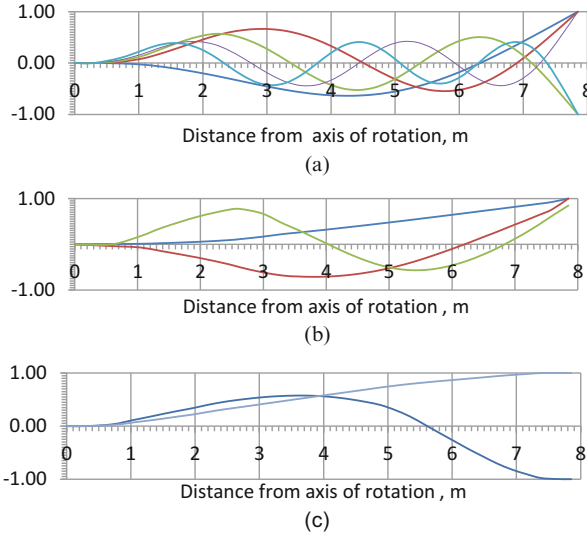


Fig. 20.5 Mode shape visualization for hingeless cantilever blade in beamwise (a), chordwise (b), and torsional (c) directions

$$MAC_{XY} = \frac{|\{\varphi\}_X^T \{\varphi\}_Y|^2}{(\{\varphi\}_X^T \{\varphi\}_X) (\{\varphi\}_Y^T \{\varphi\}_Y)}$$

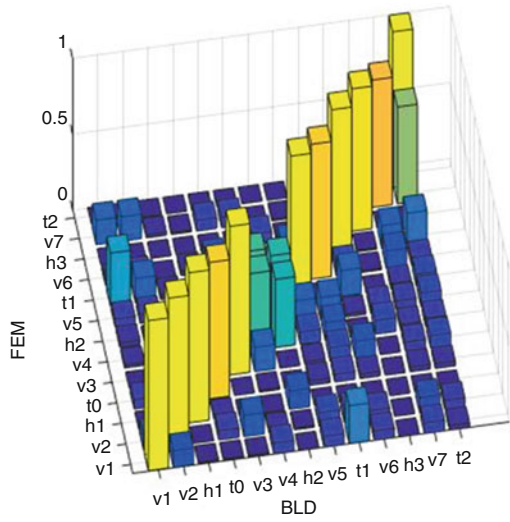
here $\{\varphi\}_X$ —mode shape vector from FEM; $\{\varphi\}_Y$ —mode shape vector from BLD.

For helicopter MR blades, the mode shapes are considered in good correlation if $MAC > 0.7$. For current analysis, almost all mode shapes are above 0.9 (Fig. 20.6). Exceptions are modes ν_4 and h_2 for which the values of natural frequencies are close to each other therefore inducing strong coupling.

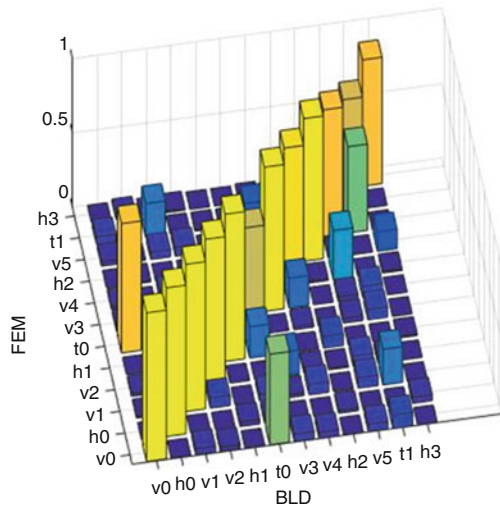
Estimation of blade vibration changes caused by active gurney flap installation is of great importance as additional mass is introduced shifting blade CG toward the toe. This could negatively influence aeroelastic stability. Several modifications were made to FEM model to simulate additional systems inside the blades. Additional point masses were introduced along blade pitch axis simulating actuators. Blade internal structure was modified as well by removing sections of honeycomb in locations of actuators and introducing slots in airfoil for flap retraction.

Modal analysis of a combined beam-3D FEM model shows that blade stiffness modification has minor influence on natural frequencies, and therefore can be neglected. Instead, blade dynamics is governed mainly by mass and CG position variations. Installation of gurney flap actuation mechanism comprising of five actuator stations with mass of approximately 350 g each causes blade center of gravity to shift by 15 mm in longitudinal direction and by 5 mm (1.1% of blade chord) in in-plane direction toward the blade toe. Natural frequencies of blade with installed actuation system decrease by 1.5% compared to basic configuration for frequency band from 3 to 50 Hz.

Fig. 20.6 Modal assurance criterion for cantilever (a) and Fully articulated (b) blade



(a)



(b)

20.2 Modal Analysis of Main Rotor

Modal analysis of four-bladed main rotor was also performed. Natural frequencies of rotating rotor are the frequencies of orthogonal, fully coupled modes of usually complex rotor structures with centrifugal force effects accounted for. The modes are coupled in the flap (out of the plane of rotation), lag (in the plane of rotation),

and pitch (motion about an axis that runs along the span of the blade) degrees of freedom (Mil et al. 1966; Johnson 1980; Bramwell et al. 2001). Flexibility of the control system also affects rotor modes, for the pitch degree of freedom in particular.

To analyze a particular rotor, it is necessary to specify the geometric and structural properties relating the manner in which the blades are mounted to the hub. Hub configuration and support system impedance characteristics are expressed as lumped mass-spring system with three basic sets of boundary conditions. Estimated modal characteristics are designated as pertaining to collective-, cyclic-, or scissor-type modes depending on which boundary condition is imposed.

Each of the three types of rotor modes—collective, cyclic, and scissors or reactionless—has a set of forcing frequencies that are integer multiples of the rotor speed. Common nomenclature for the cycles-per-rotor-revolution unit of frequency is per revolution, abbreviated/Rev.

The *cyclic modes* (Fig. 20.7) have symmetric in-plane and antisymmetric out-of-plane deflection shapes about the center of rotation. Cyclic modes have a boundary condition at the center of rotation that is pinned out of the plane of rotation and cantilevered in the plane of rotation. The hub is represented as point mass-spring system with in-plane degree of freedom. The rotor speed, $1/\text{Rev}$, is always a cyclic mode. For rotors with evenly spaced blades, the remainder of the cyclic mode forcing frequencies is the collective mode forcing frequencies $\pm 1/\text{Rev}$.

The *collective mode* (Fig. 20.8) is characterized by symmetric out-of-plane and antisymmetric in-plane deflections of opposing pairs of blades on the rotor. Collective rotor modes can be thought of as having a boundary condition at the center of rotation that is cantilevered out of the plane of rotation and pinned in the plane of rotation. In this case, hub impedance is represented as a point mass with translational degree of freedom in out-of-plane direction and in-plate torsional degree of freedom. For rotors with evenly spaced blades, collective modes have forcing frequencies that are integer multiples of the number of blades n/Rev .

Fig. 20.7 Boundary conditions for cyclic mode

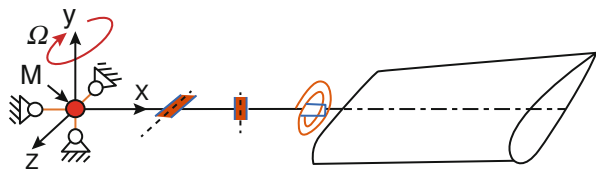


Fig. 20.8 Boundary conditions for collective mode

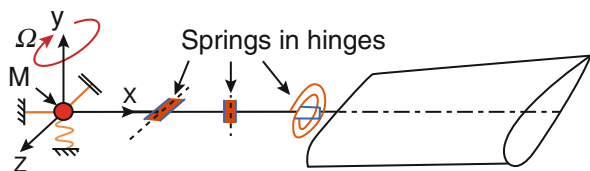
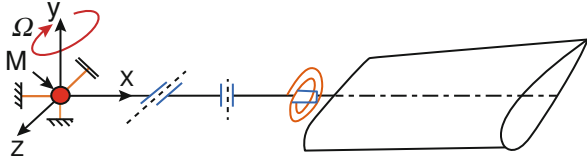


Fig. 20.9 Boundary conditions for scissors mode



Boundary conditions for collective mode (r angular DOF, d linear DOF):

- Constrained displacements at MR hub: r_x, r_z, d_x, d_z
- Spring supported d_y, r_y
- Additional stiffness in hinges to model the mast bending stiffness

A four-bladed rotor has collective mode forcing frequencies of 4/Rev and 8/Rev and would have cyclic mode forcing frequencies of 1/Rev, 3/Rev, 5/Rev, and 7/Rev.

For the *scissors* modes, the in-plane and out-of-plane boundary conditions at the center line represent clamping of the blades to an immovable hub. That is, scissors modes have a boundary condition at the center of rotation that is cantilevered both out of the plane of rotation and in the plane of rotation (Fig. 20.9). Scissors mode forcing frequencies are the integer multiples of the rotor speed that are neither collective mode forcing frequencies nor cyclic mode forcing frequencies.

As for the case with separate blade modal analysis, natural frequencies of full rotor with installed active gurney flap system slightly (by from 1 to 5 %) differ from classic main rotor configuration.

20.3 Conclusions

Natural frequencies for single blade and full rotor calculated with FEM model are in good agreement with laboratory tests and BLD results. The model of stand-alone blade with appropriate boundary conditions is suitable for modal analysis of MR with centrifugal effects accounted for.

Installation of active gurney flap system into the W-3 blade causes natural frequency decrease of about from 1 to 5 % in the frequency band from 3 to 50 Hz. The same applies to the rotating rotor with centrifugal forces. Blade aeroelastic stability parameters remain within allowable envelope after modification.

References

- Bramwell AR, Balmford D, Done G (2001) Bramwell's helicopter dynamics, 2nd edn. Butterworth Heinemann, Oxford
- Johnson W (1980) The helicopter theory. Princeton University Press, New Jersey

- Mil ML, Nekrasov AV, Braverman AS, Grodtko LN, Leikand MA (1967) In Mil ML (ed) Helicopters: calculation and design. Vibrations and dynamic strength, vol. 2. Mashinostroyeniye, Moscow
- Weller WH, Minneck RE (1978) An improved computational procedure for determining helicopter rotor blade natural modes. NASA Technical Memorandum 78670

Chapter 21

Strain Modal Analysis

Fabio L.M. dos Santos and Bart Peeters

Acronyms

ABT	Active blade twist
AFC	Active fiber composites
CFRP	Carbon fiber reinforced plastics
COMAC	Coordinate modal assurance criterion
DMA	Displacement modal analysis
DOF	Degree of freedom
ECOMAC	Enhanced coordinate modal assurance criterion
EMA	Experimental modal analysis
FBG	Fiber Bragg Grating
FEM	Finite Element Method
FRAC	Frequency response assurance criterion
FRF	Frequency response function
GF	Gauge factor
GFRP	Glass fiber reinforced plastics
GVT	Ground vibration testing
ICP	Integrated circuit piezoelectric
LS	Least squares
MAC	Modal assurance criterion
MDOF	Multiple degree of freedom
MIMO	Multiple-input multiple-output
MRB	Main rotor blade
MSF	Modal scaling factor
NDT	Non-destructive testing
OMA	Operational modal analysis

F.L.M. dos Santos (✉) • B. Peeters
Siemens Industry Software, Interleuvenlaan 68, 3001 Leuven, Belgium
e-mail: fabio.m.santos@siemens.com; bart.peeters@siemens.com

SFRF	Strain frequency response function
SHM	Structural health monitoring
SMA	Strain modal analysis
SMF	Scaling mode factor
SPA	Strain pattern analysis
UAV	Unmanned aerial vehicle

21.1 Introduction

Strain gauges and strain measurements have been commonly used in the industry for many types of applications other than modal analysis, such as load testing of mechanical systems on a component level—in Mulle et al. (2015) strain sensors are used to test a composite sandwich beam using a four point bending test, or also on a system level—in Zhang et al. (2013) strain gauges are used to measure the dynamic load on a generator rotor. Fatigue testing, durability analysis, and lifecycle and lifetime prediction analyses also commonly employ strain gauges for failure predictions (Dowling 1971) and fatigue prediction of components—in Vandepitte and Sas (1990) resonance fatigue is studied and measured using strain gauges, while in Wentzel (2013) a commercial truck is tested in such a way using strain gauges.

Another important use of strain measurements is for evaluating structural integrity or stress concentration such as in Yam et al. (1994), where the stress concentration in thin plates with holes is investigated, and in Finnveden and Pinnington (2000) the dynamic strain in pipes is the focus of the study. Strain gauges and measurements are also present in design prototype stages and also monitoring structures in operation [with Structural health monitoring systems in Li et al. (2002)], which has led to an increase in the number of dynamic strain applications and to the development of improved identification and measurement techniques: in Reich and Park (2001) a substructural strain-based system identification is proposed.

The use of strain sensors and measurements for modal testing, although less dominant when compared with the use of accelerometers, has been present in the past (Bernasconi and Ewins 1989; Vári and Heyns 1994). More recently there has been increased interest from both industry (Luczak et al. 2010) and academia (Baquersad et al. 2015; Yam et al. 1996; Zhang et al. 2015) on assessing the potential benefits of strain modal analysis. Moreover, for many of the traditional strain gauge applications, the instrumentation applied and tests performed can lead to significant additional information on product durability and dynamic performance by obtaining the modal parameters of the system.

An important contribution on the field of strain measurement are the fiber optic sensors or Fiber Bragg Grating (FBG) sensors: in Hwang et al. (2011), a fiber Bragg grating sensor is tested for dynamic strain measurements on a cantilever beam, and Suzhen and Zhishen (2005) employ the technology using long gauge

sensors. In Lae-Hyong et al. (2007), the authors use FBGs sensors to measure dynamic strain and estimate structural displacements, and in Ling et al. (2004) these sensors are embedded in a composite beam for delamination detection, while in Cusano et al. (2006) the sensors are embedded in a wing structure to measure its dynamic characteristics, including the strain mode shapes. The robustness of these sensors to magnetic interference, added to the easiness of creating a multiplexed sensor array with multiple sensors, plus the possibility of embedding these sensors in composite structures, makes them an attractive solution for use in damage identification systems such as presented in Zhang and Yang (2013), and in Mihailov (2012) the robustness of these sensors is highlighted, showing how they can be used in high temperature and high pressure environments.

Another application that makes use of dynamic strain measurements has to do with the strain–displacement relations (Pisoni et al. 1995). In many cases, the prediction of strain responses from displacements is the objective: in Lee (2007), a method using modal transformation matrices is carried out to convert displacements into strain and validated on a cantilever beam, while in Sehlstedt (2001) and Karczub and Norton (1999) this transformation is proposed using numerical differentiation. In some other cases, strain measurements can be used to estimate displacement, usually using modal transformation matrices (Foss and Haugse 1995; Tourjansky and Szechenyi 1992). This methodology is especially useful when accelerometers cannot be employed due to size constraints, such as is the case in rotating blades: in Stephan and Geeraert (2015) and Geeraert and Mauffrey (2015) this methodology is implemented on counter rotating open rotor blades to estimate their displacement based on strain measurements.

There are, however, some limitations associated with experimental strain modal analysis—these include the lack of symmetry of the strain frequency response function (SFRF) matrix, which leads to non-reciprocal measurements (Vári and Heyns 1994), which also means that the strain modes cannot be directly scaled using the conventional methodologies (Bernasconi and Ewins 1989). More recent works have shown how experimental strain modal analysis can be used and correlated with finite element models with the SFRF reconstructed from the identified parameters (Kranjc et al. 2014), and in Kranjc et al. (2013) a methodology that uses the mass-change strategy is proposed to solve the normalization problem of the strain modes.

Finally, the motivation for the use of strain gauges for dynamic characterization and other purposes is also motivated by industrial applications. In Ohno et al. (2001), the authors mention many industrial applications where strain measurements are required, such as the monitoring of concrete structures (dams, tunnels, and buildings) and of steel structures (such as ships, tanks, and bridges). In Trutzel et al. (2000), the use of FBG sensors for smart sensing applications on aviation structures is the focus. Additionally, many of the references mentioned in this section are related to or stimulated by the needs from industrial applications. Overall, these cases give very strong motivations for investigating and further developing strain-based modal analysis techniques.

This chapter of the book will give a brief introduction to classical accelerometer-based modal analysis, and will then explain the basics of strain modal analysis, modal residues, and scaling, and will show an example of experimental strain modal analysis on the PZL SW-3 Sokol helicopter main rotor blade.

21.2 Classical Modal Analysis

Modal analysis using accelerometers as output is the most common way of carrying out an experimental modal analysis. In fact, this method is so common that it is usually referred to as just modal analysis or Experimental modal analysis (EMA). However, to avoid confusion when dealing with a particular type of procedure, using accelerometers or strain-based sensors, these will be referred to accordingly—modal analysis (and displacement modes) will be referred to as the procedure using accelerometers and Strain modal analysis (SMA) (and strain modes) will be referred to as the procedure using strain gauges.

21.2.1 Displacement Modal Model

The formulation for displacement modal analysis has already been known and studied for some time (Ewins and Inman 2001; Fu and He 2001; Heylen et al. 2006; Maia and Silva 1997). Usually, the method used to obtain the modal formulation is based on lumped parameters. This can also be described as the numerical approach, where the analysis starts with the estimation of mass, stiffness, and damping matrices. In this work, the experimental approach to modal analysis will be described instead. This approach uses measurements of part of the frequency response function matrix. This matrix is described as (Heylen et al. 2006):

$$\mathbf{H}(j\omega) = \sum_{r=1}^n \frac{Q_r \phi_r \phi_r^T}{j\omega - \lambda_{\omega r}} + \frac{Q_r^* \phi_r^* \phi_r^{*T}}{j\omega - \lambda_{\omega r}^*}, \quad (21.1)$$

where n is the number of modes taken in consideration, r represents the r th mode, j is the imaginary unit, ω is the frequency variable, $\lambda_{\omega r}$ is the pole of the r th mode, Q_r is the scaling factor, ϕ_r is the r th modal vector, the superscript $*$ is the complex conjugate, and the superscript T is the transpose.

Usually, modal parameter estimation techniques will use these measurements to identify the modal parameters λ_r and ϕ_r , while the scaling factor Q_r depends on the scaling scheme (this part is better explained in Sect. 21.4).

By considering an undamped system, the frequency response function can be simplified as:

$$\mathbf{H}(j\omega) = \sum_{r=1}^n \frac{j2\omega_r Q_r \phi_r \phi_r^T}{\omega_r^2 - \omega^2} \quad (21.2)$$

which in turn can be expanded, taking also into account the number of measurement and excitation points:

$$\begin{bmatrix} H_{11} & H_{12} & \cdots & H_{1N_q} \\ H_{21} & H_{22} & \cdots & H_{2N_q} \\ \vdots & \vdots & \vdots & \vdots \\ H_{N_p1} & H_{N_p2} & \cdots & H_{N_pN_q} \end{bmatrix} = \sum_{r=1}^n \frac{j2\omega_r Q_r}{\omega_r^2 - \omega^2} \cdot \begin{bmatrix} \phi_{1r}\phi_{1r} & \phi_{1r}\phi_{2r} & \cdots & \phi_{1r}\phi_{N_q r} \\ \phi_{2r}\phi_{1r} & \phi_{2r}\phi_{2r} & \cdots & \phi_{2r}\phi_{N_q r} \\ \vdots & \vdots & \vdots & \vdots \\ \phi_{N_p r}\phi_{1r} & \phi_{N_p r}\phi_{2r} & \cdots & \phi_{N_p r}\phi_{N_q r} \end{bmatrix}_{N_p \times N_q}, \quad (21.3)$$

where N_p represents the number of measurement stations (or the number of output measurements) and N_q represents the number of excitation points (or the number of inputs).

One can also define the concept of modal participation factor. By rearranging some terms from Eq. (21.2) as:

$$\mathbf{V} = [\phi_1 \cdots \phi_n] \quad (21.4)$$

$$\text{Thedenominators: } \left[\left[\omega_r^2 \right] - \omega^2 \left[I \right] \right]^{-1} \quad (21.5)$$

$$\mathbf{L} = [j2\omega_1 Q_1 \phi_1 \cdots j2\omega_n Q_n \phi_n]^T, \quad (21.6)$$

with the term in (21.5) being a diagonal matrix containing the system natural frequencies. Then we can define the transfer function matrix:

$$\mathbf{H}(j\omega) = \mathbf{V} \cdot \left[\left[\omega_r^2 \right] - \omega^2 \left[I \right] \right]^{-1} \cdot \mathbf{L} \quad (21.7)$$

The matrices \mathbf{V} and \mathbf{L} are referred to as the modal vector matrix and the modal participation factor matrices, respectively. The first one contains the modal displacements, while the second matrix is related to the force inputs acting on the system, and it can be considered a measure of how well a degree of freedom is excited for each mode. The participation factors are a function of scaling factors Q_r and of the displacement modal vectors. This characteristic plays an important role when carrying out strain modal analysis, as the participation factor will still contain displacement modal vectors.

21.2.2 Modal Validation

Modal validation is an important part of an experimental modal analysis test campaign. Sometimes, the objectives can be to validate a Finite Element Method (FEM) model of a structure, some other times only the experimental data is available and its validity needs to be assessed. In any case, validation of the experimental results and/or comparison with FEM models is a crucial step. The most usual way to carry out such a procedure is using the Modal assurance criterion. This operation is used to measure the degree of similarity between two mode shapes. In the case of FEM model validation, we have

$$\text{MAC} = \frac{|\phi_r^{*T,t} \phi_r^s|^2}{(\phi_r^t \phi_r^{*T,t})(\phi_r^s \phi_r^{*T,s})}, \quad (21.8)$$

where the superscripts t and s represent the test and simulation mode shape vectors, respectively. The Modal assurance criterion (MAC) values range from 0 to 1, with 1 being the highest degree of similarity and 0 the lowest.

One can also use the MAC to compare a mode set with itself. In this case, this operation is referred to as the autoMAC. The autoMAC is very useful to validate experimentally obtained mode shapes, where it can be used to assess if the modes were identified correctly and are unique—the mode autoMAC value should be 1 when compared to itself and close to 0 otherwise.

There are many other types of model validation methods not presented or used in this work, such as the mode overcomplexity and modal phase collinearity, both described in Heylen et al. (2006). The first one, mode overcomplexity, is based on the sensitivity of mass changes at each response Degree of freedom (DOF) of the structure, and can give insight on whether a mode is physical, if the excitation point is close to a nodal point of the mode, or if the mode estimate might be wrong. The modal phase collinearity works in a similar way, but is only used for modes with proportional damping.

21.3 Strain Modal Analysis

21.3.1 Strain Modal Model

To obtain the strain modal formulation, one can start from the definition of the strain modes. One can define in this way the operator S as the linear spatial differentiator (Bernasconi and Ewins 1989; Kranjc et al. 2013) that relates the displacement mode vector ϕ_r to the strain mode vector ψ_r :

$$\psi_r = S \cdot \phi_r, \quad (21.9)$$

with the subscript r representing the r th mode. Then, based on Eq. (21.4), we define the strain modal vector matrix and the modal participation factor matrices:

$$\mathbf{V}^\varepsilon = [\psi_1 \cdots \psi_n] \quad (21.10)$$

$$\mathbf{L} = [j2\omega_1 Q_1 \phi_1 \cdots j2\omega_n Q_n \phi_n]^T, \quad (21.11)$$

where the superscript ε is used to identify when a parameter is related to strain modes, n indicates the number of modes, Q is the scaling factor, and $\omega_{1\dots n}$ the natural frequencies. In this way, we can define the Strain frequency response function (SFRF) function with respect to the system poles and participation factors, similar to Eq. (21.7):

$$\mathbf{H}^\varepsilon(j\omega) = \mathbf{V}^\varepsilon \cdot \left[\left[\backslash \omega_r^2 \backslash \right] - \omega^2 \left[\backslash I \backslash \right] \right]^{-1} \cdot \mathbf{L}, \quad (21.12)$$

with $\mathbf{H}^\varepsilon(j\omega)$ being the SFRF matrix. Similarly, we can define it based on the undamped case from Eq. (21.2):

$$\mathbf{H}^\varepsilon(j\omega) = \sum_{r=1}^n \frac{j2\omega_r Q_r \psi_r \phi_r^T}{\omega_r^2 - \omega^2} \quad (21.13)$$

where ω is the frequency variable and j the imaginary unit. The expansion of (21.13) in matrix form, taking into account the number of input and output measurements:

$$\begin{bmatrix} H_{11}^\varepsilon & H_{12}^\varepsilon & \cdots & H_{1N_q}^\varepsilon \\ H_{21}^\varepsilon & H_{22}^\varepsilon & \cdots & H_{2N_q}^\varepsilon \\ \vdots & \vdots & \vdots & \vdots \\ H_{N_p1}^\varepsilon & H_{N_p2}^\varepsilon & \cdots & H_{N_pN_q}^\varepsilon \end{bmatrix} = \sum_{r=1}^n \frac{j2\omega_r Q_r}{\omega_r^2 - \omega^2} \cdot \begin{bmatrix} \psi_{1r} \phi_{1r} & \psi_{1r} \phi_{2r} & \cdots & \psi_{1r} \phi_{N_q r} \\ \psi_{2r} \phi_{1r} & \psi_{2r} \phi_{2r} & \cdots & \psi_{2r} \phi_{N_q r} \\ \vdots & \vdots & \vdots & \vdots \\ \psi_{N_p r} \phi_{1r} & \psi_{N_p r} \phi_{2r} & \cdots & \psi_{N_p r} \phi_{N_q r} \end{bmatrix}_{N_p \times N_q}, \quad (21.14)$$

where N_p represents the number of strain gauge measurement stations (or the number of output measurements) and N_q represents the number of excitation points (or the number of inputs).

There are some remarks and considerations that can be obtained from the strain modal analysis theory presented:

- Each column of the matrix corresponds to SFRFs obtained from a single input excitation point and multiple strain responses;
- the SFRF matrix is not symmetric—for example, H_{12}^ε is different from H_{21}^ε (or $\psi_{1r} \phi_{2r} \neq \psi_{2r} \phi_{1r}$);
- from the item above, it can be inferred that there is no reciprocity in strain modal analysis;

- any column of the **SFRF** matrix contains all the information regarding the strain modes (ψ_r);
- any row of the **SFRF** matrix contains information about the displacement modes (ϕ_r);
- to obtain the strain mode shapes in experimental strain modal analysis, one must use a fixed excitation point and measure the multiple strain responses (for instance, using a shaker excitation);
- by using a strain gauge as a fixed reference sensor and moving the excitation point (as with roving hammer impact testing) in strain modal analysis, the displacement mode shapes can be obtained;
- the similarity of the strain modal formulation and the displacement modal formulation means that the same identification methods can be used for both types of experimental analysis (Kranjc et al. 2014).

In general, there are drawbacks but also advantages present in strain modal theory. A very important advantage is its versatility—being able to identify both displacement and strain modes with one type of output sensor (a force cell is still required to measure the input) is a property that can be used to reduce the number and types of sensors used in an experimental test campaign, and something not achieved directly with accelerometers.

Moreover, in experimental modal analysis, it is usual that the upper and lower residual term matrices are calculated. These are terms to account for the influence of modes outside the limited measurement bandwidth and they remain unchanged for strain modal analysis.

21.4 Modal Residues and Scaling

Modal scaling is a useful operation in modal analysis. The normalization of the identified modes is required in some substructuring applications (Karpel and Ricci 1997), as well as in damage detection techniques that make use of the flexibility matrix (Bernal 2002; Pandey and Biswas 1994). Structural modification prediction (Braun and Ram 2001) is also another application which makes use of the normalized modes to predict how a given mode set behaves when there are mass and stiffness changes to it (a common application is removing the mass loading effect of sensors). There are cases in which the modal scaling is not possible, usually because the driving point output measurement is not known. This is the case in operational modal analysis, where there is a lot of research effort devoted to developing procedures that can help with the mode shape scaling problem. These are usually based on the sensitivity of the modes to mass or stiffness changes (Bernal 2004; López-Aenlle et al. 2012; Parloo et al. 2002). In strain modal analysis, due to the lack of a true driving point measurement, the scaling of the strain modal vectors is still an open problem, with the most recent efforts using the mass-change technique used in operational modal analysis to scale the strain mode shapes (Kranjc et al. 2013).

In this section, some elements on how to carry out the modal scaling procedure will be explained, as well as some insight on how the procedure is carried out when dealing with strain modal analysis.

21.4.1 Displacement Modal Vector Scaling

The modal vector scaling procedure and the different scaling schemes are well described in Heylen et al. (2006). The modal vectors obtained in experimental modal analysis are scaled vectors obtained from the modal residues, which are absolute quantities. The modal residue matrix \mathbf{A}_r is defined as:

$$\mathbf{A}_r = \mathbf{Q}_r \cdot \phi_r \phi_r^T, \quad (21.15)$$

where the terms in the residue matrix \mathbf{A}_r are absolute quantities, while the modal vectors ϕ_r are scaled quantities, which depend on the scaling factor \mathbf{Q}_r . Taking into account only the element pq (representing the p th response degree of freedom and the q th input degree of freedom):

$$A_{pqr} = \mathbf{Q}_r \cdot \phi_{pr} \phi_{qr} \quad (21.16)$$

Of the many possible scaling schemes, a common one is the unity modal mass scaling scheme. For an undamped system, it can be defined as:

$$\mathbf{Q}_r = \frac{1}{2jm_r\omega_r} \quad (21.17)$$

$$\text{with } m_r = 1 \text{ and } \mathbf{Q}_r = \frac{1}{2j\omega_r} \quad (21.18)$$

$$\phi_{qr} = \sqrt{\frac{A_{qqr}}{\mathbf{Q}_r}} \quad (21.19)$$

$$\phi_{pr} = \frac{A_{pqr}}{\mathbf{Q}_r \phi_{qr}} = \frac{A_{pqr}}{\mathbf{Q}_r \sqrt{\frac{A_{qqr}}{\mathbf{Q}_r}}}, \quad (21.20)$$

where m_r is the mass component of the r th mode related to the diagonal mass matrix, and in this scaling scheme it is chosen to have unity value. Equations (21.18)–(21.20) show that the driving point measurement is normally required for the scaling procedure to be carried out [although there can be solution schemes where the driving point measurement is not necessary, such as the mass sensitivity method (Parloo et al. 2002)]. The presented scaling scheme can also be used in the case of proportionally and non-proportionally damped cases.

One can describe some practical steps to be taken to carry out the scaling procedure in experimental modal analysis. For this purpose, a full column of the residues matrix will be used and referred to (usual procedure in shaker testing), but the same procedure can be applied in the case that a full row of the matrix is instead used (usual procedure in impact testing):

- First, the column of the residues matrix for each mode is necessary. Practically speaking, the driving point residue is the most important part of this column.
- For a given excitation point q and N_p output sensors, a column vector composed of $[A_{1qr}, \dots, A_{N_pqr}]^T$ is available for each mode.
- Then, for the r th mode, the constant Q_r can be calculated using Eq. (21.18).
- Defining the subscript qq as related to the driving point, the scaled mode value at the driving point (ϕ_{qqr}) can be calculated using Eq. (21.19) and the residue A_{qqr} .
- Finally, all the other scaled mode values can be calculated using Eq. (21.20) for other residue values.

Therefore, to be able to properly scale the mode vectors, it is necessary that the FRF at the driving point is measured, which allows for the identification of the residue A_{qqr} at the location. In turn, this allows for the scaling of all the vibration modes of the system.

21.4.2 *Scaling for Strain Modal Analysis*

Having introduced the basic procedure for carrying out the unit mass scaling of displacement modes, the scaling for strain modes can be better explained. Scaling these modes can be done in similar way when compared to the displacement modes, since both of them share a lot of common elements in their formulations. The equation equivalent to (21.15) for strains that relates the strain residue matrix \mathbf{A}_r^ε to the scaling factor Q_r and to the displacement (ϕ_r) and strain modes (ψ_r) is:

$$\mathbf{A}_r^\varepsilon = Q_r \cdot \psi_r \phi_r^T \quad (21.21)$$

Once more, taking into account only the element pq (representing the p th response degree of freedom and the q th input degree of freedom), Eq. (21.21) becomes:

$$A_{pqr}^\varepsilon = Q_r \cdot \psi_{pr} \phi_{qr} \quad (21.22)$$

Analyzing Eq. (21.22), it can be understood that despite the similarity between the formulations for displacement and strain modal analysis, an additional difficulty arises in the latter case. In displacement modal analysis, the driving point measurement could be used as the basis and initial step for scaling the modes. That is, an equation with only one variable could be solved and consequently the scaled mode at the driving point could be used as the basis for calculating the scaled modes at all other measurement locations. On the other hand, with strain modal analysis there

exists no true driving point, since the **DOF** measured on the excitation point (strain) is not the same **DOF** as the excitation force. Strain measurements at the excitation point q for a strain modal analysis system yield instead:

$$\psi_{qr}\phi_{qr} = \frac{A_{qqr}^{\varepsilon}}{Q_r}, \quad (21.23)$$

which has two variables to be solved (ψ_{qr} and ϕ_{qr}), and therefore its solution is not possible.

The point where the structure is excited and strain is measured will still be referred to as the driving point in strain modal analysis, even if it does not fulfill the requirement of equal excitation and measurement **DOF**. A true driving point in strain modal analysis could be obtained by using an actuator that excites the structure on the strain **DOF**. Such is the case of PZT actuator patches, which act on the system by deforming the structure locally. This case will not be covered in this work, where instead the more usual ways of exciting the structure (shaker and impact hammer) will be used.

Generally speaking, additional operations have to be carried out or additional information has to be obtained in order to solve Eq. (21.23) and thus achieve modal scaling for the strain modes. The simplest solution to properly scale the strain modes would be to include an accelerometer measurement at the driving point. This additional sensor means that ϕ_{qr} can be calculated and consequently the strain modes can be correctly scaled according to the following relation:

$$\psi_{pr} = \frac{A_{pqr}^{\varepsilon}}{Q_r \cdot \phi_{qr}} \quad (21.24)$$

Thus, the scaling problem for strain modes can be solved by employing an additional accelerometer. However, some advantages of the strain modal analysis methodology, such as sensor size, come from the use of purely strain measurements. Therefore, it can be an advantage to be able to scale the modes using purely strain gauges. However, this is not covered in this work.

21.5 Experimental Strain Modal Analysis of a Helicopter Main Rotor Blade

This experiment had as the main goal to carry out a strain modal analysis on a composite helicopter main rotor blade, to assess how the dynamics and strain modes of the composite blade are captured by the strain sensors, and a different and newer type of sensor was tested—the **FBG** sensors. These sensors are marked in an optical fiber and a laser scans through the fiber, for a whole range of wavelengths. Relative distortions for a given wavelength are relative to the strain. The sensors, as well as the full experimental procedure, are well described in Peeters et al. (2014), dos Santos et al. (2015) and dos Santos and Peeters (2016).

Moreover, to better study the blade dynamic behavior, displacement modal analysis sensors and typical piezo ICP accelerometers were also used—one of the objectives was to identify the strain and displacement modes, to be able to understand their relations and similarities.

In total, 20 **FBG** sensors were used—these are actually gratings created within the fiber. For this case, there were two fiber lines, each containing ten sensors. Moreover, four regular resistive strain gauges were also used, collocated with the **FBG** sensors. The strain gauges were used to be able to better assess the noise floor of the **FBG** sensors, and also to synchronize them with the force measurements—since the **FBG** sensors use their own acquisition unit, while the force and other sensors are measured with the standard measurement equipment, it is important that an offline synchronization procedure is carried out to synchronize the **FBG** sensors with the force sensor. Sixteen accelerometers were collocated with the **FBG** sensors to measure both strain and acceleration at the same locations. Figure 21.1 shows a part of the blade with the above-mentioned sensors, while Fig. 21.2 shows the strain gauge collocated with the **FBG** sensor. The list of equipment used for the strain modal analysis is as follows:

- LMS SCADAS mobile with 64 measurement channels and 2 output channels
- PC with LMS Test.Lab 12A software
- 16 PCB 333B30 Accelerometers
- PCB 208C03 impedance head
- Electrodynamic shaker with stinger and amplifier
- FiberSensing BraggMETER
- Two optical fibers with ten gratings (sensors) each
- Four resistive strain gauges.

The measurement location for all the sensors is shown in Fig. 21.3—the 16 accelerometers were collocated with the **FBG** sensors, except on locations 4, 5, 14, and 15, where no accelerometers were placed, while the resistive strain gauges were collocated with the **FBG** sensors on locations 4, 7, 16, and 19. The blade was

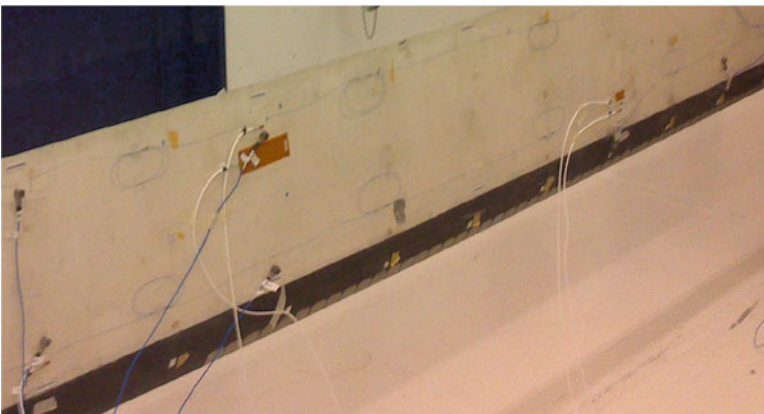


Fig. 21.1 Helicopter blade instrumented with accelerometers, strain gauges, and **FBG** sensors

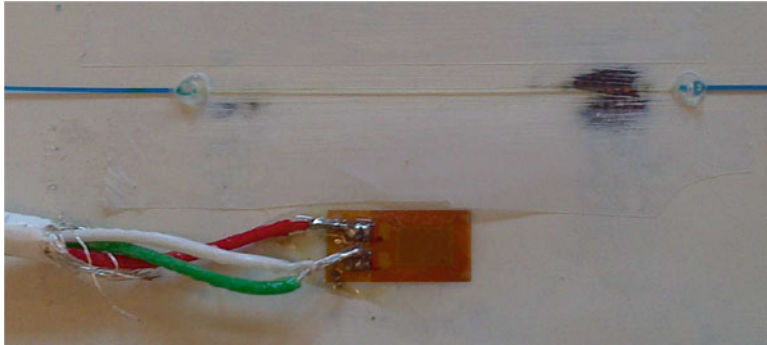


Fig. 21.2 Strain gauge collocated with FBG sensor

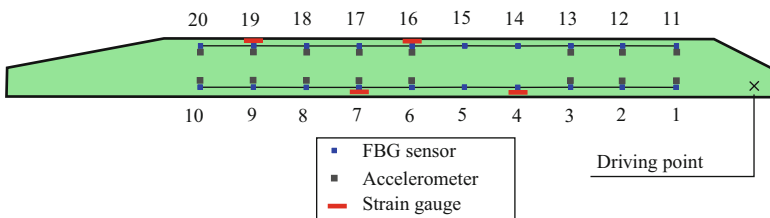


Fig. 21.3 Helicopter blade: location of FBG sensors, strain gauges, accelerometers, and driving point

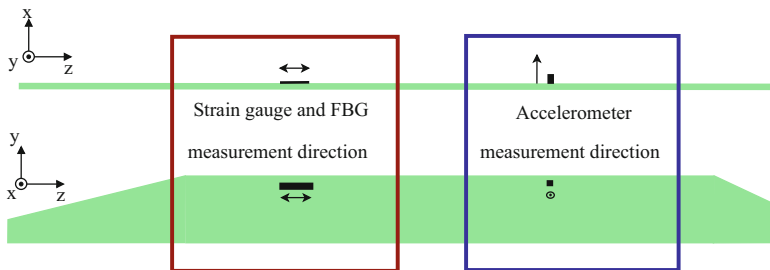


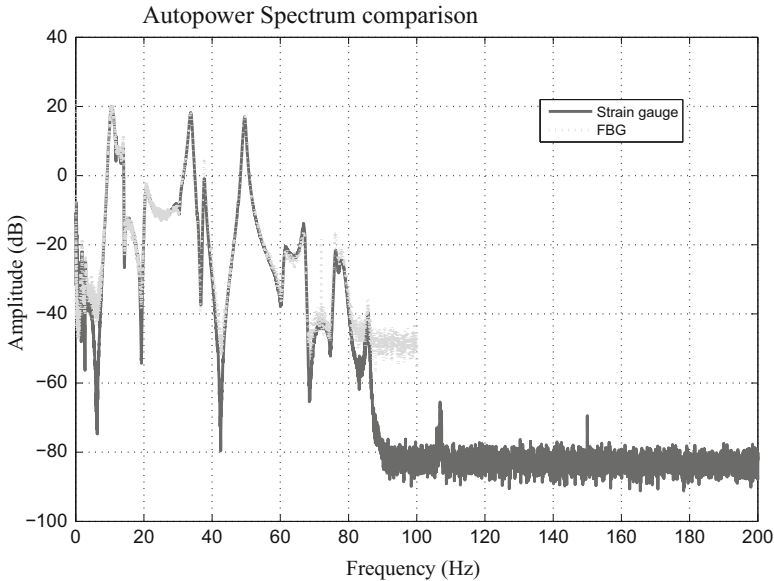
Fig. 21.4 Helicopter blade—strain gauge and accelerometer measurement directions

suspended by elastic cords to obtain an approximate free-free boundary condition. With this sort of boundary condition, strain is close to zero at the two tips of the blade and therefore, the choice was to place the sensors towards the middle of the blade, such that the measured strain would be higher. The blade was excited with an electrodynamic shaker, the force was measured using a piezoelectric force cell and the driving point is shown in Fig. 21.3.

The accelerometers were placed with the purpose of measuring on a direction perpendicular to the one measured by the strain gauge, such that they are both capturing mainly the bending modes of the structure. Figure 21.4 better depicts the

Table 21.1 Data acquisition details

Excitation signal	Burst random and sine sweep
Number of averages	20
Sampling frequency	800 Hz
Frequency range of interest	8–90 Hz
Frequency resolution	0.048 Hz
FRF estimator	H1

**Fig. 21.5** Autopower spectrum comparison between strain gauge and FBG sensor

sensor orientations. Two types of excitation signals were used for the experimental campaign—burst random and sine sweep. The data acquisition details used for the SCADAS Mobile system are shown in Table 21.1.

The frequency range of interest was limited to less than 100 Hz due to the limitations of the FBG acquisition system, which could sample at 200 Hz at the highest. Most importantly, due to the way the FBG signal is acquired, it is not possible to use an anti-aliasing filter (Buck et al. 2011), which means that care must be taken not to excite the structure past the maximum allowed bandwidth. A simple check that can be carried out to verify the quality of the measurements is to compare the autopower spectra between an FBG sensor and its collocated strain gauge. Figure 21.5 shows this comparison for the sine sweep excitation case. As it can be seen, there are no major deviations from both spectra (although there are different noise floors), which makes them suitable for the next step of processing.

The next step for the strain modal analysis using the FBG sensors is to synchronize their signals with the measured force signal. Synchronization of the input and output measurements is a crucial step in obtaining good quality of data for

the modal identification procedure. Since the resistive strain gauges, accelerometers, and force cell signals were all acquired with the same acquisition unit and are therefore synchronized, the **FBG** sensors have only to be synchronized with one of these sensors—hence, the use of the collocated strain gauges. This synchronization procedure is carried out in an offline manner, or practically speaking, after the data acquisition has already been done. The steps for the data synchronization are as follows:

- Selection of the suitable strain gauge to be used for the synchronization
- Division of the data by blocks equal to number of averages
- Synchronization (alignment) of the data, block-by-block
- Reassembly of all the blocks in one data signal
- FRF calculation
- Data import into LMS Test.Lab for modal analysis.

The strain gauge and **FBG** sensor on point 4 (from Fig. 21.3) were chosen arbitrarily for the synchronization procedure—overall, all sensor pairs were suitable to be used, but one pair had to be chosen. To properly synchronize the data, it has to be aligned from the beginning to the end. However, due to the differences in clock from both acquisition units, simply aligning the data at the beginning will lead to drifts in time at other parts. Therefore, to minimize this drift error, the data is separated by blocks and each block is aligned separately, leading to smaller drift errors. However, aligning the data by block means that some samples at the beginning or the end of the blocks must be discarded, so one must make sure that the discarded samples do not contain relevant information.

Moreover, all signals were upsampled to improve the offline synchronization efficiency. This step can also help to reduce other errors—even if both signals would have the same sampling frequency, it is still possible that the samples are taken at a different time (since they were sampled by different devices). Even if the sampling time T_s were the same for both sampling cases, they will most likely still be taken at different time instances. The maximum difference between the two sampling instances is $T_s/2$. Therefore, by reducing T_s , one can reduce this error. The resampling factor for the strain gauge was 4, and the resampling factor for the **FBG** sensor was 16, bringing both sensors' sampling frequency to 3200 Hz.

Then, the signals were divided into blocks—in total, they were divided into 20 blocks representing the 20 excitation cycles for the sine sweep. The first and last blocks were discarded, so in the end 18 blocks were used in the processing. The next step is to align each block individually. This is carried out by using the cross-correlation function. For 2 very similar signals, synchronized in time, the cross-correlation function should have its peak value exactly on the 0 lag position in the x -axis. If the signals are misaligned (which is our case), then the peak value will occur outside of the 0 lag position, but will represent how many lags (or sample differences) one of the signals should be shifted to be aligned. The result after realigning all 18 blocks and putting them back together into one signal is shown in Fig. 21.6 and a zoomed in version is shown in Fig. 21.7.

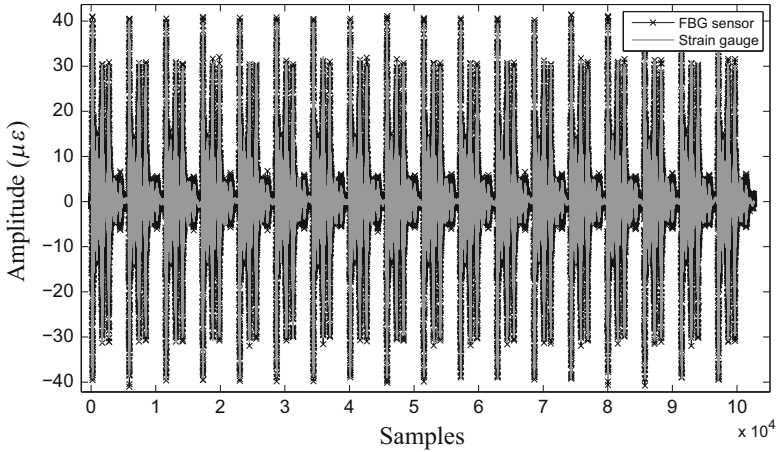


Fig. 21.6 Aligned full time signal

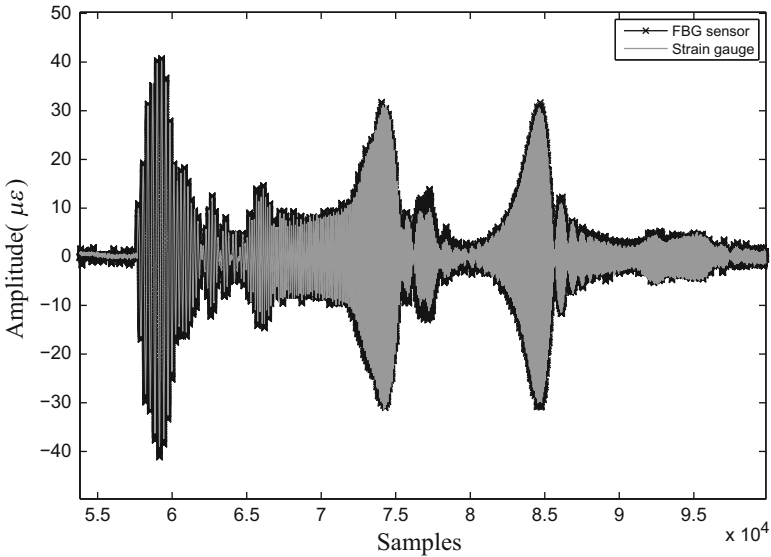


Fig. 21.7 Alignment: zoom in one of the blocks

Consequently, the Frequency response function (FRF) can be computed by using the default H1 estimator—since the FRFs were of good quality, there was no need to improve them by using a different type of estimator. To calculate the crosspower and autopower estimates to be used in the estimator calculations, a rectangular window was used and no overlap was performed. The resulting FRFs for the 4 sensor pairs and their respective coherences are shown in Figs. 21.8 and 21.9, where a comparison between the strain gauge and the FBG sensor is made. It can be seen

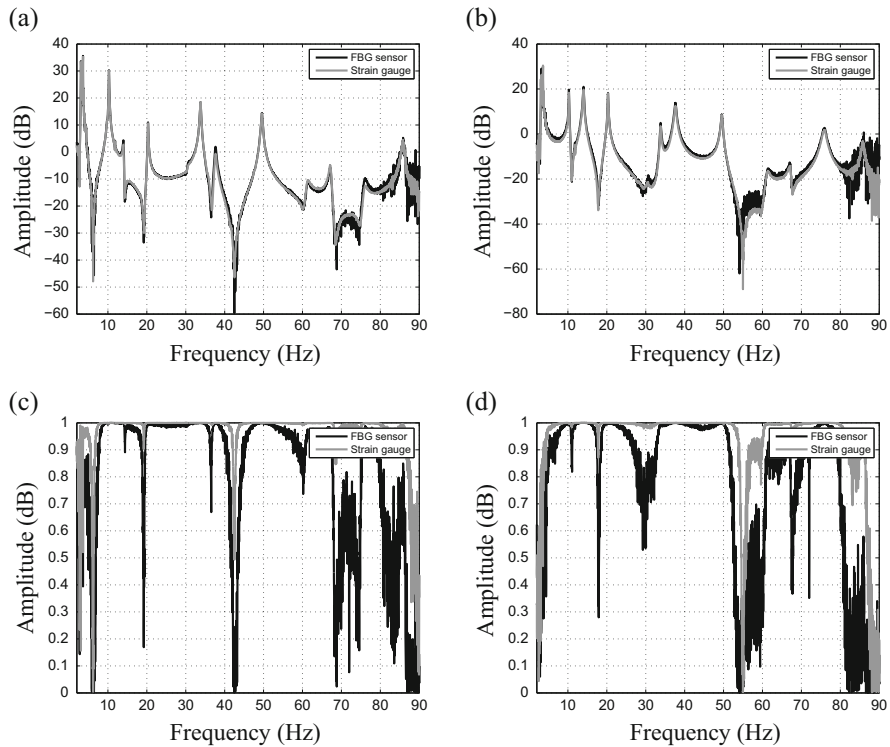


Fig. 21.8 Comparison of *SFRFs* and coherence for the first two sensor pairs. (a) *SFRF* comparison for sensor pair on point 4, (b) *SFRF* comparison for sensor pair on point 15, (c) Coherence comparison for sensor pair on point 4, (d) Coherence comparison for sensor pair on point 15

from the *FRFs* and coherence functions that the *FBG* sensors are noisier than the strain gauges. The noise levels do not depend only on the sensor type, but also on the acquisition unit. In this case, the data coming from the *FBG* acquisition unit was of lower quality, leading to worse results.

Finally, the *SFRFs* can be imported in LMS Test.Lab so that the modal analysis can be carried out. For this purpose, only the *FBG* sensor *SFRFs* are really needed, since the strain gauge measurements were only used initially for the synchronization. The procedure to identify the modes is the same as in the classic displacement modal analysis. The PolyMAX identification algorithm was used and in total 12 strain mode shapes were identified. The stabilization diagram is shown in Fig. 21.10, the natural frequencies and mode types are shown in Table 21.2 and the mode shapes are shown in Figs. 21.11, 21.12, 21.13, 21.14, 21.15, 21.16, 21.17, 21.18, 21.19, 21.20, 21.21, and 21.22, where the coloring represents the absolute values (red maximum and blue minimum strain) of strain, and the scale is relative to each mode. It can be seen from the stabilization diagram that the first bending mode could be identified at around 3 Hz, even though it was not in the initial frequency range of interest.

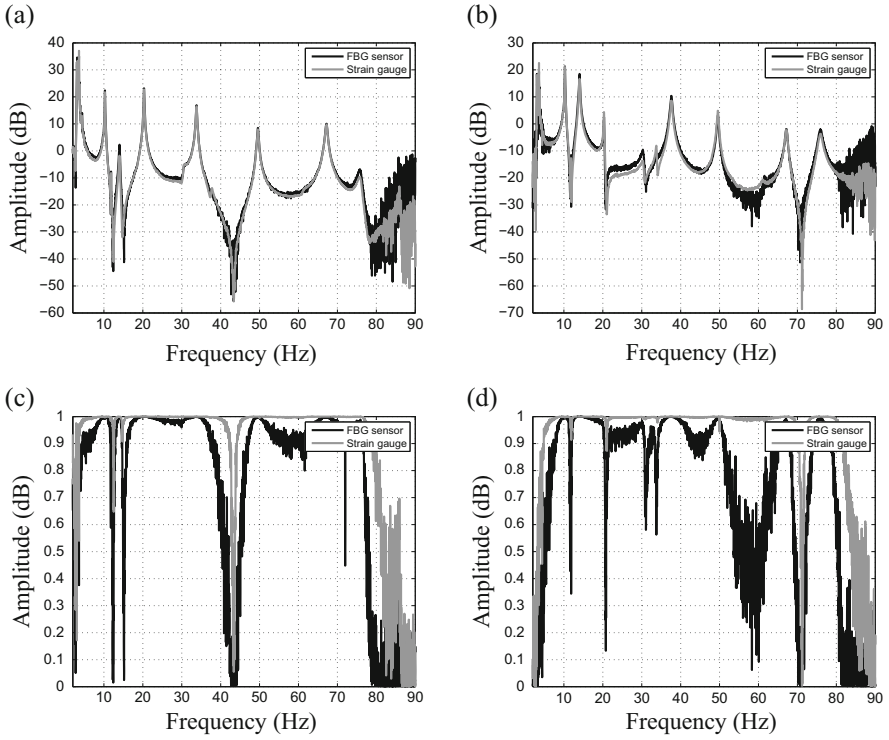


Fig. 21.9 Comparison of SFRFs and coherence for the last two sensor pairs. (a) SFRF comparison for sensor pair on point 7, (b) SFRF comparison for sensor pair on point 19, (c) Coherence comparison for sensor pair on point 7, (d) Coherence comparison for sensor pair on point 19

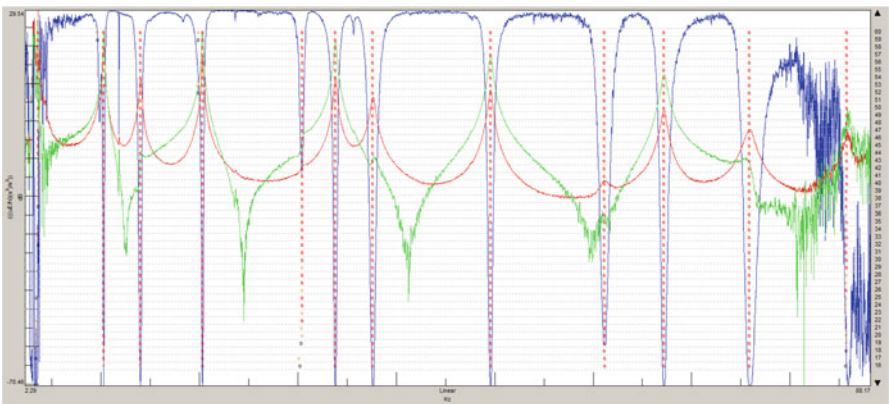


Fig. 21.10 Stabilization diagram for FBG SFRFs

Table 21.2 Identified modes from experimental modal analysis using FBG sensors

Mode number	Frequency (Hz)	Type
1	3.68	Bending
2	10.27	Bending
3	13.98	In-plane
4	20.30	Bending
5	30.44	Torsional
6	33.79	Bending
7	37.61	In-plane
8	49.55	Bending
9	61.15	Torsional
10	67.17	Bending
11	75.86	In-plane
12	85.74	Bending

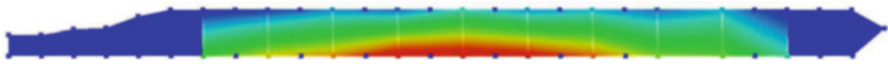


Fig. 21.11 Strain mode shape—first bending mode

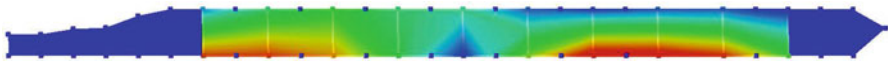


Fig. 21.12 Strain mode shape—second bending mode

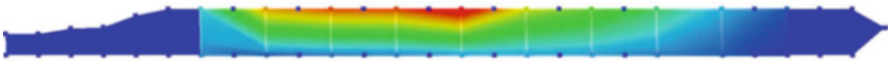


Fig. 21.13 Strain mode shape—first in-plane mode

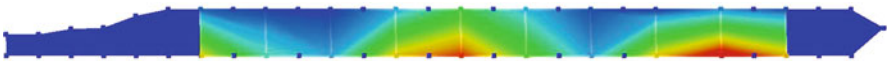


Fig. 21.14 Strain mode shape—third bending mode

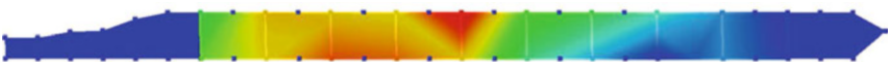


Fig. 21.15 Strain mode shape—first torsional mode



Fig. 21.16 Strain mode shape—fourth bending mode

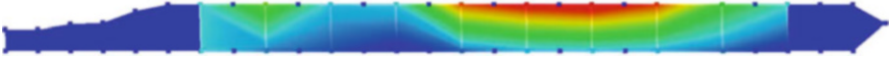


Fig. 21.17 Strain mode shape—second in-plane mode

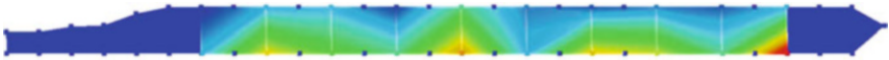


Fig. 21.18 Strain mode shape—fifth bending mode



Fig. 21.19 Strain mode shape—second torsional mode



Fig. 21.20 Strain mode shape—sixth bending mode

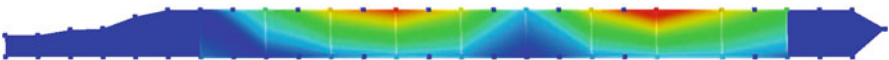


Fig. 21.21 Strain mode shape—third in-plane mode

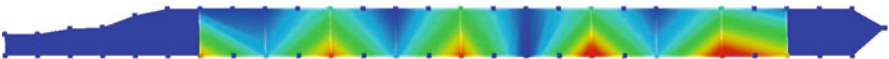


Fig. 21.22 Strain mode shape—seventh bending mode

At first, one can see that interpreting and understanding the strain mode shapes by themselves can be harder than interpreting displacement mode shapes. If the task of understanding the strain mode shapes becomes too difficult, one could combine strain sensors and accelerometers for a mixed strain/displacement modal analysis, where both strain and displacement modes can be identified and visualized concurrently.

On the other hand, the strain modes can provide information on the internal behavior of the structure, otherwise not completely present when looking at displacement mode shapes. For example, in Fig. 21.11, it is visible that there is a concentration of strain on the leading edge of the blade in bending. This is due to the D-spar that is located on the leading edge and provides most of the stiffness to the blade. A similar behavior can be seen on the higher order bending modes (Figs. 21.12, 21.14, 21.16, 21.18, 21.20, and 21.22).

The torsional modes are the hardest ones to visualize (Figs. 21.15 and 21.19)—the strain sensors were placed in a direction that cannot directly measure the shear strain generated by the torsion. However, these modes can still be measured, as normal strain is generated due to warping of the section, as can be seen on the stabilization diagram in Fig. 21.10, for the modes at approximately 30 and 61 Hz.

Finally, the strain sensors can also be used to identify the in-plane modes, shown in Figs. 21.13, 21.17, and 21.21. These modes are otherwise not easily visible when using only the accelerometers, since the motion is perpendicular to the accelerometer placement. In the case of the in-plane modes, the strain is higher on the trailing edge part of the blade. This makes sense, as the in-plane neutral line should be very close to the D-spar and leading edge of the blade, so the further away from it, the higher the strain will be.

Some additional tests were carried out using the same set-up. In this case, the objective was to verify that a strain gauge could be used as reference on a roving hammer impact test procedure, which will lead to the identification of displacement mode shapes, as pointed out in Sect. 21.3.1. For this purpose, a roving hammer impact test was carried out on the 55 test points. The direction of the impact was perpendicular to the blade (the x direction in Fig. 21.4) and the strain gauge on point 16 (from Fig. 21.3) was used as reference for the roving hammer tests. The first and second bending mode shapes, as well as the first torsional mode shapes, are shown in Figs. 21.23, 21.24, and 21.25. The resulting mode shapes were of good quality, proving that the strain gauge could be used instead of the accelerometer as reference sensor for this type of testing.



Fig. 21.23 Blade displacement mode shape first bending mode—identification using roving hammer impact test with strain gauge as reference

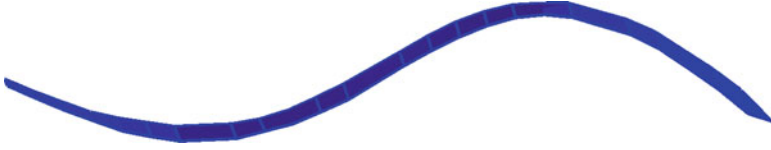


Fig. 21.24 Blade displacement mode shape second bending mode—identification using roving hammer impact test with strain gauge as reference



Fig. 21.25 Blade displacement mode shape first torsional mode—identification using roving hammer impact test with strain gauge as reference

21.6 Conclusions

This chapter presented an introduction to strain-based modal analysis. For this purpose, the strain modal model was shown, and its main characteristics were introduced—asymmetry in the Frequency response function matrix, possibility of obtaining both strain modes, and displacement modes from measurements.

Then, some experimental results on a helicopter blade were shown, where Fiber Bragg Grating sensors were used to measure the dynamic strain and then processed to identify the strain modes. The results show some characteristics that can only be captured by measuring modal strain—like the strain concentration on the blade leading edge, because of the presence of the D-spar. Moreover, a roving hammer impact test was carried out on the same blade, using a strain gauge as reference. It was shown that the displacement mode shapes can be obtained in this way.

References

- Baqersad J, Niezrecki C, Avitabile P (2015) Full-field dynamic strain prediction on a wind turbine using displacements of optical targets measured by stereophotogrammetry. *Mech Syst Signal Process* 62:284–295
- Bernal D (2002) Load vectors for damage localization. *J Eng Mech* 128(1):7–14
- Bernal D (2004) Modal scaling from known mass perturbations. *J Eng Mech* 130(9):1083–1088
- Bernasconi O, Ewins DJ (1989) Application of strain modal testing to real structures. In: *Proceedings of the 7th international modal analysis conference*, vol 2, pp 1453–1464
- Bernasconi O, Ewins DJ (1989) Modal strain/stress fields. *Int J Anal Exp Modal Anal* 4:68–76
- Braun SG, Ram YM (2001) Modal modification of vibrating systems: some problems and their solutions. *Mech Syst Signal Process* 15(1):101–119
- Buck TC, Müller MS, Perez Grassi A, Koch AW (2011) Detection of aliasing in sampled dynamic fiber Bragg grating signals recorded by spectrometers. *Measurement* 44(6):1053–1058

- Cusano A, Capoluongo P, Campopiano S, Cutolo A, Giordano M, Felli F, Paolozzi A, Caponero M (2006) Experimental modal analysis of an aircraft model wing by embedded fiber Bragg grating sensors. *IEEE Sensors J* 6(1):67–77
- dos Santos FLM, Peeters B (2016) On the use of strain sensor technologies for strain modal analysis: case studies in aeronautical applications. *Rev Sci Instrum* 87(10):102506
- dos Santos FLM, Peeters B, Gielen L, Desmet W, Góes LCS (2015) The use of fiber Bragg grating sensors for strain modal analysis. In: *Topics in modal analysis*, vol 10. Springer, Berlin, pp 93–101
- Dowling NE (1971) Fatigue failure predictions for complicated stress-strain histories. Technical Report, DTIC Document
- Ewins DJ, Inman DJ (2001) *Structural dynamics@ 2000: current status and future directions*. Research Studies Press, Baldock
- Finnveden S, Pinnington RJ (2000) A velocity method for estimating dynamic strain and stress in pipes. *J Sound Vib* 229(1), 147–182 (2000)
- Foss GC, Haugse ED (1995) Using modal test results to develop strain to displacement transformations. In: *Proceedings of the 13th international modal analysis conference*. SPIE International Society for Optical, pp 112–112
- Fu Z-F, He J (2001) *Modal analysis*. Butterworth-Heinemann, Oxford
- Geeraert A, Mauffrey Y (2015) Cror blade deformation, part 2: aeroelastic computations and comparison with experiments. In: *Proceedings of IFASD 2015*
- Heylen W, Lammens S, Sas P (2006) *Modal analysis theory and testing*. Katholieke Universteit Leuven, Department Werktuigkunde, 2006
- Hwang GS, Ma CC, Huang DW (2011) Dynamic strain measurements of a cantilever using the improved bonding fiber Bragg grating. *J Vib Control* 17(14):2199–2212
- Karczub DG, Norton MP (1999) Finite differencing methods for the measurement of dynamic bending strain. *J Sound Vib* 226(4):675–700
- Karpel M, Ricci S (1997) Experimental modal analysis of large structures by substructuring. *Mech Syst Signal Process* 11(2):245–256
- Kranjc T, Slavič J, Boltežar M (2013) The mass normalization of the displacement and strain mode shapes in a strain experimental modal analysis using the mass-change strategy. *J Sound Vib* 332(26):6968–6981
- Kranjc T, Slavič J, Boltežar M (2014) A comparison of strain and classic experimental modal analysis. *J Vib Control* 22(2):371–381
- Lae-Hyong K, Dae-Kwan K, Jae-Hung H (2007) Estimation of dynamic structural displacements using fiber Bragg grating strain sensors. *J Sound Vib* 305(3):534–542
- Lee G-M (2007) Prediction of strain responses from the measurements of displacement responses. *Mech Syst Signal Process* 21(2):1143–1152
- Li YY, Cheng L, Yam LH, Wong WO (2002) Identification of damage locations for plate-like structures using damage sensitive indices: strain modal approach. *Comput Struct* 80(25):1881–1894
- Ling HY, Lau KT, Cheng L (2004) Determination of dynamic strain profile and delamination detection of composite structures using embedded multiplexed fibre-optic sensors. *Compos Struct* 66(1):317–326
- López-Aenlle M, Brincker R, Pelayo F, Canteli AF (2012) On exact and approximated formulations for scaling-mode shapes in operational modal analysis by mass and stiffness change. *J Sound Vib* 331(3):622–637
- Luczak M, Vecchio A, Peeters B, Gielen L, Van der Auweraer H (2010) Uncertain parameter numerical model updating according to variable modal test data in application of large composite fuselage panel. *Shock Vib* 17(4–5):445–459
- Maia NMM, Silva JMM (1997) *Theoretical and experimental modal analysis*. Research Studies Press, Taunton
- Mihailov SJ (2012) Fiber Bragg grating sensors for harsh environments. *Sensors* 12(2):1898–1918

- Mulle M, Moussawi A, Lubineau G, Durand S, Falandry D, Olivier P (2015) Response of fiber Bragg gratings bonded on a glass/epoxy laminate subjected to static loadings. *Compos Struct* 130:75–84
- Ohno H, Naruse H, Kihara M, Shimada A (2001) Industrial applications of the BOTDR optical fiber strain sensor. *Opt Fiber Technol* 7(1):45–64
- Pandey AK, Biswas M (1994) Damage detection in structures using changes in flexibility. *J Sound Vib* 169(1):3–17
- Parloo E, Verboven P, Guillaume P, Van Overmeire M (2002) Sensitivity-based operational mode shape normalisation. *Mech Syst Signal Process* 16(5):757–767
- Peeters B, dos Santos FLM, Pereira A, Araujo F (2014) On the use of optical fiber Bragg grating (FBG) sensor technology for strain modal analysis. In: AIP conference proceedings, vol 1600, pp 39–49
- Pisoni AC, Santolini C, Hauf DE, Dubowsky S (1995) Displacements in a vibrating body by strain gage measurements. In: Proceedings of the 13th international conference on modal analysis
- Reich GW, Park KC (2001) A theory for strain-based structural system identification. *J Appl Mech* 68(4):521–527
- Sehlstedt N (2001) Calculating the dynamic strain tensor field using modal analysis and numerical differentiation. *J Sound Vib* 244(3):407–430
- Stephan C, Geeraert A (2015) Cror blade deformation, part 1: experimental results by strain pattern analysis. In: Proceedings of IFASD 2015
- Suzhen L, Zhishen W (2005) Structural identification using static macro-strain measurements from long-gage fiber optic sensors. *J Appl Mech* 8:943–948
- Tourjansky N, Szechenyi E (1992) The measurement of blade deflections—a new implementation of the strain pattern analysis, ONERA Technical Paper, 1
- Trutzel MN, Wauer K, Betz D, Staudigel L, Krumpholz O, Muehlmann H-C, Muellert T, Gleine W (2000) Smart sensing of aviation structures with fiber optic Bragg grating sensors. In: SPIE's 7th annual international symposium on smart structures and materials. International Society for Optics and Photonics, pp 134–143
- Vandepitte D, Sas P (1990) Case study of fracture of a mechanical component due to resonance fatigue. *Mech Syst Signal Process* 4(2):131–143
- Vári LM, Heyns PS (1994) Using strain modal testing. In: Proceedings of the 12th international conference on modal analysis, vol 2251, p 1264
- Wentzel H (2013) Fatigue test load identification using weighted modal filtering based on stress. *Mech Syst Signal Process* 40:618–627
- Yam LH, Li DB, Leung TP, Xue KZ (1994) Experimental study on modal strain analysis of rectangular thin plates with small holes. In: Proceedings of the 12th international modal analysis conference, Honolulu, Hawaii, pp 1415–1421
- Yam LY, Leung TP, Li DB, Xue KZ (1996) Theoretical and experimental study of modal strain analysis. *J Sound Vib* 191(2):251–260
- Zhang Y, Yang W (2013) Bayesian strain modal analysis under ambient vibration and damage identification using distributed fiber Bragg grating sensors. *Sens Actuators A* 201:434–449
- Zhang S, Yang J, Li Y, Li J (2013) Identification of bearing load by three section strain gauge method: Theoretical and experimental research. *Measurement* 46(10):3968–3975
- Zhang J, Xia Q, Cheng YY, Wu Z (2015) Strain flexibility identification of bridges from long-gage strain measurements. *Mech Syst Signal Process* 62:272–283

Chapter 22

Uncertainty Quantification of the Main Rotor Blades Measurements

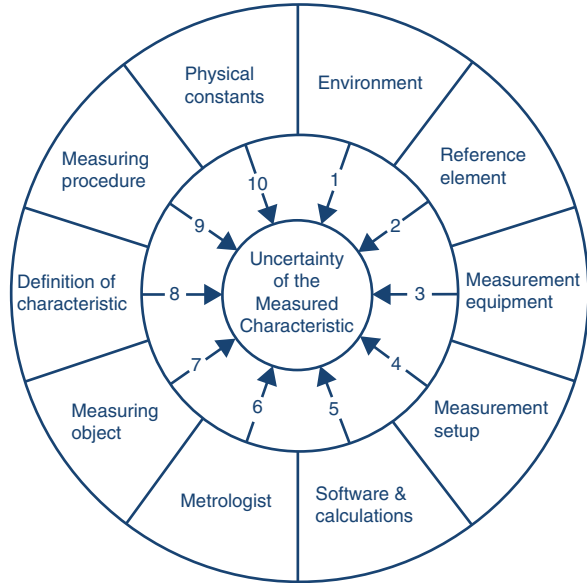
Marcin M. Luczak

22.1 Introduction

Problems presented in this chapter are the results of a research activity oriented for testing of the composite material structures (Luczak and Vecchio 2007). Competitive market forces manufacturers of the composite structures to reduce the test time and depend on much less time and cost consuming numerical simulations. However, computational models have to be validated against the experimental models to prove their reliability. Experimental Modal Analysis (EMA) technique is the established tool for the identification of dynamic properties of structures (Uhl 1997; Heylen et al. 1998; Ewins 2000). Modal models can be applied in many ways, and one of them is Finite Element Method (FEM) model updating procedure (Imregun et al. 1995; Kwon and Lin 2004; Sinha and Friswell 2003; Papadimitriou et al. 2001; Mottershead et al. 2000). The test data is used against the numerical simulation results to correct the parameters of the FE model as such it yields the results close to those from measurement. Second area of application of EMA could be Structural Health Monitoring (SHM) based on the observation of a value of modal parameter (Noh and Kwak 2006; Nahvi and Jabbari 2005; Garescì et al. 2006; Macdonald and Daniell 2005). For these two applications a reliable modal test data is of vital importance. However, test data is a subject of variability. Many factors such as production process, wear, material imperfections, environmental conditions, on one hand, and experimental setup, on the other, lead to scatter of a measurement data of nominally identical structures. Test data variabilities are subject of extensive studies in many research centers (Deraemaeker et al. 2008; Sakellariou and Fassois 2008; Gao 2007; Chen et al. 2006; Capiez-Lernout et al. 2006). Variabilities of the test

M.M. Luczak (✉)
Institute of Fluid Flow Machinery Polish Academy of Sciences, Fiszerza 14 St,
80-231 Gdańsk, Poland
e-mail: marcin.luczak@imp.gda.pl

Fig. 22.1 Sources of measurement uncertainty (McShane 2010)



data come from number of sources (Fig. 22.1). Internal source is non-repetitive production process causing that two nominally identical units have geometric and material properties within production tolerances. Example of the external source of test data variability is an environmental parameter change (Siegert et al. 2008; Xia et al. 2006; Ni et al. 2005; Sohn et al. 1999). External source of test data variability could be also test setup (Griffith and Carne 2007; Carrie and Dohrmann 1997). Within test setups there are three main components of the variability of measurement of the same specimen, i.e., boundary conditions, excitation method, and measurement technique. Within presented research the number of experimental modal models was estimated basing on the variable test data. Change of the excitation technique and the measurement technique introduced some scatter of modal parameters. These differences are presented and assessed.

22.2 Objectives

The main scientific objective of presented research outcomes is to formulate the general methodology that will identify the variability of the structural dynamic parameters measurements of the structures made of composite materials. The experimental data sets were collected during extensive dynamic testing campaigns of the investigated helicopter rotor blades.

Second scientific objective is to develop a global criteria of the measurement uncertainty for experimentally identified modal models. Proposed method examines

the important problem of quantifying uncertainties in experimentally obtained results by means of statistical methods. The dynamic testing was done on the three nominally identical composite material blades from a main rotor of the helicopter. This allows assessment of the product-to-product test data variability. For the purpose of the assessment of the test-to-test data variability of the same particular structure extensive dynamic test campaign was performed. In the experimental part, different test configurations were taken into account:

- Single-point as well as multi-point excitation,
- Different excitation signals (impulse, random, and harmonic),
- Responses obtained with different types of sensors (contact and non-contact).

The variability of the identified values resulting from these different experimental configurations was studied.

The test results from the abovementioned will be used to derive knowledge about the scatter of the values of mechanical properties of investigated structure (natural frequencies, modal damping),

Such a combination demands to take advantage of knowledge from several fields: free vibrations, composite materials, measurement methods (especially experimental modal analysis and dynamic testing), variability in measurement data, signal processing, and statistics. As a result of this research set of variable test data was assessed.

Application of the developed method in Computer Aided Engineering tools will increase the accuracy and reliability of the computer simulation results. In the design process this will allow to replace the high-cost and time-consuming real tests by its virtual representation by a computer model. Due to that it will become possible to shorten the design process duration without compromising the quality and reliability of the designed final product.

22.3 Research Methodology

The work plan of the experimental stage of the investigations encompasses structural dynamics measurements results of the structures made of composite material.

The extensive experimental data collection under investigation which was analyzed incorporates the multiple experiments done on the same object with different setups. The excitation of the structure was done by means of the electrodynamic shakers and the structure response was measured by means of contact and non-contact methods (Fig. 22.2). Excitation signal used was either random or harmonic. For several experiments one shaker was used and for the others the two shakes were applied. This allows to develop the assessment analysis of test-to-test measurement data variability accounting for the uncertainty introduced by the measurement instrumentation used on the same object. Second type of variability under investigation is product-to-product. The same setup applied for the nominally identical objects bring scatter of the results in their dynamic properties (natural frequency

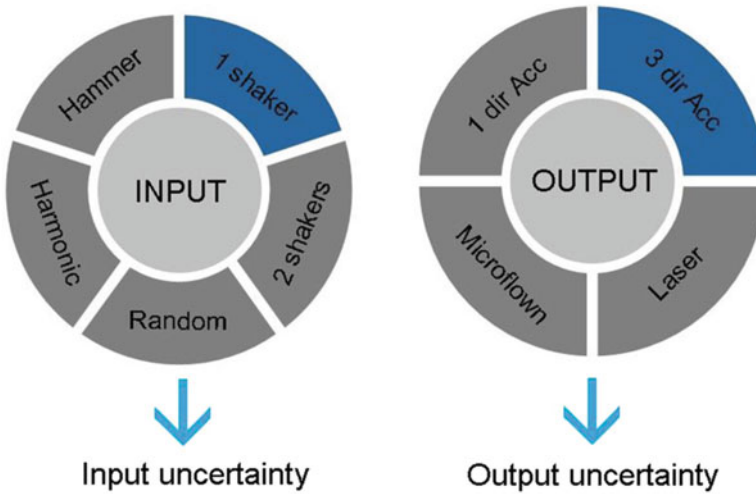


Fig. 22.2 Excitation and measurement techniques as the sources of uncertainty



Fig. 22.3 Comparison of data sets for different tests, products, and objects

values, modal damping). Three identical composite material helicopter blades were measured bringing the data collection with the scatter of the observed parameters (Fig. 22.3).

Building on the test-to-test and product-to-product analysis finally it was made possible to evaluate the object-to-object test data variability. This allows to assess the influence of the presence of subcomponents and the joints between them onto the overall test data variability. The observation made on the experimental results made possible to identify the influence of the input and output as a sources of the test variability (Fig. 22.4).

The starting point of an experimental structural dynamics assessment is modal analysis testing. The corresponding modal model results are considered to be a deterministic system description, which can be used for multiple applications, ranging from a mere verification of the fulfillment of the design criteria, to the validation and updating of Computer Aided Engineering models and the integration

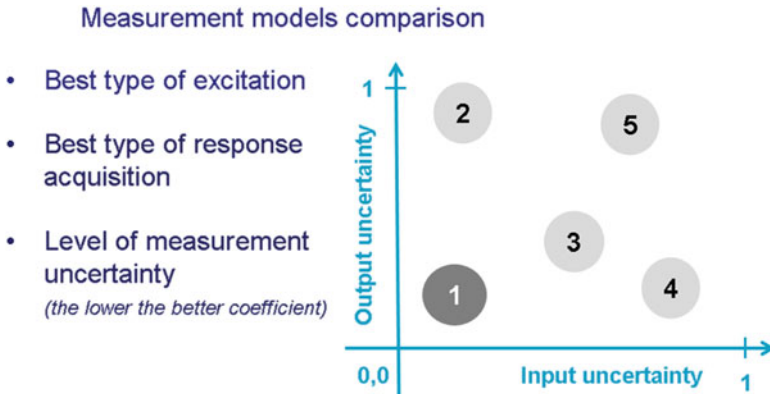


Fig. 22.4 Assessment of measurement techniques

in hybrid system models. In reality, the modal results are just an estimation of the model parameters based on a series of input-output or output-only tests and hence subject to all related testing and modeling errors. These data errors can be just stochastic disturbances on the input/output data, but can also be caused by invalid model assumptions or data processing effects. Some of the main sources of errors are: sensor location and orientation errors, test setup loading and constraining effects, sensor loading effects on the test structure, sensor calibration and data conversion errors, disturbance and distortion in the test data measurement chain, signal processing errors, and model estimation errors.

Just repeating a test and looking into test statistics will not allow the majority of these sources of uncertainty to be identified. Good practice is hence to repeat tests in slightly different test configurations, by adopting different excitation or sensing configurations and evaluate resulting model differences to assess the robustness of the test procedure and confidence in the test results. In the present study, two kinds of such test variation are executed. The first is by analyzing the variation of global system parameters (resonance frequencies, damping values) as a function of changes in the instrumentation (type of response sensors, contact vs. non-contact, number and orientation of shakers, and excitation signal). The second is by analyzing the variation of global system parameters when splitting up the measurement in several sections (“patches”). The variations between particular patches (Fig. 22.5) cause the inconsistencies of the global analysis on the complete data set (Cauberghe et al. 2002; Van der Auweraer et al. 2000).

From a rigorous statistical point of view such analysis may not yet provide the means to derive stochastic bounds on results. The related spread in the data and the models influences the adequate identification of the representative in the daily measurement practice (Fig. 22.6).

In order to characterize the variability of the results, one can obviously look into the distribution of the modal parameters as a function of test condition. This requires the adoption of very reliable and robust modal parameter estimation methods that

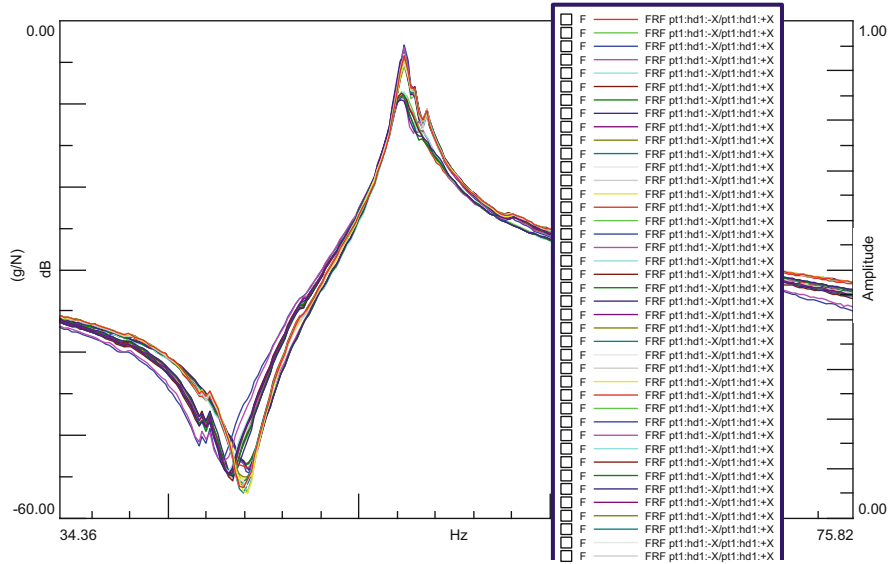


Fig. 22.5 Frequency response function plot for the impedance head 1 for measurements in several sections

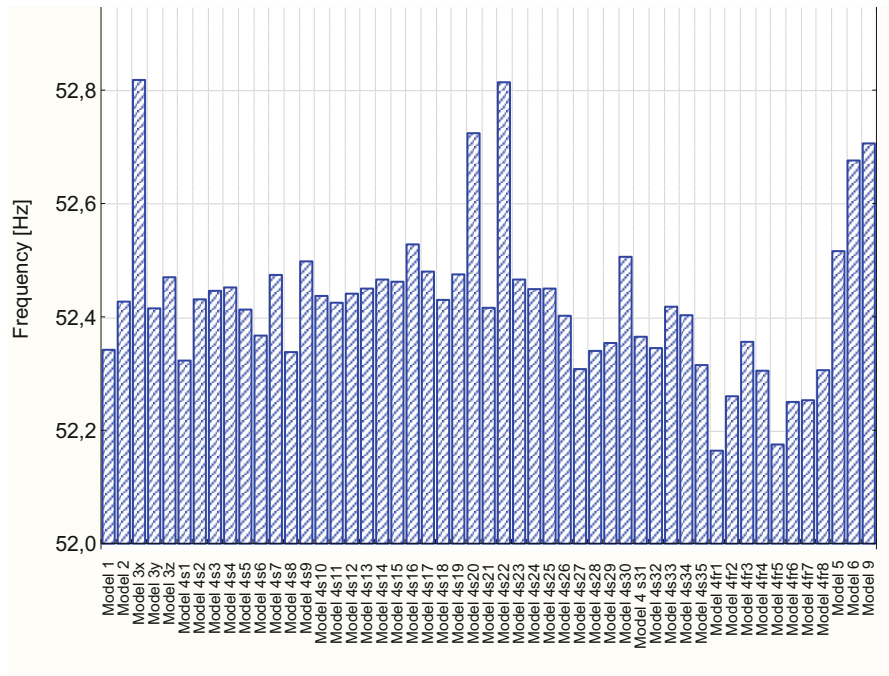


Fig. 22.6 Natural frequencies plot for measurements in several patches

allows to easily identify modal parameters from complex multi-mode data sets. An example is the discrete frequency domain rational polynomial model technique, referred to as PolyMAX (Peeters et al. 2004). Its fast and robust identification process allows the application to analyzing large and multiple data sets, making variability and statistical analysis possible.

The search for unique qualifiers for the variability of a multi-test data set has led to the definition of a new parameter named Variability Level which characterizes a particular structure in view of its variability. It is calculated as the mean value of a standard deviation Type A of the frequency and damping. Mean values of the standard deviations of the frequency is Variability Level.

Presented measure of the variability is also applicable to different cases than investigated in this research. In case of measuring the modal parameters of the nominally identical structures it can be used to assess the non-repeatability of the manufacture process. This is especially valid for the composite material structures which suffer from scatter of the design parameters resulting from the limitations of the manufacturing technology. It also allows assessing the influence of the environmental factors like temperature or humidity on the obtained results of measurement of the same structure in different weather conditions.

The final use of many experimental models is to validate and update numerical models, precisely because the latter are subject to many sources of modeling uncertainty. However, when the experimental models themselves are subject to uncertainty, this introduces another level of uncertainty.

Research tools used in the investigation are in quite extent available and some require purchasing. The research activity used the supercomputing resources from CI TASK where MSC Nastran and Matlab software is installed with multiprocessor licenses. In IMP PAN the LMS Test.Lab and LMS Virtual.Lab software is installed. The Optimus and Statistical packages were applied as well.

22.4 State of the Art

This chapter presents a novel approach in the field of experimental investigation of mechanical properties of structures made of composite material. It takes into account test data variability observed in the structural dynamic properties measurement. The main goal of the conducted research is to investigate the variability of dynamic properties of load carrying structures made of fiber reinforced composites. Non-destructive experimental methods are used hereto. Different test configurations were taken into account. The excitation was performed by means of impact, random and harmonic, single and multi-point stimuli while the response measurement was done through contact and non-contact acceleration and velocity. The test results were applied for the structural identification of the object. The sources of the test data variability were related to the excitation and measurement technique applied for

the investigated object. A number of variable test modal models were statistically assessed to investigate variability source onto modal model parameters and model accuracy.

Aerospace is fast growing sectors of the economy and challenges many technical innovations. It faces many challenges driven by the increasing number of people traveling by airplanes and the demand of reducing the cost of production and operation of the aircrafts (Agarwal 2012). The aerospace industry is paying a lot of attention to growing public concern about the impact the air transport has on environment issues such as air pollution, noise, and climate change. The volume of man-made CO₂ and other Green House Gases emissions related to air traffic is expected to increase with the steady growth of aviation. This poses several challenges regarding weight reduction and cost of production in aerospace industry. Weight reduction of the aircraft can be achieved by application of the composite materials (Degenhardt et al. 2014; Marsh 2010; Vankan and de Wit 2010).

Recently a significant advantage in the field of application of fiber reinforced composite materials can be observed (Maillot et al. 2011). Fiber reinforced composites are strong, durable, and damage tolerant and offer high strength to weight ratio. They have become an increasingly attractive alternative to metal materials and can be easily adapted to innovative manufacturing techniques in aerospace (Fig. 22.7), automotive, and domestic industry (Hollaway and Teng 2008).

Because they are combination of strong and light-weighted carbon or poly-aromatic-amide fiber with high performance polymer matrixes it is possible to change their parameters like material of fiber, material of matrix, number of layers, and orientation of fibers in individual layers (Meyer and Gaudin 2010). These fea-

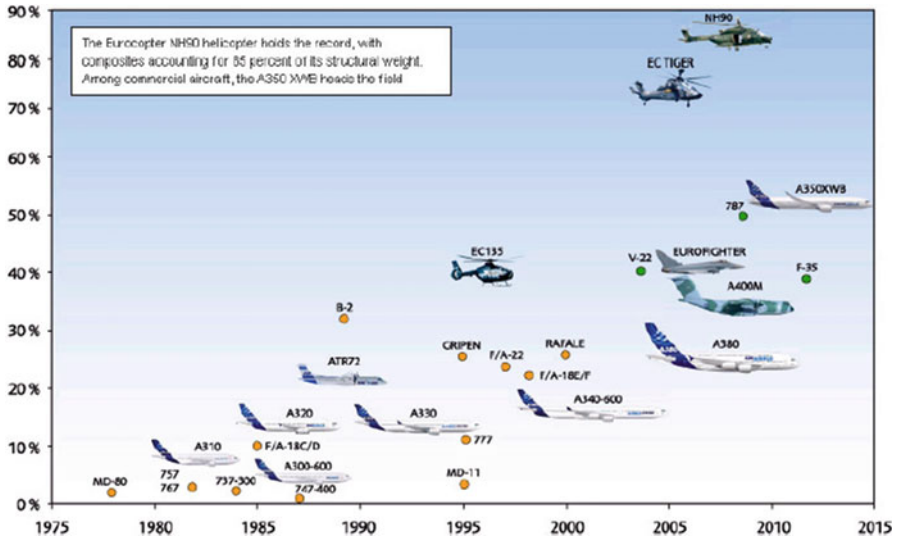


Fig. 22.7 Evolution of the use of CFRP in aircrafts (Maillot et al. 2011)

tures allow to design a composite to get the particular stiffness characteristics, value of elastic modulus according to the individual requirement. Due to it composite mechanical properties are anisotropic.

Except advantages composite materials have some disadvantages. One of them is not quite repetitive production process. The result of this imperfection can be a not homogenous distribution of mechanical properties. Heterogeneities cause that composites are considered to be of statistical nature.

Many scientists lead their research in the field of composite materials but rapid progress in composite technology causes an introduction of many new designs whose mechanical characteristics given by a manufacturer are often incomplete. New generations of composite materials require novel techniques of testing and simulating. Presented research is an interdisciplinary contribution into knowledge of experimental methods better describing complex nature of load carrying structures made of composite materials.

Metal blades are cheap and easy to manufacture. Despite these benefits they suffer from design and structural problems as poor fatigue resistance and low strength to density ratio. Composite material helicopter blades offer high stiffness to weight ratio, desirable properties, and better fatigue characteristics compared to metal blades. In the deterministic analysis of structures made of composite material the nominal material properties are used. The effective material properties of composites are uncertain in nature due to the variations of the fiber and matrix material properties, ply orientation, and variation in ply thickness. Manufacturing process is yet another source of voids, incomplete curing of resin, and excess resin between plies (Sarangapani and Ganguli 2013; Gayathri et al. 2010; Murugan et al. 2012; Sriramula and Chryssanthopoulos 2009). Elastic moduli of a lamina can vary by 5–15% according to Onkar et al. (2007). Variability of the material properties is very important for the reliable analysis and design of aircraft components made of composite materials. Structural characteristics of composite rotor blades depends on the variations associated with the material and structural properties of composite rotor blade and can be identified by testing of numerous nominally identical items. The identified variabilities can be assessed and considered in the experimental global modal model of the structure. Blades are getting larger and more flexible and are typically built-up, composite structures and made of materials that are anisotropic and non-homogeneous. There have been many investigations in the helicopter sector (Hodges 1990; Kunz 1994; Johnson 2012).

Industrial certification testing for new blade designs is a straightforward (if time consuming) task for commercial test centers; however, the demand for more complex (for example, combined) load investigations and better understanding of the blade response under different load conditions is growing, and this results in a need for more advanced test centers providing greater interest in sensors for structure tests. Improving the understanding of blade response (and hence influencing the future, optimized designs) requires a combination of modeling and testing of materials and structures across a huge scale. Material response under

different load regimes must be investigated to identify the key properties controlling various possibilities in polymer composites. A multidisciplinary approach where experimental modal models can be correlated with numerical models of the blades is necessary to predict dynamic behavior of the blade.

22.5 Experimental Techniques

Modal testing utilizes wide variety of experimental techniques (Heylen et al. 1998; Ewins 2000). They cover object excitation and response measurement devices. Main methods to excite structure comprise impact, random, and periodic:

- Impact hammer with force transducer (Tirelli and Vaddillo 2013),
- Electrodynamic shaker (Reynolds and Pavic 2000),
- Electromagnets (Firrone and Berruti 2012a),
- Piezo-actuators (Castanier and Pierre 2006),
- Acoustic speaker excitation (Amraoui and Lieven 2003; Ozdoganlar et al. 2005; Firrone and Berruti 2012b),
- Pressurized air excitation (Vanlanduit et al. 2007).

Different physical principles in sensor operation encompass (Morris and Langari 2011):

- Capacitive sensors
- Resistive sensors
- Magnetic sensors
- Piezoelectric transducers
- Strain gauges
- Piezoresistive sensors
- Optical sensors (air path)
- Three-dimensional (3D) digital image correlation (DIC) and 3D point-tracking (3DPT) (Wang et al. 2012; Warren et al. 2011).

The range of available sensors for measuring various physical quantities in modal vibration response measurements for characterization of structures includes (Fraden 2010):

- Force (Bi et al. 2013)
- Displacement (Carrella and Ewins 2011)
- Velocity (Sracic et al. 2012)
- Acceleration (Yin et al. 2011)
- Strain (Rovšček et al. 2013)
- Microflow (Pierro et al. 2009; Raangs et al. 2003).

In practice piezoelectric force, acceleration sensors, and Laser Doppler Vibrometer (Allen and Sracic 2010) are in common use for modal testing. Each of the measurement technique has its limitations and drawbacks. One of them is a mass

loading effect of the transducers attached to the test item (Warren et al. 2011; Bi et al. 2013; Cakar and Sanliturk 2005). Laser Doppler Vibrometer has systematic errors (Allen and Sracic 2010) which only recently begun to be appreciated (Yang and Allen 2011).

22.6 Uncertainty and Variability

Many authors use term of uncertainty not distinguishing their categories. It introduces the lack of international consensus on the definitions of uncertainties in measurement. Oberkampf (Oberkampf et al. 1999; Oberkampf et al. 2002) proposed terminology distinguishing between aleatory and epistemic uncertainty.

Term aleatory uncertainty is used to describe the inherent variation associated with the physical system or the environment under consideration. It covers unknowns which are different for each realization of the same experiment as described by Moens and Vandepitte (2005). The exact value of quantity is within the range of the distributed possible values which vary from experiment to experiment. Example of aleatory uncertainty is related to manufacturing tolerances. In theory fabrication process produces identical structures but in the industrial floor reality not all design parameters and material properties are precisely repeated. Another example of the aleatory uncertainty is related to environmental effects like temperature. Aleatory uncertainty is referred in literature as statistical uncertainty, irreducible uncertainty, inherent uncertainty, variability, and stochastic uncertainty.

Term epistemic uncertainty is used to describe a potential inaccuracy in any phase of the process that is due to the lack of knowledge. The inaccuracy may or may not occur which is stressed by word potential. Despite the lack of knowledge there may be no inaccuracy. Epistemic uncertainty is mainly due to the incomplete information caused by vagueness (imprecisely defined information), non-specific data (variety of alternatives), or dissonance (conflicting evidence). Epistemic uncertainty is referred in literature as reducible uncertainty, systematic uncertainty, subjective uncertainty, and cognitive uncertainty.

The usefulness of structural dynamics test and analysis results for solving noise and vibration problems or for performing a design assessment or a design optimization depends largely on the confidence that one can have in these results. In other words, the results must be characteristic for the actual problem (and not be the result of testing artifacts) and the models must be representative for the actual behavior of the investigated structure(s). This problem of modeling uncertainty has consequently been the subject of major research efforts.

Essentially, two types of problems are distinguished: (1) the test and modeling data are subject to experimentation and analysis errors and (2) the tested (or modeled) structure is not representative for the actual structure.

The first problem concern experimentation and analysis uncertainty (Mehrez et al. 2012; Piovan et al. 2013; Coleman and Steele 2009; Donders 2008; Van der Auweraer et al. 2005). The “true” test result can in principle never be achieved.

The level of the uncertainty associated with the test result is, however, not easy to quantify. A multitude of totally different causes may be at the origin of major bias and/or variance errors in the analysis (Luczak et al. 2010; Adhikari et al. 2009; Michaelides and Fassois 2008). Adequate testing and analysis procedures may reduce (at least some of) these errors, but proper overall uncertainty quantification is hard to issue. Also in building numerical simulation models (e.g., based on the Finite Element approach), uncertainty is introduced by discretization effects, through imperfectly known material, geometry, or loading parameters, or through uncertainty in the applicable model formulations. Various approaches based on stochastic or possibilistic methodologies have been developed to address this (Mehrez et al. 2012; Verhaeghe et al. 2013; Möller and Reuter 2008; Schueller 2007; Soize 2005).

The second problem is this of product variability (Szkudlarek et al. 2009), introducing changes in the structural dynamics characteristics because of differences in material, geometric, manufacturing, or even operational use (loading, temperature, etc.) parameters when compared to the “nominal” case. It is important to have at least an idea on the magnitude of these changes and their impact on the final product behavior when assessing and optimizing the design based on an “ideal” product model. While statistical product testing may reveal such performance spread, this is in general very hard to realize.

A third (and often neglected) potential problem with the significance of the analysis results can originate from a violation of the assumptions used to model the structure. One of the most prominent examples is the effect of nonlinear structural behavior on a linear (e.g., modal) model identification process.

The review of relevant scientific literature in the field points out that in most practical engineering application there is a serious lack of experimental data that would enable a correct quantification and characterization of stochastic system properties (Chen et al. 2006; Michaelides and Fassois 2013; Mao and Todd 2013; Adhikari and Phani 2010; Pintelon et al. 2007; Arici and Mosalam 2005; Collins et al. 1974). Despite of the reported achievement, the research aiming at structural uncertainty identification is vaguely reported. Experimental analysis of the sources of uncertainty may be found in Govers et al. (2006).

The current research work introduces a novel approach in the field of experimental and numerical investigation of mechanical properties of composite structures. It takes into account test data variability resulting from structural dynamic properties measurement and uses them to quantify influence on the in model parameters updating (Fang et al. 2012; Govers and Link 2010).

22.7 Structural Dynamics

This section presents the experimental investigations done on the structures made of composite material encompassing experimental campaign and assessment of the measurement uncertainty.

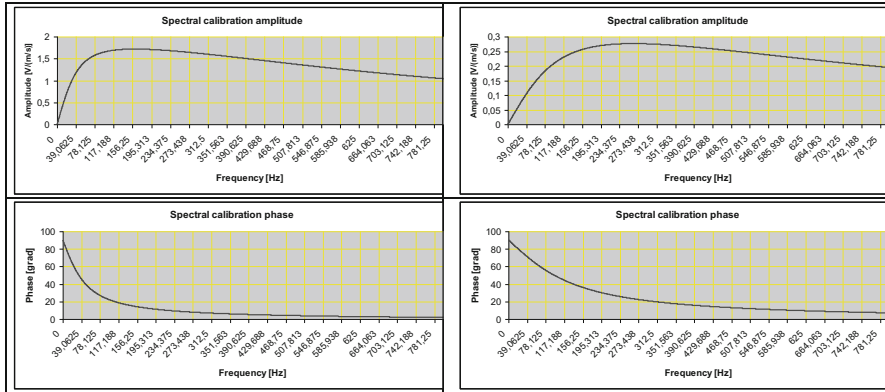


Fig. 22.8 Calibration curve for PTU (left) and USP (right) probes

Applied measurements represent both novel and well-established techniques. In structural dynamics test campaigns the following measurement and analysis tools were used.

Unlike the laser vibrometer and piezoceramic accelerometers for the microflow probes there is no single value of the sensitivity. Sensitivity of the microflow is frequency dependent function therefore it is a set of calibration values for each spectral line. During the measurement the value of the signal is set to 1 and calibration is done by means of data postprocessing. The calibration curve is being calculated for the spectral resolution defined for the measurement. Signal data is then divided by a calibration data to obtain the calibrated signal data. Microflow probes calibration curves are presented in Fig. 22.8.

22.8 Object of the Investigation: 3 GFRP Helicopter Blades

Three blades from main rotor of the helicopter are the object of this investigation. Three of them are from main rotor from helicopter PZL Swidnik W-3. They are approximately 7300 mm long, and weight approximately 75 kg. Figure 22.9 presents helicopter PZL W-3 Sokol (Polish for “Falcon”) which is a Polish medium-size, twin-engine, multipurpose helicopter manufactured by PZL-Swidnik.

There are two primary goals for modal testing of the helicopter blades:

1. To derive a natural frequencies and corresponding damping factors obtained with different test realizations. Experimental data collection allow to estimate the standard uncertainty Type A related to the each particular natural frequency and damping derived from individual tests done both on the same blade and different blades,



Fig. 22.9 PZL W-3. Photo Copyright © PZL Świdnik

2. To measure the blade with different experimental techniques of both the excitation method of the structure and response signal collection which allow to assess the influence of particular method on the uncertainty Type A value.

Achieving aimed goals requires particular design of the test setups and test campaigns capable of providing data which contains the statistically sufficient number of observations. The number of measurement points and frequency resolution is defined with purpose to avoid aliasing.

22.9 Test Rig and Equipment

In this test campaign the following measurement and analysis tools were used (Table 22.1):

1. One or two bungee cords to provide free-free boundary conditions for big blades
2. One metal frame to provide fixed-free end boundary condition for small blade
3. One or two electromagnetic shakers with amplifiers
4. Modal hammer
5. 25 uniaxial modal piezoelectric accelerometers (PCB)
6. One or two impedance heads incorporating acceleration and force sensor in the same housing to measure driving point FRFs
7. Frontend LMS SCADA III with 64 channels
8. Frontend LMS SCADA Mobile with 16 channels
9. Computer with a Test.Lab acquisition and analysis suite.

Main rotor blades were setup in different configurations. First setup concerns one shaker and blade supported with two bungee cords. Second setup concerns two shakers and blade supported with two bungee cords. Blades have different stiffness in the flapwise and edgewise direction. The deflection under blades own weight in flapwise direction is larger than in the edgewise. Therefore the blades were

Table 22.1 Hardware and software for experimental techniques

Electromagnetic shakers with amplifiers	
Shaker 1: Ling Electronics Model LS-100 Amplifier 1: Yamaha Power Amplifier P2500S Shaker 2: Brüel and Kjær Type 4808 Amplifier 2: Brüel and Kjær Type 2719	
Impedance head incorporating acceleration and force sensor in the same housing to measure driving point FRFs	
ICP [®] impedance head, force/accel, Model PCB 288D01	
Triaxial modal piezoelectric accelerometers	
Triaxial, high sensitivity, ceramic shear ICP [®] accel, 100 mV/g, Model PCB 356A15	
Uniaxial modal piezoelectric accelerometers	
Modal array, ceramic shear ICP [®] accel, 100 mV/g, Model PCB 333B32 Modal array, ceramic shear ICP [®] accel, 100 mV/g, Model PCB 333B30	
Scanning Laser Vibrometer	
OFV-055, Scanning Vibrometer OFV 303.8 Laser Scanning Head OFV3001SF Vibrometer Controller OFV042 Vibrometer Interface	
Microflow probes	
PU-mini NT0712-44 2 channel signal conditioner E0712-44 USP-mini UT0608-01 4 channel signal conditioner E0707-22	
ICP piezoelectric strain sensor	
ICP [®] piezoelectric strain sensor, titanium housing Model: 740B02	
Frontend LMS SCADAS III with 64 channels	
Type SC316, SN: 41021204 QDAC—1 module PQFA—4 modules PQA—11 modules BPROC—1 module	
Desktop PC and software	
LMS Cada-X and LMS Test.Lab acquisition and analysis suite	

Fig. 22.10 Test setup of blade from main rotor from helicopter PZL Swidnik W-3

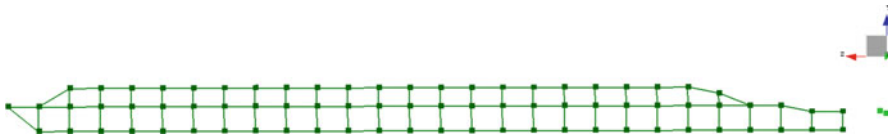
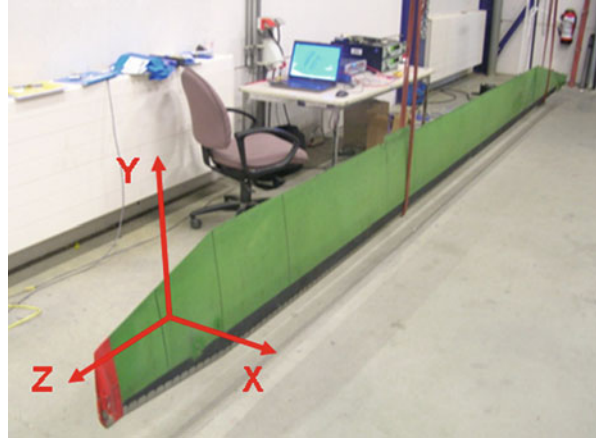


Fig. 22.11 Cartesian coordinate system for piezoelectric, microflow, and laser sensors

supported with the leading edge pointing towards ground as presented in Fig. 22.10. Electrodynamic shakers were also supported on the elastic cords to minimize the effect of constraining the degree of freedom of structure. Excitation points were located at the root of the blade.

22.10 Geometry Definition

A dense grid of measurement points was defined all over the blade surface, in order to precisely identify the dynamic properties of this large dimensions structure. Measurement points were set with a distance of 0.25 [m] one from another in the spanwise (Z) direction and 0.1 [m] in the edgewise direction (Y). Geometry definition for blade is presented in Fig. 22.11.

It consists of 77 acquisition locations and two driving points where force was injected to the system. There was no need to reduce the number of points for microflow probes measurements.

Curvature of the surface of the airfoil shaped blade regarding length and width is negligible therefore no Euler angles were defined. Similarly to the large fuselage panel measurement to minimize the mass loading effect of the attached sensors and cables the total number of measurement points was subdivided into sets (Fig. 22.12).

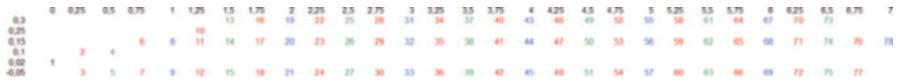


Fig. 22.12 Concept of the measurement points sets for the blade

Table 22.2 Experimental models collection summary for main rotor helicopter blades A, B, and C

Modes	15	15	15	15	15	15
Model	A1	A2	A3	A4	A6	A9
Runs/sets	$2 \times 5 \times 8 = 80$	$2 \times 5 \times 8 = 80$	$2 \times 5 \times 8 = 80$	$2 \times 7 = 14$	$1 \times 8 = 8$	$1 \times 8 = 8$
Model	B1	B2	B3			
Runs/sets	$1 \times 2 \times 8 = 16$	$1 \times 2 \times 8 = 16$	$1 \times 2 \times 8 = 16$			
Model	C1	C2	C3			
Runs/sets	$1 \times 2 \times 8 = 16$	$1 \times 2 \times 8 = 16$	$1 \times 2 \times 8 = 16$			

22.11 Test Setups

There were 15 modes identified for the helicopter main rotor blades (denoted H1–H15). Each model (A1–C3) consists of 7–8 measurement sets. The following experimental models were estimated:

- A1, B1, C1—Burst random excitation, 1 shaker, 2 dir. of measurement (ACC),
- A2, B2, C2—Burst random excitation, 2 shakers, 2 dir. of measurement (ACC),
- A3, B3, C3—Periodic chirp excitation, 1 shaker, 2 dir. of measurement (ACC),
- A4—Hammer excitation, 2 dir. of measurement (ACC),
- A6—Burst random excitation, 1 shaker, 1 dir. of measurement (LAS),
- A9—Burst random excitation, 1 shaker, 1 dir. of measurement (MIC).

The measurement campaign resulted in the collection of 366 experimental models. The breakdown of the models is presented in Table 22.2.

Acquisition parameters for models used in Test Lab Spectral Acquisition for three types of measure devices: ICP accelerometers, laser vibrometers (velocity), and microflown probe (velocity). Frequency limit of 200 Hz was selected based on the preliminary impact pre-test of the structure which revealed presence of numerous modes within 100 Hz. Accordingly to Nyquist Sampling Theorem, the frequency of 200 Hz allow to avoid aliasing.

The parameters of acquisition with ICP accelerometers are the following:

- Bandwidth: 0–200 [Hz]
- Spectral lines: 4096
- Frequency resolution: 0.0488281 [Hz]
- Number of averages: 10
- Burst: 50 %

The parameters of acquisition with laser vibrometer are the following:

- Bandwidth: 0–200 [Hz]
- Spectral lines: 4096
- Resolution: 0.0488281 [Hz]
- Averages: 5
- Burst: 50 %

The parameters of acquisition with microflown are the following:

- Bandwidth: 0–200 [Hz]
- Spectral lines: 4096
- Resolution: 0.0488281 [Hz]
- Averages: 5
- Burst: 50 %

Data measured and stored: Time, Spectrum, Cross power, Auto power, FRF, Coherence. For providing high signal to noise ratio the FRFs were measured repeatedly for number of times and averaged.

22.12 Quality Verification of Experimental Data Collection and Modal Models

Assessment of the variability of the experimental model collection starts with the evaluation of the accuracy of collected data. Observation and analysis of the experimental data is the substantial tool for extraction of the sought information characterizing the measurement results variability. Model quality assessment is an integrated part of the main goal of this investigation. The measured data variability influences results of the modal analysis. In other words the same set of data can lead to different values of modal model parameters. Therefore quality check of the estimation procedure at each of its steps is very important. In this research such procedure was applied for all estimated models, but in this section in details was described only one example for the one model of the blade.

The important remark is to be done at this point. All measurements are prone to systematic error. A systematic error is any biasing effect in the methods of observation or instruments used which introduces error into an experiment and is such that it always affects the results of an experiment in the same direction.

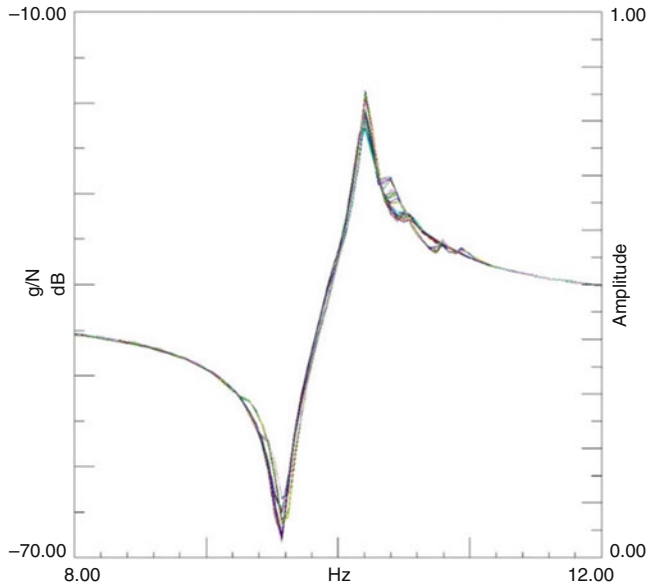


Fig. 22.13 FRF plot for the impedance head for all the measured sets for a selected point

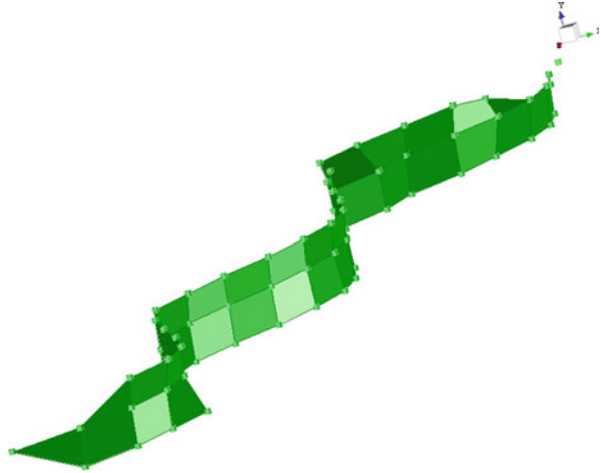
Accelerometer recording of the system's response required 8 sets of sensor locations in order to cover the entire grid of measurement points. Maximum number of 10 sensors was used. Weighted mass of all sensors and wiring system is 0.06 [kg]. This distributed mass is moved along the eight blade regions, which are characterized by a different flexibility. Additional mass always causes local structural modification which results in natural frequencies shift. Frequency shift due to mass loading for the driving point FRFs is presented in Fig. 22.13, for the second natural mode (second flapwise mode, around 10.2 Hz).

Except this, moving sensors from one location to another requires decoupling the shaker from a structure because it was not possible to provide a required quality of the sensor-structure wax connection with shaker coupled. Recoupling the shaker also alternates the connection's dynamic characteristic which consequently contributes to the measured signal. In other words the physical, real life conditions of the test realization forced the situation that each location of the sensors measurement is in fact a measurement of the slightly different assembly of the structure, sensors, wiring system, and shaker fastening.

First stage of data quality evaluation was done by means of observing individual measurement points coherence functions and their average calculated for all measurement points as presented in Fig. 22.16.

Coherence function is expected to be high. High values (close to 100% or 1) indicate both a high quality of the measurement signals and stationary operating conditions (not changing during the averaging). Values of the coherence of the

Fig. 22.14 Error of the curvature correction in laser measurement



signals are close to 1 proving the fulfillment one of the basic assumptions of modal analysis which is time invariance. Coherence check was examined for each run within entire test campaign.

The surface of the blades is curved. It was divided into three regions (assumed to be flat with a satisfactory approximation) along the spanwise direction, in order to minimize effect of curvature correction algorithm applied in LDV measurement. Therefore for each of these sets a slightly difference velocity field was obtained (Fig. 22.14). The microflow probe measurements were also not completely error free. Direct result of the sensing principle of the microflow probes is a non-correct measurement of the low frequency mode.

Vibration measure of the blades done was different for all three techniques. Therefore it is difficult to present the direct comparison of the acquired response signal for the particular point. Signal from a microflow probes is a subject of postprocessing. For this sensor there is no single frequency independent sensitivity value. The calibration of the signal data is being computed afterwards and is multiplied by frequency dependent curve. Measurement results shown in Fig. 22.15 clearly confirm the mass loading effect of the piezoceramic sensors.

Driving points FRFs for both contactless measurement techniques have higher resonant frequency values than piezoceramic sensors FRFs towards increasing frequency range which is mass influence area (Fig. 22.15).

22.13 Estimated Experimental Modal Models

In the following step of experimental modal analysis procedure, an identification of the modes of the structure was done. For this purpose the selected measured FRFs (preferably all) were used to compute SUM function. The real part of the SUM is the

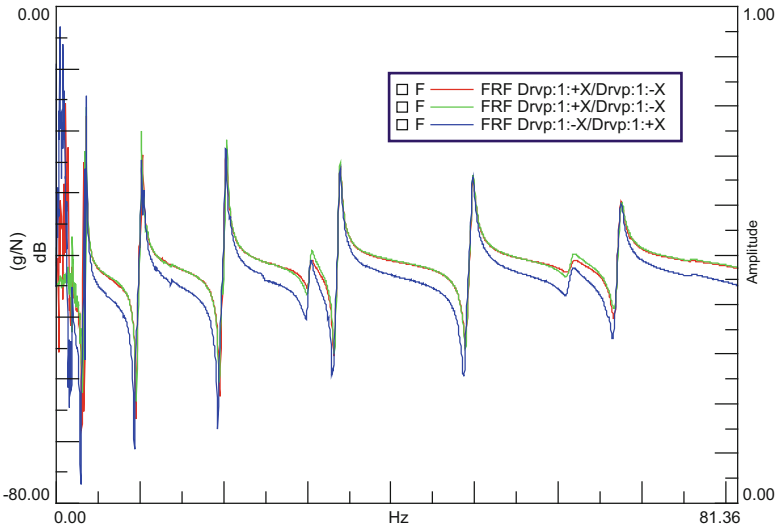


Fig. 22.15 Mass influence within investigated frequency range for driving point. Piezoceramic accelerometers measurement and microflow probes measurements are the upper curves, the laser vibrometer measurement is the lower curve

mean of the absolute value of the real part of all FRFs and the imaginary part of the SUM is the mean of the absolute value of the image of all FRFs. Resonance peaks in the SUM function plot indicate possible modes of the structure. Within bandwidth a number of resonance peaks are present on SUM plot indicating the model order.

Stabilization diagram was constructed comprising structural and computational poles. Diagram indicates modes for which the frequency and damping values of the physical modes do not change significantly. Poles of modes were repeatedly plotted for different model orders (Fig. 22.19). Poles not changing significantly were assumed to be physical modes.

It is due to model order which should be equal to number of poles within analyzed bandwidth but it is unknown a priori. Structural poles refer to structural resonances and computational poles are result of applied algorithm and noise in the measured data. Therefore during the acquisition the Hv estimator was applied assuming noise presence both on input and output signal. Source of a noise in the input signal can be nonperfect quality of a bond connection of an impedance head to the structure and the fixation of a shakers core with the impedance head due to some backlash. On the input signal the source of the noise could be a wax connection which is sensitive to the thickness of the applied wax layer. PolyMAX frequency domain algorithm was used for the computation of stabilization diagram. Generally structural poles are repeated in consequent model orders while computational ones are not stabilizing. Correct choice of the poles is of vital importance for the following steps since eigenfrequencies and damping ratios are chosen. This choice is strongly dependent on operator’s experience. To help distinguish computational

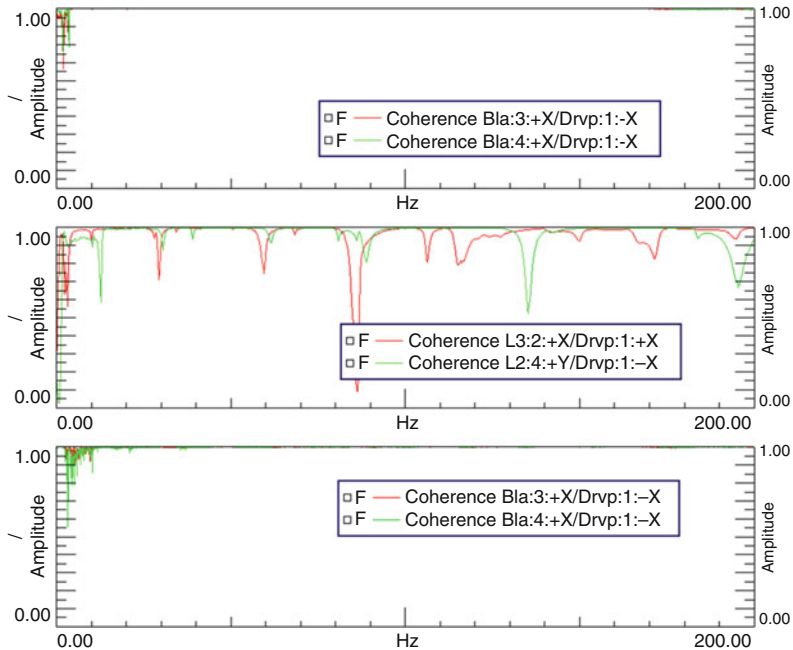


Fig. 22.16 Ordinary coherence functions for measurement points of for model A1 (*top*), A4 (*mid*), and A9 (*bottom*) for the bandwidth of interest [Hz] range

and structural poles a number of means was developed to support quality assessment of estimated modes. According to Uhl (1997) and Heylen et al. (1998) they can be divided into the following groups:

- Localization of the value of natural frequency (SUM, MMIF, and CMIF)
- Global modal indicators for total model (MAC, Synthesis)
- Assessment of correctness of the estimated mode (MPC, MOV)
- Assessment of the properties of a modal vector (MPD).

In the following, an outline of the theoretical background of the modal analysis validation tools is given. Only some of the basic working principles are presented (Heylen et al. 1998; Tirelli and Vadillo 2013; Uhl 2004; LMS International 2007). Reason for this detailed data collection quality investigation is that correct assessment of the test data variability is possible only on validated consistency of the data.

SUM: This is weighted summation of all available data, either by real or imaginary parts of measured FRFs. An important indication of the accuracy of the natural frequency estimates is their coincidence with resonance peaks in the FRF measurements. These resonance peaks can be enhanced by a SUM. Problems like missing modes, erroneous frequency estimates, or shifting resonances because of mass loading by the transducers can easily be detected this way.

MIF (Mode Indicator Functions) are frequency domain functions that exhibit local minima at the natural frequencies of real normal modes. The number of MIFs that can be computed for a given data set is equal to the number of input locations that are available. The so-called primary MIF will exhibit a local minimum at each of the structure's natural frequencies. The secondary MIF will have local minima only in the case of repeated roots. Depending on the number of input (reference) locations for which data is available, higher order MIFs can be computed to determine the multiplicity of the repeated root. So a root with a multiplicity of four will cause a minimum in the first, second, third, and fourth MIF, for example.

MMIF (Multivariant MIF) Looking directly for real normal mode, by minimizing the ratio of out-of-phase energy to total energy.

CMIF (Complex MIF) Components of the CMIF are evaluated by singular value decomposition of FRFs matrix. Local maxima of the maximum singular values function are indicating the structural resonance.

MAC (Modal Assurance Criterion) can be used to compare two modal models. If a linear relationship exists between the two complex vectors X and Y , the MAC value will be near to one. If they are linearly independent, the MAC value will be small (near zero).

FRF Synthesis quality of FRFs synthesized can be evaluated by means of the error and correlation values between measured and calculated FRFs.

MOV (Mode Overcomplexity Value) is defined as the (weighted) percentage of the response stations, for which a mass addition indeed decreases the natural frequency for a specific mode. MOV index should be high (near 100%) for high quality modes. Low value of MOV can indicate a modal point.

MPC (Modal Phase Collinearity) is an indicator that checks the degree of complexity of modes. It expresses the linear functional relationship between the real and the imaginary parts of the unscaled mode shape vector. This index should be high (near 100%) for real, normal modes. A low MPC index indicates a rather complex mode, due either to local damping elements in the tested structure, to errors in the data measurement, or to mistakes in the analysis procedure.

MPD (Mean Phase Deviation) is the indicator for the complexity of unscaled mode shape vectors. This index is the statistical variance of the phase angles for each mode shape coefficient from their mean value, and indicates the phase scatter of a mode shape. This MPD value should be low (near 0°) for real normal modes.

MP (Modal Participation) is defined as the sum of all residue values for a specific reference for each mode and expresses that mode's contribution to the response. When a comparison is made of the residue sums for one mode at all the references, it evaluates the reference point selection for that mode. The reference with the highest residue sum is the best one to excite that mode. *MIMO* (multi input multi output) is relevant to properly excite all the modes of the structure within the bandwidth of interest. Each shaker can contribute at different level of modal participation. When a modal participation value referring to a particular mode is low it means that this particular mode was not properly excited by a specific shaker. Values of above 20% for each shaker are considered to represent a sufficient degree of the excitation of the system.

The summation (SUM), multivariate mode indicator (MIF), and the complex mode indicator (CMIF) functions were used for identification uncertainty levels of the modes in the modal model.

Comprehensive measurement campaign conducted on the three nominally identical composite material blades allows to focus on the assessment of the influence of the following test parameters on the variability observed in measured results:

- Multiple realizations of the measurements of the same specimen,
- Measurement number of nominally identical specimens within the same test setup.

Measurement uncertainties of particular natural frequencies and damping factors (or ratios) were calculated according to Guide to the Expression of Uncertainty in Measurement JCGM 100:2008 (ISO 1995). Definitions used in the Guide are taken from the International vocabulary of basic and general terms in metrology (abbreviated VIM). According to it a measurement is a set of operations having the object of determining a value of a quantity, measurand is particular quantity subject to measurement, and result of a measurement is a value attributed to a measurand, obtained by measurement. Uncertainty of measurement is defined as the parameter, associated with the result of a measurement, that characterizes the dispersion of the values that could reasonably be attributed to the measurand. The uncertainty of the result of a measurement reflects the lack of exact knowledge of the value of the measurand. The result of a measurement after correction for recognized systematic effects is still only an estimate of the value of the measurand because of the uncertainty arising from random effects and from imperfect correction of the result for systematic effects. Recommendation INC-1 (1980) of the Working Group on the Statement of Uncertainties defines the key uncertainty components into two categories based on their method of evaluation, "A" and "B". The uncertainty of a correction for a known systematic effect may in some cases be obtained by a Type A evaluation. Type A evaluation of uncertainty is a method of evaluation of uncertainty by the statistical analysis of series of observations. The estimated variance u^2 characterizing an uncertainty component obtained from a Type A evaluation is calculated from series of repeated observations and is the familiar statistically estimated variance s^2 . The estimated standard deviation u , the positive square root of u^2 , is thus $u = s$ and for convenience is sometimes called a Type A standard uncertainty. The individual observations q_k differ in value because of random variations in the influence quantities, or random effects. The experimental variance of the n independent observations q_k observations, which estimates the variance σ^2 of the probability distribution of q , is given by

$$s^2(q_k) = \frac{1}{n-1} \sum_{j=1}^n (q_j - \bar{q})^2 \quad (22.1)$$

This estimate of variance and its positive square root $s(q_k)$, termed the experimental standard deviation, characterize the variability of the observed values q_k , or more specifically, their dispersion about their mean \bar{q} .

Although the variance $s^2(\bar{q})$ is the more fundamental quantity, the standard deviation $s(\bar{q})$ is more convenient in practice because it has the same dimension as q and a more easily comprehended value than that of the variance. Type A standard uncertainty is given by:

$$s(q) = \sqrt{\frac{1}{n-1} \sum_{j=1}^n (q_j - \bar{q})^2} \quad (22.2)$$

The result of a measurement can unknowably be very close to the value of the measurand (and hence have a negligible error) even though it may have a large uncertainty.

Measurement uncertainties of particular natural frequencies and damping factors (or ratios) are standard deviation of the mean value of the observed measurand (particular quantity subject to measurement).

Uncertainty level (mean value of uncertainty) for the overall modal model is calculated based on the formula for the arithmetic mean (Eq. (22.3)) of particular Type A uncertainties calculated for individuals modes according to Eq. (22.2).

$$A = \frac{1}{n} \sum_{i=1}^n a_i \quad (22.3)$$

The summation (SUM), multivariate mode indicator (MIF), and the complex mode indicator (CMIF) functions were used for identifying modes (Figs. 22.17 and 22.18).

Stabilization diagrams calculated using PolyMAX algorithm are presented in Fig. 22.19.

Structure is of moderate modal density within analyzed band. Several mode shapes are clear global modes of an entire blade. With the rise of frequency the mode shapes become increasingly more and more local. From the stabilization diagram it

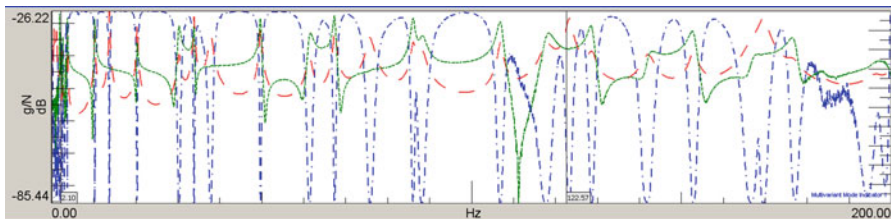


Fig. 22.17 Summation function (SUM) and multivariate mode indicator function (MIF) for the total bandwidth of interest, 000 ÷ 200 [Hz] range

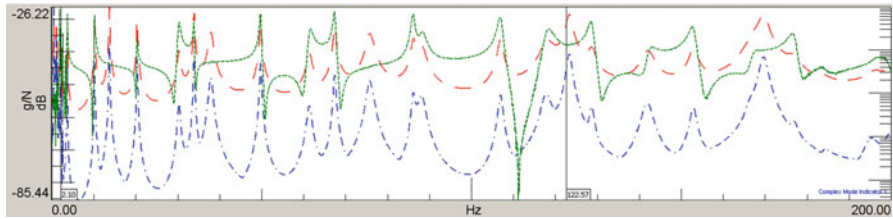


Fig. 22.18 Summation function (SUM) and complex mode indicator function (CMIF) for the total bandwidth of interest, 000 ÷ 200 [Hz] range

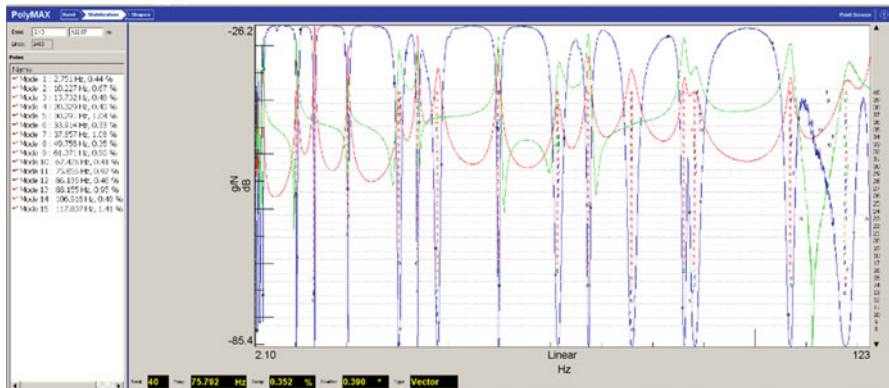


Fig. 22.19 Stabilization diagram, SUM, and MIF within the bandwidth of interest, 0 ÷ 200 [Hz]

can be read that the stable poles appear already below model order of 17. Within bandwidth of 0 ÷ 200 [Hz] poles are very well identified. The FRFs synthesized in this frequency range are well correlated with measured FRFs (Fig. 22.20) for the majority of cases.

The data presented in previous section was used for the estimation of the modal models. Local minima of MIF indicators are well corresponding with local maxima of SUM and in addition with number of individual FRFs peaks. Estimated natural frequencies and damping are listed in Figs. 22.21 and 22.22.

Table 22.3 presents a part of the comparison of the natural frequency and damping ratio values for the identified modes. Data for these models were acquired by means of contact and non-contact techniques.

22.14 Comparison of the Modal Vectors

Within the bandwidth of interest there are all modes (except the first one using the microflow sensor) successfully identified for all modal models. Visual inspection of the mode shapes is presented in Table 22.4. Both non-contact sensors are

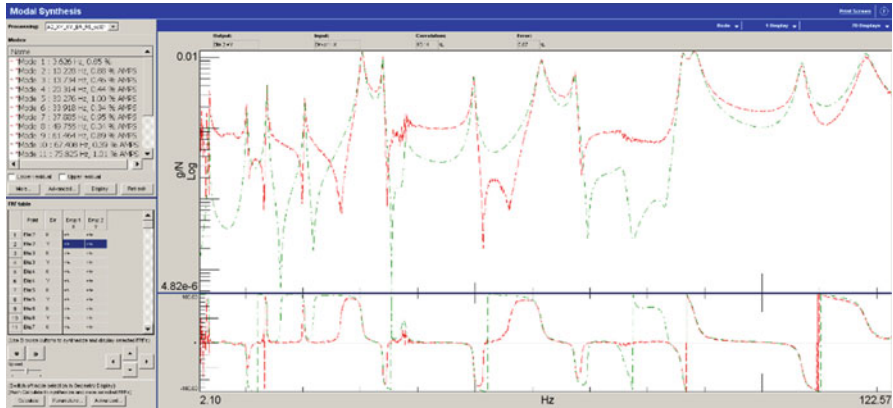


Fig. 22.20 Example of FRFs synthesis for the model A2_XY_R1

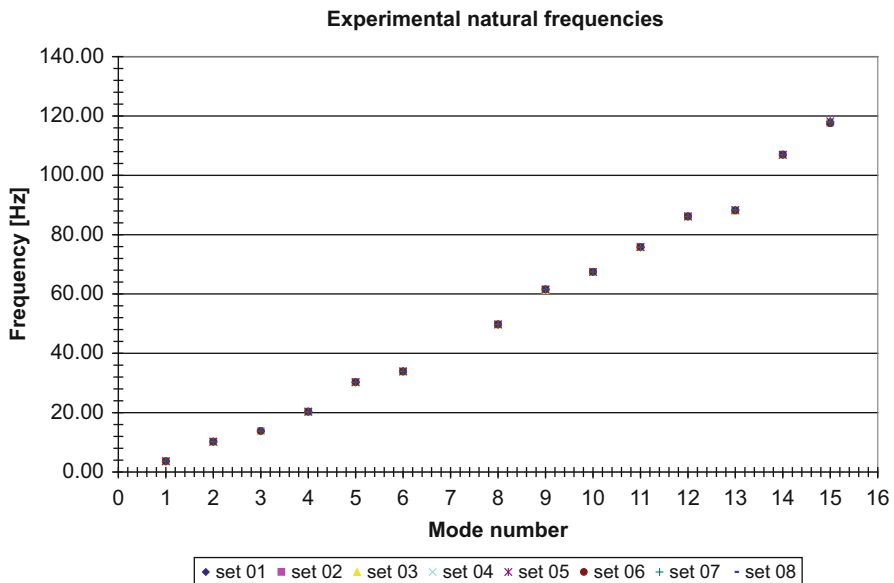


Fig. 22.21 Estimated experimental natural frequencies for the blade A, model A1_X_Y_R1

measuring only out-of-plane direction displacement. In-plane direction of displacement was therefore not captured by laser and microflown probes in edgewise modes. These modes were recorded properly with the contact vibration acceleration sensors.

Discussed systematic errors do not influence the correctness of the model estimation which can be observed in MAC matrix plots in Table 22.5.

MAC matrix comparison also confirms that both contactless measurement models coincide better than contact, piezoceramic accelerometer model.

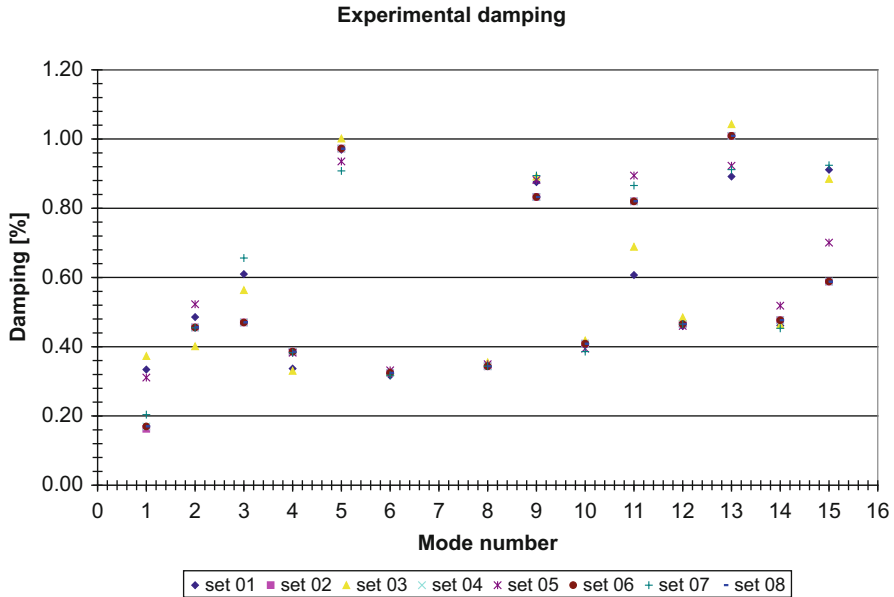


Fig. 22.22 Estimated experimental damping for the blade A, model A1_X_Y_R1

22.15 Uncertainty Levels for Models

In previous sections investigation on coupon and component level test items were presented. Main rotor helicopter blades represent the level of fully assembled structure of the highest structure complexity. Extensive measurement campaign conducted on the helicopter blades was adopting combination of previously used comparison criteria, namely:

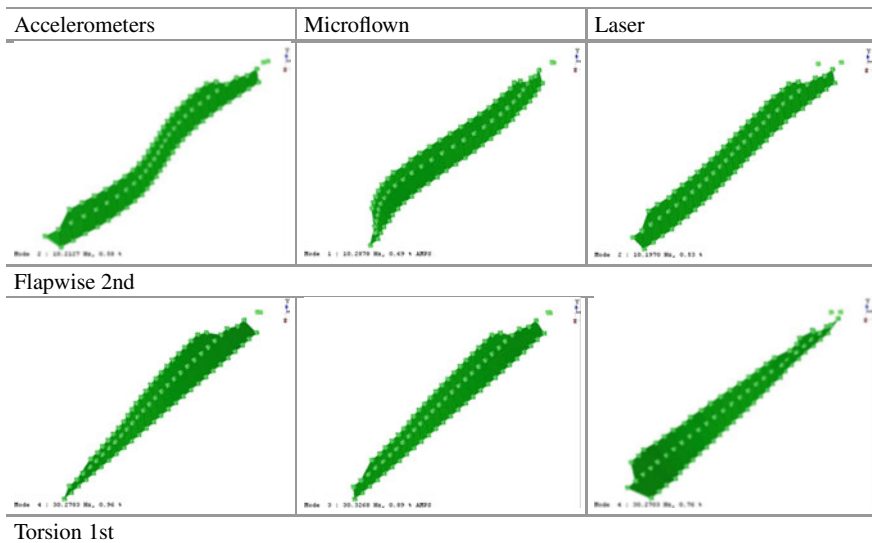
- Single vs. multiple input,
- Multiple realizations of the measurements of the same specimen,
- Measurement number of nominally identical specimens within the same test setup.
- Random vs. harmonic excitation signal as input,
- Impact vs. electrodynamic shaker excitation,
- Contact vs. non-contact response measurement,
- Vibration acceleration vs. velocity based measurement,
- Different principles of non-contact sensor operation and related signal processing.

Investigated helicopter blades were mounted in the main rotor of the helicopter. The selection of the blades for the rotor is a subject of strict procedures (Johnson 2012). Most intense experimental campaign was conducted on the blade defined as blade A.

Table 22.3 Experimental natural frequencies and damping

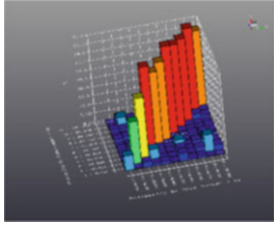
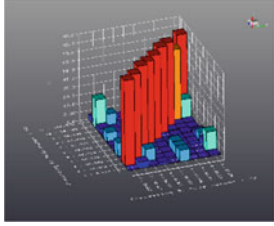
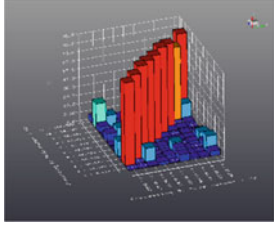
Mode number	Mode type	Accelerometer	Laser	Microflow	Accelerometer	Laser	Microflow
		Frequency Hz			Damping %		
H1	Flapwise 1st	3.69	3.61	—	1.31	0.25	—
H2	Flapwise 2nd	10.23	10.21	10.28	0.70	0.66	0.67
H3	Edgewise 1st	13.74			0.51	—	—
H4	Flapwise 3rd	20.33	20.28	20.31	0.40	0.36	0.44
H5	Torsion 1st	30.35	30.28	30.32	0.98	0.76	0.89
H6	Flapwise 4th	33.91	33.91	33.92	0.34	0.33	0.40
H7	Edgewise 2nd	37.87	—	—	1.01	—	—
H8	Flapwise 5th	49.76	49.75	49.78	0.35	0.31	0.36
H9	Torsion 2nd	61.47	61.44	61.55	0.88	0.55	0.89
H10	Flapwise 6th	67.43	67.40	67.42	0.41	0.32	0.39
H11	Edgewise 3rd	75.87	—	75.98	0.96	—	0.34
H12	Flapwise 7th	86.13	86.15	86.16	0.47	0.28	0.49
H13	Torsion 3rd	88.33	88.16	88.41	0.94	0.50	1.01
H14	Flapwise 8th	106.93	106.92	106.95	0.48	0.27	0.46
H15	Torsion 4th	118.10	117.94	118.00	1.26	0.56	0.99

Table 22.4 Mode shapes



Single Input Multiple Output burst random excitation was applied for flapwise X or edgewise Y directions. In Multiple Input Multiple Output measurement two electrodynamic shakers were used. Response signals for both SIMO and MIMO models were collected in flapwise and edgewise direction.

Table 22.5 MAC criterion for modal vectors comparison

		
Acceleration (A) vs LASER (B)	Acceleration (A) vs. Microflow (B)	Laser (A) vs. Microflow (B)

In Fig. 22.23 two high values of frequency uncertainty could be observed for modes H7, H11, H9, H13, and H15 in all five runs. Mode H7 and H11 are edgewise bending (Y direction). Damping ratio estimation for mode H7 in model A1X (Fig. 22.24) is also significantly higher than for the remainder of the modes. While modes H7 and H11 in edgewise excited model A1Y are low valued modes H9, H13, and H15 uncertainties remain high in both A1X and A1Y models. Modes H9, H13, and H15 are torsional modes and their high frequency uncertainty for both flapwise and edgewise excitation directions could be explained by relatively weak excitation of the torsional modes. This observation is confirmed by high value of the frequency uncertainty for modes H9, H13, and H15 in both flap and edgewise excitation directions (Figs. 22.23 and 22.25) and two directions excited in the same test A2 XY (Fig. 22.27). In case of harmonic excitation used in models A3X and A3Y (Figs. 22.29 and 22.31) the high level of modes H9, H13, and H15 could still be observed. It confirms that despite of different excitation signal the torsional modes are weakly excited by means of shakers attached in flap and edgewise direction. The H7 edgewise mode frequency uncertainty is also high similarly to models with random signal excitation. Model A4X and Y was estimated from experiments with the use of the modal hammer as an excitation method. Impacts of the hammer provide impulse type of input signal. In practice it is difficult to maintain the precise of flapwise direction impacts and this could be reason of reduction of frequency uncertainty Type A values for modes H9 and H13. It means that the excitation is provided also in the both X and Y directions despite exciting X direction. It allowed to better excite the modes in Y direction (Fig. 22.32). However, mode H15 reached double frequency uncertainty Type A value in edgewise direction (Fig. 22.33).

Interesting observation regards damping ratios uncertainty Type A values. In measurement results of blade A in number of cases (Figs. 22.23, 22.24, 22.25, 22.26, 22.28 and 22.30) the damping ratio uncertainty is higher than frequency uncertainty. Exception is mode H15 (Fig. 22.32).

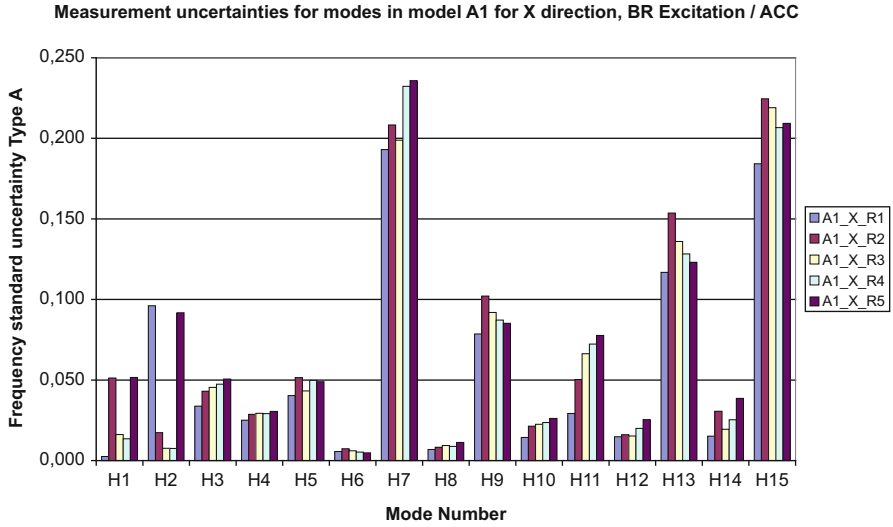


Fig. 22.23 Blade model A1 X frequency uncertainty Type A (Eq. (22.2))

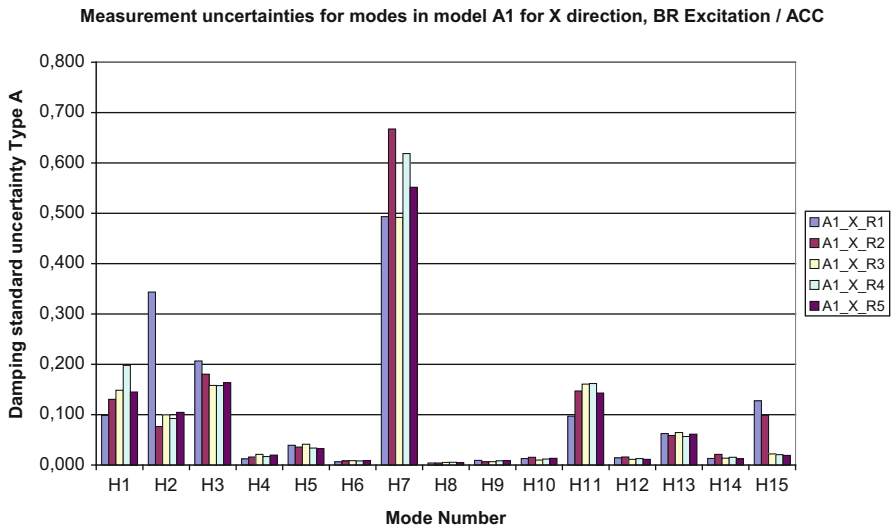


Fig. 22.24 Blade model A1 X damping uncertainty Type A (Eq. (22.2))

Models A6 and A9 were estimated on the test conducted with laser vibrometer (Figs. 22.35 and 22.36) and microflown probes (Figs. 22.37 and 22.38). Both sensors were not able to capture the response of the structure for edgewise direction modes H3, H7, and H11. This is due to the principle of operation of both sensors capable of measuring out-of-plane direction. Despite this fact the order of

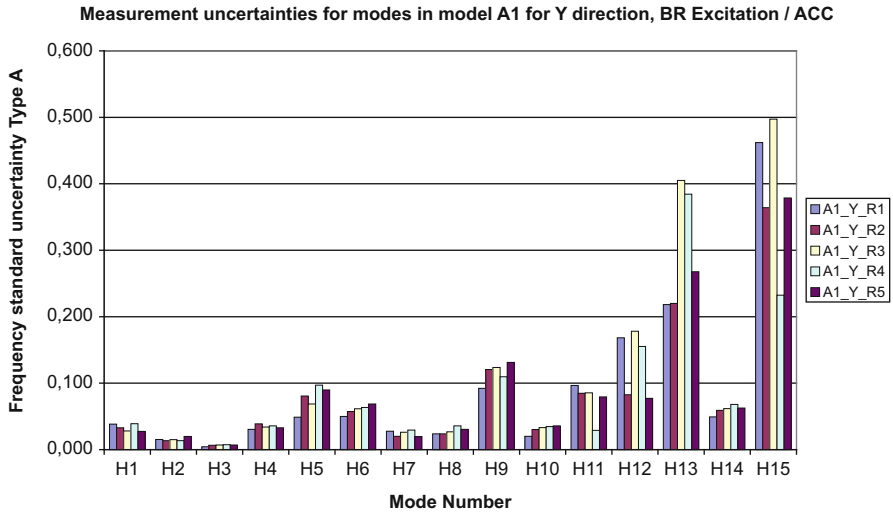


Fig. 22.25 Blade model A1 Y frequency uncertainty Type A (Eq. (22.2))

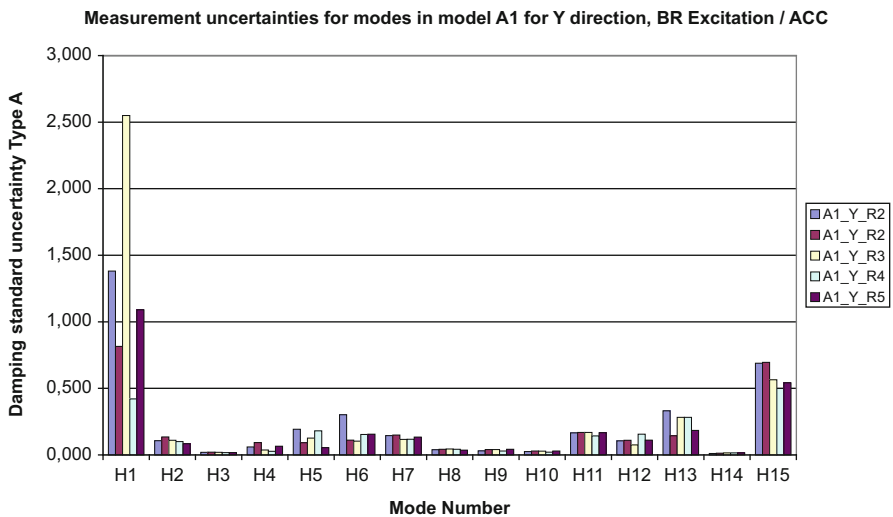


Fig. 22.26 Blade model A1 Y damping uncertainty Type A (Eq. (22.2))

frequency uncertainty Type A values are hundredths of Hertz while for the contact measurements they were tenths of Hertz. It confirms the observation made in results of panel measurement where significant decrease of uncertainty in non-contact methods results was also present. Mass of the single blade is approximately 70 kg. Presented results indicate that the smaller the ratio of test specimen mass over mass of the sensors the lower the uncertainty of frequency measurement.

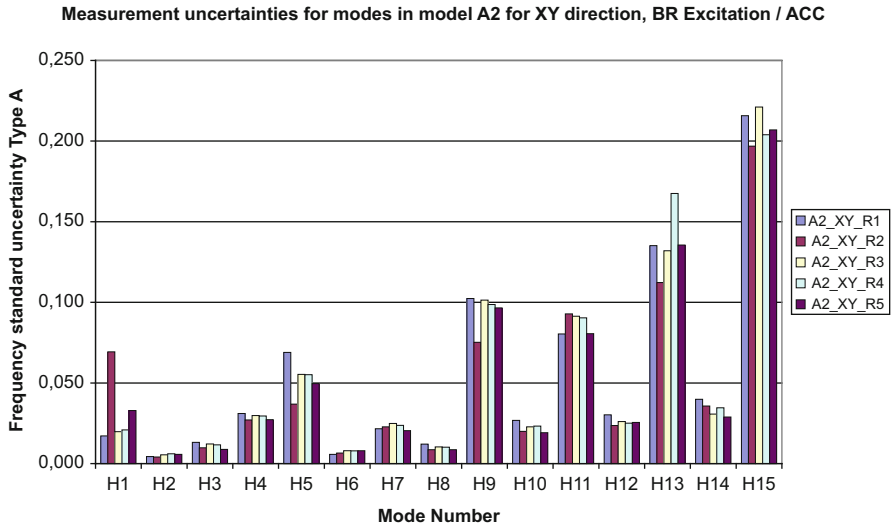


Fig. 22.27 Blade model A2 XY frequency uncertainty Type A (Eq. (22.2))

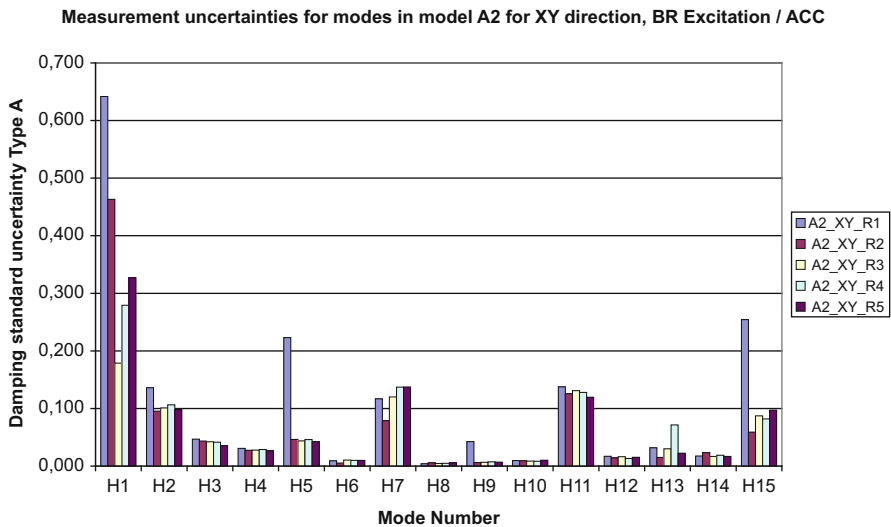


Fig. 22.28 Blade model A2 XY damping uncertainty Type A (Eq. (22.2))

Blade A was subject of extensive multiple tests campaign. Different measurement techniques, structure exciting methods input numbers, and driving signals were investigated. In the next step two blades B and C from the same rotor were measured. The main objective of this part of research was to assess the differences of uncertainty Type A values observed in measurement of nominally identical test

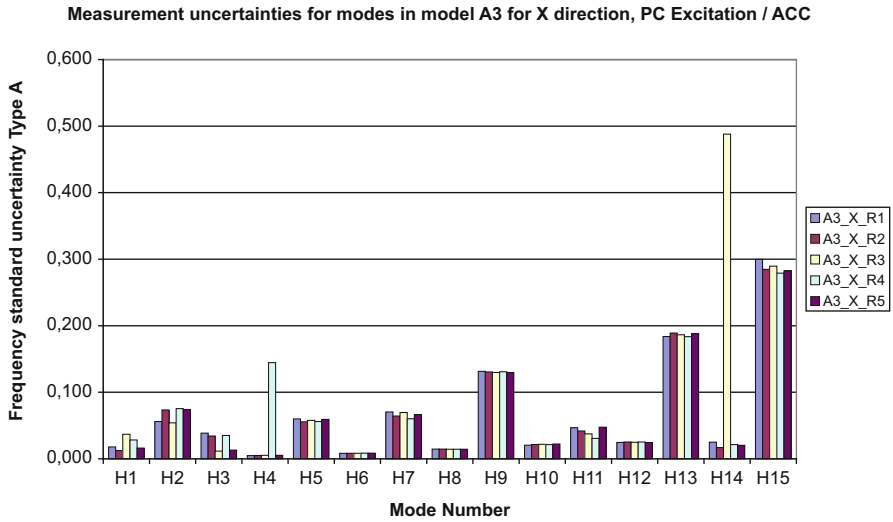


Fig. 22.29 Blade model A3 X frequency uncertainty Type A (Eq. (22.2))

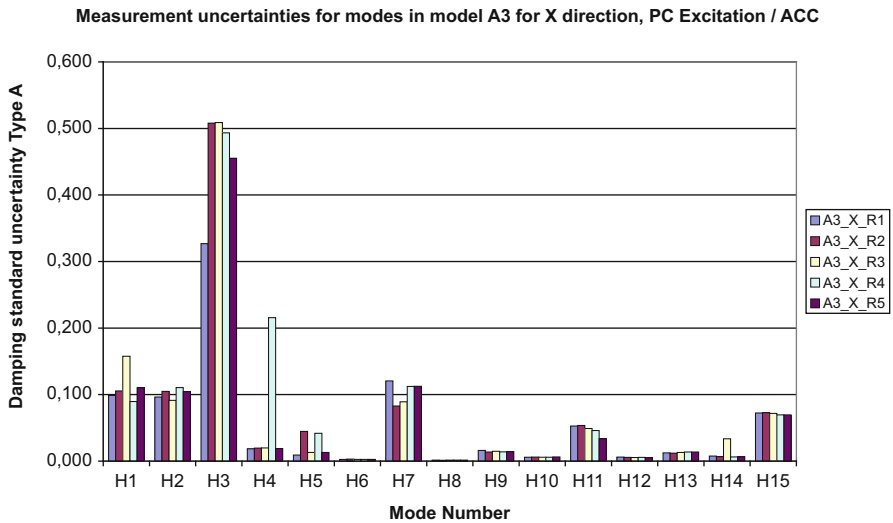


Fig. 22.30 Blade model A3 X damping uncertainty Type A (Eq. (22.2))

items. For all three blades A, B, and C the estimated modal models consisted of the same number of identified modes of very similar frequencies.

Plots of the frequency uncertainty level for blades B and C tested within identical test setup as blade A could be compared to their blade A counterparts. Referencing Model B1X (Figs. 22.39, 22.40–22.44) and C1X (Fig. 22.45) to model A1X (Fig. 22.23) it is possible to notice similarities. Mode H7, edgewise

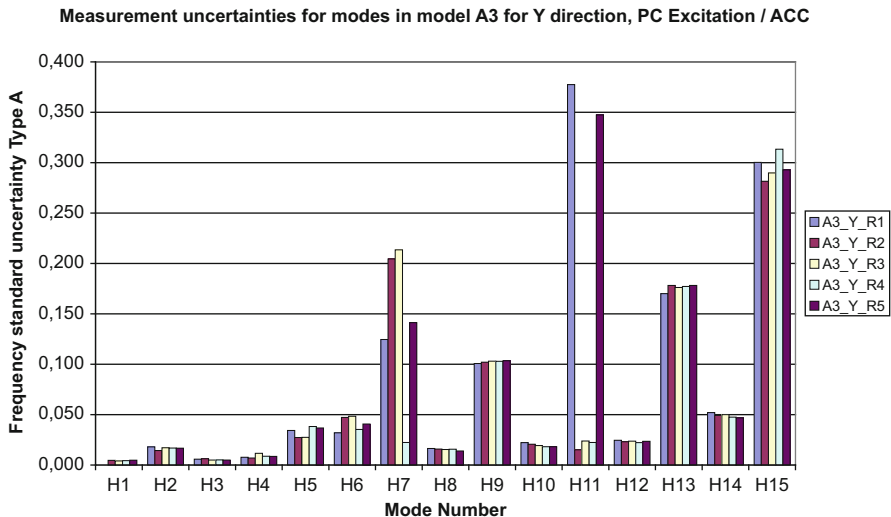


Fig. 22.31 Blade model A3 Y frequency uncertainty Type A (Eq. (22.2))

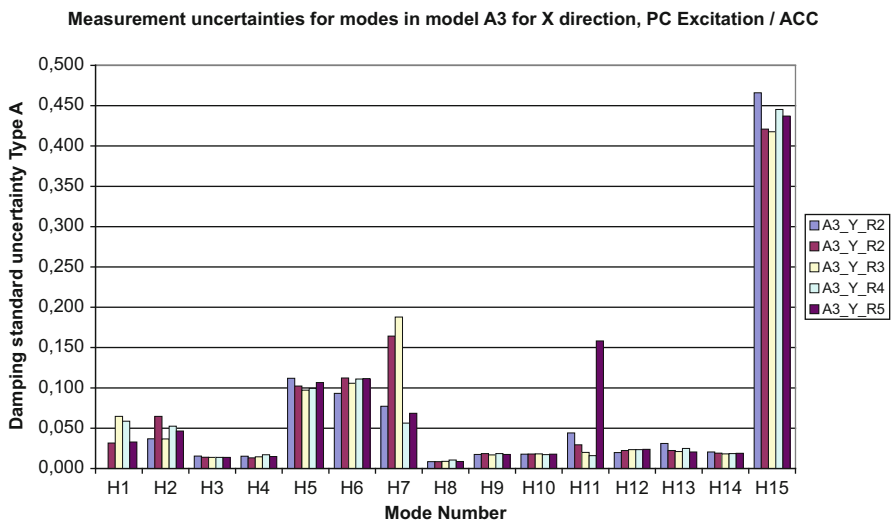


Fig. 22.32 Blade model A3 Y damping uncertainty Type A (Eq. (22.2))

bending in Y direction, has the high frequency uncertainty in case of flapwise (X) direction. Torsional modes H9, H13, and H15 demonstrate high levels of frequency uncertainties for both SIMO/MIMO and random/harmonic signal models B1, B2, B3 and C1, C2, and C3. Alike models of blade A the highest frequency uncertainty manifests for mode H15. Multiple input excitation configurations brought the

Measurement uncertainties for modes in model A4 for X and Y direction, IMPACT Excitation / ACC

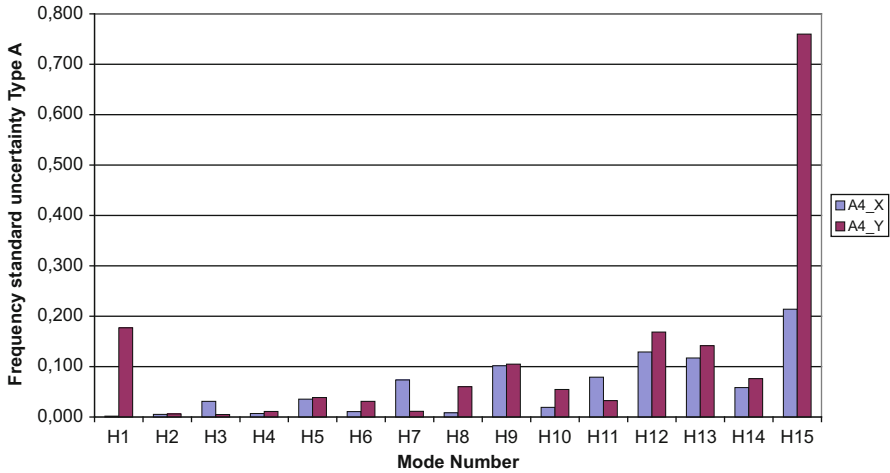


Fig. 22.33 Blade model A4 X and Y frequency uncertainty Type A (Eq. (22.2))

Measurement uncertainties for modes in model A4 for X and Y direction, IMPACT Excitation / ACC

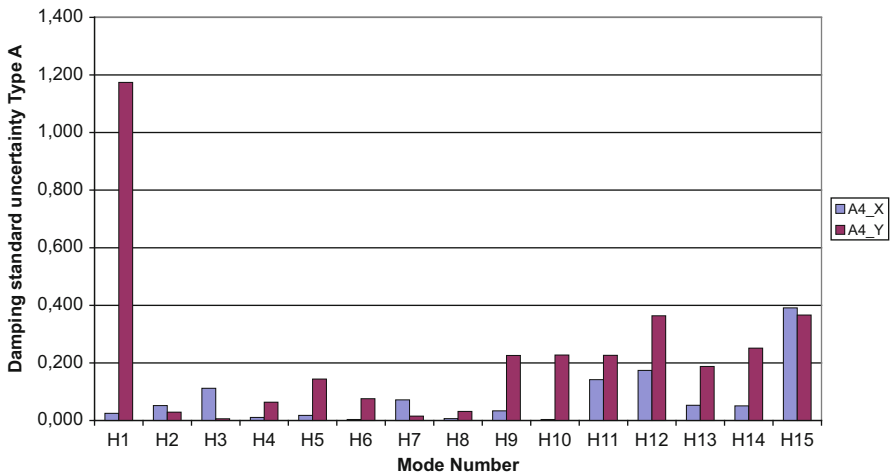


Fig. 22.34 Blade model A4 X and Y damping uncertainty Type A (Eq. (22.2))

decrease of the uncertainties in B2 and C2 models comparing to single input models B1 and C1 which was also notified for models A2 and A1, respectively.

Multiple tests run performed on blade A made it possible to study differences in uncertainty levels between particular tests done by means of various experimental techniques. Analysis of models A1, A2, and A3 reveal details about influence of

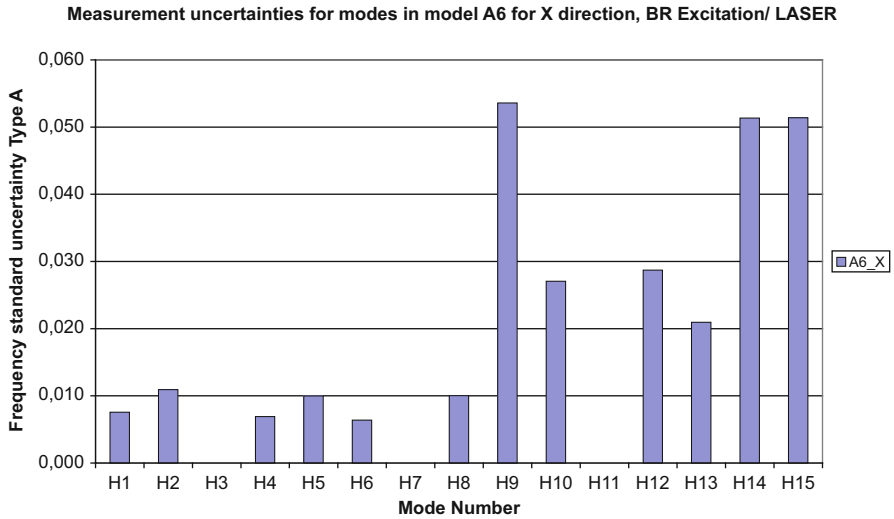


Fig. 22.35 Blade model A6 frequency uncertainty Type A (Eq. (22.2))

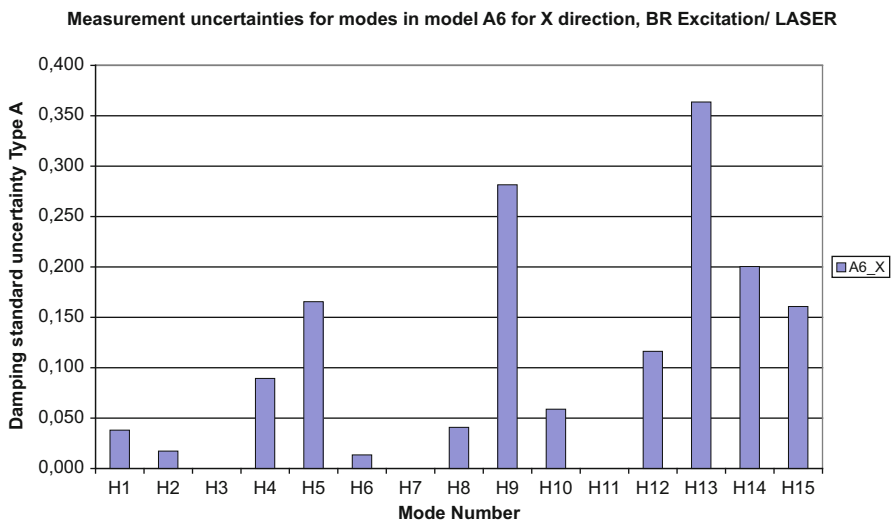


Fig. 22.36 Blade model A6 damping uncertainty Type A (Eq. (22.2))

applied excitation method on the results variations. In A1 model *X* direction random excitation with *XY* direction measurement the uncertainty of frequency is lower than *Y* direction random excitation and *XY* direction response for all realizations of the tests. This remark is not applicable for the harmonic signal excitation in SIMO

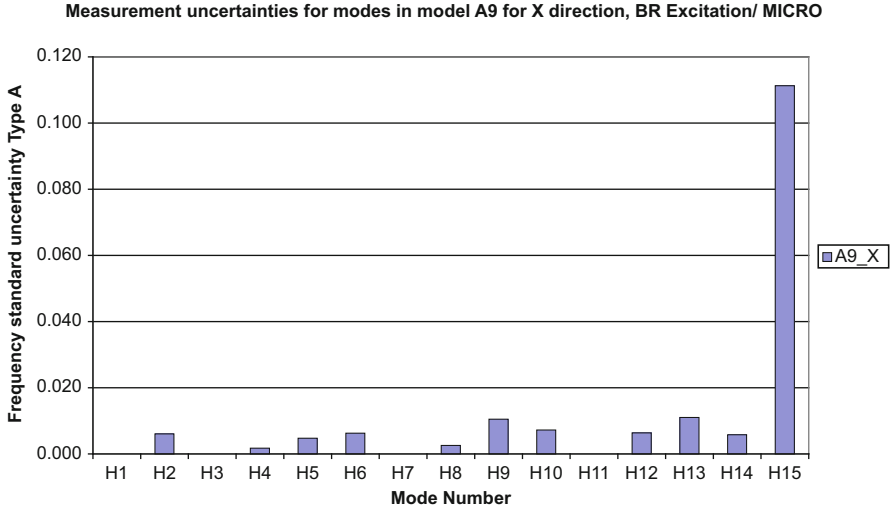


Fig. 22.37 Blade model A9 frequency uncertainty Type A (Eq. (22.2))

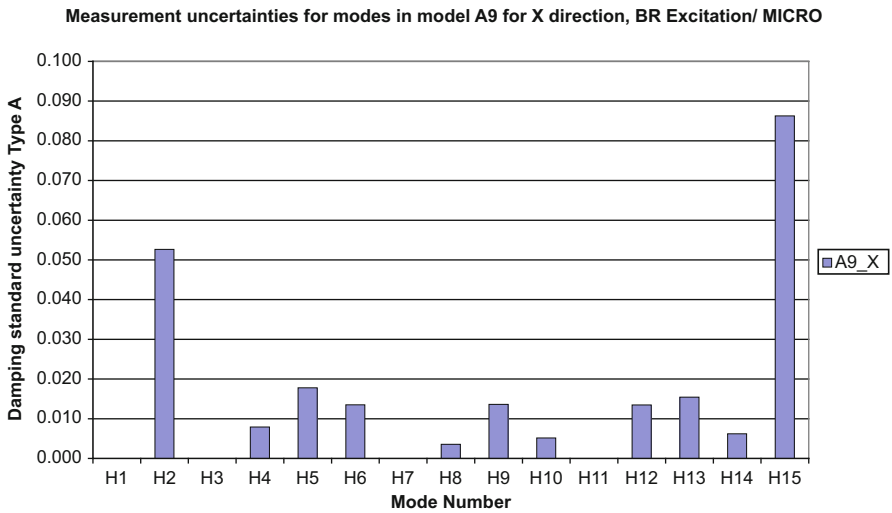


Fig. 22.38 Blade model A9 damping uncertainty Type A (Eq. (22.2))

configuration (Figs. 22.46, 22.47, 22.48, 22.49, and 22.50). The uncertainty levels estimated for the XY MIMO A2 model (Fig. 22.53) were of half of the values for the SIMO (Figs. 22.51, 22.52, 22.53, 22.54, and 22.55).

Measurement uncertainties for modes in model B1 for X and Y direction, BR Excitation / ACC

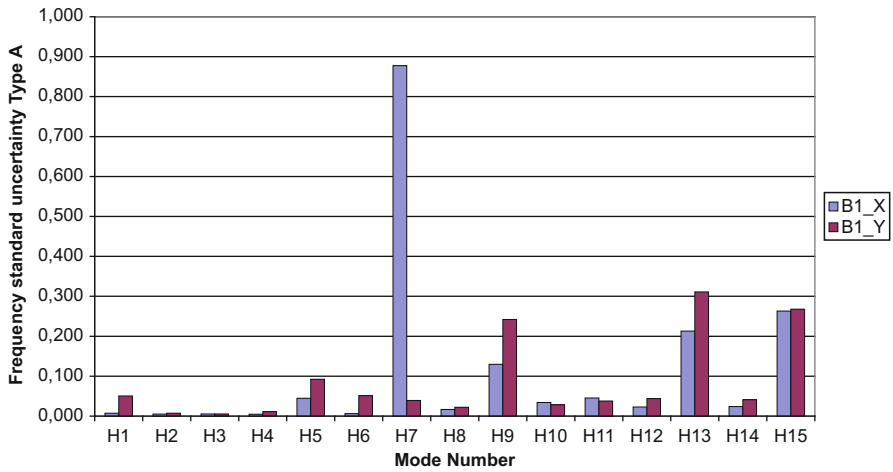


Fig. 22.39 Blade model B1 X and Y frequency uncertainty Type A (Eq. (22.2))

Measurement uncertainties for modes in model B1 for X and Y direction, BR Excitation / ACC

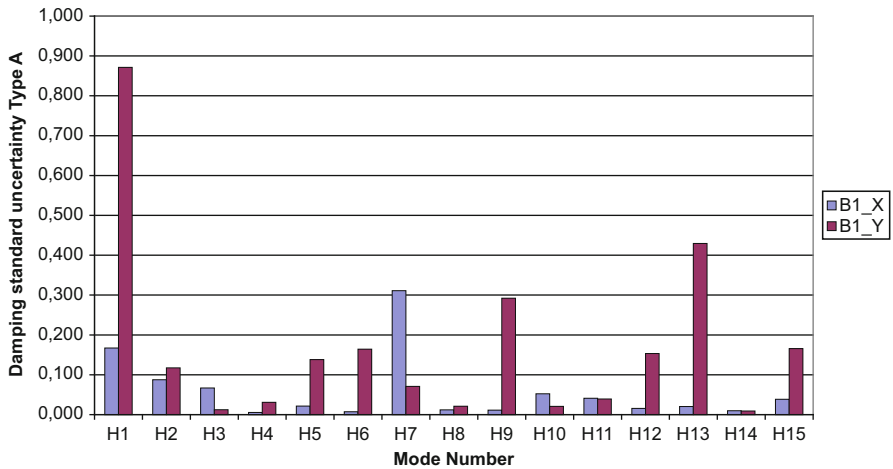


Fig. 22.40 Blade model B1 X and Y damping uncertainty Type A (Eq. (22.2))

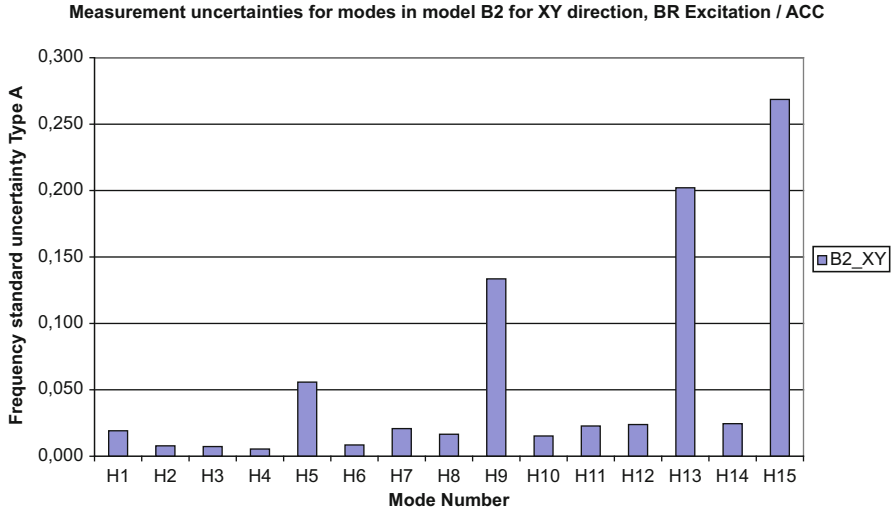


Fig. 22.41 Blade model B2 XY frequency uncertainty Type A (Eq. (22.2))

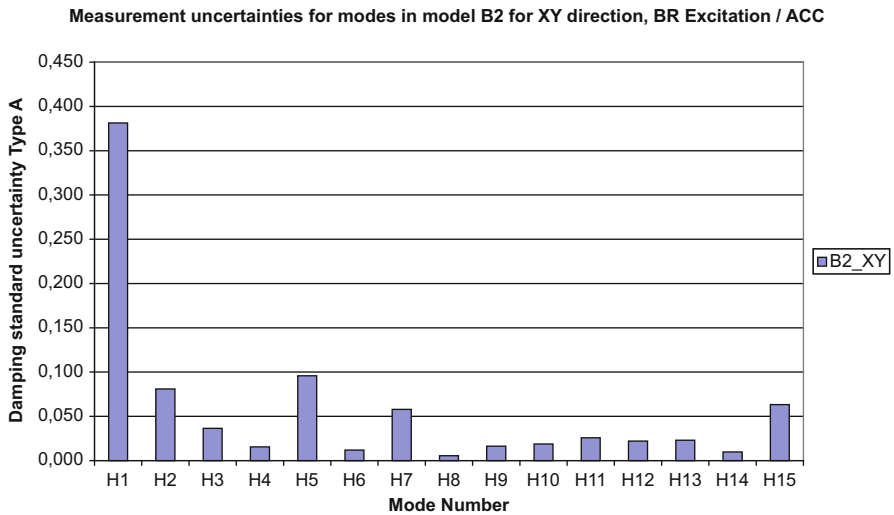


Fig. 22.42 Blade model B2 XY damping uncertainty Type A (Eq. (22.2))

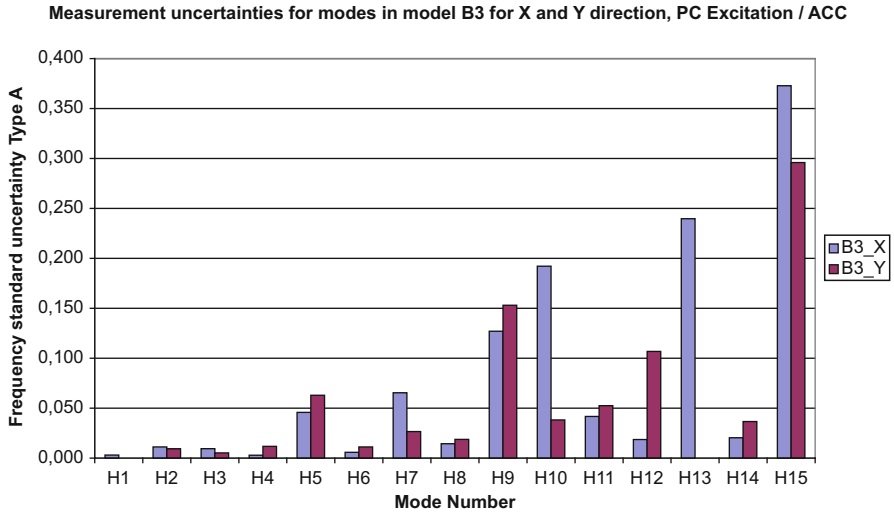


Fig. 22.43 Blade model B3 X and Y frequency uncertainty Type A (Eq. (22.2))

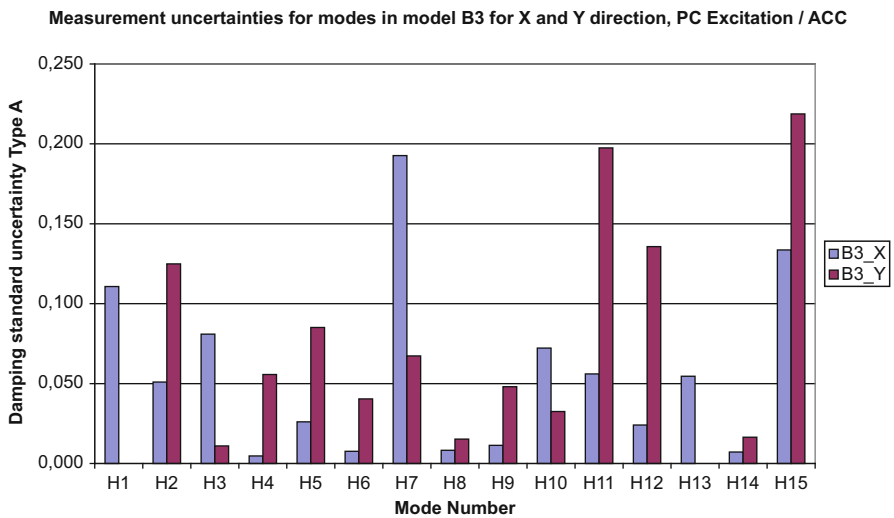


Fig. 22.44 Blade model B3 X and Y damping uncertainty Type A (Eq. (22.2))

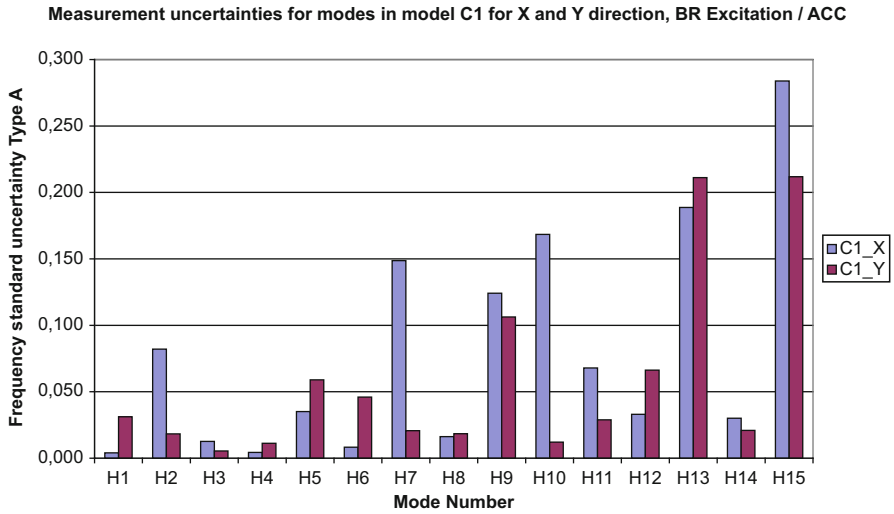


Fig. 22.45 Blade model C1 X and Y frequency uncertainty Type A (Eq. (22.2))

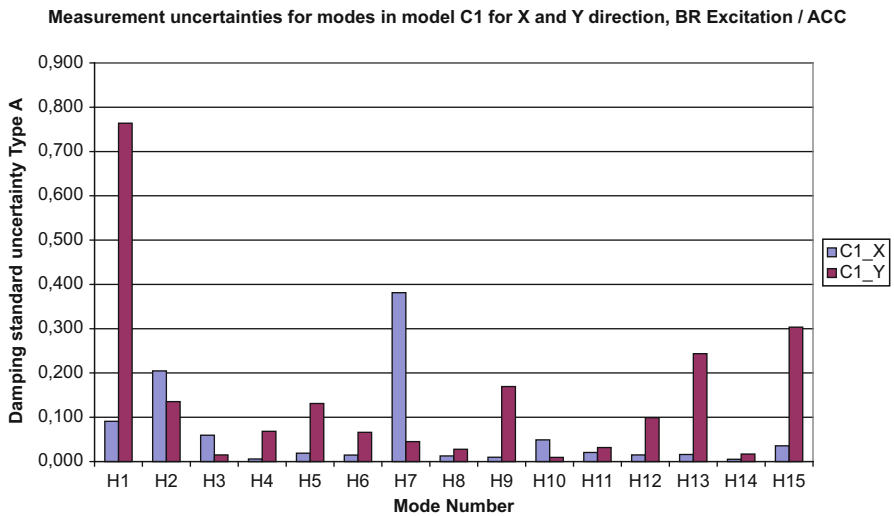


Fig. 22.46 Blade model C1 X and Y damping uncertainty Type A (Eq. (22.2))

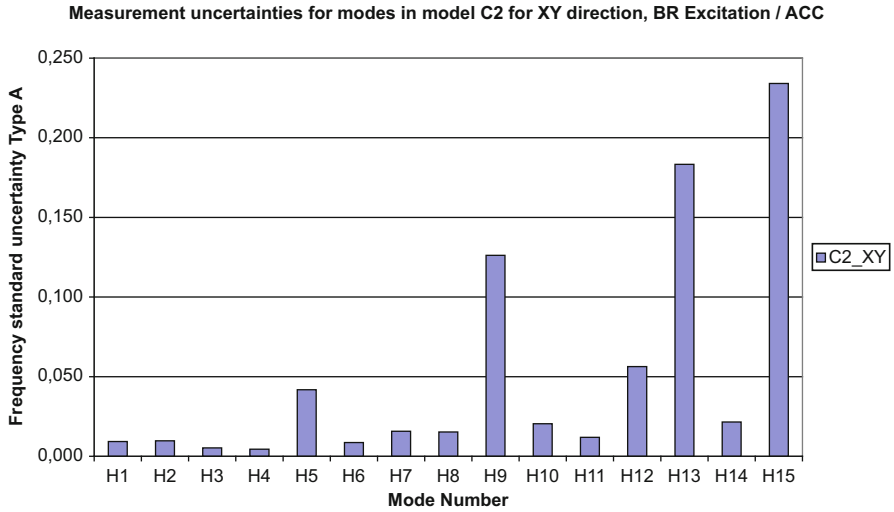


Fig. 22.47 Blade model C2 XY frequency uncertainty Type A (Eq. (22.2))

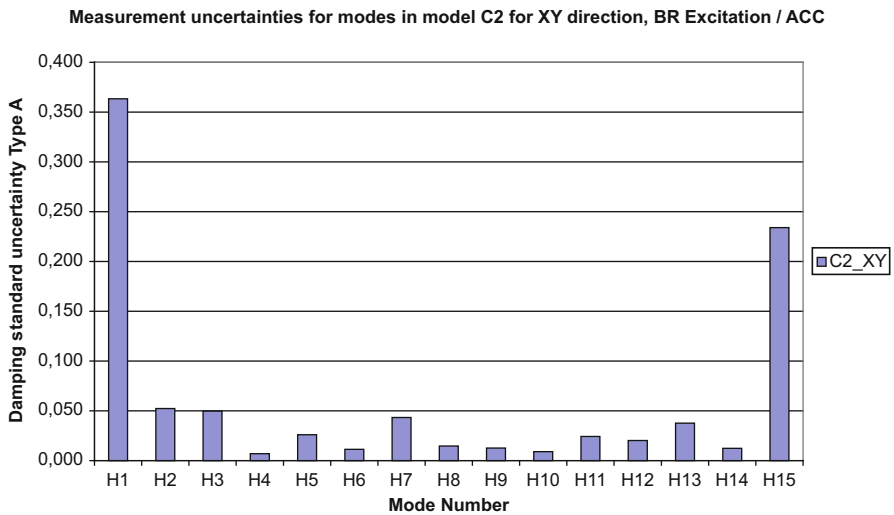


Fig. 22.48 Blade model C2 XY damping uncertainty Type A (Eq. (22.2))

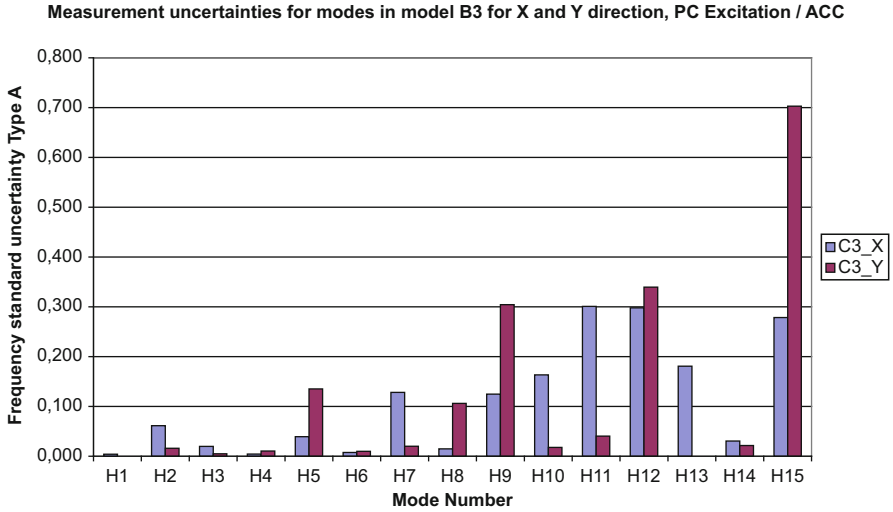


Fig. 22.49 Blade model C3 X and Y frequency uncertainty Type A (Eq. (22.2))

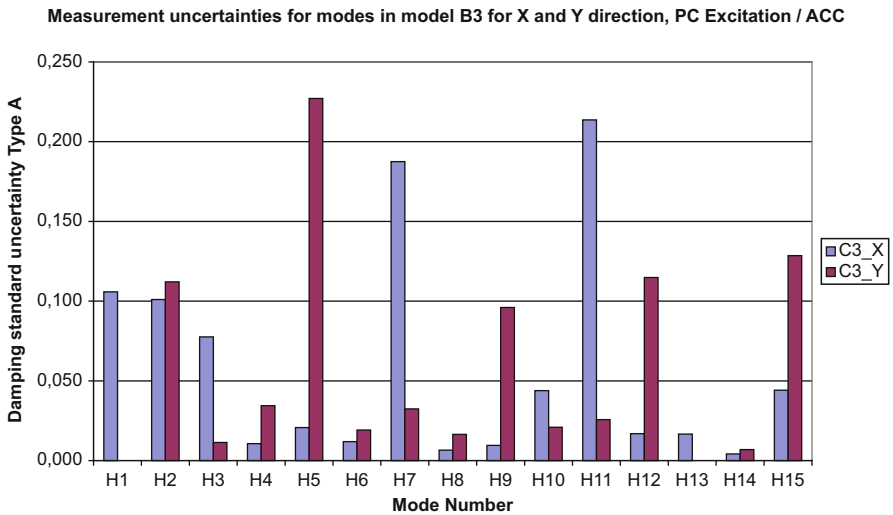


Fig. 22.50 Blade model C3 X and Y damping uncertainty Type A (Eq. (22.2))

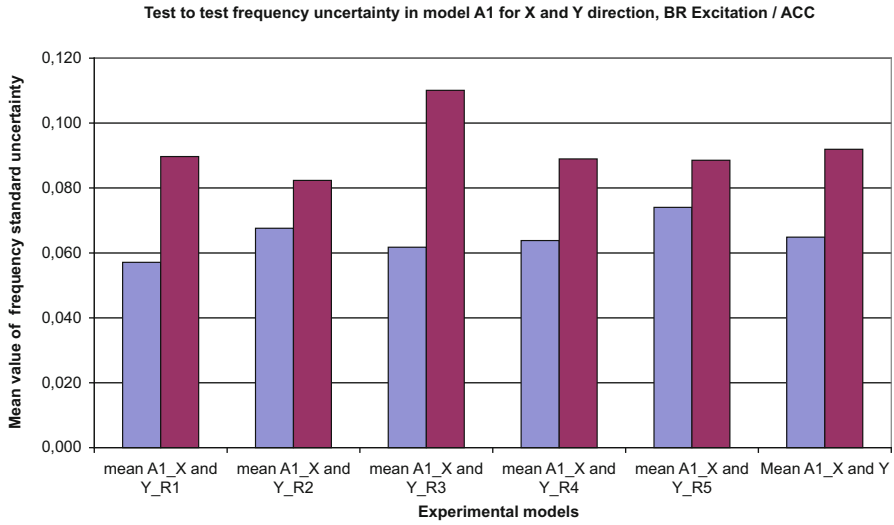


Fig. 22.51 Blade A1 test-to-test frequency uncertainty level

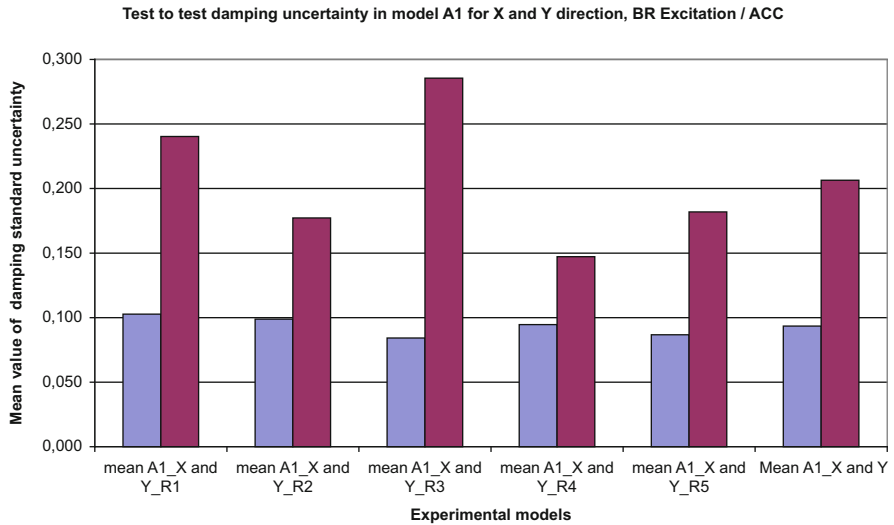


Fig. 22.52 Blade A1 test-to-test damping uncertainty level

To complete the multicriteria study of influence of applied technique onto uncertainty of measured results the comparison of uncertainty mean values for investigated blades was made (Figs. 22.56, 22.57, and 22.58). Mean values of uncertainties for blades A, B, and C were plotted. Lowest value of uncertainty is associated with blade A, while for blades B and C are almost identical. The reason of slightly smaller blade A uncertainties is incorporation of the non-contact

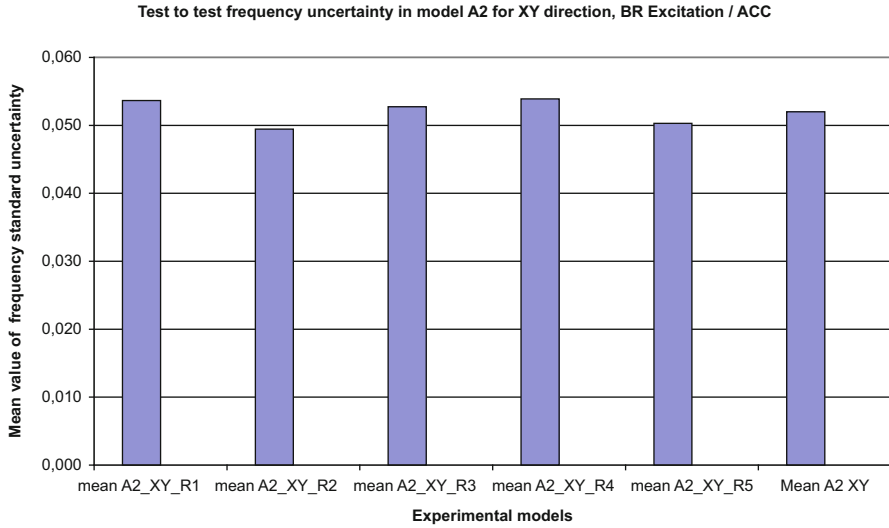


Fig. 22.53 Blade A2 test-to-test frequency uncertainty level

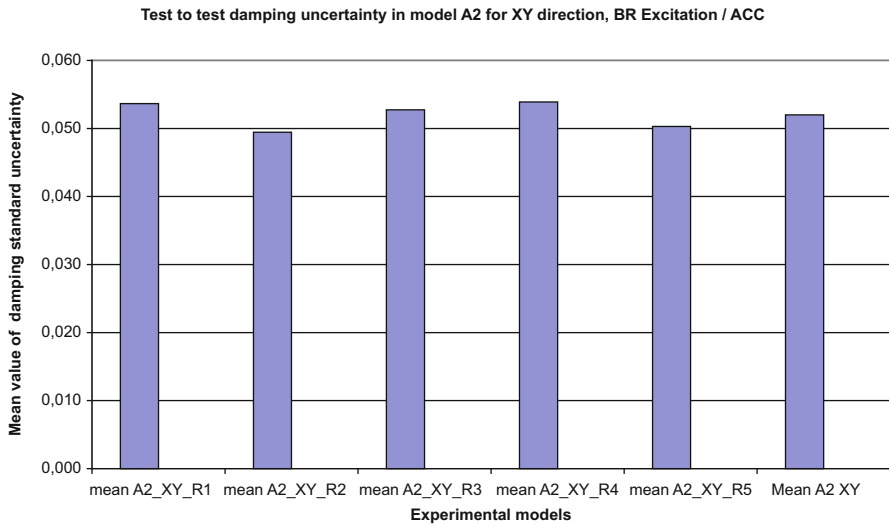


Fig. 22.54 Blade A2 test-to-test damping uncertainty level

measurements. Laser and microflow probes measurements uncertainties were order of magnitude lower than the accelerometer tests and are counted in the calculation of the mean uncertainty Type A value. It could also be noticed that the overall uncertainty level for the blades amounts to 0.08 [Hz].

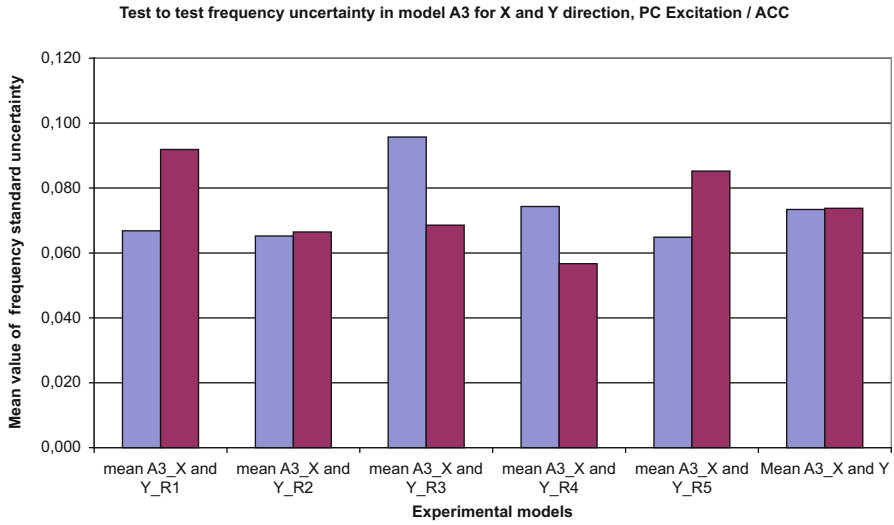


Fig. 22.55 Blade A3 test-to-test frequency uncertainty level

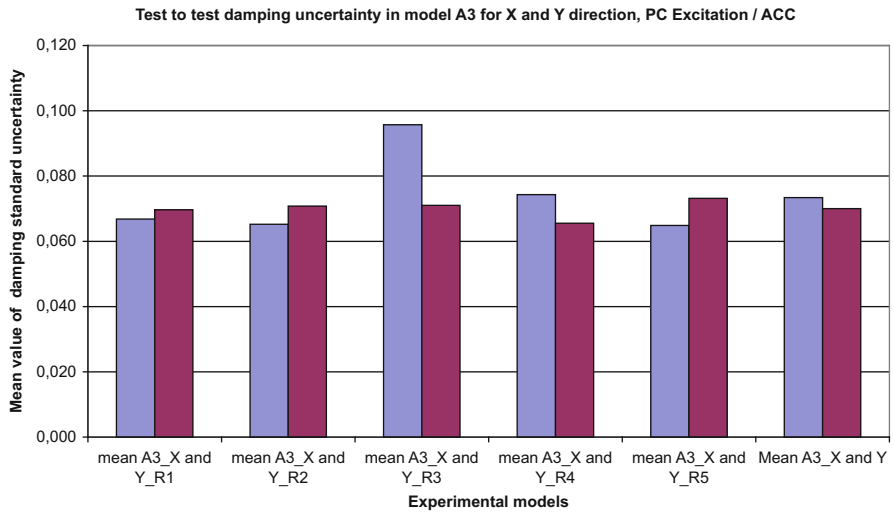


Fig. 22.56 Blade A3 test-to-test damping uncertainty level

Another relevant comparison method for these models is a correlation plot shown in Fig. 22.59. For contact and non-contact models the correlation plot of damping ratio and frequency is being drawn. Damping ratios for the torsional modes are clearly demonstrating the significantly higher value with respect to the translational modes. This concerns all the considered models. A new observation comes from the comparison between the microflow and laser measurement models. Both are

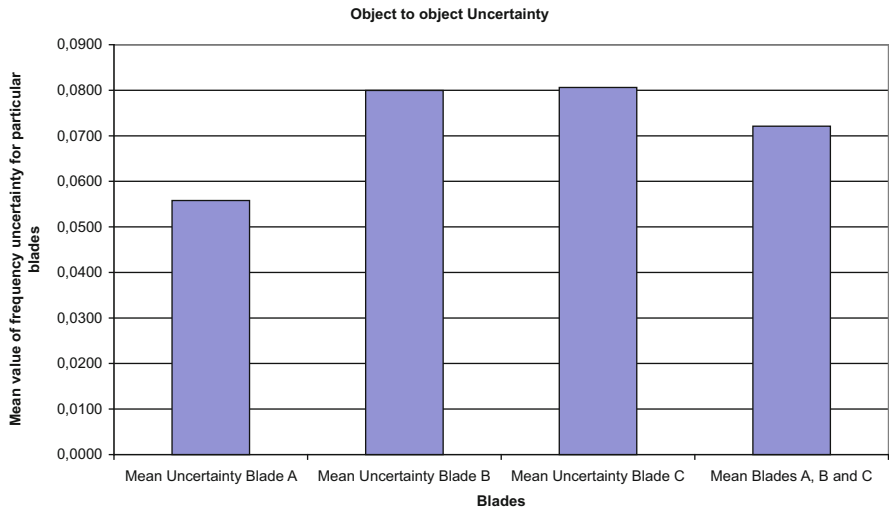


Fig. 22.57 Object-to-object frequency uncertainty levels

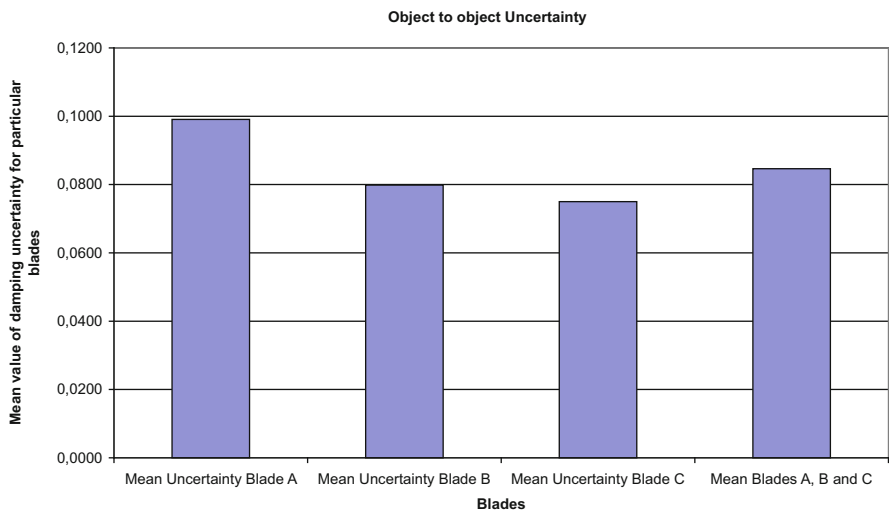


Fig. 22.58 Object-to-object damping uncertainty levels

non-contact techniques, therefore, the same values of estimated damping ratio could be expected for both models. This is not a case and what is more, the higher is the frequency of the mode the larger the difference becomes (see the trend line of the difference on the bottom part of Fig. 22.59).

The explanation for this could be looked into the plots of measured and reported (Raangs 2005; Visser 2004) data. Both reported laser and microflown measured velocity signals comparisons are done for the constant distance of a probe from a

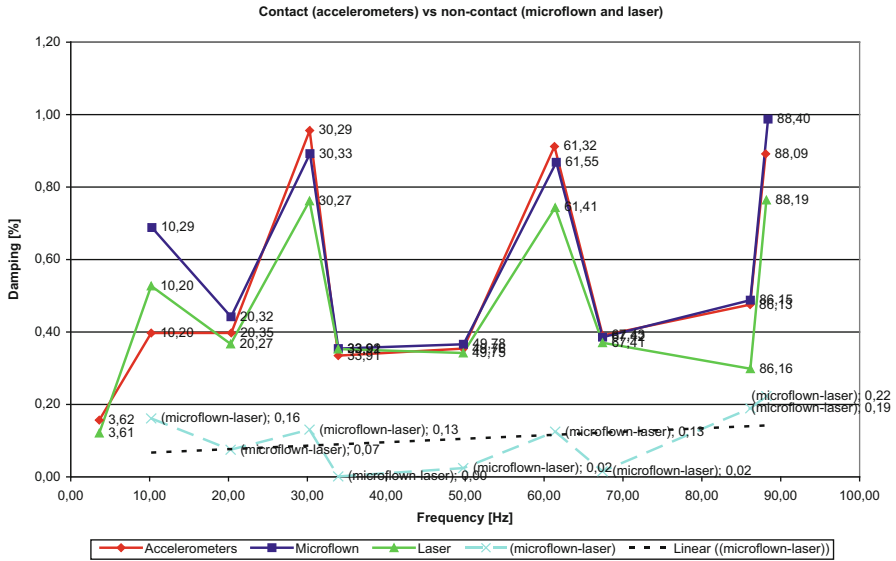


Fig. 22.59 Assessment of the laser vibrometer, microflow probes, and piezoceramic measurement on modal parameters. It is also assessment of acceleration and velocity measurement

surface. Due to the curvature of a large blade surface it is difficult to maintain exactly the same distance between the probe and the surface all over the measurements. Therefore this variability also contributes to a final modal model quality and especially the damping ratio is affected. Both the abovementioned reasons result in increasing differences of estimated mode shapes (see damping ratios in Fig. 22.59).

22.16 Conclusions and Contribution

Focus of this section was on identification and modeling of structural dynamics of structures using measured variable data for modal model parameter estimation of tested structures. Structures for applications in aerospace were investigated at level fully assembled system represented by three composite blades of main rotor of medium-size helicopter. For each blade the extensive experimental campaign was implemented resulting in development of variable test data collection. Measurement uncertainties were quantified by means of statistical analysis. Main contribution of this section is the new method of uncertainty assessment incorporating modal model parameters within frequency bandwidth. This is an extension of existing approach based on the uncertainty quantification based on the statistical analysis of particular measurand.

Results of measurements with particular applied technique and object brought the specific knowledge regarding the influence of the individual test. Different test

data variability was observed and quantified by means of standard uncertainty Type A. One of the main objectives of the presented research effort was to propose a new method of uncertainty assessment which would be applicable for the modal model. Modal model is a collection of individual modes composed of the mode shape, natural frequency, and damping ratio. Type A standard uncertainty quantifies each value separately. The proposed method extends this approach by means of statistical analysis and provides the overall uncertainty level within for entire modal model.

The overall objective of the presented research was to demonstrate the existence of the influence of variability present in structural dynamics measurement results on the accuracy of numerical model updating. The most important research objectives are listed below:

- Development of novel method of characterizing the test data variability (experimental data collection) by means of the “uncertainty level” indicator derived from mathematical statistics based analyses,
- Describing the dependencies between applied measurement technique and introduced “uncertainty level” by means of the mathematical statistics based methods.

References

- Adhikari S, Phani AS (2010) Random eigenvalue problems in structural dynamics: experimental investigations. *AIAA J* 48:1085–1097
- Adhikari S, Friswell M, Lonkar K (2009) Experimental case studies for uncertainty quantification in structural dynamics. *Probab Eng Mech* 24:473–492
- Agarwal RK (2012) Review of technologies to achieve sustainable (Green) aviation. INTECH Open Access Publisher
- Allen MS, Sracic MW (2010) A new method for processing impact excited continuous-scan laser doppler vibrometer measurements. *Mech Syst Signal Process* 24:721–735
- Amraoui YM, Lieven NA (2003) Noncontacting excitation and measurement of light structures. *J Vib Acoust* 125:114–119
- Arici Y, Mosalam KM (2005) Statistical significance of modal parameters of bridge systems identified from strong motion data. *Earthq Eng Struct Dyn* 34:1323–1341
- Bi S, Ren J, Wang W (2013) Elimination of transducer mass loading effects in shaker modal testing. *Mech Syst Signal Process* 38:265–275
- Cakar O, Sanliturk K (2005) Elimination of transducer mass loading effects from frequency response functions. *Mech Syst Signal Process* 19:87–104
- Capiez-Lernout E, Pellissetti M, Pradlwarter H (2006) Data and model uncertainties in complex aerospace engineering systems. *J Sound Vib* 295:923–938
- Carrella A, Ewins D (2011) Identifying and quantifying structural nonlinearities in engineering applications from measured frequency response functions. *Mech Syst Signal Process* 25:1011–1027
- Carrie TG, Dohrmann CR (1997) Support conditions, their effect on measured modal parameters
- Castanier MP, Pierre C (2006) Modeling and analysis of mistuned bladed disk vibration: current status and emerging directions. *J Propuls Power* 22:384–396
- Cauberghe B, Guillaume P, Dierckx B (2002) Identification of modal parameters from inconsistent data. In: Proceedings of the 20th international modal analysis conference (IMAC20), Anonymous

- Chen C, Duhamel D, Soize C (2006) Probabilistic approach for model and data uncertainties and its experimental identification in structural dynamics: case of composite sandwich panels. *J Sound Vib* 294:64–81
- Coleman HW, Steele WG (2009) Experimentation, validation, and uncertainty analysis for engineers. John Wiley & Sons Incorporated, New York, NY
- Collins JD, Hart GC, Haselman T (1974) Statistical identification of structures. *AIAA J* 12:185–190
- Degenhardt R, Castro SG, Arbelo MA (2014) Future structural stability design for composite space and airframe structures. *Thin-Walled Struct* 81:29–38
- Deraemaeker A, Reynders E, De Roeck G (2008) Vibration-based structural health monitoring using output-only measurements under changing environment. *Mech Syst Signal Process* 22:34–56
- Donders S (2008) Computer-aided engineering methodologies for robust automotive NVH design. https://irias.kuleuven.be/bitstream/1979/1698/1/donders_phd_20080221.pdf (Simulatiemethoden Voor Robuust Vibro-Akoestisch Ontwerp Van Voertuigen)
- Ewins DJ (2000) Modal testing: theory, practice, and application. Research Studies Press, Baldock, pp xiii, 562
- Fang S, Ren W, Perera R (2012) A stochastic model updating method for parameter variability quantification based on response surface models and Monte Carlo simulation. *Mech Syst Signal Process* 33:83–96
- Firrone C, Berruti T (2012a) An electromagnetic system for the non-contact excitation of bladed disks. *Exp Mech* 52:447–459
- Firrone CM, Berruti T (2012b) Non contact measurement system with electromagnets for vibration tests on bladed disks. In: Haq MZ (ed) Applied measurement systems. InTech, Rijeka, Croatia, pp 77–108
- Fraden J (2010) Handbook of modern sensors. Springer, NY
- Gao W (2007) Natural frequency and mode shape analysis of structures with uncertainty. *Mech Syst Signal Process* 21:24–39
- Garescì F, Catalano L, Petrone F (2006) Experimental results of a damage detection methodology using variations in modal parameters. *Exp Mech* 46:441–451
- Gayathri P, Umesh K, Ganguli R (2010) Effect of matrix cracking and material uncertainty on composite plates. *Reliab Eng Syst Saf* 95:716–728
- Govers Y, Link M (2010) Stochastic model updating—covariance matrix adjustment from uncertain experimental modal data. *Mech Syst Signal Process* 24:696–706
- Govers Y, Böswald M, Füllekrug U (2006) Analysis of sources and quantification of uncertainty in experimental modal data. In: International conference on noise and vibration engineering, ISMA2006, Katholieke Universiteit Leuven, Anonymous, pp 18–20
- Griffith DT, Carne TG (2007) Experimental uncertainty quantification of modal test data. In: 25th international modal analysis conference, Anonymous
- Heylen W, Lammens S, Sas P (1998) Modal analysis theory and testing. Departement Werktuigkunde, Katholieke Universiteit Leuven, Leuven
- Hodges DH (1990) Review of composite rotor blade modeling. *AIAA J* 28:561–565
- Hollaway LC, Teng J (eds) (2008) Strengthening and rehabilitation of civil infrastructures using fibre-reinforced polymer (FRP) composites. Elsevier
- Imregun M, Visser W, Ewins D (1995) Finite element model updating using frequency response function data: I. Theory and initial investigation. *Mech Syst Signal Process* 9:187–202
- BIPM & ISO (1995) BIPM, ISO Guide to the expression of uncertainty in measurement. International Organization for Standardization, Geneva
- Johnson W (2012) Helicopter theory. Courier Corporation, North Chelmsford, MA
- Kunz DL (1994) Survey and comparison of engineering beam theories for helicopter rotor blades. *J Aircr* 31:473–479
- Kwon K, Lin R (2004) Frequency selection method for FRF-based model updating. *J Sound Vib* 278:285–306
- LMS International (2007) LMS Test.Lab. LMS International, Leuven, Belgium

- Luczak M, Vecchio A (2007) UNVICO-2 Data variability and parameter uncertainty in composite shaft structural vibration measurement and numerical model updating. http://cordis.europa.eu/project/rcn/82499_en.html
- Luczak M, Vecchio A, Peeters B (2010) Uncertain parameter numerical model updating according to variable modal test data in application of large composite fuselage panel. *Shock Vib* 17:445–459
- Macdonald JH, Daniell WE (2005) Variation of modal parameters of a cable-stayed bridge identified from ambient vibration measurements and FE modelling. *Eng Struct* 27:1916–1930
- Maillot A, Luinge H, Schulte K (2011) CNT modified carbon fiber Reinforced composites for aerospace applications. In: Conference proceedings 16th international conference on composite structures (ICCS16), Porto, Portugal, Anonymous, pp 28–30
- Mao Z, Todd M (2013) Statistical modeling of frequency response function estimation for uncertainty quantification. *Mech Syst Signal Process* 38:333–345
- Marsh G (2010) Airbus A350 XWB update. *Reinf Plast* 54:20–24
- McShane JJ (2010) Metrology and reporting uncertainty. <http://www.thetruthaboutforensicscience.com/metrology-and-reporting-uncertainty/>
- Mehrez L, Moens D, Vandepitte D (2012) Stochastic identification of composite material properties from limited experimental databases, Part I: Experimental database construction. *Mech Syst Signal Process* 27:471–483
- Meyer C, Gaudin J (2010) Tools for manufacturing a composite panel, in particular of an aircraft fuselage. US Patent Application 12/968,579
- Michaelides PG, Fassois SD (2008) Stochastic identification of structural dynamics from multiple experiments—experimental variability analysis. *Analysis* 8, E10
- Michaelides P, Fassois S (2013) Experimental identification of structural uncertainty—an assessment of conventional and non-conventional stochastic identification techniques. *Eng Struct* 53:112–121
- Moens D, Vandepitte D (2005) A survey of non-probabilistic uncertainty treatment in finite element analysis. *Comput Methods Appl Mech Eng* 194:1527–1555
- Möller B, Reuter U (2008) Prediction of uncertain structural responses using fuzzy time series. *Comput Struct* 86:1123–1139
- Morris AS, Langari R (2012) Measurement and instrumentation: theory and application. Academic, Waltham
- Mottershead J, Mares C, Friswell M (2000) Selection and updating of parameters for an aluminium space-frame model. *Mech Syst Signal Process* 14:923–944
- Murugan S, Chowdhury R, Adhikari S (2012) Helicopter aeroelastic analysis with spatially uncertain rotor blade properties. *Aerosp Sci Technol* 16:29–39
- Nahvi H, Jabbari M (2005) Crack detection in beams using experimental modal data and finite element model. *Int J Mech Sci* 47:1477–1497
- Ni Y, Hua X, Fan K (2005) Correlating modal properties with temperature using long-term monitoring data and support vector machine technique. *Eng Struct* 27:1762–1773
- Noh H, Kwak H (2006) Response variability due to randomness in Poisson's ratio for plane-strain and plane-stress states. *Int J Solids Struct* 43:1093–1116
- Oberkampf W, DeLand S, Rutherford B, Diegert K, Alvin K (1999) A new methodology for the estimation of total uncertainty in computational simulation. AIAA Paper No 99-1612, Anonymous AIAA/ASME/ASCE/AHS/ASC structures, structural dynamics, and materials conference and exhibit
- Oberkampf WL, DeLand SM, Rutherford BM (2002) Error and uncertainty in modeling and simulation. *Reliab Eng Syst Saf* 75:333–357
- Onkar A, Upadhyay C, Yadav D (2007) Stochastic finite element buckling analysis of laminated plates with circular cutout under uniaxial compression. *J Appl Mech* 74:798–809
- Ozdoganlar OB, Hansche BD, Carne TG (2005) Experimental modal analysis for microelectromechanical systems. *Exp Mech* 45:498–506
- Papadimitriou C, Beck JL, Katafygiotis LS (2001) Updating robust reliability using structural test data. *Probab Eng Mech* 16:103–113

- Peeters B, Van der Auweraer H, Guillaume P (2004) The PolyMAX frequency-domain method: a new standard for modal parameter estimation? *Shock Vib* 11:395–409
- Pierro E, Mucchi E, Soria L (2009) On the vibro-acoustical operational modal analysis of a helicopter cabin. *Mech Syst Signal Process* 23:1205–1217
- Pintelon R, Guillaume P, Schoukens J (2007) Uncertainty calculation in (operational) modal analysis. *Mech Syst Signal Process* 21:2359–2373
- Piovan M, Ramirez J, Sampaio R (2013) Dynamics of thin-walled composite beams: analysis of parametric uncertainties. *Compos Struct* 105:14–28
- Raangs R (2005) Exploring the use of the Microflown. Ph.D. dissertation, University of Twente
- Raangs R, Druyvesteyn W, De Bree H (2003) A low-cost intensity probe. *J Audio Eng Soc* 51:344–357
- Reynolds P, Pavic A (2000) Impulse hammer versus shaker excitation for the modal testing of building floors. *Exp Tech* 24:39–44
- Rovšček D, Slavič J, Boltežar M (2013) The use of strain sensors in an experimental modal analysis of small and light structures with free–free boundary conditions. *J Vib Control* 19:1072–1079
- Sakellariou J, Fassois S (2008) Vibration based fault detection and identification in an aircraft skeleton structure via a stochastic functional model based method. *Mech Syst Signal Process* 22:557–573
- Sarangapani G, Ganguli R (2013) Effect of ply-level material uncertainty on composite elastic couplings in laminated plates. *Int J Comput Methods Eng Sci Mech* 14:244–261
- Schueller G (2007) On the treatment of uncertainties in structural mechanics and analysis. *Comput Struct* 85:235–243
- Siebert D, Mevel L, Goursat M (2008) Experimental validation of damage monitoring techniques in variable temperature conditions. In: *Proceedings of IMAC XXVI a conference and exposition on structural dynamics*
- Sinha JK, Friswell MI (2003) The use of model updating for reliable finite element modelling and fault diagnosis of structural components used in nuclear plants. *Nucl Eng Des* 223:11–23
- Sohn H, Dzwonczyk M, Straser EG (1999) An experimental study of temperature effect on modal parameters of the Alamosa Canyon Bridge. *Earthq Eng Struct Dyn* 28:879–897
- Soize C (2005) A comprehensive overview of a non-parametric probabilistic approach of model uncertainties for predictive models in structural dynamics. *J Sound Vib* 288:623–652
- Sracic MW, Allen MS, Sumali H (2012) *Topics in nonlinear dynamics*, vol 3. Springer, NY pp 269–286
- Sriramula S, Chryssanthopoulos MK (2009) Quantification of uncertainty modelling in stochastic analysis of FRP composites. *Compos A: Appl Sci Manuf* 40:1673–1684
- Szkudlarek W, Kahsin M, Luczak M (2009) Vibration-based damage detection in multi-layer composite material. In: *16th international congress on sound and vibration ICSV16*, Anonymous ICSV16
- Tirelli D, Vadillo I (2013) *Nondestructive testing of materials and structures*. Springer, New York, pp 999–1006
- Uhl T (1997) *Komputerowo wspomagana identyfikacja modeli konstrukcji mechanicznych*. Wydawnictwa Naukowo Techniczne, Warszawa, p 320
- Uhl T (2004) The use and challenge of modal analysis in diagnostics. *Diagnostyka* 30:151
- Van der Auweraer H, Leurs W, Mas P (2000) Modal parameter estimation from inconsistent data sets. In: *Proceedings, 18th international modal analysis conference*, Anonymous, pp 763–771
- Van der Auweraer H, Peeters B, Donders S (2005) Importance of uncertainty in identifying and using modal models. In: *Proceedings of the INCE symposium on managing uncertainties in noise measurements and prediction*, Anonymous
- Vankan W, de Wit A (2010) Assessment of optimisation strategies suited for application on composite fuselage panels. <http://reports.nlr.nl/xmlui/handle/10921/175>
- Vanlanduit S, Daerden F, Guillaume P (2007) Experimental modal testing using pressurized air excitation. *J Sound Vib* 299:83–98
- Verhaeghe W, Desmet W, Vandepitte D (2013) Interval fields to represent uncertainty on the output side of a static FE analysis. *Comput Methods Appl Mech Eng* 260:50–62

- Visser R (2004) A boundary element approach to acoustic radiation and source identification. University of Twente
- Wang W, Mottershead JE, Siebert T (2012) Frequency response functions of shape features from full-field vibration measurements using digital image correlation. *Mech Syst Signal Process* 28:333–347
- Warren C, Niezrecki C, Avitabile P (2011) Comparison of FRF measurements and mode shapes determined using optically image based, laser, and accelerometer measurements. *Mech Syst Signal Process* 25:2191–2202
- Xia Y, Hao H, Zanardo G (2006) Long term vibration monitoring of an RC slab: temperature and humidity effect. *Eng Struct* 28:441–452
- Yang S, Allen MS (2011) *Modal analysis topics*, vol 3. Springer, NY pp 47–64
- Yin ZJ, Tang ZC, Chen B (2011) Modal analysis and testing of large-span space steel structure. *Adv Mater Res* 154:386–389

Chapter 23

Temperature Compensation Methods for Elastic Wave Based SHM

Codruț Alexandru Dan and Paweł Kudela

23.1 Introduction

Pushed into the spotlight by the recent technological advances in sensing systems, Structural Health Monitoring (SHM) is emerging as a viable extension to classical Non-Destructive Testing (NDT). As defined in the first published SHM standard, health monitoring is, (SAE-International 2013)

the process of acquiring and analysing data from on-board sensors to determine the health of a structure.

Ultimately, SHM aims to integrate NDT on a structure, be it aircraft, automobile, ships or civil infrastructure. Such a scenario is expected to produce the shift from scheduled maintenance to condition based maintenance, a cheaper and more effective structural integrity surveillance strategy.

Many NDT methods have been developed in order to assess structural parts made out of metallic or composite materials. For this purpose techniques such as ultrasound testing (Dong et al. 2015; Meola et al. 2015), eddy currents (Heuer et al. 2015), active thermography (Meola et al. 2015), X-ray tomography (Uhry et al. 2015), terahertz spectroscopy (Dong et al. 2015, 2016; Opoka et al. 2015) and guided waves have been utilised.

We can distinguish two dimensions regarding the health of a structure (Farrar and Worden 2007; Rytter 1993; Staszewski et al. 2004)

- The health of the structure now. In this case, the questions to be answered are:
 - Is there any defect? (SHM level 1)
 - Where is the defect located? (SHM level 2)

C.A. Dan • P. Kudela (✉)

Institute of Fluid Flow Machinery, Polish Academy of Sciences, Fiszerza 14, Gdansk, Poland

e-mail: dancodrut@imp.gda.pl; pk@imp.gda.pl

- What are the type and dimension of defect (SHM level 3).
- And the health of the structure in the future, i.e.
 - Prognosis: what is the remaining useful life? (SHM level 4).

Elastic wave based structural diagnostic has the potential to reach all the four levels of SHM. This method is based on the fact that any kind of discontinuity like damage is a source of changes of guided wavefield. Due to long range distance of guided (elastic) waves and sensitivity to relatively small defects elastic wave based methods have been of particular interest of many researchers over the past years.

23.1.1 Elastic Wave Propagation

Elastic wave based SHM performance using sparse array systems has already been proven effective in many references (Giurgiutiu 2005; Ostachowicz et al. 2009; Staszewski et al. 2004; Su and Ye 2009), but the sensitivity of the method to environmental changes like temperature, moisture or loading is still a problem to be quantified.

Temperature is the most detrimental environmental effect (Croxford et al. 2007, 2010; Konstantinidis et al. 2006; Lu and Michaels 2005) because, as it will be shown here, changes in temperature expected to occur naturally, even during the course of the day, can cause signal distortions that practically disable the capabilities of an elastic wave based SHM system.

Elastic waves are mechanical harmonic perturbations that propagate through a medium that has inertia and elasticity. By means of excitation forces, particles that are displaced can transfer momentum to adjoining particles whilst are themselves restored to their original position (Parker 2003). When elastic waves propagate, the energy of elastic deformation is transferred between particles without any flow of matter. Every harmonic wave has amplitude and a vibration frequency of the particles. Depending on the medium travelled, the wave will have a characteristic wavelength, phase and group velocities, which will be determined by laws governing the distribution of displacements and stresses over the wave front. There are two basic types of elastic waves that are categorised in terms of the movement of the particles with respect to the propagation direction:

Pressure, or longitudinal, waves in which the particles vibrate in the direction of the propagation. For a 3D structure, node locations (i.e. particles that don't move) extend across the entire cross-section (Fig. 23.1-left). Particles moving towards the node tend to come closer together and the local particle density increases (compression) while the particles moving outward the node come further apart (rarefaction).

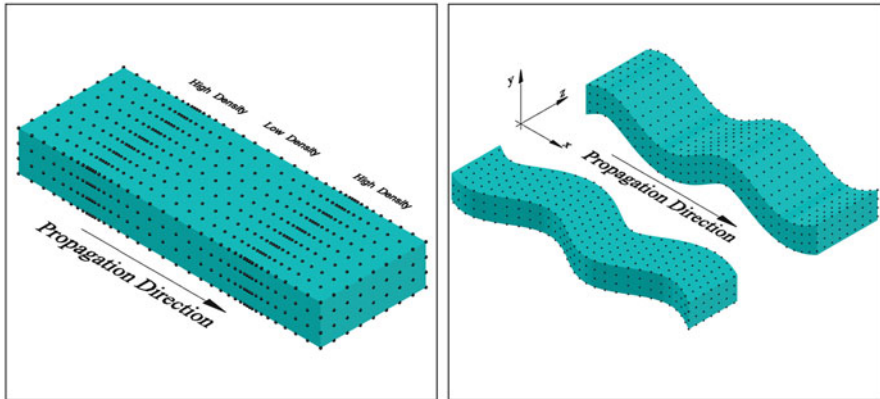


Fig. 23.1 Pressure (*left*) and shear (*right*) waves

Shear, or transverse, waves in which the particles vibrate perpendicular to the propagation direction. These can have a flexural behaviour, when the direction of the particle movement is in the direction of the thickness and shear horizontal (SH) when the movement of the particles is perpendicular to both propagation direction and thickness direction.

Usually, in guided wave based SHM, diagnostic frequencies are in the range where the wavelength is comparable with the structural dimensions. In such cases, shear and pressure waves are coupled at the boundaries and the resulting displacement field is a “combination” of uniform compression or extension and pure shear deformation. The waves formed in such a way are referred to as *guided waves*.

The most important types of elastic waves are Rayleigh and Lamb waves.

23.1.2 Lamb Waves

Lamb waves (Lamb 1917), named in honour of their discoverer, Horace Lamb, are guided waves that travel between the surfaces of a plate. Lamb waves dispersion relations result imposing that stresses at the boundaries vanish.

The dispersion relations can be represented in two ways, as a frequency-wavenumber $\omega-k$ plot (Fig. 23.2), or in a phase velocity versus frequency-thickness product $c_p - fd$. As it can be seen in Fig. 23.3, the Lamb waves are dispersive, since the phase velocity depends on the frequency of the wave. Also, multiple modes exist at a given frequency-thickness product. Moreover, the number of modes increases with the increase in the frequency of the wave. From the point of view of SHM these characteristics are drawbacks, because they translate in an increased complexity of the recorded time traces, which are more difficult to process.

Fig. 23.2 Lamb waves frequency–wavenumber relationship

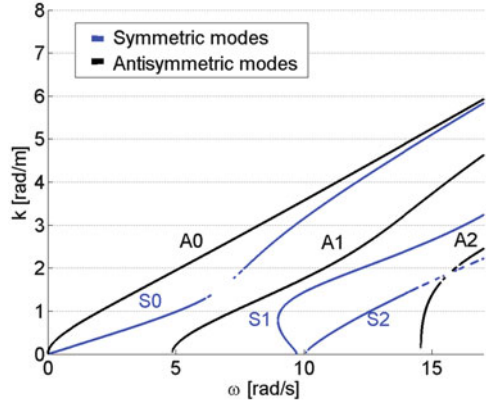
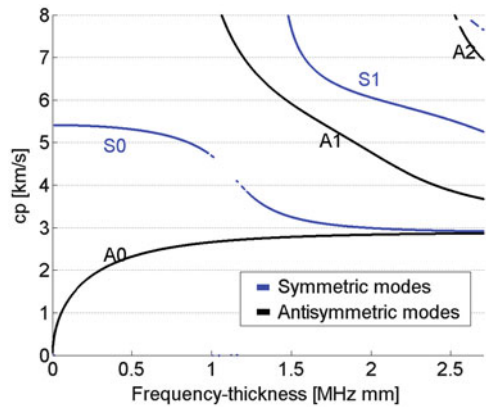


Fig. 23.3 Lamb waves dispersion curves



23.2 Temperature Effects on Lamb Waves

Solids upon change of temperature experience modifications in their mechanical properties, of interest being here the elastic and shear moduli and the density, which in turn cause changes in the two main elastic wave properties of any given material, wave attenuation and wave velocity. Thus, the problem of compensation of temperature effects on guided waves can be split into two problems, the change in the phase of the recorded time signal with temperature, occurring with the modification of bulk shear and longitudinal velocities and changes in amplitude of the propagating waves with temperature, occurring not only as a result of the modifications in the wave attenuation coefficient but also as a result of changes occurring in sensor properties and in the bonding layer (Marzani and Scalea 2011; Scalea and Salamone 2012).

There are several aspects that make the analytic compensation of temperature effect on wave propagation in complex structures a challenging endeavour:

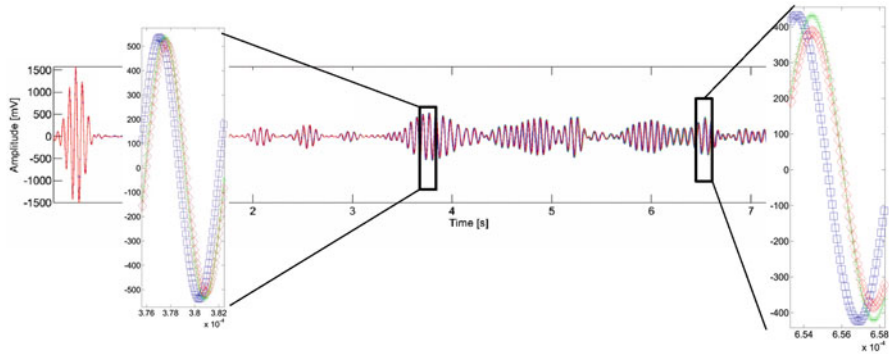


Fig. 23.4 Temperature effects on Lamb wave signal (blue—lower temperature recording, red—higher temperature recording)

The recorded time traces stretch with propagation distance, Fig. 23.4. Any correction of the baseline time traces is difficult with signals containing multiple reflections. Even if boundary reflection paths can be determined, reflections of structural features like bolts, rivets or reinforcing elements are difficult to anticipate. Thus, the prediction of the time shift in the later arrivals in the time signal is challenging.

The change in the wave velocity with temperature depends on frequency of the wave. Lower frequencies will be less affected by temperature than higher frequencies. That is, considering $c_{p0} = c_p(\theta_0)$ and S_{c_p} the phase velocity temperature coefficient defined as,

$$S_{c_p} = \frac{1}{c_{p0}} \frac{\delta c_p}{\delta \theta} \tag{23.1}$$

and developing in terms of angular frequency (see Dan 2015) we obtain

$$\frac{\delta \omega}{\delta \theta} = \frac{\omega^2}{\omega_0} (\alpha - S_{c_p}) \tag{23.2}$$

Equation (23.2) can be computed at reference conditions,

$$\frac{\delta \omega}{\delta \theta} = \left. \frac{\delta \omega}{\delta \theta} \right|_{\theta=\theta_0} = \omega_0 (S_{c_p} - \alpha) \tag{23.3}$$

The new *observed* frequency $\omega(\theta)$ can be predicted using only one parameter, the frequency-temperature coefficient or, as it will be further referred, the *Rayleigh-Lamb thermal coefficient*—given by:

$$S_\omega = \frac{1}{\omega_0} \frac{\delta\omega}{\delta\theta} = S_{c_p} - \alpha \quad (23.4)$$

S_ω incorporates both thermal expansion effect and the change in the phase velocity with temperature. Usually, the effect of thermal expansion is considerably smaller (at least one order of magnitude) than the effect of the phase velocity. In metals the difference between the two is of two orders of magnitude, thus the effect of the thermal expansion can be ignored. Also, the coefficient underlines from a physical point of view the effect that one can expect to get in a registered signal, as a result of environmental temperature change:

- the change in phase follows the change in temperature—if temperature increases, the signals will present phase delay, and vice versa;
- the change in phase has an opposite trend with thermal expansion of the body.

The Rayleigh–Lamb thermal coefficient has been determined analytically [full development available in Dan (2015)],

$$S_\omega = S_\omega^A = S_\omega^S = S_{c_L} \frac{\hat{C}}{\hat{C} + \hat{D} + \hat{E}} + S_{c_T} \frac{\hat{D} + \hat{E}}{\hat{C} + \hat{D} + \hat{E}} \quad (23.5)$$

where

$$\begin{aligned} \hat{C}(h, \omega) &= \frac{4k^2\omega^2 p_0}{c_{T_0}^2 q_0} \\ \hat{D}(h, \omega) &= \frac{4k^2\omega^2 q_0}{c_{L_0}^2 p_0} \\ \hat{E}(h, \omega) &= \frac{4\omega^2 \left(-2k^2 + \frac{\omega^2}{c_{T_0}^2} \right)}{c_{T_0}^2}. \end{aligned}$$

The above relation represents the straightforward computation of the Lamb wave thermal coefficient from the temperature material coefficients, if the material properties and the corresponding thermal coefficients are available.

In the equations above, c_{T_0} , c_{L_0} are the velocities of the pressure and shear waves (see Sect. 23.1.1) computed at reference temperature θ_0 . They are given by (λ and μ are the Lamé coefficients and ρ is the material density),

$$c_L^2(\theta) = \frac{\lambda(\theta) + 2\mu(\theta)}{\rho(\theta)} \quad \text{and} \quad (23.6)$$

$$c_T^2(\theta) = \frac{\mu(\theta)}{\rho(\theta)} \quad (23.7)$$

Table 23.1 Lamb wave thermal coefficient for various materials

Material	α [$10^{-5} \frac{1}{^\circ\text{C}}$]	S_Y [$10^{-4} \frac{1}{^\circ\text{C}}$]	S_G [$10^{-4} \frac{1}{^\circ\text{C}}$]	S_{c_L} [$10^{-4} \frac{1}{^\circ\text{C}}$]	S_{c_T} [$10^{-4} \frac{1}{^\circ\text{C}}$]	S_ω [$10^{-4} \frac{1}{^\circ\text{C}}$]
Aluminium	2.31	-4.8	-5.2	-1.2	-2.2	-2.54
Copper	1.65	-3	-3.1	-0.9	-1.3	-1.72
Gold	1.42	-4.8	-3.3	-18.9	-1.4	-3.1
Iron	1.18	-2.3	-2.8	-0.1	-1.2	-1.2
Platinum	0.88	-0.98	-1	-0.27	-0.36	-0.62
Silver	1.89	-7.5	-4.5	-13.8	-1.9	-4.6
Steel (general)	1.2	2.4	2.6	-0.69	-1.12	-1.3

While q_0 and p_0 are phase factors notations utilised for equations simplification, $p^2 = \frac{\omega^2}{c_L^2} - k^2$ and $q^2 = \frac{\omega^2}{c_T^2} - k^2$.

Table 23.1 presents the Lamb wave thermal coefficient, S_ω for various metallic materials where α is the thermal expansion coefficient, S_Y is Young’s modulus thermal coefficient and S_G is the shear modulus thermal coefficient.

23.3 The Equivalent Wave Method for Phase Delay Compensation

Firstly, the methods developed to find the phase velocity of the wave at any temperature are introduced.

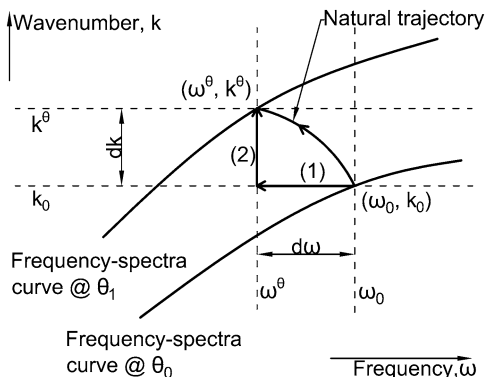
The main idea behind the proposed method starts from the assertions that:

- Lamb wave velocity has a decreasing linear trend with temperature
- for every frequency ω exists a phase velocity c_p that satisfies the Rayleigh–Lamb equations.

The Equivalent Wave Method (EWM) proposes to look for a new frequency, ω^θ , that is equivalent (hence the name) to the changes in wave speed caused by temperature to the initial wave at ω_0 . This idea is represented in Fig. 23.5.

To predict the behaviour of the Lamb waves at a given temperature θ knowing the behaviour at θ_0 , it is necessary to (Step 1) implement the frequency-temperature model [Eq. (23.2)] into the new-variable Rayleigh–Lamb equations, and (Step 2) to solve for k^θ using $\omega^\theta = \omega^\theta(\omega, \Delta\theta)$.

Fig. 23.5 The two step Equivalent Wave Method



23.4 Compensation of Temperature Effects on Lamb Wave Signals

The compensation strategy relies on the idea that the compensation should be performed in frequency domain rather than in time domain, in order to discard the necessity for the distance of propagation.

To compensate for environmental temperature changes, the following parameters need to be known a priori:

- the temperature change, $\Delta\theta$, between the baseline state of the structure and the current state;
- the ultrasonic thermal coefficient, S_ω , of the structure. Not always the relevant material coefficients are available to determine S_ω using the above relations. In fact, in practical situations, prior knowledge on material temperature coefficients S_Y , S_μ and S_ρ does not exist. In such cases a prior calibration procedure is needed to determine experimentally the value of S_ω . As a general approach, a calibration method should utilise the proposed compensation model to optimise for S_ω . A detailed procedure can be found in Dan (2015).

First, the signal is written in frequency domain using the discrete Fourier transform (Prandoni and Vetterli 2008),

$$X[k] = \sum_{n=0}^N x[t] \omega_N^{nk} \tag{23.8}$$

where $\omega_N = e^{\frac{(-2\pi i)}{N}}$ is the N th root of unity.

In order to increase accuracy of the compensation, the recorded signal $x(t)$ is zero-padded. This will approximate better the DFT of the signal.

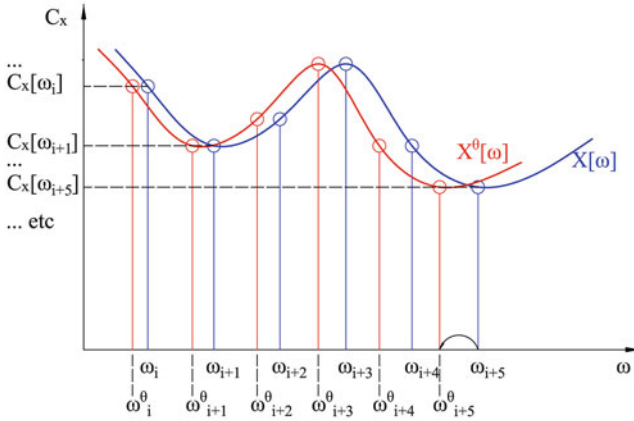


Fig. 23.6 Signal temperature compensation procedure

The Fourier coefficients of the signal are retrieved,

$$C_x(\omega) = \frac{1}{N}|X(\omega)| \tag{23.9}$$

and each coefficient is shifted from ω_0 to ω^θ , where

$$\omega^\theta = \omega_0 e^{S_\omega \Delta\theta} \tag{23.10}$$

This procedure is described graphically in Fig. 23.6.

Thus, the shifted Fourier coefficients of the compensated signal are obtained: $C_x^\theta = C_x[\omega^\theta]$, which will give the compensated spectrum, $X^\theta[k]$.

Finally, the compensated signal is obtained by using the inverse Fourier transform on the new, compensated spectrum:

$$x^\theta[t] = \sum_{n=0}^N X^\theta[k] \omega_N^{nk} \tag{23.11}$$

23.5 Experiments and Validation

An experimental analysis was conducted on a 1 mm thick Aluminium plate of planar dimensions 1 m by 1 m with SMART Layer[®] and SMART Suitcase from Acellent Technologies, Inc. (Lin et al. 2005). Measurements over large temperature range show that the time of arrival change with temperature is linear for the same moment in time, Fig. 23.7.

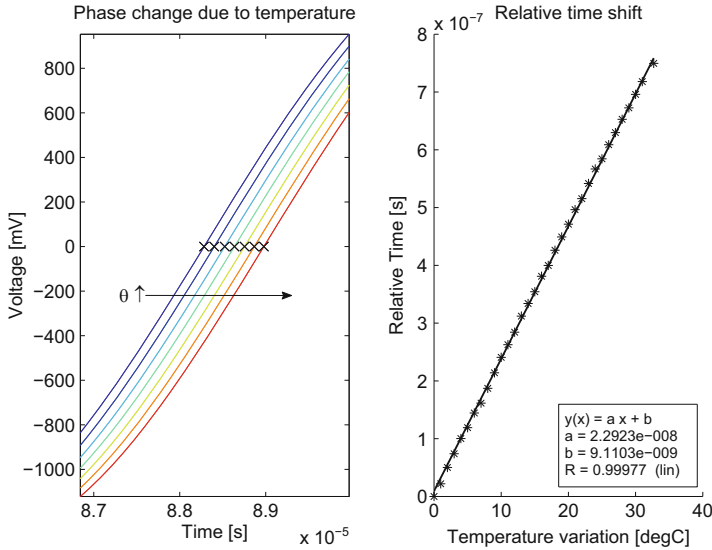


Fig. 23.7 Phase change and linear behaviour of thermally induced time shift

On the other hand, the beginning parts of the signal are less affected than the ones accounting for longer time of flight, so the overall effect is perceived as a time-stretch.

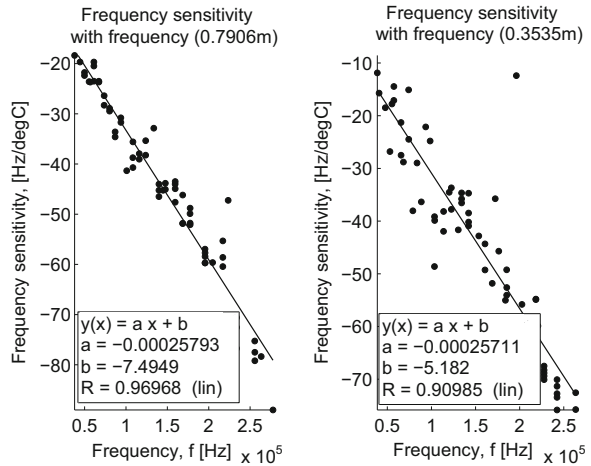
This observation is explained theoretically by the Croxford et al. model (Croxford et al. 2007). The theoretical model is relating time of arrival with temperature change through the derivation of the speed equation with respect to temperature. This approach, though, enables the correction only of first incoming packages, and for a robust detection strategy, this is not enough.

One way to circumvent the problem of distance dependence in the model is, as mentioned, to perform the correction not in the time domain but in the frequency domain.

The rate of apparent change of frequency with temperature has been seen to change with frequency. Plots of the recorded frequency sensitivities with respect to frequency unveil the linear characteristic of this change, Fig. 23.8. An important observation is that the second order dependency, the slope of the frequency sensitivity versus frequency line, is not dependent on the propagation distance. The slope of the linear fit in Fig. 23.8 represents the Lamb wave thermal coefficient, S_ω given by,

$$S_\omega = \frac{1}{\omega_0} \frac{\delta \omega}{\delta \theta} \tag{23.12}$$

Fig. 23.8 Frequency thermal sensitivity over a 200 kHz band



23.5.1 Damage Detection in Temperature Variable Environment

In guided wave based structural monitoring, damage is detected through identification of special patterns of propagation of the travelling wave (reflection, attenuation, mode conversion, etc.).

Diagnostic signals were collected with and without damage and detection and localisation strategies relying on baseline subtraction were utilised.

Signals were recorded at various room temperatures, in a range of 10 °C temperature change. It is shown that only 2 °C of change in environment temperature manage to critically disturb the diagnostic procedure. The compensation strategies proposed manage to retrieve the damage information that would otherwise be concealed by the thermal changes of the structure.

First we show a qualitative assessment presenting the compensation procedure over 10 °C together with the residual comparison between compensated and uncompensated signals. Figure 23.9 shows that the compensation strategy proposed improved by an average of -14 dB the residual resulting from subtraction of two sets of data registered on undamaged plate, but at a 10 °C temperature difference.

On the 1 mm Aluminium-alloy plate with installed SMART Layer®, signals for each sensor-actuator path were collected. In total, 132 unique time traces can be recorded for damage detection. Signals of sound structure (baselines) at a reference temperature were collected.

Subsequently, damage was introduced on the plate and time traces were recorded at various room temperatures. The damage was simulated using various neodymium magnets that were attached to the plate in various positions. The mass of the magnets, regarded as the level of damage, varied from 0.12 to 1.6% of the 1 mm Aluminium plate mass.

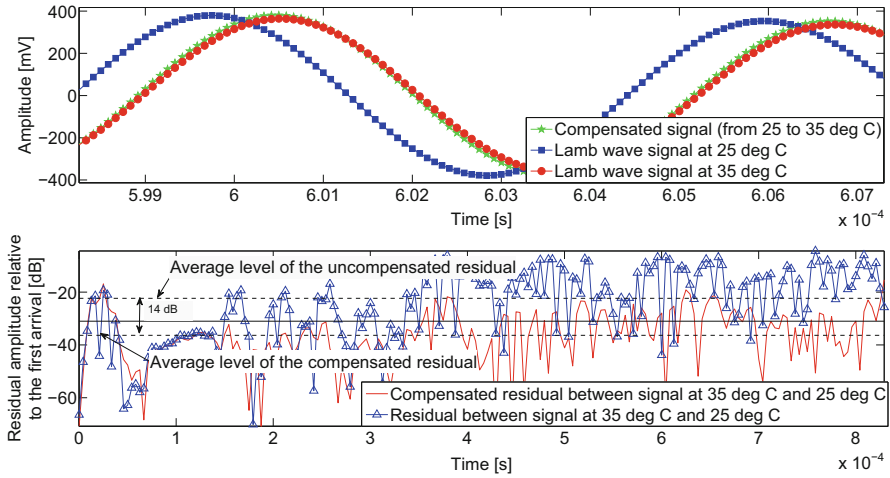
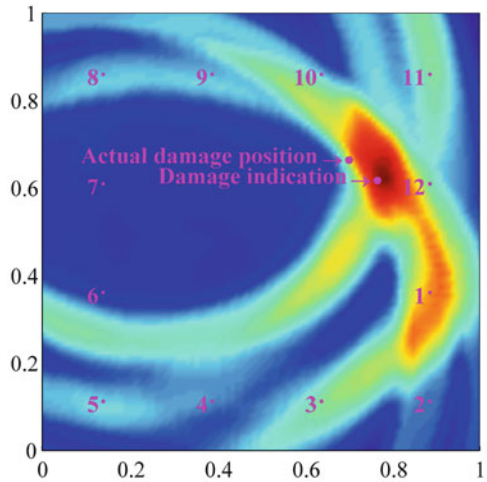


Fig. 23.9 Temperature compensation of Lamb wave signals

Fig. 23.10 Control test:
baseline at 26.3 °C vs
damage at 26.4 °C



The compensation strategy was employed on all 132 paths of the SMART Layer[®], and damage influence maps showing the location and level of damage were constructed (Kudela et al. 2008; Malinowski et al. 2008; Michaels and Michaels 2007; Ostachowicz et al. 2009). Figures 23.10, 23.11, and 23.12 present the damage detection using the S0 mode propagation with and without compensation.

Fig. 23.11 Environmental effects test: baseline at 24.7°C vs damage at 26.4°C

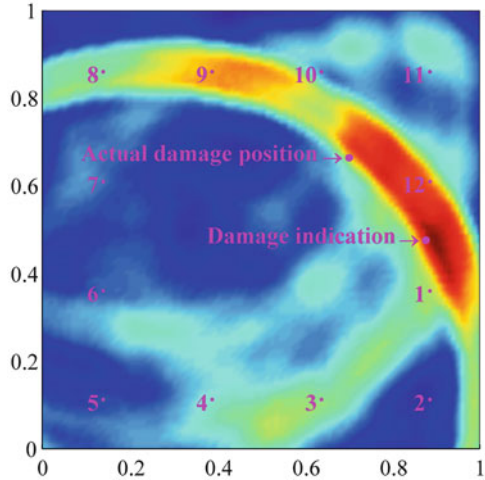
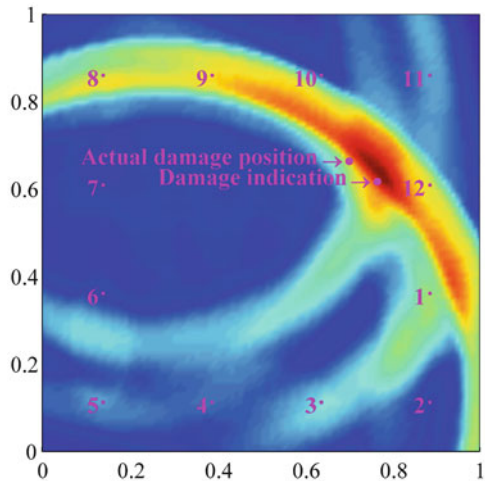


Fig. 23.12 Compensation validation: corrected baseline at 24.7°C vs damage at 26.4°C



23.6 Conclusions

Structural Health Monitoring is one of the main objectives behind the development of smart structures, and elastic wave based SHM is the most promising in terms of cost versus benefits, having the potential of reaching the highest levels of insight of structural diagnostic.

It is shown that temperature compensation of guided wave based SHM systems is compulsory for components exposed to environmental conditions, since only few degrees of change in the ambient temperature are capable of disturbing entirely the damage detection procedure.

The existing compensation models have been extended with a frequency compensation method that is independent on travel distance and by providing analytic expressions relating the phase delay observed with sparse array sensor networks with the material thermal coefficients. The phase distortion observed with sparse array sensor systems can be expressed in terms of only one parameter, the Rayleigh–Lamb thermal coefficient. This is further utilised as fundamental building block for the development of the compensation methods.

The new compensation strategy for the temperature effects on Lamb waves, the Equivalent Wave Method (EWM) allows the prediction of the Lamb wave behaviour with temperature without prior knowledge on the temperature dependencies of the material properties. Analytic simulations show a good agreement with measurements.

The experiments considered to observe the wave behaviour with temperature revealed that the phase velocity varies linearly with temperature. The linearity observed in the Lamb wave velocity is transferred from the linearity of the shear and longitudinal velocities which compose the normal wave.

For 1 mm thick Aluminium plate, the proposed signal processing improved by an average of -14 dB the residual resulting from subtraction of two sets of data recorded at a 10 °C temperature difference.

The frequency-domain based temperature compensation strategy is independent on travel distance, thus it can be implemented on an entire sensor array, like a SMART Layer[®]. It has been shown that the correction of the thermally induced phase distortion alone ensures the necessary level of compensation for an S_0 based damage detection for the 1 mm thick Aluminium plate.

References

- Croxford A, Wilcox P, Drinkwater B, Konstantinidis G (2007) Strategies for guided-wave structural health monitoring. *Proc R Soc A Math Phys Eng Sci* 463(2087):2961–2981 [Online]. Available: <http://rspa.royalsocietypublishing.org/cgi/doi/10.1098/rspa.2007.0048>
- Croxford AJ, Moll J, Wilcox PD, Michaels JE (2010) Efficient temperature compensation strategies for guided wave structural health monitoring. *Ultrasonics* 50(4–5):517–28 [Online]. Available: <http://www.ncbi.nlm.nih.gov/pubmed/20031182>
- Dan CA (2015) Elastic wave propagation including temperature effect compensation. Ph.D. Dissertation, Institute of Fluid Flow Machinery, Polish Academy of Sciences, 2015
- Dong J, Kim B, Locquet A, McKeon P, Declercq N, Citrin DS (2015) Nondestructive evaluation of forced delamination in glass fiber-reinforced composites by terahertz and ultrasonic waves. *Compos Part B* 79:667–675
- Dong J, Locquet A, Citrin D (2016) Enhanced terahertz imaging of small forced delamination in woven glass fibre-reinforced composites with wavelet de-noising. *J Infrared Millim Terahertz Waves* 37:289–301
- Farrar C, Worden K (2007) An introduction to structural health monitoring. *Phil Trans R Soc A* 365:305–315
- Giurgiutiu V (2005) Tuned lamb wave excitation and detection with piezoelectric wafer active sensors for structural health monitoring. *J Intell Mater Syst Struct* 16(4):291–305 [Online]. Available: <http://jim.sagepub.com/cgi/doi/10.1177/1045389X05050106>

- Heuer H, Schulze M, Pooch M, Gäßler S, Nocke A, Bardl G (2015) Review on quality assurance along the CFRP value chain – non-destructive testing of fabrics, preforms and CFRP by HF radio wave techniques. *Compos Part B* 77:494–501
- Konstantinidis G, Drinkwater BW, Wilcox PD (2006) The temperature stability of guided wave structural health monitoring systems. *Smart Mater Struct* 15(4):967–976 [Online]. Available: <http://stacks.iop.org/0964-1726/15/i=4/a=010?key=crossref.fa69455081060dae9cfe4bfea3e10c56>
- Kudela P, Ostachowicz W, Żak A (2008) Damage detection in composite plates with embedded PZT transducers. *Mech Syst Signal Process* 22(6):1327–1335 [Online]. Available: <http://linkinghub.elsevier.com/retrieve/pii/S0888327007001173>
- Lamb H (1917) On waves in an elastic plate. *Proc R Soc* 93:114–128
- Lin M, Qing X, Kumar A, Beard SJ (2005) Smart layer and smart suitcase for structural health monitoring applications. Technical Report 408, Missile Defense Agency, Arlington, VA, USA
- Lu Y, Michaels JE (2005) A methodology for structural health monitoring with diffuse ultrasonic waves in the presence of temperature variations. *Ultrasonics* 43(9):717–731 [Online]. Available: <http://www.ncbi.nlm.nih.gov/pubmed/15992847>
- Malinowski P, Wandowski T, Ostachowicz W (2008) Multi-damage localization with piezoelectric transducers. In: *Proceedings of the 4th European workshop on structural health monitoring*, Krakow, Poland, pp 716–723
- Marzani A, Scalea FLD (2011) Numerical prediction and experimental verification of temperature effect on plate waves generated and received by piezoceramic sensors. *Mech Syst Signal Process* 30:204–2017 [Online]. Available: [doi:10.1016/j.ymsp.2011.11.003](https://doi.org/10.1016/j.ymsp.2011.11.003)
- Meola C, Boccardi S, Carlomagno GM, Boffa ND, Monaco E, Ricci F (2015) Nondestructive evaluation of carbon fibre reinforced composites with infrared thermography and ultrasonic. *Compos Struct* 134:845–853
- Michaels JE, Michaels TE (2007) Guided wave signal processing and image fusion for in situ damage localisation in plates. *Wave Motion* 44:482–492
- Opoka S, Wandowski T, Malinowski P, Ostachowicz W (2015) Terahertz spectroscopy for damage assessment in composite materials. In: *4th International conference on engineering against failure (ICEAF IV)* 24–26 June 2015
- Ostachowicz W, Kudela P, Malinowski P, Wandowski T (2009) Damage localisation in plate-like structures based on PZT sensors. *Mech Syst Signal Process* 23(6):1805–1829 [Online]. Available: <http://linkinghub.elsevier.com/retrieve/pii/S0888327008002719>
- Parker SP (2003) *McGraw-Hill dictionary of scientific & technical terms*. McGraw-Hill, New York
- Prandoni P, Vetterli M (2008) *Signal processing for communications*, 1st edn. EPFL Press, Lausanne
- Rytter A (1993) *Vibration based inspection of civil engineering structures*. Ph.D. Dissertation, Department of Building Technology and Structural Engineering, Aalborg University, Denmark
- SAE-International (2013) Arp6461: guidelines for implementation of structural health monitoring on fixed wing aircraft, September 2013
- Scalea FLD, Salamone S (2012) Temperature effects in ultrasonic lamb wave structural health monitoring systems. *Am J Phys* 80(913):161–174 [Online]. Available: <http://dx.doi.org/10.1119/1.4733357>
- Szaszewski WJ, Boller C, Tomlinson GR (2004) *Health monitoring of aerospace structures, smart sensor technologies and signal processing*. Wiley, New York
- Su Z, Ye L (2009) *Identification of damage using lamb waves*, 1st edn. Springer, Berlin
- Uhry C, Guillet F, Duvauchelle P, Kaftandjian V (2015) Optimisation of the process of X-ray tomography applied to the detection of defects in composites materials. In: *Proceedings of digital industrial radiology and computed tomography (DIR 2015)*

Index

A

- Abaqus, 288
- Acoustic box, 329–330
- Active Gurney flaps, 15–16, 105–106
 - actuation mechanism, 106–107
 - dynamic force analysis, 111–118
 - position analysis, 107–109
 - velocity analysis, 109–111
 - blade section, 118–120
 - flight test data, 73–75
 - forward flight
 - elastic blade, 78–85
 - rigid blade, 75–78, 82
 - numerical methods, 70
 - coupling with structural dynamics, 71
 - trimming method, 72–73
 - W3 main rotor, 73
- Actuation mechanism, 106–107
 - dynamic force analysis, 111–118
 - position analysis, 107–109
 - velocity analysis, 109–111
- Adjoint (AD) method
 - advantages and disadvantages, 339–340
 - aircraft and rotorcraft applications, 341–342
 - flow equations, 339
 - forward mode, 340–341
 - HMB2 flow solver, 342–343
 - Hover computations
 - ONERA 7AD rotor, inviscid flow, 350–352
 - S-76 rotor, 353
 - treatment, 349–350
 - implementation, 340
 - linear problem, 338
 - reverse mode, 341
 - sensitivity problem, 338–339
 - tangent formulation
 - fixed-point iterative schemes, 343
 - flow-equation residual Jacobian, 344
 - Jv , 344–347
 - $J^T v$, 347–348
- Aerodynamic noise, 325, 329, 332
- Aerodynamic performance, 40, 43, 45, 46
- Aeroelastic calculations
 - application, 61–62
 - elastic blade, 62–66
- AH-1G helicopter rotor blade, 166, 167
- Airflow, 331–332
- Airfoils
 - analysis, 126
 - Caradonna–Tung model rotor, 149
 - computational domain, 150
 - contour map and numerical validation, 151
 - flow separation, 149, 152
 - friction coefficient and streamlines, 151–153
 - polar graph, 151, 154
- Air-jet vortex generators (AJVGs), 7–9
 - configuration, 142–144
 - schematic view, 139
- AJVGs. *See* Air-jet vortex generators (AJVGs)
- Aleatory uncertainty, 441
- Algebraic multigrid (AMG) method, 126, 268
- ANSYS Fluent, 204–205
- ANSYS Mechanical, 288
- APA500L piezostack actuator, 106
- Average over rotation, 288

B

- Bailey model, 98
- Bistable linear moving magnet (BLMM)
 - actuator, 177–178
- BLD software, 399–400
- Bousman's dynamic stall function, 4, 5
- Box refinements, 329

C

- Cantilever blade with hinges, 399
- Caradonna and Tung (C–T) model
 - experimental data, 160
 - flow control case, 163–166
 - reference case, 160–163
- CEDRAT Technologies (CEDRAT nd), 177
- Cell-centered finite volume approach, 342–343
- CFD. *See* Computational fluid dynamic (CFD)
- Collective mode, 404
- Combined beam-3D FEM model, 402
- Complex mode indicator function (CMIF), 453, 456
- Composite materials, 439
- Computational aeroacoustics (CAA), 329
- Computational fluid dynamic (CFD), 325, 329, 332

AJVG

- configuration, 142–144
 - schematic view, 139
- analysis, 266–268
- forward flight conditions
 - flow control case, 169–172
 - reference case, 168–169
- hover conditions
 - flow control case, 163–166
 - reference case, 160–163
- mesh updating, 272–274
- NACA 4415 airfoil, 299–300
- numerical methods, 23–24
 - HMB solver, 24–25
 - implementation, 26–33
 - proposed methods, 25–26
 - two dimensions, 33–38

RVG

- boundary layer, 147–149
 - configuration, 143–145
 - pressure distribution, 147, 149
 - schematic view, 139
 - separation control, 148, 150
 - shock wave, 145
 - 3D view, 146
 - 2D view, 145
- simulations, 204, 205

3D computations

- observations, 45–49
- pitching–translating wing computations, 41–45
- static computations, 38–41
- turbine blades, 315–317
- W3-Sokol rotor, 56, 79, 89
- Computer-aided design (CAD) model, 325–326
- Computer Aided Engineering tools, 433
- Constant volume tetrahedron (CVT) method, 53, 71
- Continuous approach (CA)
 - advantages and disadvantages, 339–340
 - flow equations, 339
 - forward mode, 340–341
 - implementation, 340
 - reverse mode, 341
- CouplingEnvironment
 - best-fit interpolation method, 285
 - co-simulation problems, 285
 - coupling algorithms, 285
 - coupling analysis solutions, 285–286
 - simulation codes, 286–287
- Cyclic modes, 404
- Czech Technical University (CTU), 233

D

- Degree of freedom (DOF), 412, 417
- Discrete adjoint method
 - advantages and disadvantages, 339–340
 - aircraft and rotorcraft applications, 341–342
 - flow equations, 339
 - forward mode, 340–341
 - HMB2 flow solver, 342–343
 - hover computations
 - ONERA 7AD rotor, inviscid flow, 350–352
 - S-76 rotor, 353
 - treatment, 349–350
 - implementation, 340
 - linear problem, 338
 - reverse mode, 341
 - sensitivity problem, 338–339
 - tangent formulation
 - fixed-point iterative schemes, 343
 - flow-equation residual Jacobian, 344
 - Jv , 344–347
 - $J^T v$, 347–348
- Doppler effect, 366–367
- Dynamic mesh model, 125
- Dynamic stall vortex (DSV), 11

E

- Elastic wave propagation
 - pressure/longitudinal waves, 486, 487
 - shear/transverse waves, 487
- Element-based boundary conditions, 291
- Environmental effects test, 496, 497
- Epistemic uncertainty, 441
- Equivalent wave method (EWM), 491, 492
- Euler approach. *See* Passenger car model
- Experimental modal analysis (EMA), 412, 431
- Experimental modal models
 - estimation
 - CMIF, 453, 456
 - experimental damping, 456, 458, 459
 - experimental natural frequencies, 456, 457, 459
 - FRF synthesis, 453, 456, 457
 - MAC, 453
 - MIF, 453
 - MMIF, 453, 455
 - MOV, 453
 - MP, 453
 - MPC, 453
 - MPD, 453
 - PolyMAX frequency domain algorithm, 451
 - stabilization diagrams, 455, 456
 - structural poles, 451, 452
 - SUM function, 450–452, 455, 456
 - Type A evaluation, 454
 - Type A standard uncertainty, 454–455
 - uncertainty of measurement, 454
 - MAC matrix plots, 457, 460
 - mode shapes, 456, 459
 - quality verification, 448–450
- Experimental model collection
 - quality verification
 - assessment, 448
 - coherence functions, 449–450, 452
 - curvature correction algorithm, 450
 - data quality evaluation, 449
 - FRF plot, 449
 - microflown probes measurement, 450, 451
 - piezoceramic accelerometers
 - measurement, 450, 451
 - sensor-structure wax connection, 449
 - systematic error, 448
 - test setups, 447

F

- FEA model. *See* Finite element analyses (FEA) model
- FEM. *See* Finite element method (FEM)
- Fiber Bragg grating (FBG) sensors, 377, 408–409
- Fiber optic sensors, 408
- Fine/Open package, 328–329
- Finite element analyses (FEA) model
 - HIRENASD benchmark cases, 293–294
 - NACA 4415 airfoil, 298
 - turbine blades, 318–319
- Finite element method (FEM), 412, 431
 - ANSYS Multiphysics software, 373
 - piezoelectric actuator Sonox P502, 361–364
 - PZL-W-3/W-3A helicopter, 399–401
 - sound transducer LD-BZPN-2030, 364–365
- Finite volume method, 331
- Fixed Gurney flaps
 - aeroelastic calculations
 - application, 61–62
 - elastic blade, 62–66
 - hover flight calculations
 - rigid blade computations, 56–61
 - W3-Sokol MRB geometry, 54–56
 - numerical methods
 - coupling with structural dynamics, 52–53
 - modelling, 52
 - trimming method, 53–54
- FLIGHTLAB
 - model, 94–98
 - validation, 98–99
- Flight test data, 73–75
- Flow control technology, 3–4
 - air-jet vortex generators, 7–9
 - nonfluidic devices
 - Gurney flaps, 14–17
 - leading edge geometries, 13–14
 - plasma technology, 12–13
 - surface blowing circulation, 10–11
 - surface suction, 11–12
 - synthetic jets, 9–10
 - vortex generators, 4–7
- FLOWer code, 158, 160
- Flow-field, 315, 328

- Fluid–solid interaction (FSI) simulations
 - CFD
 - analysis, 266–268
 - mesh updating, 272–274
 - cycle flowchart, 265
 - displacements interpolation
 - node projection scheme, 271–272
 - structural surface displacements
 - and interpolated fluid surface deformation, 272, 273
 - explicit coupling procedure, 265
 - flow domain, 264
 - loose coupling approach, 263–264
 - requirements, 264–265
 - results
 - blade section parameters, 275
 - coefficient of lift, 275
 - dynamic simulation with static preload, 278, 280
 - excessive displacement simulation, 276, 277
 - force and moment coefficient evolution *vs.* time, 275, 276
 - lift coefficient evolution *vs.* time, 276, 278
 - lift coefficient hysteresis *vs.* incidences and pitching cycle, 276, 278
 - low torsional stiffness and impact load, 276
 - NACA 23012 airfoil aeroelastic behavior, 275
 - Reynolds number, 275–276
 - static fluid and structural models, 278
 - velocity contours, airfoil motion, 278, 279
 - structural analysis, 270–271
 - structural domain, 264
 - surface pressure integration
 - compatibility of velocity field, 269
 - concentrated mass, 268
 - distributed fluid load, 270
 - equilibrium of tractions, 269
 - force vector, 270
 - section inertia and stiffness properties, 268–269
 - temporal coupling and updating, 269
 - time step, 269
 - tightly coupled (monolithic) approach, 263
 - Fluid–structure interactions (FSI) coupling
 - HIRENASD benchmark cases, 294–296
 - modeFRONTIER, 311–313
 - NACA 4415 airfoil
 - aluminum, 300–303
 - applied flow control devices, 299
 - Young’s modulus, 302–308
 - Forward flight
 - conditions
 - CFD (*see* Computational fluid dynamic (CFD))
 - flow characteristics, 156, 157
 - test data, 166–168
 - elastic blade, 78–85
 - rigid blade, 75–78, 82
 - Frequency response function (FRF), 422
 - FSIMapper
 - average over rotation, 288
 - co-simulation, 287
 - EMAG result format, 288
 - Fourier transformation, 288
 - periodic passage, 288–289
 - robust and efficient interpolation, 288
 - thermal and mechanical loads, 288
 - FSI simulations. *See* Fluid–solid interaction (FSI) simulations
 - Full-flux method, 30–32
- G**
- Gauss–Seidel coupling scheme, 285
 - Generic light utility helicopter (GLUH), 98
 - closed loop control, 99–100
 - control law, synthesis, 101
 - FLIGHTLAB
 - model, 94–98
 - validation, 98–99
 - handling qualities, 101–103
 - Globally explicit coupling method, 285
 - Gurney flaps
 - aerodynamic force, 127, 128
 - density-based solution methodology, 126–127
 - drag coefficients, 128, 129
 - dynamic stall analysis, 132–133
 - lift coefficient, 127–130
 - moment coefficients, 127–130
 - NACA 23012 airfoil, 129, 131–133
 - normal force, 129, 130, 132
 - numerical methods, 23–24
 - HMB solver, 24–25
 - implementation, 26–33
 - proposed methods, 25–26
 - two dimensions, 33–38
 - retracting gurney flap
 - deployment and retraction position, 124
 - dynamic mesh model, 125
 - NACA 23012 airfoil, 123

- SST $k-\omega$ model, 128–129
 - 3D computations
 - observations, 45–49
 - pitching-translating wing computations, 41–45
 - static computations, 38–41
 - trailing edge flaps, 14–17, 121, 122
 - URANS turbulence methods, 132
 - wind tunnel tests, 122
 - Gurney flaps, helicopter flight
 - closed loop control, 89–91
 - controller, 99–100
 - 2D, 91–92
 - W3-Sokol, 92–94
 - control law, synthesis, 101
 - FLIGHTLAB
 - model, 94–98
 - validation, 98–99
 - handling qualities, 101–103
 - structural properties of blade, 88–89
- H**
- Helicopter
 - performance, 4, 106
 - surface suction, 11
 - W3 Sokol, 42, 57, 79
 - Helicopter flight envelope (Gurney flaps)
 - closed loop control, 89–91
 - controller, 99–100
 - 2D, 91–92
 - W3-Sokol, 92–94
 - control law, synthesis, 101
 - FLIGHTLAB
 - model, 94–98
 - validation, 98–99
 - handling qualities, 101–103
 - structural properties of blade, 88–89
 - Helicopter Multi-Block solver version 2.0 (HMB2) flow solver, 342–343
 - Helicopter PZL Swidnik W-3, 443, 444
 - Helicopter PZL W-3 Sokol, 443
 - Helicopter rotor blade measurements
 - acquisition parameters, 447–448
 - aerospace industry, 438
 - aleatory and epistemic uncertainty, 441
 - analysis results, 442
 - composite materials, 439
 - computer aided engineering models and integration, 434–435
 - data errors, 435
 - excitation, 433, 434
 - experimental modal (*see* Experimental modal models)
 - experimental model collection (*see* Experimental model collection)
 - experimental structural dynamics assessment, 434, 435
 - experimental techniques, 440–441
 - experimentation and analysis uncertainty, 441–442
 - fiber reinforced composite materials, 438
 - frequency response function plot, 435, 436
 - geometry definition, 446–447
 - 3 GFRP helicopter blades, 443–444
 - industrial certification testing, 439
 - LMS Test.Lab and LMS Virtual.Lab software, 437
 - natural frequencies plot, 435, 436
 - non-destructive experimental methods, 437
 - PolyMAX, 437
 - product variability, 442
 - research tools, 437
 - scientific objective, 432–433
 - SMA
 - accelerometers, 418, 419
 - data acquisition, 420
 - data synchronization, 420–421
 - driving point, 418, 419
 - equipment, 418
 - FBG sensors, 408–409, 418–420
 - frequency response function, 422
 - mode identification, 423, 425
 - PolyMAX identification algorithm, 423
 - SFRF, 409–413, 422–424
 - signal alignment, 421, 422
 - stabilization diagram, 423, 424
 - strain gauges, 418–420
 - strain mode shape, 423, 425–428
 - structural dynamics, 442–443
 - test rig and equipment, 444–446
 - test-to-test vs. product-to-product, 433–434
 - test variation, 435
 - uncertainty levels
 - blade A1 test-to-test damping, 468, 475
 - blade A2 test-to-test damping, 468, 476
 - blade A3 test-to-test damping, 475, 477
 - blade A1 test-to-test frequency, 468, 475
 - blade A2 test-to-test frequency, 468, 476
 - blade A3 test-to-test frequency, 468, 477
 - blade model A6 damping, 461, 467
 - blade model A9 damping, 461, 468
 - blade model A6 frequency, 461, 467
 - blade model A9 frequency, 461, 468
 - blade model A4 X and Y damping, 466

- Helicopter rotor blade measurements (*cont.*)
 uncertainty levels (*cont.*)
 blade model A4 *X* and *Y* frequency, 460, 466
 blade model A1 *X* damping, 460, 461
 blade model A3 *X* damping, 460, 464
 blade model A1 *X* frequency, 460, 461, 464
 blade model A3 *X* frequency, 460, 464
 blade model A2 *XY* damping, 460, 463
 blade model A2 *XY* frequency, 460, 463
 blade model A1 *Y* damping, 460, 462
 blade model A3 *Y* damping, 460, 465
 blade model A1 *Y* frequency, 460, 462
 blade model A3 *Y* frequency, 460, 465
 blade model B1 *X* and *Y* damping, 464, 469
 blade model B3 *X* and *Y* damping, 464, 471
 blade model B1 *X* and *Y* frequency, 464, 469
 blade model B3 *X* and *Y* frequency, 464, 471
 blade model B2 *XY* damping, 464, 470
 blade model B2 *XY* frequency, 464, 470
 blade model C1 *X* and *Y* damping, 468, 472
 blade model C3 *X* and *Y* damping, 468, 474
 blade model C1 *X* and *Y* frequency, 464, 472
 blade model C3 *X* and *Y* frequency, 468, 474
 blade model C2 *XY* damping, 468, 473
 blade model C2 *XY* frequency, 468, 473
 laser vibrometer Assessment, 478, 479
 microflow probes, 478, 479
 MIMO, 459
 object-to-object damping, 475, 478
 object-to-object frequency, 475, 478
 piezoceramic measurement, 478, 479
 SIMO, 459
 Variability Level, 437
 variable test modal models, 438
 Helicopter rotor blades, RVG. *See* Rod vortex generator (RVG)
 Helmholtz frequency, synthetic jet actuator
 cavity resonant frequency, 210
 contours of velocity magnitude
 one membrane, 212, 213
 two membrane, 213, 214
 flow separation, 211
 jet velocity
 for one membrane, 210, 211
 for two membranes, 211, 212
 model parameters, 210
 velocity magnitude and velocity
 y-component, 210–211
 Hexpress/Hybrid tool, 328–329
 High Reynolds Number Aerostructural Dynamics (HIRENASD) benchmark cases
 CFD simulations, 294
 description, 292–293
 FEA, 293–294
 FSI coupling, 294–296
 Hingeless cantilever blade, 399
 HMB CFD solver, 23–26
 Hover computations
 ONERA 7AD rotor, inviscid flow, 350–352
 S-76 rotor, 353
 treatment, 349–350
 Hover conditions
 CFD
 flow control case, 163–166
 reference case, 160–163
 experimental data, 160
 Hovering rotors
 aeroelastic calculations
 application, 61–62
 elastic blade, 62–66
 flight calculations
 rigid blade computations, 56–61
 W3-Sokol MRB geometry, 54–56
 numerical methods
 coupling with structural dynamics, 52–53
 modelling, 52
 trimming method, 53–54
 Hybrid meshing. *See* Passenger car model
- I**
 ICP accelerometers, 448
 Implicit iterative coupling method, 285
 Incomplete lower–upper (ILU) factorization scheme, 126, 268
 Industrial certification testing, 439
 Initial and updated synthetic jet models
 ANSYS Fluent, 204–205
 boundary condition, 206
 CFD simulations, 204, 205
 initial membrane deformation profile, 205, 206

MDM method, 204, 205, 220
 re-meshing method, 206
 SST $k-\omega$ model, 205
 updated deformation profile, 205, 206
 Integral quantities, 290–291

J
 Jacobi coupling scheme, 285

L
 Lagrangian–Eulerian formulation, 24
 Lamb waves
 dispersion curves, 487, 488
 frequency–wavenumber, 487, 488
 temperature effects, 488–491
 Laser Doppler anemometry (LDA), 7
 Laser Doppler vibrometer, 441
 Laser vibrometer(s)
 acquisition parameters, 448
 advantage, 366
 assessment, 478, 479
 Doppler effect, 366
 harmonic vibration, 367–368
 piezoelectric actuator Sonox P502, 367
 Polytec 3D laser vibrometer, 366, 367
 LD-BZPN-2030, 372
 Leading edge geometries, 13–14, 54
 Lead zirconate titanate (PZT) actuator, 16, 417
 LEM. *See* Lumped element modeling (LEM)
 LMS Imagine Lab AMESim, 177
 LMS software
 Imagine Lab AMESim, 180
 displacements, 183, 184
 electrical and mechanical parts, 180
 friction characteristics, 182
 geometrical and material parameters,
 182–183
 input signal submodels, 180, 181
 mass submodel, 181–182
 positions, 183
 rod activation time, 184–185
 spring-damper, 182, 183
 voltage source submodel, 180, 181
 Virtual Lab (*see* Virtual Lab (VL))
 LMS Test.Lab software, 437
 LMS Virtual.Lab software, 437
 Lumped element modeling (LEM)
 equivalent electrical circuit, 227, 228
 synthetic jet generator, preliminary design,
 209, 224, 225

M
 MAC. *See* Modal assurance criterion (MAC)
 Main rotor blade (MRB), 53–66, 76–78, 81–83
 MDM method. *See* Moving–Deforming–Mesh
 (MDM) method
 Mean phase deviation (MPD), 453
 Microelectromechanical systems (MEMS),
 138
 Microflow probes, 448, 478, 479
 Micro vortex generators, 6
 Modal assurance criterion (MAC), 453
 for cantilever, 402, 403
 values, 412
 between vectors, 401–402
 Modal participation (MP), 453
 Modal phase collinearity (MPC), 453
 modeFRONTIER
 design space, 310–311
 FSI loop, 311–313
 optimization work, 308–310
 Pareto front, 314–315
 performances, 308
 solution block, 307
 Mode indicator functions (MIF), 453
 Mode overcomplexity value (MOV), 453
 Moving–Deforming–Mesh (MDM) method,
 204, 205, 220

MpCCI
 applications, 284
 association, 289–290
 commercial and open-source simulation
 codes, 284
 CouplingEnvironment
 best-fit interpolation method, 285
 co-simulation problems, 285
 coupling algorithms, 285
 coupling analysis solutions, 285–286
 simulation codes, 286–287
 data transfer, 284
 FSIMapper
 average over rotation, 288
 co-simulation, 287
 EMAG result format, 288
 Fourier transformation, 288
 periodic passage, 288–289
 robust and efficient interpolation, 288
 thermal and mechanical loads, 288

HIRENASD benchmark cases
 CFD simulations, 294
 description, 292–293
 FEA, 293–294
 FSI coupling, 294–296

MpCCI (*cont.*)

- interpolation, 290–292
- modeFRONTIER
 - design space, 310–311
 - FSI loop, 311–313
 - optimization work, 308–310
 - Pareto front, 314–315
 - performances, 308
 - solution block, 307
- NACA 4415 airfoil
 - CFD simulations, 299–300
 - FEA model, 298
 - FSI simulation, 299–308
 - innovative rotor blades, 297
- one-way/bi-directional coupling, 284
- turbine blades
 - CFD simulation, 315–317
 - FEA simulation, 318–319
 - mapping, 317–318
 - problem description, 315–316
 - rotating and stationary components, 314–315
- MRB. *See* Main rotor blade (MRB)
- MSC.Nastran model, 294
- Multiple input multiple output (MIMO), 459
- Multivariate mode indicator function (MMIF), 453, 455

N

- NACA 4415 airfoil
 - CFD simulations, 299–300
 - FEA model, 298
 - FSI simulation
 - aluminum, 300–303
 - applied flow control devices, 299
 - Young's modulus, 302–308
 - innovative rotor blades, 297
- NACA 23012 airfoil, 129, 131–133
- NACA23012M, 39, 44
 - aerofoil, 37, 38, 40–43, 75, 91
 - sections, 97
 - wing, 39, 41, 45–48
- Nastran, 288
- NASTRAN code, 52, 53, 61–63, 71, 88
- Newton–Raphson process, 72
- Non-destructive testing (NDT) method, 485
- Nonfluidic devices
 - Gurney flaps, 14–17
 - leading edge geometries, 13–14
- Non-integral quantity, 290–291
- Numeca International, 325, 326, 329, 331
- Nyquist Sampling Theorem, 447

O

- OASPL. *See* Overall sound pressure level (OASPL)
- Object-to-object damping *s*, 475, 478
- Object-to-object frequency *s*, 475, 478
- ONERA stall model, 7, 10, 13, 94
- Orphan node, 292
- Overall sound pressure level (OASPL)
 - at exterior car surface, 334
 - at floor surface, 333
 - at ground surface, 332–333
 - at rearview mirror surface, 334–335
 - root-mean-square definition, 332

P

- Parallel algorithm, 285
- Part-flux method, 30–32
- Passenger car model
 - acoustic analysis
 - at exterior car surface, 334
 - at floor surface, 333
 - at ground surface, 332–333
 - at rearview mirror surface, 334–335
 - root-mean-square definition, 332
 - computational domain, 327–329
 - steady flow solution, 331–332
 - surface grid, 329–330
 - surface model and hole searcher, 325–327
 - surface refinements, 327–328
 - volume grid generation process, 329–331
 - volume refinements, 329
- PID controller, 101–102
- Piezoceramic measurement, 478, 479
- Piezoelectric actuator Sonox P502
 - experimental equipment
 - description, 365–368
 - design, 376–377, 384–385
 - piezoelectric actuators, 368–371
 - resonance frequencies, 371–372
 - numerical simulation
 - ANSYS Multiphysics software, 373
 - brass diaphragm, 363–364
 - CeramTec, 361
 - diaphragm oscillation, 360
 - piezoceramic material, 361
 - piezo disc, 361–362
 - resonance frequencies, 361, 363, 371–372
 - sound transducer LD-BZPN-2030, 364–365
 - vibration modes, 361–362
 - thermal analysis, 378–380, 385–391

- “Ping-Pong” algorithm, 285
- Plasma technology, 12–13
- PolyMAX identification algorithm, 423, 437, 455
- PZL-W-3/W-3A helicopter
 - active gurney flap installation, 402
 - with beam elements, 398
 - combined beam-3D FEM model, 402
 - coupled bending-torsion modal analysis, 399
 - effective modal mass, 400–401
 - FEM and BLD, 399–400
 - laboratory modal tests, 399
 - MAC, 401–403
 - modal analysis, 403–405
 - natural mode shapes, 400–402
 - with 3D middle section, 398
 - vibration plane, 400
- R**
- Retractable rod vortex generator (RrVG)
 - active and passive methods, 175
 - BLMM actuator, 177–178
 - cascade model, 176
 - electromechanical actuators, 176
 - friction force, 178–179
 - LMS Imagine Lab AMESim, 180
 - displacements, 183, 184
 - electrical and mechanical parts, 180
 - friction characteristics, 182
 - geometrical and material parameters, 182–183
 - input signal submodels, 180, 181
 - mass submodel, 181–182
 - positions, 183
 - rod activation time, 184–185
 - spring-damper, 182, 183
 - voltage source submodel, 180, 181
 - LMS Virtual Lab (*see* Virtual Lab (VL))
 - material parameters, 178–179
 - numerical tools, 177
- Reynolds-averaged Navier–Stokes (RANS)
 - equations, 157, 268
- Rigid blade computations
 - analysis, 57–61
 - performance, 56–57
- Rod vortex generator (RVG)
 - configuration, 143–145
 - curved wall nozzle
 - boundary layer, 147–149
 - pressure distribution, 147, 149
 - separation control, 148, 150
 - shock wave, 145
 - 3D view, 146
 - 2D view, 145
 - forward flight conditions
 - flow characteristics, 156, 157
 - flow control case, 169–172
 - reference case, 168–169
 - test data, 166–168
 - Gurney flaps, 156
 - helicopter rotor blades, 157
 - hover conditions
 - experimental data, 160
 - flow control case, 163–166
 - reference case, 160–163
 - numerical model
 - background component grid, 158
 - blade component grid, 158, 159
 - boundary conditions, 159–160
 - detailed view, 159
 - FLOWer code, 158
 - LEA $k-\omega$ turbulence model, 157
 - RANS equations, 157
 - schematic view, 139
- RrVG. *See* Retractable rod vortex generator (RrVG)
- Runge–Kutta method, 157
- Runge–Kutta type integration, 331
- RVG. *See* Rod vortex generator (RVG)
- S**
- S-76 blade, 88, 89, 103
- SCADAS Mobile system, 420
- Scissors modes, 404, 405
- Second-order accuracy, 331–332
- Serial algorithm, 285
- SFRF matrix. *See* Strain frequency response function (SFRF) matrix
- Shape-function interpolation method, 292
- Signal temperature compensation procedure, 493
- Single input multiple output (SIMO), 459
- SMA. *See* Strain modal analysis (SMA)
- Sound transducer LD-BZPN-2030, 376–377, 381, 384
- Spalart–Allmaras model, 294
- SST $k-\omega$ turbulence model, 128–129
- Strain frequency response function (SFRF)
 - matrix, 409, 413, 422–424
- Strain modal analysis (SMA)
 - classical modal analysis
 - displacement modal analysis, 410–411
 - modal validation, 412

- Strain modal analysis (SMA) (*cont.*)
 - dynamic strain measurements, 409
 - helicopter main rotor blade
 - accelerometers, 418, 419
 - data acquisition, 420
 - data synchronization, 420–421
 - driving point, 418, 419
 - equipment, 418
 - FBG sensors, 408–409, 418–420
 - FRF, 422
 - mode identification, 423, 425
 - PolyMAX identification algorithm, 423
 - SFRF, 409–413, 422–424
 - signal alignment, 421, 422
 - stabilization diagram, 423, 424
 - strain gauges, 418–420
 - strain mode shape, 423, 425–428
 - modal participation factor matrices, 21
 - modal residues and scaling
 - displacement modal vector scaling, 415–416
 - DOF, 417
 - structural modification prediction, 414
 - SMA theory, 413–414
 - strain modal vector matrix, 21
- Sub-boundary layer vortex generator (SBVG), 6–7
- Surface blowing circulation, 10–11
- Surface grid, 329–330
- Surface hole searcher, 325–327
- Surface model, 325–327
- Surface refinements, 327–328
- Surface suction, 11–12
- Synthetic jet actuator
 - bump, flow separation
 - CFD model of wind tunnel, 215, 216
 - contours of static pressure, 219
 - dimensions, 215
 - model of, 215
 - separation bubble, inflow velocity, 217, 218
 - velocity magnitude contours, 215–218
 - initial and updated synthetic jet models
 - ANSYS Fluent, 204–205
 - boundary condition, 206
 - CFD simulations, 204, 205
 - initial membrane deformation profile, 205, 206
 - MDM method, 204, 205, 220
 - re-meshing method, 206
 - SST $k-\omega$ model, 205
 - updated deformation profile, 205, 206
 - parametric study
 - Helmholtz frequency (*see* Helmholtz frequency)
 - LEM method, 209
 - membrane structural resonance, 209–210
 - numerical simulations, 207–208
 - piezoelectric membrane displacement, 208
 - vibrating membrane amplitude, 208
 - with perpendicular and parallel membranes, 203, 204
 - shape optimization
 - actuator with one and two membranes, 207, 209
 - duct geometry with 45° edge inclination, 206, 207
 - duct geometry with 60° edge inclination, 206, 208
 - duct geometry with rounded edge, 206, 208
 - geometry parameters, 206, 209
 - velocity magnitude vectors, 206, 207
- Synthetic jet generator, 223, 224
 - amplitude-frequency characteristic, dependence of velocity, 229
 - conjugate power variables, 228
 - equivalent electrical circuit, 227
 - impedance, 228
 - LEM, 227, 228
 - minimum power and maximum intensity, 227
 - vortex shedding phenomena, 229–230
- Synthetic jet generator with loudspeakers
 - amplitude-frequency modulation, 233
 - bump model, 233, 234
 - efficiency, 235, 236
 - specific saved-up work, 235
 - temperature field, 234, 236
 - total pressure distribution, 234, 235
 - total pressure fields, 234
- Synthetic jet generator with piezo-membranes
 - amplitude-frequency characteristics, 238, 239
 - cavity with one output orifice, 237, 240
 - drag coefficient of helicopter, 235–236
 - experimental data
 - amplitude-frequency characteristic, 250, 252
 - change of velocity output, 251, 253
 - efficiency of energy conversion, 253
 - optimization lower resonant frequency, 254

- output velocity dependence, 250, 251
 - power input dependence, 250, 252
 - sound measurements, 256–258
 - time-mean output velocities, 251, 253
 - flow control parameters and data measurements, 258–259
 - longitudinal and transversal vortex structure, 236, 237
 - measurement campaign, 248–249
 - measurement techniques
 - CTA measurements, 241
 - fan controller, 241, 242
 - fan (WP-8-E) dimensions and characteristics, 241
 - MiniCTA 54T30 DANTEC, StreamLine 90N10 Frame, and CTA probe DANTEC, 241–243
 - NetScanner System 9116, 241–243
 - pressure measurement, 242
 - smoke flow field visualization, 241
 - smoke generator, 241, 242
 - model shape, 237
 - model with controlled boundary layer, 236–237
 - numerical simulation, 237
 - parametric study, 256
 - piezo-membrane deflections dependency, 238, 239
 - software development
 - constants, calculation of, 244
 - CTA probe calibration, 244
 - data acquisition, 246
 - data and power spectra pages, 248
 - data collection, 244
 - excitation signal generation, 247
 - user-defined miniCTA DANTEC software, 243
 - velocity measurement, 245–247
 - wind tunnel
 - arrangement, 240, 241
 - CTA measurements, 239
 - flow field visualization, 255, 256
 - frequency spectra of flow field, 254
 - maximum velocity, 239
 - pressure distribution, 255
 - pressure measurement, 240
 - radial fan, 240
 - synthetic jet influence to flow, 255, 256
 - Synthetic jets (SJ), 9–10
 - advantage, 223
 - amplitude modulation, 223
 - experimental equipment description, 365–368
 - design, 376–377, 384–385
 - piezoelectric actuators, 368–371
 - resonance frequencies, 371–372
 - flow control efficiency, 223
 - local loss coefficient, 230
 - specific work loss, 231
 - total pressure rake probe, 230
 - frequency and intensity
 - amplitude-frequency characteristic, dependence of velocity, 226, 229
 - criteria of existence, 226–228
 - longitudinal vortex structures, 224, 225
 - lumped element mode, 226, 228
 - momentum coefficient, 226, 227
 - nondimensional frequency, 226, 227
 - Reynolds number, 226–227
 - Stokes number, 226–227
 - Strouhal number, 227
 - transversal vortex structures, 224, 225
 - vortex shedding frequency, 225
 - generator (*see* Synthetic jet generator)
 - LEM, 224, 225
 - numerical simulation
 - ANSYS Multiphysics software, 373
 - diaphragm oscillation, 360
 - piezoelectric actuator Sonox P502, 361–364
 - resonance frequencies, 371–372
 - sound transducer LD-BZPN-2030, 364–365
 - thermal analysis
 - piezoelectric actuator Sonox P502, 378–380, 385–391
 - sound transducer LD-BZPN-2030, 381, 384, 391–395
 - vortex structures, 224
- T**
- Temperature compensation methods
 - Croxford et al. model, 494
 - damage detection, 495–497
 - elastic wave propagation
 - pressure/longitudinal waves, 486, 487
 - shear/transverse waves, 487
 - EVM, 491, 492
 - frequency thermal sensitivity, 495
 - lamb waves
 - dispersion curves, 487, 488
 - frequency–wavenumber, 487, 488
 - temperature effects, 488–491
 - phase change and linear behaviour, 493, 494

- Temperature effects
 - analytic compensation, 488–489
 - lamb wave signals, 491–493
 - lamb wave thermal coefficient, 490, 491
 - q_0 and p_0 phases, 491
 - Rayleigh–Lamb thermal coefficient, 489, 490
 - record time, 489
 - wave velocity changes, 489
 - Test data variability, 431–432, 437
 - Tip Aerodynamics and Acoustics Test (TAAT), 166, 167
 - Transfinite interpolation (TFI), 53, 71
 - Translational spring-damper-actuator (TSDA), 191
 - Turbine blades
 - CFD simulation, 315–317
 - FEA simulation, 318–319
 - mapping, 317–318
 - problem description, 315–316
 - rotating and stationary components, 314–315
- U**
- UFAST project, 140
 - UH-60 Black Hawk helicopter, 16, 98–99
 - Uncertainty quantification, of rotor blades measurements
 - blade A1 test-to-test damping, 468, 475
 - blade A2 test-to-test damping, 468, 476
 - blade A3 test-to-test damping, 475, 477
 - blade A1 test-to-test frequency, 468, 475
 - blade A2 test-to-test frequency, 468, 476
 - blade A3 test-to-test frequency, 468, 477
 - blade model A6 damping, 461, 467
 - blade model A9 damping, 461, 468
 - blade model A6 frequency, 461, 467
 - blade model A9 frequency, 461, 468
 - blade model A4 X and Y damping, 466
 - blade model A4 X and Y frequency, 460, 466
 - blade model A1 X damping, 460, 461
 - blade model A3 X damping, 460, 464
 - blade model A1 X frequency, 460, 461, 464
 - blade model A3 X frequency, 460, 464
 - blade model A2 XY damping, 460, 463
 - blade model A2 XY frequency, 460, 463
 - blade model A1 Y damping, 460, 462
 - blade model A3 Y damping, 460, 465
 - blade model A1 Y frequency, 460, 462
 - blade model A3 Y frequency, 460, 465
 - blade model B1 X and Y damping, 464, 469
 - blade model B3 X and Y damping, 464, 471
 - blade model B1 X and Y frequency, 464, 469
 - blade model B3 X and Y frequency, 464, 471
 - blade model B2 XY damping, 464, 470
 - blade model B2 XY frequency, 464, 470
 - blade model C1 X and Y damping, 468, 472
 - blade model C3 X and Y damping, 468, 474
 - blade model C1 X and Y frequency, 464, 472
 - blade model C3 X and Y frequency, 468, 474
 - blade model C2 XY damping, 468, 473
 - blade model C2 XY frequency, 468, 473
 - laser vibrometer Assessment, 478, 479
 - microflown probes, 478, 479
 - MIMO, 459
 - object-to-object damping, 475, 478
 - object-to-object frequency, 475, 478
 - piezoceramic measurement, 478, 479
 - SIMO, 459
 - User-defined function (UDF), 125
- V**
- Vane vortex generators (VVGs), 138
 - Variability Level, 437
 - Variable droop leading edge (VDLE), 13
 - Vehicle surface model, 325–327
 - VGs. *See* Vortex generators (VGs)
 - Virtual Lab (VL), 177
 - closed model, 185, 187
 - connectivity and accuracy, 186
 - dynamic analysis
 - body locations and mass properties, 189
 - conditions, 192
 - control signals, 191, 192, 198, 199
 - degrees of freedom, 194
 - displacement characteristics, 195, 196
 - force elements, 190
 - with friction force, 194–197
 - Point-to-Point Contact force, 191
 - Scalar Expression Force, 190–191
 - spring performance, 192
 - TSDA, 191
 - without friction forces, 191, 193
 - kinematic analysis
 - algebraic constraints and joints, 187–188
 - characteristics, 189, 190
 - displacements, 189, 190
 - driver constraints, 188–189
 - 3D model, 187, 188
 - Volume grid generation process, 329–331

- Volume refinements, 329
 - Vortex generators (VGs), 4–7
 - airfoils
 - Caradonna–Tung model rotor, 149
 - computational domain, 150
 - contour map and numerical validation, 151
 - flow separation, 149, 152
 - friction coefficient and streamlines, 151–153
 - polar graph, 151, 154
 - CFD investigation (*see* Computational fluid dynamic (CFD))
 - experimental setup, 140–141
 - vs. Gurney flaps, 39–40
 - numerical model, 139–140
 - type of, 138
 - VVGs, 138
 - VVGs. *See* Vane vortex generators (VVGs)
- W**
- Weighted-element mapping algorithms, 292
 - W3 main rotor, 45, 73, 74
 - W3-Sokol blade, 57, 62, 63, 88–94
 - W3-Sokol MRB geometry, 52, 54–58
- Z**
- Zero net mass flux jets, 360